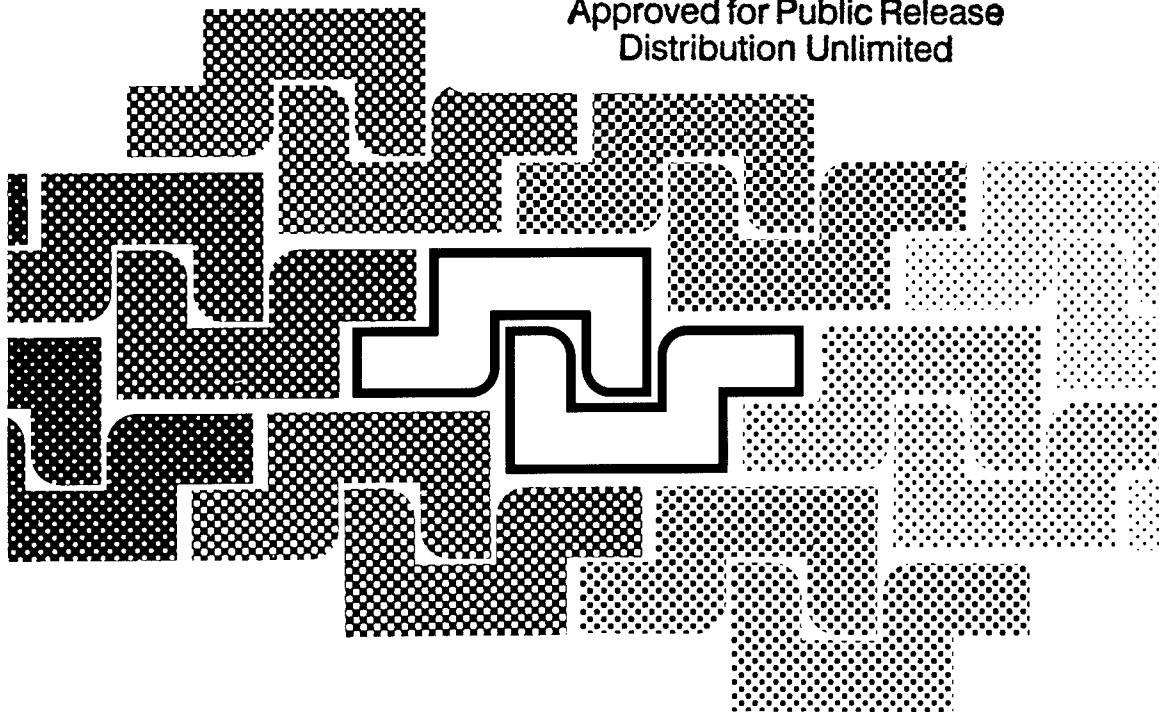


**DISTRIBUTION STATEMENT A**

Approved for Public Release  
Distribution Unlimited



20011203 225

# **Nanostructured Films and Coatings**

Edited by

**Gan-Moog Chow, Ilya A. Ovid'ko  
and Thomas Tsakalakos**

# REPORT DOCUMENTATION PAGE

Form Approved OMB No. 0704-0188

Public reporting burden for this collection of information is estimated to average 1 hour per response, including the time for reviewing instructions, searching existing data sources, gathering and maintaining the data needed, and completing and reviewing the collection of information. Send comments regarding this burden estimate or any other aspect of this collection of information, including suggestions for reducing this burden to Washington Headquarters Services, Directorate for Information Operations and Reports, 1215 Jefferson Davis Highway, Suite 1204, Arlington, VA 22202-4302, and to the Office of Management and Budget, Paperwork Reduction Project (0704-0188), Washington, DC 20503.

1. AGENCY USE ONLY (Leave blank)			2. REPORT DATE	3. REPORT TYPE AND DATES COVERED
			6 July 1999	Conference Proceedings
4. TITLE AND SUBTITLE			5. FUNDING NUMBERS	
NATO Advanced Research Workshop on Nanostructured Films and Coatings			F61775-99-WF023	
6. AUTHOR(S)				
Conference Committee – editors: Chow, Ovid'ko, Tsakalakos				
7. PERFORMING ORGANIZATION NAME(S) AND ADDRESS(ES)			8. PERFORMING ORGANIZATION REPORT NUMBER	
Institute of Problems of Mechanical Engineering, RAS Bolshoj 61, Vas. Ostrov St. Petersburg 199178 Russia			N/A	
9. SPONSORING/MONITORING AGENCY NAME(S) AND ADDRESS(ES)			10. SPONSORING/MONITORING AGENCY REPORT NUMBER	
EOARD PSC 802 BOX 14 FPO 09499-0200			CSP 99-5023	
11. SUPPLEMENTARY NOTES				
These proceedings are published as volume 78 of a series of scientific publications by NATO Science Committee.				
12a. DISTRIBUTION/AVAILABILITY STATEMENT		12b. DISTRIBUTION CODE		
Approved for public release; distribution is unlimited.		U.S. Government Rights License This work relates to Department of the Air Force Grant/Contract issued by the European Office Aerospace Research and Development (EOARD). The United States Government has a royalty-free license throughout the world in all copyrightable material contained herein		
A				
13. ABSTRACT (Maximum 200 words)				
The Final Proceedings for NATO Advanced Research Workshop on Nanostructured Films and Coatings, 28 June 1999 - 30 June 1999				
This is an interdisciplinary conference. Topics include nanostructure synthesis and processing, modeling, characterization and properties (mechanical, biological, chemical, electronic and magnetic), and applications.				
14. SUBJECT TERMS			15. NUMBER OF PAGES	
EOARD, Electronic Devices, Nanotechnology			394	
			16. PRICE CODE	
			N/A	
17. SECURITY CLASSIFICATION OF REPORT	18. SECURITY CLASSIFICATION OF THIS PAGE	19. SECURITY CLASSIFICATION OF ABSTRACT	20. LIMITATION OF ABSTRACT	
UNCLASSIFIED	UNCLASSIFIED	UNCLASSIFIED	UL	

NSN 7540-01-280-5500

Standard Form 298 (Rev. 2-89)  
Prescribed by ANSI Std. Z39-18  
298-102

## **Nanostructured Films and Coatings**

## NATO Science Series

*A Series presenting the results of activities sponsored by the NATO Science Committee. The Series is published by IOS Press and Kluwer Academic Publishers, in conjunction with the NATO Scientific Affairs Division.*

<b>A. Life Sciences</b>	IOS Press
<b>B. Physics</b>	Kluwer Academic Publishers
<b>C. Mathematical and Physical Sciences</b>	Kluwer Academic Publishers
<b>D. Behavioural and Social Sciences</b>	Kluwer Academic Publishers
<b>E. Applied Sciences</b>	Kluwer Academic Publishers
<b>F. Computer and Systems Sciences</b>	IOS Press
<b>1. Disarmament Technologies</b>	Kluwer Academic Publishers
<b>2. Environmental Security</b>	Kluwer Academic Publishers
<b>3. High Technology</b>	Kluwer Academic Publishers
<b>4. Science and Technology Policy</b>	IOS Press
<b>5. Computer Networking</b>	IOS Press

### NATO-PCO-DATA BASE

The NATO Science Series continues the series of books published formerly in the NATO ASI Series. An electronic index to the NATO ASI Series provides full bibliographical references (with keywords and/or abstracts) to more than 50000 contributions from international scientists published in all sections of the NATO ASI Series.

Access to the NATO-PCO-DATA BASE is possible via CD-ROM "NATO-PCO-DATA BASE" with user-friendly retrieval software in English, French and German (WTV GmbH and DATAWARE Technologies Inc. 1989).

The CD-ROM of the NATO ASI Series can be ordered from: PCO, Overijse, Belgium



# **Nanostructured Films and Coatings**

edited by

**Gan-Moog Chow**

Department of Materials Science,  
National University of Singapore,  
Kent Ridge, Republic of Singapore

**Ilya A. Ovid'ko**

Laboratory for Theory of Defects in Materials,  
Institute for Problems of Mechanical Engineering,  
Russian Academy of Sciences,  
St. Petersburg, Russia

and

**Thomas Tsakalakos**

Department of Ceramics and Materials Engineering,  
Rutgers University,  
New Jersey, U.S.A.

**DISTRIBUTION STATEMENT A**  
Approved for Public Release  
Distribution Unlimited



**Kluwer Academic Publishers**

Dordrecht / Boston / London

Published in cooperation with NATO Scientific Affairs Division

AQ F02-02-0283

Proceedings of the NATO Advanced Research Workshop on  
Nanostructured Films and Coatings  
Santorini, Greece  
June 28-30, 1999

A C.I.P. Catalogue record for this book is available from the Library of Congress.

ISBN 0-7923-6265-9 (HB)  
ISBN 0-7923-6266-7 (PB)

Published by Kluwer Academic Publishers,  
P.O. Box 17, 3300 AA Dordrecht, The Netherlands.

Sold and distributed in North, Central and South America  
by Kluwer Academic Publishers,  
101 Philip Drive, Norwell, MA 02061, U.S.A.

In all other countries, sold and distributed  
by Kluwer Academic Publishers,  
P.O. Box 322, 3300 AH Dordrecht, The Netherlands.

*Printed on acid-free paper*

**U.S. Government Rights License**

This work relates to Department of the Air  
Force Grant/Contract issued by the European  
Office Aerospace Research and Development  
(EOARD). The United States Government  
has a royalty-free license throughout the world  
in all copyrightable material contained herein

All Rights Reserved

© 2000 Kluwer Academic Publishers

No part of the material protected by this copyright notice may be reproduced or utilized in  
any form or by any means, electronic or mechanical, including photocopying, recording or  
by any information storage and retrieval system, without written permission from the  
copyright owner.

Printed in the Netherlands.

---

## TABLE OF CONTENTS

Preface	ix
List of NATO ARW proceedings contributors	xi
<i>Chapter 1. Gas phase synthesis of nanostructured films and coatings</i> <i>H. Hahn, M. Winterer, S. Seifried, V.V. Srdic</i>	1
<i>Chapter 2. Electrodeposited nanostructured films and coatings: synthesis, structure, properties and applications</i> <i>U. Erb, G. Palumbo, K.T. Aust</i>	11
<i>Chapter 3. Nanostructured carbon coatings</i> <i>Y. Gogotsi</i>	25
<i>Chapter 4. Semiconductor quantum dot heterostructures (growth and applications)</i> <i>V.M. Ustinov</i>	41
<i>Chapter 5. Chemical processing of nanostructured coatings</i> <i>L.K. Kurihara</i>	55
<i>Chapter 6. Nanostructured coatings of inner surfaces in microporous matrixes</i> <i>Yu. A. Kumzerov</i>	63
<i>Chapter 7. Electroless deposited nanostructured NiCo films</i> <i>G.M. Chow</i>	77
<i>Chapter 8. Nanoscaled magnetic electrodeposited structures on the basis of ion group metals: preparation, structure, magnetic and magnetoresistive properties</i> <i>V. M. Fedosyuk</i>	85
<i>Chapter 9. Nanodispersed refractory compounds in the electrodeposited metal coatings</i> <i>I. Vitina, I. Zalite, V. Belmane, J. Grabis, V. Rubene, O. Kovalova</i>	103
<i>Chapter 10. Thermal sprayed nanostructured hard coatings</i> <i>B.H. Kear, W.E. Mayo</i>	113
<i>Chapter 11. Synthesis and characterization of nanocomposite coatings</i> <i>J. He, M. Ice, E J. Lavernia</i>	131

<i>Chapter 12.</i> Nano-engineered thermoelectric coating <i>M. Toprak, Yu Zhang, M. Muhammed, A.A. Zakhidov, R.H. Baughman, I. Khayrullin</i>	149
<i>Chapter 13.</i> Photoluminescence from pressure-annealed nanostructured silicon dioxide and nitride films <i>A. Misiuk, L. Rebohle, A. Iller, I.E. Tyschenko, J. Jun, A. Panas</i>	157
<i>Chapter 14.</i> CoPt and FePt thin films for high density recording media <i>J. A. Christodoulides, Y. Zhang, G. C. Hadjipanayis, I. Panagiotopoulos, D. Niarchos</i>	171
<i>Chapter 15.</i> Unidirectional anisotropy in manganite based ferromagnetic- antiferromagnetic multilayers <i>I. Panagiotopoulos, C. Christides, M. Pissas, D. Niarchos</i>	177
<i>Chapter 16.</i> Surface characterization of nanostructured coatings: study of nanocrystalline SnO <sub>2</sub> gas sensors <i>M.I. Baraton</i>	187
<i>Chapter 17.</i> Phase differentiation and characterization of nanostructured composites by synchrotron radiation techniques <i>Y.K. Hwu, G.M. Chow, W.C. Goh, T.S. Cho, J.H. Je, D.Y. Noh, H.-M. Lin, C. K. Lin</i>	203
<i>Chapter 18.</i> X-ray study of microstructure and grain boundary statistics in nanocrystalline materials <i>A.P. Zhilyaev, I.V. Alexandrov, R.Z. Valiev</i>	215
<i>Chapter 19.</i> XRD strain and stress determination in nanostructured films and coatings <i>T. Tsakalakos, M. Croft</i>	223
<i>Chapter 20.</i> Interfaces in nanostructured films and coatings <i>I.A. Ovid'ko</i>	231
<i>Chapter 21.</i> Nanoscale elastic properties of dislocations and disclinations <i>M. Yu. Gutkin, E.C. Aifantis</i>	247
<i>Chapter 22.</i> Study of porous silicon formation and silicon-on-porous silicon epitaxy (computational modelling) <i>P.L. Novikov, L.N. Aleksandrov, A.D. Dvurechenskii, V.A. Zinoviev</i>	255

<i>Chapter 23.</i> Evolution of phase composition and associated properties in the process of growth of nanostructured films <i>S.A. Kukushkin, A.V. Osipov</i>	267
<i>Chapter 24.</i> Review of fatigue of coatings/substrates <i>K. Sadananda, R.L. Holtz</i>	283
<i>Chapter 25.</i> Nanoindentation /nanoscratching and stress studies in monolithic and nanolayered amorphous carbon films <i>S. Logothetidis, C. Charitidis, M. Gioti</i>	297
<i>Chapter 26.</i> Formation of nanostructured surface regions under a concentrated load <i>M.SH. Akchurin, V.R. Regel</i>	309
<i>Chapter 27.</i> Non-destructive mechanical characterisation of mechanical properties of non-homogeneous nanostructured coatings <i>S.M. Aizikovich, J.-P. Celis, L.I. Krenov, N.A. Serova</i>	315
<i>Chapter 28.</i> High refractive index Si/SiO <sub>x</sub> based nanocomposites <i>T. Phely-Bobin, D.E. Bhagwagar, F. Papadimitrakopoulos</i>	323
<i>Chapter 29.</i> Preparation and characterisation of metallic thin films for electroluminescent devices based on porous silicon <i>I. Kleps, A. Angelescu, M. Miu</i>	337
<i>Chapter 30.</i> Photoelectrochemical behavior of chlorophyll a in thin films <i>L. Tugulea</i>	347
<i>Chapter 31.</i> Lean-burn natural gas engine exhaust remediation using nanostructured catalysts and coatings <i>M.D. Fokema, A. J. Zarur, J. Y. Ying</i>	355
<i>Chapter 32.</i> Polymer-layered silicate nanocomposites: emerging scientific and commercial opportunities <i>E.P. Giannelis</i>	367
<i>Chapter 33.</i> Office of Naval Research initiative on wear resistant nanostructured materials <i>L. T. Kabacoff</i>	373
Subject Index	379

## Preface

The NATO Advanced Research Workshop on Nanostructured Films and Coatings (Santorini, Greece, June 28-30, 1999) successfully reviewed the state-of-the-art of many topics in this rapidly growing high-tech area. Nanostructured films and coatings may possess unique properties due to the size and the interface effects. They find many advanced applications such as electronics, catalysis, protection, data storage, optics and sensors. The focus of the Workshop was placed on the synthesis and processing; advanced characterization techniques; properties (including mechanical, chemical, electronic, thermal, catalytic, and magnetic); modeling of intralayer and interlayer interfaces; and applications.

Nanostructured films can be synthesized by vapor phase and solution chemistry methods. Solution approach allows the complex and hidden surfaces to be coated since it does not have the limitation of line-of-sight deposition as in the vapor methods. Vapor deposition such as sputtering, chemical vapor condensation and solution chemistry such as sol-gel, electrodeposition and electroless deposition were reviewed. Template-mediated approach was also discussed. Thick coatings were prepared using thermal spraying of nanostructured powders. Increasing attention is given on the use of liquid precursors for thermal spraying.

Advanced characterization techniques of nanostructured films and coatings were addressed. These included, for example, magnetic domain imaging; structural and residual stress study using synchrotron radiation techniques; and surface chemistry using surface FTIR. It was noted that some conventional techniques may not accurately determine the structure of nanostructured alloys and composites, and new techniques need to be developed for better characterization of nanostructured materials.

Enhanced material properties of nanostructured films and coatings were reported in many areas. The understanding and control of the intralayer and interlayer interfaces in multilayered, multifunctional nanostructured films and coatings are critical to the optimization of material properties and performances. Tailor-design of interfaces in these materials through modelling and experimental efforts is receiving growing interest.

The participation in the Workshop was by invitation. This NATO ARW publication includes most of the invited lecture and invited poster papers.

We would like to acknowledge the significant contribution of the organizing committee: Lawrence Kabacoff (USA), A. K. Vasudevan (USA), Lynn K. Kurihara (USA) and Alexei Romanov (Russia). We gratefully acknowledge the major financial support of this ARW by the NATO High Technology Program, and the co-sponsorship by the International Field Office (Europe), U.S. Office of Naval Research; European Research Office of the U.S. Army; European Office of Aerospace Research and Development, and U.S. Air Force Office of Scientific Research, U.S. Air Force Research Laboratory. We thank Yannis Papaoannou, Tourlite International (USA) for his assistance with the travel and lodging for the participants, and many others who provided their support in the preparation and conduction of the Workshop. We also thank Deborah K. Chow for the editorial assistance with the proceedings.

Gan-Moog Chow  
ARW director  
National University of Singapore

Ilya A. Ovid'ko  
ARW co-director  
Russian Academy of Sciences

Thomas Tsakalakos  
ARW co-director  
Rutgers University

---

## List of NATO ARW proceedings contributors

Professor Gan-Moog Chow  
Department of Materials Science, National University of Singapore, Kent Ridge, Singapore 117543,  
Republic of Singapore  
Phone: (65) 874 3325, Fax: (65) 776 3604, Email: [mascgm@nus.edu.sg](mailto:mascgm@nus.edu.sg)

Professor Thomas Tsakalakos  
Department of Ceramics and Materials Engineering , 98 Brett Rd, Rutgers University, Piscataway,  
NJ 08855-8058, USA  
Phone: 1(732)445-2888, Fax: 1 (732)445-3229, Email: [tsakalak@rci.rutgers.edu](mailto:tsakalak@rci.rutgers.edu)

Dr. Ilya A. Ovid'ko (CP country co-director)  
Laboratory for Theory of Defects in Materials, Institute for Problems of Mechanical Engineering  
Russian Academy of Sciences, Bolshoj 61, Vas.Ostrov, St.Petersburg 199178, Russia  
Fax: +(7 812)321 4771, Email: [ovidko@def.ipme.ru](mailto:ovidko@def.ipme.ru)

Professor U. Erb  
NSERC / Ontario Hydro Industrial Chair in Microengineered Materials  
University of Toronto, Dept. of Metallurgy & Materials Science, 184 College St. Room 140  
Toronto, Ontario M5S 3E4, Canada  
Phone: 416 978 4430 Office, Fax. 416 978 4155, email : [erb@ecf.utoronto.ca](mailto:erb@ecf.utoronto.ca)

Prof. Dr. Horst Hahn  
Darmstadt University of Technology  
Department of Materials Science, Thin Films Division, Petersenstr. 23, 64287 Darmstadt, Germany  
Phone: +49 6151 16-6336, Fax.: +49 6151 16-6335, Email: [hhahn@hrzpub.tu-darmstadt.de](mailto:hhahn@hrzpub.tu-darmstadt.de)

Dr. Victor Ustinov  
Ioffe Physico-Technical Institute, Russian Academy of Sciences, Polytechnicheskaya 26  
St.Petersburg 194021, Russia  
Fax: +(7 812)247 8640, Email: [ymust@beam.ioffe.rssi.ru](mailto:ymust@beam.ioffe.rssi.ru)

Professor Yuri Gogotsi, Materials Research Center, Kiev, Ukraine  
Present Address:Department of Mechanical Engineering, University of Illinois at Chicago, Chicago, IL  
60607, USA  
Fax: +(1 312)413 0447, Email: [ygogotsi@uic.edu](mailto:ygogotsi@uic.edu)

Professor Marie-Isabelle Baraton  
SPCTS-UMR 6638 CNRS, University of Limoges, France.  
Email: [baraton@unilim.fr](mailto:baraton@unilim.fr)

Dr. Dimitris Niarchos  
Director Institute of Materials Science , NCSR Demokritos , Aghia Paraskevi, Attikis 15310, Greece  
Fax: 30-1-6519430, Email: [dniarchos@ims.demokritos.gr](mailto:dniarchos@ims.demokritos.gr)

Professor Mamoun Muhammed  
Materials Chemistry Division, Royal Institute of Technology, Brinellvägen 23, II, SE-100 44 Stockholm -  
Sweden  
Fax: +46-8-790 9072 Email: [mamoun@matchem.kth.se](mailto:mamoun@matchem.kth.se)

Professor Emmanuel Giannelis  
Department of Materials Science and Engineering, Cornell University, 247 Bard Hall, Ithaca, NY 14853  
USA  
Fax : (607) 255-2365. Email: [emmanuel@msc.cornell.edu](mailto:emmanuel@msc.cornell.edu)

Professor George Hadjipanayis  
Department of Physics & Astronomy, University of Delaware Newark, DE 19716 USA  
Fax : 302 832 1637; Email: [hadjii@udel.edu](mailto:hadjii@udel.edu)

Dr. Lawrence Kabacoff  
Materials Science and Technology Division, code 332, Office of Naval Research, 800 North Quincy Street,  
Arlington, Virginia 22217, USA  
Phone: 1(703)696-0283, Fax: 1(703)696-0934, Email: [kabacol@onr.navy.mil](mailto:kabacol@onr.navy.mil)

Professor Bernard H. Kear  
State of New Jersey Professor, Department of Ceramic and Materials Engineering, Rutgers University  
607, Taylor Road, Piscataway, NJ 08854-8065, USA  
Phone: (732) 445-2245, Fax: (732) 445-5977, Email: [bkear@rci.rutgers.edu](mailto:bkear@rci.rutgers.edu)

Dr. Lynn Kurihara  
Naval Research Laboratory, Code 6323, Washington, DC 20375, USA  
Email: [kurihara@anvil.nrl.navy.mil](mailto:kurihara@anvil.nrl.navy.mil)

Professor Enrique Lavernia  
Department of Chemical and Biochemical Engineering and Materials Science, University of California,  
Irvine, CA 92697-2575, USA  
Email: [lavernia@uci.edu](mailto:lavernia@uci.edu)

Professor Fotios Papadimitrakopoulos  
Co-Director, Nanomaterials Optoelectronics Laboratory, Institute of Materials Science, U-136, University  
of Connecticut, Storrs, CT 06269-3136, USA.  
Phone: (860)-486-3447, Fax: (860)-486-4745, Email: [papadim@mail.ims.uconn.edu](mailto:papadim@mail.ims.uconn.edu)

Dr. K. Sadananda  
Code 6323, Naval Research Laboratory, Washington D.C. 20375, USA  
Phone: (202)767-2117, Fax:(202)767-2623, Email: [sada@anvil.nrl.navy.mil](mailto:sada@anvil.nrl.navy.mil)

Professor Jackie Ying  
Department of Chemical Engineering, Massachusetts Institute of Technology, 77 Massachusetts Avenue,  
Cambridge, MA 02139, USA  
Email: [jying@mit.edu](mailto:jying@mit.edu)

Professor Valerii Fedosyuk  
Institute of Solid State Physics and Semiconductors, National Academy of Sciences of Belarus  
P.Brovka Street 17, Minsk 220072, Belarus  
Phone: +(172)84 2791, Fax: +(172)84 0888, Email: [fedosyuk@iftpp.bas-net.by](mailto:fedosyuk@iftpp.bas-net.by)

Professor A.Misiuk  
Institute of Electron Technology, Al. Lotnikow 32/46, 02-668 Warszawa, Poland  
Email: [misiuk@ite.waw.pl](mailto:misiuk@ite.waw.pl)

Professor Anatoly V. Dvurechenskii  
Institute of Semiconductor Physics, Siberian Branch of Russian Academy of Science, 630090, Novosibirsk,  
Lavrent'ev prospekt 13, Russia.  
Phone: 7-3832- 33 24 66, Fax: 7-3832-33 27 71, Email: [dvurech@isp.nsc.ru](mailto:dvurech@isp.nsc.ru)

Professor Sergei Kukushkin  
Institute of Problems of Mechanical Engineering, Russian Academy of Sciences, Bolshoj 61, Vas.Ostrov ,  
St. Petersburg, 199178, Russia  
Fax: +7 (812) 3214771, Email: [ksa@math.ipme.ru](mailto:ksa@math.ipme.ru)

Professor Yuri Kumzerov  
Ioffe Physico-Technical Institute, Russian Academy of Sciences, Polytechnicheskaya 26  
St.Petersburg 194021, Russia  
Fax: +(7 812)515 6747, E-mail: [kumz@infopro.spb.su](mailto:kumz@infopro.spb.su)

Dr. Y. K. Hwu  
Institute of Physics, Academia Sinica, Nankang, Taipei 11529, Taiwan, R.O.C.  
Email: [phhwu@ccvax.sinica.edu.tw](mailto:phhwu@ccvax.sinica.edu.tw)

Dr. Stergios Logothetidis  
Laboratory for Thin Films and Coatings, Materials Characterization and Metrology, Solid State Physics  
Section, Department of Physics, Aristotle University of Thessaloniki, Greece.  
Email: [logot@ccf.auth.gr](mailto:logot@ccf.auth.gr)

Dr. I. Zalite  
Institute of Inorganic Chemistry of the Riga Technical University, Mierailea 34, Salaspils,  
LV 2169, Latvia, Salaspils, LV 2169, Latvia  
Phone: (371-2) 944773, Fax: (371) 7901257, Email: [ilmars@iich.sal.lv](mailto:ilmars@iich.sal.lv)

Dr. Irina Kleps  
Institute of Microtechnology (IMT), P.O. Box 38-160, Bucharest 72225, Romania  
Email: [irinak@imt.ro](mailto:irinak@imt.ro)

Dr. Laura Tugulea  
Faculty of Physics-University of Bucharest, P.O. Box MG-11, Bucharest-Magurele, 76900 Romania  
Email: [laur@scut.fizica.unibuc.ro](mailto:laur@scut.fizica.unibuc.ro)

Dr. Sergei Aizikovich  
Mechanics and Applied Mathematics Institute, Rostov State University, P.O. Box 4845  
Rostov-on-Don 344090, Russia  
Phone: +(7 8632) 285955, Email: [aizsm@gis.rnd.runnet.ru](mailto:aizsm@gis.rnd.runnet.ru)

Dr. Marat Akchurin  
Institute of Crystallography, Russian Academy of Sciences, Leninskii pr. 59, Moscow 117333  
Russia  
Phone: +(7 095)330 8274, Fax: +(7 095)135 1011, Email: [public@mechan.incr.msk.su](mailto:public@mechan.incr.msk.su)

Dr. M.Yu. Gutkin  
Institute for Problems of Mechanical Engineering, Russian Academy of Sciences  
Bolshoj 61, Vas.Ostrov, St.Petersburg 199178, Russia  
Fax: +(7 812)321 4771, Email: [gutkin@def.ipme.ru](mailto:gutkin@def.ipme.ru)

Dr. A.P. Zhilyaev  
Institute for Physics of Advanced Materials, Ufa State Technical University, 12, K. Marks St., Ufa 450000  
Russia  
Phone: +(7 347)223 5244, Fax: +(7 347)223 3422, Email: [AlexZh@anrb.ru](mailto:AlexZh@anrb.ru)

## GAS PHASE SYNTHESIS OF NANOSTRUCTURED FILMS AND COATINGS

H. HAHN, M. WINTERER, S. SEIFRIED, V.V. SRDIC\*

*Darmstadt University of Technology*

*Materials Science Department*

*Thin Films Division, Petersenstr. 23*

*64287 Darmstat, Germany*

*(<sup>\*</sup> permanent address: University of Novi Sad, Novi Sad, Yugoslavia)*

### 1. Introduction

Nanocrystalline materials have become increasingly important both in fundamental and applied research because of their interesting properties which are altered compared to conventional microstructures due to effects of grain size and due to the disordered atomic structure of the interfacial regions. For many years the research was concentrated on the synthesis and properties of nanocrystalline materials in bulk form which were prepared by consolidation and sintering of nanocrystalline powders prepared by wet chemical, gas phase and mechanical routes. Recently, as a response to the need of constantly improving the properties and performance of thin films and coatings, a potential for nanocrystalline materials in the area of novel synthesis and microstructures of films and coatings was identified. Many different techniques for the preparation of thin and thick films are readily available both for industrial applications and basic research and provide an excellent base for the development and application of new methods. The potential of nanocrystalline films and coatings can be identified in a wide range of technologies based on friction and wear properties, other mechanical properties such as superplasticity, and thermal conductivity for thermal barrier coatings, and optical, magnetic, electronic and catalytic properties.

In principle many different structures in thin films such as multilayers in electronic materials and for magneto-resistance effects (GMR, TMR etc.) should be included in a complete review of the topic of nanostructured films and coatings, because the characteristic dimensions are in the nanometer regime. However, it is beyond the scope of this paper to give a complete overview of all these structures and the corresponding processing techniques which are available for the synthesis of thin films and coatings. Therefore, the reader is referred to the literature on physical and chemical vapor processing techniques [1, 2]. Nevertheless, for the understanding of gas phase synthesis processes presented in the following sections it is worthwhile to note that the physical and chemical vapor deposition routes (PVD, CVD) have achieved a high degree of control and excellent reproducibility. Therefore, these techniques are widely spread in both research and production. The PVD and CVD techniques have capabilities to design materials at the atomic level by depositing atomic building units in a layer by layer growth to obtain atomically sharp interfaces between chemically or structurally dissimilar materials. In particular the design of semiconductor interfaces and magnetic multilayers has led to sophisticated artificial materials and unique applications associated with the well-defined nanostructures. As a disadvantage for production on a large scale, the processes for controlled growth are relatively slow.

Additionally, the microstructures which can be obtained include single crystalline, epitaxial layers and columnar grain structures depending on the crystallographic relationships between the substrate and the growing film and the synthesis conditions (temperature, pressure, growth rate etc.). However, based on the knowledge of nanocrystalline materials in bulk form, it is anticipated that novel microstructures with grain sizes in the nanometer regime, controlled porosity with narrow size distributions and control of the chemical composition and the elemental distribution on the scale of the nanometer sized grains will open new areas of application. In this paper the opportunities for the growth of films and coatings with nanometer sized microstructures based on chemical vapor processing is reviewed.

## 2. The Chemical Vapor Synthesis Process

The process for film growth is based on the Chemical Vapor Synthesis (CVS) which has been described in detail in the literature [3]. The CVS technique itself is similar to the process of Chemical Vapor Deposition (CVD) which is widely employed to prepare thin films and coatings at a high level of control. The conditions for CVD growth have been determined for many materials systems and detailed knowledge exists for the dependence of the growth rate as a function of precursor partial pressure and temperature as well as other quantities influencing the growth of films on substrates. In the simplest form of a hot wall reactor the substrate is located in a cylindrical reactor tube heated with an external furnace. Other activation source such as microwave plasma can be employed as well. The complex growth process includes multiple steps such as decomposition of the metalorganic precursor molecules, gas diffusion to the hot substrate, deposition of the atomic species on the surface of the substrate and surface diffusion of the species to energetically favored sites on the surface such as steps and kinks. The growth rate of a film on a substrate depends on many parameter. It is shown schematically in Figure 1 as a function of the inverse temperature and the partial pressure of the precursor. Several distinct growth regimes can be identified in the dependence on the precursor pressure: (1) a regime in which the growth rate depends linearly on the precursor partial pressure; (2) a regime in which the growth rate on the substrate ceases to increase with increasing partial pressure and (3) a regime in which a rapid decrease at the highest partial pressures occurs. The best conditions for CVD growth are in the initial linear regime because the precursor decomposes and the reaction products are solely deposited at the surface of the growing films. Over a wide range of pressure no change in the mode of growth is observed and conditions for stable growth are given. In the plateau regime additional formation of nanoparticles occurs in the gas phase and consequently the growth rate of the film does not increase with increasing precursor partial pressure. At the highest partial pressures film growth is further suppressed and most of the precursor is transformed into nanoparticles because fewer precursor molecules reach the substrate surface. While this regime is not desirable in conventional film growth because of the incorporation of the nanoparticles into the films, this regime is used for the formation of nanoparticles by CVS. In this process the particles are collected from the gas phase after exiting from the hot wall reactor and can be processed further by consolidation and sintering.

The temperature dependence of the growth rate by CVD shows a similar behavior: (1) film growth occurs in the first two regimes with surface reaction control and gas diffusion control as rate determining steps. At higher temperatures the film growth rate decreases rapidly due to the homogeneous formation of nanoparticles in the gas phase. Therefore, optimum conditions for particle formation in the gas phase, i.e. CVS, require high temperatures and high precursor partial pressures.

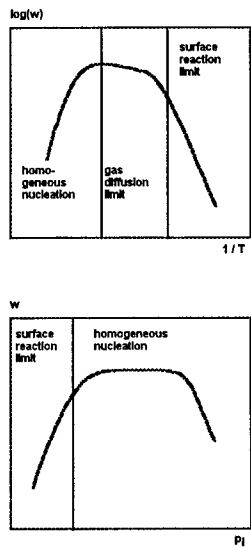


Figure 1: Schematic dependence of the film growth rate on a substrate by CVD growth as a function of the inverse temperature (top) and the precursor partial pressure  $P_i$  (bottom).

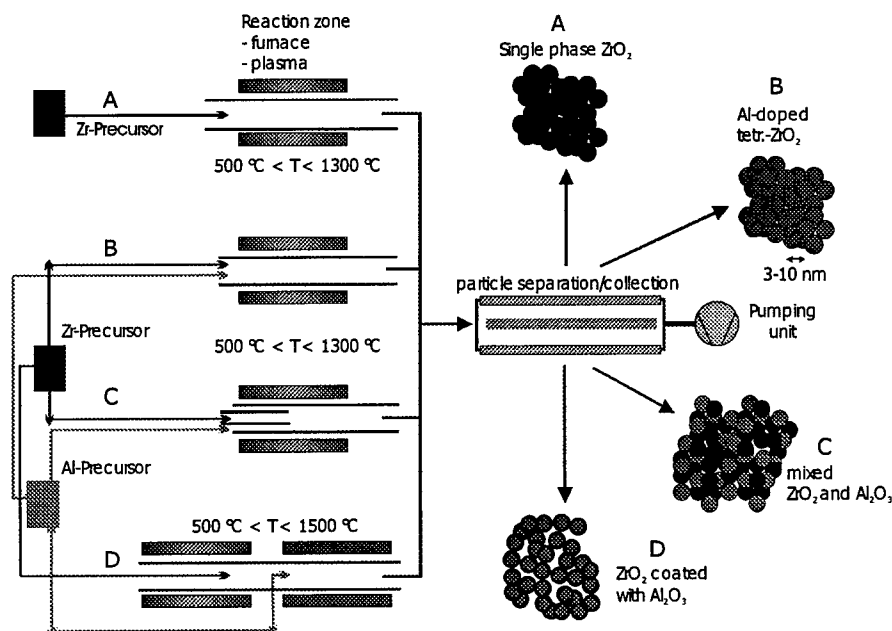
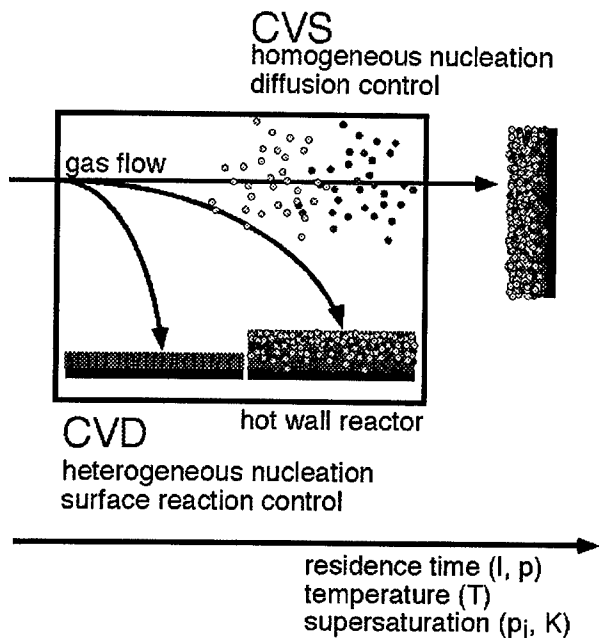


Figure 2: Opportunities of the CVS processing for the synthesis of nanocrystalline oxides with different elemental distributions of Zr- and Al-ions in the individual nanoparticles and the corresponding geometry of the various reactor designs.

The opportunities which result from the unique design of a hot wall CVS reactor for nanoparticle synthesis are illustrated schematically in Figure 2. The design is applicable in general for many materials systems, but as an example the consequences for the microstructure of the nanoparticles are shown for the  $ZrO_2/Al_2O_3$  system, which is immiscible according to the equilibrium phase diagram. By changing the reactor geometry it is possible to synthesize oxide nanoparticles with different elemental distributions of the Zr- and Al-ions: crystalline and amorphous Al-doped zirconia, mixed pure oxides and coated nanoparticles. The possibility to control the elemental distributions within the nanoparticles opens many opportunities for the engineering of properties.



*Figure 3:* Various synthesis techniques based on chemical vapor processing: CVD for pure film growth with epitaxial or columnar grain structure, CVS for homogeneous formation of nanoparticles and CVD/CVS for nanoparticle deposition on a substrate with instantaneous sintering.

An interesting opportunity arises by the careful control of the synthesis parameter in the regime where CVD growth coincides with nanoparticle formation in the gas phase. At high precursor partial pressures and high temperatures, i.e. at high growth rates, it is possible to incorporate nanoparticles into the growing film, thus increasing the film growth rates compared to pure CVD growth. It has been demonstrated that nanoparticles which are formed in the gas phase can be deposited on the surface of a substrate held at high temperatures. Depending on the processing temperature it is possible to obtain porous or dense nanocrystalline coatings. The complete range of possibilities from epitaxial and columnar coatings grown by CVD, nanoparticles in the gas phase by CVS and the intermediate range of CVD/CVS as discussed above is summarized in Figure 3, highlighting the relationship between the different techniques. An important feature of the CVD/CVS regime is the high growth rate, because the total rate is determined by the sum of the film growth (CVD) and the

nanoparticle deposition. In the parameter window of CVD/CVS growth rates exceeding those of CVD growth by far can be achieved. The general equipment for all three techniques is similar and includes the precursor sources, the hot wall reactor with a tubular reaction zone, process control equipment for pressure, temperature and mass flow and pumping. Depending on the precursor in use, the precursor delivery must be quite elaborate and consists of a bubbler arrangement for liquid precursors with high vapor pressures, mass flow controller for gaseous and volatile precursors or liquid precursor delivery systems exhibiting accurate delivery by precursor pumping and fast evaporation. As in CVD-processing extremely accurate control with reproducible parameters such as total and partial pressures, temperature, residence time, pumping speed, precursor and reactive gas flows etc. is possible and guarantees nanopowders and films of high quality. Further advantages of the CVS process compared to other gas condensation processing are better scalability, operator independent control of parameter, higher production rates (10 to 20 g/hr in a laboratory reactor).

### 3. Results

Different ceramics such as the simple oxides  $ZrO_2$ ,  $Al_2O_3$ ,  $Y_2O_3$ ,  $TiO_2$ , doped oxides such as  $Y-ZrO_2$  and  $Eu-Y_2O_3$  and coated oxides nanoparticles such as  $ZrO_2$  coated with  $Al_2O_3$  and  $ZrO_2$  coated with  $Y_2O_3$  have been synthesized using the CVS process. It is important to note that the median and the width of the size distribution of nanopowders prepared by CVS is drastically improved compared to the values of powders prepared by Inert Gas Condensation (IGC) [4]. As can be seen in Figure 4, the particle size distributions of oxide nanopowders obtained by IGC have average particle sizes of approx. 10 nm and 8 nm for standard and optimum synthesis conditions, respectively, with a geometric standard deviation of approx. 1.8. The average particle sizes of CVS-powders are approx. 5 nm with  $\sigma=1.3$ . In combination with the reduced degree of agglomeration and the excellent cleanliness and crystallinity, the sintering behavior of the nanopowders are improved compared to IGC-powders, which have been shown to be improved compared to conventional powders. A sequence of samples in different stages of sintering shows that during the entire sintering process transparency is

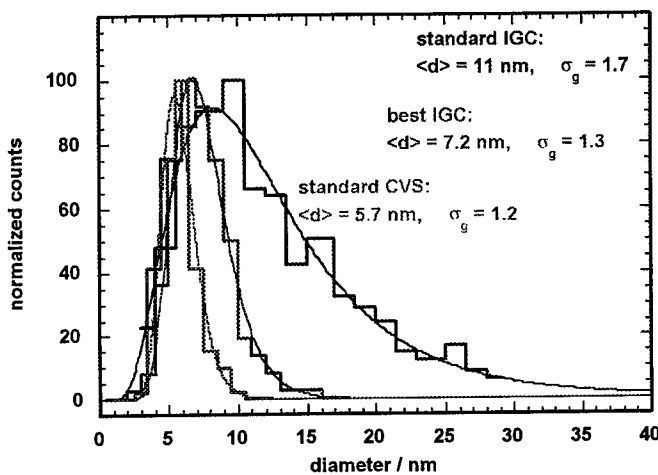


Figure 4: Particle size distributions for nanocrystalline  $ZrO_2$  determined by TEM prepared by different gas phase routes: inert gas condensation (IGC) under standard and optimized (best) conditions and chemical vapor synthesis (CVS) under non-optimized conditions.

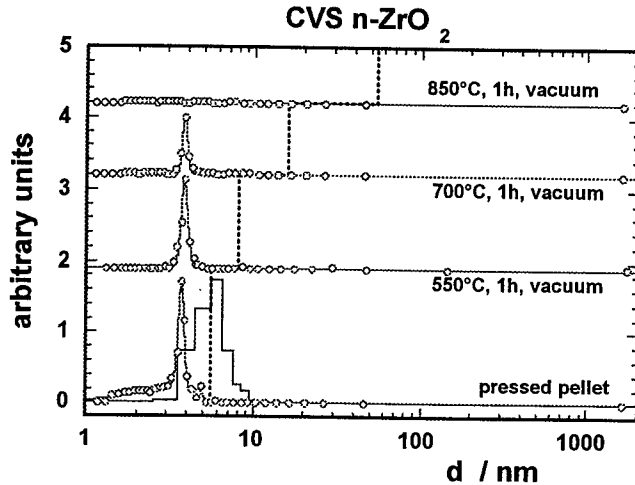


Figure 5: Pore size distributions of nanocrystalline  $\text{ZrO}_2$  in the compacted state and after different sintering treatments determined by nitrogen adsorption. Included as dashed lines are also the average grain sizes at the different temperatures determined from the line broadening of XRD using the Scherrer formula. For the pressed pellet the grain size distribution determined by HRTEM is given as well.

maintained indicating that the pore size distributions are not changed significantly as has been observed in earlier sintering studies. Detailed analysis using nitrogen adsorption confirms this result as can be seen in Figure 5 for the pore size distribution of pure nanocrystalline zirconia obtained by BET/BJH analysis. The microstructural features, i.e. average particle size, size distribution, agglomeration, crystallinity etc., which have been described above for pure oxides can be maintained in the doped, mixed and coated nanoparticles as well. As an example, Figure 6 shows a high resolution transmission electron micrograph of  $\text{Al}_2\text{O}_3$ -coated  $\text{ZrO}_2$  nanoparticles prepared by sequential deposition as described above (see Figure 2). The crystalline core of a  $\text{ZrO}_2$ -nanoparticle with a Al-rich amorphous coating layer can be clearly identified in the micrograph. The existence of a coating layer has also been demonstrated using EXAFS analysis with Reverse Monte Carlo (RMC) data evaluation, as described by Winterer [5]. It could be shown that depending on the processing conditions, a thin layer of  $\text{Y}_2\text{O}_3$  on  $\text{ZrO}_2$  nanoparticles can be obtained [6]. Even though the two precursors were introduced simultaneously into the reactor the slower decomposition kinetics of the Y-precursor resulted in a sequential deposition and formation of a coating on the  $\text{ZrO}_2$  nanoparticles.

One of the main challenges during sintering of nanopowders is the prevention/suppression of grain growth during the high temperature processing necessary to obtain high densities. Due to the large fraction of interfaces, both the driving forces for grain growth and sintering are large. Consequently, during pressureless sintering the average grain sizes grow to the  $\mu\text{m}$  regime during the final stages of sintering. Different techniques such as pressure assisted sintering, hot-isostatic pressing and creep deformation have been employed to densify nanocrystalline oxides while minimizing grain growth. An interesting effect has been observed if a structural phase transformation under high pressure occurs at the sintering temperature. In this case which was observed for nanocrystalline  $\text{TiO}_2$ , a smaller grain size in



Figure 6: High resolution transmission electron micrograph of a  $\text{ZrO}_2$  nanoparticle coated with a layer of  $\text{Al}_2\text{O}_3$  prepared by CVS. (HRTEM: Courtesy of Dr. Miehe, Structural Analysis Division at Materials Science Department of Darmstadt University of Technology).

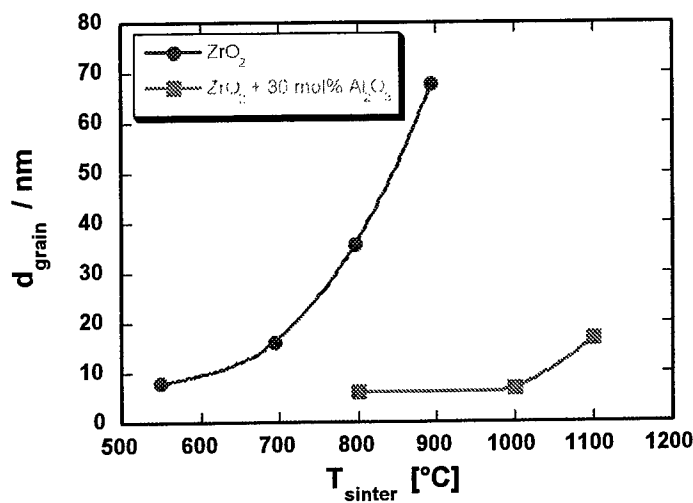


Figure 7: Grain size of pure nanocrystalline  $\text{ZrO}_2$  and  $\text{ZrO}_2$  doped with 30 mol%  $\text{Al}_2\text{O}_3$  prepared by CVS. The grain growth can be suppressed effectively by the doping and grain sizes in the range of 20 nm can be stabilized even at temperatures of 1100 °C.

the dense ceramic than the original grain size in the powder was obtained due to a high nucleation density [7]. However, due to the high cost of pressure assisted sintering equipment, restrictions of sample size and time constraints, pressureless sintering is favorable. Consequently, grain growth has to be inhibited by other means, such as grain boundary segregation and addition of second phase nanoparticles with low solubility in the matrix. Both methods have been employed for various material systems and are based on the reduction of grain boundary mobility. It has been demonstrated that a crystalline  $ZrO_2$  ceramic doped with up to 10 mol%  $Al_2O_3$  can be sintered to theoretical density at 1100 °C with grain sizes below 40 nm, while a  $ZrO_2$  ceramic doped with more than 15 mol%  $Al_2O_3$  sintered to only 75 % density with grain sizes below 20 nm [8]. The results of these studies are summarized in Figure 7. The pore structure consisting of nanopores with average pore diameter below 10 nm was stable at sintering temperatures of 1100 °C. It should be mentioned that both microstructures, i.e. dense ceramics with nanometer sized grains and ceramics with a porosity in the nanometer regime, which are stable at high temperatures are of interest for advanced applications. Further investigations with mixed and coated nanoparticles are in progress.

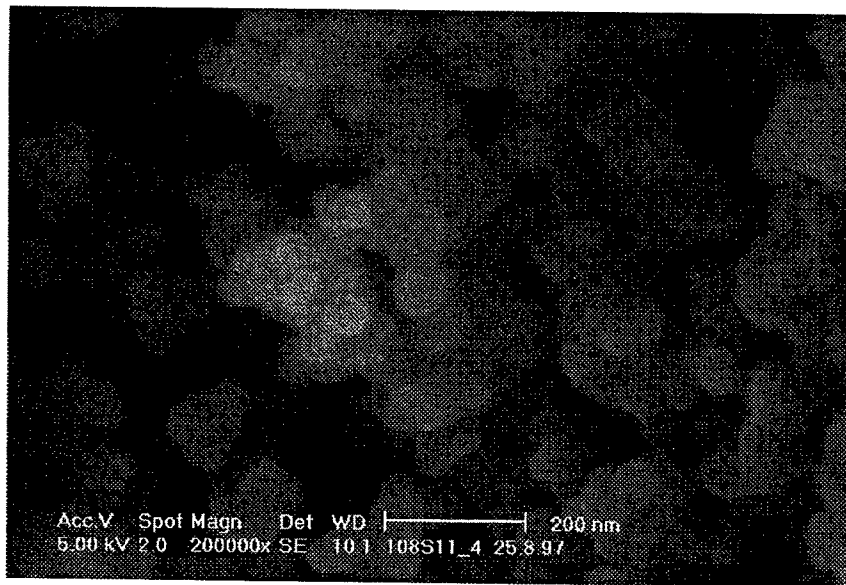


Figure 8: Backscattering image of the cross section through a Si-C-B gradient on a silicon substrate; position along the reactor axis 150 mm.

In relation to the synthesis of nanocrystalline films and coatings it is important that the microstructural features which are relevant for the sintering behavior of consolidated nanopowders also facilitate the densification of nanoparticles deposited on the surface of substrates during CVD/CVS processing. Similar to the results on bulk ceramics it has been shown that fully dense coatings can be readily obtained at sintering temperatures below 0.4  $T_m$ . Additionally, the exact control of the precursor fluxes into the reactor, i.e. by adjusting the mass flow rates of precursors and reacting gases and composition of the precursors, allows a change of the growth mode. Similarly, a temperature ramp during deposition results in a change of the growth mode from pure CVD film growth to CVS nanoparticle deposition as indicated in Figure 1. As a consequence of the change of the growth mode the grain morphology changes from a columnar grain structure with intergranular porosity to a porous or dense nanocrystalline microstructure. Furthermore, employing this principle a gradient

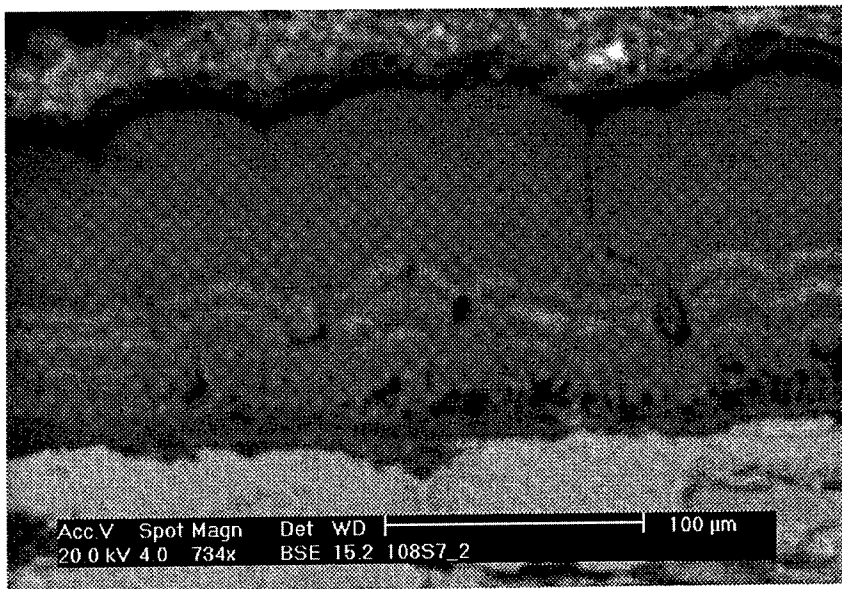


Figure 9: Transmission electron micrograph of the cross section close to the interface between the Si-C-B gradient film and the silicon substrate; position along the reactor axis: 250 mm.

structure with different grain morphologies was obtained for  $\text{TiO}_2$  by changing the temperature profile continuously during deposition. Similarly, the composition can be changed by adjusting the flow rates of two different precursors during the deposition at constant temperature. The step-like gradient shown in the scanning electron micrograph of Figure 8 results from the distinct changes of the flow rates. However, with computer controlled equipment it is possible to design continuous linear compositional gradients across the thickness of the coatings. The high resolution scanning electron micrograph of Figure 9 shows clearly the nanocrystalline grains in the coating. The exact growth mode of the nanocrystalline coating is not yet established and it is not clear where the nanoparticles are formed. The size of the particles formed in the gas phase (by CVS) and the grain size in the coatings are similar which indicates that the nanoparticles are formed in the gas phase and are subsequently deposited onto the substrate. Since the deposition temperatures are high, appropriate means to suppress grain growth as discussed have to be taken to ensure the deposition of a nanocrystalline coating.

#### 4. Acknowledgements

The authors are grateful for the financial support of the research by the Deutsche Forschungsgemeinschaft. One of the authors (VVS) is thankful for a research fellowship by the Alexander von Humboldt Stiftung.

#### 5. References

[1] Herman, M.A. and Sitter, H. (1989) *Molecular Beam Epitaxy – Fundamentals and Current Status*, Springer, Berlin.

- [2] Hitchman, M.L. and Jensen, K.-F. (eds.) (1993) *Chemical Vapor Deposition – Principles and Applications*, Academic Press, London.
- [3] Klein, S., Winterer, M. and Hahn, H. (1998) Reduced-pressure chemical vapor synthesis of nanocrystalline silicon carbide powders, *Chemical Vapor Deposition* 4, 143-149.
- [4] Nitsche, R., Rodewald, M., Skandan, G., Fuess, H., and Hahn, H. (1996) HRTEM study of nanocrystalline zirconia powders, *Nanostructured Materials* 7, 535-546.
- [5] Winterer, M. (1999), Reverse Monte Carlo analysis of EXAFS spectra of monoclinic and amorphous zirconia, submitted to *Journal of Physics: Condensed Matter*.
- [6] Benker, A. (1999) Diploma Thesis, Darmstadt University of Technology, Materials Science Department.
- [7] Liao, S.-C., Chen, Y.-J., Mayo, W.E., and Kear, B.H. (1999) Transformation-assisted consolidation of bulk nanocrystalline titania, *Nanostructured Materials*, accepted.
- [8] Srdic, V.V., Winterer, M. and Hahn, H. (1999), Sintering behavior of nanocrystalline zirconia doped with alumina prepared by chemical vapor synthesis, *Journal of the American Ceramic Society*, submitted.

## ELECTRODEPOSITED NANOSTRUCTURED FILMS AND COATINGS: SYNTHESIS, STRUCTURE, PROPERTIES AND APPLICATIONS

U. ERB<sup>1</sup>, G. PALUMBO<sup>2</sup> AND K. T. AUST<sup>1</sup>

<sup>1</sup>*University of Toronto  
Dept of Metallurgy & Materials Science*

*184 College St, Toronto, Ontario, Canada, M5S 3E4*

<sup>2</sup>*Integran Technologies  
1 Meridian Rd  
Toronto, Ontario, Canada M9W 4Z6*

### 1. Introduction

Major advances in materials design are often the result of innovation in material synthesis and processing technologies. For example, over the past three decades, enormous progress has been made in the development of novel electronic materials and devices after vacuum technology and various thin film deposition methods had reached the level of sophistication that enabled the synthesis of extremely thin layers of metals, dielectrics, semiconductors and insulators. Here, the precise control of thickness, defect structure and chemical composition of the materials were of utmost importance and required unique solutions in processing technology. In contrast, other advanced materials of high innovation potential can be derived from a particular premise to achieve desirable structure-property-performance relationships in the material through microstructural design. The synthesis methods to achieve innovation in these materials are then often of secondary concern; they may still be novel but in many cases they are simply modifications of well-established and mature technologies.

A good example for advanced materials falling into the latter category are nanostructured materials. This field was first introduced by Gleiter [1] almost two decades ago. The original premise in Gleiter's approach was to synthesize a new solid state structure – an interfacial material – which differs from the crystalline and amorphous counterparts of the same chemical composition. Gleiter's proposal to achieve such a new structure by introducing very large volume fractions of grain boundary or interface atoms by crystal size reduction was based on the understanding of grain boundary structure – property relationships at that time. If one further considers that "not all grain boundaries are created equal" [2] (i.e. their structure and properties depend greatly on the misorientation between adjacent grains) one can categorize fully dense nanostructured materials as a subgroup of grain boundary engineered (GBE) materials. The innovation in GBE materials is then the precise engineering of average grain size, grain boundary volume fraction and character distribution for desired application-specific material performance. In other words, by controlling the type and / or volume fraction of grain boundaries of conventional engineering materials, using modifications

of existing processing technology (such as thermomechanical processing, ball milling, rapid solidification, electrodeposition), unique material performance characteristics in bulk materials as well as films and coatings can be achieved.

This paper deals with electrodeposited nanostructures. After reviewing the chemistry and physics involved in the synthesis of these materials, a brief summary of some of the unique mechanical, physical and chemical properties will be given. Several practical applications of these materials will also be presented.

## 2. Synthesis

Electrodeposition is a low temperature processing route to produce nanostructured materials, most often in a single step requiring no secondary consolidation. Usually two electrodes are involved (one anode and one cathode) which are immersed in an aqueous electrolyte containing the material to be produced in ionic form. Important processing parameters include bath composition, pH, temperature, overpotential, bath additives, etc. Numerous examples listing electrochemical processing windows leading to nanocrystals have been previously published for pure metals (e.g. Ni [3-5], Co [6], Pd [7], Cu [6]), binary alloys (e.g. Ni-P [8, 9], Ni-Fe [10], Zn-Ni [11], Pd-Fe [12], Co-W [13]) and ternary alloys (e.g. Ni-Fe-Cr [14, 15]). Even multilayered or compositionally modulated alloys (e.g. Cu-Pb [16], Cu-Ni [17, 18], Ag-Pd [19], Ni-P [20]), metal matrix composites (e.g. Ni-SiC [3]), ceramics (e.g. ZrO<sub>2</sub> [21]) and ceramic nanocomposites (e.g. Tl<sub>a</sub>Pb<sub>b</sub>O<sub>c</sub> [22]) have been successfully produced by electrodeposition methods.

Electrocrysallization occurs either by the build up of existing crystals or the formation of new ones [23]. These two processes are in competition with each other and are influenced by different factors such as plating parameters and substrate pre-treatment. The two key mechanisms which have been identified as the major rate determining steps for nanocrystal formation are charge transfer at the electrode surface and surface diffusion of adions on the crystal surface [23, 24]. The other important factor in nanocrystal formation during electrocrysallization is overpotential [23, 24]. Grain growth is favoured at low overpotential and high surface diffusion rates for adions, while high overpotential and low diffusion rates promote the formation of new nuclei. In many systems these conditions can be achieved by using (1) pulse plating where the peak current density can be considerably higher than the limiting current density attained in the same electrolyte during direct current plating and / or (2) surface active bath additions or alloying elements which lower the surface diffusion of adions. Under these conditions, which lead to massive nucleation and reduced grain growth, the effect of the substrate on the resulting bulk electrodeposit becomes often negligible [e.g. 25].

A thin coating (thickness up to ~100µm) electroplated onto on a substrate to modify specific surface properties is probably the most widely known application of electrodeposition technologies. However, it should be noted that there are several other processes (e.g. brush plating, electrowinning and electroforming) which can be used to produce nanocrystalline materials as thick coatings (several mm or cm thick) or in freestanding forms such as sheet, foil, tubes, wire, mesh, plate and foam. Several examples are listed in table 1 and Fig. 1.

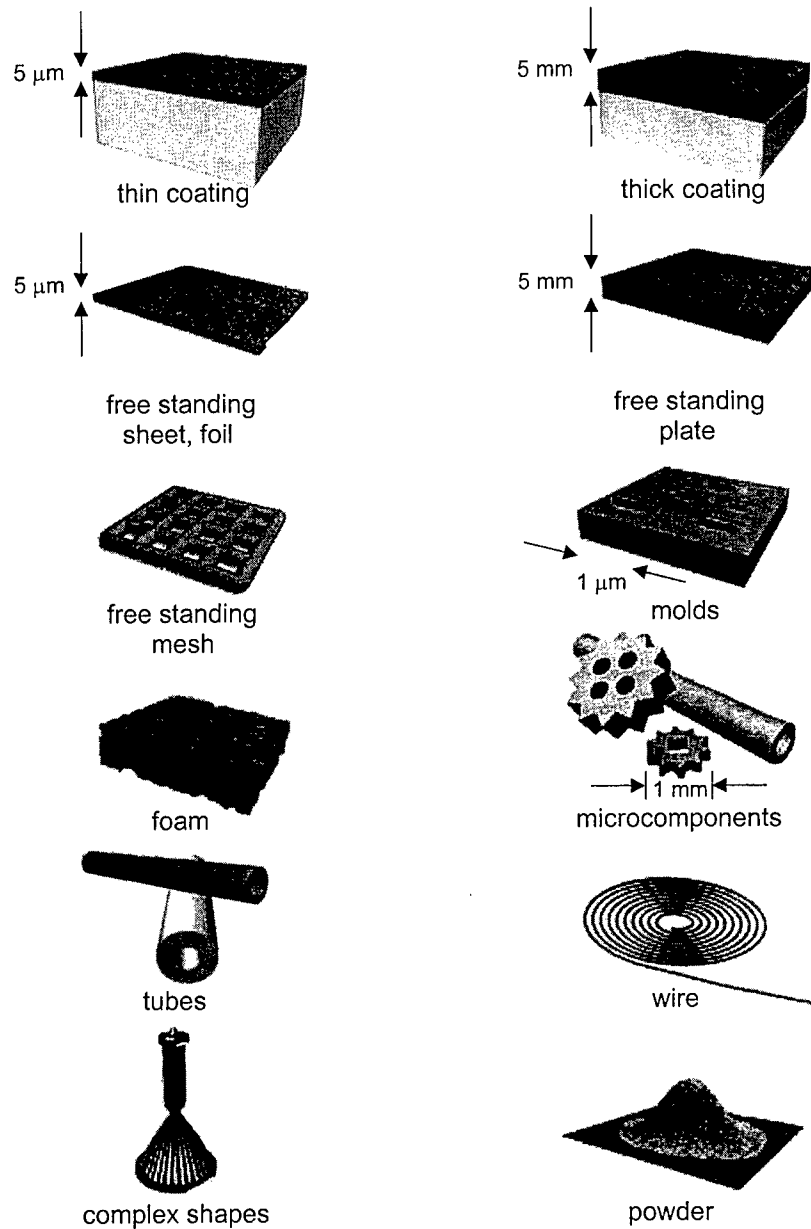


Figure 1. Various shapes of electrodeposited products

TABLE 1. Various Shapes and Applications of Electrodeposited and Electroformed Products

Shapes	Applications
<b>Thin Coatings</b> (on Substrate)	Surface Modification for Wear and Corrosion Resistance; Catalytic Surfaces
<b>Thick Coatings</b> (on Substrate)	Electrosleeve™; Repair of Worn Components
<b>Sheet, Foil</b> (Free-Standing)	Gaskets; Pressure Control Membranes; Hydrogen Purification Membranes
<b>Tubes, Wire</b> (Free-Standing)	Thermal Barriers; Solar Energy Absorbers; Microfoils; Soft Magnets
<b>Tubes, Wire</b> (Free-Standing)	Surgical Tools; Missile Guidance Systems; Miniature Gamma Radiation Sources
<b>Mesh</b> (Free-Standing)	Filters; Precision Sieve Screens; Razor Foils; Printing Screens; Centrifuge Screens
<b>Plate</b> (Free-Standing)	Structural Applications
<b>Foam</b> (Free-Standing)	Filters; Electromagnetic Shielding; Battery Electrodes; Catalyst Carriers
<b>Molds</b> (Free-Standing)	CD Stampers; Embossing Tools for Holograms; Compression, Injection and Pattern Molds
<b>Free Forms</b>	Precision Bellows; Erosion Shields for Helicopters; Thrust Chambers for Rocket Engines; Components for Micro-magnetic Motors, Microoptics, Microactuators and Microfiltration; Shaped Charge Liners; Precision Reflectors and Mirrors; Nozzles.
<b>Powder</b>	Catalysts; Reinforcements

The Electrosleeve™ applications will be discussed in section 5.1.

### 3. Structure

In the as-plated condition electrodeposited nanocrystals are fully dense materials, usually with negligible porosity [26, 27] unless they are deliberately produced in powder form. They are non-equilibrium structures which is primarily manifested in the small crystal size and the associated large volume fraction of grain boundaries and triple junctions [28, 29] and considerable extension of the solid solubility range as observed, for example, in Ni-P [8, 9], Zn-Ni [11] and Ni-Mo [30]. Grain size distributions are usually very narrow exhibiting log normal behaviour and average grain size and crystallographic texture can be controlled by various plating parameters, for example bath pH, current density, etc., [31]. High resolution electron microscopy has revealed that the grain boundary structures in electrodeposited nanocrystals are similar to the structures found in conventional polycrystalline materials [32]. Cross-sectional examination of thin ( $\sim 2.5 \mu\text{m}$ ) and thick ( $>1\text{mm}$ ) coatings has shown that the nanocrystalline structure is fully established right at the interface with the substrate and that the grain size is essentially independent of coating thickness [33]. This is in contrast to conventionally produced electrodeposits which often show considerable grain coarsening with increasing coating thickness [34]. Purities of 99.9% or better can be achieved by proper bath control and choice of electroplating parameters.

### 4. Properties

A comparison of the microstructures of nanomaterials produced by consolidation of precursor nanocrystalline powders and electrodeposition shows that the main difference is the porosity in the final product; porosity usually being negligible in electrodeposited nanocrystals. Consequently, considerable differences in some properties have been observed in both groups of materials [see e.g. 35]. For example, the initially reported large changes in Young's modulus, thermal expansion, specific heat, saturation magnetization and Curie temperature observed on consolidated nanocrystals were not found in electrodeposited nanostructures. In fact, the grain size independence of saturation magnetization and Curie temperature are fully consistent with the results of recent first principle calculations which showed that the magnetic moment of atoms in grain boundary structures is not strongly affected by the structural disorder associated with various boundary types [36]. It has been concluded [35] that the differences in certain properties measured on consolidated and electrodeposited nanostructures were mainly due to porosity and associated impurity effects rather than the presence of large volume fractions of grain boundaries and triple junctions.

What is commonly observed in both groups of materials, however, are the remarkable improvements in hardness, yield strength, ultimate tensile strength and wear rate. For example, table 2 shows a comparison of some mechanical properties of conventional polycrystalline and two grades of nanocrystalline Ni with 100nm and 10nm grain size, respectively. Fig. 2 shows the hardness as a function of grain size in the usual Hall-Petch [37, 38] plot for nanocrystalline Ni. The observed transition from regular to inverse Hall-Petch relationship has also been observed for Ni-P [29], Ni-Fe [10] and Ni-Mo [30] alloys. The corresponding reduction in the dry wear rate for Ni from about  $130 \times 10^{-5} \text{ mm}^3/\text{mm}$  at an average grain size of  $10\mu\text{m}$  to an extremely low value of

$0.8 \times 10^{-5}$  mm<sup>3</sup>/mm at 10nm grain size is shown in Fig. 3, together with the concurrent decrease in the coefficient of friction [39]. In nanocrystalline Ni-1% P alloys (10nm grain size) the hardness can be further increased from about 700 VHN in the as-plated material to over 1200 VHN by appropriate annealing treatment (400°C, 20 minutes) as shown in Fig. 4 [40]. The increase in hardness was found to be the result of grain growth to 30nm and simultaneous formation of Ni<sub>3</sub>P precipitates as per equilibrium phase diagram [41]. Further annealing at 400°C as well as annealing at 500°C and 600°C resulted in excessive microstructure coarsening indicated by a decrease in hardness.

TABLE 2. Mechanical Properties of Conventional and Nanocrystalline Nickel

Property	Conventional <sup>a</sup>	Nano-Ni	
		100nm	10nm
Yield Strength, MPa (25°C)	103	690	>900
Yield Strength, MPa (350°C)	-	620	-
Ultimate Tensile Strength, MPa (25°C)	403	1100	>2000
Ultimate Tensile Strength, MPa (350°C)	-	760	-
Tensile Elongation, % (25°C)	50	>15	1
Elongation in Bending, % (25°C)	-	>40	-
Modulus of Elasticity, GPa (25°C)	207	214	204
Vickers Hardness, kg/mm <sup>2</sup>	140	300	650
Work Hardening Coefficient	0.4	0.15	0.0
Fatigue Strength, MPa (10 <sup>8</sup> cycles/air/25°C)	241	275	-
Wear Rate (dry air pin on disc), $\mu\text{m}^3/\mu\text{m}$	1330	-	7.9
Coefficient of Friction (dry air pin on disc)	0.9	-	0.5

a: ASM Metals Handbook, ASM International, Metals Park, OH, Vol. 2, p. 437 (1993).

The corrosion behaviour of nanocrystalline Ni has been extensively studied using potentiostatic and potentiodynamic polarizations in various corrosive environments (2N H<sub>2</sub>SO<sub>4</sub> solution [pH=0], 30-wt% KOH solution [pH=13] and 3wt% NaCl solution [pH=7]) [30, 42-44]. It has been demonstrated that, as far as overall corrosion rate is concerned, the excellent corrosion performance of Ni is not compromised significantly by grain size reduction. These tests, together with further corrosion tests (ASTM G28 – susceptibility to intergranular attack; ASTM G35, G36 and G44 – susceptibility to stress corrosion cracking) have shown that nanostructured Ni is intrinsically resistant to intergranular attack and intercrystalline stress corrosion cracking [45]. The material was also found to be resistant to pitting attack and only slightly susceptible to crevice corrosion (ASTM G48) [45].

Nanocrystalline Ni electrodeposits having an average grain size of 20nm are also observed to display higher electrocatalytic behaviour when compared to cold worked, fine grained and fully annealed reference structures, with regards to the hydrogen evolution reaction (HER) for alkaline water electrolysis at room temperature [46]. The enhanced HER kinetics observed here are considered to be the direct result of the high area fraction of grain boundaries (and to some extent, triple junctions) which

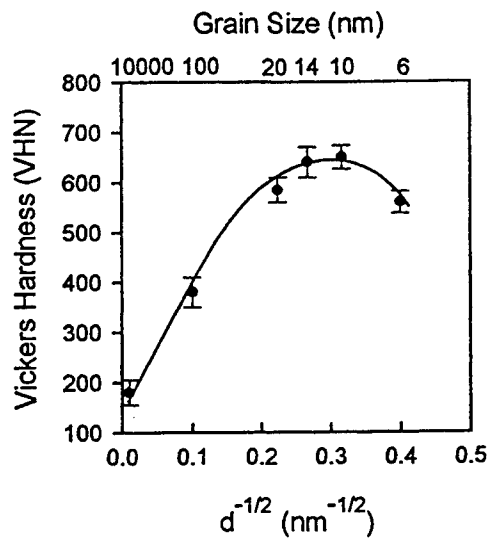


Figure 2. Hardness of nanocrystalline Ni a function of grain size [31]

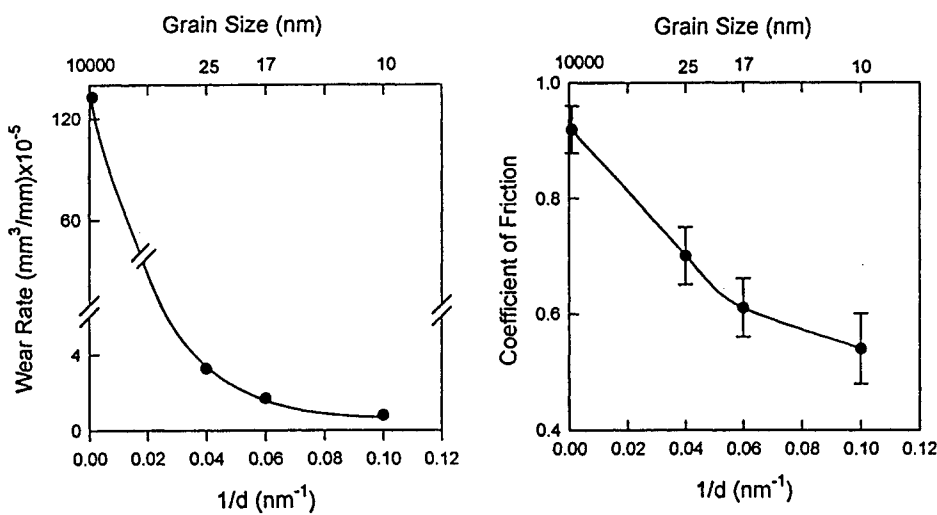


Figure 3. a) Wear rate of Ni electrodeposits as a function of grain size [39].  
b) Corresponding coefficients of friction [39].

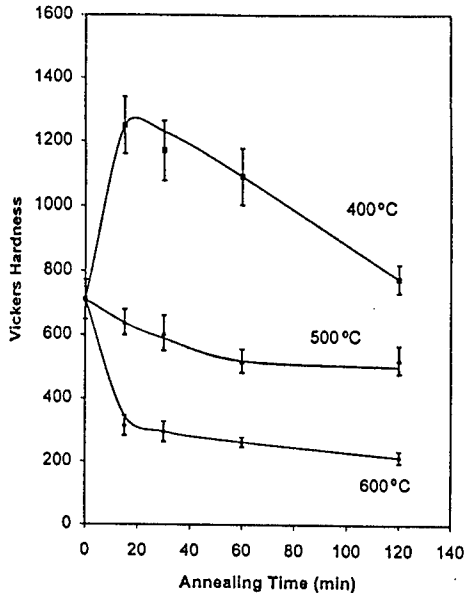


Figure 4. Hardness of nanocrystalline Ni - 1%P having a starting grain size of 10nm as a function of annealing treatment [40].

intersect the free surface of the electrode. It has been further shown [30] that the HER kinetics can be further enhanced by alloying nanocrystalline Ni with molybdenum.

## 5. Applications

Electrodeposited nanostructures have advanced rapidly to commercial application as a result of (1) an established industrial infrastructure (i.e., electroplating and electroforming industries), (2) a relatively low cost of application whereby nanomaterials can be produced by simple modification of bath chemistries and electrical parameters used in current plating and electroforming operations, (3) the capability in a single-step process to produce metals, alloys, and metal-matrix composites in various forms (i.e., coatings, free-standing complex shapes), and most importantly (4) the ability to produce fully dense nanostructures free of extraneous porosity. The importance of the latter cannot be overemphasized with regard to industrial application since, as has been outlined in previous section, many of the extraordinary properties initially attributed to nanostructures have since been demonstrated to be an artifact of residual porosity in these materials. From the outset, the fully dense nanomaterials produced by electrodeposition have displayed predictable material properties based upon their increased content of intercrystalline defects. This 'predictability' in ultimate material performance has accelerated the adoption of nanomaterials by industry, whereby, such extreme grain refinement simply represents another metallurgical tool for microstructural optimization. In this section, an overview of some current and emerging

practical applications for electrodeposited nanocrystalline materials are presented and discussed in light of the importance of property-specific grain size 'optimization' rather than grain miniaturization for its own sake.

### 5. 1. STRUCTURAL APPLICATIONS

As would be expected from Hall-Petch considerations, numerous practical applications for nanocrystalline materials are based upon opportunities for high strength coatings and free-standing structural components. The superior mechanical properties of these electrodeposited nanostructures have led to one of their first large scale industrial applications—the Electrosleeve™ process for in-situ repair of nuclear steam generator tubing [47]. This proprietary process [48] has been successfully implemented in both Canadian CANDU and U.S. Pressurized Water Reactors, and has been incorporated as a standard procedure for pressure tubing repair [49]. In this application, nanocrystalline Ni (100nm) is electroformed as a thick coating (0.5–1mm) on the inside surface of steam generator tubes to effect a complete structural repair at sites where the structural integrity of the original tube has been compromised (e.g., corrosion, stress corrosion cracking etc.). The high strength and good ductility of this 100nm grain size material (see table 2) permits the use of a thin 'sleeve' (0.5-1mm) which minimizes the impact on fluid flow and heat transfer in the steam generator.

Recent geometric models and experimental findings [50, 51] have shown that nanostructured materials can also possess a high resistance to intergranular cracking processes, including creep cracking. Several emerging applications for nanocrystalline materials possessing high intergranular cracking resistance include, lead-acid battery (positive) grids, and shaped charge liners (Cu, Pb, Ni) for military and industrial applications (e.g., demolition, oil well penetrators etc.); applications in which durability and performance are frequently compromised by premature intergranular failure.

### 5. 2. FUNCTIONAL APPLICATIONS

Some of the most promising industrial applications for nanostructured materials are in the area of soft magnets for high efficiency transformers, motors, etc. Anticipated reductions in magnetocrystalline anisotropy and coercivity as grain size is reduced below the mean thickness of a magnetic domain wall in conventional materials, have generated considerable development activity in this area. The main advantage of electrodeposited nanocrystals is their uncompromised saturation magnetization. The industrial use of these high performance ferromagnetic materials in motor, transformer and shielding applications has been accelerated by the recent development of a drum plating process for cost-effectively producing large quantities of sheet, foil, and wire in nanocrystalline form.

Another major application for drum-plated nanocrystalline material is in the production of copper foil for printed circuit boards, where enhanced etching rates and reduced line spacing/pitch can be achieved by reducing grain size. For this application grain size has been optimized on the basis of calculated electrical resistivity for nanocrystalline Cu [52]. A 50nm to 100nm grain size provides optimum etchability while maintaining good electrical conductivity.

As has been previously discussed, the high density of intercrystalline defects present within the bulk, and intersecting the free surface of nanostructured materials provides considerable opportunity in catalytic and hydrogen storage applications. Several applications are being developed for the use of these materials, either as an electrodeposited coating or electroformed free-standing component in Nickel Metal Hydride battery systems, and as alkaline fuel cell electrodes.

### 5. 3. COATING APPLICATIONS

The improved hardness, wear resistance and corrosion resistance coupled with undiminished saturation magnetization and predictable thermal expansion, elastic properties and electrical resistivity make nanocrystalline coatings ideal candidates for protective and functional coatings. Examples include hard facing on softer, less wear resistant substrates, recording heads, electronic connectors, replacement coatings for chromium and cadmium in automotive, aerospace, and defense applications, in particular for non line-of-sight applications such as crevices, angles, bores, etc. In the latter application the drive is primarily environmental, where much more stringent workplace and emission / effluent standards are putting pressure on hard chrome and cadmium plating. In North America, these regulations still permit the use of these materials but in some European Countries, materials such as cadmium have already been banned.

## 6. Fully Grain Boundary Engineered Nanostructures

Until recently the primary GBE concept applied to electrodeposited nanocrystals was the consideration of the grain boundary and triple junction volume fraction enhancement by grain size reduction. The structure-property relationships presented in the previous sections were mainly for nanostructures in the as-plated conditions with little consideration of the second concept of grain boundary engineering – the grain boundary character distribution. For conventional polycrystalline materials, the optimization of grain boundary character distribution to achieve a high population of low  $\Sigma$  CSL (Coincidence Site Lattice) boundaries has recently emerged as a technically viable and cost-effective means of achieving significant performance improvements (e.g. enhanced ductility, creep resistance, fracture resistance) in practical engineering materials [53]. For polycrystalline materials it has been shown that mobility differences between low  $\Sigma$  and general grain boundaries during grain growth can be used to optimize conventional metallurgical thermomechanical processes in order to achieve significant increases in the population of low  $\Sigma$  CSL boundaries [54]. In order to assess the possibility to achieve high frequencies of special boundaries in nanocrystalline materials by annealing, a series of experiments have been conducted on nanocrystalline Ni-15wt% Fe having an initial average grain size of 30nm. Specimens were annealed at 600°C for annealing times in the range of 5s to 900s and subsequently analyzed by electron backscatter diffraction [54]. Preliminary results from this analysis as shown in Fig. 5 are very encouraging. The low  $\Sigma$  CSL population is shown to initially increase with increasing grain size in the range of 150nm to 300nm and then subsequently decrease with increasing grain size in the range 300nm to 7 $\mu$ m.

Further experimentation is currently underway to (1) extend measurements to grain sizes below 100nm, (2) evaluate the effect of annealing temperature on the phenomenon, (3) to observe if similar effects can be observed with other nanocrystalline electrodeposits and (4) to evaluate the effect of optimized grain boundary character distribution in nanocrystals on the materials performance.

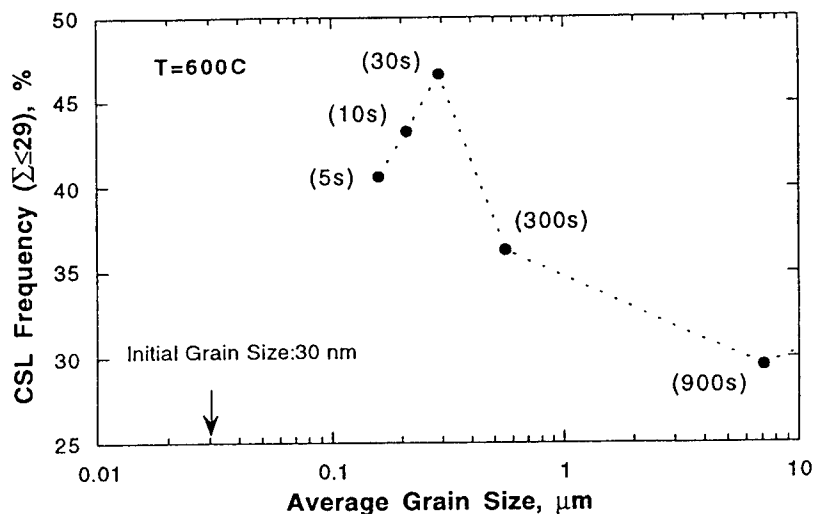


Figure 5. CSL frequency as a function of average grain size for Ni – 15%Fe. Values in parentheses present annealing times [54].

## 7. Conclusions

Electrodeposition of fully dense nanocrystalline materials can be considered a distinct form of grain boundary engineering resulting in interfacial materials containing large volume fractions of grain boundaries and triple junctions. Materials produced by electrodeposition exhibit excellent mechanical, wear, corrosion, catalytic and magnetic properties. Several economically viable electrodeposition technologies are already available to produce large quantities of various pure metals, alloys and composites in many different forms and shapes including thin and thick coatings, free-standing foil, sheet, tubes and wires as well complex geometries. Post deposition annealing of nanostructured electrodeposits is proposed as a means of optimizing grain boundary character distributions which could result in further property improvements of these materials.

### Acknowledgements

Financial support from NSERC and Ontario Hydro is gratefully acknowledged. The authors would also like to acknowledge the contributions of Dr. P. Lin and Messrs D. Clark, A. Robertson and D. Limoges to this work.

### References

- 1) Gleiter, H., (1991) in "Deformation of Polycrystals: Mechanisms and Microstructures" Proc. 2<sup>nd</sup> Risø Int. Symp. on Metallurgy and Materials Science, Risø National Laboratory, Roskilde Denmark **15**
- 2) Erb, U. and Palumbo, G. (eds) (1993) "Grain Boundary Engineering" Canadian Institute of Mining, Metallurgy and Petroleum, Montreal
- 3) El-Sherik, A. M., Erb, U., Palumbo, G., and Aust, K. T., (1992) *Scripta Metall. et Mater.*, **27**, 1185
- 4) Erb, U. and El-Sherik, A. M., (1994) US Patent No. 5,352,266
- 5) Bakonyi, E. Toth-Kadar, T. Tarnoczi, L. K. Varga, A. Cziraki, I. Geroes and B. Fogarassy, (1993), *Nanostr. Mat.*, **3**, 155
- 6) Bakonyi, E., Toth-Kadar, J., Toth, T., Tarnoczi and Cziraki A., (1996) in "Processing and Properties of Nanocrystalline Materials", C. Suryanarayana et al. (eds). TMS, Warrendale 465
- 7) Würschum, R., Gruss, S., Gissibl, B., Natter, H., Hempelmann, R. and Schäfer, H. E., (1997) *Nanostr. Mat.*, **9** 615
- 8) McMahon, G. and Erb, U., (1989) *Microstr. Sci.*, **17**, 447
- 9) McMahon, G. and Erb U., (1989) *J. Mat. Sci. Lett.*, **8**, 865
- 10) Cheung, C., Djuanda, F., Erb, U. and Palumbo, G. (1995) *Nanostr. Mat.*, **5**, 513
- 11) Alfantazi , A.M., El-Sherik A. M. and Erb, U. (1994) *Scripta Metall. et Mater.*, **30**, 1245
- 12) Bryden, K. J. and Ying, J. Y. (1997) *Nanostr. Mat.*, **9**, 485
- 13) Osmola, D., Renaud, E., Erb, U., Wong, L., Palumbo G., and Aust, K. T., (1993) *Mat. Res. Soc. Symp. Proc.*, **286**, 161
- 14) Cheung, C., Erb, U. and Palumbo, G. (1994) *Mat. Sci. Eng.*, **A185**, 39
- 15) Cheung, C., Palumbo, G., and Erb, U. (1994) *Scripta Metall. et Mater.*, **31**, 735
- 16) Despic, R. and Jovic, V. D. (1987) *J. Electrochem. Soc.*, **134**, 3004
- 17) Lashmore, D. S. and Dariel, M. P. (1988) *J. Electrochem. Soc.*, **135**, 1218
- 18) Yahalom, J. and Zadok, O. J. (1987) *Mat. Sci.*, **22**, 499
- 19) Cohen, U., Koch, F. B. and Sand, R. J. (1983) *Electrochem. Soc.*, **130**, 1987
- 20) Haseeb, B., Blanpain, G., Wouters, J. P., Celis and Roos, J. R., J. (1993) *Mat. Sci. Eng.*, **A168**, 137
- 21) Shirkhanzadeh, M., (1993) *Mat. Lett.*, **16**, 189
- 22) Switzer, J. A. (1992) *Nanostr. Mat.*, **1**, 43
- 23) Choo, R. T. C., El-Sherik, A. M., Toguri, J. and Erb, U., (1995) *J. Appl. Electrochem.*, **25**, 384
- 24) Bockris J. O. M., and Razumney, G. A., (1967) "Fundamental Aspects of Electrocristallization", Plenum Press, New York 27
- 25) Alfantazi, A.M., Brehaut, G., Erb, U. (1997) *Surf. Coat. Techn.* **89**, 239

26) Haasz, T. R., Aust, K. T., Palumbo, G., El-Sherik, A. M. and Erb, U., (1995) *Scripta Metall. et Mater.*, **32**, 423

27) Turi, T., (1997) "Thermal and Thermodynamic Properties of Fully Dense Nanocrystalline Ni and Ni-Fe Alloys", Ph.D. Thesis, Queen's University, Kingston, Ontario, Canada

28) Palumbo, G., Thorpe, S. J. and Aust, K. T., (1990) *Scripta Metall. et Mater.*, **24**, 1347

29) Palumbo, G., Erb, U. and Aust, K. T., (1990) *Scripta Metall. et Mater.*, **24**, 2347

30) Wang, S., "Electrochemical Properties of Nanocrystalline Nickel and Nickel-Molybdenum Alloys", Ph.D. Thesis, Queen's University, Kingston, Ontario, Canada, 1997

31) Erb, U., El-Sherik, A. M., Palumbo, G. and Aust K. T., (1993) *Nanostr. Mat.*, **2**, 383

32) Mehta, S. C., Smith, D. A. and Erb, U., (1995) *Mat. Sci. Eng.*, **A204**, 227

33) Loewen, K., (1996) "The Grain Size Evolution of Nanocrystalline Materials as a function of the Electrodeposited Layer Thickness", B.Sc Thesis, Queen's University, Kingston, Ontario, Canada

34) Merchant, H. K., (1995) in "Defect Structure, Morphology and Properties of Deposits", H. D. Merchant (ed.), TMS, Warrendale 1

35) Erb, U., Palumbo, G., Szpunar, B. and Aust, K. T., (1997) *Nanostr. Mat.*, **9**, 261

36) Szpunar, B., Erb, U., Palumbo, G., Aust. K. T. and Lewis, L. J., (1996) *Phys. Rev. B*, **53**, 5547

37) Hall, E. O., (1951), *Proc. Phys. Soc. London*, **B65**, 747

38) Petch, N. J., (1953) *J. Iron Steel Inst.*, **174**, 25

39) El-Sherik, A. M. and Erb, U., (1997) in "Nickel-Cobalt 97-Vol. IV, Applications and Materials Performance", F. N. Smith et al. (eds.), The Metallurgical Society of CIM, Montreal 257

40) Erb, U. and Palumbo, G., to be published

41) Hansen, M. and Anderko, K., (1958) "Constitution of Binary Alloys" McGraw Hill, New York, 1027

42) Rofagha, R., Langer, R., El-Sherik, A. M., Erb, U., Palumbo, G. and Aust, K. T., (1991) *Scripta Metall. et Mater.*, **25**, 2867

43) Rofagha, R., Langer, R., El-Sherik, A. M., Erb, U., Palumbo G. and Aust, K. T., (1992) *Mat. Res. Soc. Symp. Proc.*, **238**, 751

44) Wang, S. Rofagha, R. Roberge P. R. and Erb, U. (1995) *Electrochem. Soc. Proc.*, **95-8**, 224

45) Gonzalez, F., Brennenstuhl, A. M., Palumbo, G., Erb, U. and Lichtenberger, P. C., (1996) *Mat. Sci. Forum*, **225-227**, 831

46) Doyle, D. M., Palumbo, G., Aust, K. T., El-Sherik, A. M. and Erb, U., (1995) *Acta Metall. et Mater.*, **43** 3027

47) Palumbo, G., Gonzalez, F., Brennenstuhl, A. M., Erb, U., Shmayda W. and Lichtenberger, P. C., (1997) *Nanostr. Mat.*, **9**, 737

48) Palumbo, G., Lichtenberger, P.C., Gonzalez, F., and Brennenstuhl, A.M., US Patents: 5,527,445 (1996); 5,516,415 (1996); 5,538,615 (1996)

49) ASME Code Case 96-189-BC96-206 Case N-569; Section XI, Division 1; Alternative Rules for Repair by Electrochemical Deposition of Class 1 and 2 Steam Generator Tubing (1996).

---

- 50) Palumbo, G., King, P.J., Aust, K.T., Erb, U. and Lichtenberger, P.C., (1991) *Scripta Metall.*, **25**, 1775
- 51) Palumbo, G., Lehockey, E.M., Lin, P., Erb, U. and Aust, K.T., (1997) *Mat. Res. Soc. Symp. Proc.* **458**, 273
- 52) McCrea, J., M.A.Sc. Thesis (in progress) Department of Metallurgy and Materials Science, University of Toronto
- 53) Palumbo, G., Lehockey, E. M., Lin, P., (1998) *JOM*, **50**, 40
- 54) Palumbo, G. and Aust K. T., (1998) in "Grain Growth in Polycrystalline Materials III, Weiland, H. et al. (eds.), TMS, Warrendale, Ohio, 311

## NANOSTRUCTURED CARBON COATINGS

YURY GOGOTSI

*University of Illinois at Chicago, Department of Mechanical  
Engineering M/C 251, 842 West Taylor St., Chicago,  
IL 60607-7022  
YGogotsi@uic.edu*

### Abstract

This paper provides an overview of nanocrystalline and nanostructured carbon coatings and explores a very broad range of potentially important carbon nanostructures that may be used in future technologies. A new method for the synthesis of nanostructured carbon coatings on the surface of SiC and other metal carbides is described. This method is accomplished through the extraction of metals from carbides by supercritical water or halogens in a high temperature reactor.

This is a versatile technology because a variety of carbon structures can be obtained on the surface of carbides in the same reactor. Not only simple shapes or fibers, but also powders, whiskers and components with complex shapes and surface morphologies can be coated. This technology allows for the control of coating growth on the atomic level, monolayer by monolayer, with high accuracy and controlled structures.

Ordered and disordered graphite, nanoporous carbon (specific surface area of 1000 m<sup>2</sup>/g and more) and hard carbon can be formed depending on the temperature and gas composition. These carbon coatings can be used as tribological coatings having a low-friction coefficient for a variety of applications, from heavy-load bearings to nanocoatings for MEMS; protective coating for sensors and tools, intermediate thin films for further CVD deposition of diamond, weak coatings on SiC reinforcements for composite materials, coatings on SiC powders for improved sinterability, catalyst supports, molecular membranes for sensors, etc. The structure and properties of carbon coatings obtained on the surface of SiC have been investigated using an array of analytical techniques.

### 1. Introduction

Nanotechnology has been recognized as an emerging technology of the next century [1]. Control over the structure of materials on nanoscale can open opportunities for the development of nanocrystalline materials with controlled properties, if the structure/property relations are known. The coating industry is a major industry worldwide. Coatings are needed to prevent wear, erosion and corrosion, to provide

---

electrical or thermal insulation, to act as selective membranes, etc. There is a need for coatings with improved performance [2]. Typically, materials with the structural elements ranging from 1 to 100 nm are considered to be nanocrystalline. Such structural features are smaller by factors of 10 to 1000 compared to microcrystalline materials. This can offer potential for significant improvements or modification of certain properties, since most of them are controlled by the structural features of materials.

Carbon is among the most important and widely used materials in all areas: chemistry (catalyst support, absorbent), electrochemistry (electrodes), bioengineering (biocompatible implants), mechanical engineering (C/C composites), tribology (solid lubricant), metallurgy (crucibles and heaters), glass industry (mold coating), electronics (substrates) and in many other fields. In some of these applications, carbon coatings are as important as bulk materials, and sometimes only thin coatings can be used. For instance, carbon layers with a high specific surface area are important in catalysis and hard diamond-like modifications are useful for wear resistant parts [3, 4] as coatings with an adjustable hardness. Carbon coatings have a variety of structures, with diamond and graphite being the main industrial products. However, new carbons are challenging the traditional materials and an enormous growth of applications and manufacturing techniques have emerged in this area during the past decade. Some of them will be analyzed in this paper.

Novel carbon materials, including nanostructured films, are manufactured under severe control for purity, structure and texture to achieve the ultimate properties or give them new functions. In Japan, a New Carbon Forum was established in 1988 to coordinate all activities in the area of novel carbon materials. It consists of representatives of leading Japanese companies and selected academics, and contributes significantly to the growth of this area and in attracting increasingly significant funding. A new term Carbon Alloys [5] was introduced by Japanese scientists in 1992 to describe the variety of carbon materials, including ones containing additives of other elements. In most countries, including the US, activities in the areas of traditional carbons (graphite), diamond and fullerenes/nanotubes are separated and scientists working in these areas belong to different professional societies and rarely meet at the same conference. As a result, according to the recent assessment of R&D status and trends in nanoparticles [1], Japan is leading in the area of carbon-based nanoparticles for coating and devices, followed by Europe and then the US. This paper attempts to provide a short crosscutting overview through all areas and all kinds of nanocrystalline carbon films, both high-tech, such as nanocrystalline diamond, and low-tech, such as soot.

It is important to distinguish between “nanocrystalline” and “nanostructured” materials. Carbon is intrinsically a nanocrystalline material. Most industrial carbons, except diamond crystals, well-ordered graphite and amorphous coatings, are nanocrystalline. For example, common carbon black has a particle size of about 30 nm. Moreover, it is much easier to produce nanocrystalline carbon than a well-crystallized one. Scientists traditionally worked on obtaining large crystals, particularly in the case of diamond, to achieve the ultimate properties. Thus, the size of crystals in the nano range does not bring an advantage by itself. However, it can be advantageous in the case of the use of nanotechnology to tailor the nanostructure to satisfy property requirements.

## 2. Review of Nanostructured Carbon Coatings

### 2.1. NANOPOROUS FILMS AND HIGH SURFACE AREA MATERIALS

High surface area (300-2000 m<sup>2</sup>/g) materials are used in applications that require rapid and responsive sampling, selective separation, and catalytic processing. The growing area of chemical sensors requires new nanostructured materials, particularly thin films.

Nanoporous carbons, also often referred to as carbon molecular sieves, can be considered amorphous, that is, they have no long-range order. However, they display a remarkable regularity in the distribution of pore dimensions, having a pore size of about 0.5 nm [6]. These carbons have a requisite pore diameter to provide shape selective effects in the transport and adsorption of small molecules. TEM shows that these carbons contain "wormlike" structures. The combination of short persistence length and regions of high curvature gives rise to incoherence and structural complexity [6]. Hence, the materials are simultaneously regular (on the nanoscale and below) and x-ray amorphous. Thus, calling such carbon films amorphous is not strictly appropriate, given the regularity of structure.

### 2.2. FULLERENES

Fullerene films can be prepared by vacuum deposition on a variety of substrates [7]. Photoinduced polymerization of solid fullerene films can increase their stability to organic solvents such as boiling toluene [8]. Our recent work demonstrated the stability of fullerenes in supercritical water at temperatures of up to 500°C [9]. However, applications for these films are still to be found.

Onion-like carbon particles [10], which can be considered as giant fullerenes or their relatives, are not produced in large quantities and it is not clear what benefits can be achieved by using them. Further research into both, synthesis and property characterization of these carbon structures is required.

### 2.3. NANOTUBES AND NANOFIBERS

Single- and multiwall nanotubes represent the small-size part of this group, while graphite filaments can have diameters ranging from a few nm to hundreds of nm. Although these fibrous materials cannot be considered as a typical coating, they can be grown as a layer on a substrate (Fig. 1a) and find use in sensors, catalyst supports, etc. Moreover, carbon nanotubes are primarily grown on a substrate in fixed-bed reactors [11].

The structure of the graphite filaments can be varied from a cylindrical hollow-cored to ribbon like with stacking of graphite layers perpendicular to the ribbon surface [12]. Fishbone structure of nanotubes has been also reported [11]. Graphite nanofibers consisting of graphite platelets 3-50 nm in width are capable of sorbing and retaining in excess of 20 l/gram of hydrogen when exposed to the gas pressures of 120 atm at room temperature [13]. Carbon filaments with periodic conical internal voids (Fig. 1b,c) have been produced by decomposition of paraformaldehyde under hydrothermal conditions at

700-750°C under 100 MPa [14]. Application of nanotubes and nanofibers as catalyst support is currently considered [11].

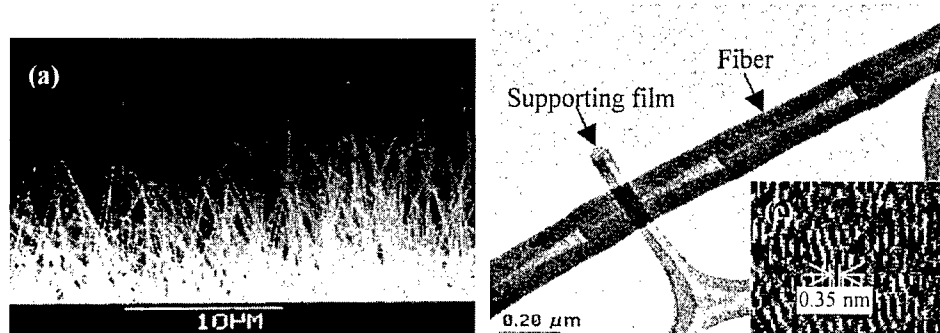


Figure 1. SEM (a) and TEM (b,c) micrographs of carbon fibers (about 200 nm thick) grown on a substrate by hydrothermal decomposition of paraformaldehyde [14].

#### 2.4. NANOCRYSTALLINE DIAMOND AND DLC FILMS

Nanocrystalline diamond films can provide very smooth coatings having high hardness and other properties of polycrystalline diamond films, and a very low friction coefficient of 0.1 or less [3].

As is shown in the work conducted at Argonne National Laboratory [15, 16] nanocrystalline diamond can be obtained from  $C_{60}$  by chemical vapor deposition (CVD). The deposition mechanism proposed is through the carbon dimer,  $C_2$ , which forms by microwave fragmentation of vapor phase  $C_{60}$  followed by growth on a heated silicon substrate. There is no incorporation of hydrogen into these nanocrystalline diamond films. This is due to the fact that it is not present in the growth environment or present in only very small quantities. High growth rates are attributed to the mechanism of direct incorporation of the  $C_2$  species into a hydrogen-free diamond lattice, which is in contrast to the mechanism of growth by adsorption of  $CH_3$  radicals which requires subsequent desorption of the hydrogen as a step in the process. The films produced in this process are nanocrystalline for which nucleation rates of  $\sim 10^{10} \text{ cm}^{-2} \text{ sec}^{-1}$  are indicated to account for the microstructure. The direct insertion of  $C_2$  dimers into (100) faces is supported by theoretical calculations [17] which also provide an explanation for the absence of a graphitic phase in this process.

The instantaneous transformation of  $C_{60}$  to bulk polycrystalline diamond under rapid nonhydrostatic compression has been reported [18]. A sample of  $C_{60}$  held in a graphite capsule was compressed in a diamond anvil with slightly non-parallel faces which applied a pressure gradient while compressing the sample to 20 GPa. The application of a pressure gradient results in non-hydrostatic stress on  $C_{60}$  molecules which collapse and undergo a phase transformation into diamond. Thin ( $\sim 5 \mu\text{m}$ ) and transparent nanocrystalline diamond films can also be obtained by shock compression of fullerene films [7]. With the fall in cost of fullerene powders, this method may become important in the future as a method to produce nanocrystalline diamond free of metal impurities.

Diamondlike carbon (DLC) films are often considered to be amorphous. These films can be deposited at lower temperatures compared to diamond. Recent work shows that if electron cyclotron resonance plasma is used, DLC films obtained at room temperature can contain nanocrystalline cubic or hexagonal diamond [19]. Amorphous DLC (a-C:H) films can be crystallized by laser treatment producing a mixture of diamond nanocrystals of 2-7 nm in size and graphite particles of 2-4 nm in size. Thus, amorphous carbon films can be nanostructured through the control of manufacturing or post-growth modification.

## 2.5. CARBON-BASED NANOCOMPOSITES

### 2.5.1. *Diamond-like Nanocomposites*

DLC coatings modified by Si and other metals are produced under the commercial name Dylyn® by Advanced Refractory Technologies [20] and are marketed in the US and worldwide. Their mechanical, electrical and optical properties can be tuned over a wide range by changing deposition conditions and composition, such as doping with metals. This kind of coating is a good example of property control achieved by material modification on the nanolevel. In particular, they have a low friction coefficient of 0.05-0.2 and excellent wear resistance.

### 2.5.2. *Silicon-containing Composites*

Up to 11% Si can be nanodispersed in CVD carbon [21]. Small clusters of a few silicon atoms are located in regions of disordered carbon, which separate small regions of organized graphene layers. This material is promising for electrode applications, particularly in advanced lithium batteries.

It is necessary to mention that most of silicon carbide materials made from polymeric precursors (Tyranno®, Blackglas®, Nicalon® and other) are in fact SiC-C-SiO<sub>x</sub> composites. Interlayers of carbon determine many properties of these important materials. Many of them are used for manufacturing protective coatings. The attractive prospect of polymer decomposition to carbon-based composites is that the polymer can first be applied in thin films and then would be transformed to carbon by laser or thermal pyrolysis.

### 2.5.3. *Encapsulated Metals and Carbides*

Synthesis of nanometer-size single crystals encapsulated in carbon cages or nanotubes has been achieved [22]. Those crystal particles are primarily carbides (WC, TaC, YC<sub>2</sub>, SiC [23] and other) and metals (Fe, Ni, Co, [24], and Pd [25]). Carbon encapsulation can help to prevent interaction of nanoparticles with the environment, accelerate sintering of carbides, or prevent grain growth during sintering. Magnetic metal or carbide particles are of interest for potential applications in which iron oxide particles are currently used: in magnetic data storage, for magnetic toner in xerography, in ferrofluids and as contrast agents in magnetic resonance imaging [26]. Several metal particles can be encapsulated in continuous carbon structures known as carbon socks [27] or in multiwall carbon nanotubes. Typically, the particles are covered by a few well-ordered layers of graphitic carbon.

## 2.6. CONVENTIONAL NANOCRYSTALLINE CARBON COATINGS

Not only high-tech carbons are nanocrystalline. There exists a large market for conventional nanocrystalline carbon coatings for a variety of applications. Fig. 2 shows a typical soot coating which can be produced by combustion of acetylene in oxygen-lean flames [28]. The average particle size is 30-50 nm. The structure of the coating can

be controlled by changing the acetylene/ oxygen ratio and flame temperature. Acetylene/oxygen ratio of about 1:1 would result in the formation of diamond if the substrate is properly cooled [29]. Polycrystalline diamond films may be grown at the rate of tens of microns per hour at atmospheric pressure. It was found that the morphology of the deposit depended on the substrate temperature and gas. Thus, flame synthesis of carbon coatings allows for control over the arrangement of carbon atoms and can produce a variety of structures from graphitic carbon to diamond.

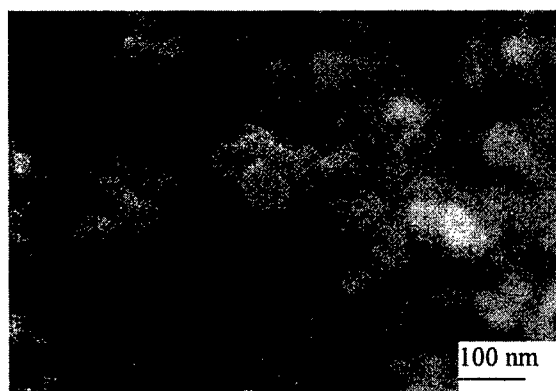


Figure 2. Field emission scanning electron micrograph (FESEM) of a soot coating produced using acetylene flame.

## 2.7. ANALYSIS OF NANOSTRUCTURED CARBON

Advanced analytical techniques must be used to study all nanocrystalline materials. However, the analysis of carbon requires considerable care and caution due to the variety of existing carbon allotropes. Analysis of nanocrystalline carbons by X-ray diffraction is usually inconclusive because many nanostructured carbons are X-ray amorphous. For this purpose electron microscopy, especially TEM combined with SAD and EELS is useful, but it is a slow and expensive method. FESEM is more valuable to examine the growth habit of larger structures ( $> 10$  nm). AFM can be a valuable tool for surface studies as well.

Investigators generally apply Raman spectroscopy to study carbons due to its speed and simplicity of use. Diamond gives a sharp peak at  $1332\text{ cm}^{-1}$  [30], which is shifted to lower wavenumbers and accompanied by a band at about  $1140\text{ cm}^{-1}$  in the nanocrystalline state [31]. Nanocrystalline graphite gives bands at  $\sim 1580\text{ cm}^{-1}$  (G-band) and  $\sim 1355\text{ cm}^{-1}$  (D-band). The D-band is reported to occur over the range 1343-1360 using the 514 nm wavelength excitation [32] depending on the degree of disorder and/or stress. The G-band at  $1582\text{ cm}^{-1}$  appears to shift up with increasing disorder. The degree of graphitization has been correlated to the ratio of intensities of the G and D-bands [33], where in highly amorphous carbon, the D-band is stronger than the G-band. Recent analysis of graphitic carbons has explored the linear dependence of the D-band on the laser excitation energy [34]. Conventional visible wavelength Raman

spectroscopy fails to determine nanocrystalline diamond when it is mixed with graphite. In this case, UV excitation Raman spectroscopy can provide greater sensitivity [35].

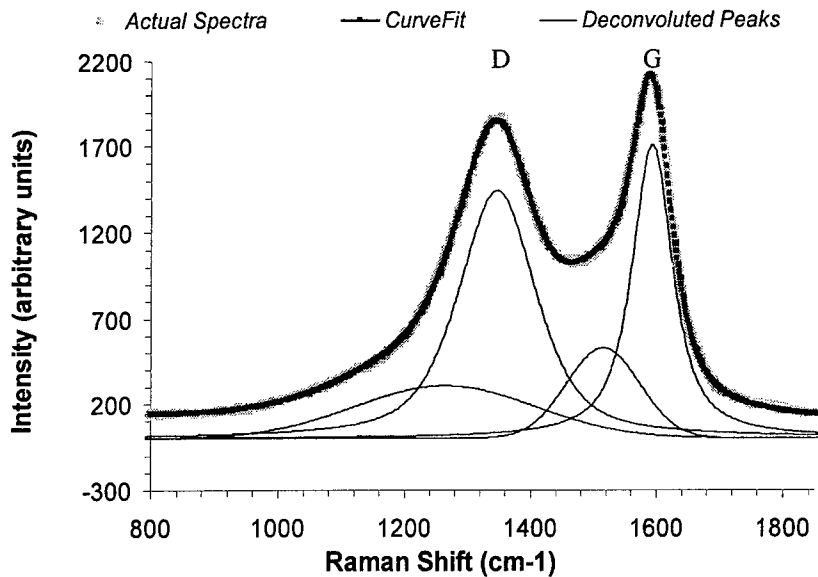


Figure 3. Deconvoluted Raman spectra for a sintered SiC specimen treated in 3.5%  $\text{Cl}_2$ -Ar for 5 hours at 1000°C [36].

A typical spectrum of nanocrystalline carbon in Fig. 3 shows characteristic D ( $1343 \text{ cm}^{-1}$ ) and G ( $1600 \text{ cm}^{-1}$ ) bands for graphite, however, detailed examination of the spectrum shows that its shape cannot be accurately matched by these two bands alone. Better agreement was achieved when the spectrum was deconvoluted with the addition of two broad bands centered at  $1225 \text{ cm}^{-1}$  and  $1500 \text{ cm}^{-1}$ . These bands are associated with disorder in carbon, and are consistent with nanocrystalline or amorphous graphite or with  $sp^3$  bonding which would provide improved hardness, exceeding that of SiC, to the carbon layer [36].

Fullerenes [9] and single wall carbon nanotubes [37] have characteristic Raman spectra with multiple bands, while Raman spectra of multiwall nanotubes are similar to that of nanocrystalline graphitic carbon.

### 3. Synthesis of Carbon Coatings by Selective Leaching of Carbides

Many carbon coatings are applied to the surface of carbides. Carbide ceramics such as SiC,  $\text{B}_4\text{C}$ , WC and TiC have good wear resistance and find a number of applications because of their high hardness. However, their dry friction coefficient is about 0.6-0.7. Better tribological performance can be expected if the ceramic is coated with a carbon film to reduce the friction coefficient. Tungsten carbide tools are often coated with diamond films to reduce the wear. Mechanical and chemical stability are also limiting

factors for high surface area materials and new methods of synthesis can help to overcome this problem.

In particular, the nanostructured carbon coatings obtained on the surface of silicon carbide can be used for the following purposes:

- Diamond coatings would be important in SiC electronic devices, as protective coating for sensors and tools, for “diamondization” of SiC powders for abrasive applications, and intermediate thin films for further CVD deposition of diamond.
- Ordered and disordered graphitic carbon coatings can be used on SiC reinforcements for composite materials (fibers, whiskers, platelets), as tribological coatings for a variety of applications (e.g., seals), and coatings on SiC powders for improved sinterability.
- Nanoporous carbon coatings (specific surface area of 1000 m<sup>2</sup>/g and more) can be used as catalyst supports, molecular membranes for sensors, or interlayers for the micro-joining of SiC components to Si wafers through reacting carbon with Si.
- Hydrogenated (a-C:H) and diamond-like carbon films have potential as tribological coatings having a low-friction coefficient for a variety of applications, from heavy-load bearings to nanocoatings for MEMS.

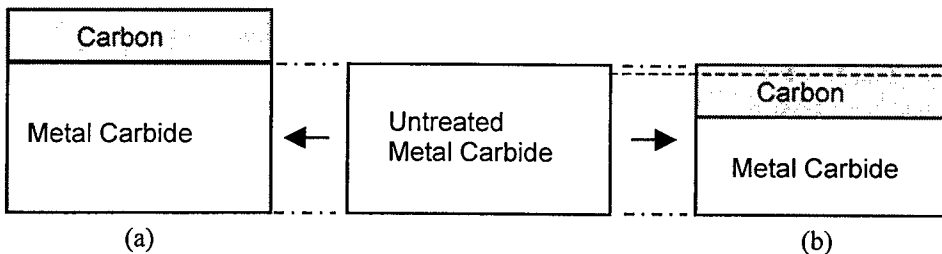


Figure 4. Carbon coating via vapor deposition (a) and selective leaching of carbides (b).

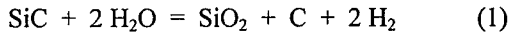
CVD or physical vapor deposition PVD are used to obtain a variety of carbon coatings ranging from diamond to graphite and amorphous carbon. However, adhesion of vapor deposited coatings is always a problem. Additionally, the size of the coated component increases (Fig. 4a) which is not always desirable, especially when these objects are thin, e.g., SiC fibers or MEMS devices. There is no current technology allowing to produce uniform carbon coatings within pores in a porous ceramic body, or on whiskers/platelets/fiber preforms without bridging the particles/fibers. Thus, the search for new methods of producing nanostructured carbon coatings continues.

Since carbides contain carbon in their structure, it is possible to produce a carbon coating by leaching the metal and leaving carbon layer behind. Such coating is not deposited onto the surface, rather the surface is transformed into carbon (Fig. 4b). As a result, the thickness of the coated component does not increase. It remains the same or decreases slightly. The structure and composition of the coating can be controlled with high precision, leaching metal layer by layer. This technique is particularly good for nanostructured coatings. We suggested this method 5 years ago, using supercritical

water for leaching [38], and later expanded it for the use of halogens [39]. A brief overview of the structure of nanocrystalline coatings produced by leaching carbides will be given in the following sections.

### 3.1. HYDROTHERMAL SYNTHESIS

Hydrothermal leaching of silicon carbide has been studied in detail [38], [40-44]. In these experiments, SiC samples were placed in capsules with distilled water and treated at temperatures of 300-850°C and pressures of 10-500 MPa. The following reaction was predicted by thermodynamic calculations [45] for the Si-C-H-O system to lead to solid carbon formation:



This reaction is thermodynamically favored at relatively low water/carbon ratios. The critical factor here is that as soon as silica is formed, it dissolves in the fluid. Thus, the reaction (1) tends to move further to the right, leading to the growth of the carbon coating.

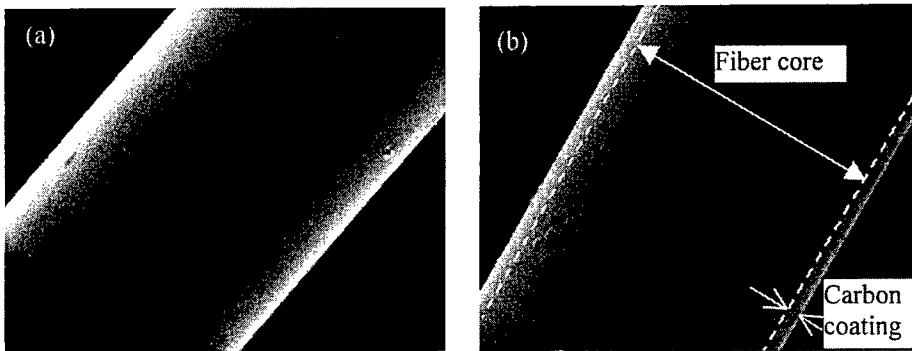
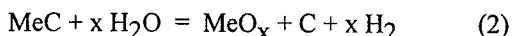


Figure 5. Typical SEM micrographs of a desized Tyranno® SiC fiber (a) and a fiber after hydrothermal treatment at 400°C. The fiber shown in (b) has a carbon coating of about 500 nm, but the surface roughness did not change after treatment. Fiber diameter is 11  $\mu\text{m}$ .

Carbon formation during hydrothermal leaching of SiC demonstrates that the hydrothermal method can be useful for producing carbon coatings. In particular, we used this approach to obtain carbon coatings on SiC fibers (Fig. 5) and particles [43]. Carbon films on SiC fibers with thickness of 10 nm to 1  $\mu\text{m}$  were obtained and used for interfacial engineering in ceramic matrix composites, to ensure fiber pull-out and gracious fracture of composites [46]. The treatment temperature can be reduced from 350-400°C to 250°C by using alkaline solutions instead of pure water [47]. The carbon layer produced is very smooth and uniform (Fig. 5b). AFM study [48] showed that the surface topology of the fiber remains unchanged after leaching. This is possible because the size of graphite crystallites, according to Raman spectroscopy analysis, does not exceed 5 nm and is typically about 2 nm. Thus, removal of Si as  $\text{Si}(\text{OH})_4$  or similar species at low temperatures does not cause collapse of crystals producing a nanoporous films similar to those described in Section 2.1. A similar shape retention was observed

for SiC powders, even when those were completely transformed to carbon [23]. TEM analysis showed that SiC powders can be coated with 3-4 monolayers of graphite providing carbon encapsulation [23] described in Section 2.5.3.

This method can potentially be applied to other carbides as well [45]. The reaction (1) can be written in the general form for hydrothermal leaching of carbides with the formation of carbon as following:



The use of large-volume autoclaves instead of small pressure vessels that were used in our experiments can make this method attractive for industrial use. However, the hydrothermal method can only be applied to the carbides that form soluble or volatile hydroxides, e.g.,  $\text{Si}(\text{OH})_4$ . This limits the range of materials to be coated. Thermodynamic analysis [39] predicts that the extraction of metals from carbides by halogens (e.g.,  $\text{Cl}_2$ ) or their compounds (e.g.,  $\text{HCl}$ ) can also lead to the formation of free carbon. This method can be used to obtain carbon coatings on TiC and other carbides that form volatile halides, but do not form soluble or volatile oxides.

### 3.2. LEACHING BY HALOGENS

Carbon films can be produced on SiC surfaces by high temperature chlorination because  $\text{SiCl}_4$  is more thermodynamically stable than  $\text{CCl}_4$  at elevated temperatures, so that chlorine reacts selectively with the Si at SiC surfaces according to the reactions:



leaving carbon behind. The structure of the carbon layer is affected by temperature and the composition of the chlorinating gas mixture. Carbon films have been produced on  $\beta$ -SiC powders [39] as well as SiC based fibers [46] and monolithic CVD and sintered ceramics [49] exposed to  $\text{Ar}-\text{H}_2-\text{Cl}_2$  gas mixtures at atmospheric pressure at temperatures between 600 and 1000°C.

After a treatment of  $\beta$ -SiC in 3.5%  $\text{Cl}_2$  at 600°C (Fig. 6a), the XRD pattern was similar to that of as-received powder. After reacting with 3.5%  $\text{Cl}_2$ -Ar at 800°C and 1000°C (Fig. 6b) the intensity of  $\beta$ -SiC reflections diminished and they disappeared with increasing reaction time. However, no other peaks were detected. Only long-term treatment of bulk ceramics resulted in some well-crystallized graphite that could be detected by XRD.

In the Raman spectra of the powders treated in 3.5 %  $\text{Cl}_2$  at 600°C and 1000°C, bands of disordered graphite were observed (Fig. 3). The average size of graphite crystallites formed in the treatment with 3.5%  $\text{Cl}_2$  was estimated as 2-4 nm (Table 1) using the Tuinstra-Koenig equation [33].

The TEM micrographs show that as the temperature increases, thicker and better ordered carbon films grow due to the reaction with  $\text{Cl}_2$  atmosphere (Fig. 6b). These films produce electron diffraction patterns of graphite.

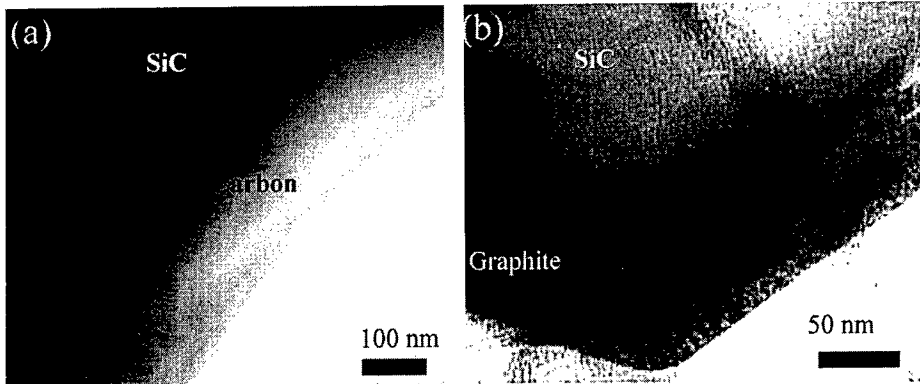


Figure 6. Bright field TEM micrographs showing an amorphous carbon film on  $\beta$ -SiC after treatment in Ar/3.5%Cl<sub>2</sub> at 600°C for 27 hrs (a) and a graphitic film after treatment at 1000°C for 72 h (b) [39].

TABLE 1. Surface area and size of graphite crystallites in SiC powders treated in Ar/Cl<sub>2</sub> and Cl<sub>2</sub>/H<sub>2</sub> gases [39].

Experimental conditions			BET measured specific surface of powder (m <sup>2</sup> /g)	Carbon content (%)	Calculated surface area of carbon (m <sup>2</sup> /g)	L <sub>a</sub> (nm)
Gas	Temp. (°C)	Time (hrs)				
3.5% Cl <sub>2</sub> /Ar	600	27	48	8	400	2.0 - 2.5
3.5% Cl <sub>2</sub> /Ar	600	48	140	11	1163	2.4 - 2.6
3.5% Cl <sub>2</sub> /Ar	1000	20	990	98	1010	2.0 - 4.5
2%Cl <sub>2</sub> /2%H <sub>2</sub> /Ar	1000	72	12	< 5	10	1.0 - 4.5
As-received $\beta$ -SiC			13	< 3		2.0

It can be seen in Table 1 that the powder treated at 1000°C in Cl<sub>2</sub> has a specific surface area in excess of 1000 m<sup>2</sup>/g. This value is typical for nanoporous carbons (Section 2.1). Other experiments with Cl<sub>2</sub> produced powders with the surface area of 100-200 m<sup>2</sup>/g. However, these powders contained various amounts of non-reacted SiC. To determine the carbon content in the powders, the samples treated with the Cl<sub>2</sub> gas were oxidized in air in a temperature range from room temperature to 750°C and the weight changes were measured by TGA [39]. We found that all porous carbon coatings on SiC particles have a high surface area, but the surface area increases with increasing time and/or temperature of the treatment in Cl<sub>2</sub> (Table 1), probably due to slow etching of carbon.

Carbon films have also been formed on the surfaces of commercially available monolithic SiC specimens by high temperature chlorination at atmospheric pressure in Ar-Cl<sub>2</sub> and Ar-H<sub>2</sub>-Cl<sub>2</sub> gas mixtures [49]. The carbon film forms in two layers, with the outer layer being a loosely adherent, coarse graphitic carbon. The lower layer, which is strongly adherent to the SiC, is nanocrystalline and hard. Raman spectroscopy and X-ray diffraction identified it as highly disordered carbon with characteristics of nanocrystalline graphite. Pin-on-disk tribology testing using a spherical silicon nitride

indenter showed that the presence of this layer reduced the friction coefficient by a factor of approximately six and the wear rate by more than an order of magnitude [36].

The kinetics of the growth of the dense carbon layer on SiC at 1000°C was found to be linear with time up to thickness in excess of 50  $\mu\text{m}$ . This suggests the chemical reaction controlled process and not a diffusion controlled one [49]. Thus, the carbon film allows penetration of  $\text{CCl}_4$  molecules through the layer as thick as 50  $\mu\text{m}$  and is expected to be a nanoporous film. However, since the size of the  $\text{SiCl}_4$  molecule is smaller than that of a hydrated silica molecule penetrating through the carbon layer in the case of hydrothermal leaching, the carbon film is expected to have a smaller pore size and hence, higher mechanical strength. Again, TiC and other carbides can be coated as thermodynamic modeling and preliminary experiments show [50].

### 3.3. DISCUSSION

We summarized typical carbon nanostructures that we observed in leaching experiments in Fig. 7. Although we observed all these structures in our experiments, this paper does not give us enough space to explain why and how this variety of carbon structure is formed. Reactions (1-4) lead to the formation of free carbon, that may maintain the  $sp^3$ -structure which it has in carbide and form diamond. Alternatively, it can be transformed to the graphite, which is thermodynamically stable under these pressures or form various amorphous or disordered structures intermediate to diamond and graphite. By changing the experimental conditions, it is possible to tune the structure of the coating. For example, high temperatures will favor the formation of graphite, while amorphous coatings will be formed at low temperatures, when surface reconstruction is slow. Presence of hydrogen in the environment will stabilize  $sp^3$  bonding leading to the formation of diamond or DLC [39, 51].

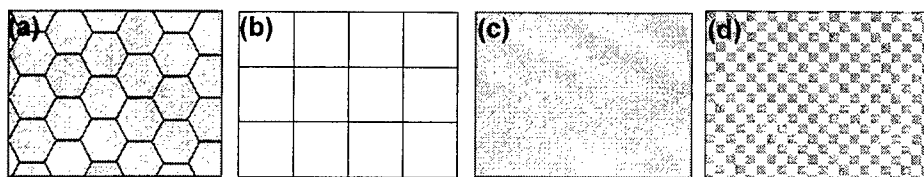


Figure 7. Schematic presentation of structures of carbon films that can be produced by leaching carbides. a - graphite, b - diamond or hard carbon, c - uniform amorphous carbon, d - nanoporous films with controlled pore size and surface area.

If the carbon atoms stay on their sites after metal is extracted from the lattice, one-dimensional growth of a porous carbon structure with a pore size comparable to the lattice parameter of the carbide substrate or molecules of the gaseous species that escape from the reaction interface. Thus, by changing the carbide we change the distance between the carbon atoms in the structure (Fig. 8) and the size of gaseous  $\text{MeCl}_x$  molecules penetrating through the film. By replacing chlorine with other halogens (F, Br or I) or supercritical water we gain additional control over the porous structure of the

film. Thus, it should be possible to control the pore size by selecting an appropriate gas/carbide couple.

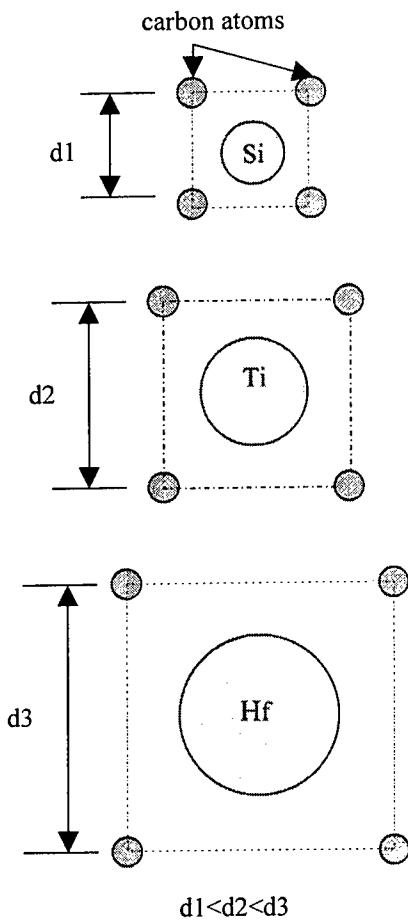


Figure 8. Structural templating of nanoporous carbon films.

approach has been demonstrated using SiC as an example. Supercritical water and chlorine were used for leaching a variety of SiC materials.

It has been shown that hydrothermal leaching produces smooth and uniform carbon films on SiC. Similar coatings have been obtained through the chlorination of SiC. Thermodynamic simulation shows that the suggested method can be applied to a variety of carbides, and other halogens can be used.

It allows us to solve the problems of uniformity and adherence of coatings, as well as avoid the bridging of filaments and/or particles. The principal difference between the

Differences in the composition and structure of carbide materials determine the differences in the reaction kinetics in different environments and structure of the coating. In general, the hydrothermal method worked better for polymer derived fibers. Extraction of silicon by chlorine was more efficient for CVD fibers and monolithic ceramics.

Synthesis of carbon coatings by leaching carbides is potentially an inexpensive technology because:

- The process is conducted at moderate or ambient pressures;
- It does not require plasma or other high-energy sources;
- The process can be scaled up to virtually any volume.

This is a more versatile process than CVD or PVD synthesis because:

- Almost any possible carbon structure can be obtained;
- Fibers, powders, whiskers and platelets, as well as complex shapes can be coated.

#### 4. Conclusions

A new approach to the synthesis of carbon coatings on the surface of carbides has been developed. It is based on the idea of extracting metal atoms from the surface layer of carbides and subsequent conversion of the carbide surface into carbon. This

described method and other approaches is that the coating is not deposited on the surface of the carbide; rather the carbide surface is converted into carbon. This method can provide a simple and inexpensive route to carbon coatings (thickness from 1 nm to 100  $\mu\text{m}$ ) for a wide range of applications. Depending on the carbide substrate and the experimental conditions, dense or porous carbon coatings with a varying  $\text{sp}^2/\text{sp}^3$  carbon ration can be produced.

## Acknowledgments

Experimental help of UIC students Joseph Libera, Daniel Ersoy and Yvonne Aratyn is appreciated. I wish to acknowledge fruitful cooperation with Prof. M. Yoshimura, Tokyo Institute of Technology, Prof. K.G. Nickel, University of Tübingen, and Prof. M. McNallan, University of Illinois at Chicago. This research was supported in part by the National Science Foundation under Grant # CMS-9813400 and the Research Institute of Solvothermal Technology via the Tokyo Institute of Technology, Japan.

## References

1. Siegel, R.W., Hu, E., and Roco, M.C. (eds.) (1998) *R&D Status and Trends in Nanoparticles, Nanostructured Materials, and Nanodevices in the United States*. International Technol. Res. Inst: Baltimore.
2. Gell, M. (1997) Nanostructured Coatings, in *R&D Status and Trends in Nanoparticles, Nanostructured Materials, and Nanodevices in the United States*. Washington, DC: International Technol. Res. Inst. pp. 124-130.
3. Erdemir, A., Bindal, C., Fenske, G.R., Zuiker, C., Csensits, R., Krauss, A.R., and Gruen, D.M. (1996) Tribological Characterization of Smooth Diamond Films Grown in Ar-C<sub>60</sub> and Ar-CH<sub>4</sub> Plasmas, *Diam. Films Techn.*, **6**, 31-47.
4. Bull, S.J. (1995) Tribology of Carbon Coatings: DLC, Diamond and Beyond, *Diam. Rel. Mater.*, **4**, 827-835.
5. Yasuda, E. (ed.) (1998) *Carbon Alloys*. Satellite meeting of Carbon '98, Nov. 12, 1998. Tokyo Institute of Technology: Tokyo.
6. Eckert, J. (1999) Partially Disordered Inorganic Materials, *MRS Bulletin* (May), 31-41.
7. Hirai, H., Kondo, K., Kim, M., Koinuma, H., Kurashima, K., and Bando, Y. (1997) Transparent Nanocrystalline Diamond Ceramics Fabricated from C<sub>60</sub> Fullerene by Shock Compression, *Appl. Phys. Lett.*, **71**(20), 3016-3018.
8. Rao, A.M., Zhou, P., Wang, K.A., Hager, G.T., Holden, J.M., Wang, Y., Lee, W.-T., Bi, X.-X., Elkund, P.C., Cornett, D.S. (1993) Photoinduced Polymerization of Solid C<sub>60</sub> Films, *Science*, **259**, 955-957.
9. Suchanek, W.L., Yoshimura, M., and Gogotsi, Y.G. (1999) Stability of Fullerenes under Hydrothermal Conditions, *J. Mater. Res.*, **14**(2), 323-326.
10. Zhang, M., He, D.W., Ji, L., Wei, B.Q., Wu, D.H., Zhang, X.Y., Xu, Y.F., and Wang, W.K. (1998) Macroscopic Synthesis of Onion-like Graphitic Particles, *NanoStructured Materials*, **10**(2), 291-297.
11. de Jong, K.P. (1999) Synthesis of Supported Catalysts, *Current Opinion in Solid State and Materials Science*, **4**, 55-62.
12. Murayama, H. and Maeda, T. (1990) A Novel Form of Filamentous Graphite, *Nature*, **345**, 791-793.
13. Chambers, A., Park, C., Baker, R.T.K., and Rodriguez, N.M. (1998) Hydrogen Storage in Graphite Nanofibers, *J. Phys. Chemistry B*, **102**(22), 4253-4256.

14. Gogotsi, Y.G. and Nickel, K.G. (1998) Formation of Filamentous Carbon from Paraformaldehyde under High Temperatures and Pressures, *Carbon*, **36**(7), 937-942.
15. Gruen, D.M. (1994) Diamonds from Dust, *Mater. Tech.*, **9**, 149-151.
16. Gruen, D.M., Liu, S., Krauss, A.R., and Pan, X. (1994) Buckyball Microwave Plasmas: Fragmentation and Diamond-film Growth, *J. Appl. Phys.*, **75**(3), 1758-1763.
17. Redefern, P.C., Horner, D.A., Curtiss, L.A., and Gruen, D.M. (1996) Theoretical Studies of Growth of Diamond (110) from Dicarbon, *J. Phys. Chem.*, **100**, 11654-11663.
18. Regueiro, M.N., Monceau, P., and Hodeau, J.-L. (1992) Crushing C<sub>60</sub> to Diamond at Room Temperature, *Nature*, **355**, 237-239.
19. Zarabian, M., Fourches-Coulon, N., Turban, G., Marhic, C., and Lancin, M. (1997) Observation of Nanocrystalline Diamond in Diamondlike Carbon Films Deposited at Room Temperature in Electron Cyclotron Resonance Plasma, *Appl. Phys. Lett.*, **70**(19), 253-255.
20. ART (1999) DYLYN® - A New Family of Diamond-Like Coatings, Advanced Refractory Technologies, <http://www.art-inc.com/products/coatings.html>
21. Wilson, A.M., Way, B.M., Dahn, J.R., and van Buuren, T. (1995) Nanodispersed Silicon in Pregraphitic Carbons, *J. Appl. Phys.*, **77**(6), 2363-2369.
22. Yosida, Y., Shida, S., and Ohsuna, T. (1994) Synthesis, Identification, and Growth Mechanism of Fe, Ni, and Co Crystals Encapsulated in Multiwalled Carbon Nanocages., *J. Appl. Phys.*, **76**(8), 4533-4539.
23. Gogotsi, Y.G., Nickel, K.G., Bahloul-Hourlier, D., Merle-Mejean, T., Khomenko, G.E., and Skjerlie, K.P. (1996) Structure of Carbon Produced by Hydrothermal Treatment of β-SiC Powder, *J. Mater. Chem.*, **6**(4), 595-604.
24. Li, Z.Q., Zhang, H.F., Zhang, X.B., Wang, Y.Q., and Wu, X.J. (1998) Nanocrystalline Tungsten Carbide Encapsulated in Carbon Shells, *NanoStructured Mater.*, **10**(2), 179-184.
25. Wang, Y. (1994) Encapsulation of Palladium Crystallites in Carbon and Formation of Wormlike Nanostructures, *J. Am. Chem. Soc.*, **116**, 397-398.
26. Nuhfer, N.T., Graef, M.D., McHenry, M.E., Majetich, S.A., Artman, J.O., and Staley, S.W. (1994) Electron Microscopy Study of Carbon Coated Magnetic Nanoparticles Produced by the Kratschmer-Arc Process, in *13th Internat. Congress on Electron Microscopy*. Paris, France: Les editions de physique. pp. 313-314.
27. Botton, G.A., Burnell, G., Humphreys, C.J., Yadav, T., and Withers, J.C. (1994) From Carbon Socks to Web-like Wires: The Microstructure of Multi-Metal Filled Carbon Nanostructures by TEM and EELS, in *13th International Congress on Electron Microscopy*. Les editions de physique. pp. 321-322.
28. Libera, J. and Gogotsi, Y., (1999) Characterization of Flame Deposited Carbon Soot Films, University of Illinois at Chicago, Chicago, Nonpublished work.
29. Zhang, B. and Chen, S. (1996) Morphological Evolution of Diamonds in Combustion Synthesis, *J. Appl. Phys.*, **79**(9), 7241-7247.
30. Badzian, A. and Badzian, T. (1993) Diamond Homoepitaxy by Chemical Vapor Deposition, *Diamond and Related Materials*, **2**, 147-157.
31. Nemanich, R. J., Glass, J. T., Lucovsky, G. and Shroder, R. E. (1988) Raman Scattering Characterization of Carbon Bonding in Diamond and Diamondlike Films, *J. Vac. Sci. Technol. A*, **6** (3), 1783-1787.
32. Basca, W.S. (1994) Diamond-Like Carbon Bonds, *Science*, **266**, 1256.
33. Tuinstra, F. and Koenig, J.L. (1970) Raman Spectrum of Graphite, *J. Chem. Physics*, **53**(3), 1126-1130.
34. Pocsik, I., Hundhausen, M., Koos, M., and Ley, L. (1998) Origin of the D peak in the Raman Spectrum of Microcrystalline Graphite., *J. Non-Crystalline Solids*, **227-230**, 1083-1086.

---

35. Prawer, S., Nugent, K.W., and Jamieson, D.N. (1998) The Raman Spectrum of Amorphous Diamond, *Diamond and Related Materials*, **7**, 106-110.

36. Ersoy, D.A., McNallan, M.J., and Gogotsi, Y. (1999) Characterization of Carbon Produced by High Temperature Chlorination of SiC, in *196th Meeting of The Electrochemical Society*. Honolulu, Hawaii: The Electrochemical Society. (in press).

37. Dresselhaus, M.S., Pimenta, M.A., Marucci, A., Matthews, M.J., Brown, S.D.M., Rao, A.M., Eklund, P.C., Dresselhaus, G., Saito, R., and Endo, M. (1998) Raman Scattering as a Characterization Tool for New Forms of Carbon, *Extended Abstracts, International Symposium on Carbon*. Tokyo, Japan, Carbon Soc. Japan. pp. 94-95.

38. Gogotsi, Y.G. and Yoshimura, M. (1994) Formation of Carbon Films on Carbides under Hydrothermal Conditions, *Nature*, **367**, 628-630.

39. Gogotsi, Y.G., Jeon, J.D., and McNallan, M.J. (1997) Carbon Coatings on Silicon Carbide by Reaction with Chlorine-Containing Gases, *J. Mater. Chem.*, **7**(9), 1841-1848.

40. Gogotsi, Y.G. (1994) Hydrothermale Korrosion von SiC - Betrachtung der schädlichen und nützlichen Aspekte, in *Korrosion und Verschleiss von keramischen Werkstoffen*. Aachen: Deutsche Keramische Gesellschaft. pp. 114-122.

41. Gogotsi, Y.G., Kofstad, P., Yoshimura, M., and Nickel, K.G. (1996) Formation of  $sp^3$  - bonded carbon upon hydrothermal treatment of SiC, *Diamond and Related Materials*, **5**, 151-162.

42. Kraft, T., Nickel, K.G. and Gogotsi, Y.G. (1998) Hydrothermal Degradation of CVD SiC Fibers, *J. Mater. Sci.*, **33**, 4357-4364

43. Gogotsi, Y.G., Yoshimura, M., Kakihana, M., Kanno, Y., and Shibuya, M. (1995) Hydrothermal Synthesis of Carbon Films on SiC Fibers and Particles, in *Ceramic Processing Science and Technology*, H. Hausner, G.L. Messing, and S.-I. Hirano (Eds.), Am. Ceram. Soc., Westerville, OH, pp. 243-247.

44. Roy, R., Ravichandran, D., Badzian, A., and Breval, E. (1996) Attempted Hydrothermal Synthesis of Diamond by Hydrolysis of beta-SiC Powder, *Diamond Relat. Mater.*, **5**, 973 - 976.

45. Jacobson, N.S., Gogotsi, Y.G., and Yoshimura, M. (1995) Thermodynamic and Experimental Study of Carbon Formation on Carbides under Hydrothermal Conditions, *J. Mater. Chem.*, **5**(4), 595-601.

46. Gogotsi, Y., Welz, S., Daghfal, J., McNallan, M.J., Jeon, I.D., Nickel, K.G., and Kraft, T. (1998) Formation of Carbon Coatings on SiC Fibers by Selective Etching in Halogens and Supercritical Water, *Ceram. Eng. Sci. Proc.*, **19**(3), 87-94.

47. Yoshimura, M., Sakai, K., Nakagawa, Y., Hara, T., Gogotsi, Y., Yamamoto, S., Yashima, M., Kakihana, M., Kanno, Y., and Shibuya, M. (1998) Dense Carbon Coating on Silicon Carbide Fibers by Hydrothermal Treatment, in *Extended Abstracts, Internat. Symp. on Carbon*. Tokyo, Carbon Soc. of Japan. pp. 552-553.

48. Gogotsi, Y.G. (1997) Formation of Carbon Coatings on Carbide Fibers and Particles by Disproportionation Reactions, in *NATO ARW: Advanced Multilayered and Fiber-Reinforced Composites*. Dordrecht: Kluwer. pp. 217-230.

49. Ersoy, D.A., McNallan, M.J., and Gogotsi, Y. (1998) High Temperature Chlorination of SiC for Preparation of Tribological Carbon Films, in *Electrochemical Society Proceedings*. Vol. 98-9, Ed. P.Y. Hou et al., pp. 324-333.

50. McNallan, M., Gogotsi, Y., and Jeon, I.D. (1998) Formation of Carbon Films on Ceramic Carbides by High Temperature Chlorination, in *Tribology Issues and Opportunities in MEMS*, Ed. B. Bhushan, Kluwer, Dordrecht pp. 559-565.

51. Gogotsi, Y.G., Kofstad, P., Nickel, K.G., and Yoshimura, M. (1996) Formation of  $sp^3$ -Bonded Carbon upon Hydrothermal Treatment of SiC, *Diamond and Relat. Mater.*, **5**(2), 151-162.

---

## SEMICONDUCTOR QUANTUM DOT HETEROSTRUCTURES (GROWTH AND APPLICATIONS)

V.M.USTINOV

*A.F.Ioffe Physico-Technical Institute  
Politekhnicheskaya 26, 194021 St. Petersburg, Russia*

### Abstract

The reduction of dimensionality of the carrier motion in quantum nanostructures brings new, interesting effects in semiconductor physics. In addition, it opens an exciting possibility of improving the device performance. It has been predicted that the delta-function like density of states inherent for the objects with three-dimensional quantum confinement (quantum dots) should lead to the decrease in threshold current density, and improvement of its temperature stability (for semiconductor injection lasers when the quantum dot heterostructures are used as an active region).

In the present work we discuss the synthesis of InAs/GaAs quantum dots by using self-organization phenomena at the initial stages of strained layer heteroepitaxy. We show that the driving force for the island formation is strain accumulating during the deposition of the lattice mismatched material. Quantum dot size and shape are presented and their optical properties are discussed. The characteristics of quantum dot injection lasers are shown. The ways to reduce threshold current density and improve its temperature stability are demonstrated. The band-gap and strain engineering are shown to be effective tools for controlling the quantum dot optical emission range.

### 1. Introduction

When the motion of charge carriers is confined by the size of the order of de-Broigle wavelength of the particle the energy spectrum and other main characteristics of the system shows size dependence. This is a manifestation of the quantum size effect.

Semiconductor devices whose operation is based on the quantum size effect are currently widely used in various applications. For example, semiconductor diode lasers are used in optical fiber communications and compact disc players, high electron mobility transistors are used in satellite communication systems, etc. In these devices quantum size effect manifests itself in one direction, i.e. in the direction normal to the structure surface. Meanwhile, in the plane of the semiconductor layer the carrier motion is free. The new breakthrough in characteristics of semiconductor devices and appearance of new applications are associated with semiconductor structures where quantum size effect manifests itself in all three directions. These structures are called quantum dots (QDs).

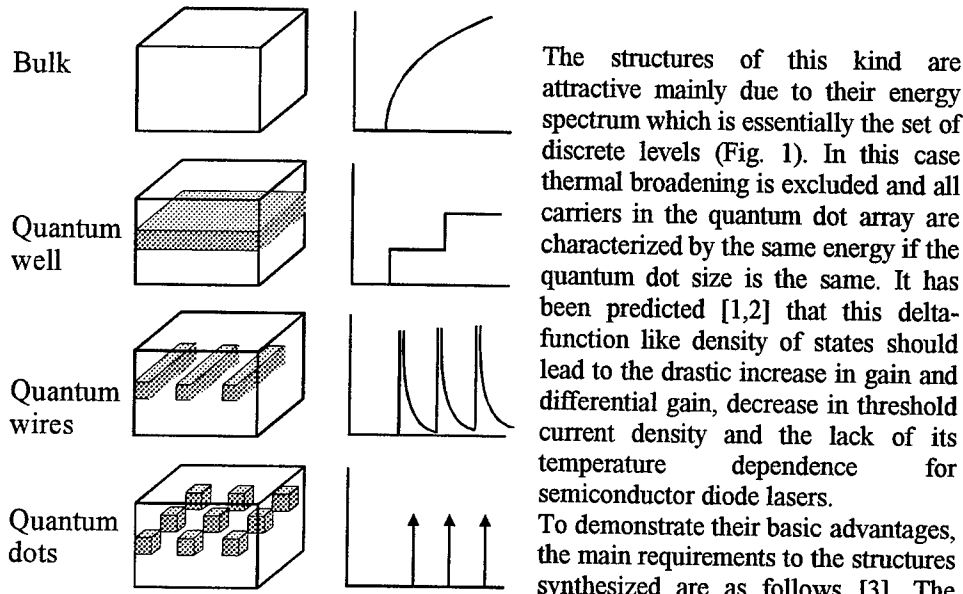


Figure 1. Effect of size quantization on density of states.

The structures of this kind are attractive mainly due to their energy spectrum which is essentially the set of discrete levels (Fig. 1). In this case thermal broadening is excluded and all carriers in the quantum dot array are characterized by the same energy if the quantum dot size is the same. It has been predicted [1,2] that this delta-function like density of states should lead to the drastic increase in gain and differential gain, decrease in threshold current density and the lack of its temperature dependence for semiconductor diode lasers.

To demonstrate their basic advantages, the main requirements to the structures synthesized are as follows [3]. The minimal size of a quantum dot is determined by the presence of at least one confined state. The maximal size

is limited by the lack of thermal population of adjacent states in a quantum dot. In addition, device applications exclude the exceptional amount of defects and dislocations as well as considerable interface recombination velocity. The quantum dot array should be uniformly dense to provide sufficient gain, since strong fluctuations in quantum dot size and shape would lead to the strong broadening of the spectrum. Extremely important is also the possibility for the matrix to provide the current flow and collection of carriers into the quantum dot states.

In the present work we discuss the synthesis of semiconductor quantum dots by using the effect of spontaneous transformation of the growth surface at the initial stages of lattice mismatched heteroepitaxy. The alternative methods of formation of quantum dots (e.g. etching the quantum well structures, growth in V-grooves or glass matrices) are beyond the scope of this work. Optical properties of self-organized quantum dots and their applications in diode lasers will also be discussed.

## 2. Synthesis of InAs/GaAs self-organized quantum dots

### 2.1. EPITAXIAL GROWTH MODES

Three possible mechanisms have been described so far in the theory of epitaxial growth: layer by layer or Frank van der Merwe (FvdM) growth mode, island or Volmer-Weber (VW), and island combined with layer or Stranski-Krastanov (SK) growth mode, Fig. 2. The type of epitaxial growth will be determined by the interface energy parameters and lattice mismatch. If the epitaxial layer and the substrate are lattice matched, the islands will be formed provided the surface energy of the substrate is less than the surface

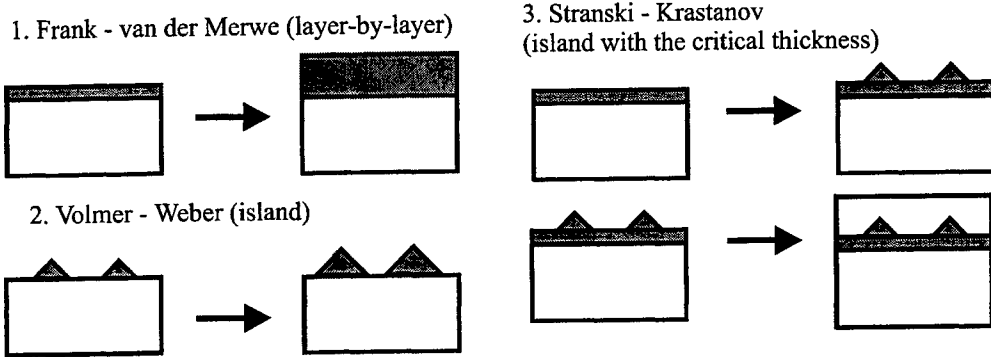


Figure 2. Possible mechanisms of epitaxial growth.

energy of the epitaxial layer and the interface energy. Variation of this energy relation leads to change in the growth from the VW to the FvdM mode. If the epitaxial layer and the substrate are lattice mismatched the growth initially proceeds in a layer by layer mode. However, increasing the layer thickness leads to the accumulation of large strain energy and it becomes energetically favorable for the system to reduce its energy by the formation of isolated islands due to strain relaxation. In the theory of the SK growth this process should be accompanied by the formation of misfit dislocations at the interface. However, it has been shown that for the lattice mismatched growth of semiconductors (e.g., Ge/Si, InAs/GaAs, etc) the critical layer thickness for the island growth is less than the critical thickness for the formation of dislocations [4, 5]. Thus, within a certain layer thickness coherent islands are formed on the growth surface. In this case the strain relaxation occurs either in the substrate adjacent to the island or in the island itself [4,5,6].

## 2.2. FORMATION OF ARRAYS OF InAs/GaAs SELF-ORGANIZED QUANTUM DOTS *IN SITU* BY MOLECULAR BEAM EPITAXIAL GROWTH

### 2.2.1. Structural characterization of quantum dots

The onset of the island growth mode upon the deposition of InAs on GaAs is usually monitored by high energy electron diffraction (HEED) patterns during the molecular beam epitaxial (MBE) growth (Fig. 3). The appearance of dashes and spots on the HEED pattern instead of streaks characteristic of the layer by layer growth is indicative of the formation of microscopic islands on the growth surface. If the deposition of InAs is interrupted at this stage, and the InAs islands obtained are overgrown by GaAs then the system of InAs islands in GaAs can be considered as a quantum dot array of low band-gap material in a large band-gap matrix.

Studying the initial stages of deposition of  $In_xGa_{1-x}As$  on GaAs by HEED has shown that the increase in the In content ( $x$ ) in the epilayer leads to a decrease in the critical layer thickness for the island growth from 4 monolayers (ML) ( $x=0.5$ ) to 3 ML ( $x=0.6$ ) [7] and 1.7 ML ( $x=1$ ) [8].

Transmission electron microscopy (TEM) studies show that structural characteristics of  $In_xGa_{1-x}As$  quantum dots in GaAs strongly depend on  $x$  and effective layer thickness, Fig. 4 [8]. Just exceeding the critical layer thickness the QD ensemble is characterized by pronounced lateral nonuniformities and small size of individual islands. Increasing the effective layer thickness to 4 ML (InAs) leads to the formation of about 60 Å high pyramidal quantum dots with square

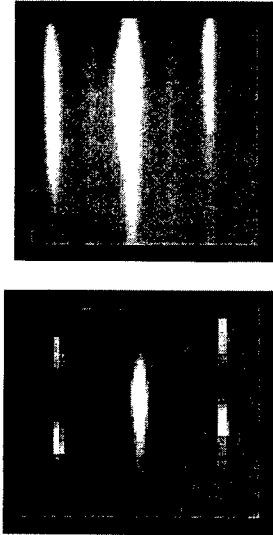


Figure 3. Change in HEED pattern with the deposition of InAs on GaAs surface due to the transition from layer-by-layer (1.6 ML, upper part) to island (1.7 ML, lower part) growth mode.

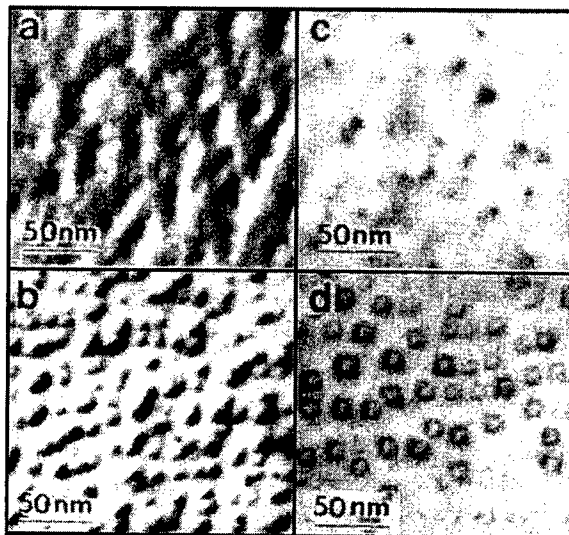


Figure 4. Plan-view TEM images of In(Ga)As QD arrays in a GaAs matrix: In0.5Ga0.5As QDs (3.3 ML (a), 7.3 ML (b)); InAs QDs (2 ML (c), 4 ML (d)).

bases ( $\sim 120$  Å). The islands form two-dimensional primitive square lattice, and their size distribution is relatively narrow (dispersion less than 20%).

Thus, the formation of InGaAs/GaAs self-organized quantum dots is controlled by the composition of the deposited layer and its effective thickness; the driving force for the formation of quantum dots is the strain energy accumulating upon the epitaxial growth of lattice mismatched semiconductor materials.

## 2.2.2. Optical properties of quantum dots

Coherent QDs usually show high (close to 100%) effectiveness of radiative recombination at low temperatures. The energy position of the photoluminescence (PL) peak strongly depends on the size of the islands [9]. Just after the formation of islands the PL peak becomes broadened and red shifted as compared to the quantum well case (Fig. 5a). Further increasing the effective thickness of InGaAs leads to gradual long wavelength shift of the PL line until the critical layer thickness for the dislocation formation is achieved (Fig. 5b). In this case the PL intensity is drastically decreased due to the large number of nonradiative recombination centers. The dots of smaller sizes usually exhibit a broader and weaker PL line as compared to the large dots with lower size dispersion. Integral PL intensity of the InAs/GaAs quantum dot heterostructures is almost independent of temperature until 100 K. However, increasing the temperature beyond 100 K leads to the decrease in the PL intensity characterized by the activation energy of about 80 – 90 meV. This value is close to the valence band discontinuity at the heterojunction InAs QD – GaAs matrix estimated theoretically [6] thereby indicating the effective evaporation of

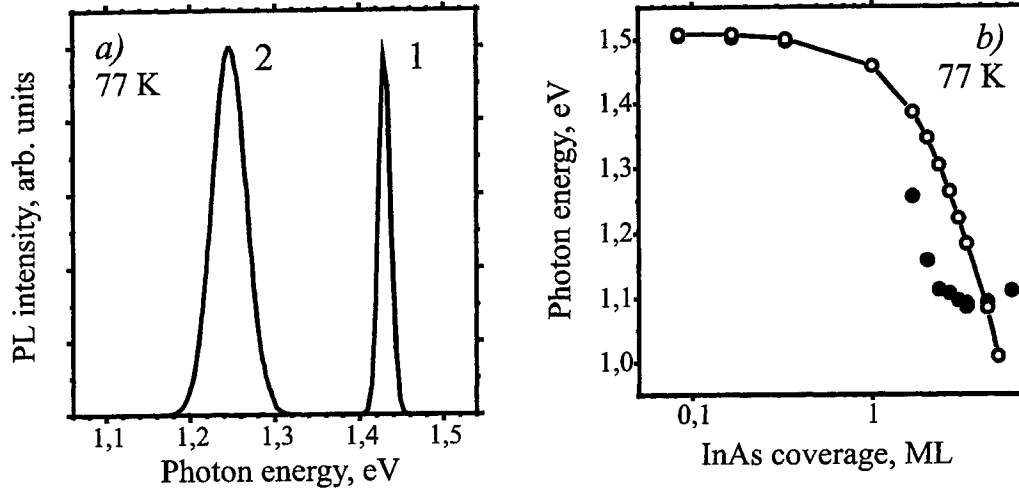


Figure 5. (a) PL spectra of heterostructures containing two-dimensional layer (curve 1) or QD array (curve 2) of InGaAs in a GaAs matrix.

(b) Dependence of PL peak position from InAs insertion in GaAs: (●) measured experimentally; (○) calculated in assumption of two-dimensional coverage.

carriers from quantum dots at elevated temperatures [10]. Nevertheless, the room temperature PL intensity remains sufficiently high which allows the use of quantum dot structures in diode lasers.

#### 2.2.3. Vertically coupled quantum dots

TEM studies have shown that typical InAs/GaAs quantum dots are characterized by relatively low aspect ratio (maximum base size  $\sim 140$  Å, maximum height  $\sim 60$  Å). Further increasing the effective thickness of deposited InAs leads to the formation of misfit dislocations. However, increasing the aspect ratio should lead to the increase in the carrier localization energy thereby suppressing the thermal evaporation of carriers from the QDs. This in turn should improve the room temperature characteristics of diode lasers.

It has been found that successive deposition of the InAs dot sheets and thin GaAs spacers leads to the formation of the islands of the subsequent sheet just above the islands of the previous sheet if the spacer thickness is less than or equal to the height of the island, Fig.6 [11]. The reason for this phenomenon is that the growth of the second InAs layer proceeds under the influence of the strain fields due to the presence of the previous QD sheet. This leads to the preferential migration of the In atoms to the places just above the location of the island of the previous layer.

The energy of the ground state transition has been found to depend on the number of the dot sheets and the spacer width. The PL peak shifts to the longer wavelengths with the increase in the number of QD sheets due to the decrease in the size quantization energy owing to the increase of the effective height of the quantum dot. The red shift of the PL line is also observed with the decrease in the spacer thickness due to the enhancement of the electronic coupling

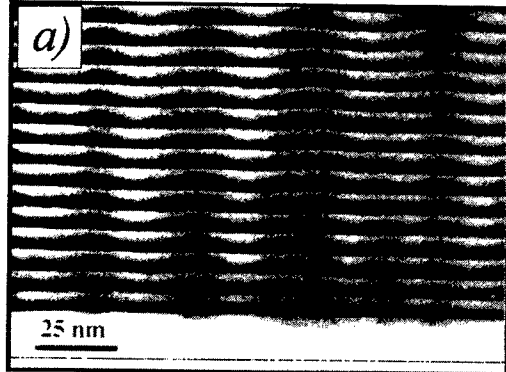
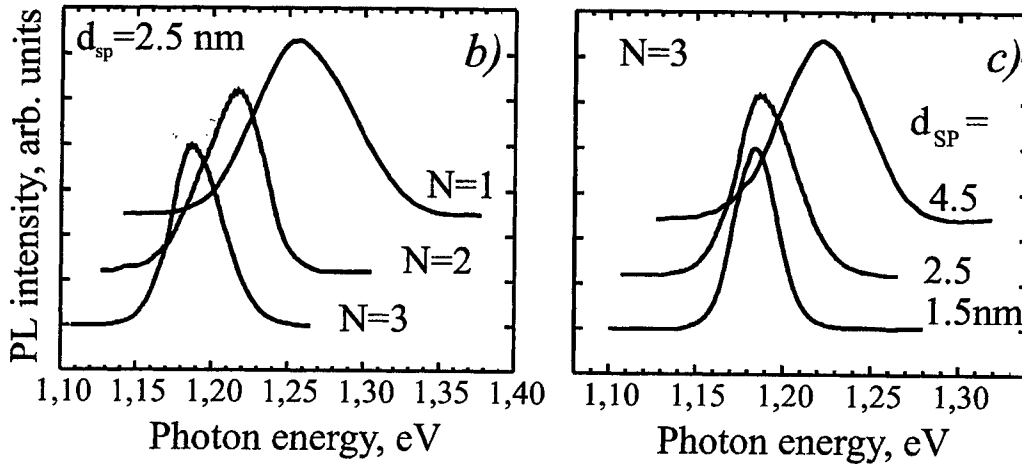


Figure 6. Cross-section TEM image of the structure containing more than 10 planes of InAs QDs separated by 5 nm-thick GaAs spacers (a) and evolution of PL spectrum of stacked QD array with the number of QD planes (b) and the spacer thickness (c).



between the dots of the adjacent layers. These effects are indicative of the fact that the vertically coupled quantum dot with strongly increased aspect ratio is a single quantum mechanical object characterized by a joint system of energy levels.

#### 2.2.4. Density of states spectrum of individual quantum dots

The PL spectrum of a quantum dot ensemble is a broad line (Fig. 5) which is the result of inhomogeneous broadening due to the size and shape fluctuations of the self-organized islands. Experimental evidence indicates that the energy spectrum of an individual quantum dot is a set of discrete energy levels due to three-dimensional quantization. This has been observed when studying cathodoluminescence (CL) under high spatial resolution of electron beam [12]. If only several tens of quantum dots are excited by a highly focused electron beam (under routine PL conditions  $10^7$  –  $10^8$  dots are within the laser spot) the CL spectrum is the set of ultra narrow lines (FWHM < 0.15 meV) which is indicative of the lack of inhomogeneous broadening, Fig. 7. No increase in the width of the luminescence lines is observed with the increase in the temperature. This observation confirms that there is a lack of thermal broadening due to the delta function like density of states owing to the three dimensional quantization.

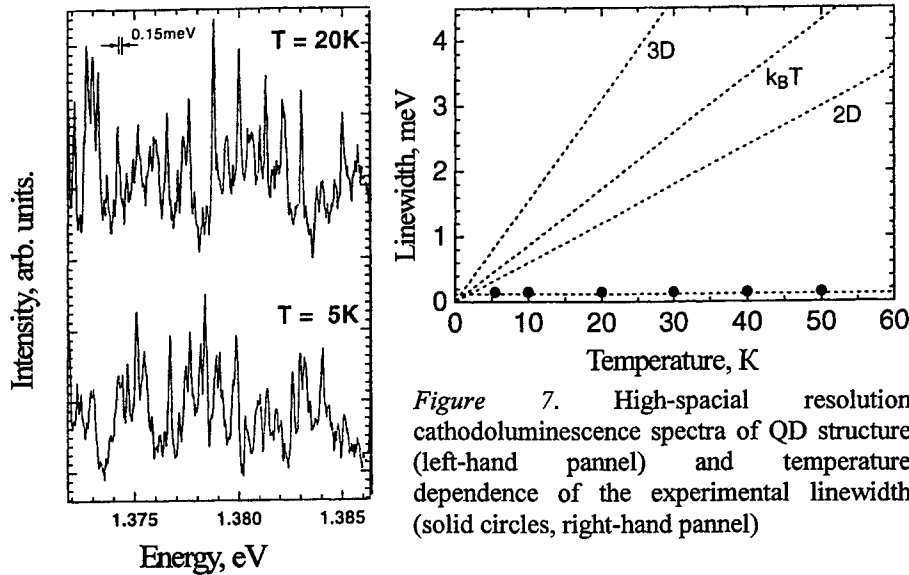


Figure 7. High-spatial resolution cathodoluminescence spectra of QD structure (left-hand pannel) and temperature dependence of the experimental linewidth (solid circles, right-hand pannel)

### 3. Formation of InAs quantum dots on silicon

Silicon is a key material in modern semiconductor technology. The important properties of silicon (high thermal conductivity, high stiffness, stable oxide formation, and developed technology for preparing inexpensive large-area dislocation-free substrates) make this material advantageous for numerous applications in microelectronics. On the contrary, the indirect bandgap of Si makes its application in optoelectronics very difficult. However, the luminescence efficiency of an indirect gap matrix can be dramatically improved by inserting a narrow- and direct-gap material (e.g. GaAs layers in AlAs). Nonequilibrium carriers are trapped in the direct-gap regions, and the luminescence efficiency may be extremely high, even

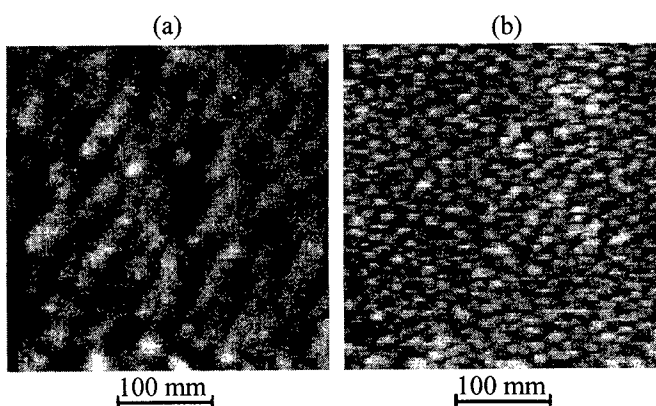


Figure 8. STM images of the surface morphology of InAs deposits on a Si (100) surface for 60 ML of InAs deposited at  $470\text{ }^{\circ}\text{C}$  (a) and 5.5 ML InAs deposited at  $250\text{ }^{\circ}\text{C}$  (b).

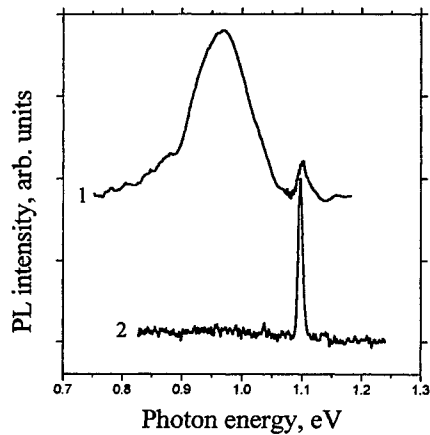


Figure 9. PL spectra of InAs QD array in a Si matrix (curve 1) and bare Si substrate (curve 2) at 77 K.

when the relative total thickness of the narrow gap material is small. Using the QD approach may be advantageous in overcoming the problems of lattice mismatch and anti-phase domains which are the main limiting factors for the growth of III-V materials on silicon. When studying the growth regimes for InAs quantum dots on Si we have found that at moderate arsenic fluxes and substrate temperatures (470°C) (typical for the growth of InAs/GaAs quantum dots) InAs grows on Si (100) surface in the Stranski-Krastanow growth mode with the formation of mesoscopic dislocated clusters on top of a two-dimensional periodically corrugated InAs wetting layer. In contrast, at lower temperatures (250°C) a dense array of self-organized nanoscale InAs quantum dots of uniform size and shape is formed, Fig. 8. These quantum dots, when grown on a Si buffer layer and covered with a Si cap, give a PL line at about 1.3  $\mu$ m, Fig. 9 [13].

#### 4. Quantum dot diode lasers

##### 4.1. THRESHOLD CHARACTERISTICS

To study the diode lasers based on self-organized quantum dots, the quantum dot array was inserted into an active region of a GRIN SCH GaAs-(Al,Ga)As laser, Fig. 10. This allowed us to realize lasing via the ground state of quantum dots at low temperatures. Lasing wavelength was in the vicinity of the maximum of QD photoluminescence (PL) spectrum recorded at low excitation densities, and the threshold current density was found to be practically temperature insensitive in the temperature range up to  $\sim 100$  K. However, at higher temperatures we observed a steep increase in the threshold current density accompanied by a blue shift of lasing wavelength. Room temperature lasing energy was close to optical transition energy in a wetting layer (WL) [10]. Extremely high material and differential gain have been reported for these lasers, however, poor optical confinement factor led to moderate values of modal gain [14].

Important improvements in threshold characteristics of quantum dot diode lasers became possible due to the use of vertically coupled quantum dots in the active region [15]. These lasers show ground state lasing up to room temperature and the lasing wavelength follows the temperature dependence of the GaAs band-gap. The threshold current density steeply decreases and the range of its thermal stability increases with an increase in the number of QD layers (Fig. 11). The threshold current density ( $J_{th}$ ) is as low as 90-100 A/cm<sup>2</sup> at room temperature for N=10 which is 10 times less than that for N=1.

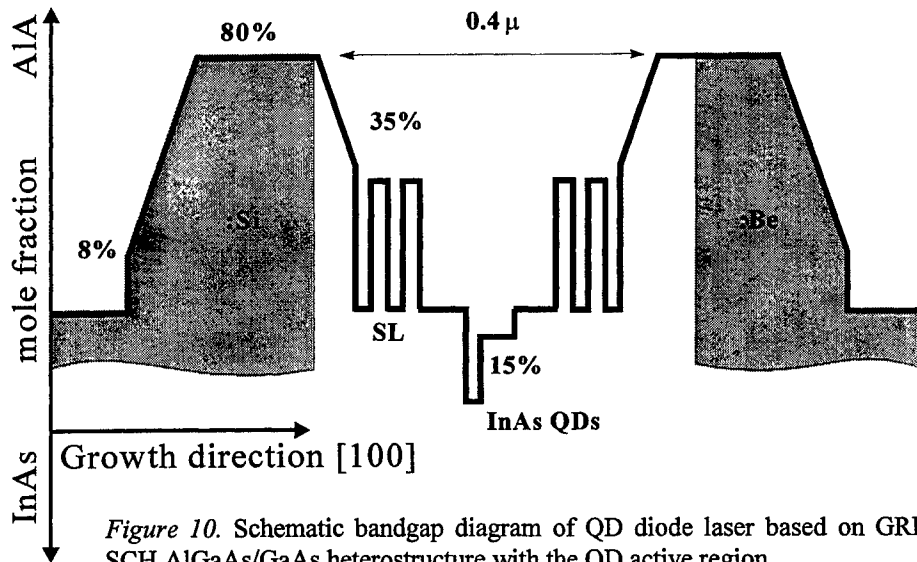


Figure 10. Schematic bandgap diagram of QD diode laser based on GRIN-SCH AlGaAs/GaAs heterostructure with the QD active region.

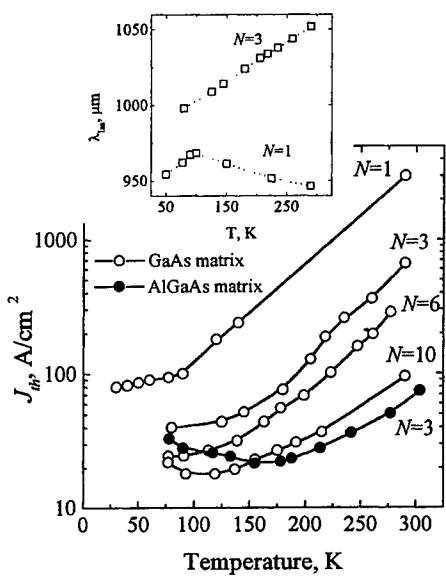


Figure 11. Temperature dependence of the threshold current density and the lasing wavelength (insert) for the lasers based on  $N$  layers of InAs QDs in GaAs or AlGaAs matrix.

Further decrease in threshold current density of quantum dot diode lasers was achieved by using the AlGaAs instead of the GaAs as a matrix for InGaAs QDs. This allowed for the increase in the barrier height for the carriers in the quantum dot states which reduces the carrier evaporation from quantum dots. The problem of low-temperature growth of AlGaAs is solved by *in situ* annealing during the high-temperature growth of the second emitter of the laser structure. This approach allowed us to achieve a room temperature threshold current density as low as  $60 \text{ A/cm}^2$ , and a differential efficiency of more than 60% for a quantum dot diode laser [15]. The value of the threshold current density well corresponds to the best values reported for the quantum well lasers.

Studying the main mechanisms of internal carrier losses and leakage from the ground state of quantum dots has shown that the threshold current density can be reduced down to about  $15 \text{ A/cm}^2$  at room temperature by reducing the non-radiative recombination and improving the carrier localization [16].

#### 4.2. CONTINUOUS WAVE OPERATION OF QUANTUM DOT DIODE LASERS

The high quality of diode lasers, characterized by low threshold current density and reasonable differential efficiency, allowed us to demonstrate for the first time continuous wave (CW) operation of the QD lasers. Output power of about 1 W for the InGaAs/AlGaAs QD laser was reported [17].

One of the dominant mechanisms limiting output power of the semiconductor laser is spectral hole burning, associated with the finite capture time of charge carriers into the active states. Since the capture time into the ground state of In(Ga)As QDs is relatively large and the QDs themselves are characterized by a certain number of states determined by their surface density (typical value is  $3\div 5 \times 10^{10} \text{ cm}^{-2}$ ), there is a maximum current capability of the QD active region. The increase in the surface density of QDs should allow us to increase the maximal possible current, which, in the turn, will increase the light output power. In [18] we have proposed the method to increase the surface density of QDs using denser InAlAs QDs as the

centers for stimulated formation of In(Ga)As QDs. The density of such composite vertically coupled QDs is set by the InAlAs islands ( $1\div 1.5 \times 10^{11} \text{ cm}^{-2}$ ), whereas the optical transition energy is determined by the In(Ga)As QDs. Following this method we formed the active region of the laser which demonstrated maximum output power with uncoated facets in CW and pulsed regimes ( $10^\circ \text{C}$ ) as high as 3.5 and 4.8 W, respectively, Fig. 12. The maximum value of output power was limited by catastrophic optical mirror damage (COMD). The internal loss for these diodes was estimated to be as low as  $1.3 \pm 0.3 \text{ cm}^{-1}$ . The internal quantum efficiency was estimated to be about 75% [19]. Thus, QD lasers can be used for high-power applications.

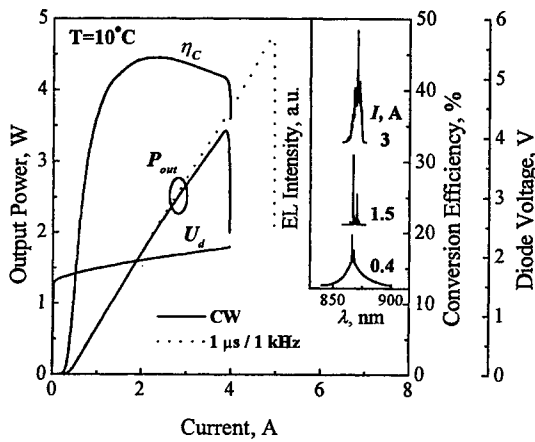


Figure 12. Output power,  $P_{out}$ , diode voltage,  $U_d$ , and conversion efficiency,  $\eta_C$ , vs drive current for the QD diode laser operating in CW regime at room temperature.

#### 4.3. QUANTUM DOT DIODE LASERS FOR OPTICAL FIBER COMMUNICATIONS

Extension of the optical emission range available for the GaAs-based optoelectronic devices to  $1.3 \mu\text{m}$  is currently a subject of strong interest due to matching the transparency window of optical fibers. A number of attempts have been made to find an alternative to InGaAsP material system for laser diodes to overcome its strong temperature sensitivity due to insufficient electron confinement in the active region. Moreover, the use of GaAs-based lasers emitting at  $1.3 \mu\text{m}$  would eliminate the use of expensive InP substrates and the sophisticated technique of fusion of Bragg reflectors and active regions for vertical cavity devices. The approach based on

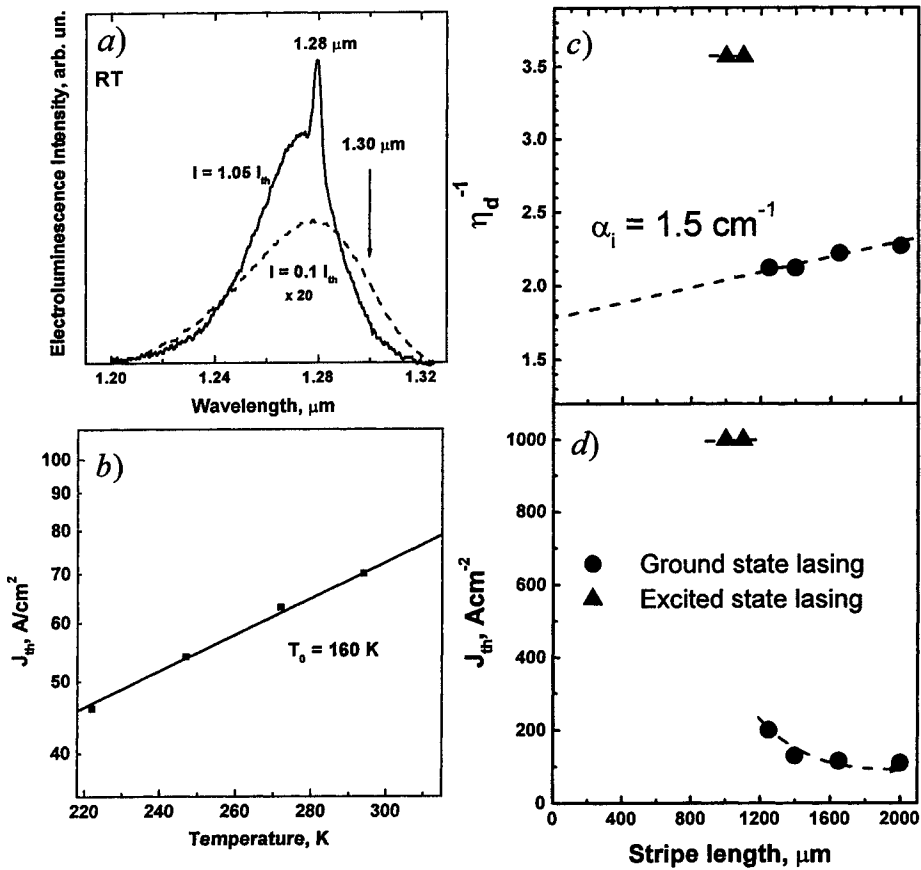


Figure 13. Electroluminescence (EL) spectra for four-side cleaved devices at room temperature (a), temperature dependence of the threshold current (b), dependence of the inverse differential efficiency (c) and the threshold current density (d) on the cavity length for the laser based on InAs QDs covered with InGaAs QW layer.

strained InGaAs/GaAs quantum well structures did not allow the necessary wavelength range to be reached due to the intrinsic limitation of the quantum well width associated with the border for pseudomorphic growth.

InAs/GaAs quantum dots are the promising candidates for extending the long wavelength border for the GaAs based light emitters. Once the InGaAs nanoscale islands are formed the pronounced red-shift of the luminescence peak position relative to that in strained InGaAs/GaAs quantum well is observed. We have proposed and realized a method to extend the optical emission range for the InGaAs/GaAs structures based on the effect of reduction of the energy of optical transition in a quantum dot when the bandgap of the surrounding matrix is decreased. We placed an InAs quantum dot (QD) array into external InGaAs strained quantum

well which allowed us to control the quantum dot emission wavelength by varying the InGaAs composition and to achieve the emission wavelength as long as  $1.3\text{ }\mu\text{m}$ , Fig. 13 [20]. Using these InAs/InGaAs/GaAs quantum dots in the active region of a diode laser allowed us to realize low threshold current density ( $J_{th} = 65\text{ A/cm}^2$ ) operation near  $1.3\text{ }\mu\text{m}$  at room temperature. The lasing occurred via the QD ground state for cavity length  $L > 1\text{ mm}$ . Differential efficiency is 40% and internal losses are  $1.5\text{ cm}^{-1}$ . Characteristic temperature near RT is 160 K, Fig. 13, [21]. Thus, the GaAs-based QD laser emitting near  $1.3\text{ }\mu\text{m}$  demonstrated properties superior to those of InP-based QW devices.

#### 4.4. QUANTUM DOT DIODE LASERS FOR NEAR-IRFARED OPTICAL RANGE

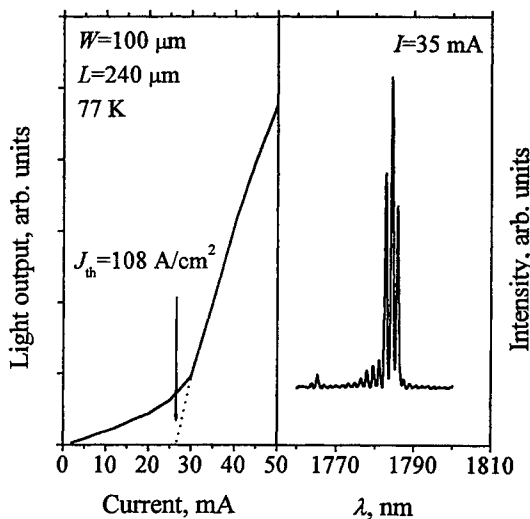


Figure 14. Light output vs drive current curve (left-hand panel) and above-threshold EL spectrum (right-hand panel) for 240- $\mu\text{m}$ -long stripe diode based on InAs QDs in an InGaAs/InP matrix.

Using the idea of the dependence of the quantum dot emission wavelength on the matrix band-gap allowed us to further increase the emission wavelength of a quantum dot laser. We used InGaAs ternary lattice matched to InP substrate as a matrix for InAs quantum dots. In this case the matrix band-gap was only  $\sim 0.8\text{ eV}$  and consequently the QD emission wavelength should be considerably increased as compared to the InAs/GaAs case. We have shown experimentally that for the InAs/InGaAs/InP QDs the optical emission range can be extended to  $\sim 2\text{ }\mu\text{m}$  [22]. Having inserted these quantum dots into the InP/InAlAs/InGaAs laser structure we managed to observe lasing in the 77-200 K temperature range. Low threshold currents and emission wavelength at  $1.8\text{ }\mu\text{m}$  (77 K), Fig. 14, [23], show that the wavelength of the InAs QD lasers can be extended to the near-infrared optical range.

#### 5. Conclusions

InAs quantum dots have been successfully grown by MBE on GaAs, InP, and Si substrates. Growth regimes for the formation of coherent islands have been studied. Energy spectrum, structural, and optical properties have been evaluated. Diode lasers based on self-organized quantum dots have been fabricated and characterized. The possibility to obtain ultra low threshold current densities by optimizing the structural design and growth regimes has been demonstrated. Quantum dot lasers have demonstrated high output power performance comparable to the quantum well lasers. In addition, quantum dot lasers have extended the

optical emission range of the GaAs based lasers to wavelengths necessary for optical fiber communications.

## 6. Acknowledgements

This work in different parts is supported by Volkswagen Foundation (grant 1/73-631), INTAS (grants 96-0467 and 96-0242), BMBF 13 N 7231, NanOp CC, Russian Foundation for Basic Research (grant 99-02-16799), and the Program of Ministry of Science of Russia "Physics of Solid State Nanostructures".

The author is grateful to the Directors and Organizing Committee of the NATO Advanced Research Workshop "Nanostructured Films and Coatings" (Santorini, Greece, June 28-30, 1999) for financial support.

The author also gratefully acknowledges his colleagues whose contribution to this work was extremely important: A.Yu.Egorov, A.E.Zhukov, A.R.Kovsh, N.A.Maleev, S.S.Mikhrin, D.V.Denisov, M.V.Maximov, A.F.Tsatsul'nikov, I.L.Krestnikov, B.V.Volovik, D.A.Bedarev, Yu.M.Shernyakov, A.V.Lunev, E.Yu.Kondrat'eva, S.V.Zaitsev, N.Yu.Gordeev, V.I.Kopchatov, D.A.Lifshits, Yu.G.Musikhin, A.A.Suvorova, A.O.Kosogov, S.S.Ruvimov, N.A.Bert, P.S.Kop'ev, N.N.Ledentsov, and Zh.I.Alferov – Ioffe Institute, St. Petersburg, Russia; G.E.Cirlin and A.O.Golubok – Institute for Analytical Instrumentation, St. Petersburg, Russia; N.Kirstaedter, R.Heitz, M.Grundmann, and D.Bimberg – Technical University of Berlin, Berlin, Germany; P. Werner – Max-Planck Institute, Halle, Germany; Z.Liliental-Weber and E.R.Weber – Lawrence Berkeley National Laboratory, Berkeley, CA, USA.

## 7. References

1. Arakawa, Y. and Sakaki, H. (1982) Multidimensional quantum well laser and temperature dependence of its threshold current, *Appl. Phys. Lett.* **40**, 939-941.
2. Asada, M., Miyamoto, Y., and Suematsu, Y. (1986) Gain and the threshold of the three-dimensional quantum-box lasers, *J. Quantum Electron.* **QE-22**, 1915-1921.
3. Ledentsov, N.N. (1996) Ordered arrays of quantum dots, in M. Scheffler and R. Zimmerman (eds.), *Proceedings of the 23<sup>rd</sup> International Conference on the Physics of Semiconductors* **1**, Berlin, Germany, 19-26.
4. Eaglesham, D.J. and Cerullo, M. (1990) Dislocation-free Stranski-Krastanow growth of Ge on Si (100), *Phys. Rev. Lett.* **64**, 1943-1946.
5. Guha, S., Madhukar, A., and Rajkumar, K.C. (1990) Onset of incoherency and defect introduction in the initial stages of molecular beam epitaxial growth of highly strained  $In_xGa_{1-x}As$  on GaAs (100), *Appl. Phys. Lett.* **57**, 2110-2112.
6. Grundmann, M., Stier, O., and Bimberg, D., (1995) InAs/GaAs pyramidal quantum dots: Strain distribution, optical phonons, and electronic structure, *Phys. Rev. B* **52**, 11969-11981.
7. Egorov, A.Yu., Zhukov, A.E., Kop'ev, P.S., et al. (1994) Effect of deposition conditions on the formation of (In,Ga)As quantum clusters in a GaAs matrix, *Semiconductors* **28**, 809-811.

- 8 Ruvimov, S.S., Werner, P., Scheerschmidt, K., et al. (1995) Structural characterization of (In,Ga)As quantum dots in a GaAs matrix, *Phys. Rev. B* **51**, 14766-14769.
- 9 Egorov, A.Yu., Zhukov, A.E., Kop'ev, P.S., et al. (1996) Optical emission range of structures with strained InAs quantum dots in GaAs, *Semiconductors* **30**, 707-710.
- 10 Bimberg, D., Ledentsov, N.N., Grundmann, M., et al. (1996) InAs-GaAs quantum pyramid lasers: in situ growth, radiative lifetimes, and polarization properties, *Jpn. J. Appl. Phys., Part 1* **35**, 1311-1319.
- 11 Ustinov, V.M., Egorov, A.Yu., Zhukov, A.E., et al. (1996) Formation of stacked self-assembled InAs quantum dots in GaAs matrix for laser applications, *Mat. Res. Soc. Symp. Proc.* **417**, 141-146.
- 12 Grundmann, M., Christen, J., Ledentsov, N.N., et al. (1995) Ultranarrow luminescence lines from single quantum dots, *Phys. Rev. Lett.* **74**, 4043-4046.
- 13 Cirlin, G.E., Dubrovskii, V.G., Petrov, V.N., et al. (1998) Formation of InAs quantum dots on a silicon (100) surface, *Semicond. Sci. Technol.* **13** 1262-1265.
- 14 Kirstaedter, N., Schmidt, O.G., Ledentsov, N.N., et al. (1996) Gain and differential gain of single layer InAs/GaAs quantum dot injection lasers, *Appl. Phys. Lett.* **69**, 1226-1228.
- 15 Ustinov, V.M., Egorov, A.Yu., Kovsh, A.R., et al. (1997) Low-threshold injection lasers based on vertically coupled quantum dots, *J. Cryst. Growth* **175**, 689-695.
- 16 Zaitsev, S.V., Gordeev, N.Yu., Kopchatov V.I., et al. (1997) Vertically coupled quantum dot lasers: first device oriented structures with high internal quantum efficiency, *Jpn. J. Appl. Phys. Part 1* **36**, 4219-4220.
- 17 Maximov, M.V., Shernyakov, Yu.M., Tsatsul'nikov, A.F., et al. (1998) High-power continuous-wave operation of a InGaAs/AlGaAs quantum dot laser, *J. Appl. Phys.* **83**, 5561-5563.
- 18 Kovsh, A.R., Zhukov, A.E., Egorov, A.Yu., et al. (1998) MBE growth of composite (In,Al)As/(In,Ga)As vertically coupled quantum dots and their application in injection lasers, *Proc. of 10<sup>th</sup> Int. Conf. MBE, Abstract Book*, 175. (to be published in *J.Crys.Growth*, 1999).
- 19 Kovsh, A.R., Zhukov, A.E., Livshits, D.A., et al. (1999) 3.5 W CW operation of a quantum dot laser, *Electron. Lett.* (to be published)
- 20 Ustinov, V.M., Maleev, N.A., Zhukov, A.E., et al. (1999) InAs/InGaAs quantum dot structures on GaAs substrates emitting at 1.3  $\mu$ m, *Appl. Phys. Lett.* **74**, 2815-2817.
- 21 Shernyakov, Yu. M., Bedarev, D.A., Kondrat'eva, E.Yu., et al. (1999) 1.3  $\mu$ m GaAs-based laser using quantum dots obtained by activated spinodal decomposition, *Electron. Lett.*, in press
- 22 Ustinov, V.M., Zhukov, A.E., Tsatsul'nikov, A.F., et al. (1997) Arrays of strained InAs quantum dots in an (In,Ga)As matrix grown on InP substrates by molecular beam epitaxy, *Semiconductors* **31**, 1080-1083.
- 23 Ustinov, V.M., Zhukov, A.E., Egorov, A.Yu., et al. (1998) Low threshold quantum dot injection laser emitting at 1.9  $\mu$ m, *Electron. Lett.* **34**, 670-672.

## CHEMICAL PROCESSING OF NANOSTRUCTURED COATINGS

LYNN K. KURIHARA

*Code 6354, Multifunctional Materials Branch  
Naval Research Laboratory  
Washington DC 20375 USA  
Email: kurihara@anvil.nrl.navy.mil  
Also at  
Potomac Research International  
Fairfax VA 22030 USA*

### 1. Introduction

Nanostructured materials, often characterized by a physical dimension of 1-100 nm (such as grain size) and significant amount of surfaces and interfaces, have been attracting much interest because of their demonstrated or anticipated unique properties compared to the conventional materials (1-3). Nanophase coatings can enhance the surface properties and yet retain the bulk properties of the coarse grained substrate material.

Nanostructured films can be prepared by evaporative technologies, glow discharge, gas-phase processes and liquid phase chemical routes. There has been a growing interest in chemical routes because of the many advantages it has over the other technologies. The advantages of chemical routes include: the ability to control the chemical composition, the particle size distribution, agglomerate size distribution, particle morphology, porosity, and the advantages of low temperature processing and cost-effective bulk quantity production. Examples of chemical routes used for preparing nanostructured coatings are: sol-gel processing, polyol, electroplating, electroless plating, electrophoretic deposition and electrolytic anodization. The scope of this chapter will be restricted to sol-gel processing and polyol chemistry.

### 2. Sol-Gel Processing of Nanostructured Coatings

Sol-gel processing involves the synthesis of an inorganic network by chemical reactions in a solution at low temperature (4). The solution or sol is a dispersion of solid particles in a liquid, and the gel is the result of the formation of a three dimensional network which spans the entire solution volume. The reaction usually takes place at room temperature. The traditional precursors for sol-gel reactions have been metal alkoxides. Although, a variety of metal precursors can be used, such as metal nitrate or other metal-organic compounds. Sol-gel is a versatile technique. Using sol-gel techniques, many types of materials may be made. They include aerogels, xerogels, powders, glasses, coatings, fibers, whiskers, monoliths, hollow spheres and foams. Depending on the synthesis conditions, coatings, porous solids, powders, fibers, bulk materials may be prepared. From solution, coatings may be applied to a substrate, or fibers may be drawn if the viscosity of the sol is high enough. If the sol is allowed to start to gel, a porous solid or a powder can be formed from the gel. The porous solid or nanopowder can also be used as a starting material for some coating techniques.

There are many types of sol-gel coatings in the literature ranging from IR imaging to anti-scratch to smart windows and waveguides. Uhlmann and Towee have taken a survey of the sol-gel community (5) and found that it was considered that coatings were the most important present products using sol-gel processing, and it was also reported that functional coatings would be considered the most important commercial product in ten years. The reasons behind these choices were that, with sol-gel, coatings could be obtained with compositions that are not obtainable by other means; sol-gel provides the ability to do integrated multilayers at a lower cost than vacuum techniques and sol-gel can easily be combined with other preparative systems. Painting, spinning, dipping, spraying, electrophoresis (6), and ultrasonic pulverization (7) may be employed to put down coatings and films from sol-gel solutions. The last two techniques have

recently been getting more attention, as they can be used to prepare thicker coatings. The most common deposition techniques are that of spinning or dipping. A drawback of these techniques is that they are generally limited to the deposition of axially or radically symmetric substances. Sol-gel processing is especially adaptable for coating formation. Films and coatings represent the earliest commercial use of sol-gel processing. Sol-gel techniques offer the following advantages. Controlling the pore volume, pore size and the surface area can control microstructure; that is, the film properties can be tailored. It is also possible to obtain compositions that are not available by other routes such as gas condensation. Thin films use very small quantities of raw materials and can be processed quickly, and very large and irregularly shaped surfaces can be coated. Dense pinhole free layers can be prepared at low temperatures using sol-gel processing. Porous films can be prepared by changing the reaction conditions. This approach is particularly useful to obtain homogeneous multicomponent coatings. To avoid cracking caused by large capillary stresses during evaporation of solvent in the drying process, either slow evaporation (slow process) or supercritical drying (fast process) is used. As-deposited oxide coatings are typically amorphous. Thermal and thermochemical post-synthesis treatment can be carried out to obtain nanostructured oxide, carbide or nitride coatings. Hybrid coatings can be fabricated by doping the sol with material of a different phase, followed by gelation and densification. Because of the large capillary stress during solvent evaporation that can cause cracking, sol-gel process has been traditionally used for preparing thin films and coatings. Generally, the film thickness is less than a micron. To prepare thick coatings, the problems of shrinkage and cracking and the limitation of coating thickness can be mitigated by increasing particle loading in sol-gel process (8-10). This approach involved dispersing large ceramic powders in sol-gel solution, and the mixture was applied onto the substrate by various techniques such as dipping and spraying. Coatings with thickness up to 200  $\mu\text{m}$  were fabricated. The sol-gel film formed strong bonds to both oxide powders and substrates by interaction with functionalized surface hydroxyl groups on the oxide powders and the oxide layer of substrates. The strong bond reduced cracking. The shrinkage problem associated with conventional sol-gel approach was minimized due to the high loading of ceramic powders. One way to prepare thicker coatings is to add powders into the sol. This helps to reduce the capillary stresses associated with drying. Chen and coworkers (9) have prepared thick coatings by adding nanosized boehmite, alumina, zirconia or silicon carbide into an inorganic-organic hybrid matrix. A two dimensional sol-gel process was also used to fabricate thick films of titania (11). In this process, the traditional sol-gel hydrolysis and condensation reactions took place at an air-water interface. The gel films formed could then be deposited onto substrates using Langmuir Blodgett techniques.

The ability to process at room temperature has also opened up the biomaterials aspect of sol-gel chemistry. Proteins and enzymes can be encapsulated in silica glass (12), while still retaining their activity. Sol-gel coatings (13,14) of hydroxyapatite should also aid in the implantation of artificial bones or joints with of the surrounding tissue.

As previously mentioned, the processing of sol-gel coatings can be controlled to form porous coatings. The porosity may be used as a template or reaction site for other materials or chemical reactions to take place or this porosity may be used to change physical properties. The real advantage of sol-gel processing is that this porosity can be controlled. Films with pore sizes below 10 nm and patterned (15,16) can be prepared. These pores can be filled by surface adsorption from aqueous solutions of the desired cations. The doping time and temperature, and solution pH can control this doping process.

Composite coatings can be prepared by doping other materials into a porous matrix. Metal clusters of Ag, Cu and Ag-Cu have been prepared in silica films (17). These metal clusters have enhanced third order nonlinear susceptibility, and these properties can be tuned by controlling the cluster size. The nanocluster size can be controlled by temperature and annealing atmosphere in the processing of these materials. Conducting polymers such as polyaniline can also be entrapped in the porous silica coating (18). This hybrid system improves the conductivity and stability of the conducting polymer.

Ferroelectric films have many potential applications in a variety of solid state devices such as RAM, sensors, and actuators. Sol-gel preparation of films of ferroelectric materials is generating a lot of interest because of the ease of integrating the films into microelectronics manufacturing processes. Adding nanoporosity in ferroelectric coatings is one way to change the dielectric constant in a coating while keeping the thermal and mechanical properties of the coatings. Sol-gel processing can be used to prepare polymeric organic-inorganic hybrids with controlled morphologies. Using a thermally labile macromolecule template for the vitrification of a silsequioxane precursor allows this to be achieved (19). The organic moiety can be removed by heat treatment to leave a nanoporous structure. The pore size is controlled by the template polymerization. However, it may not be advantages to add a nanoporous coating to a device.  $\text{Pb}(\text{Zr}_{53}\text{Ti}_{47})\text{TiO}_3$  thin films with crystallite sizes of 23 nm at 800°C can be prepared

by using the methoxyethoxides of the starting elements (20). It was found that the annealing temperature is the important parameter. However, defects or uncontrolled porosity can lead to short circuits (21). It was determined that having a film with low porosity and nanosized pores can decrease the number of short circuits. This can be done by control the hydrolysis reactions in the precursor gel by regulating the pH and the water to alkoxide ratio. Lead titanate films with crystallite size of 160 nm at 800C had a  $\epsilon = 190$  and a  $\tan \delta$  of 8%. Sol-gel processing has also been used to prepare fine-grained (<70 nm) polycrystalline barium titanate films (22-24). These films generally have the cubic perovskite structure instead of the ferroelectric tetragonal structure. It was noted that the dielectric properties of barium titanate films also decreased as the grain size decreased. A detailed TEM (24) study of nanocrystalline barium titanate films showed that the microstructure was independent of variations in processing parameters, such as: amount of water, precursor type, solvent, and pH. In-situ TEM studies showed a intermediate carbonate phase is formed around 600°C that decomposes to leave nanoporosity in the final film at higher temperatures and the nanocrystalline barium titanate is formed by nucleation on this intermediate phase.

## 2.1 Sol-gel processing of thermal barrier coatings

Thermal barrier coatings (TBC) generally consist of zirconia ( $ZrO_2$ ) or yttria-stabilized zirconia (YSZ) and more recently alumina-stabilized zirconia (ASZ).  $ZrO_2$  is of particular interest for TBCs because of its chemical and temperature stability, hardness and low thermal conductivity. However, pure zirconia has a very serious drawback, related to high temperature phase stability. That is, depending on the temperature, that  $ZrO_2$  has three distinct crystal structures. In the past, different approaches have been tried to stabilize the high temperature phase of zirconia. The most common method for this phase stabilization is alloying zirconia with yttria. However, yttria is severely attacked by hot corrosion and mechanical failures of the TBC are caused by scale between the  $Al_2O_3$  scale on the bond coat and the YSZ. One advantage of using alumina as the stabilizer instead of yttria would be that the mismatch between the TBC and the bondcoat would be removed, besides not suffering from the hot corrosion problem associated with YSZ.

Sol-gel routes have been used to prepare alumina-stabilized zirconia (25,26). Nanophase alumina stabilized zirconia should show increased resistance to cracking due to better thermal-mechanical matching with the substrate material, and should have enhanced mechanical properties, such as increased fracture toughness and higher modulus of elasticity, as well as increased resistance to oxidation and hot corrosion attack.

Coatings of ASZ were prepared on stainless steel 304 coupons by dip coating. X-ray diffraction (XRD) and scanning electron microscopy (SEM) were used to characterize the samples. The coatings prepared on the SS substrates were transparent and adherent as deposited. Figure 1 shows the results of 10% $Al_2O_3$ -90% $ZrO_2$  after a heat treatment at 1200°C for 2 hours. Only the tetragonal phase of  $ZrO_2$  and the stainless steel substrate peaks are present. The average crystallite size from XRD line broadening was found to be 32 nm.

In an attempt to prepare thick coatings of zirconia, zirconia sols were loaded with solid particles of either a sol-gel-derived boehmite (amorphous) and a commercially available nanocrystalline alumina. Preliminary results are given in Table I. It was found that the amorphous sol-gel derived boehmite helped to stabilize the tetragonal phase of zirconia as well as aiding in the production of a thicker coating. Further research is being done to optimize solids loading as well as coating thickness (10).

Table I. Effects of solids loadings on zirconia phase.

Solid Dopant	Amount (vol%)	Phase of $ZrO_2$ After 1200°C/2hr	Ave. crystallite size (nm)	Coating thickness (nm)
None	None	Monoclinic	22	40
n-SG ALOOH	1	Monoclinic	23	46
n-SG ALOOH	20	Tetragonal Monoclinic Alpha alumina	29 35 11	525
37 nm $Al_2O_3$	20	Monoclinic Alpha alumina	140 38	876

Relative Intensities

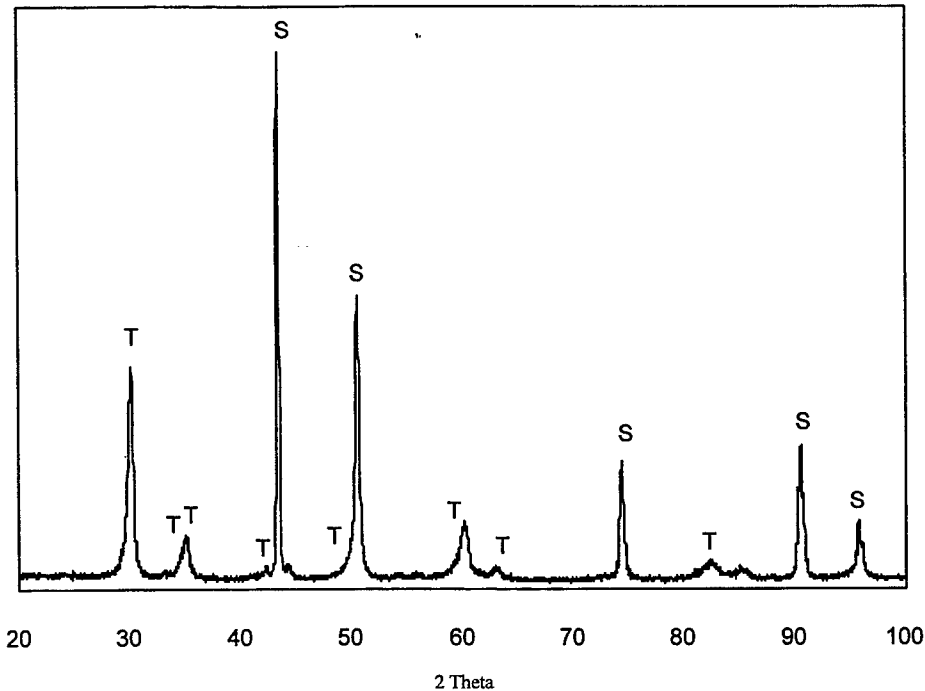


Figure 1. X-ray diffraction pattern of 10% $\text{Al}_2\text{O}_3$ -90% $\text{ZrO}_2$ . The tetragonal peaks of zirconia are marked as well as the stainless steel substrate peaks.

### 3. Polyol Method for Preparing Nanocrystalline Metallic Coatings

Another chemical route for preparing nanostructured coatings is the polyol method. In this method, the metal precursors are first suspended in ethylene glycol. As the temperature is increased toward the reflux temperature, a soluble species is formed that is then reduced by the ethylene glycol. This method can be used to prepare nanocrystalline powders, coatings, and composite materials (27-30).

Nanocrystalline films of copper on AlN were prepared using the polyol method (30,31). Grazing incidence X-ray scattering (GIXS) techniques and small angle scattering techniques were used to determine the evolution of structure as a function of depth as well as the presence of nanometer size structures in the films. Copper is deposited on AlN substrates suspended inside the refluxing solution for a specific amount of time. The substrate is either placed horizontally (H) or vertically (V) with respect to the bottom of the solution flask. The resulting films have thickness that range between 2 and 4 microns.

In order to investigate the nature and origin of the textured region of the coatings, GIXS was used to look at the in-plane structure of the 20 and 30-minute films. Figures 2a-d show the GIXS contour scan of the Cu (200) on 20 and 30 minute samples grown in both a horizontal (Figure 2a, c) as well as vertical (Figures 2 b, d) substrate respectively. The scans consist of a number of peaks, whose d-spacings correspond to strains ranging between +0.1% to -0.6%. Figure 2 also shows that the intensity and location of the different peaks depend on the azimuthal orientation of the sample with respect to the incoming beam.

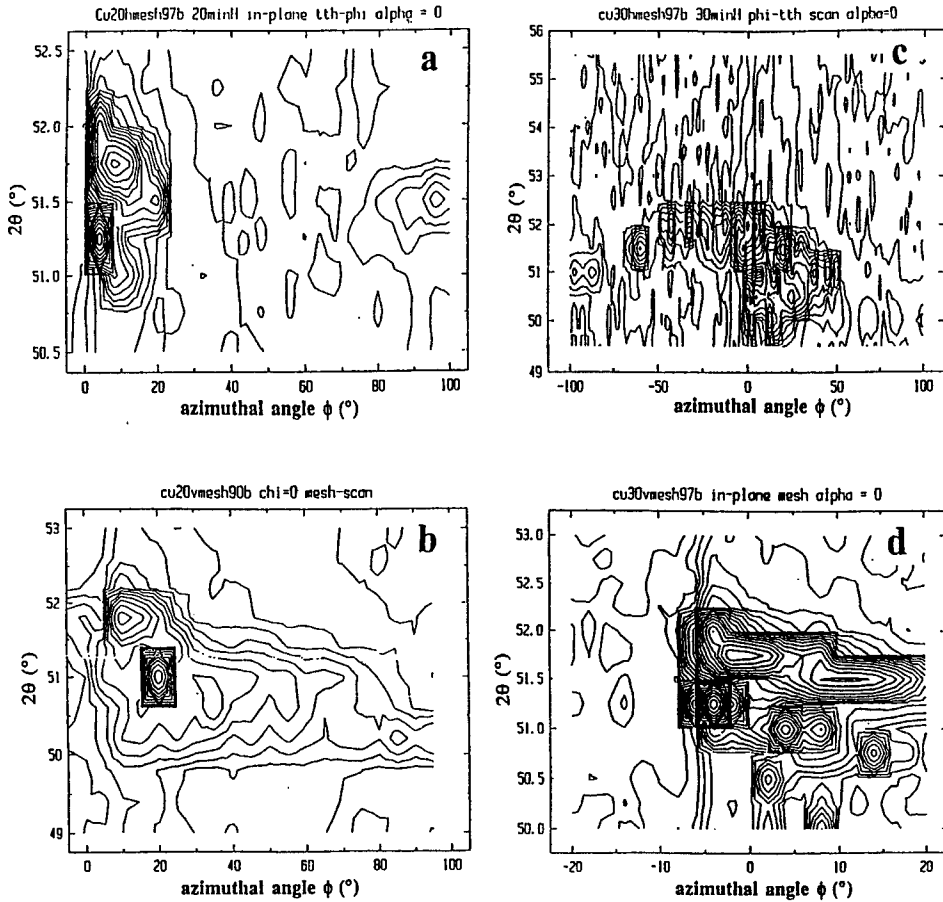


Figure 2. In plane  $2\theta$ - $\phi$  contour maps of the Cu (200) at different deposition times and substrate orientations: a. 20 minute H; b. 20 minute V; c. 30 minute H; d. 30 minute V.

The azimuthal distribution varies both as a function of metallization time as well as substrate orientation. The 20-minute H sample has an azimuthal distribution of approximately  $20^\circ$ , whereas this distribution is  $80^\circ$  in the 20 minute V sample. This suggests that the horizontally prepared sample have in-plane texturing (a preferred azimuthal/stress orientation). This orientation becomes less evident as the metallization time increases, as seen on the 30-minute samples (Figures 2c-d). The 30-minute samples show a broad azimuthal distribution for both H samples and for the interior regions of the V samples. In-situ experiments are currently underway to elucidate film growth (32).

#### 4. Summary

Chemical routes offer many advantages for processing nanostructured coatings. By controlling the synthetic conditions, the microstructure, composition and properties of the coatings can be tuned. Sol-gel techniques were used to prepare alumina-stabilized zirconia for thermal barrier applications and the polyol method was used to prepare nanocrystalline copper coatings on AlN.

#### 5. Acknowledgements

The support of NRL core program on Nanoscale Hybrid Coatings and the ONR Affordability Initiative program on Nanostructured Coatings is acknowledged. The author would like to thank Dr. Luz Martinez-Miranda and Dr. David Lewis III for useful discussions in the course of writing this chapter.

#### References

- Muhammed, M. and Rao, K. V. (Eds) (1999) Proceedings of Nano98, Nanostructured Materials, **12**.
- Chow, G.M. and Noskova, N. I. (Eds) (1998) *Nanostructured Materials, Science and Technology*, Kluwer Academic Publishers, Dordrecht.
- Edelstein, A. S. and Cammarata, R. C. (Eds) (1996) *Nanomaterials: Synthesis, Properties and Applications*, Institute of Physics Publishing, Bristol and Philadelphia.
- Brinker, C. J., Hurd, A. J., Schunk, P. R., Frye, G. C., and Ashley, C.S. (1992) Review of sol-gel film formation, *Journal of Noncrystalline Solids*, **147 & 148**, 424-436.
- Uhlmann, D. R. and Towee, G. (1998) Sol-gel science and Technology: Current State ad Future Prospects, *Journal of Sol-Gel Science and Technology*, **13**, 153-162.
- Nishinari, H., Tatsumisago, M., and Minami, T. (1996) Heat treatment effect of dispersed particles of thick silica films by using electrophoretic sol-gel deposition, *Journal of Material Science*, **31**, 6529-6533.
- Marage, P., Langlet, M., Joubert, J. C. (1994) A new route for the deposition of SiO<sub>2</sub> sol-gel coatings, *Thin Solid Films*, **238**, 218-227.
- Barrow, D. A., Perloff, T.E., and Sayer, M. (1997) Thick ceramic coatings using sol-gel based ceramic –ceramic 0-3 composite, *Surface and Coating Technology*, **76-77**, 113-118.
- Chen, Y., Jin L and Xu Y (1998) Sol-gel processing of organic- inorganic nanocomposite protective coating, *Journal of Sol-Gel Science and Technology*, **13**, 735-738.
- Kurihara, L. K. (1999) unpublished results.
- Moriguchi, I., Maeda, H., Teraoka, Y., and Kagwa, S. (1997) Preparation of a TiO<sub>2</sub> nanoparticulate film using a two dimensional sol-gel process. *Chemistry of Materials*, **9**, 113-118.
- Lan, E.H., Bakul, C. D., Fukuto, J. M., Dunn, B., Zink, J. I., and Valentine, J. S., (1999) Synthesis of sol-gel encapsulated heme proteins with chemical sensing properties, *Journal of Materials Chemistry*, **9**, 45-53.
- Haddow, D. B., Vanes, P. F., Van Noort, R (1998) Sol-gel derived calcium phosphate coatings for biomedical applications, *Journal of Sol-Gel Science and Technology*, **13**, 261-65.
- Lolpatin, C. M., Pizziloni, V., Alford, T. L., and Lawson, T (1998) Hydroxyapatite powders ad thin films prepared by sol-gel techniques, *Thin Solid Films*, **326**, 227-232
- McCarthy O. and Yeatman, E. M. (1998) Control of dopant adsorption from aqueous solution into nonporous sol-gel films, *Journal of Sol-Gel Science and Technology*, **13**, 579-584.
- McCarthy O. and Yeatman, E. M. (1997) Selected area doping of porous sol-gel films for integrated optics. *Optics Letters*, **22**, 1864-1872.
- De, G. (1998) Sol-gel synthesis of metal nanocluster-silica composite films, *Journal of Sol-Gel Science and Technology*, **11**, 289-298.
- Hori, T., Kuramoto, N., Tagaya, H., Karase, M., Kadokawa, J-I. And Chiba, K. (1999) Preparation of conducting films composed of polyaniline and metal oxide by sol-gel method, *Journal of Materials Research*, **14**, 5-7.
- Hedrich, J. L., Miller, R. D., Hawker, C. J., Carter, K. R., Volksen, W., Yoon, D. Y., and Trollsas, M. (1998) Templating Nanoporosity in thin film dielectric insulators, *Advanced Materials*, **10**, 1045-1053.
- Ontalu, V., Cabianii, C., Vasilire, F., Parlog, C. (1996) Crystallization behavior and phase coexistence at morphotropic phase boundaries in PZT thin films prepared by sol-gel processing. *Journal of Materials Science*, **31**, 3639-3642.
- Saegusa, K., (1997) Effect of preparation conditions on short circuits in sol -gel –derived lead titanate thin films, *Journal of Materials Science*, **32**, 5961-68.
- Yamanashi, A., Tanaka, K., Nagatomo, T., and Omoto, O (1993) BaTiO<sub>3</sub> films on silicon –on-insulator structure, *Japanese Journal of Applied Physics. Part 1*, **32**[9B] 4179-81.
- Xu, Z., Chae, H. K., Frey, M. H. and Payne, D. A., 1991, "Chemical Processing and Properties of Nanocrystalline BaTiO<sub>3</sub>," pp. 339-44 in Better Ceramics Through Chemistry V, Proceedings of the Materials Research Society Symposium, Vol. 271 (San Francisco CA 1992) M. H. Hampden-Smith, W. G. Klempner and C. J. Brinker, MRS Pittsburgh,
- Gust, M. C., Evans, N. D., Momoda, L. A., Mecartney, M. L. (1997) In-situ transmission electron microscopy crystallization studies of sol-gel derived barium titanate, *Journal of the American Ceramic Society*, **80**, 2828-2836.
- Kuo, J., and Bourrell, D. L. (1997) Structural evolution during calcination of sol-gel synthesize alumina and alumina-8 vol% zirconia composite. *Journal of Materials Science*, **32**, 2687-2692.

---

26. Paterson, M. J., and Ben-Nissan, B. (1996) Multilayer sol-gel zirconia coatings on 316 stainless steel, *Surface and Coatings Technology*, **86-87**, 153-158.

27. Kurihara, L. K., Chow, G.M., and Schoen, P. E. (1995) Nanocrystalline metallic powders and films produced by the polyol method, *Nanostructured Materials*, **5**, 607-613.

28. Chow, G. M., Schoen, P.E. and Kurihara, L. K. (June 1, 1998) Nanostructured metallic powders and films via a alcoholic solvent process, US Patent 5,759,230.

29. Kurihara, L. K. and Everett, R. K., (1999) unpublished results.

30. Chow, GM, Kurihara, L. K., Ma, D, Fen, C. R., Schoen, P. E. and Martinez-Miranda, L. J. (1997) Alternative approach to electroless Cu metallization of AlN by a nonaqueous polyol process, *Applied Physics Letters*, **70**, 2315-2317.

31. Martinez-Miranda, L. J., Li, Y., Chow, G. M., and Kurihara, L. K. (1999) A depth profile study of the structure and strain distribution in chemically grown Cu films on AlN, *NanoStructured Materials*, **12**, 653-657.

32. Martinez-Miranda, L. J., and Kurihara, L. K., unpublished results.

---

## NANOSTRUCTURED COATINGS OF INNER SURFACES IN MICROPOROUS MATRIXES.

Yu.A. KUMZEROV

*A.F.Ioffe Physico-Technical Institute, Russian Academy of Sciences,  
194021 St.Petersburg, Russia*

### 1. Introduction

There is growing interest in the physical properties of extremely small structures. The experimental realisation of new effects relies on the ability to create new types of structures and devices. Our understanding of material processing in the pursuit of ultra-small structures is continually advancing. Sophisticated epitaxial growth and lateral microstructuring techniques have made it possible to realise low-dimensional electronic systems with quantum confined energy structure i.e. quantum wells, quantum wires and quantum dots. Low-dimensional systems can also be obtained by confining a solid or liquid within the nanometer-sized pores of different porous materials (see [1]). Systems with size-selected nanoparticles embedded in a porous matrix via chemical coating have received some attention these past few years. In this case the confined materials penetrate into the pores due to wetting processes. In the case of non-wetting there is the possibility of using a mechanical coating of inner surfaces of porous materials when some external pressure forces non-wetting liquid into the pores [2]. Mechanical coating means that the mechanical energy of the piston forcing the liquids into the pores transforms to the energy of some new surface arising due to filling process (Fig.1). Since the total surface energy is proportional to the highly developed inner surface of the porous matrix, to surface tension of embedded materials and inversely proportional to the characteristic diameters of pores, for very small diameters a relative amount of surface energy may be very large and even comparable with some traditional sources of energy (Fig.1). For example, liquid mercury embedded into the pores of zeolites (needed pressure is about 20 kbars) accumulates of about 0.4 kJ/g mechanical energy in the form of a surface energy. Such a situation may be used for mechanical energy accumulation [3]. On the other hand the materials coating the inner surfaces of the pores in different porous matrixes may be interesting themselves as some physical objects with the characteristic sizes in nanometre scale i.e. as some new types of nanostructures. The advantages of such nanostructures are connected with the possibility to produce the following:

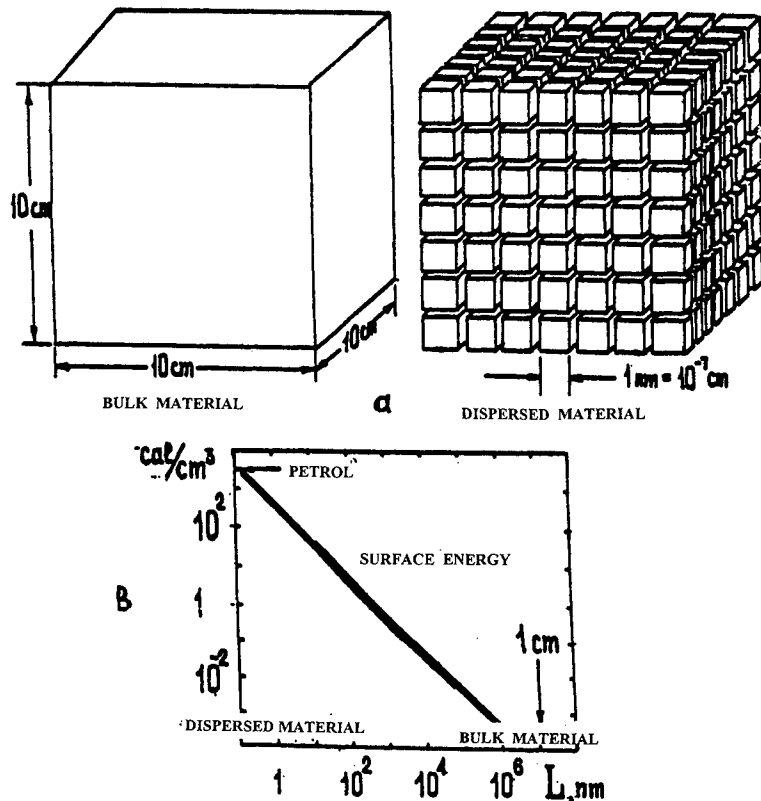


Figure 1. a) Surface arising due to process of material dispersion.  
 b) Surface energy per  $\text{cm}^3$  of dispersed material versus characteristic size of dispersed particles

- nanostructures with different geometries ( two-dimensional film-like structures, one-dimensional wire-like structures, zero-dimensional small particles-like structures).
- nanostructures with a large range of characteristic sizes ( from approximately 1 nm to approximately 100-150 nm).
- nanostructures with very large total amount of nanomaterial ( up to some cubic cm). Such situations permit the use some experimental methods ( neutron scattering, heat capacity measurements) that require a large amount of nanostructures.
- nanostructures from different substances ( from metals, including superconductors, from semiconductors, from insulators, including ferroelectrics etc). Further, examples of such nanostructures, and their physical properties will be presented.

## 2. Irregular systems of small particles in porous glasses.

Small particles or film-like objects can be obtained by confining a solid or liquid within the nanometer-sized pores of porous glasses. Porous silica glasses have often been used for this purpose because of their relatively well-characterised pore structure, large specific pore volumes and availability over several orders of magnitude in the mean pore diameter (about their structure see [4]). The porous matrix usually is prepared from a sodium borosilicate glass. This glass is produced from a melt of 75%  $\text{SiO}_2$ , 20%  $\text{B}_2\text{O}_3$  and 5%  $\text{Na}_2\text{O}$ . Heat treatment leads to a separation in a silicon-rich phase and a boron-rich one. After removing the boron-rich phase, there remains an interconnected solid skeleton of nearly pure  $\text{SiO}_2$  with a rather homogeneous distribution of mass and pores. The pores have a rather narrow size distribution and the pore diameters may be varied from 4 nm to about 100 nm. The pores together with narrow necks, which connect the pores, form a random interconnected network in a glass bulk.

Phase transitions in materials confined within porous glasses have been studied intensively. The melting and freezing within porous glasses have been observed for materials such as water, organic liquids [5,6], metals with low melting point [7-11], helium [12], oxygen and some other simple liquids [13-15]. The ferroelectric phase transition within porous glass has been observed for  $\text{NaNO}_2$  and  $\text{K}_2\text{HPO}_4$  [16,17]. Superconductivity for some metals confined within porous glass has also been observed [18].

## 3. Regular systems of small particles in opals.

The regular systems of identical nanoparticles may be obtained by confining some substances within the pores of opal. Opal itself consists of identical silica balls with diameters (D) ranging from 150 to 350 nm (about its structure, see [19]). The size homogeneity of these spheres allows their assembly in a close three-dimensional lattice, usually with FCC symmetry. Empty voids exist between neighbouring balls which, in turn, form their own regular lattice. There are two types of interpenetrating voids in the opal lattice: eight-fold co-ordinated large voids each connected with eight four-fold co-ordinated small voids. A large void has the form of a truncated tetrahedron with four windows to four large voids. The diameters of spheres inscribed in the larger and smaller voids are  $d_1=0.41D$  and  $d_2=0.23D$  respectively. The diameter of a circle inscribed in the triangular window is  $d_3=0.15D$ . The density of voids in opal is typically  $10^{14}\text{cm}^{-3}$ . The porosity of the ideal package of balls is 26% of the whole volume.

This matrix itself is interesting as a material for so-called photonic crystals, that behave with respect to photons like a dielectric crystal does with respect to electron

waves and demonstrates the photonic gap phenomenon [20]. The lattices of nanosize metal particles may be prepared by impregnation of the opal matrix by molten metal under high hydrostatic pressure conditions [21-25]. The shape of the metal grains is a precise copy of the void configuration since the metal occupies all free matrix volume. Thus, a three-dimensional metal replica of the matrix is formed. According to the matrix structure, each section consisting of two adjacent grains contains a constricted region which may be considered as a weak link i.e. the element of S-c-S ( S-superconductor, c- constriction) type. Owing to the matrix these elements are arranged in a crystalline manner and form a macrosystem. The density of weak links in this material is near  $10^{14} \text{ cm}^{-3}$ . Defects of this secondary lattice are the same as those of ordinary atomic crystals, and therefore the samples are polycrystals consisting of crystallites with characteristic size near 0.01 cm [23]. This object demonstrated properties characteristic of the Josephson systems [21, 23, 24]. The oscillating dependence of the critical current magnitude on the external magnetic field for such samples was observed and its example is shown in Fig.2 ( from [23]). Such dependence may be connected with a regular structure of investigated materials.

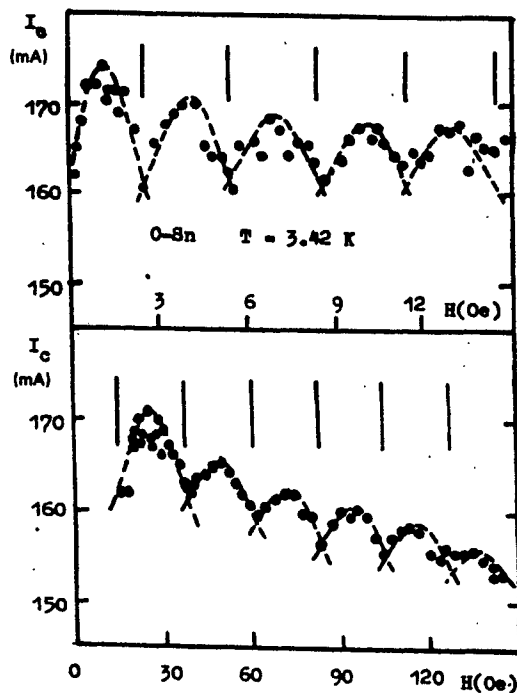


Figure 2. Critical current ( $I_c$ ) vs magnetic field ( $H$ ) for Sn-based sample. The upper plot corresponds to narrow and the lower plot to the wide scale of the magnetic field. The measured points are connected by lines to guide the eye. The sections indicate the periodicity.

#### 4. Nanoclusters in zeolites.

The further type of microporous materials are the crystalline framework solids such as zeolites (about their structure, see [26]), that have found great utility as catalysts and sorption media because of their large internal surface area. They have regular arrays of identical voids, forming three-dimensional channel networks with very small sizes compared with the diameters of the atoms. For example, the channels in NaA zeolite have maximum diameter of 11.4 Å, run in three perpendicular directions, and are interrupted by narrow diaphragms having a diameter 4.2 Å. The cavities in NaX zeolite form a diamond lattice and have a maximum diameter of 13 Å, the diaphragms have a diameter of 8 Å.

Wetting liquids such as water will spontaneously fill the channels and cavities of zeolites essentially completely. It was shown in [27,28] that non-wetting liquids (mercury, gallium, bismuth) can be introduced into the regular channels of zeolites at sufficiently high pressures. The pressures at which mercury and gallium fill NaA zeolite are 14.5 kbar and 23 kbar, respectively. The critical pressures for NaX zeolite are 12.5 kbar (Hg) and 20 kbar (Ga). These values can be estimated from well-known porometric equation, based on the concepts of surface tension and wettability of liquid [27]

$$P_c = 0.4\sigma/d,$$

where  $P_c$  is critical pressure (kbar),  $\sigma$  is surface tension (dyn/cm) and  $d$  is the channel diameter (Å). After the external pressure is removed, some of the liquid metal leaves the zeolite channels. Nevertheless, the density of the zeolites shows that about half of the metal which was in the zeolite remains there. The rest of the metal collects in cavities and drops as a result of surface tension thus forming some ordered secondary crystal.

Some of the physical properties of such materials were investigated. For Hg and Ga drops a phase transition was observed [29]. It was manifested by singularities in the temperature dependence in the electrical conductivity and specific heat. The singularities were observed at temperatures much lower than the melting point of the bulk metal. It was concluded that the phase transition occurred in a system of interacting drops composed of metal atoms, and the interaction stabilised the system against fluctuations. The absorption spectra of Se drops in the zeolites NaA and NaX [30] were investigated. The form of the spectra obtained is typical of absorption spectra of crystals in the region of the optical absorption edge. It was concluded that the lattice of the clusters produced in the zeolite cavities is also a crystal, and the obtained spectral curves correspond to the absorption spectra of such cluster crystals in the region of the interband transitions.

A strong nonlinearity of the current-voltage characteristic of the cluster superlattice of tellurium in NaX zeolite was observed [31]. The characteristic was a series of current peaks rising in increasing amplitude in the field. This behaviour is

demonstrated in Fig.3 ( from [31]). It was shown that these peaks appeared periodically when considered as a function of  $1/E$  ( $E$  is electric field intensity). The periodicity of the current peaks ( on the  $1/E$  scale) of the current-voltage characteristic for Te in NaX zeolite was discussed on the basis of a theory of electrophonon resonance.

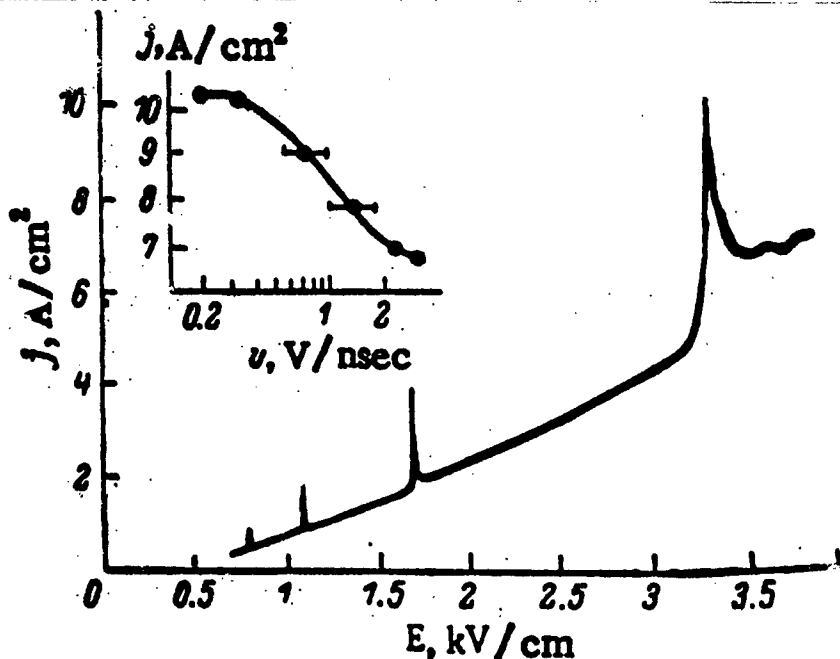


Figure 3. Oscillogram of the current-voltage characteristic obtained using sawtooth voltage pulses with a leading edge  $\tau_1 \sim 50$  nsec. The inset at the top of the figure gives the dependence of the amplitude of the  $n=1$  peak on the rate of the rise of the voltage  $v$ .

## 5 Quantum wires in chrysotile asbestos.

Quantum wires of a wide class of materials can be prepared in porous matrices. This is natural chrysotile asbestos mineral ( composition  $Mg_3Si_2O_5(OH)_4$  ). It is a regular set of closely packed parallel ultrathin dielectric tubes with external diameters of  $\approx 30$  nm ( this value determines the distance between the centres of the neighbour channels), and with internal channel diameters of 2-10 nm depending of the origin of the mineral ; its structure is described in [32, 33]. Chrysotile asbestos tubes constitute single-crystal alumino-silicate sheets ( the thickness of one sheet is 7A), which owing to their structural characteristics twist themselves into rolls until the radius of curvature of the outer and inner layers starts differing appreciably from their optimum value. The tubes of natural chrysotile asbestos reach lengths of several centimetres.

When we fill the channels with molten materials (Hg, Sn, Bi, In, Pb, InSb, Se, Te) under high pressure conditions we have the possibility of obtaining a regular system of ultrathin parallel wires. Fig.4 demonstrates the model of this system. The reduction in the pressure of the molten metals after their introduction into the asbestos leads to a loss of sample conductivity on account of the oozing of the liquid metals from the channels; it is therefore essential to carry out the conductivity measurements directly under pressure, using the autonomous chamber with a reserve valve.

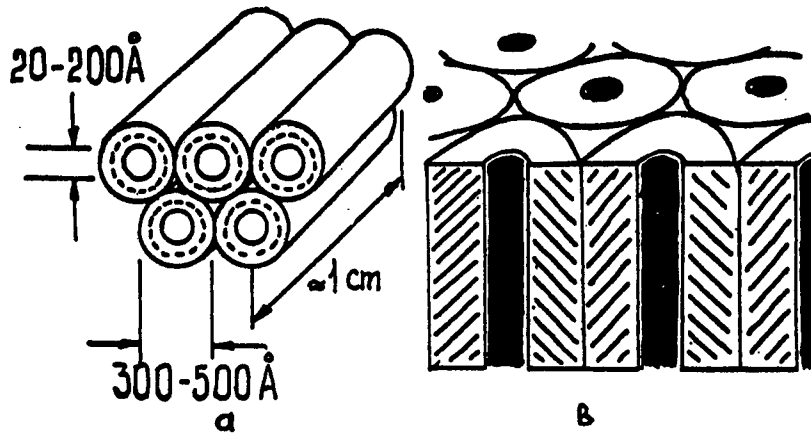


Figure 4. a) Close packed tubes of chrysotile asbestos.  
b) System of ultrathin wires within the channels of chrysotile asbestos

The superconducting transitions of a complete series of such samples by the contact method were studied [34-40]. Particularly, the superconducting transition of metals in asbestos channels has a temperature spread that is due to fluctuations which are significant for such thin elements [35]. Fig.5 demonstrates such behaviour for mercury wires of 80 Å diameter. The measurements performed on mercury wires with diameters 20 Å [35] show that their superconducting transition is smeared from ~2 K to ~6 K that  $\Delta T/T_c \sim 1$ , where  $\Delta T$  is the width of critical region. Some attempts of theoretical description of the fluctuation smeared superconducting transition are known [41-43] and the theoretical dependence is shown in Fig.5 by the solid line. It may be seen that the theoretical curve in the low temperature region is quite consistent with the experimental data. The critical temperature of the ultrathin wires was determined from resistance dependence on temperature, using some theoretical description of the fluctuation smeared superconducting transition [40]. Critical temperatures vs diameter were measured for mercury, tin and indium with wires from 20 Å to 150 Å. They are demonstrated in Fig.6. The critical temperature of tin wires increases with decreasing diameter and critical temperature on diameter dependence.

for mercury and indium wires have a maximums at 4.6K for diameter  $\approx 40\text{A}$  (Hg) and at 6.2K for diameter  $\approx 20\text{A}$  (In).

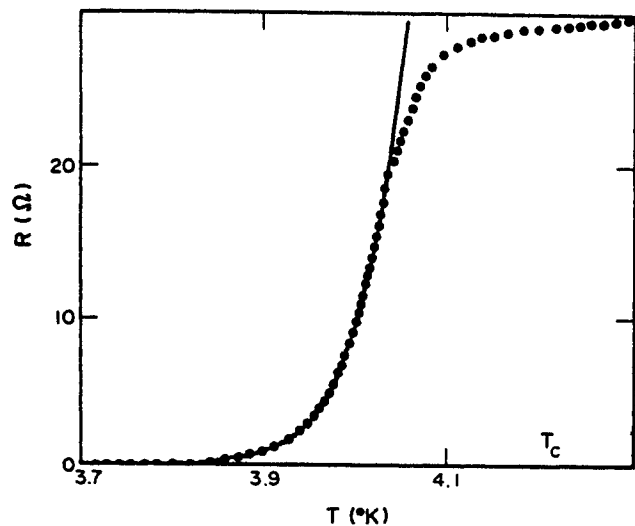


Figure 5. Resistance as a function of temperature for mercury wires of 80A diameter in the superconducting region

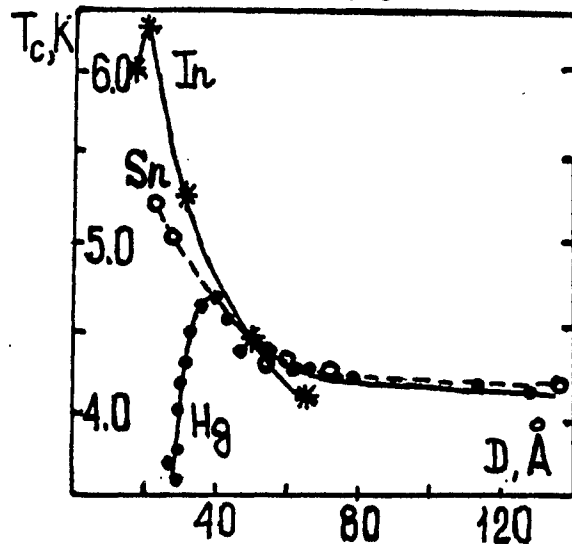


Figure 6. Superconducting critical temperature dependence on the diameter of mercury, tin and indium wires.

Some increase of resistance and non-linearity of current-voltage characteristics with decreasing temperature were observed on mercury ultrathin wires [35,44]. The temperature dependence of mercury 25A wires resistance in the region below 60K is shown in Fig.7. In the temperature range 10-60K the experimental data are well described by  $T^{-3/2}$  dependence. Below 10K the

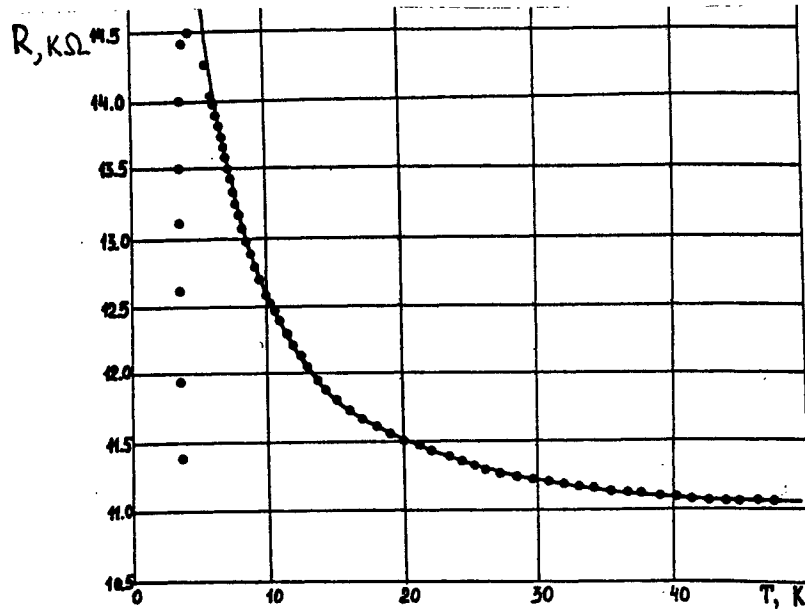


Figure 7. The dependence of resistance of 25A mercury wires on temperature (the solid line corresponds to  $\Delta R/R \sim T^{-3/2}$  dependence).

superconducting fluctuations dominate the conductivity. As to wires with larger diameters, their negative temperature derivative of resistivity decreases with the diameter. These results were explained as the display of localisation effects in disordered one-dimensional system. The temperature dependence of resistivity of thin wire due to localisation (one-dimensional case) can be written as [46]

$$R = R_0 [1 + \rho_B (D\tau_i)^{1/2} / R_T d^2]$$

where  $\rho_B$  is the impurity scattering resistivity,  $D = v_F l / 3$  is the diffusion constant,  $v_F$  is the Fermi velocity,  $R_T = 36500 \Omega$ ,  $d$  is diameter of the wire,  $l$  is the elastic mean free path,  $\tau_i$  is the inelastic scattering time. The necessary condition for one-dimensional behaviour is  $d < (D\tau_i)^{1/2}$ . The temperature dependence of wire resistance in this equation is governed by the temperature dependence of  $\tau_i$ , so that  $\Delta R/R_0 = (R - R_0)/R_0 \sim (\tau_i)^{1/2}$ . Since we have  $\Delta R \sim T^{-3/2}$  dependence, it follows that  $\tau_i \sim T^{-3}$ . Such temperature dependence of inelastic scattering time may be due to scattering on three-dimensional

phonons. Using this equation we find  $\tau_i \sim 10^{-10}$  sec at 10K. The localisation length  $(D\tau_i)^{1/2}$  at 10K is about  $3 \times 10^{-5}$  cm which satisfies the localisation criterion for wires and so the data obtained may be interpreted in terms of one-dimensional electron localisation.

The melting and freezing as a first-order phase transition of mercury wires in the range between 20Å and 100Å [45] was investigated. The first-order phase transitions in dispersed systems have been studied considerably less extensively than the second-order phase transitions. There have been virtually no experiments of this type performed using approximately one-dimensional systems as objects of investigation. The melting region of extremely fine mercury wires was identified on the temperature curve of the resistance. It was of considerable interest to study this transition as a function of wire diameter. The samples whose wires had a small spread in diameter (not exceeding  $\sim 5\%$ ) were chosen for measurements. The melting region extends over a large temperature interval, which is probably attributable to the fluctuations whose appreciable effect on the phase transitions in one-dimensional systems has been well established. At such a highly diffuse transition, it is not clear what point should be regarded as the melting point. Since there are no physically sound criteria for determining this point on the resistance versus temperature curve in the melting region (although these criteria can be determined for second-order phase transitions in several cases [40]), we can arbitrarily assume that the melting point is that point at which the resistance changes only half as much as it does during melting.

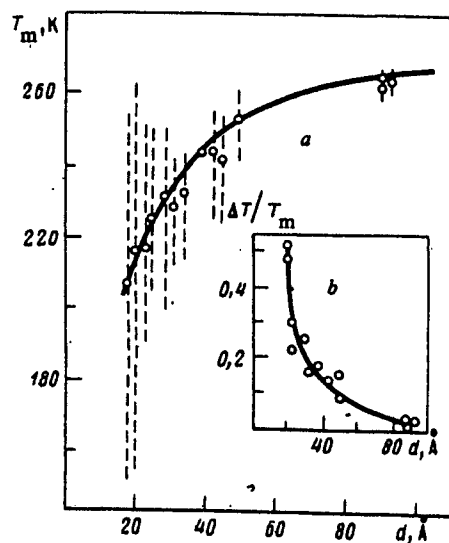


Figure 8. a) The melting point of extremely fine mercury wires versus the diameter (dashed line corresponds to the diffuse-transition region).  
 b) The diffusive melting range versus diameter

The dependence of a particular melting point on the diameter is shown in Fig.8. Also shown here is the region in which the transition becomes diffuse (dashed lines). The solid curve corresponds to the dependence  $T=T_0(1-d/d)$ , where  $d\sim 5.5\text{ \AA}$  and  $T_0\sim 280\text{ K}$ , which is equal to the melting point of bulk mercury at a pressure of  $\sim 10\text{ kbar}$ . Fig.2b is a plot of  $\Delta T/T_m$  ( $\Delta T$  is the diffuse-transition region) as a function of the diameter, and the solid curve corresponds to the relation  $\Delta T/T_m=(D/d)^2$ , where  $D\sim 14\text{ \AA}$ .

In addition some optical properties of ultrathin wires incorporated within chrysotile asbestos nanotubes were studied. Polarised optical absorption spectra of Hg, Bi and InSb wires have been studied in the spectral region 0.5-3 eV, and high anisotropy of the absorption has been observed [47,48]. InP quantum wires have been produced in channels of asbestos by metal-organic chemical vapour deposition [49]. A comparative study of Raman, optical absorption, and photoluminescence spectra revealed the dependence of the optical properties of quantum wires on interface effects, namely, atomic interaction in the wires, wire-matrix, and wire-wire interactions.

## 6. Conclusions.

The results obtained clearly show good potential for the use of the natural and artificial microporous media for the preparation of the artificial systems that are interesting for scientific investigations and potential applications. The utilisation of porous glasses, artificial opals, and chrysotile asbestos matrices allows the formation of nanostructures for measurement of electrical, optical and other properties.

## 7. Acknowledgements.

This work has been partly supported by Programme «Physics of Nanostructures» (grant- 99-1112) and RFFI ( grant 97-02-18267).

## 8. References.

1. Schwarz J.A. and Contescu C.I.(eds) (1999) *Surfaces of Nanoparticles and Porous Materials*, Marcel Dekker Inc., New-York
2. Bogomolov V.N.(1978) Liquids within ultrathin channels, *Uspehi fizicheskikh nauk* **124**, 171-182
3. Bogomolov V.N.(1993) Surface energy and prospects for its use in power generation, transport and ecology, *Sov. Technical Physics*, **38**, 224-227

---

4. Levitz P., Ehret G., Sinha S.K., Drake J.M.(1991) Porous vycor glass: the microstructure as probed by electron microscopy, direct energy transfer, small-angle scattering, and molecular adsorption, *J.Chem.Phys.*, **95**, 6151-6161
5. Mu R. and Malhorta V.M.(1991) Effects of surface and physical confinement of the phase transitions of cyclohexane in porous silica, *Phys.Rev.* **44B**, 4296-4303
6. Strange J.H., Raham M., Smith E.G.(1993) Characterisation of porous solids by NMR, *Phys.Rev.Lett.* **71**, 3589-3591
7. Borisov B.F., Charnaya E.V., HoffmannW-D., Michel D., Shelyapin A.V. and Kumzerov Yu.A.(1997) NMR and acoustic investigations of the melting-freezing phase transition of gallium in a porous glass, *J.Phys.Condens.Matter* **9**, 3377-3386
8. Borisov B.F., Charnaya E.V., Kumzerov Yu.A., Radzhabov A.K., Shelyapin A.V.(1994) Phase transitions for gallium microparticles in a porous glass, *Sol.St.Commun.* **92**, 531-533
9. Shabanova E., Charnaya E.V., Schaumburg K. and Kumzerov Yu.A.(1997) NMR studies of gallium embedded into a porous glass, *Physica* **B229**, 268-274
10. Kumzerov Yu.A., Nabereznov A.A., Vakhrushev S.B. and Savenko B.N.(1995) Freezing and melting of mercury in porous glass, *Phys.Rev.* **B52**, 4772-4774
11. Charnaya E.V., Tien C., Lin K.J., Kumzerov Yu.A.(1998) X-ray studies of the melting and freezing phase transitions for gallium in a porous glass, *Phys.Rev.* **58B**, 11089-11092
12. Beamish J.R., Mulders N., Hikata A. and Elbaum C.(1991) Vacancy diffusion and stress relaxation in  $^4\text{He}$  freezing in porous Vycor, *Phys.Rev.* **B44**, 9314-9318
13. Molz E., Wong A.P.Y., Chan M.H.W. and Beamish J.R.(1993) Freezing and melting of fluids in porous glasses, *Phys.Rev.* **B48**, 5741-5750
14. Warnock J., Awschalom D.D. and Shafer M.W.(1986) Geometrical supercooling of liquids in porous glass, *Phys.Rev.Lett.* **57**, 1753-1756
15. Schindler M., Destinger A., Kondo Y. and Pobell F.(1996) Hydrogen in porous Vycor glass. *Phys.Rev.* **B53**, 11451-11461
16. Colla E.V., Koroleva E.Yu., Kumzerov Yu.A., Savenko B.N., Vakhrushev S.B.(1996) Ferroelectric phase transitions in materials embedded in porous media, *Ferroelectric Letters* **20**, 143-147
17. Colla E.V., Fokin A.V., Kumzerov Yu.A.(1997) Ferroelectric properties of nanosize KDP particles, *Sol.St.Commun.* **103**, 127-130
18. Charnaya E.V., Tien C., Lin K.J., Kumzerov Yu.A.(1998) Superconductivity of gallium in various confined geometries, *Phys.Rev.* **B58**, 467-472
19. Balakirev V.G., Bogomolov V.N., Zhuravlev V.V., Kumzerov Yu.A., Petranovskii V.P., Romanov S.G., Samoilovich L.A. (1993) Three-dimensional superlattices within the matrixes of opal, *Kristallographia* **38**, 111-120
20. Bogomolov V.N., Gaponenko S.V., Germanenko I.N., Kapitonov A.M., Petrov E.P., Gaponenko N.V., Prokofiev A.V., Ponyavina A.N., Silvanovich N.I., Samoilovich S.M. (1997) Photonic band gap phenomenon and optical properties of artificial opals, *Phys.Rev.* **55E**, 7619-7625
21. Bogomolov V., Zhuravlev V., Zhadorozhni A., Kolla E., Kumzerov Yu. (1982) Voltage-current characteristics of regular system of weakly coupled superconducting particles, *JETP Lett.* **36**, 365-367
22. Bogomolov V.N., Kazantseva L.K., Kolla E.V., Kumzerov Yu.A.(1987) Periodic peaks of a resistive state during destruction of the superconductivity by a current in a lattice of weakly coupled indium particles, *Sov.Phys.Solid State* **29**, 359
23. Bogomolov V.N., Kumzerov Yu.A., Romanov S.G., Zhuravlev V.V. (1993) Josephson properties of the three-dimensional regular lattice of the weakly coupled nanoparticles, *Physica* **C208**, 371-384
24. Kumzerov Y., Bogomolov V., Colla E., Romanov S. (1994) Three-dimensional regular Josephson medium from identical nanoparticles, *Phys.Low-Dim.Struct.* **11/12**, 129-134

25. Babmuratov K.Kh., Zhuravlev V.V., Kumzerov Yu.A., Romanov S.G., Khachaturov S.A. (1993) Structure of a resistive superconducting transition in a regular lattice of indium nanoparticles, *Sov.Phys.Solid State* **35**, 795-797

26. Breck D.W. (1974) *Zeolite molecular sieves*, A Wiley-Interscience Publication john Wiley&Sons, New-York

27. Bogomolov V.N.(1972) Nonwetting liquids in ultrathin channels, *Sov.Phys.Solid State* **14**, 1048-1050

28. Bogomolov V.N., Zhadorozhnii A.I.(1975) Monoatomic chains of Hg and Bi in mordenite and surface tension of liquid metals, *Sov.Phys.Solid State* **17**, 1078-1079

29. Bogomolov V.N., Volkonskaya T.I., Zadorozhnii A.I., Kapanadze A.A., Lutsenko E.L. (1975) Phase transition in a system of Ga and Hg drops in zeolite cavities of 12A diameter, *Sov.Phys. Solid State* **17**, 1110-1112

30. Bogomolov V.N., Lutsenko E.L., Petranovskii V.P., Kholodkevich S.V.(1976) Absorption spectra of three-dimensionally-ordered system of 12A particles, *JETP Lett.* **23**, 482-484

31. Bogomolov V.N., Vaitekunas F.K., Zadorozhniy A.I., Pavlova T.M., Sutkus K.V. and Yashin G.Yu. (1983) Determination of the time taken to establish a current flow regime in the region of N-type peaks of the current-voltage characteristic of an NaX-Se crystal, *Sov.Phys. Solid State* **25**, 1983-1984

32. Pundsak F.L. (1961) The pore structure of chrysotile asbestos, *J.Phys.Chem.* **65**, 30-33

33. Yada K. (1967) Study of chrysotile asbestos by a high resolution electron microscope, *Acta Cryst.* **23**, 704-707

34. Bogomolov V.N., Krivosheev V.K., Kumzerov Yu.A. (1972) Superconductivity of mercury in chrysotile asbestos, *Sov.Phys. Solid State* **13**, 3148-3150

35. Bogomolov V.N., Kumzerov Yu.A. (1975) Fluctuations in mercury filaments five atoms in diameter, *JETP Lett.* **21**, 198-200

36. Bogomolov V.N., Klushin N.A., Kumzerov Yu.A. (1977) Superconducting transition of indium filaments at 6K, *JETP Lett.* **26**, 72-74

37. Bogomolov V., Kumzerov Y., Pimenov V. (1981) Splitting of the heat capacity peak of metal filaments in a dielectric matrix in the superconducting region with decreasing diameter of the filaments, *Physics Letters* **86A**, 183-184

38. Bogomolov V.N., Kvyatkovskii B.E., Kolla E.V., Ktitorov S.A., Kumzerov Yu.A. and Okuneva N.M. (1981) N-type current-voltage characteristic of ultrathin metal filaments in the superconducting state, *Sov.Phys. Solid State* **23**, 1271-1272

39. Bogomolov V.N., Kolla E.V., Kumzerov Yu.A., Okuneva N.M., Prigodin V.N. (1980) Appearance of the dielectric instability and its coexistence with the superconductivity in ultrathin metallic filaments with decreasing diameter, *Sol.St.Commun.* **35**, 363-366

40. Bogomolov V.N., Kolla E.V., Kumzerov Yu.A. (1983) Determination of the critical temperature of the ultrathin metals filaments superconducting transition and its dependence on the filament diameter, *Sol.St.Commun.* **46**, 159-160

41. Langer J.S.,Ambegaokar V. (1967) Intrinsic resistive transition in narrow superconducting channels, *Phys.Rev.* **164**, 498-510

42. McCumber D.E., Halperin B.I. (1970) Time scale of intrinsic resistive fluctuations in thin superconducting wires, *Phys.Rev.* **B1**, 1054-1070

43. Larkin A.I., Ovchinnikov Yu.N. (1973) Fluctuation conductivity in the vicinity of the superconducting transition, *J.Low Temp.Phys.* **10**, 407-421

44. Bogomolov V.N., Kolla E.V., Kumzerov Yu.A. (1983) One-dimensional effects in low-temperature conductivity of ultrathin metallic filaments, *Sol.St.Commun.* **46**, 383-384

45. Bogomolov V.N., Kolla E.V., Kumzerov Yu.A. (1985) First-order phase transition in an approximately one-dimensional system, *JETP Lett.* **41**, 34-37

46. Thouless D.J. (1980) The effect of inelastic electron scattering on the conductivity of very thin wires, *Sol.St.Commun.* **34**, 683-685

---

- 47. Kumzerov Y., Poborchii V. (1994) Ultrathin wires with near atomic diameters, *Phantoms Newsletter* **4**, 2-3
- 48. Ivanova M.S., Kumzerov Y.A., Poborchii V.V., Ulashkevich Y.V., Zhuravlev V.V. (1995) Ultrathin wires incorporated within chrysotile asbestos nanotubes: optical and electrical properties, *Microporous Materials* **4**, 319-322
- 49. Romanov S.G., Butko V.Yu., Kumzerov Yu.A., Yates N.M., Pemble M.I., Agger J.R., Anderson M.W., Sotomayor-Torres C.M. (1997) Interface phenomena and optical properties of structurally confined InP quantum wires ensembles, *Phys.Solid State* **39**, 641-648

---

## ELECTROLESS DEPOSITED NANOSTRUCTURED NiCo FILMS

G.M. Chow  
Department of Materials Science  
National University of Singapore  
Kent Ridge, Singapore 117543, Republic of Singapore

*Email:* [mascgm@nus.edu.sg](mailto:mascgm@nus.edu.sg)

### 1. Abstract

Nanostructured metal films and coatings with unique properties can be synthesized using solution chemistry. In this paper, the non-aqueous electroless polyol synthesis, characterization and properties of NiCo films are discussed.

### 2. Introduction

Nanostructured films and coatings with unique properties can be fabricated by many methods. Physical vapor techniques, such as thermal evaporation and sputtering, are generally line-of-sight processes suited for deposition on planar surfaces. The limitation in these processes is caused by the high sticking coefficients of atoms that cannot readily move around after impacting the surface. On the other hand, chemical vapor deposition and solution chemistry methods are generally free from such limitation, since the atoms have smaller sticking coefficients and higher mobility at the surface. Thus, these techniques are suitable for depositing films on not only planar but also hidden and complex surfaces. Further, high-cost vacuum technology is not needed in wet chemistry processing.

Using solution approach, nanostructured ceramic films can be prepared by sol-gel method, and metal films can be synthesized using electrodeposition and electroless deposition. Electrochemical technology finds many applications ranging from traditional surface finishing to high-tech fabrication of advanced materials for microelectronics and media storage [1].

#### 2.1. AQUEOUS ELECTRODEPOSITION

In electrodeposition [2], metal precursors in the solution are reduced by the application of an electric current, resulting in deposition of the metal film on the conductive substrate. Aqueous electrolytes are extensively used because water is a

---

good solvent for many salts and it is inexpensive. Experimental parameters, such as electrolyte composition, pH, temperature and agitation, applied potential and current, are controlled to optimize the thickness, grain size and composition of deposited films. Special care is required to deposit films on substrates with sharp corners and irregular surface, since the electric field distribution may not be uniform at these regions. For electroplating of non-conductors such as plastics and ceramics, they must be plated with metal by another process such as electroless plating. Thick deposits can be formed on a mandrel by electroforming and subsequently removed and machined for applications.

Nanostructured materials, for example, compositionally modulated multilayers [3] and GMR films [4,5], have been synthesized using electrodeposition. Polycrystalline, nanostructured Ni was synthesized by pulsed electrodeposition in a bath containing saccharin [6]. The grain size was in the range of 10 to 40 nm and showed initial rapid decrease with increasing saccharin concentration. The deposits were smooth and bright. The growth texture was dependent on the concentration of saccharin in the plating bath. Industrial applications of electrodeposited nanocrystals include, for example, corrosion and wear resistance, magnetic materials, fuel cells and catalysis [7].

## 2.2. AQUEOUS ELECTROLESS DEPOSITION

In electroless deposition (often known as electroless plating) [8], electrons are produced by chemical reactions without the application of an external current. Unlike electrodeposition, electroless metallization can be applied to both conductor and insulator. This process may occur by one of the following: deposition by ion or charge exchange, deposition by contacting the metal to be plated, and autocatalytic deposition on catalytic surfaces in solutions containing appropriate reducing agents. For autocatalytic electroless deposition, the surface to be metallized is initially treated with catalysts such as nanosized Pd colloids. Reduction of metal ions or metal complexes by the reducing agent in the plating bath results in metal deposition on the substrate surface. Each freshly deposited metal layer then becomes the catalyst for subsequent metal deposition. Electroless plating allows for the deposition of uniform films on irregular-shaped objects with complex and hidden surfaces.

Electroless films and coatings find applications in wear resistance, corrosion resistance, solar absorber optics and electronics. Nanostructured Ni and Co films were electroless deposited [9]. Self-assembled biomolecular tubular microstructures were electroless coated with nanostructured metal films for application as high-current density cathode in vacuum field emission [10,11,12]. Generally, the crystallinity and the grain size (ranging from 2 – 100 nm) can be controlled by controlling the composition of the plating bath and performing suitable post-deposition heat treatment. The control of the size of adsorbed catalysts is also critical in controlling the particle size of nanostructured electroless Ni deposits. Smaller catalysts were bound to the chemically modified substrate surface and led to a reduction of particle size in the deposits by 3-4 times [13]. Electroless deposition was also used to deposit CoNiP films consisted of oriented hcp crystallites [14]. The crystallite size decreased

from about 37 nm to 25 nm with increasing ammonia concentration. The coercivity of the films decreased from about 2600 Oe to less than 1000 Oe with decreasing crystallite size.

### 2.3. NON-AQUEOUS, ELECTROLESS POLYOL DEPOSITION

When the substrate and deposited materials are susceptible to hydrolysis and oxidation, adverse material properties may result from using aqueous chemical processes. For deposition of nanostructured metallic materials with significant amount of surfaces and interfaces, these problems may become more acute. Therefore, a simple and non-aqueous approach has been sought as an alternative to aqueous processing. The polyol method, a non-aqueous electroless process, has been used to synthesize micron, submicron and nanostructured powders [15,16,17,18]. Recently, we have extended this polyol method to synthesize nanostructured metal films [17]. The process involves the reduction of metal salts in refluxing ethylene glycol to deposit metal films on the substrates. Film deposition can occur on planar or complex surfaces of both suitable conductor and insulator substrates, without any pre-deposition surface treatment such as the catalyzation of insulator surface as in traditional electroless plating. For example, Co was deposited on WC substrate [19] and Cu was deposited on AlN [20].

In this paper we describe our work on polyol deposition of nanostructured  $\text{Ni}_x\text{Co}_{100-x}$  films [21]. Nickel-cobalt find applications as decorative bright coatings, engineered hard coatings, and magnetic films and coatings.

### 3. Experimental

Nickel (II) acetate tetrahydrate and cobalt (II) acetate tetrahydrate were suspended in 200 ml ethylene glycol. The total precursor concentration was kept at 0.1M. The nominal compositions of  $\text{Ni}_x\text{Co}_{100-x}$  films were obtained from the starting precursor molar ratio. Coarse-grained, polycrystalline Cu substrates with a (200) texture were vertically suspended in the mixtures. The mixtures were heated and refluxed at 194° C for 1 h for film deposition. For  $\text{Co}_{100}$  film, the deposition was carried out for 7 h due to the greater difficulty to reduce Co under these conditions. The structure of deposited films on Cu substrates was studied using  $\theta$ -2 $\theta$  X-ray diffraction (XRD). The diffraction peaks were analyzed using a profile fit routine. Average crystallite size (x-ray coherence length) was estimated from the XRD line broadening. The film thickness was measured from cross-sectioned films with scanning electron microscopy (SEM). The hysteresis loops were measured with vibrating sample magnetometry (VSM) at room temperature using a maximum field of  $\pm 50$  kOe. Both in-plane ( $\parallel$ ) and perpendicular-to-plane ( $\perp$ ) measurements were made. The Vickers microhardness (HV) of deposited films on substrates was measured using a load of 25 gf for 10 s.

Nickel and cobalt are miscible. The thickness of deposited  $\text{Ni}_x\text{Co}_{100-x}$  films was in the range of 0.6 to 1.6  $\mu\text{m}$ . The XRD data showed that the films had a single fcc phase with a (111) texture. Figure 1 shows the XRD results of films with  $x = 30, 50$  and 70. The (111) diffraction peaks were observed for  $x \leq 30$ . For  $x \geq 50$ , higher fcc

reflections were also observed. For  $\text{Co}_{100}$ , in addition to the predominant fcc phase, a weak signal that could be assigned to hcp phase was detected. The average crystallite size (estimated from (111) line broadening) increased with  $x$  from 15 to 64 nm (Fig. 2). Since Ni was more easily reduced than Co, a higher Ni precursor concentration favored the growth of larger Ni-rich crystallites in Ni-rich films. Because of the very close lattice parameters of fcc Ni (3.5238 Å) and fcc Co (3.5447 Å), the appearance of a single set of fcc peaks as shown in XRD results could not be used to ascertain if the films were solid solutions or composites.

When the coherent inhomogeneities of nanostructured materials are below a critical size, conventional XRD should not be used alone to determine the structure of a composite or solid solution [22]. For example, other complementary techniques such as extended x-ray absorption fine structure (EXAFS) and nuclear magnetic resonance (NMR) have been used for structure determination of nanostructured Co-Cu powder [18]. Recently, the structure of these polyol-deposited  $\text{Ni}_x\text{Co}_{100-x}$  films has been studied using anomalous x-ray scattering (AXS) [23]. The association of an element in-question with a specific Bragg peak was investigated. It was shown that nanostructured NiCo films did not necessarily form solid solution as expected from their phase diagram or suggested by the results of conventional XRD. Further work to elucidate the nanostructures of these films is currently pursued using AXS, EXAFS and high-resolution transmission electron microscopy.

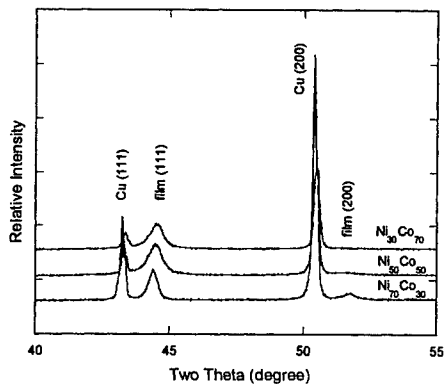


Figure 1. XRD of Ni-Co films,  
 $x = 30, 50$  and  $70$

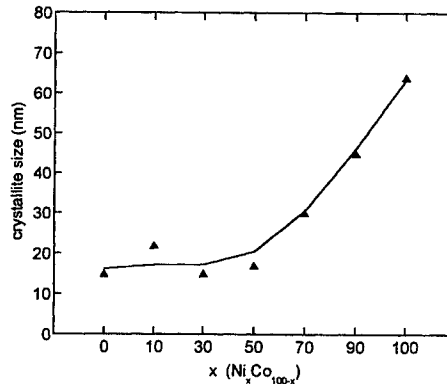


Figure 2. Dependence of crystallite size on composition

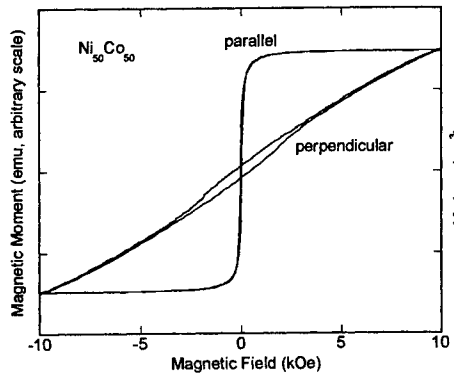


Figure 3. Hysteresis loops of  $\text{Ni}_{50}\text{Co}_{50}$  in parallel and perpendicular directions

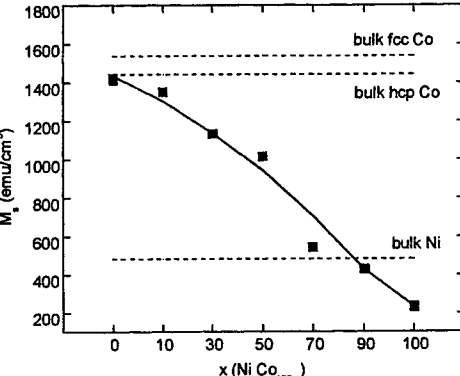


Figure 4. Dependence of  $M_{s//}$  on composition

Saturation magnetization ( $M_s$ ) of bulk fcc Ni, fcc Co and hcp Co are 484, 1538 and 1442 emu/cm<sup>3</sup>, respectively. The hysteresis loops of  $\text{Ni}_x\text{Co}_{100-x}$  films showed in-plane magnetization anisotropy. Figure 3 shows the hysteresis loops of  $\text{Ni}_{50}\text{Co}_{50}$  in the parallel and perpendicular directions. Figure 4 shows the dependence of in-plane saturation magnetization ( $M_{s//}$ ) on composition. The  $M_s$  of the  $\text{Ni}_{100}$  sample was 236 emu/cm<sup>3</sup>, but it could approach the value of bulk Ni by increasing the deposition time [24]. The  $M_s$  increased with increasing Co content and reached as high as 1421 emu/cm<sup>3</sup> for  $\text{Co}_{100}$ . For example,  $M_{s//}$  and remanent magnetization ( $M_r$ ) of  $\text{Ni}_{50}\text{Co}_{50}$  were 1016 and 636 emu/cm<sup>3</sup>, respectively, thus giving a remanence squareness ( $M_r/M_s$ ) of 0.63. The  $M_s$  of  $\text{Ni}_{50}\text{Co}_{50}$  film compared well with that reported for bulk  $\text{Ni}_{50}\text{Co}_{50}$  (997 emu/cm<sup>3</sup>) [25]. The remanence squareness of the  $\text{Ni}_{50}\text{Co}_{50}$  film suggested that some texturing existed in the film.

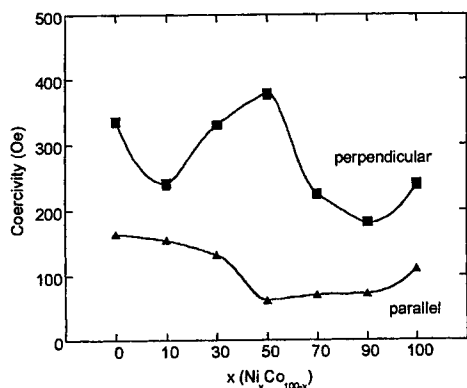


Figure 5. Dependence of coercivity on composition

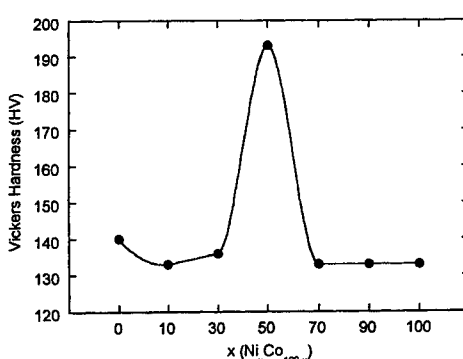


Figure 6. Dependence of microhardness on composition

The coercivity showed an interesting dependence on composition (Fig. 5).  $H_{c\perp}$  was higher than  $H_{c\parallel}$  in these films. For example,  $H_{c\perp}$  of  $\text{Ni}_{50}\text{Co}_{50}$  film was 379 Oe, which was about six times that of  $H_{c\parallel}$ . The value of  $H_c$  of electrodeposited NiCo alloy films, depending on the composition, was in the range of 200 to 500 Oe [26]. A possible explanation of the perpendicular coercivity anisotropy in our films is that these films consisted of two components: a continuous film and a small fraction of magnetically isolated particles with some form of anisotropy (such as shape) in the perpendicular direction [27].

Good film adhesion was observed, and the critical load for film delamination increased with increasing Ni concentration as determined from the microscratch tests [27]. Figure 6 shows the dependence of Vickers microhardness on film composition. The HV of the Cu substrate, bulk Ni and bulk Co samples were found to be 75, 144 and 288, respectively. The films provided enhanced surface hardness for the underlying soft Cu substrate. Interestingly, the  $\text{Ni}_{50}\text{Co}_{50}$  film had very good saturation magnetization, the highest hardness and largest magnetic anisotropy compared to other samples. These good properties can be further optimized for magnetic applications.

In vapor deposition, a constant flux of atoms to the substrate can be maintained by controlling deposition parameters. In solution deposition, film formation is a more complicated process as it depends on the chemistry of reactions. Recently we have investigated how the solution chemistry and film deposition chemistry changed with reaction (deposition) time in the polyol process. It was found that the composition and properties of  $\text{Ni}_{50}\text{Co}_{50}$  films varied with deposition time due to the change in solution chemistry with increasing time [28]. The solvent was found to have the corrosive activity on deposited Ni films when deposition time was increased [24]. Further work is needed to understand the solution chemistry and film deposition chemistry in the polyol process in order to optimize the film properties.

#### 4. Summary

The non-aqueous, electroless polyol approach has been used to deposit nanostructured metal films for various applications. Film deposition can take place on exposed or hidden, and planar or complex surfaces. In this paper the work on polyol-synthesized  $\text{Ni}_x\text{Co}_{100-x}$  films was described. The magnetic films showed in-plane magnetization anisotropy with higher perpendicular coercivity. The  $\text{Ni}_{50}\text{Co}_{50}$  film showed good magnetic properties with high hardness. Current focus is placed on understanding the solution chemistry and the effects of applied electric field in polyol deposition of nanostructured films for longitudinal and perpendicular magnetic recording.

#### Acknowledgment

The support of this work by the Academic Research Fund, the National University of Singapore, and the Office of Naval Research, USA, is gratefully acknowledged. The

author thanks J. Zhang, J. Ding and S.H. Lawrence for their valuable contributions to this work.

## References

1. Masuko, N., Osaka, T., and Ito, Y. (eds.) (1996) *Electrochemical Technology: Innovation and New developments*, Gordon and Breach Publishers, Kodansha Ltd. Tokyo, Japan.
2. Safranek, W.H. (1986) *The Properties of Electrodeposited Metals and Alloys*, second edition, American Electroplaters and Surface Finishers Society, Florida, USA.
3. Haseeb, A., Blanpain, B., Wouters, G., Celis, J.P., and Ross, J.R. (1993) Electrochemical deposition: a method for the production of artificially structured materials, *Mater. Sci. Eng. A* **168**, 137-140.
4. Schwarzacher, W., and Lashmore, D.S. (1996) Giant magnetoresistance in electrodeposited films, *IEEE Trans. Magn.* **32** 3133-3153.
5. Schwarzacher, W., Attenborough, K., Michel, A., Nabiyouni, G. and Meier, J.P. (1997) Electrodeposited nanostructures, *J. Magn. Magn. Mater.* **165**, 23-29.
6. El-Sherik A.M. and Erb, U.(1995) Synthesis of bulk nanocrystalline nickel by pulsed electrodeposition, *J. Mater. Sci.* **30**, 5743-5749.
7. Clark, D., Wood, D., and Erb, U. (1997) Industrial applications of electrodeposited nanocrystals, *Nanostruct. Mater.* **9**, 755-758
8. Mallory G.O. and Hadju, J.B. (1990) *Electroless Plating: Fundamentals and Applications*, American Electroplaters and Surface Finishers Society, Florida, USA.
9. Chow S.L., Hedgecock, N.E., and Schlesinger, M. (1972) Electron microscope study of the nucleation and growth of electroless cobalt and nickel, *J. Electrochem. Soc.* **119**, 1614-1619.
10. Krebs, J.J., Rubenstein, M., Lubitz, P., Harford, M.Z., Baral, S., Shadhidhar, S., Ho, Y.S., Chow, G.M., and Qadri, S. (1991) Magnetic properties of permalloy coated organic tubules, *J. Appl. Phys.* **70**, 6404-6406.
11. Chow, G.M., Stockton, W.B., Price, R., Baral, S., Ratna, B., Schnur, J.M., Bergeron, G.L., Czarnaski, M.A., Hickman, J.J., and Kirkpatrick, D.A. (1992) Fabrication, characterization and field emission properties of biologically-based microstructure composites, *Mater. Sci. Eng. A* **158**, 1-6.
12. Kirkpatrick, D.A., Bergeron, G.L., Czarnaski, M.A., Hickman, J.J., Chow, G.M., Price, R., Ratna, B.R., Schoen, P.E., Stockton, W.B., Baral, S., Ting, A.C., and Schnur, J.M. (1992) Demonstration of vacuum field emission from a self-assembling biomolecular microstructure composite, *Appl. Phys. Letts.* **60**, 1556-1558.
13. Brandow, S.L., Dressick, W.J., Marrian, C.R.K., Chow, G.M., and Calvert, J.M. (1995) The morphology of electroless Ni deposition on a colloidal Pd (II) catalyst, *J. Electrochem. Soc.* **142**, 2233-2343.
14. Homma, T., Sezai, Y., and Osaka, T. (1997) A study on growth process of CoNiP perpendicular magnetic anisotropy films electroless-deposited at room temperature, *Electrochim. Acta* **42**, 3041-3047.
15. Fiévet, F., Lagier, J.P., and Figlarz, M. (1989) Preparing monodisperse metal powders in micrometer and submicrometer sizes by the polyol process, *Mater. Res. Soc. Bull.* December, 29-34.
16. Viau, G., Ravel, E., Acher, O., Fiévet -Vincent, F., and Fiévet, F. (1994) Preparation and microwave characterization of spherical and monodisperse  $Co_{20}Ni_{80}$  particles, *J. Appl. Phys.* **76**, 6570-6572.
17. Kurihara, L.K., Chow, G.M., and Schoen, P.E. (1995) Nanocrystalline metallic powders and films produced by the polyol method, *Nanostruct. Mater.* **5**, 607-613.
18. Chow, G.M., Kurihara, L.K., Kemner, K.M., Schoen, P.E., Elam, W.T., Ervin, A., Keller, S., Zhang, Y.D., Budnick, J., and Ambrose, T. (1995) Structural, morphological and magnetic study of nanocrystalline cobalt-copper powders synthesized by the polyol process, *J. Mater. Res.* **10**, 1546-1554.
19. Eriksson, G., Siegbahn, H., Andersson, S., Turkki, T., and Muhammed, M. (1997) The reduction of  $Co^{2+}$  by polyalcohols in the presence of WC surfaces studied by XPS, *Mater. Res. Bull.* **32**, 491-499.

---

20. Chow, G.M., Kurihara, L.K., Ma, D., Feng, C.R., Schoen, P.E., and Martinez-Miranda, L.J. (1997) Alternative approach to electroless Cu metallization of AlN by a nonaqueous polyol process, *Appl. Phys. Lett.* **70**, 2315-2317.
21. Chow, G.M., Ding, J., Zhang, J., Lee, K.Y. and Surani, D. (1999) Magnetic and hardness properties of nanostructured Ni-Co films deposited by a non-aqueous electroless method, *Appl. Phys. Lett.* **74**, 1889-1891.
22. Michaelson, C. (1995) On the structure and homogeneity of solid solutions: the limits of conventional x-ray diffraction, *Phil. Mag. A.* **72**, 813-828.
23. Chow, G.M., Goh, W.C., Hwu, Y.K., Cho, T.S., Je, J.H., Lee, H.H., Kang, H.C., Noh, D.Y., Lin, C.K., and Chang, W.D. (1999) Structure determination of nanostructured Ni-Co films by anomalous x-ray scattering, *Appl. Phys. Lett.* **75**, 2503-2505.
24. Zhang, J., Chow, G.M., Lawrence, S.H. and Feng, C.R. (1999) Nanostructured Ni films by polyol electroless deposition, *submitted*.
25. Sadron, C. (1942) *Ann. Phys. (Paris)* **17**, 371.
26. Safranek, W.H. (1974) *The Properties of Electrodeposited Metals and Alloys*, Elsevier, New York, p. 291.
27. Chow, G.M., Zhang, J., Li, Y.Y., Ding, J. and Goh, W.C. (1999) Electroless polyol synthesis and properties of nanostructured  $Ni_xCo_{100-x}$  films, *submitted*.
28. Zhang, J. and Chow, G.M. (1999) Electroless polyol deposition and magnetic properties of nanostructured  $Ni_{50}Co_{50}$  films, *submitted*.

---

## **NANOSCALED MAGNETIC ELECTRODEPOSITED STRUCTURES ON THE BASIS OF ION GROUP METALS: PREPARATION, STRUCTURE, MAGNETIC AND MAGNETORESISTIVE PROPERTIES**

V.M.Fedosyuk

Institute for Solid State Physics and Semiconductors of the Belorussian Academy of Sciences  
220072 Minsk, Belarus, P.Brovki, 17

### **1. Introduction**

At the present time the emphasis of the investigations in almost all the branches of science, including magnetism, is shifted towards the study of 'nanoscaled', or so called 'nanosized' objects. The interest in such materials derives from the unusual, often unique properties associated with the relatively high ratio of the numbers of surface and bulk atoms. The classification of nanoscaled objects is not clearly defined, but a general definition may be given as follows: nanoscaled materials are those in which any parameter, e.g. the grain size, layer thickness, the size of columnar crystal, diameter of magnetic inclusion, etc., is of the same order as the fundamental constants of the substance - such as free electron path, Fermi wave vector, etc.

Magnetic nanosized materials that are based on transition metals may be divided into six main groups (Fig.1). They are: films with columnar type of crystal structure (1), multilayers (2), granular or so called inhomogeneous alloyed films (3), quasi- or semigranular films (4), nanocrystalline films (5) (which are produced after partial crystallization of amorphous soft magnetic films and foils) and, finally, nanowires (6). There is no sharp boundary (transition) between these types of nanosized materials: for example, it is possible to produce multilayered nanowires and columnar type films. Multilayers with very thin alternate magnetic and nonmagnetic layers look like, and behave like, granular films. Therefore, the investigation of each separate nanosized magnetic material, and also of the permanent transitions from one type to another, can give us additional information about each individual material, and also about the common properties of the class of materials.

It is necessary to say that all of the above mentioned classes of nanoscaled materials can be produced in a variety of forms by the electrodeposition method, and some of them (e.g. nanowires) may be prepared exclusively by electrochemical means.

The advantages of electrodeposition, such as low cost, potentially high productivity, and the ease of automation of the process make electrodeposition a very attractive technique with possible commercial viability. Preparation of nanoscaled materials by electrodeposition technique becomes increasingly widespread all over the world, for example, in UK, France, Switzerland, Japan, USA, Holland, Germany, etc.

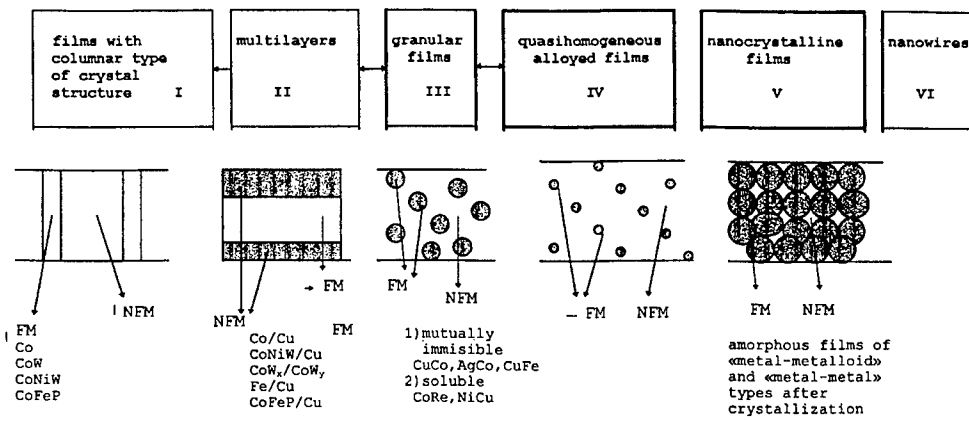


Fig.1. The scheme of nanosized electrodeposited materials.

## 2. Films with columnar type of crystal structure

One of the ways to increase the magnetic recording density in storage devices is to use a new, vertical mode of recording. The data-storage capacity of a device using such a mode could be increased by more than an order of magnitude over similar systems that use the traditional horizontal recording mode. It is necessary to use recording media with the unusual magnetic property of high perpendicular anisotropy for such applications, so as to allow a stable remanent magnetization component to be achieved perpendicular to the plane of the film. The crystalline anisotropy of ferromagnetic metals, (i.e. [002] texture of hcp-Co structure), alone would be insufficient to provide the required magnetic properties; since the demagnetization energy  $E_{dm} \sim 2\pi M_s^2 \sim 10^7$  erg/cc would be still higher than the crystallographic energy  $E_A \sim 4.2 \times 10^6$  erg/cc. It is possible to overcome the demagnetization energy, which tends to arrange the magnetization vector into the plane of the films, by decreasing the magnetization of the material (but this is not the best way), or by adding to crystallographic energy some other contribution. This could be, for example, the shape anisotropy energy of columnar grains in recording media. Films exist in which nanosized (~10nm) 'needle-like' crystallites - columns, which pass through the full thickness of the film, are surrounded by regions with lower, or even zero, magnetization, (Fig.2). In such a case the sum of

crystallographic energy plus the shape anisotropy energy of columnar grains can overcome the demagnetization energy.

Films with columnar type of crystal structure can be produced also by electrodeposition method [7]. There are two requirements for this. The rate of appearance of new grains must be much smaller than the rate of growth of existing crystallites; and the velocity of growth of grains perpendicular to the plane of the film must be much higher than the in-plane growth rate. This may be achieved by choosing electrodeposition regimes where passivation of the growth surface is very extensive due to the formation of hydroxides.

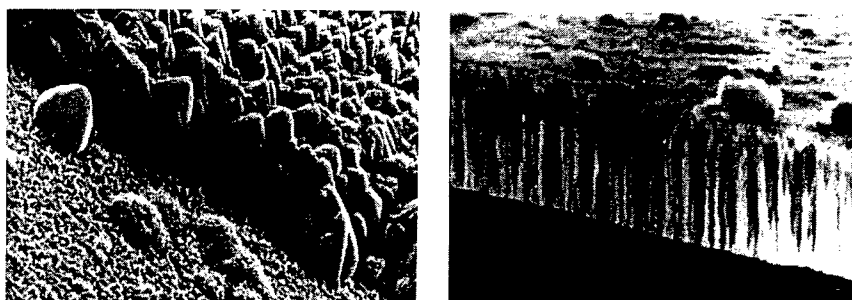


Fig.2. Films with different types of crystal structure. Magnification - 50000<sup>x</sup>

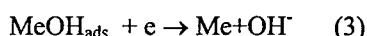
A possible interpretation of the mechanism of columnar structure growth for electrodeposited film (such as Co/Ni) is as follows. In electrolytes with high pH, the formation of metal-hydroxide complexes (in our case of Co and Ni) of the form  $\text{MeOH}^+$  and  $\text{Me}_4\text{OH}^{4+}$  is highly probable. These positively charged complexes are formed by reactions of the type shown below,



(where Me are Co and Ni). These complexes migrate towards the cathode, where they capture an electron and are adsorbed onto the cathode surface,



The adsorbed complexes are then further reduced by the reaction



Thus, besides the reduction of hydrogen, alkalization also occurs at the cathode. It should also be noted that the diffusion coefficient of complexes of type (1) is some

orders of magnitude higher than that of simple metal ions; therefore reduction of metal atoms (Co, Ni, Fe) is most likely to take place not from metal ions but from their complexes with hydroxide groups. It has been established experimentally that the number of the adsorbing complexes of  $\text{Me(OH)}^+$  and  $\text{Me}_4\text{OH}_4^{4+}$  on the most closely packed (001) face is about 1.8 times higher than on the others. Therefore, the recovery of Co and Ni ions, occurring through the formation and subsequent fission of their hydroxide complexes, will result in a more rapid growth of closely packed planes. Thus, the pH value of the electrolyte being relatively high and the quantity of the adsorbing  $\text{Me(OH)}^+$  and  $\text{Me}_4\text{OH}_4^{4+}$  complexes formed being large, is therefore expected to result in the development of the [001] texture, (the closely packed planes will be parallel to the cathode surface). Addition of alkaline at the cathode due to reaction (3) causes an increase in pH by 3-4, i.e. with a pH of the electrolyte in the volume equal to  $\sim 6.0 - 7.0$  pH, it increases, locally, at the cathode, to between 9 and 10. It has been well documented, that the reaction of the type:



accelerates rapidly at pH = 7.

It is therefore necessary to ensure that the rate of reaction (4) in the electrolytes used is very high, so as to achieve the required texture. The hydroxides of cobalt and nickel, forming in great quantities, migrate from the areas of active crystal growth (i.e. from the grain center with [001] texture) to the crystallite periphery, where the growth rate is lower (the faces with orientations of (100) and (101) grow approximately 1.8 times slower). Accumulating in large quantities, they are trapped during the growth and thereby form rather broad inter-grain regions. The resulting structure is of columns of [001] cobalt surrounded by regions which are highly enriched in nonmagnetic hydroxide  $\text{Co(OH)}_2$  and  $\text{Ni(OH)}_2$ . Under optimum deposition conditions, this mechanism of structural growth is sufficiently stable. When the electrolysis conditions deviate from the optimum, two possible modes of growth are observed. Normal growth of crystallites occurs when the crystallite growth is very much greater than the rate of formation of new crystallites ( $D \leq 3 \text{ mA/cm}^2$ ) and deposits obtained are large-grained, not textured, since the growth rate of different faces is about the same. Dendrite growth occurs for  $D \geq 100 \text{ mA/cm}^2$ , where the rate of growth is very much less than the rate of formation of new crystallites; the resulting structure is fine-grained, not textured. The columnar crystallite growth (Fig.2) is intermediate between the normal and dendrite types of growth. The increase in the ratio of crystallite growth over that of crystallite formation is characteristic of it. It is essential, however, to note that under conditions of columnar growth the growth rate for different faces varies widely. When the electrochemical conditions of formation are in marked contrast to those that are optimum for the columnar growth of the films, i.e. when the quantity of the adsorbing  $\text{Me(OH)}^+$  and  $\text{Me}_4\text{OH}_4^{4+}$  complexes is small, the experimentally observed development of structure

and texture of deposits can be accounted for in terms of the models of normal and tangential crystallite growth [8].

Depending on the conditions of preparation, (both composition and regimes of electrodeposition - pH,  $D_k$  and T), it is possible to regulate not only the type of crystal structure but also to determine, over a wide range, the diameter of grain columns and the intercolumnar distance. As a result, the magnetic properties of films, including the perpendicular or in-plane anisotropy, could be varied over a wide spectrum. We were able to measure magnetic parameters such as the remanent magnetization perpendicular to film plane direction  $M_{r\perp} = 0.1 - 0.3$  ( $M_{r\perp} > M_{r\parallel}$ , by 2 - 3 times) and coercive force in the same direction  $H_{C\perp} = 1000 - 2000$  Oe ( $H_{C\perp} > H_{C\parallel}$ ) [9]. The indicated parameters of electrodeposited Co-Ni hard magnetic films with perpendicular anisotropy and a columnar type of crystal structure suggest their applicability to vertical-mode storage devices.

### 3. Multilayered films

Relatively recently, extensive work on the development of methods for deposition and study of physical properties of multilayered magnetic structures with ultrafine (<1 nm) alternating magnetic and non-magnetic layers has been carried out. These structures are remarkable, not only from a fundamental viewpoint, but also because they have a wide practical application due to their unique magnetic, mechanical, electronic and other properties.

The initial approach to achieving high perpendicular anisotropy in multilayers was influenced by experience with the hard magnetic films with the columnar structure described above[10]. This approach relies upon the so-called surface anisotropy. In very thin magnetic films, (of the order of a few nanometers), regardless of whether they are single-layered or multilayered, the component of the magnetization vector that is perpendicular to the plane of the film increases as an inverse function of film thickness. In multilayered thin film structures, consisting of alternate magnetic and nonmagnetic layers, every magnetic layer has two surface sublayers (at each interface boundary). If the thickness of magnetic layers is such that the material at the boundary between layers is a significant proportion of the bulk volume of the layer, high anisotropy can be achieved after the growth of many such alternate layers.

One feasible, and technologically simple, method of producing multilayered structures is electrodeposition in a pulse regime. A multilayer can be obtained in this way from a single electrolyte. Ferromagnetic metals such as Co, Fe and Ni or their alloys, and copper or (Ag, Au, Pd) can be used for magnetic and nonmagnetic layers, respectively. Electrochemical deposition of such structures relies upon the fact that the equilibrium reduction potentials of the ferromagnetic and non-ferromagnetic ions differ by more than 400 eV. In general, electrolytes that are saturated in copper are used in the multilayer deposition process. This is due to transport difficulties in the electrolyte, which limit the current density for copper deposition when the solution is dilute in

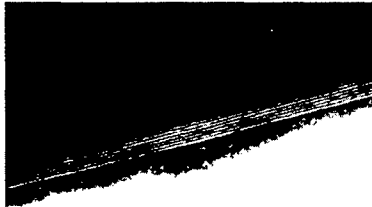


Fig.3. Multilayered Co/Cu film.  
The thickness of layers in 5 nm.

copper ions. The concentration of the ferromagnetic ions (in this case Co) must be very much less than that of the Cu ions. In this case, if a current density of  $0.53 \text{ mA cm}^{-2}$  is used during the Cu deposition pulse, this will be much less than the minimum current density of cobalt deposition, which is about  $5 \text{ mA cm}^{-2}$ . This, therefore, results in a pure Cu layer. For deposition potentials as low as circa 0.87 V, only copper will deposit and above this both copper and cobalt deposit. The current density used during the deposition of the magnetic layer was  $100 \text{ mA cm}^{-2}$ , hence the deposition rate of the ferrometal exceeded by about two orders of magnitude that of copper. The

proportion of copper in cobalt layers could not therefore exceed a fraction of a percent. In such a manner, using a single solution and pulse regime of electrodeposition we are able to obtain the desired Co/Cu multilayered structure (Fig.3), where the layer thickness was determined by pulse duration.

The X-ray diffraction patterns of the Co/Cu multilayered films reveal two features: the absence of any reflection in a small-angle range and satellite reflections near the basic structure reflections of Co. When the thickness of the Co layers was changed, with a constant Cu layer thickness ( $d_{\text{Cu}}=1.5 \text{ nm}$ ), the X-ray diagram was as follows. The first reflections appeared at  $T \approx 80 \text{ nm}$  ( $d_{\text{Co}}=1.5 \text{ nm}$ ), with a corresponding cobalt deposition pulse time of  $T_{\text{Co}} \approx 200 \text{ ms}$  ( $d_{\text{Co}}=2.5 \text{ nm}$ ); there were three obvious reflections of different intensities. The reflections at  $2\theta = 49.5^\circ$  and  $53.8^\circ$  are the satellite reflections of the structure peak at  $2\theta = 52.1^\circ$  for (111) fcc Co (tabulated  $2\theta = 51.95^\circ$ ). With further increases in  $T_{\text{Co}}$  (up to 400 ms), the picture becomes more distinct. Apart from the satellite reflections of the peak for (111) fcc Co, one more reflection appears for (200) fcc Co ( $2\theta = 60.7^\circ$ ) with satellite reflections ( $2\theta^- = 58.5^\circ$ ,  $2\theta^+ = 62.5^\circ$ ). In all the investigated Co and Cu layer thickness ranges, (up to 10 nm), the multilayer Co/Cu structures, (obtained by electrodeposition from a single solution), were structures based on fcc Co and fcc Cu. In addition, the conjugation of Co and Cu layer structures took place on more compact planes ((111) fcc Co || (111) fcc Cu).

The presence of a satellite reflection is confirmed by the fact that the modulation period of the inter-plane distances of the Co/Cu, calculated from the satellites for different reflections, are consistent with the compositional modulation obtained using Auger spectroscopy.

According to the Auger profile some amount of one element may be present in the layers of the other element (5 - 15%), but this experimental result may be explained in another way. When the thicknesses of the alternate layers are very small, irregularities on the sub-micron scale result in protrusions of material from one layer to the next. The diameter of the Auger microscope probe was  $1 \mu\text{m}$  and some of these protrusions are,

therefore, necessarily sampled by the Auger process. The irregularities of the thin layers in periodic structure can be estimated to be up to  $\sim 15\%$ .

From an analysis of these figures and the magnetic behavior reported below, it is shown that the ultrathin alternating Co/Cu multilayers are 'island'-type layers. When the layer thickness is less than 1 nm, the irregularity of the layers is of the order of  $\sim 50\%$ . Structural investigations using transmission electron microscopy confirmed the island-like type structure of the layers. At Co deposition pulse times of less than 200 ms, the Co layer forms islands of 15 - 30 nm in diameter. Microdiffraction studies show the presence of crystallites of fcc Co.

The value of the total magnetic anisotropy constant of an ultrathin magnetic layer in Co/Cu multisystems can be given as the sum of the crystallographic strain, and surface anisotropy components. The contribution of the surface anisotropy constant to the perpendicular magnetic anisotropy becomes predominant when the magnetic layer thickness in the multilayers is of the order of a few nm. As the thickness of the Co layer decreases, the perpendicular anisotropy and coercive force increase (Fig.4). Additional evidence of the development of perpendicular magnetic anisotropy can be seen from the magnetization reversal curves parallel and perpendicular to the coating directions.

As the thickness of the magnetic layers of Co decreases, the remanent magnetization  $M_r$  and  $H_c$  in the direction perpendicular to the surface of films increases. Simultaneously, the equivalent in-plane parameters decrease. This is typical of magnetic structures with increasing perpendicular anisotropy. Analyses of these figures show that the decrease in the Co layer thickness leads to an increase in the perpendicular magnetic

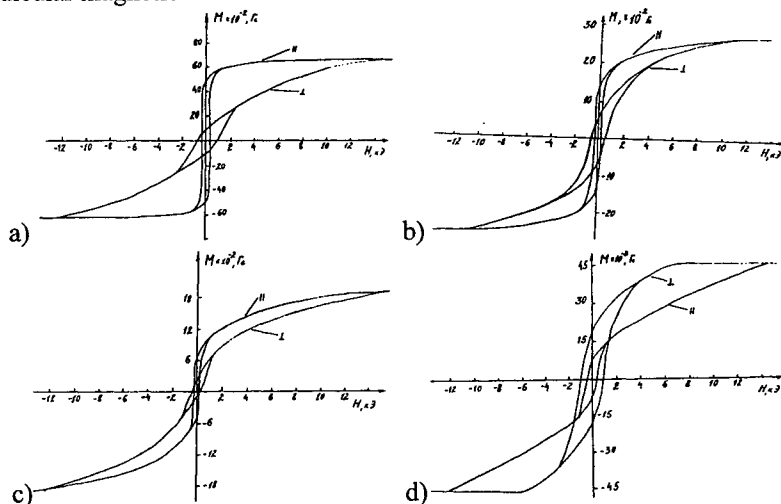


Fig.4 Magnetization curves of Co/Cu multilayers with time of pulse Co deposition:  
a -  $t_{Co} = 10$  ms, b - 40, c - 15 and d - 10 ms;  $t_{Cu} = 5$  s = const.

anisotropy constant. Furthermore, in our opinion, the increase in the discontinuity of these layers is the reason for the increase in coercivity of the island-type structure. This fact is an important result for the use of the investigated multilayer films as materials for vertical magnetic recording.

We reported on studies of multilayered films of the Co/Cu, Fe/Cu, CoFeP/Cu and CoNiW/Cu systems. An anomalous temperature dependence of the magnetization of the Co/Cu films was found [12]. One of the possible explanations was based on the existence of indirect exchange (RKKY) coupling observed at thickness of Co and Cu layers that led to the antiferromagnetic ordering of magnetization vectors of adjacent layers. This coupling is also responsible for GMR in multilayered films. Therefore, we continued our experiments with the investigation of the magnetoresistance of multilayered Co/Cu films [13]. To study the magnetoresistance, we used films deposited on a pyroceram substrate with a chemically deposited layer of amorphous nickel phosphide as well as on an aluminum foil substrate that was later dissolved in a 10% NaOH solution. The measurements showed virtually identical results for the films deposited on nickel phosphide and on aluminum because of the low shunting effect of the nickel phosphide layer. Thus, the films deposited on the pyroceram substrate were of better practical use in our experiments. The magnetoresistance was measured in a temperature range of 300 – 10 K in fields of up to 1.3 T, (in steps of 0.005 T), by the four-point method. We used three configurations, differing in the orientations of the current  $I$ , field  $H$ , and the film plane. They were designated  $\Delta R_{\parallel\parallel}$  (where both current and field were parallel to the film plane),  $\Delta R_{\perp\perp}$  (where the current was perpendicular to the in-plane field); and  $\Delta R_{\perp\parallel}$  (where the field was perpendicular to the in-plane current).

It is known that, in contrast to the anisotropic magnetoresistance of ferromagnetic metals and alloys, the giant magnetoresistance of multilayered films is not only characterized by a large value (more than 60%), but is also isotropic for measurements using any combination of relative directions of the applied magnetic field, current, and film plane (i.e.,  $\Delta R_{\parallel\parallel}$ ,  $\Delta R_{\perp\perp}$  and  $\Delta R_{\perp\parallel}$ ).

Figure 5 shows  $\Delta R_{\parallel\parallel}$  as a function of the thickness of the cobalt and copper layers. Negative magnetoresistance (its decrease upon magnetic saturation) which is a prerequisite of the GMR, was observed for the films consisting of cobalt and copper layer thickness of 14.0 and 15.0 nm (Fig.5(a,c)) and 0.2 and 1.5 nm (Fig.5(b)) respectively. The  $\Delta R_{\parallel\parallel}(H)$  dependence (Fig.5(a)) shows a positive magnetoresistance typical of the conventional anisotropic magnetoresistance of a film consisting of the cobalt and copper layers of the thickness indicated. The  $\Delta R_{\parallel\parallel}(H)$  dependence (Fig.5(b)) characterized by a broad "triangular" reversible maximum without saturation and hysteresis, (observed at both 300 and 100 K), may be typical of the following two cases. First, the absence of hysteresis may be explained by a strong antiferromagnetic coupling of magnetic layers. In the studies of the structure of periodic Co/Cu multilayered films described above, it was shown that ultrathin cobalt layers (less than 1 nm in thickness) consisted of isolated "islands" of Co, whose diameter was an order of magnitude greater than the film thickness. These magnetic "islands" of Co in the copper

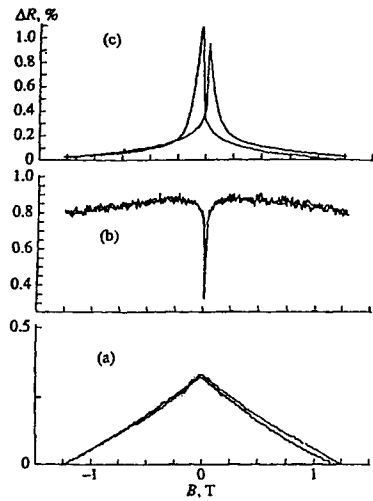


Fig.5. Field dependence of magnetoresistance taken at room temperature in field parallel to the in-plane current for the Co/Cu multilayered films with various thickness of the layers:

- (a)  $d_{Co} = 0.2$  nm and  $d_{Cu} = 1.5$  nm;
- (b)  $d_{Co} = 2.5$  nm and  $d_{Cu} = 1.5$  nm;
- (c)  $d_{Co} = 14$  nm and  $d_{Cu} = 15$  nm.

matrix may be ordered antiferromagnetically because of the magnetostatic coupling through their stray fields. Without an applied magnetic field, the magnetic single-domain particles will have antiparallel mutual orientations because the energy of the system on the whole tends to a minimum. The electrical resistivity of such a film in the initial state is higher than after its magnetization to saturation. The electron scattering on such magnetic inhomogeneities is isotropic ( $\Delta R_{II} \approx \Delta R_{\perp}$ ) and thus represents a possible mechanism for the giant magnetoresistance in the Co/Cu films with cobalt and copper layers of 0.2 and 1.5 nm in thickness, respectively. Secondly, such a field dependence  $\Delta R_{II}(H)$  is also typical of granular (heterogeneous) alloys that display giant magnetoresistance. In these alloys, the effect of GMR is attributed to a superparamagnetic state of magnetic granules surrounded by a nonmagnetic matrix. The increase in the giant magnetoresistance and weak hysteresis observed at a temperature of 10 K in our samples are typical of granular alloys. Thus, the Co/Cu film consisting of the cobalt and copper layers of 0.2 and 1.5 nm in thickness, respectively, may be considered to be a granular multilayered material.

Figure 5(b) shows the field dependence  $\Delta R_{II}(H)$  for the Co/Cu films with  $d_{Co} = 2.5$  nm and  $d_{Cu} = 1.5$  nm. As is seen, the increase in the thickness of the magnetic layer resulted in the transition from isotropic (negative  $\Delta R_{II}$  and  $\Delta R_{\perp}$ ) to anisotropic (positive  $\Delta R_{II}$ ) magnetoresistance typical of homogeneous magnetic materials. The disturbance of the mechanism causing GMR is likely to be due to the imperfect structure of the copper interlayer and the formation of ferromagnetic Co "bridges" between the layers. These "bridges" connect the layers in a uniform interacting medium, yielding the usual anisotropic magnetoresistance typical of ferromagnetic materials. To obtain information on the quality of the structure of this  $Co_{2.5\text{ nm}}/Cu_{1.5\text{ nm}}$  multilayered system, we studied the films by nuclear magnetic resonance, using  $^{59}\text{Co}$  as a source (Fig.6).

The maximum observed at 21.6 T is close to that observed in bulk fcc Co ( $B_{hf} = 21.6$  T). However, the peak is very broad and extends over the range of hyperfine fields from 18.4 to 22.6 T; the extreme points of this range correspond to bulk hcp Co (22.6 T) and to Co atoms having 1 or 2 nearest-neighbor nonmagnetic atoms of Cu ( $B = 18.4$  T). Because of the enhanced imperfection of the structure and the presence of a large concentration of Co atoms that have one or two Cu atoms in their nearest neighborhood, as well as the possible existence of ferromagnetic «bridges» between the cobalt layers, such a system exhibits the conventional anisotropic magnetoresistance. The experimental data confirm that, on increasing thickness of the nonmagnetic layer to 2.5 nm (at  $d_{Co} = 2.5$  nm), the structure becomes more perfect and ferromagnetic “bridges” between the magnetic layers disappear, and the negative giant magnetoresistance appears instead of the positive anisotropic magnetoresistance (Fig. 5(b)). Interesting data were obtained for multilayered films consisting of relatively “thick” ( $\sim 10.0$  nm) layers. These results show that the antiferromagnetic coupling is by no means necessary for giant magnetoresistance to arise. The magnetoresistance curve differs from the bell-shaped curves typical of the films with strong antiferromagnetic coupling between the magnetic layers; it has two maxima located at fields  $\pm H_c$  ( $H_c$  is the coercive force or the switching field at which the magnetization passes through zero). Thus, the maximum values of the magnetoresistance correspond to the state at which the domains of the adjacent magnetic layers are oriented randomly. An abrupt change in magnetization leads to an abrupt decrease in electrical resistivity. The magnetoresistive sensitivity, i.e. the change in the magnetoresistance per unit magnetic field, is an important parameter of magnetoresistive materials used in magnetic-field sensors. It was important that, in contrast to these films, the decrease in the electrical resistivity in the films studied in this work occurs at low fields ( $H < 0.01$  T). The highest magnetoresistive sensitivity was equal to 1.5% at magnetic field changes of  $\pm 1$  T; the saturation field was 0.025 T.

In summary, we observed the giant magnetoresistance in Co/Cu multilayered

films produced by pulsed electrodeposition from a single electrolyte. For the first time, we found the low-field giant magnetoresistance. This is of great practical interest. It is obvious that electrodeposition shows promise as a production method of giant magnetoresistive films. It is interesting to produce and study magnetic multilayered films with magnetic layers having a low coercivity. Electrodeposited CoFe/Cu multilayered films, exhibiting a low coercive force and high thermal stability, are expected to be promising materials with a low-field giant magnetoresistance higher than that of the Co/Cu films. Moreover, electrodeposition may be used to

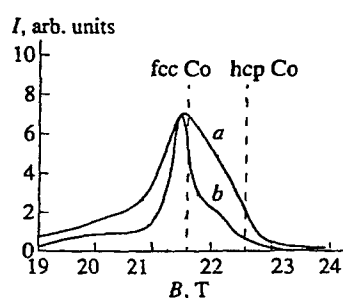


Fig. 6. NMR spectra for the Co/Cu multilayered films with  $d_{Co} = 0.2$  nm and  $d_{Cu} = 1.5$  nm (a) and  $d_{Co} = 10$  nm and  $d_{Cu} = 7$  nm (b).

produce even more promising multilayered films exhibiting "spin-valve" magnetoresistance effects [14]. These films consist of five or more alternating layers, for example, magnetically soft/nonmagnetic/ magnetically soft/magnetically hard/nonmagnetic layers. The "spin-valve" magnetoresistance may be observed in such films as  $(CoFeP_x/Cu/CoFeP_x/CoFePy/Cu)_n$  and  $CoW_x/Cu/CoW_x/CoW_y/Cu)_n$ , where the magnetic alloys with  $x > 20$  at.% have low coercive force and those with  $y < 5$  at.% have high coercivity. The composition and magnetic properties of the alternate layers may be varied by controlling the amplitude of applied current pulses. The investigations of the above mentioned films are now in progress and the results will be reported in further papers.

#### 4. Granular films.

As we showed in section 3 of the present paper, multilayered films which are produced under very short pulse duration are really 'island-like' type multilayered films; and their behavior looks like typical granular (or inhomogeneous alloyed) films - i.e. they show 'bell-like' triangle unsaturated dependence of magnetoresistance.

Upon consideration of our study of granular films and taking into account the complete mutual insolubility of Co and Cu our first idea was to try to get granular Cu-Co films not in a pulse regime, but at constant current density. This was successful.

In previous work on Co-Fe-P and Co-W [15,16] and also other systems where ED films have been produced under constant deposition conditions, it was found that all films were homogeneous. It thus seemed likely that in the Cu-Co system, produced under similar conditions, the same degree of inhomogeneity would be obtained. However, as we shall show, in the case of the Cu-Co system, we also produced samples with a range of inhomogeneities.

The electrolytic composition was:  $CuSO_4 \cdot 5H_2O$  30 g/l,  $CoCl_2 \cdot 6H_2O$  3.3 g/l,  $H_3BO_3$  6.6 g/l,  $MgSO_4 \cdot 7H_2O$  23.3 g/l,  $CoSO_4 \cdot 7H_2O$  10 to 30 g/l [17]. The composition range of the samples investigated was obtained by varying the  $CoSO_4$  concentration in the electrolyte; all other chemical concentrations were held constant. The electrolyte had a pH value of 6.0 and deposition was performed at  $20^0C$  with a current density of 5 mA  $cm^{-2}$ . The films produced had thickness typically of the order 1  $\mu m$ .

Magnetization loops were measured for all samples in the temperature range from 5 to 300 K; all loops had similar characteristics. Some typical results, for a  $Co_{11}Cu_{89}$  sample are given in Fig.7. The hysteretic behavior at low temperatures, combined with the reversible part of the magnetization curve, which extends over a wide field-range (Fig.7(a)) suggests that we have a mixture of ferromagnetic and superparamagnetic particles. Whereas, at higher temperatures (Fig.7(b)) above the blocking temperature, we observe only superparamagnetism. It is also important to note, in this context, that no sample could be magnetically saturated, even at a temperature of 5 K and the maximum applied field of 5 T.

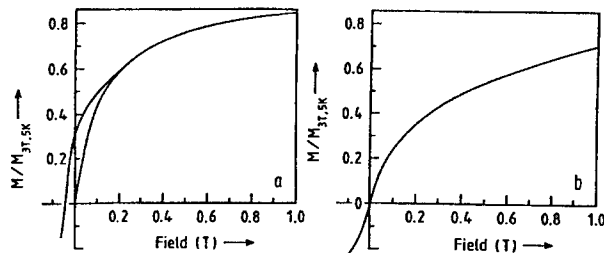


Fig.7. Typical reduced magnetization curves for  $\text{Co}_{11}\text{Cu}_{89}$  granular film: a - at 5 K; b - at 300 K

The temperature dependence of the remanence of different granular compositions is shown in Fig.8. We observe curves of continuously varying slope which also differ from sample to sample. This suggests that we have a range of blocking temperatures, depending upon the Co concentration. We have attempted to estimate the maximum blocking temperature for each sample by extrapolating the remanence curves to zero; the maximum blocking temperature increases with increasing Co concentration. The fact that all remanence curves, except that for composition  $\text{Co}_{20}\text{Cu}_{80}$ , show strong curvatures, suggests a range of blocking temperatures for each sample and a corresponding range of particle sizes present in the films, which we are able to control by varying the deposition conditions.

This also indicates, in our opinion, that we have been successful in producing, immediately after deposition, inhomogeneous alloy systems. The linear variation of the remanence for sample  $\text{Co}_{20}\text{Cu}_{80}$  suggests an approximately uniform size of particles in that film.

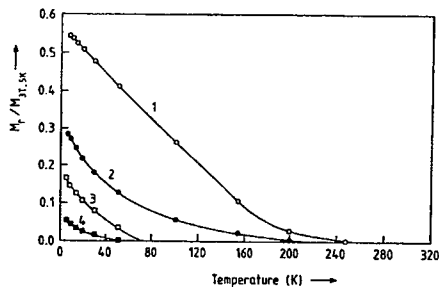


Fig.8. Temperature dependence of the remanence for various samples investigated; values have been normalized with respect to the magnetization at  $H = 3\text{ T}$  and  $T = 5\text{ K}$ : 1 -  $\text{Co}_{20}\text{Cu}_{80}$ , 2 -  $\text{Co}_{11}\text{Cu}_{89}$ , 3 -  $\text{Co}_8\text{Cu}_{92}$ , 4 -  $\text{Co}_6\text{Cu}_{94}$ .

In order to estimate the maximum particle size in each sample, we have used the well-known expression:  $-K_A v = 25 k_B T_B$ , where  $K_A$  is the anisotropy energy density,  $v$  is the critical particle volume and  $T_B$  is the blocking temperature. A value of  $K_A$  appropriate for f.c.c. Co has been assumed. The results are summarized in Table1.

Table 1

Summary of the results obtained for series of CuCo films produced by electrodeposition. The values quoted for the Co concentrations are the averages of chemical and X-ray analyses

Compositions	T <sub>B</sub> (K)	granular diameter (nm)
Co <sub>6</sub> Cu <sub>94</sub>	55 ± 5	7.6
Co <sub>8</sub> Cu <sub>92</sub>	80 ± 10	8.7
Co <sub>11</sub> Cu <sub>89</sub>	210 ± 20	12.0
Co <sub>20</sub> Cu <sub>80</sub>	260 ± 25	12.8

Fig.9 shows the magnetization for an annealed Co<sub>0.94</sub>Cu<sub>0.06</sub> film as a function of reduced field and as measured at different temperatures well above the maximum blocking temperature of the sample, 50 ± 5 K. These curves do not superimpose and we conclude that the sample does not exhibit pure superparamagnetism (SPM). Such behavior was typical for the whole range of concentrations investigated, both before and after annealing. In Fig.10 the temperature dependence of the reciprocal of the FC (field cooled) susceptibility is plotted as a function of anneal for sample Co<sub>0.94</sub>Cu<sub>0.06</sub>. On the assumption that at high temperatures the susceptibility can be represented by a Curie-Weiss law:  $\chi \propto (T - T_{int})^{-1}$  where T<sub>int</sub> is an interaction temperature, T<sub>int</sub> is obtained by extrapolating the linear part of the curve.

While some caution must be exercised over the interpretation of the results, values obtained for T<sub>int</sub> are: 20 ± 2 K for the unannealed sample, and 35 ± 4 K and 50 ± 5 K after annealing at 200 and 400°C. On annealing of the sample, there is a gradual increase in curvature of the  $\chi^{-1}$  plots. Measurements were also made after

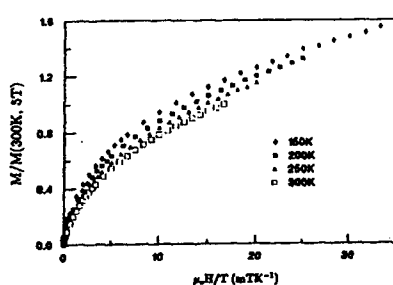


Fig.9. Dependence of magnetization of unannealed Co<sub>6</sub>Cu<sub>94</sub> film as function of reduced magnetic field for the temperature indicated. The magnetization is normalized to its value at H = 5T and T = 300K.

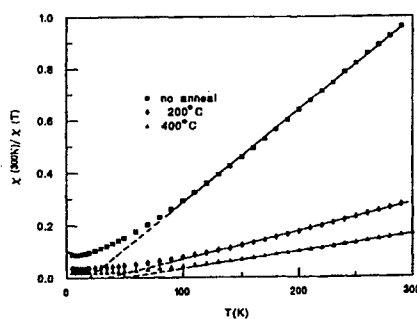


Fig.10. Low-field reciprocal (ZFC-FC) susceptibility as measured in a field of 5 mT for Co<sub>6</sub>Cu<sub>94</sub> film as a function of anneal at the temperature indicated.

annealing at 600°C, but in this case, we were unable to cool from above the maximum blocking temperature.

So, the temperature interaction is positive and equal  $\approx +20$  K for the unannealed Co<sub>6</sub>Cu<sub>94</sub> composition, hence, the energy of the cluster interaction is estimated as  $E_{int} = T_{int} \cdot k_B \approx 1.7 \times 10^{-3}$  eV. This value is comparable with the energy of the magnetic anisotropy of the clusters.

Therefore, at a relatively large positive, i.e. direct ferromagnetic, interaction between the clusters, the second condition of the pure superparamagnetism (Fig.9) does not have to be satisfied. Let us note that Cu<sub>94</sub>Co<sub>6</sub> films were fabricated by electrolytic deposition under stationary conditions. During the formation and growth of Cu and Co crystals some clusters can touch each other due to possible anisotropy of their shape (elongation) or formation of a Cu-Co metastable magnetic alloy between certain Co clusters. It is obvious that the interaction between Co clusters in the Cu matrix ought to depend on Co concentration. The size of the magnetic particles depends upon both the electrolytic composition and the detail of the deposition parameters, but typical values, from previous work, are 7 nm for  $x = 0.06$ , 12 nm for  $x = 0.12$  and 15 nm for  $x = 0.35$ , i.e. they are of the same order of magnitude as the electron mean-free path in transition metals. This is clearly the reason that the spin-dependent component of the electrical conductivity tensor is predominant and this is the basis of the GMR mechanism [18,19].

On annealing of the samples, there is an increase in the GMR (Fig.11), although even after annealing at 600°C, there is no saturation observed in the available field (1.3 T). This is in contrast to the magnetization which, after a corresponding anneal, both increases and saturates in fields of less than 1 T. There is also an increase in the coercivity. This can be understood in terms of a growth of magnetic particle size on annealing. It is well established that the magnitude of the GMR is determined by magnetic cluster sizes, their distribution and also by the sharpness of the composition profile in the vicinity of the particle-matrix boundary; these factors are strongly dependent upon annealing. Work on maximizing GMR by an investigation of these various parameters is in progress and will be reported in due course.

It has been shown that it is possible to produce inhomogeneous alloyed CuCo film by electrodeposition at constant current density from a single solution. Such films have typical superparamagnetic behavior and giant isotropic magnetoresistive properties. It is obvious that the same is also possible for mutually insoluble Cu-Fe system [20]. But it was not unexpected that we would be successful in producing granular alloys from such a completely soluble system as Co-Re [21]. We believe that this is not the limit of the electrodeposition technique and it would be possible to produce homogeneous alloyed films from immiscible metals. We suppose that the above-mentioned Cu-Co system could be obtained not only as a granular system, but also as a homogeneously distributed system. More exactly, we have observed the permanent transition from the multilayered to a granular state in the Co/Cu  $\rightarrow$  Co-Cu system and the similar transition from granular Co-Cu to homogeneous Co-Cu alloy. It is also possible to vary the sizes of Co clusters in Cu matrix or vice versa - Cu

inclusions in a Co-matrix, by changing the electrochemical regime or preparation conditions.

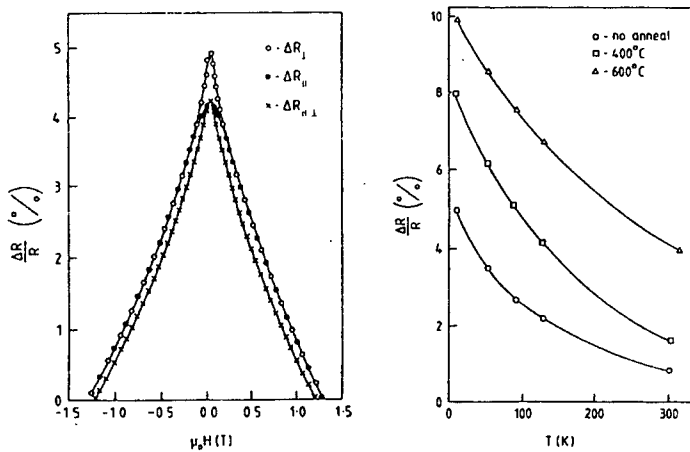


Fig.11. Magnetoresistance of as-deposited  $\text{Co}_{20}\text{Cu}_{80}$  film measured at 5K as a function of magnetic field for various orientation indicated (a); and the temperature dependence of the magnetoresistance as a function of annealing for 30 min at a temperature indicated measured with  $\mathbf{J} \perp \mathbf{H}$  and both in the film plane.

## 5. Nanowires

One of the main aims of early studies of nanowires was to achieve a CPP (current perpendicular to plane) giant magnetoresistance, which was expected to be much greater than the conventional CIP (current in plane) effect. Some groups (mainly from Bristol, UK and Jausannu, Switzerland) were successful in this. They produced a wide range of multilayered nanowires. We have demonstrated a further advantage of electrodeposition, namely the possibility of preparing heterogeneous alloys in the form of nanowires having lengths of several mm or tens of mm, and diameters of only a few tens of nm. These nanowires exhibit GMR, the magnitude of which increases on annealing.

Co-Cu heterogeneous alloy nanowires having lengths of several tens of mm and diameters of 20 or 200 nm were deposited in the pores of commercially available anodic aluminum oxide membranes. Unlike the nuclear-track-etched polycarbonate membranes used in previous studies of nanowire, these can be used in annealing studies. Prior to sample growth, all membranes were coated with an evaporated Au layer on the side that was not to be exposed to the electrolyte, in order to produce a conducting substrate for electrodeposition.



Fig. 12. Transmission electron micrograph of Co-Cu heterogeneous alloy nanowires electrodeposited in a nuclear track-etched polycarbonate membrane with quoted pore diameter 10 nm and pore density  $6 \times 10^8 \text{ cm}^{-2}$ .

nanowires would be measured in parallel. It is immediately apparent that although the absolute magnitude of the MR is small (less than 1%), in both configurations it is negative, showing that we do indeed have GMR, as expected for a heterogeneous Co-Cu alloy. There appears to be symmetric 'shoulders' either side of the central peak in both MR curves, which may be related to details of the magnetization reversal mechanism. This is currently investigated.

This apparent anisotropy in the magnetization reversal process suggests that the nanowire geometry does influence the magnetic properties of the heterogeneous alloy. This could be because some of the Co-rich particles approach the size of the nanowire diameter (20nm); or possibly because even if the nanowire diameter is much larger than the particle dimensions, it may be less than the range over which magnetic interactions are important. Alternatively, during electrodeposition and subsequent annealing, the nanowire geometry could influence the shapes and distributions of the Co-rich magnetic particles, or could lead to stress induced anisotropy in these particles.

Although porous aluminum oxide membranes do allow annealing studies, they have the disadvantage that it is relatively difficult to dissolve the aluminum oxide to release the nanowires for structural studies. Some nanowires were therefore electrodeposited in nuclear-track-etched polycarbonate membranes, which can easily be dissolved using chloroform to facilitate characterization by transmission electron microscopy (TEM). Figure 12 shows a TEM image of heterogeneous alloy nanowires electrodeposited at a nominal current density of  $3.3 \text{ A cm}^{-2}$ , and having a measured room temperature GMR of under 0.5%. It is apparent that the nanowires are highly polycrystalline. No evidence of oxide, reported to be present in some continuous electrodeposited Co-Cu films, was found in these as-deposited nanowires.

Following growth, the room temperature magnetoresistance (MR) of the nanowires was measured with one contact made using Ag DAG to the caps at the tops of the nanowires and the other to the Au layer at the base of the wires. This configuration meant that generally the MR of several

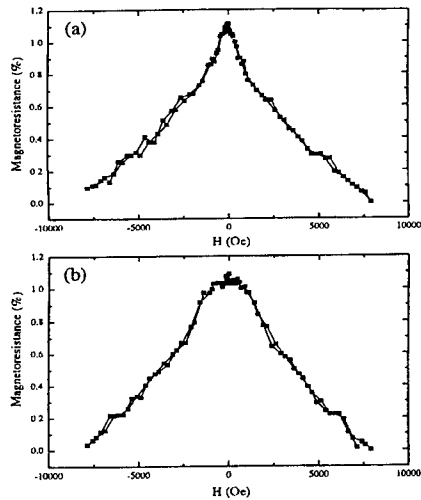


Fig.13. Percentage magnetoresistance for Co-Cu heterogeneous alloy nanowires electrodeposited in an aluminum oxide membrane with quoted pore diameter 200 nm and pore density  $10^9 \text{ cm}^{-2}$  following by anneal at  $400^\circ\text{C}$  for 30 min measured at room temperature with the magnetic field applied (a) parallel and (b) perpendicular to the long axis of

## 6. Conclusion

A wide range of nanoscaled electrodeposited materials have been discussed. It is clear that all of the above-mentioned types of nanosized structures are constantly being developed in increasing numbers. Research has been undertaken to both obtain additional information about existing materials and to develop new materials with practical application. W. Schwarzacher *et.al.* reported, (still unpublished), a magnetoresistive effect at room temperature of about 70% in multilayered CoNi/Cu nanowires. In previous work by W. Schwarzacher and K. Attenborough, [22], a high sensitivity of about 0.67%/Oe was achieved in electrodeposited (Cox/Cu/Coy/Cu)n multilayers of the 'spin-valve' type. There are several possible ways in which to develop nanoscaled materials with improved properties. For example, work is currently in progress by the authors on multilayered nanowires of spin-valve type [14].

The author would like to acknowledge financial support from INTAS(grant No. 97-0553).

## References

1. Schwarzacher W., Lashmore S. (1996) Giant magnetoresistance in electrodeposited films, IEEE Trans.Magn., 32, 3133-3157.
2. Lenczowski S.K.I., Schonenberger C., Gijs M.A.M., de Jonge W.I.M. (1995) Giant magnetoresistance of electrodeposited Co/Cu multilayers, J.Magn.Magn.Mater., 148, 455-465.
3. Nallet P., Chassaing E., Wals M.G., Hytch M.I. (1996) Interface characterization in electrodeposited Co-Cu multilayers, J.Appl.Phys., 79, 6884-6889.
4. Moffat T.P. Electrochemical production of single-crystal Cu-Ni strained-layer superlattices on Cu(100) (1995), J.Electrochem.Soc., 142, 3767-3770.

---

5. Ansermet J-Ph, Doudin B., Meier I.P. Magnetic and transport properties of electrodeposited nanostructured nanowires (1998), IEEE Trans.on Magn., 34, 968-972.
6. Jyoko Y., Kashiwabara S., Hayashi Y. (1997) Preparation of giant magnetoresistance Co/Cu multilayers by electrodeposition, J.Electrochem.Soc., 144, L5-L9.
7. Fedosyuk V.M., Boltushkin A.V., Shadrow V.G. (1989) Hard magnetic Co-W and CoNiW films with perpendicularly magnetic anisotropy, Phys.Stat.Sol.(a), 25, 359-363.
8. Fedosyuk V.M., Kasyutich O.I., Sheleg M.U. (1989), J.Electrochem.Soc., 137, 395.
9. Fedosyuk V.M., Sheleg M.U., Kasyutich O.I. (1991) Electrochemically plated films for data storage media, J.Inf.Record.Materials, 19, 455-463.
10. Fedosyuk V.M., Kasyutich O.I. (1991) Deposition and study of multilayers Co/Cu structures, J.Mater.Chem., 1, 795-797.
11. Fedosyuk V.M., Kasyutich O.I. (1993) Hard magnetic Co/Cu superlattices, J.Magn.Magn.Mater., 125, 330-334.
12. Fedosyuk V.M., Kasyutich O.I. (1991) Magnetic properties of multilayered Co/Cu films, J.Phys.of Metals and Metallography (in Russian), 12, 43-49.
13. Kasyutich O.I. (1996) Giant magnetoresistance in electrodeposited Co/Cu multilayered films, J.Phys.of Metals and Metallography (in Russian), 182, 90-98.
14. Fedosyuk V.M., Kasyutich O.I. (1996) New idea in electrodeposition – “spin-valve” structures, In Proceed. Of 6<sup>th</sup> Intern.Symp.on Surface Nanocontrol and Related Materials, Iketani, 25-27 November, Japan, rep. Np4.
15. Fedosyuk V.M., Riveiro J.M. (1994), Structure and thermal stability of amorphous  $Co_{80-x}W_x + \{Ni,Fe,Re\}_{20}$  films. In Proceed. Of the 14<sup>th</sup> Gen.Conf. Condens. Mat. Division, 28-31 Murch, Madrid.
16. Fedosyuk V.M., Riveiro J.M. (1996), Mossbauer study of the microstructure of electrodeposited  $Co_{92-x}W_x Fe_8$  films., J.Non.-Cryst.Solids, 204, 99-104.
17. Fedosyuk V.M., Blythe H.I. (1994), Magnetic investigation of electrodeposited inhomogeneous alloyed CuCo films, Phys.Stat.Sol.(a), 146, K13-K17.
18. Fedosyuk V.M., Blythe H.I., Kasyutich O.I., (1996), Chemically-deposited CuCo granular films: an alternative route to GMR. Mater.Science Letters, 26, 69-72.
19. Fedosyuk V.M., Kasyutich O.I., Blythe H.I. (1996), Giant magnetoresistance in granular electrodeposited CuCo films. J.Magn.Magn.Mater., 156, 345-346.
20. Fedosyuk V.M., Blythe H.I., Williams J.M. (1996) J.Magn.Magn.Mater., 155, 355-357.
21. Fedosyuk V.M., Blythe H.I., Jones G.A. (1998) An investigation of the structure and magnetic properties electrodeposited  $Co_xRe_{100-x}$  films. J.Magn.Magn.Mater., 184, 28-40.
22. Attenborough K., Boever H., Boect I. (1998) Ultra-sensitive spin-valve structures grown on GaAs by single bath electrodeposition. In Proceed. Of Eur.Conf. on Magn.Sensors and Actuators, 13-15 July, Sheffield, UK, rep.N A2.3.

## NANODISPERSED REFRACTORY COMPOUNDS IN THE ELECTRODEPOSITED METAL COATINGS

I. VITINA, I. ZALITE, V. BELMANE, J. GRABIS, V. RUBENE, O. KOVALOVA

*Riga Technical University, Institute of Inorganic Chemistry  
34 Miera Street, Salaspils-1, LV-2169, Latvia*

### 1. Introduction

The electrodeposition technique has a great theoretical and practical significance to obtain composite coatings on metal, metallized ceramic or polymer surfaces. The composite coatings can provide surface properties from both the electrodeposited metal and inorganic compound. The electrodeposition method of composite coating metal - inorganic compounds is used for modifying the surface [1-5].

New dispersed compounds with high electroconductivity, for example,  $\text{NbTi}$ ,  $\text{NbC}_x\text{N}_y$ ,  $\text{PbMo}_6\text{S}_8$ ,  $(\text{Pb}_{1.2}\text{Mo}_{6.4}\text{S}_8)$ ,  $\text{TiN}/\text{NbN}$ ,  $\text{Cu}_{1.8}\text{Mo}_6\text{S}_8$ ,  $\text{Sn}_{1.2}\text{Mo}_{6.4}\text{S}_8$ ,  $\text{YBa}_2\text{Cu}_3\text{O}_{7-x}$  and  $\text{Cr}_3\text{C}_{1.6}\text{N}_{0.4}$  have been prepared by the method of high temperature ion chemical synthesis and the plasma chemical method [5-9].

The aim of our investigations was to determine the possibilities of composite electrodeposition in systems  $\text{Sn-PbMo}_6\text{S}_8$ ,  $\text{Sn-NbC}_x\text{N}_y$ ,  $\text{Sn-TiN}$ ,  $\text{Sn-Ti}_{0.63}\text{Nb}_{0.34}\text{C}_{0.38}\text{N}_{0.58}$  and the characteristics of the electrodeposited thin layers' surface structure. These inorganic compounds were chosen to ensure electronic conductivity, solderability and black colour of the coatings.

The complexity of chrome-plating technologies and the necessity of obtaining chromium coatings with different functional properties motivate the search for new types of electrolytes to enable co-deposition of other elements, for example, Cd, Zn, Mo and particles of diamond,  $\text{B}_{6.5}\text{C}$ ,  $\text{B}_4\text{C}$ ,  $\text{AlB}_{12}$ ,  $\text{SiC}$  and  $\text{Al}_2\text{O}_3$  in amount of 0.1-0.5 % for preparation of composite coatings [4, 5].

Our investigations were aimed towards preparation of an electrolyte which allows for the attainment of electrodeposited coatings of  $\text{Cr-Cr}_3\text{C}_{1.6}\text{N}_{0.4}$  at temperature 25-30°C.

### 2. Experimental

The complex electrolyte  $\text{Sn(IV)-K}_4\text{P}_2\text{O}_7$  ( $\text{Sn}$  - 0.3M,  $\text{K}_4\text{P}_2\text{O}_7$  - 1.7M) was used to electrodeposit composites  $\text{Sn-Ti}_{0.63}\text{Nb}_{0.34}\text{C}_{0.38}\text{N}_{0.58}$  on copper substrate. The cation active organic compounds were added at 0.6 to 2.5 wt%. To obtain  $\text{Sn-NbC}_x\text{N}_y$  and  $\text{Sn-Ti}_x\text{N}_y$  the complex electrolyte of  $\text{Sn(II)-K}_4\text{P}_2\text{O}_7$  was used with concentrations:  $\text{Sn}$ -0.3M,  $\text{K}_4\text{P}_2\text{O}_7$ -0.8M. Alkybenzyltrimethylammonium chloride and alkyldiethanolbenzylammonium chloride were used as cation active organic compounds. The chemical dissolution of dispersed particles does not occur if the electrolyte pH range is 7.0 - 9.0.

The powders of  $\text{NbC}_x\text{N}_y$ ,  $\text{Ti}_x\text{N}_y$ ,  $\text{Ti}_{0.63}\text{Nb}_{0.34}\text{C}_{0.38}\text{N}_{0.58}$ ,  $\text{Cr}_3\text{C}_{1.6}\text{N}_{0.4}$  were prepared in the Institute of Inorganic Chemistry by plasma chemical synthesis. The characteristic shape of prepared  $\text{Ti}_x\text{N}_y$ ,  $\text{Ti}_{0.63}\text{Nb}_{0.34}\text{C}_{0.38}\text{N}_{0.58}$  is cubic, but particles of  $\text{Cr}_3\text{C}_{1.6}\text{N}_{0.4}$  have spherical form (Fig. 1). The average particle size of powders was in the range of 0.01-0.6  $\mu\text{m}$ . The characteristics of the dispersed particles of the inorganic compounds was studied by transmission electron microscopy.

The electrolyte containing (g/l):  $\text{CrO}_3$  - 200-250,  $\text{H}_2\text{SO}_4$  - 2.0-2.5,  $\text{NH}_4\text{F}$  - 4.0 was used as the electrolyte for electrodeposition of  $\text{Cr-Cr}_3\text{C}_{1.6}\text{N}_{0.4}$  coatings. Different from the usual electrolytes of the

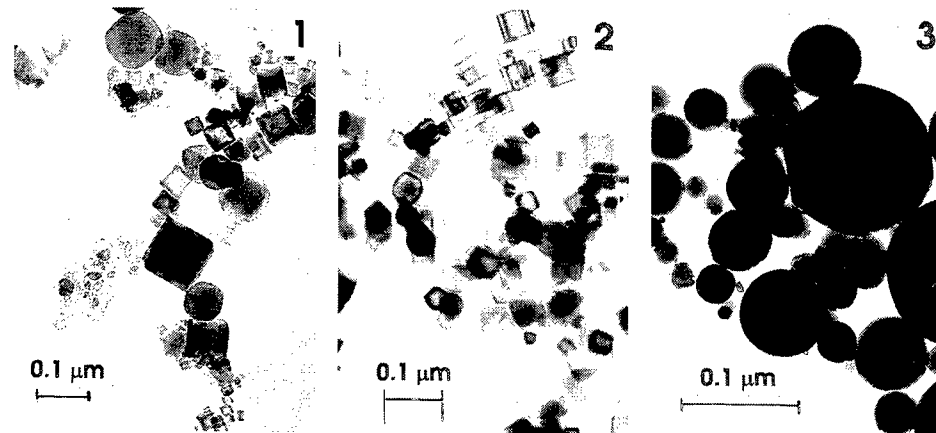


Figure 1. Characteristic shapes and sizes of disperse inorganic compounds: (1) for  $Ti_{0.63}Nb_{0.34}C_{0.38}N_{0.58}$ ; (2) for  $Ti_xN_y$ ; (3) for  $Cr_3C_{1.6}N_{0.4}$ .

electrodeposition of chromium, our electrolyte contains pyrophosphoric acid  $H_4P_2O_7$ . The electrodeposition was carried out at temperature of 25-30°C and at cathodic current density  $D_c=10-30\text{ A/dm}^2$ .

The charge and velocity of the disperse phase particles were investigated by the microelectrophoresis method. To determine the charge of disperse particles by means of electrophoresis, the horizontally mounted flat cell was used [10]. The content of the disperse inorganic phase in composite coatings was determined by chemical analysis. The quantitative content of chromium carbonitride in composite coatings was determined measuring the amount of carbon by method of combustion in oxygen flow. The surface structure of electrodeposited thin layers was investigated by scanning electron microscopy. We carried out the electrodeposition process in a simple bath of  $500\text{ cm}^3$  volume with mechanical stirring. A cathode and an anode were suspended vertically in the bath.

### 3. Results and Discussion

#### 3.1. THE COMPOSITE COATING Sn-DISPERSE INORGANIC COMPOUNDS

It has been shown in the microelectrophoresis method, that in a Sn(IV)- $K_4P_2O_7$  complex  $K_8[Sn(P_2O_7)_3]$  solution and in a Sn(II)- $K_4P_2O_7$  complex  $K_6[Sn(P_2O_7)_2]$  solution the particles of inorganic compounds  $NbC_xN_y$  and  $Ti_{0.63}Nb_{0.34}C_{0.38}N_{0.58}$  possess negative charge, determined by the absorption of complex anions  $[Sn(P_2O_7)_3]^{8-}$ ,  $[Sn(P_2O_7)_2]^{6-}$  on the surfaces of particles.

The surface charge of disperse particles does not change in the presence of cation active organic compounds alkylbenzyltrimethylammonium and alkyldiethanolbenzylammonium chlorides in the electrolyte. Particles maintain their negative charge, but their velocity towards the positively charged electrode decreases. The velocity of the particles is determined by the competition of adsorption processes between complex anions  $[Sn(P_2O_7)_3]^{8-}$ ,  $[Sn(P_2O_7)_2]^{6-}$  and cation active organic compounds or the formation of their associates on the surface of disperse particles.

The discharge of tin on the cathode from the complex anion adsorbed on disperse particle in the process of electrodepositing promotes simultaneous particle attachment to the cathode surface and their incorporation in a metal coating. The mechanism of the cathode process in this case determines the possibility of electrodepositing coatings with a high content of disperse particles of inorganic compound in the composite coatings Sn-inorganic compound.

### 3.2. THE COMPOSITE COATINGS $\text{Sn}-\text{Ti}_{0.63}\text{Nb}_{0.34}\text{C}_{0.38}\text{N}_{0.58}$

The inorganic compound  $\text{Ti}_{0.63}\text{Nb}_{0.34}\text{C}_{0.38}\text{N}_{0.58}$  content in the electrodeposited composite layer does not change significantly with its concentration in the  $\text{Sn}(\text{IV})-\text{K}_4\text{P}_2\text{O}_7$  electrolyte if pH is 6.5 to 7.0 and a cathodic current density in the range of 3.0 to 17.0  $\text{A}/\text{dm}^2$  is used (Fig. 2). The results were obtained from three parallel experiments. The results are relevant to  $\text{Ti}_{0.63}\text{Nb}_{0.34}\text{C}_{0.38}\text{N}_{0.58}$  used in this study.

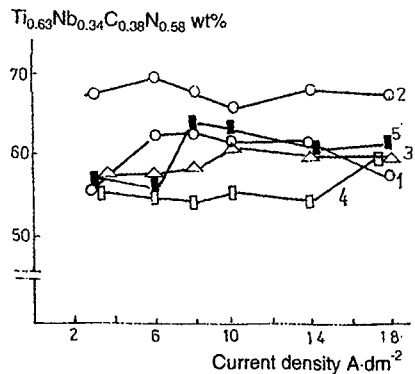


Figure 2. The  $\text{Ti}_{0.63}\text{Nb}_{0.34}\text{C}_{0.38}\text{N}_{0.58}$  content in the composite coating  $\text{Sn}-\text{Ti}_{0.63}\text{Nb}_{0.34}\text{C}_{0.38}\text{N}_{0.58}$  and its dependence on the concentration of  $\text{Ti}_{0.63}\text{Nb}_{0.34}\text{C}_{0.38}\text{N}_{0.58}$  in the electrolyte and the current density  $D_c$ :

- (1)  $\text{Ti}_{0.63}\text{Nb}_{0.34}\text{C}_{0.38}\text{N}_{0.58}$  55 g/l, pH 7.0;
- (2)  $\text{Ti}_{0.63}\text{Nb}_{0.34}\text{C}_{0.38}\text{N}_{0.58}$  75 g/l, pH 7.0;
- (3)  $\text{Ti}_{0.63}\text{Nb}_{0.34}\text{C}_{0.38}\text{N}_{0.58}$  75 g/l, pH 7.0;
- (4)  $\text{Ti}_{0.63}\text{Nb}_{0.34}\text{C}_{0.38}\text{N}_{0.58}$  75 g/l, pH 6.5;
- (5)  $\text{Ti}_{0.63}\text{Nb}_{0.34}\text{C}_{0.38}\text{N}_{0.58}$  100 g/l, pH 7.0.

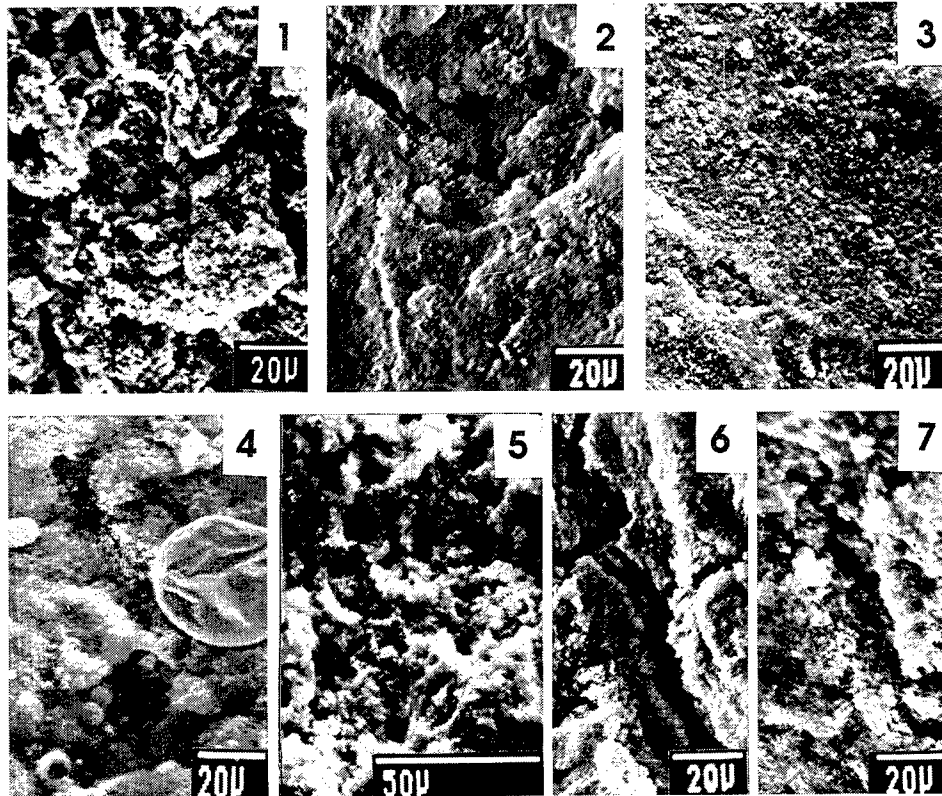


Figure 3. The structure of the composite coating  $\text{Sn}-\text{Ti}_{0.63}\text{Nb}_{0.34}\text{C}_{0.38}\text{N}_{0.58}$  and its dependence on the current density ( $D_c$ )  $\text{A}/\text{dm}^2$ : (1) 2.5; (2) 3.5; (3) 6.5, after thermal treatment at  $260^\circ\text{C}$  4 h +  $280^\circ\text{C}$  5 h; (4) 20.0, after thermal treatment at  $260^\circ\text{C}$  4 h; (5) the coating presented at "4" after thermal treatment  $280^\circ\text{C}$  5 h +  $310^\circ\text{C}$  6 h; (6) 24; (7) the coating presented at "6" after thermal treatment  $260^\circ\text{C}$  4 h +  $280^\circ\text{C}$  5 h.

Addition of the cation active compound alkylbenzyltrimethylammonium chloride (I) to the electrolyte does not essentially affect the amount of the disperse phase  $Ti_{0.63}Nb_{0.34}C_{0.38}N_{0.58}$  in the composite layer, but facilitates formation of a homogeneous surface structure without pores and characteristic cracks, if the cathodic current density is 8.0-10.0  $A/dm^2$  (Fig. 3(2)).

The increase of cathodic current density  $>10 A/dm^2$  is the reason for porous layer formation. The formation of crack-isolated large grains can be observed (Fig. 3(4), (5)). The pore formation is determined by considerable hydrogen evolution on the cathode during electrodeposition of the composite layer. Pores and cracks in the composite layer can be eliminated by 9 hours of thermal treatment at 260, 280, 310°C (Fig. 3(3), (5), (7)). At the beginning of the thermal treatment we can observe the occlusion of organic compound, which is adsorbed on the particles of the disperse phase and cathode surface during the electrodeposition process (Fig. 3(4) A). This could be the reason for the increase in the number of pores, if the thermal treatment is insufficient. The electrodeposited composite layers are electroconductive. The investigations of these layers' properties are continuing.

### 3.3. THE COMPOSITE COATINGS Sn-Ti<sub>x</sub>N<sub>y</sub>

It is possible to electrodeposit composite coatings with disperse phase content of up to 42 - 70 wt% from the Sn(II)-K<sub>4</sub>P<sub>2</sub>O<sub>7</sub> complex electrolyte, where the amount of inorganic compound Ti<sub>x</sub>N<sub>y</sub> is from 100 to 180 g/l and the concentration of organic substances alkylidi-( $\beta$ -hydroxyethyl)benzylammonium chloride mixture with alkylidi-( $\beta$ -hydroxyethyl)amin 0.6-2.5 wt%. The dependence of titanium nitride content in a composite coating on the concentration of organic substances in electrolyte and the cathodic current density are demonstrated in Figure 4. The electrodeposited composite layers Sn-Ti<sub>x</sub>N<sub>y</sub> have a characteristic heterogeneous surface structure and cracks in the coating. The coating can easily become homogeneous by thermal treatment at 250-280°C for 1 h (Fig. 5). Micropores and cracks have been filled after the treatment. The coatings (10-20  $\mu m$ ) can prevent corrosion and with a content of Ti<sub>x</sub>N<sub>y</sub> up to 30 wt% have a good solderability.

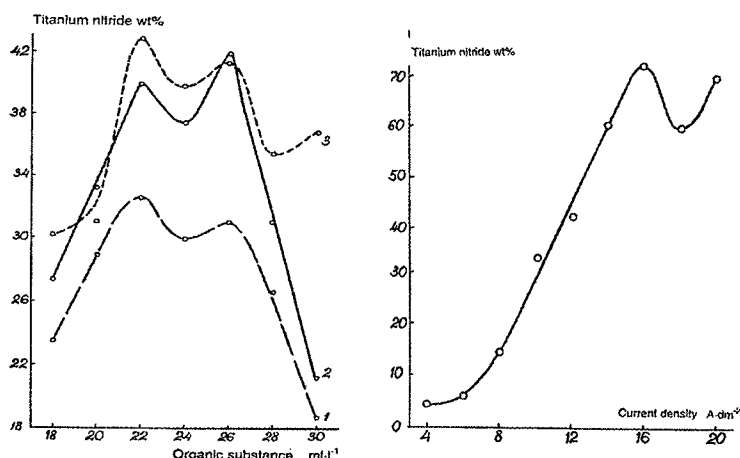


Figure 4. The content of titanium nitride in composite coating Sn-Ti<sub>x</sub>N<sub>y</sub> in dependence on the content of organic substance in electrolyte and the density of cathodic current.

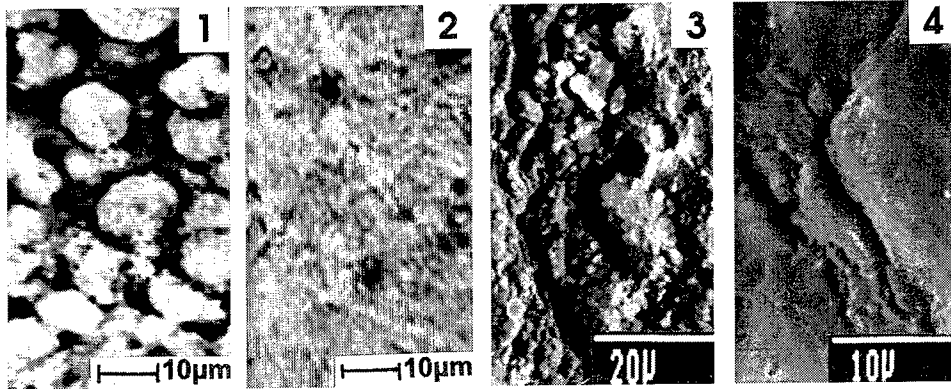


Figure 5. The structures of composite coating in dependence on the content of titanium nitride and thermal treatment: (1) 5.9 wt% without thermal treatment; (2) 5.9 wt% after thermal treatment at 280°C 1 h; (3) 53.6 wt% + 0.5 μm sputtered Sn without thermal treatment; (4) 53.6 wt% + 0.5 μm sputtered Sn after thermal treatment at 250°C 1 h.

### 3.4. THE COMPOSITE COATINGS $\text{Sn-NbC}_x\text{N}_y$

It is possible to electrodeposit composite coatings with disperse phase contents of up to 85-88 wt% (Fig. 6) from the  $\text{Sn}(\text{II})\text{-K}_4\text{P}_2\text{O}_7$  complex electrolyte, where the amount of inorganic compound  $\text{NbC}_x\text{N}_y$  is from 100.0 to 180.0 g/l and the concentration of alkylbenzyltrimethylammonium chloride (I) is from 6.4 to 9.0 g/l. Independent of the content of the disperse phase the electrodeposited composite layers  $\text{Sn-NbC}_x\text{N}_y$  have a characteristic heterogeneous surface structure and cracks in the coating. The coatings can easily become homogeneous by thermal treatment at 280°C for 4 - 10 hours (Fig. 7). These thin layers are electroconductive and solderable at  $300 \pm 10^\circ\text{C}$ , if the  $\text{NbC}_x\text{N}_y$  content is  $< 30$  wt%. Homogenized coatings on copper are corrosion resistant, when tested for 30 days at  $40 \pm 2^\circ\text{C}$ , relative humidity of 98%. They are structure-stable at  $-50^\circ\text{C}$ .

### 3.5. THE COMPOSITE COATINGS $\text{Cr-Cr}_3\text{C}_{1.6}\text{N}_{0.4}$

The electrophoretic investigation of chromium carbonitride surface properties depending on ion composition of solution gave the following results. Solutions of polychromium acids in the presence

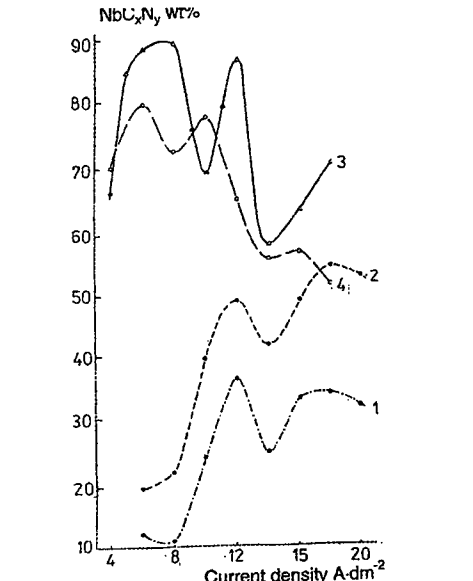


Figure 6. The niobium carbonitride content in the composite coating  $\text{Sn-NbC}_x\text{N}_y$  and its dependence on the concentrations of the ultradisperse phase, the organic substance (I) and the current density  $D_c$ : (1)  $\text{NbC}_x\text{N}_y$  100, (I) 6.4; (2)  $\text{NbC}_x\text{N}_y$  120, (I) 6.4; (3)  $\text{NbC}_x\text{N}_y$  180, (I) 8.0; (4)  $\text{NbC}_x\text{N}_y$  180, (I) 9.0 g/l.

of  $H_2SO_4$  and  $NH_4F$  or without these additions are strongly acidic and chromium carbonitride particles are positively charged. The chromium carbonitride particles move towards the negative electrode in the electric field with the velocity of 12.1 points/s.

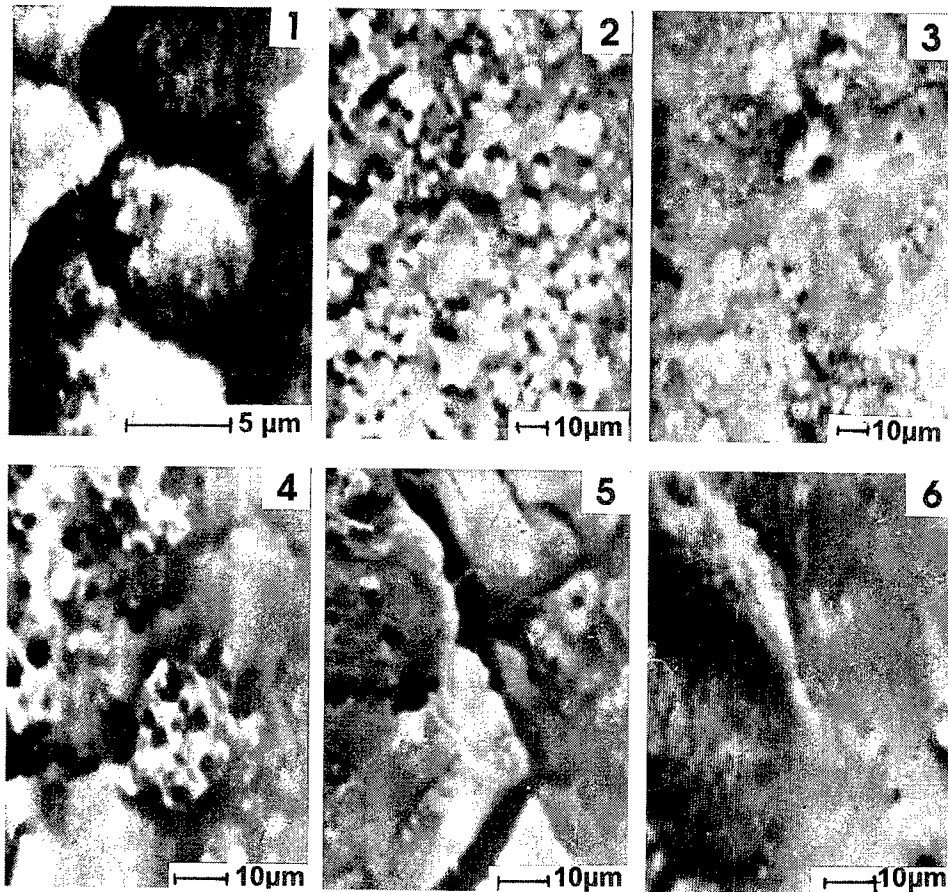


Figure 7. The structure of the composite coating and its dependence on the niobium carbonitride content in the coating  $Sn-NbC_xNy$ : (1) 9.64 wt% without thermal treatment; (2) 56.96 wt% without thermal treatment; (3) the coating presented at "2" after thermal treatment at  $280^\circ C$ ; (4) 38.4 wt% without thermal treatment; (5) 72.96 wt% without thermal treatment; (6) the coating presented at "5" after thermal treatment at  $280^\circ C$ .

In the presence of pyrophosphoric acid  $H_4P_2O_7$ ,  $H_2SO_4$  being absent, chromium carbonitride particles also have the positive charge, but their velocity decreases to 8.4 points/s. In the electrolyte containing  $H_2SO_4$  (concentration 2.8 g/l) and  $H_4P_2O_7$ , chromium carbonitride particle motion velocity is determined by the presence of  $P_2O_7^{4-}$ . The co-deposition of chromium carbonitride in the course of electrodeposition of chromium composite coatings as well as during formation of other metal coatings is determined by the complicated mechanism of cathode process and coatings growth [11].

The obtained data reveal that chromium carbonitride percentage in coatings depends on its content in electrolyte, cathodic current density and concentration of  $H_4P_2O_7$  (Fig. 8, Fig. 9).

The co-deposition of disperse phase in chromium coating (concentration of disperse phase in electrolyte from 5.0 to 50.0 g/l) is considerably influenced by the cathodic current density. Only when the current density is increased up to 8.0-10.0 A/dm<sup>2</sup> the formation of homogeneous coatings on the entire surface to be covered begins. At further increase of the cathodic current density up to 20-30 A/dm<sup>2</sup> the composite coatings are homogeneous in structure without changes on the sharp edges. The highest

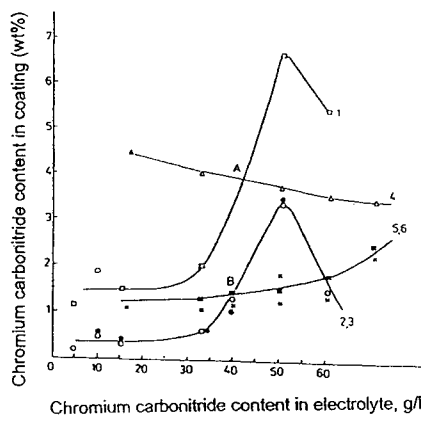


Figure 8. Dependence of chromium carbonitride content in composite coatings on chromium carbonitride and pyrophosphoric acid concentration in electrolyte and cathodic current density:  
 (1-3)  $\text{H}_3\text{P}_2\text{O}_7$  content 3.6 g/l, (1) — 10 A/dm<sup>2</sup>,  
 (2) —○— 20 A/dm<sup>2</sup>, (3) —●— 30 A/dm<sup>2</sup>,  
 (4-6) —  $\text{H}_4\text{P}_2\text{O}_7$  content 5.4 g/l, (4) —Δ— 10 A/dm<sup>2</sup>,  
 (5) —■— 20 A/dm<sup>2</sup>, (6) —×— 30 A/dm<sup>2</sup>.

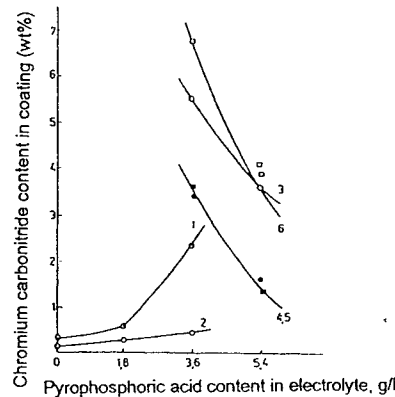


Figure 9. Influence of pyrophosphoric acid concentration in electrolyte on the content of co-deposited chromium carbonitride in composite coatings: (1, 2) concentration of chromium carbonitride 10 g/l, (1) 10 A/dm<sup>2</sup>, (2) 20 A/dm<sup>2</sup>,  
 (3-5) concentration of chromium carbonitride 50 g/l,  
 (3) —□— 10 A/dm<sup>2</sup>, (4) —●— 20 A/dm<sup>2</sup>,  
 (5) —■— 30 A/dm<sup>2</sup>, (6) —○— concentration of chromium carbonitride 60 g/l,  $D_c=20$  A/dm<sup>2</sup>.

possible degree of co-deposition of chromium carbonitride (up to 6.6 wt%) occurs at its concentration in solution of 50.0 g/l and cathodic current density of 10.0 A/dm<sup>2</sup>. When the content of chromium carbonitride in electrolyte is 40.0 g/l and concentrations of  $\text{H}_4\text{P}_2\text{O}_7$  are 3.6 and 5.4 g/l the content of disperse phase in coatings is mainly determined by cathodic current density.

The structures of electrodeposited coatings give additional information on mechanism of composite coating formation and purposefulness of the choice of concentration of disperse phase of inorganic compound and additional anion in electrolyte (Fig. 10). The structure (2) is determined by rivaling processes of electrodeposition of glittering chromium coatings versus the formation of chromium-chromium carbonitride composition with co-deposition of disperse phase in amounts of 0.2 wt%. The increase of chromium carbonitride concentration in electrolyte up to 50.0 g/l (the content of  $\text{H}_4\text{P}_2\text{O}_7$  being 5.4 g/l and cathodic current density 20.0 A/dm<sup>2</sup>) ensures the co-deposition of chromium carbonitride up to 3.5 wt% (structures (7) and (8)). In this case the increase of  $\text{H}_4\text{P}_2\text{O}_7$  concentration up to 12.0 g/l changes the character of structure and ensures its homogeneity and compactness (structure (9)). When the chromium carbonitride and pyrophosphoric acid concentrations are simultaneously increased up to 95.0 g/l and 15.0 g/l respectively at cathodic current density of 26.0 A/dm<sup>2</sup> the structure is homogeneous with round, sheet-shape crystal grains over all the surface, compact, without pores (Fig. 10, structures (11) and (12)).

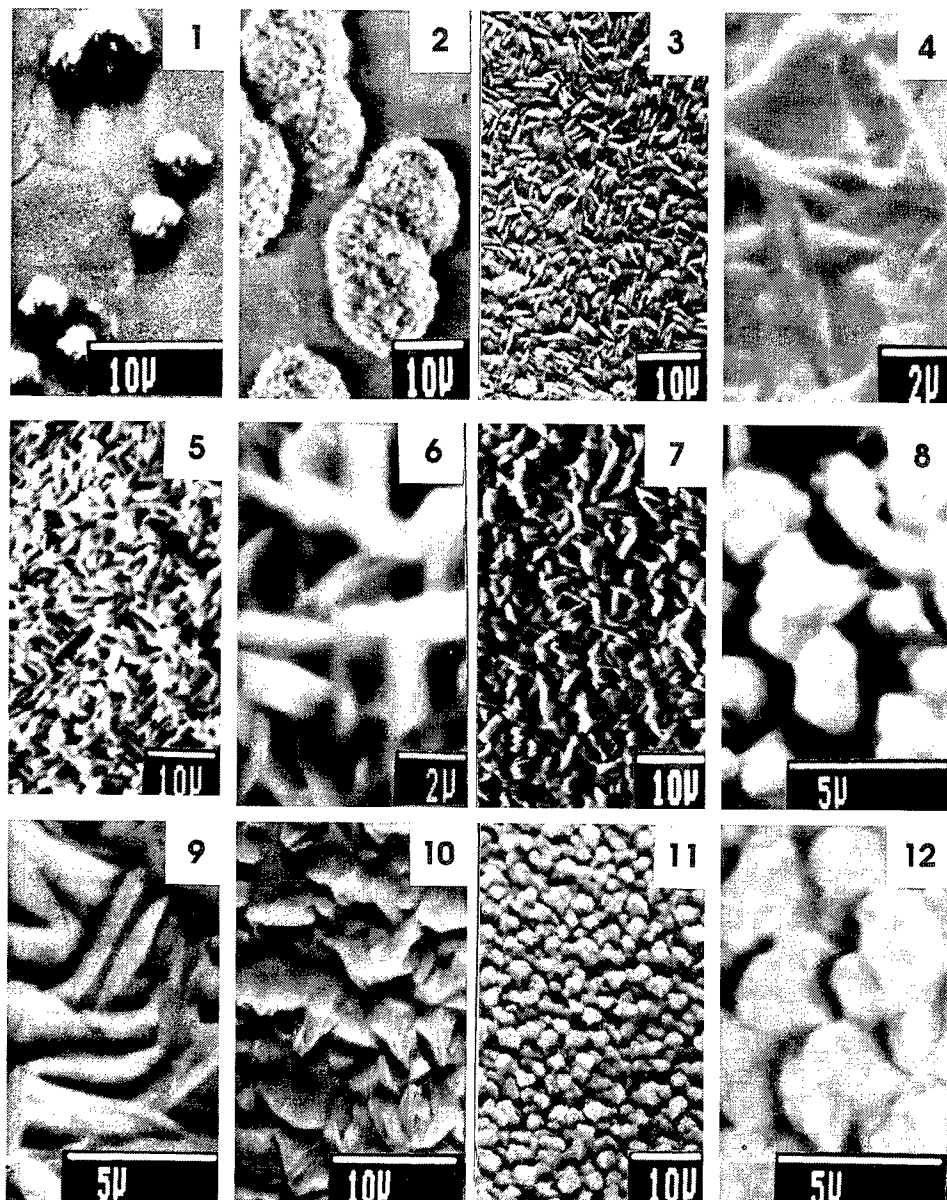


Figure 10. Changes of the surface structure of chromium-chromium carbonitride composite coating depending on chromium carbonitride  $\text{Cr}_3\text{C}_{1.6}\text{N}_{0.4}$  and pyrophosphoric acid  $\text{H}_4\text{P}_2\text{O}_7$  content in electrolyte (g/l) and cathodic current density ( $D_c$ ): (1) the electrolyte not containing  $\text{Cr}_3\text{C}_{1.6}\text{N}_{0.4}$  and  $\text{H}_4\text{P}_2\text{O}_7$  at  $D_c=3.5 \text{ A/dm}^2$ , (2) content  $\text{Cr}_3\text{C}_{1.6}\text{N}_{0.4} - 6.0$  without  $\text{H}_4\text{P}_2\text{O}_7$  at  $D_c=10 \text{ A/dm}^2$ , (3, 4)  $\text{Cr}_3\text{C}_{1.6}\text{N}_{0.4} - 6.0$ ,  $\text{H}_4\text{P}_2\text{O}_7 - 1.8$ ,  $D_c=10 \text{ A/dm}^2$ , (5, 6)  $\text{Cr}_3\text{C}_{1.6}\text{N}_{0.4} - 7.4$ ,  $\text{H}_4\text{P}_2\text{O}_7 - 10.0$ ,  $D_c=26 \text{ A/dm}^2$ , (7, 8)  $\text{Cr}_3\text{C}_{1.6}\text{N}_{0.4} - 50.0$ ,  $\text{H}_4\text{P}_2\text{O}_7 - 3.6$ ,  $D_c=20 \text{ A/dm}^2$ , (9)  $\text{Cr}_3\text{C}_{1.6}\text{N}_{0.4} - 50.0$ ,  $\text{H}_4\text{P}_2\text{O}_7 - 12.6$ ,  $D_c=20 \text{ A/dm}^2$ , (10)  $\text{Cr}_3\text{C}_{1.6}\text{N}_{0.4} - 39.0$ ,  $\text{H}_4\text{P}_2\text{O}_7 - 0.0$ ,  $D_c=15-20 \text{ A/dm}^2$ , (11, 12)  $\text{Cr}_3\text{C}_{1.6}\text{N}_{0.4} - 96.0$ ,  $\text{H}_4\text{P}_2\text{O}_7 - 12.6$ ,  $D_c=26 \text{ A/dm}^2$ .

#### 4. Conclusions

1. It is possible to obtain the following nanocomposite surface coatings by electrodeposition on copper as the base metal:
  - $\text{Sn-Ti}_{0.63}\text{Nb}_{0.34}\text{C}_{0.38}\text{N}_{0.58}$  with the  $\text{Ti}_{0.63}\text{Nb}_{0.34}\text{C}_{0.38}\text{N}_{0.58}$  content from ~55 to 70 wt% from the  $\text{Sn(IV)-K}_4\text{P}_2\text{O}_7$  electrolyte;
  - $\text{Sn-NbC}_x\text{N}_y$  with the  $\text{NbC}_x\text{N}_y$  content from ~10 to 88 wt% from the  $\text{Sn(II)-K}_4\text{P}_2\text{O}_7$  electrolyte;
  - $\text{Sn-Ti}_x\text{N}_y$  with the  $\text{Ti}_x\text{N}_y$  content from ~42 to 70 wt% from the  $\text{Sn(II)-K}_4\text{P}_2\text{O}_7$  electrolyte.
2. The formation of the electrodeposited composite layers' surface structure is determined by the applied cathode current density, hydrogen evolution in the electrolysis process and the amount of the disperse phase in the composite.
3. Pores and cracks in the composite layers can be eliminated by 4-40 h thermal treatment at 260-310°C.
4. The electrolyte based on  $\text{CrO}_3$  in the presence of  $\text{H}_2\text{SO}_4$  and  $\text{NH}_4\text{F}$  at temperature of 20 to 30°C and cathodic current density of 10 to 30  $\text{A}/\text{dm}^2$  result in deposition of the chromium-chromium carbonitride composite coatings. The disperse phase content varies from 0.2 to 6.8 wt% depending on the content of chromium carbonitride and additional anion  $\text{P}_2\text{O}_7^{4-}$  in electrolyte.

#### 5. References

1. Kurosawa, K. (1990) *The Journal of the Surface Finishing Society of Japan*, **41**(11), 1094-1100.
2. Sadowska-Mazur, J. and Warwick, M.E. (1985) *Plating and Surface Finishing*, **72** (5), 120-125.
3. Doong, J.C., Duh, J.G. and Tsai, S.Y. (1993) *Surface and Coatings Technology*, **58**, 151-155.
4. Schulze-Berge, K. and Schneider, E. (1989) *Metalloberfläche*, **43**, 6, 249.
5. Сайфуллин, Р.С. (1983) *Неорганические композиционные покрытия*, Химия, Москва.
6. Wahl, G. and Schmaderer, F. (1989) *Galvanotechnik*, **80** (9), 3018-3028.
7. Chu, X., Barnett, S.A., Wong, M.S. and Sproul, W.D. (1993) *Surface and Coatings Technology*, **57**, 13-18.
8. Weyten, H., Adriansens, W., Cornelis, J. and Leysen, R. (1993) *Journal of Materials Science*, **28** (5), 1252-1256.
9. Chaim, R. and Ezer, Y. (1993) *Journal of Materials Science*, **28**, 4205-4211.
10. Hunter, K.J. (1981) *Zeta potential in colloid science*, Academic Press, London.
11. Vitina, I., Zalite, I., Vilstone, R., Karklina, I. and Rubene, V. (1994) Electrodeposition and structure of chromium-chromium carbonitride composite coatings, *Latvijas Kimijas zurnals*, **2**, 186-196.

---

## **THERMAL SPRAYED NANOSTRUCTURED HARD COATINGS**

B.H. Kear and W.E. Mayo  
Rutgers, The State University of New Jersey  
Center for Nanomaterials Research  
607 Taylor Road  
Piscataway, NJ 08854-8065

### **1. Abstract**

Hardcoatings of WC/12Co and  $\text{Al}_2\text{O}_3/13\text{TiO}_2$ , produced by High Velocity Oxy-Fuel (HVOF) and High Energy Plasma (HEP) spraying, have been investigated. In HVOF spraying, nanostructured WC/Co coatings experience more extensive decarburization than conventional coatings, whereas in HEP spraying, just the opposite effect occurs. This is explained in terms of the influence of temperature on the decarburization mechanism. In the  $\text{Al}_2\text{O}_3/13\text{TiO}_2$  case, HEP spraying generates a metastable coating, due to rapid quenching of the plasma melted particles on the substrate. The metastable phase has a defect spinel structure and a nanocrystalline grain size. When heated, it decomposes into an equilibrium two-phase structure, consisting of  $\alpha\text{-Al}_2\text{O}_3$  and  $\beta\text{-Al}_2\text{O}_3\text{-TiO}_2$ . Both nanostructured cermets and ceramics have potential as wear-resistant coatings.

### **2. Introduction**

Materials with fine-scale structures have long been recognized to exhibit remarkable and technologically attractive properties. Over the past decade [1-3], interest has been growing in a new class of materials that are composed of ultra-fine grains or particles. A feature of such *nanostructured* materials is the high fraction of atoms that reside at grain boundaries or interfaces in the materials. Although much of today's R&D activity is focused on the synthesis and processing of nanostructured bulk materials [3,4], there is a growing interest in the fabrication of nanostructured coatings.

This paper presents a progress report on work being conducted on thermal spraying of nanostructured hardcoatings at Rutgers' Center for Nanomaterials Research, in collaboration with several industrial partners. Our work in this area has been focussed primarily on developing wear-resistant coatings of WC/12Co and  $\text{Al}_2\text{O}_3/13\text{TiO}_2$ .

### 3. Experimental

*Feed powders* of conventional and nanostructured WC/12Co were obtained from Surface Engineering (2400 grade) and Nanodyne (Nanocarb<sup>®</sup>), respectively. These powders have strikingly different characteristics, which are a consequence of different production methods.

Conventional WC/Co powder is produced by mechanical mixing of WC and Co particles in a fluid medium, spray drying to form solid agglomerates, and heat treatment to consolidate the agglomerated particles. Nanostructured WC/Co powder is produced by spray drying an aqueous solution mixture of salts of the constituent elements to develop a homogeneous precursor powder, followed by fluid bed thermochemical conversion (pyrolysis, reduction and carburization) of that powder to form the desired nano-WC/Co end-product powder [5,6]. During the cool-down cycle in the reactor, the high surface area powder is passivated with oxygen-rich species. Without this precautionary measure, the powder is susceptible to spontaneous combustion when exposed to air.

The as-produced conventional powder consists of solid agglomerates, which are screened to a relatively narrow size distribution, typically within the range 15-40  $\mu\text{m}$ . Within each particle the carbide grain size is from 2-5  $\mu\text{m}$ . In contrast, the as-produced nanostructured powder has a porous, spherical shell morphology, and particle size of 5-30  $\mu\text{m}$ . The individual WC grains residing within each nanocomposite particle are about 30-50 nm.

*Thermal spraying* was carried out at A&A Company Inc., using both HVOF and HEP guns. Plasma spraying was performed with a Metco 3M gun, using both Ar/10% He and N<sub>2</sub>/12% H<sub>2</sub> as feed gases. The much longer particle residence time in the hot zone of the N<sub>2</sub>/H<sub>2</sub>-plasma, due to release of recombination energy downstream in the plasma jet, heats up the particles to much higher temperatures. Therefore, the trend in thermal spraying, represented by HVOF, Ar/He-plasma and N<sub>2</sub>/H<sub>2</sub>-plasma, reflects a sharp increase in the mean particle temperature achieved during spraying.

## 4. Results and Discussion

### 4.1 WC/12Co COATINGS

#### 4.1.1 HVOF Deposition

Coating tests were performed with an HVOF gun, using both conventional and nanostructured powder feeds of the same nominal composition, WC/12Co; actual compositions are given in Table I. Metallographic examination of cross-sections of the two types of coatings revealed some important differences in their microstructures.

In the nano-coating case, a typical microstructure consisted of alternating bands of speckled and clear material, and inter-band porosity, Figure 1. Under high resolution in the SEM, a speckled region of the microstructure was revealed to be a highly porous aggregate of WC and Co particles, Figure 2(a), reminiscent of the original particle structure. Moreover, it appeared that many of the WC nanoparticles were experiencing

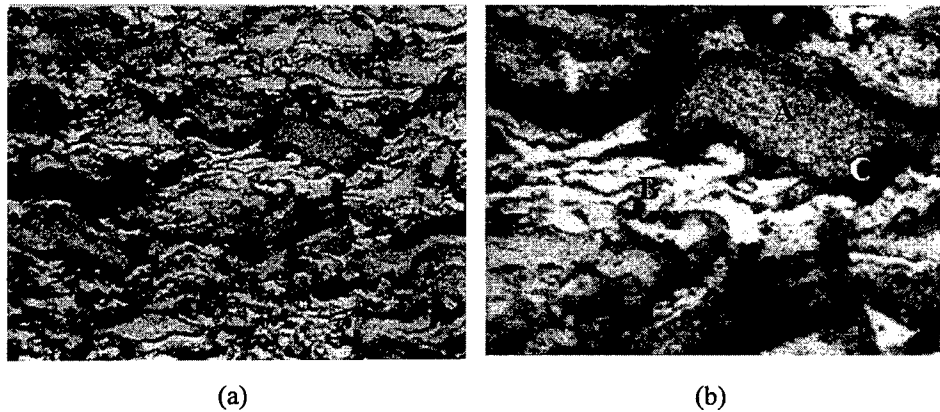


Figure 1. Optical micrographs (etched and re-polished) of HVOF-sprayed WC/12Co nano-coating; (a) low magnification (400x) micrograph showing "banded" structure of coating, and (b) same area at higher magnification (1000x) showing speckled band (A), clear band (B), and inter-band porosity (C).

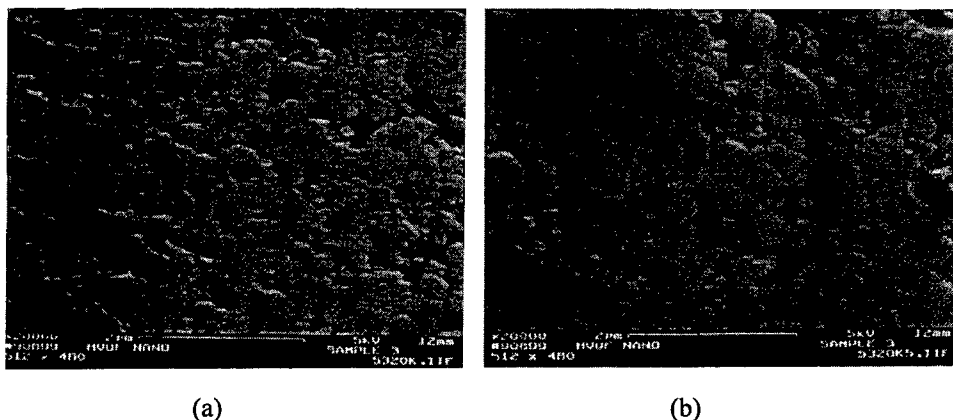


Figure 2. SEM micrographs of the different regions in Figure 1, showing (a) extensive micro-porosity in a speckled band (A), and (b) the absence of such porosity in a clear band (B). Both bands show the presence of a fine distribution of WC particles, but they appear to be coarser in the pore-free band of the microstructure.

coarsening by a particle rearrangement and coalescence mechanism. Evidence for this mechanism is indicated in Figure 2(a), where clusters of WC nanoparticles appear to be coalescing to form larger particles, apparently assisted by the presence of liquid Co. In contrast, a clear region of the microstructure, Figure 2(b), was composed of a pore-free, sintered mass of WC particles in a Co matrix phase, although the amount of Co phase was larger than expected. As will be shown later, this is explicable on the grounds that

these regions must have been exposed to high temperatures during spraying, thus causing some dissolution of the WC particles in the liquid Co to form more liquid phase. Another feature is the larger average particle size in Figure 2(b) relative to Figure 2(a), which is consistent with a higher temperature of exposure of the latter during thermal spraying. A surprising finding is the faceting of many of the WC particles, down to the smallest particle size observable, which is indicative of good wetting between the WC particles and the liquid Co phase. Such an effect is commonly observed in the near-equilibrium conditions encountered in liquid phase sintering of bulk materials [7].

Table I

Material	Composition (wt.pct)				
	W	Co	Total C	Free C	O/N (ppm)
Surface Eng. powder feed (WC/15Co)	Starting powder	79.87	14.94	5.19	0.04
	HVOF coating	79.98	15.1	4.85	0.07
	Plasma coating	98.17	0.55	1.28	0.05
Nanodyne powder feed (WC/12Co)	Starting powder	82.63	12	5.37	0.04
	HVOF coating	84.44	11.66	3.9	0.09
	Plasma coating	92.6	4.76	2.65	0.12

These observations are interpreted to be evidence for non-uniform melting of the original shell-like particles during spraying. As indicated in Figure 3, only the liquid phase sintered part of a heated particle would be expected to yield a dense structure when it impacts the chilled substrate. In contrast, the heated, but not necessarily melted part of that same particle should retain at least some, if not all, of its original micro-porosity. In agreement with this model, the hardness in the clear regions was ~1050 VHN (1 kg load), whereas that in the speckled regions was ~ 650 VHN (1 kg load)--the latter reflecting 'softening' of the region by virtue of the presence of a fine distribution of micro-pores. In other words, despite a relatively uniform distribution of WC particles, the presence of micro-porosity substantially reduces the measured hardness of the coating.

If the temperature of any region of a heated particle exceeds the melting temperature of the pseudo-binary eutectic in the WC-Co system [8], rapid dissolution of the WC nanoparticles in the liquid Co is to be expected, assisted by the high surface area of contact between the two phases. Thus, the amount of liquid Co, and its enrichment in W and C, should both increase progressively with degree of superheat above the eutectic temperature. Such an effect would explain the variations in WC particle size and distribution in the clear regions of the microstructure. Moreover, enrichment of the liquid Co in W and C should generate a high population density of strong tungsten/carbon clusters in the liquid phase, making it highly susceptible to

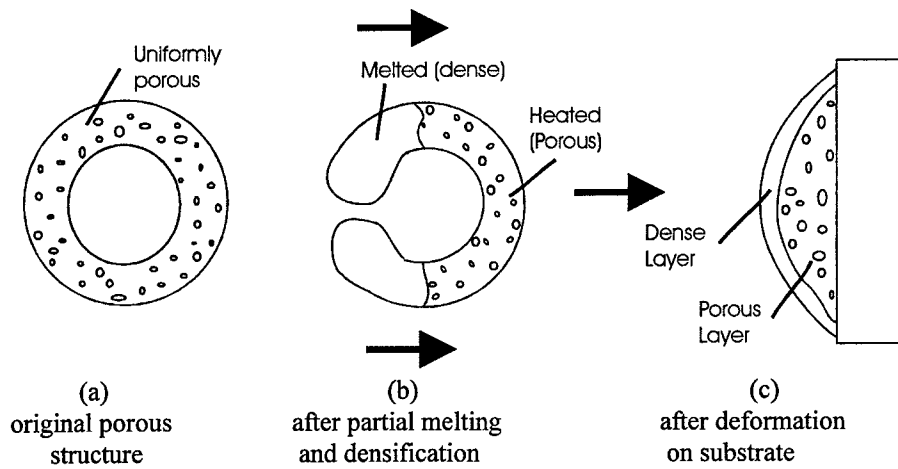


Figure 3. Schematic representation of the formation of a "banded" coating structure when a partially melted and densified nano-WC/Co particle impacts on the substrate surface.

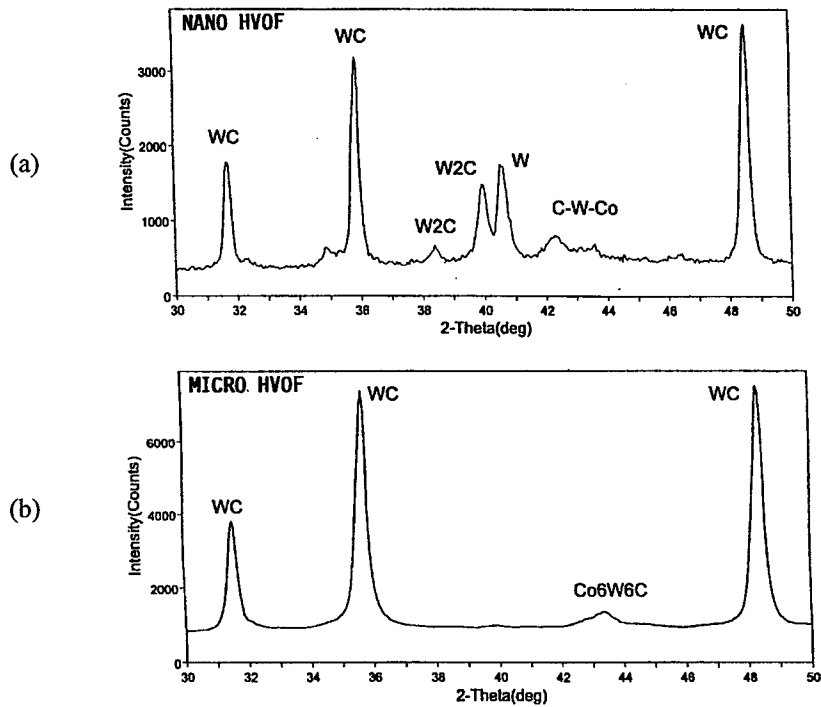
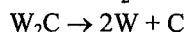
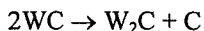


Figure 4. X-ray diffraction patterns of HVOF-deposited WC/12Co coatings, showing evidence for more decarburization in the nano-coating sample (a), relative to the micro-coating sample (b).

amorphization during subsequent solidification. Since the Co-rich liquid experiences splat-quenching on the chilled substrate, it seems inevitable that an amorphous Co-rich matrix phase will be developed, as in fact has been reported in the literature [9,10]. On the other hand, if the quenching rate is not high enough, then crystallization of mixed-metal carbide nanophases is to be expected. Evidence for  $\eta$ -carbide formation on an ultra-fine scale has been found in X-ray diffraction patterns of some of the coatings.

X-ray diffraction patterns of the two types of coatings showed that decarburization was more pronounced in the nano-coating material than in the micro-coating material, Figure 4. The most prominent feature in the diffraction pattern of the nano-coating material is the evidence for  $W_2C$  and W formation, which accounts for about 30% of the total carbide content in the material. This behavior is believed to be a consequence of two effects. First, loss of WC phase can occur by high temperature reaction with oxygen in the HVOF environment, leading to the formation of  $W_2C$  and even W. This includes impurity oxygen in the feed gases, on the surfaces of the passivated nanoparticles, and by mixing of ambient air with the combustion flame. Second, if the temperature is high enough, then the WC particles can undergo thermal decomposition, according to the following reactions:



The instability of WC phase at high temperatures is well known [11], but what is not known is how this is affected by the presence of liquid Co. It seems likely that dissolution of WC in liquid Co must play a role, but the details are unclear at this time.

In the nano-coating case, it is believed that the high surface area of the nano-WC/Co particles makes decarburization by reaction with impurity oxygen the dominant mechanism, thus accounting for the observed higher degree of decarburization relative to that of the micro-coating case, Figure 4. On the other hand, under the conditions encountered in plasma spraying, where particle temperatures are much higher, the dominant decarburization mechanism is thermally-induced decomposition of the WC phase, as will be shown later.

Because of the importance of the microstructural features discussed above, coating samples from several thermal spray companies were examined. Without exception, all HVOF-derived nano-coatings showed a heterogeneous microstructure, similar to that of Figure 1. However, different samples showed varying degrees of inter-band porosity and relative volume fractions of speckled (micro-porous) and clear (dense) regions, which is taken to be an indication of the importance of controlling thermal spray parameters to produce nano-coatings with reproducible microstructures, properties and performance.

The observations on the HVOF-deposited micro-coatings were similar to that reported in the literature [12]. The most significant feature was the relatively uniform distribution of coarse WC particles in the Co matrix phase. An important difference was the absence of significant dissolution of WC particles in the liquid Co, because of the low surface area of contact between the two phases. Another factor was the relatively low enrichment of the Co phase in W and C in the starting powder, relative to that of the nano-powder, which is enriched in W and C by virtue of the chemical route used in its production.

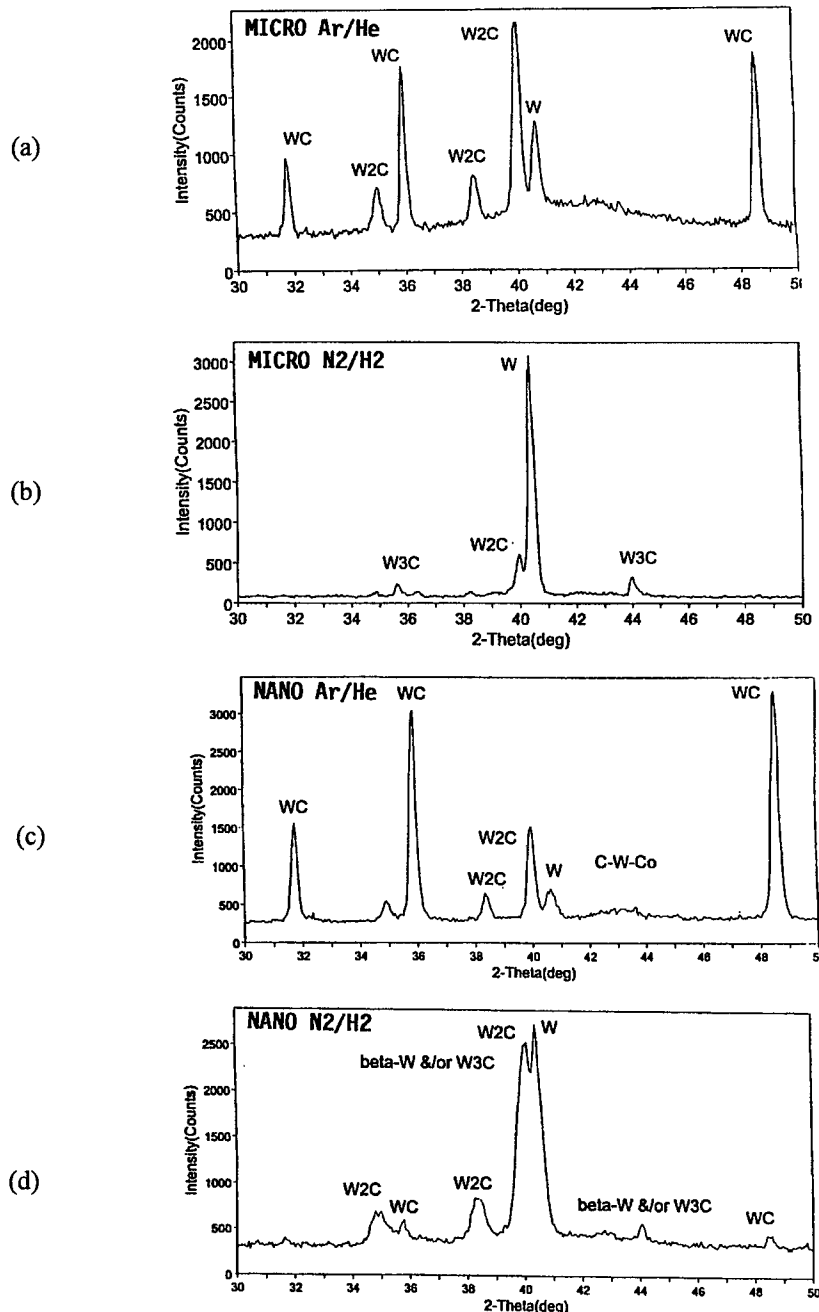


Figure 5. X-ray diffraction patterns of HEP-deposited WC/12Co coatings, showing evidence for more extensive decarburization in the micro-coating samples (a) and (b), relative to the nano-coating samples (c) and (d).

#### 4.1.2 HEP deposition

Coating tests were performed with an HEP gun, using Ar/10% He and N<sub>2</sub>/12% H<sub>2</sub> feed gases.

X-ray diffraction patterns showed evidence for extensive decarburization in the HEP-deposited coatings, but the effect was more pronounced in micro-coatings than in nano-coatings, Figure 5, which was the opposite of that found for HVOF-deposited coatings, Figure 4. The sequence of phase changes was strikingly different in the two cases. In the micro-coating case, decarburization involved the formation of W<sub>2</sub>C and W at the expense of WC. However, the major phase was W<sub>2</sub>C in the Ar/He plasma coating, and W in the N<sub>2</sub>/H<sub>2</sub> plasma coating. In contrast, in the nano-coating case, decarburization to form W<sub>2</sub>C and W was not as pronounced.

Chemical analysis of HVOF and N<sub>2</sub>/H<sub>2</sub> plasma coatings confirmed the trend in decarburization indicated by the X-ray analysis. Moreover, there was clear evidence for a major loss of Co, which was quite remarkable in the micro-coating case. As shown in Table I, the amount of Co decreases from 15 wt.% in the starting powder to 0.55 wt.% in the N<sub>2</sub>/H<sub>2</sub>-plasma coating, and there is a corresponding decrease in carbon content from 5.19 wt.% to 1.28 wt.%. Similar losses of Co and C occurred in the nano-coating case, but not as much as that in the micro-coating case.

The microstructure of a N<sub>2</sub>/H<sub>2</sub>-plasma coating was quite different from that of an HVOF coating, irrespective of the type of powder feed used, i.e. nano- versus micro-powder. This was most clearly seen in a comparison of etched samples of the nano-coating material. The HVOF coating showed a uniform distribution of WC particles, Figure 6(a), whereas there was little or no evidence for such particles in the N<sub>2</sub>/H<sub>2</sub>-plasma coating, Figure 6(b). A similar difference in microstructure was seen in an HVOF overlay coating on a N<sub>2</sub>/H<sub>2</sub>-plasma coating, Figure 6(c). This difference in etching behavior is consistent with Figure 5, which shows that the major phases are W and W<sub>2</sub>C, with only a small amount of residual WC phase due to extensive decarburization. Similar observations were made for the micro-coating material, except that banding of the microstructure was more pronounced. The microstructures of the corresponding Ar/He -plasma coatings more closely resembled the HVOF coatings than the N<sub>2</sub>/H<sub>2</sub>-plasma coatings, particularly in the nano-coating case, again consistent with the X-ray data.

Hardness measurements on both nano- and micro-coatings showed consistently higher values for HVOF coatings relative to N<sub>2</sub>/H<sub>2</sub>-plasma coatings, reflecting the more extensive decarburization experienced in plasma spraying. Moreover, there was little difference in hardness between transverse and in-plane sections of the microstructure, Table II, despite the presence of microstructural banding. In a few cases, the dependence of hardness on coating thickness was examined. A surprising finding was the reproducible decrease in hardness with coating thickness for both micro-coating and nano-coating samples, with a HVOF coating consistently displaying higher hardness than a N<sub>2</sub>/H<sub>2</sub>-plasma coating. It should be noted that the hardness values obtained at low loads were consistently higher than that at high loads, due to the influence of porosity in the coatings. Nevertheless, the trends in hardness observed were the same whatever the magnitude of load applied.

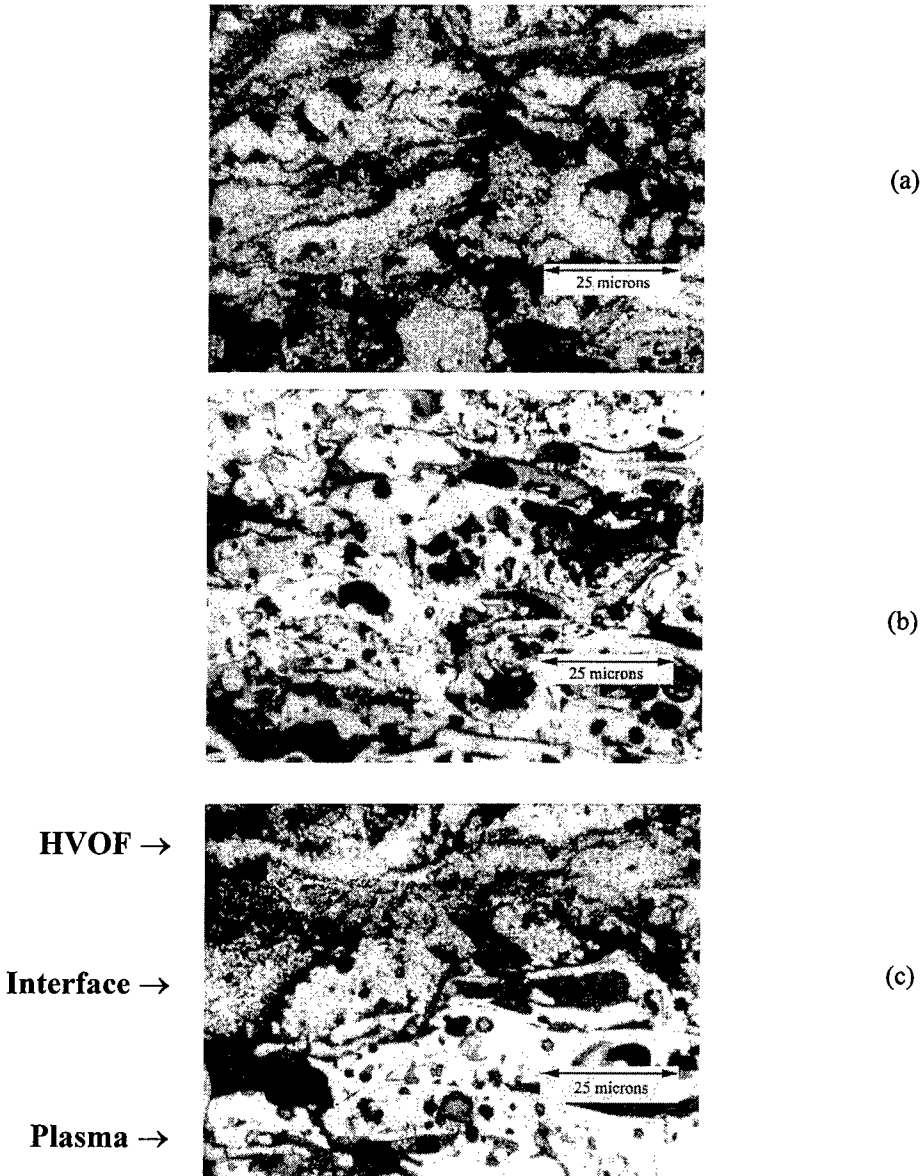


*Figure 6.* Optical micrographs of WC/12Co nano-coating samples, comparing microstructures (etched condition) of (a) HVOF coating, (b) N<sub>2</sub>/H<sub>2</sub>-plasma coating, and (c) HVOF overlay coating on N<sub>2</sub>/H<sub>2</sub>-plasma coating. Note uniform distribution (speckled appearance) of fine WC particles in (a), and the absence of WC particles in (b), due to extensive decarburization in the N<sub>2</sub>/H<sub>2</sub>-plasma coating.

**Table II**

Coating	Transverse section		In-plane section	
	VHN <sub>100</sub>	VHN <sub>1000</sub>	VHN <sub>100</sub>	VHN <sub>1000</sub>
HVOF	1233	744	1156	644
Plasma	937	414	871	474
HVOF + Plasma	1187 946	666 414	---	---

The variations in hardness with coating thickness in nano- and micro-coating samples are not understood. It is conceivable that the build-up of internal stresses during incremental coating deposition is a contributing factor. This will be checked by further experiments.

#### 4.1.3 Decarburization mechanism

Taken together, these observations provide strong evidence for the decarburization model discussed above. A key factor is the much higher average particle temperature achieved during plasma spraying, relative to HVOF spraying, which causes more extensive decarburization. A surprising result is the almost complete decarburization of the micro-coating using a N<sub>2</sub>/H<sub>2</sub>-plasma, as well as the gross loss of Co. Evidently, in this case, particle temperatures are so high that vaporization of Co and C occur to an unusual degree, even during the very short residence times in the hot zone of the plasma. It is proposed that the reduced susceptibility of the nano-coating to these compositional changes reflects the lowering of the vapor pressure of the liquid Co because of its enrichment in W and C. The mechanism of C gasification needs further investigation, but it may be enhanced by reactions with the ionized gas species in the plasma.

#### 4.1.4 Coating thickness effect

There have been indications that much thicker coatings can be produced using nanostructured powder feed than conventional powder feed. This is a useful result, since in many applications there are requirements for thick coatings that are beyond today's capabilities. A feature of the microstructure that needs more attention is the presence of micro-porosity in the thermal sprayed nano-coating material. Since these micro-porous regions are not as hard and stiff as the adjacent melted and quenched regions, this raises interesting questions concerning the potential for relaxation of internal stresses in the softer regions during coating deposition. In other words, the build up of internal stresses during incremental deposition may be lessened, so that the coating may be less prone to cracking and/or de-bonding at the coating/substrate interface. This topic is currently under investigation.

## 4.2 Al<sub>2</sub>O<sub>3</sub>/13TiO<sub>2</sub> COATINGS

Agglomerated powder feed of Al<sub>2</sub>O<sub>3</sub>/13TiO<sub>2</sub>, (Metco 130, particle size -53 µm + 15 µm) was obtained from Sulzer Metco. An X-ray diffraction pattern of this powder

showed that it was composed of a micron-scale mixture of  $\alpha$ -Al<sub>2</sub>O<sub>3</sub> (corundum) and TiO<sub>2</sub> (anatase) grains.

Plasma spraying was carried out at A&A Company Inc. using a Metco 3M gun. The powder was fed into a high energy N<sub>2</sub>/10%H<sub>2</sub> plasma, with a protective argon shroud, and sprayed into cold water and onto a chilled substrate, located at about 23 cm. from the gun nozzle. The resulting powders, splats and coatings were characterized by X-ray diffraction, using CuK<sub>α</sub> radiation (40 kV, 30 mA), and JADE (version 3.1) for phase identification. Vickers hardness measurements were performed on polished sections using a Leco micro-hardness tester.

#### 4.2.1 Effect of cooling rate

During the short residence time in the plasma jet, the feed particles were completely melted and homogenized. When the liquid droplets were water quenched, they solidified in one of two microstructural forms. Particles experiencing moderate cooling rates ( $\sim 10^4$  °K/sec) displayed a well-defined dendritic microstructure, and exhibited some phase separation. However, particles experiencing somewhat higher cooling rates developed a cellular-dendritic microstructure. Both of these microstructures are shown in Figure 7. When the cooling rate was exceptionally high,  $\sim 10^6$  °K/sec, as in splat-quenching on a metal chill plate, the microstructure was featureless. In other words, it appears that segregation-less (plane-front) solidification occurs only under the highest cooling rates characteristic of splat-quenching [13].

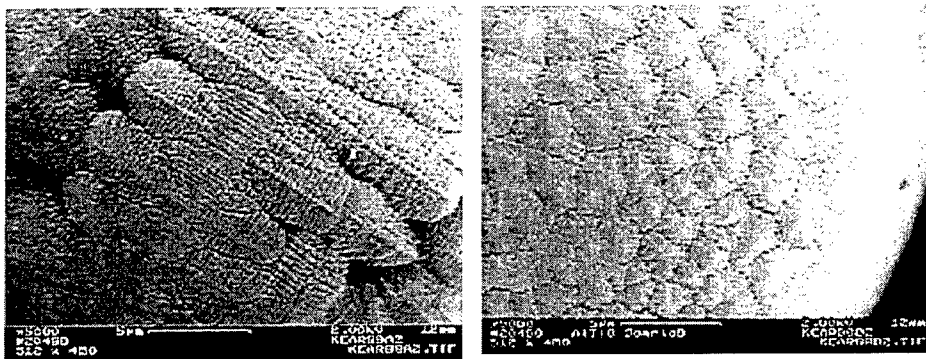


Figure 7. SEM micrographs of plasma-melted and water-quenched particles of Al<sub>2</sub>O<sub>3</sub>/TiO<sub>2</sub>, showing dendritic (left) and cellular-dendritic (right) microstructures, depending on cooling rate.

An X-ray diffraction pattern of the water-quenched powder, Figure 8, shows that the dendritic structure is composed of an amorphous component,  $\alpha$ -Al<sub>2</sub>O<sub>3</sub>, and metastable Al<sub>2</sub>O<sub>3</sub>•TiO<sub>2</sub>, which we call  $\chi$ -phase. Our calculations indicate that the powder has approximately 50% amorphous content, 40%  $\chi$ -phase, and 10%  $\alpha$ -Al<sub>2</sub>O<sub>3</sub>. The grain size of  $\alpha$ -Al<sub>2</sub>O<sub>3</sub> is approximately 60 nm, whereas that of the  $\chi$ -phase is about 24 nm. In contrast, the corresponding X-ray diffraction pattern of splat-quenched

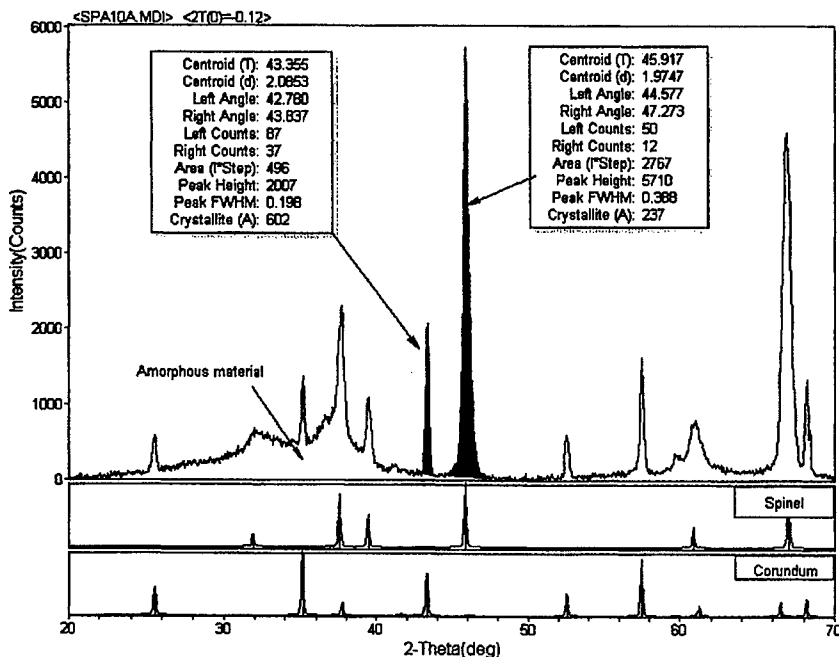


Figure 8. X-ray diffraction pattern of  $\text{Al}_2\text{O}_3/\text{TiO}_2$  powder, after plasma melting and water quenching. Shown for comparison are the reference diffraction patterns for the spinel and corundum ( $\alpha\text{-Al}_2\text{O}_3$ ) structures.

powder, Figure 9, shows evidence for a strong amorphous component plus  $\chi$ -phase (28 nm grain size), but no  $\alpha\text{-Al}_2\text{O}_3$ . The absence of  $\alpha\text{-Al}_2\text{O}_3$  phase is believed to be a consequence of the much higher average cooling rate experienced by splat-quenched material, relative to water-quenched material.

X-ray diffraction patterns similar to that of  $\chi$ -phase have been reported in the literature. In particular, Zhou and Snyder [14] have given a detailed analysis of the diffraction patterns of chemically synthesized  $\eta\text{-Al}_2\text{O}_3$  and  $\gamma\text{-Al}_2\text{O}_3$  powders, Figure 10. Both phases have a cubic structure - spinel with  $\text{Fd}3\text{m}$  space group. In this structure, the oxygen ions form a cubic close-packed sub-lattice, and the aluminum ions partially occupy both octahedral and tetrahedral sites. The broad peaks indicate a high degree of structural disorder, so that the material is more properly described as having a defect spinel structure. An exception is the sharp (222) reflection, which is due to scattering from ordered domains of the oxygen sub-lattice.

In the present case, Figure 9, the relative intensities of the (400) and (440) reflections are the opposite of that displayed by the  $\eta$  and  $\gamma$  phases. Computer simulations indicate that there is a preference for octahedral coordination of the cations, and that there is random occupancy of Ti on the Al lattice sites. It may be concluded, therefore, that  $\chi$ -phase is a metastable solid solution of  $\text{Al}_2\text{O}_3$  and  $\text{TiO}_2$ . There are

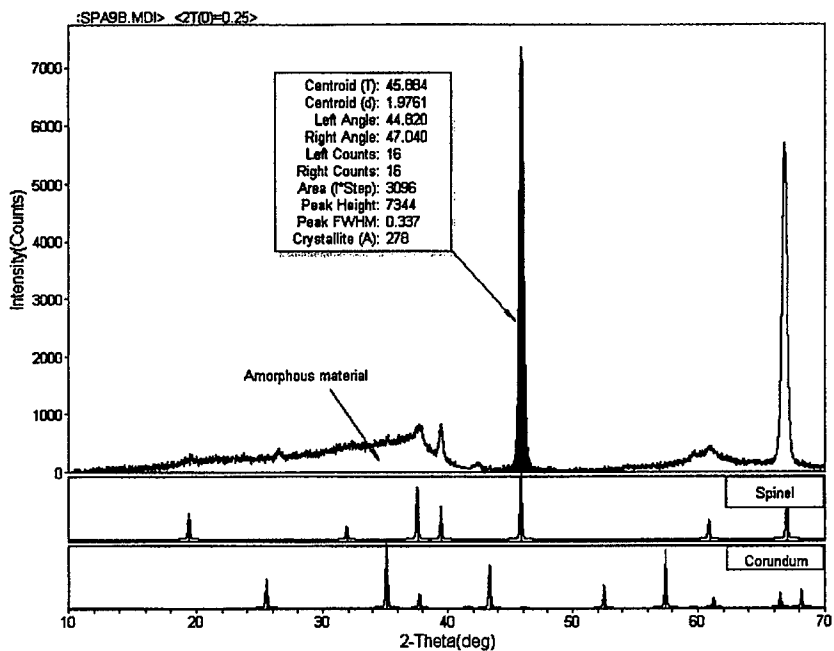


Figure 9. X-ray diffraction pattern of  $\text{Al}_2\text{O}_3/\text{TiO}_2$  powder, after plasma melting and splat quenching on a copper chill plate. Shown for comparison are the reference diffraction patterns for the spinel and corundum ( $\alpha\text{-Al}_2\text{O}_3$ ) structures.

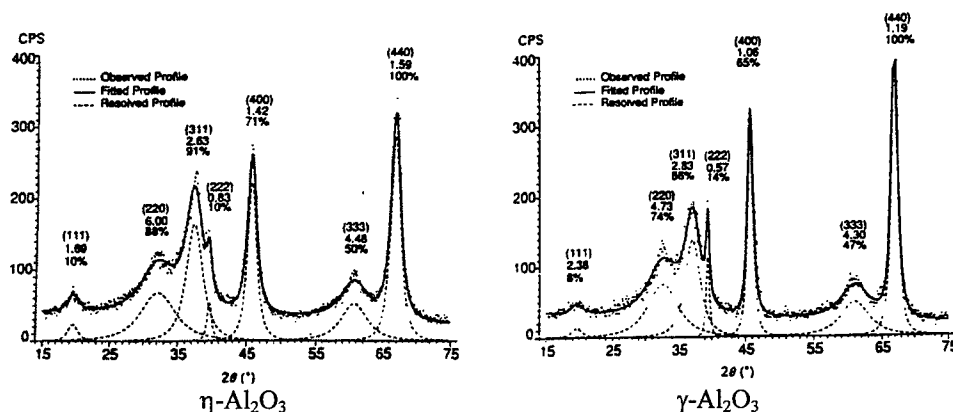


Figure 10. X-ray diffraction patterns of chemically-synthesized  $\eta\text{-Al}_2\text{O}_3$  and  $\gamma\text{-Al}_2\text{O}_3$  powders, after Zhou and Snyder [14].

several features in the diffraction pattern that indicate a strongly disordered structure, which is far from equilibrium. First, note the presence of an amorphous phase, as indicated by the "hump" in the diffraction pattern at  $35^\circ$ . Also, the diffraction peaks are strong only for the spinel peaks at approximately  $46^\circ$  and  $66.5^\circ$ . All the other peaks for this phase have very low intensity.

An X-ray diffraction pattern of a typical plasma-sprayed coating showed similar features to that of the splat-quenched powder. This is to be expected, since a coating is formed by the superposition of splat-quenched particles. On the other hand, thick coatings produced by multiple passes showed some indications of  $\alpha$ - $\text{Al}_2\text{O}_3$  formation, which probably reflects heating of the substrate, and hence lowering of the average quench rate.

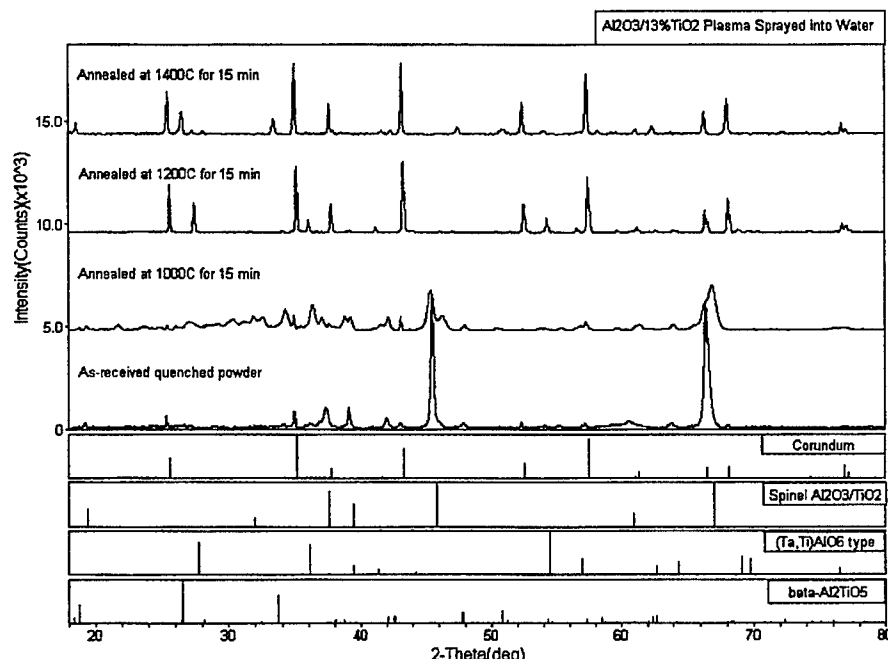


Figure 11. X-ray diffraction patterns of water-quenched and heat treated  $\text{Al}_2\text{O}_3/\text{TiO}_2$  powder, showing decomposition reactions with increasing temperature.

#### 4.2.2 Effect of heat treatment

When water-quenched powder is heated at temperatures below  $1200^\circ\text{C}$ , a series of intermediate phases are formed, Table III. At  $1000^\circ\text{C}$ , the first such intermediate phase to appear has an unknown structure, with no known structural analogue. At  $1200^\circ\text{C}$ , a tetragonal phase appears, which is similar to the  $(\text{Ta},\text{Ti})\text{Al}_2\text{O}_6$  crystal structure described in Powder Diffraction File #32-0028 [15]. This phase is also metastable, and further decomposes at  $1400^\circ\text{C}$  into the equilibrium two-phase structure, consisting of

**Table III**  
**Summary of Heat Treatment Data**  
**Water-quenched powder**

Annealing Temperature	Qualitative Composition (Main Phases)		Approximate Quantitative Composition	Color
RT	x-phase	$\alpha$ -Alumina	10:1	blue
800°C	x-phase	$\alpha$ -Alumina	4:1	blue
1000°C	x-phase	$\alpha$ -Alumina unidentified phase(s)	2:1:1	blue-grey
1200°C	$\alpha$ -Alumina	y-phase	1:1	yellow-white
1400°C	$\alpha$ -Alumina	$\beta$ -Aluminum Titanate y-phase	10:10:1	white

x-phase: cubic,  $a_0=7.94\text{ \AA}$ ;  $\text{Al}_2\text{O}_3 \cdot \text{TiO}_2$

cell dimensions close to those of  $\gamma$ -alumina (defect spinel structure)

y-phase: tetragonal  $a_0=4.59$ ,  $c_0=2.96$ ;  $\text{Al}_2\text{O}_3 \cdot \text{TiO}_2$

cell dimensions close to that of  $\text{AlTiTaO}_6$ .

**Table IV**  
**Summary of Heat Treatment Data**  
**Splat-quenched coating**

Annealing Temperature	Qualitative Composition (Main Phases)		Approximate Quantitative Composition	Hardness (kg/mm <sup>2</sup> , 1 kg load)
RT	x-phase			700
800°C	x'-phase*			720
1000°C	$\alpha$ -Alumina	x-phase or $\gamma$ -Alumina unidentified phase(s)	5:1:1	850
1200°C	$\alpha$ -Alumina	$\text{Ti}_3\text{O}_5$	10:1	940
1400°C	$\alpha$ -Alumina	$\beta$ -Aluminum Titanate	1:1	990

x-phase: cubic,  $a_0=7.94\text{ \AA}$ ;  $\text{Al}_2\text{O}_3 \cdot \text{TiO}_2$

cell dimensions close to those of  $\gamma$ -alumina (defect spinel structure)

\*x'-phase: cell dimensions close to x-phase

$\beta$ -phase: orthorhombic  $a_0 = 9.439$ ,  $b_0 = 9.647$ ,  $c_0 = 3.592$

approximately 1:1 mixture of  $\alpha$ - $\text{Al}_2\text{O}_3$  and  $\beta$ - $\text{Al}_2\text{O}_3 \bullet \text{TiO}_2$  (orthorhombic structure, PDF #41-0258). Thus, the final structure consists of primary  $\alpha$ - $\text{Al}_2\text{O}_3$  (micrometer scale), and secondary  $\alpha$ - $\text{Al}_2\text{O}_3$  that co-precipitates with the  $\beta$ - $\text{Al}_2\text{O}_3 \bullet \text{TiO}_2$ . Figure 11 illustrates these phase transitions via their respective X-ray diffraction patterns.

When splat-quenched material (powder or coating) is heated, thermal decomposition of the original  $\chi$ -phase follows a somewhat different path, Table IV. The most notable change is the appearance of  $\alpha$ - $\text{Al}_2\text{O}_3$  at 1000 °C as a major phase. Again, however, the equilibrium two-phase structure is established at 1400 °C. These phase transitions with increasing temperature are accompanied by a progressive increase in hardness, as indicated in Table IV. It is significant that the final structure at 1400 °C has a Vickers hardness of 990 kg./mm<sup>2</sup>, which represents about a 40% increase over that of the as-sprayed coating. An important feature is the absence of micron-scale primary  $\alpha$ - $\text{Al}_2\text{O}_3$  in the final nanocomposite material, which is a reflection of the structural uniformity of the original splat-quenched material.

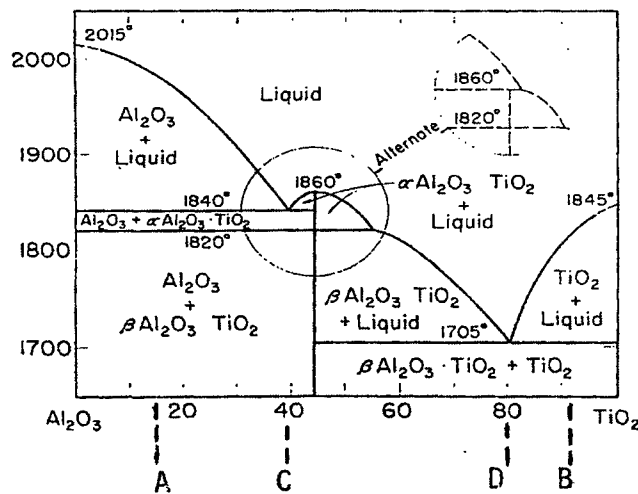


Figure 12. Phase diagram for the  $\text{Al}_2\text{O}_3$ - $\text{TiO}_2$  system, after Lang, Fillmore and Maxwell [15].

#### 4.2.3 Compositional effect

The location of the  $\text{Al}_2\text{O}_3/13\text{TiO}_2$  composition on the equilibrium phase diagram is indicated in Figure 12. The presence of the nanocrystalline  $\alpha$ - $\text{Al}_2\text{O}_3$  phase in the water-quenched powder, Figure 8, can be interpreted as a consequence of significant undercooling of the melt prior to nucleation of primary  $\alpha$ - $\text{Al}_2\text{O}_3$  grains followed by dendritic growth of the principal  $\chi$ - $\text{Al}_2\text{O}_3/\text{TiO}_2$  phase. This being the case, the volume fraction of the much harder  $\alpha$ - $\text{Al}_2\text{O}_3$  phase may be increased by shifting the composition towards the  $\text{Al}_2\text{O}_3$ -rich side of the phase diagram. It is difficult to predict the composition requirement to realize say a 50:50 mixture of the two phases, because

of the modification of the phase diagram under supercooling conditions. However, it seems that a starting composition of about  $\text{Al}_2\text{O}_3/7\text{TiO}_2$  might serve the purpose. Experiments are underway to check this concept.

## 5. Acknowledgements

Support from the Office of Naval Research (contract numbers N00014-97-1-0249; N00014-97-1-0844; and N00014-98-3-0005) is gratefully acknowledged.

## 6. References

1. Gleiter, H. (1989) Nanocrystalline materials, *Progress in Materials Science*, **33**, (4) 223.
2. Kear, B.H. and Strutt, P.R. (1995) Nanostructures, the next generation of high performance bulk materials and coatings, *KONA Powder and Particle*, **13**, pp. 45-55.
3. Siegel, R.W. (1993) Synthesis and properties of nanophase materials, *Mat. Sci. Eng. A: Structural Materials: Properties, Microstructure and Processing*, **2**, pp. 189-197.
4. Sadangi, R.K., McCandlish, L.E., Kear, B.H. and Seegopaul, P. (1998) Grain growth inhibition in liquid phase sintered nanophase WC/Co alloys, in Oakes, J.J. and Reinshagen, J.H. (eds.) *Proc. 1998 Int. Conf. on Powder Metallurgy and Particulate Materials*, MPIF, pp. 1-51.
5. McCandlish, L.E., Kear, B.H. and Bhatia, J., Spray conversion process for production of nanophase WC-Co powders, US Patent No. 5,352,269.
6. McCandlish, L.E., Kear, B.H. and Kim, B.K. (1990) Chemical processing of nanophase WC-Co composite powders, *Mats. Sci. & Tech.*, **6**, pp. 953-957.
7. German, R.M. (1985) *Liquid Phase Sintering*, Plenum Press, New York.
8. Schwarzkopf, P. and Keiffer, R. (1960) *Cemented Carbides*, Macmillan, London.
9. McCandlish, L.E., Kear, B.H., Kim, B.K. and Wu, L. (1990) Low pressure plasma sprayed coatings of nanophase WC-Co, in Yazici, R.M. (ed.), *Protective Coatings: Processing and Characterization*, The Minerals, Metals and Materials Society, pp. 113-143.
10. Li, C.J., Ohmori, A. and Harada, Y. (1996) Formation of an amorphous phase in thermally sprayed WC-Co coatings, *Journal of Thermal Spray Technology* **5**,(1), pp. 69-73.
11. Binary phase diagram of W-C, (1992) ASM Handbook, **3**, p. 2.115.
12. Sampath, S. and Herman, H. (1992) *Thermal Spray Technology*, ASM, Materials Park, OH.
13. Cohen, M., Kear, B.H. and Mehrabian, R. (1980) Rapid solidification processing--an outlook, *Proc. Second Int. Conf. on Rapid Solidification Processing*, Reston, VA, p. 1.
14. Zhou, R.-S. and Snyder, R.L. (1991) Structures and transformation mechanisms of the  $\eta$ ,  $\gamma$  and  $\theta$  transition aluminas, *Acta Cryst. B* **47**, pp. 617-630.
15. Lang, S.M., Fillmore, C.L. and Maxwell, L.H. (1952) *J. Research Natnl. Bur. Standards*, **48**, (4) p. 301; RP 2316.

## SYNTHESIS AND CHARACTERIZATION OF NANOCOMPOSITE COATINGS

J. HE, M. ICE, AND E. J. LAVERNIA

*Department of Chemical and Biochemical Engineering and Materials Science, University of California Irvine, Irvine, CA 92697-2575*

### Abstract

The synthesis of nanocomposite coatings is described in this paper. The nanocomposite feedstock powders are synthesized using mechanical milling, and the characteristics of the milled powders, i.e., morphology, agglomeration behavior, powder size, grain size and structural evolution during milling, are analyzed using X-ray diffraction, SEM and TEM. Using high velocity oxygen fuel (HVOF) spraying, the nanocomposite coatings are sprayed, and the microstructures and properties of the resulting coatings are characterized.

### 1. Introduction

In thermal spraying technology, molten or semi-molten powders are deposited onto a substrate to produce a two-dimensional coating or in some cases, a three-dimensional self-standing material. The microstructure and properties of the material depend on the thermal and momentum characteristics of the impinging particulate [1], which are determined by the spraying methodology and the type of feedstock materials employed. Powders, rods and wires can be used as feedstock materials. Metals and alloys in the form of rods or wires are commonly used in arc spraying (AS) and flame spraying (FS). Powders of metals, alloys, ceramic oxides, and cements are often employed in thermal spraying to form a homogeneous microstructure in the resulting coatings. In most cases, the sprayed surface should be degreased, masked and roughened prior to spraying to maximize the bonding strength between the coating and the substrate material. Various techniques for pre-spraying treatment have been described [2]. Today, a number of thermal spraying techniques are available. Flame spraying (FS), arc spraying (AS), detonation gun spraying (DGS), continuous detonation spraying (CDS), atmospheric plasma spraying (APS), twin wire arc spraying (TWAS), low pressure plasma spraying (LPPS) or vacuum plasma spraying (VPS), controlled atmosphere plasma spraying (CAPS), high velocity flame spraying (HVFS) and high velocity oxygen fuel spraying (HVOF) are widely used to produce various coatings for different industrial applications. The process and parameters of the spraying techniques mentioned above are summarized in Refs [1, 3]. HVOF spraying is the most significant development in thermal spraying industry since the development of plasma spraying [1] and it has been the topic of many

excellent investigations in the recent past years [4-6]. HVOF is characterized by high particle velocity and low thermal energy when compared to plasma spraying. The applications of HVOF have expanded from the initial use of tungsten carbide coatings to include different coatings that provide for wear or erosion/corrosion resistance [7]. HVOF uses an internal combustion jet fuel (propylene, acetylene, propane, and hydrogen gases) to generate hypersonic gas velocities of 1830 m/s. When burned in conjunction with pure oxygen, these fuels can produce a nominal gas temperature greater than 3029 K. The powder particles are injected axially into the jet gas, heated, and propelled toward the substrate. With the relatively low temperatures of the flame gas associated with the HVOF systems, superheating or vaporization of individual particles are often prevented [8]. Furthermore, the lower particle temperatures present lead to carbide coatings that exhibit less carbide loss than that of the plasma sprayed coatings. In essence, the advantages of HVOF process over conventional plasma spraying are higher coating bond strength, lower oxide content, and improved wear resistance due to a homogeneous distribution of carbides [9,10]. In recent work [11], it was reported that the velocity and temperature of the HVOF sprayed particle powders could be controlled independently.

Nanostructured materials are characterized by a microstructural length scale in the 1-100 nm regime [12]. More than 50 volume percent of atoms are associated with grain boundaries or interfacial boundaries when the grain is small enough, thus a significant amount of interfacial component between neighboring atoms associated with grain boundaries contributes to the physical properties of nanostructured materials [13]. Using nanostructured feedstock powders, thermal spraying has allowed researchers to generate coatings with higher hardness, strength and corrosion resistance than the corresponding conventional coatings [3, 14]. A number of techniques that are capable of producing nanostructured materials include gas condensation, mechanical alloying/milling, crystallization of amorphous alloys, chemical precipitation, spray conversion processing, vapor deposition, sputtering, electro-deposition, and sol-gel processing techniques [15]. Mechanical alloying/milling techniques have been used to produce large quantities of nanocrystalline materials for possible commercial use [15]. Mechanical alloying/milling is a high energy ball milling process, in which elemental or pre-alloyed powders are welded and fractured to produce metastable materials with controlled microstructures. Today, mechanical alloying/milling has been widely used to synthesize amorphous alloys, intermetallic compounds and nanocrystalline materials [16-18]. During mechanical milling, particle welding and fracturing result in severe plastic deformation. Using mechanical milling,  $\text{Cr}_3\text{C}_2$ -NiCr and WC-Co nanocomposites were successfully synthesized [19-21] in our laboratories.

The objective of this paper is to describe the complete synthesis history of a nanocomposite coating, consisting of the synthesis of nanocomposite using mechanical milling, characteristics of the milled powder, thermal spraying process and characterization of the resulting coatings.

## 2. Synthesis and characteristics of nanocomposite powder

Pre-alloyed  $\text{Cr}_3\text{C}_2$ -25(Ni20Cr) powders (Dialloy 3004, Sulzer Metco (US) Inc. with a nominal particle size of (-45+5.5) microns are chosen for this study. The powders are

immersed in Hexane [ $\text{H}_3\text{C}(\text{CH}_2)_4\text{CH}_3$ ] and mechanically milled with a modified Szegvari attritor model B at a rate of 180 rpm for 20 hours in a stainless steel tank with stainless steel balls. The ball to powder mass ratio is 20:1. To monitor the synthesis process, samples are taken from the tank every two hours for SEM, X-ray and TEM examination. SEM analysis performs on a Philips XL 30 FEG microscope. X-ray diffraction measurements are carried out using a Siemens D5000 diffractometer equipped with a graphite monochromator using  $\text{Mo K}\alpha$  ( $\lambda=0.070923$  nm) radiation. General scans with a step size of  $0.01^\circ$  and a step time of 1s are conducted for phase identification; and detailed scans with a step size of  $0.01^\circ$  and a step time of 5s are conducted for grain size measurements. The milled powders to be analyzed by TEM are dispersed in Methanol, deposited on carbon grid substrates, and TEM observation is performed using a Philips CM20 microscope operated at 200 keV.

## 2.1 MORPHOLOGY OF THE MILLED POWDER

Figure.1 (a) shows the morphology of as-received powder which consists of a  $\text{Cr}_3\text{C}_2$  carbide phase and a Ni20Cr phase (a solution of 20% Cr in Ni). A small amount of the powder exhibits a spherical morphology while the remainder shows an irregular morphology with sharp facets.

Figure. 1 (b) shows the result of X-ray (EDS) dot mapping of Ni. There is a high Ni in the regions where spherical particles appear. While almost no Ni appears at the sites where irregular-shaped particles are present. This indicates that the Ni20Cr phase shows a spherical morphology and  $\text{Cr}_3\text{C}_2$  carbides are present in form of irregular-shaped particles. Figure 1 (c) and (d) shows the changes in the powder after milling

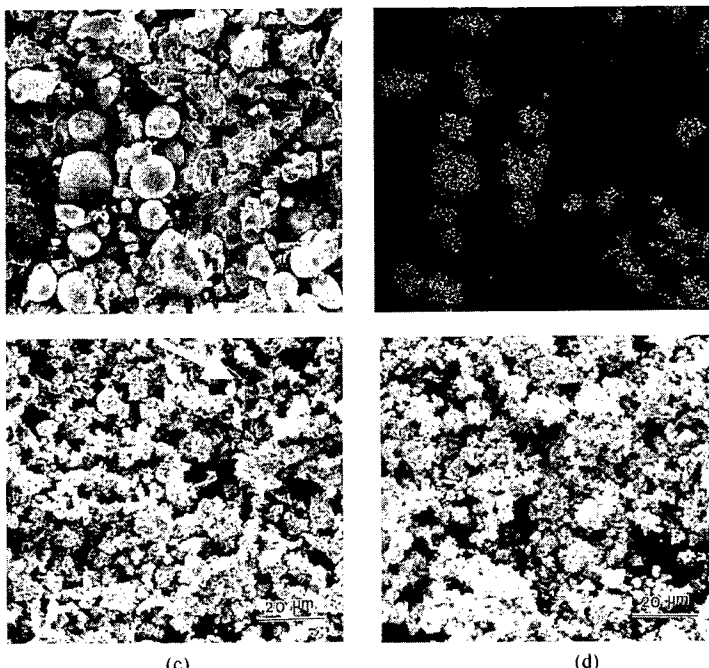


Figure 1. Morphology of the powders following different milling times: (a) as-received powder; (b) Ni-map of (a); (c) 8 hour milled powder and (d) 16 hour milled powder.

8 and 16 hours, respectively. In Figure 1(c) a large as-received powder particle is evident (see arrow) illustrating the morphology of the powders after 8 hours milling. X-ray

mapping reveals that this particle, with sharp facets, is a carbide. This featured particle with sharp facets is not observed in the powder that is milled for 16 hours.

## 2.2 AGGLOMERATION BEHAVIOR AND AVERAGE SIZE OF MILLED POWDER

During mechanical milling, powder agglomeration is often observed. Two types of self-agglomeration behavior are observed in the present powder system, referred as binder-induced agglomeration and metallurgical agglomeration in this paper. Figure 2 shows SEM images illustrating binder-induced agglomeration. After 4 hours milling, see Figure 2(a), a large proportion of the small particles are self-agglomerated. However, the larger carbide particles, with sharp facets, remain non-agglomerated. A detailed view of the agglomerated powder, indicated by the arrow in Figure 2 (a), is shown in Figure 2(b). The presence of regular rectangular parallelepiped particles, indicated by arrows, is

thought to be  $\text{Cr}_3\text{C}_2$  carbides with an orthorhombic crystal structure that fracture along low Miller index planes, possibly  $\{100\}$  planes, during milling. X-ray dot mapping confirms that these particles are carbides. Figure 2 (c) shows almost complete self-agglomeration in the powder that has been milled for 20 hours.

A magnification

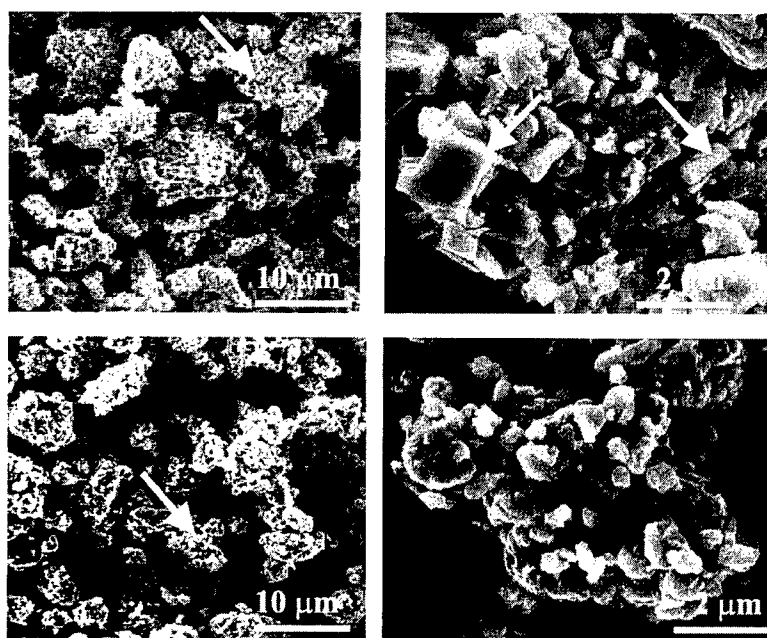


Figure 2. Morphology of the binder-induced self-agglomerated powders. (a) 4 hour milled powder; (b) magnification of (a); (c) 20 hour milled powder and (d) magnification of (c).

of the agglomerated powder indicated by the arrow in Figure 2(c) is shown in Figure 2 (d); X-ray mapping results indicate that the particles in Figure 2 (d) are neither pure carbide nor pure NiCr phase.

The self-agglomerated powders, shown in Figure 2, are not very dense, and referred as binder-induced agglomeration in this paper. The binder-induced agglomeration is primarily bonded by milling media, and can easily be decomposed back to its original powder form. For example, to make TEM samples, the powder is immersed into Methanol and vibrated by a supersonic instrument for a few minutes; under these

conditions, the agglomerates are broken down.

Figure 3 are TEM images illustrating the process of metallurgical agglomeration. An agglomerated powder is made of particles A, B, C and D. The SAD pattern on the interface of powders A and B is shown on the bright field image. This is a complex pattern of polycrystal diffraction rings and single crystal diffraction spots. On the side of powder A, the pattern comes from a polycrystal. A number of sharp carbide fragments can be observed. While, on the side of powder B, the pattern is essentially one of a f.c.c. single crystal. Similar complex SAD patterns are also diffracted on the interfaces of powder A with C, and A with D. Therefore, powder A is a polycrystal nanocomposite, and powder B, C and D are essentially single crystal NiCr solid solutions that are embedded with a few fragments of carbide particles. The interface of powders A and B is completely continuous and without microcracks or microvoids. The continuous and smooth interfaces between the powder particles in the agglomerates provide direct evidence that mechanical milling promotes metallurgical bonds between ductile NiCr solid solution materials and polycrystal composite powders. The self-agglomerated powder in Figure 3 is characterized by the metallurgical bond between the powders, and referred to as metallurgical agglomeration in this paper. The self-agglomeration process is primarily controlled by cold welding and fracturing that occurs during the milling process, and can not easily be decomposed because of the presence of metallurgical bonds between powders.

The average sizes of self-agglomerates and particles are shown in Figure 4. In the powder milled for two hours there is no evidence of self-agglomeration. However, in the powder milled for four hours a large portion of the smaller particles self-agglomerate; the larger carbide particles remain segregated. In an individual powder system, the size of the binder-induced agglomeration powder is thought to depend on the dynamic factors in the milling process, such as rotation, ball to

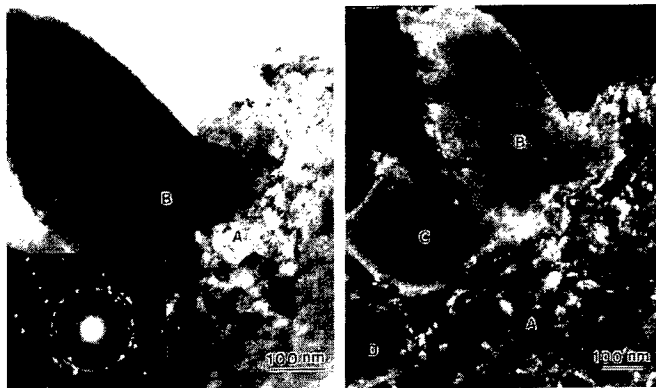


Figure 3. TEM micrograph of metallurgical agglomeration powders:  
(a) bright field image and (b) dark field image.

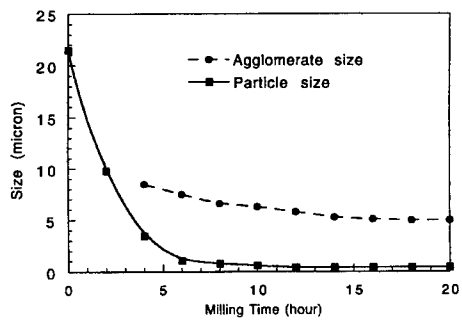


Figure 4. Variation of average sizes of agglomerate and particle.

powder mass ratio, tank dimensions, and the behavior of the milling media used. Dry inert gas, air, liquid nitrogen, liquid chemicals (such as Methanol, Acetone and Hexane) are often used as milling media. The behavior of the milling media affects the size of the agglomerates. In special case, binder chemicals are often added into the powder to change behavior of the binder-induced agglomeration. However, a systematic study on the binder-induced agglomeration is currently unavailable. Under the present conditions, the size of the binder-induced agglomeration particles approaches a constant value of 5 micron after 8 hours of milling. Interestingly, the particle size also approaches a constant value of 0.5 micron. The fact that the average particle size approaches a constant value is an indication that the smaller particles grow while the larger particles fracture. Benjamin [16] introduced an assumption to explain the stabilization of the average particle size. Fracture strain of particles decreased with increasing particle size, while the strain value at which cold welding occurred was constant, hence, average the particle size tended to stabilize as milling time increased. Apparently, both fracture and weld strains depend strongly on powder characteristics and milling conditions. In related studies, it was reported that the average powder size of Ni-based superalloys, containing a small amount of  $Y_2O_3$ , increased and approached a constant value of between 110 and 130 microns as milling progressed [16]. Brittle powder systems, such as the present 75%  $Cr_3C_2$ -25% Ni20Cr system, possess low fracture strain, therefore, the average particle size approaches a constant value on the order of 1 micron. By contrast, a continuous decrease in powder size for both ductile-ductile (Ti-Al) and ductile-brittle (Ti-Si) systems [22] occurred with increasing milling time. Lau *et al.* [14] indicated that the milling media affected the dependence of average powder size versus milling times of Ni powders. As milling time increased, Ni powder size decreased when milled in Methanol, whereas the powder size increased when milled in liquid nitrogen. Due to a number of changeable experimental parameters, it is difficult to estimate an average size of milled powder.

### 2.3. STRUCTURAL AND CHEMICAL COMPOSITION CHANGES OF THE POWDERS DURING MILLING

X-ray diffraction (XRD) spectrums of the powders following different milling times are shown in Figure 5. Figure 5 (a) indicates that as-received  $Cr_3C_2$ -NiCr powder consists of the  $Cr_3C_2$  carbide phase and a NiCr solid solution. The  $Cr_7C_3$  carbide phase can not be simply identified by this XRD spectrum because all the diffraction peaks from  $Cr_7C_3$  carbide overlap those from  $Cr_3C_2$  carbide or the NiCr solid solution. Guilemany and Calero [23] analyzed commercial  $Cr_3C_2$ -NiCr powder by EPMA and distinguished three phases, mainly  $Cr_3C_2$ , some  $Cr_7C_3$ , and NiCr solid solution. These three phases were identified by the presence of three regions with distinct chemical composition.

$Ni20Cr$  solid solution has a f.c.c. structure with lattice constant of  $a=0.35454$  nm, while the lattice constant of pure Ni crystal is 0.35238 nm, based on JCPDS file provided by International Centre for Diffraction Data [PDF#04-0850]. The substitution of Cr for 20% Ni leads to 0.6% increase in lattice constant.  $Cr_3C_2$  and  $Cr_7C_3$  carbides are well documented in JCPDS files. They have orthorhombic and hexagonal crystal structures, respectively.

With increasing milling time, XRD peaks from NiCr solid solution show a larger change compared with those from  $Cr_3C_2$  carbide. The XRD peaks broaden and decrease

drastically, then nearly disappear in the powder following 16 hours of milling. This indicates that there is a larger change in the structure of NiCr solid solution powder than in  $\text{Cr}_3\text{C}_2$  carbide. During milling, the NiCr solid solution powder, with lower hardness, is subjected to double milling from both the stainless steel balls and the hard chromium carbide particles. Hence, the NiCr solid solution powder undergoes more severe plastic deformation. The intensity of the strongest diffraction peak, which is located at the position of  $2\theta=19.96^\circ$  and belongs to both NiCr solid solution and  $\text{Cr}_7\text{C}_3$  carbide, decreases in comparison with the diffraction peaks of  $\text{Cr}_3\text{C}_2$ . The peak does not disappear in the powder milled for 16 hours. This confirms a heavier deformation in NiCr powder and the presence of  $\text{Cr}_7\text{C}_3$  carbide in the system.

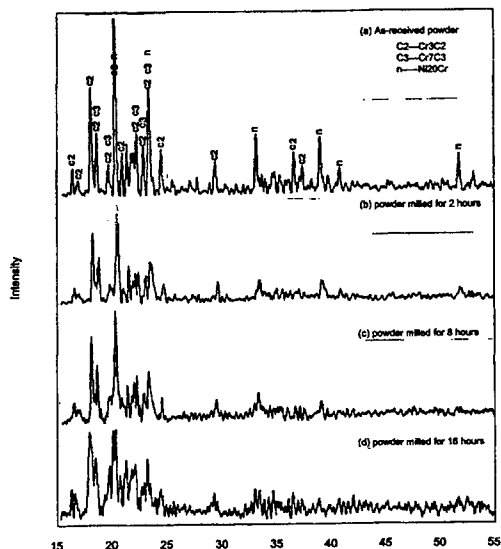


Figure 5. X-ray diffraction spectrums of the powders following different milling times.

Hard and brittle chromium carbides fracture during milling. Figure 6 shows detailed views of XRD spectrums between the diffraction angle ( $2\theta$ ) range of 15 to 25 degrees for the as-received powder and the same powder milled for 16 hours. The diffraction peaks from the milled powder broaden noticeably. The grain sizes of the milled powders following different milling times are determined on the basis of the Scherrer equation [24], and the results are plotted in Figure 7.

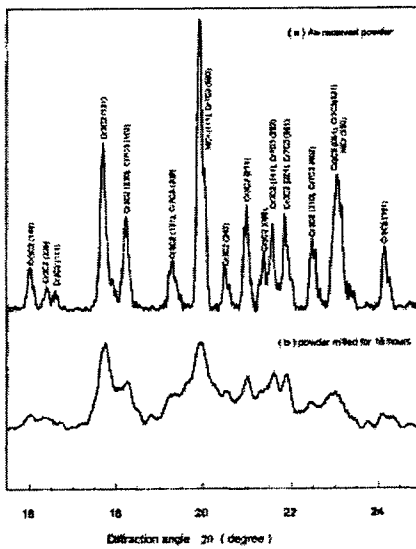


Figure 6. Detailed view of XRD spectrums.

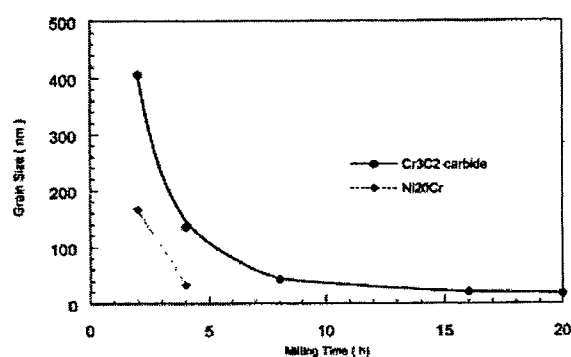


Figure 7. Dependence of grain sizes on milling time.

Grain size of  $\text{Cr}_3\text{C}_2$  carbide ranges from 406 nm in the powder milled for 2 hours down to 17 nm in the powder milled for 20 hours. Grain sizes of the NiCr solid solution milled for 2 and 4 hours are calculated to be 166 and 33 nm, respectively. It is not possible to determine the grain size of the NiCr solid solution for longer milling times because the individual diffraction peaks from the NiCr solid solution cannot be differentiated for milling times in excess of 6 hours. The grain size of  $\text{Cr}_7\text{C}_3$  carbide can not be measured by X-ray because there is no separation between  $\text{Cr}_7\text{C}_3$  carbide diffraction peaks in the XRD spectrum. However, it may be reasonably assumed that the grain size of  $\text{Cr}_7\text{C}_3$  carbide in the powder milled for 20 hours is smaller than 50 nm because the grain sizes of  $\text{Cr}_3\text{C}_2$  carbide and NiCr solid solutions are less than 50 nm.

Contamination is unavoidable during the milling process. To profile the contamination extent under Hexane [ $\text{H}_3\text{C}(\text{CH}_2)_4\text{CH}_3$ ] milling, the changes of chemical composition with milling times are listed in Table 1. According to Table 1, as milling time increases, the percentage of carbon decreases while the percentage of nitrogen and oxygen increases. This indicates that decarburization and contamination occur during milling. However, no new peaks appear in the X-ray spectrum of the milled powder, proving that the amount of contaminants is less than the minimum limit (around 5%) which X-ray diffraction can detect. In related studies, nitride and oxide phases in nanostructured materials played a beneficial role in retarding grain growth [25-26].

Table 1. Dependence of chemical composition on milling time (wt. %)

Milling time (h)	Cr	Ni	C	N	O
0	70.0	19.2	9.83	0.20	0.21
8	66.2	19.7	9.71	0.38	1.11
20	64.3	18.8	9.36	0.51	1.93

#### 2.4. MILLING MECHANISM OF $\text{Cr}_3\text{C}_2$ -NiCr

Figure 8 (a) shows a bright field consisting primarily of the NiCr solid solution in the 2 hour milled powder, and Figure 8 (b) and (c) are the corresponding selected area diffraction (SAD) patterns of powders A and B in Figure (a). Based on the SAD patterns, powder A is nearly a single crystal of NiCr solid solution although a few fragments from other powders can be seen. Carbide particles can be identified as being embedded into powder B because ambiguous diffraction rings overlap the SAD pattern of single crystal NiCr solid solution. With increasing milling time, more carbide

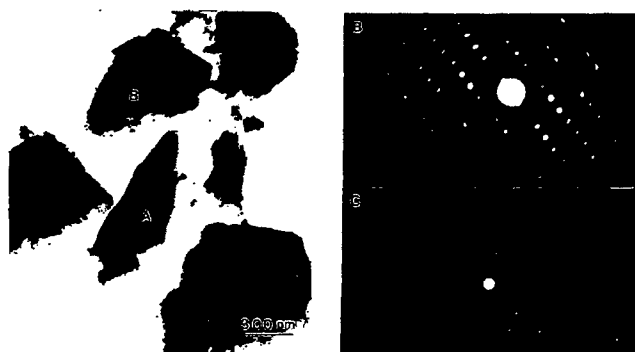


Figure 8. TEM image of NiCr solid solution in the 2 hour milled powder: (a) bright field micrograph; (b) SAD pattern of powder A and (c) SAD pattern of powder B.

particles are embedded into the NiCr solid solution. Figure 9 (a) displays a bright field image of the 4 hour milled powder, and Figure 9 (b) shows the corresponding dark field image, using a carbide diffraction spot, in which many carbide particles can be seen. In this figure, clearer carbide diffraction rings, which overlap the SAD pattern of single crystal NiCr solid solution, can be seen.

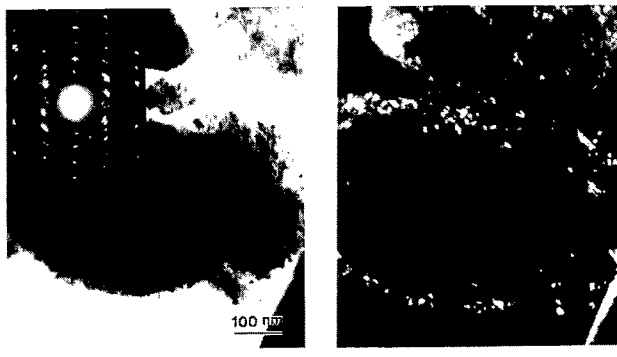


Figure 9. Micrograph of the powder following 4 hours of milling: (a) bright field; (b) dark field image.

Figure 10 shows that a carbide powder, in the 8-hour milled powder, fractures into a number of fragments that are embedded into the NiCr solid solution. It can be verified that the carbide and binder metal combine into a polycrystal nanocomposite powder because the SAD pattern is made completely of diffraction rings. The carbide fragments in the polycrystal nanocomposite have a sharp shape. Figure 11 (a) and (b) display a bright field and the corresponding dark field image of a polycrystal nanocomposite powder after 20 hours of milling. Large proportions of carbide fragments have transformed into round carbide particles. The average size of these round carbide particles was approximately 15 nm, which agrees with the X-ray measurements. Apparently, the

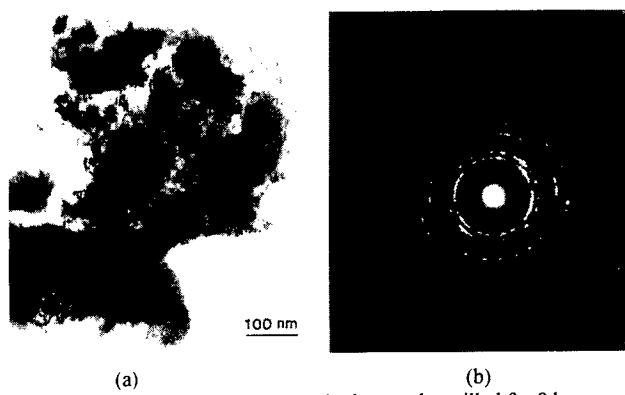


Figure 10. Carbide fragments in the powder milled for 8 hours: (a) bright field image; (b) SAD pattern.

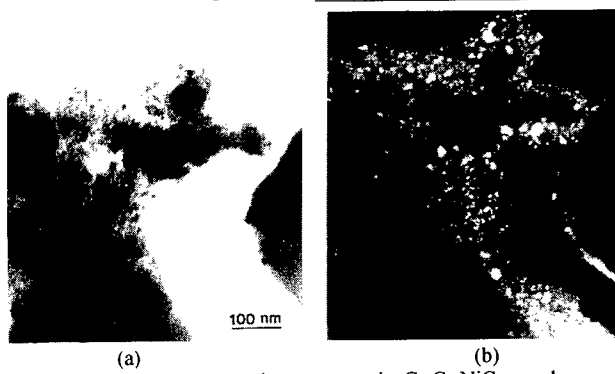


Figure 11. Polycrystal nanocomposite  $\text{Cr}_3\text{C}_2\text{-NiCr}$  powder: (a) bright field image; (b) dark field image.

micrograph and SAD patterns shown in Figures 8 through 10 exhibit transition microstructures of the powders during milling. The milled powders are found to continually overlap, cold weld, fracture, and gradually transform into polycrystal nanocomposites, in which round nanostructured carbide particles are uniformly distributed. The milling mechanism is schematically shown in Figure 12.

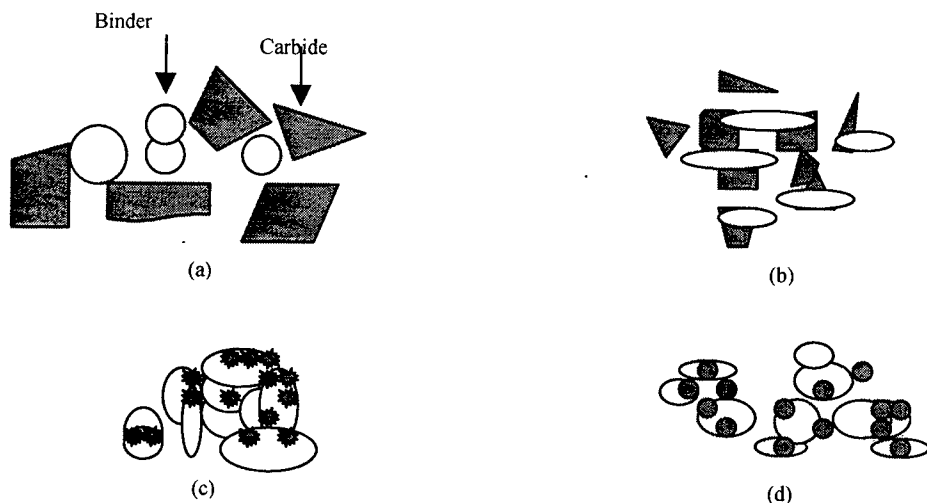


Figure 12. Schematic of milling mechanism for duplex structure powder: (a) Initial stage; (b) NiCr overlap and deform,  $\text{Cr}_3\text{C}_2$  fracture and embed into NiCr; (c) Binders deform, fracture, and weld, carbide fracture further; (d) Nanocomposite powder.

### 3. Thermal Spraying of Nanocomposite Powder

Nanostructured and conventional  $\text{Cr}_3\text{C}_2$ -NiCr (Dialloy 3004 blended  $\text{Cr}_3\text{C}_2$ -25 (Ni20Cr), with a nominal particle size of  $(-45+5.5)$   $\mu\text{m}$ , produced by Sulzer Metco (US) Inc.) powders were used for spraying using HVOF.

#### 3.1 AGGLOMERATION

The thermal spray process typically requires a powder size within the range of 10-50  $\mu\text{m}$ . The as-synthesized nanostructured  $\text{Cr}_3\text{C}_2$ -NiCr powder is approximately 5  $\mu\text{m}$  and hence not suitable for thermal spraying in the as-synthesized condition. Accordingly, a procedure was established for the agglomeration of the  $\text{Cr}_3\text{C}_2$ -NiCr powder into larger-sized particles. Using a 2% methyl cellulose solution in  $\text{H}_2\text{O}$ , the powder is made into a slurry. This slurry was annealed in a vacuum furnace at a temperature of 80°C for a time period ranging from 24 to 48 hours. The annealing time is a function of the quantity of the slurry to be baked. As a result of the annealing, a solid block of material was formed. This block is relatively brittle and can easily be crushed into powder. This powder was then sieved through a sub-50  $\mu\text{m}$  mesh. The resulting powder was found to have an adequate particle size (approximately 40  $\mu\text{m}$ ) to flow in the HVOF system used.

### 3.2 HVOF THERMAL SPRAY PROCESS

To spray the  $\text{Cr}_3\text{C}_2\text{-NiCr}$  coatings, a Sulzer Metco Diamond Jet HVOF thermal spray facility is used. As shown in Figure 13, the Diamond Jet brings in oxygen, air and fuel, in this experiment propylene, from the DJC into the rear of the gun in the proper stoichiometric ratios. This gaseous mixture is ignited by an arc current creating a hypersonic, low temperature flame with gas velocities of 1830m/s and temperatures around 2700 K. From the 9-MP hopper powder feed unit, nitrogen carrier gas brings the agglomerated powder into the rear of the gun and then axially into the flame. The powder is heated in the gun barrel then sprayed out onto a stainless steel substrate. The spraying parameters are summarized in Table 2.

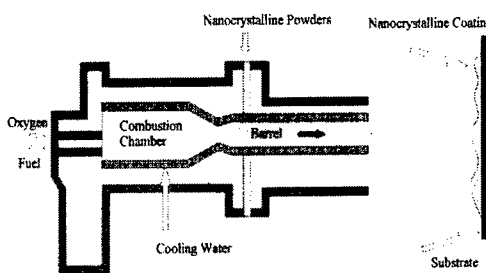


Figure 13. Schematic of HVOF process

Table 2 Spraying parameters used to produce  $\text{Cr}_3\text{C}_2\text{-25(Ni20Cr)}$  coatings

Gas	Pressure(psi)	FMR*	SCFH**	Parameter	Setting
Air	100	48	857	Powder feed rate	2.5 lbs/hr
Fuel	100	40	176	X-Y traverse speed	200 ft/min
Nitrogen	150	55	28	Spraying distance	9 in
Oxygen	150	40	578		

FMR: flow meter reading; \*\*SCFH: standard cubic feet/hour.

### 4. Coating Characterization

The cross-sections of the coatings are examined using Philips XL 30 FEG SEM. The microhardness is tested on a Buehler Micromet 2004 Microhardness tester using a load of 300 gram. Each microhardness value is obtained from an average value of 30 tests. After removal of the substrate by polishing, the TEM specimens are prepared by cutting out a section of the coating and forming 3-mm diameter disks. The disks are dimpled to around 30  $\mu\text{m}$  thick using a dimpler fitted with diamond grinders. The grinding size descends from 6  $\mu\text{m}$  grade, down to 3  $\mu\text{m}$ , and finally to 1  $\mu\text{m}$  grade. The final thinning perforation process is performed using an argon ion miller. With the prepared samples, TEM observation is carried out on the Philips CM20 microscope operated at 200 keV.

#### 4.1. MICROSTRUCTURE OF COATINGS

The microstructures of conventional and nanostructured  $\text{Cr}_3\text{C}_2\text{-NiCr}$  coatings, examined using SEM, are shown in Figure 14. A uniform and dense microstructure is observed in the nanostructured coatings, compared to the conventional  $\text{Cr}_3\text{C}_2\text{-NiCr}$  coating which is observed to have an inhomogeneous microstructure. Five carbide (dark phase) and

binder areas (bright phase) are randomly chosen for SEM EDS analysis of their chemical composition. The results of this analysis are listed in Table 3. The distributions of Cr and Ni in carbide particle and binder phase are obtained from the average value of 5 readings. The row labeled "average" in Table 3 is obtained from low magnification analysis (A number of carbide phases and binder phases are enclosed) and is also the average value of 5 readings.

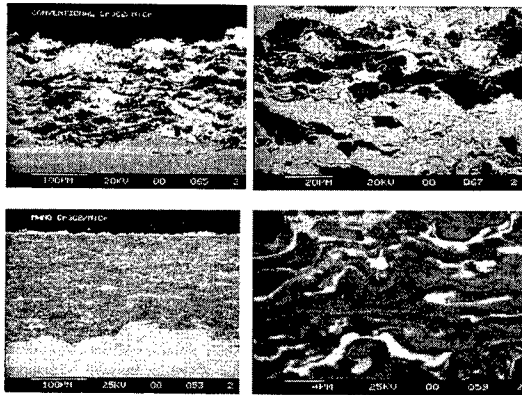


Figure 14. Microstructure of  $\text{Cr}_3\text{C}_2$ -25(Ni20Cr): (a) conventional coating; (b) magnification of (a); (c) nanostructured coating and (d) magnification of (c).

Table 3 Chemical composition of  $\text{Cr}_3\text{C}_2$ -25(Ni20Cr) coatings (wt %)

	Conventional coating		Nanostructured coating	
	Cr	Ni	Cr	Ni
Average	46.3	53.7	76.25	23.75
Binder	16.21	83.79	31.12	68.88
Carbide	99.15	0.85	94.34	5.66

In the binder phase of the conventional coating, the contents of Cr and Ni are close to the nominal chemical composition of pure NiCr solid solution (80% Ni and 20% Cr), thus the binder phase is considered to be the NiCr solid solution phase. A minor amount of Ni exists (0.85%) in the carbide phase. For the nanostructured coating, a higher Cr content in the binder phase and a higher Ni content in the carbide phase are observed. During milling, carbide particles are fractured and embedded into binder phases. Thus the most of binder phases combine with fractured carbide particles to form nanocomposite, and a relatively small amount of binder phases are still present in the nanocomposite feedstock powder. However, the binder phases are not completely pure NiCr solid solution, which contains more or less carbide particles. This causes a higher Cr content in the binder phases within the nanostructured coating. Similarly, binder phases are present in gaps between fractured carbide particles in the nanocomposite feedstock powder, thus Ni is observed in the carbide phase of the nanostructured coating. In addition to, the measurement of elements in individual phase of the nanostructured coating is partly affected by the beam size limitations of the EDS. Since both the binder phase and carbide phase are extremely fine in the nanostructured coating, a pure binder phase area or carbide phase area can not be perfectly isolated for SEM EDS analysis. Thus, the constituents of the binder phase in the nanostructured coating likely include a carbide phase, or *vice versa*.

To compare the average chemical composition (labeled "average" in Table 3) of the

coatings with those of the feedstock powders listed in Table 1, a simple correction for data in Table 3 is made because the light elements, such as C, N, and O, are not included in the EDS analysis. In Table 3, the sum of Cr and Ni content is 100%. Actually, the sum of Cr and Ni content is 89.2 % in the conventional feedstock powder, and 83.1% in the nanocomposite feedstock powder, see Table 1. Therefore, the content of Cr and Ni is multiplied by factors of 0.892 in the conventional coating, and 0.831 in the nanostructured coating. This correction represents a simple approximation because it implies that there are no changes in the contents of all elements during thermal spraying, whereas in practice, this may not be the case. After making this simple correction, the average contents of Cr and Ni are 41.3% and 47.9% in the conventional coating, and 63.4% and 19.8% in the nanostructured coating, respectively. It is worth noting that there is a large average chemical composition difference between the conventional and nanostructured coatings. The average contents of Cr and Ni in the nanostructured coatings are close to those of feedstock nanocomposite powder. However, those same values found for the conventional coating differ markedly from the conventional feedstock powder. Because the contents of Ni and Cr in both the binder and the carbide phase are close to their nominal contents, the chemical composition difference between the conventional coating and feedstock powder is attributed to a decrease in the volume fraction of the carbide phase in the conventional coating. In related studies, the decarburation of tungsten carbide is widely reported [27-28], whereas chromium carbide is quite stable during thermal spraying [23]. Therefore, the measured decrease in the volume fraction of the carbide phase in the conventional coating may not be attributed to decarburation or oxidation of chromium carbide. Individual, large-sized regularly shaped carbide particles and spherically shaped binder phase particles are present in blended  $\text{Cr}_3\text{C}_2$ -NiCr powder. During spraying, the large-sized carbide particles, with a high melting point of 2200 K ( $T_1$ ), may remain solid or semi-molten in the HVOF system (short dwell time and low temperature flame), yielding low adherence with the substrate surface. Conversely, melt binder phase droplets (melting point is 1690 K) have a more fluid characteristic than the carbide particles. The greater fluidity can result in effective contact of binder phase with the substrate surface. Thus, the volume fraction of the carbide phase decreases in the conventional coatings as a fraction of the carbide particles fail to adhere, and simply bounce-off from the substrate. In the case of the nanocomposite feedstock powder, there is high probability that the nanoscale carbide particles will be completely surrounded by the binder phase, as a result of their extremely small size (15 nm). The nanoscale particles are therefore co-coated with the binder phase and effectively adhere onto the substrate surface. Thus the improved fluidity leads to the nanostructured coating to have a close composition to the feedstock powder. Current efforts are aimed at providing quantitative support to this suggestion via studies of carbide particle size distribution during milling.

The commercially available blended  $\text{Cr}_3\text{C}_2$ -NiCr powders are mixtures of  $\text{Cr}_3\text{C}_2$  and NiCr solid solution and these mixtures are inherently difficult to handle because of segregation during storage, transportation and spraying [29, 30]. Consequently, these mixtures usually produce an inhomogeneous microstructure characteristic [29, 30]. In this study, the decrease in the volume fraction of the carbide phase in the conventional coating is an indicative of a non-uniformity in the microstructure. Coating performance is known to be very susceptible to the non-uniformity of microstructure [29-31]. A few

pre-treatment methods have been developed to overcome these types of microstructural variations. Two such methods, referred to as “pre-alloying” [30] and “cladding” [29], are widely used. Using the “pre-alloying” method, the powders are first agglomerated using an organic polymeric binder and then heated and pre-sintered in hydrogen. The powders are then densified using a plasma flame in an inert atmosphere, and are finally milled, screened and classified to yield the desired particle size. In related study [30], the hardness of a plasma-sprayed  $\text{Cr}_3\text{C}_2\text{-NiCr}$  coating, using the “pre-alloyed” powder, increased from 594 to 796 DPH<sub>300</sub>. In the “cladding” method, each  $\text{Cr}_3\text{C}_2$  carbide particle is clad with an essentially continuous layer of NiCr solid solution; therefore, the  $\text{Cr}_3\text{C}_2$  carbide is present as a discrete second phase particle randomly embedded in a NiCr solid solution. In related work [29], the hardness of a plasma-sprayed  $\text{Cr}_3\text{C}_2\text{-NiCr}$  coating increased from 620 to 860 DPH<sub>300</sub>, and the wear resistance was also improved as compared to the standard blend coating method, presumably as a result of the uniform “clad” powder [29]. Using a Metco Diamond Jet system, Sasaki *et al.* [31] compared the behavior of HVOF thermally sprayed coatings made using four different types of  $\text{Cr}_3\text{C}_2\text{-NiCr}$  feedstock powders (blend, agglomerated/sintered, sintered/crushed and sintered/crushed/clad). They found that the coating made of the sintered/crushed/clad powder showed the best characteristics as compared with those coatings sprayed by other three types of powders. Therefore, regardless of the spraying method employed, the uniformity of microstructure in a coating has a significant positive influence on its performance.

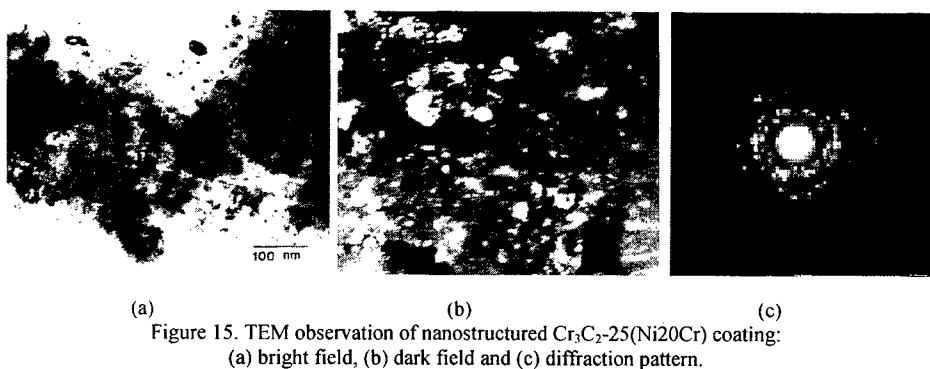


Figure 15. TEM observation of nanostructured  $\text{Cr}_3\text{C}_2\text{-25(Ni20Cr)}$  coating:  
(a) bright field, (b) dark field and (c) diffraction pattern.

In the present study, the  $\text{Cr}_3\text{C}_2\text{-NiCr}$  nanocomposite powder is synthesized using mechanical milling and agglomeration following the milling process. In this approach, the carbides in the nanocomposite powder are uniformly distributed in the NiCr solid solution. In essence, our approach yields a “clad” powder and hence a uniform microstructure is obtained in the nanostructured coating. In other words, the synthesis method of nanocomposite feedstock powder used in the present study provides a beneficial role in the uniformity of microstructure of the coatings.

The TEM bright field image of the nanostructured coating, the corresponding dark field image and diffraction pattern are shown in Figure 15 (a), (b) and (c), respectively. The average carbide particle size is approximately 24 nm. This indicates that the coating has a nanostructured microstructure. In the nanostructured WC-12%Co coating [20], TEM examination revealed a microstructure consisting of nano sized WC carbide

particles in an amorphous matrix phase. While in the nanostructured  $\text{Cr}_3\text{C}_2\text{-NiCr}$  coatings, the diffraction pattern does not exhibit clearly the presence of an amorphous matrix phase. Guilemany and Calero [23] also observed amorphous matrix phases in a conventional HVOF thermally sprayed  $\text{Cr}_3\text{C}_2\text{-NiCr}$  coating. Instead of an amorphous matrix phase, a few discontinuous elongated amorphous phases are observed in the nanostructured  $\text{Cr}_3\text{C}_2\text{-NiCr}$  coating, shown in Figure 16 (a) and (b). The inserted diffraction patterns, which are from the elongated phases marked A, show diffuse rings. Many fine diffraction spots are sharply imaged in the diffraction patterns, this indicates that the diffraction patterns are well focused. The diffuse rings are thus indicative of an amorphous phase rather than a false appearance caused by under/over focusing. These elongated amorphous phases, which have dimensions of around 100 nm wide and 1  $\mu\text{m}$  long, are discontinuously distributed in the coating.

#### 4.2 MICROHARDNESS

The average microhardness of the nanostructured  $\text{Cr}_3\text{C}_2\text{-NiCr}$  coating, taken on the cross-section, increases from a value of 846 for the conventional  $\text{Cr}_3\text{C}_2\text{-NiCr}$  coating to 1020  $\text{DPH}_{300}$  for the nanostructured coating. Hence nanostructured coating exhibits to a 20.5 % increase in microhardness as compared with the corresponding conventional coating. Several published hardness values of  $\text{Cr}_3\text{C}_2\text{-NiCr}$  coatings are listed in Table 4. The spraying methodology and the type of feedstock powder used (blend, agglomeration or clad) have very a significant influence on the hardness of coatings on the basis of the data in Table 4. Effects of spraying method [32, 33] and type of feedstock powder [28-31] on hardness has been extensively investigated. HVOF is characterized by high particle velocity and low thermal energy, this combination of high kinetic energy and low thermal energy leads to a high hardness [27]. The clad feedstock powders produce uniform  $\text{Cr}_3\text{C}_2\text{-NiCr}$  coatings and hence high hardness [29, 31]. It has been reported that the hardness of nanostructured materials often exhibits a 2-5 fold increase compared with that of the conventional materials although it is lower than that predicted using the classical Hall-Petch equation [34-36]. In a related study, Kear and McCandlish [37] also indicated that nanostructured WC-23%Co coatings have a higher hardness than that of the conventional coating of the same composition. Therefore, the high hardness of the nanostructured  $\text{Cr}_3\text{C}_2\text{-NiCr}$  coatings results primarily from two aspects: (1) uniformity of microstructure, caused by the synthesis process of nanocomposite feedstock powder; and (2) the intrinsically high hardness of nanostructured materials.

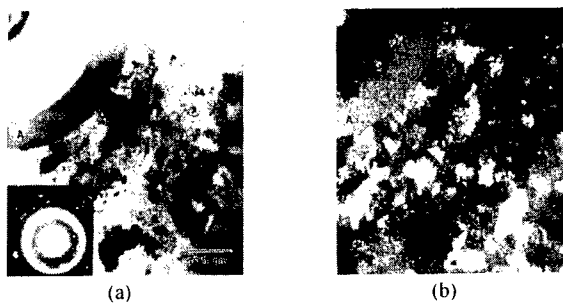


Figure 16. Elongated amorphous phase in nanostructured  $\text{Cr}_3\text{C}_2\text{25(Ni20Cr)}$  coating: (a) bright field and (b) dark field.

Table 4 Published hardness data of Cr<sub>3</sub>C<sub>2</sub>-25(Ni20Cr) coatings

Spraying method	Powder	Hardness	Source
High Velocity Oxygen Fuel	Commercial	855 (HV <sub>300</sub> )	[38]
High Velocity Oxygen Fuel	Commercial (sintered/crushed/clad)	950 (DPH <sub>300</sub> )	[31]
High Velocity Oxygen Fuel	Commercial (blend)	700 (DPH <sub>300</sub> )	[31]
High Velocity Oxygen Fuel	Commercial (agglomeration)	914 (DPH <sub>300</sub> )	[28]
High Velocity Oxygen Fuel	Commercial (blend)	697(DPH <sub>300</sub> )	[28]
Detonation gun spraying	Commercial (powder size: 10-44 $\mu$ m)	800 (HV <sub>300</sub> )	[39]
Atmospheric Plasma Spraying, Ar/H <sub>2</sub>	Commercial	830(HV <sub>300</sub> )	[32]
Atmospheric Plasma Spraying, Ar/He	Commercial	871(HV <sub>300</sub> )	[32]
Continuous detonation spraying	Commercial	828(HV <sub>300</sub> )	[32]
Atmospheric Plasma Spraying, Ar/H <sub>2</sub>	Commercial	837(HV <sub>300</sub> )	[33]
Atmospheric Plasma Spraying, Ar/He	Commercial	943 (HV <sub>300</sub> )	[33]
Continuous detonation spraying	Commercial	889 (HV <sub>300</sub> )	[33]
Detonation gun spraying	Commercial	945 (HV <sub>300</sub> )	[33]
High Velocity Oxygen Fuel	Commercial (blend)	846 (DPH <sub>300</sub> )	This study
High Velocity Oxygen Fuel	Nanostructured	1020 (DPH <sub>300</sub> )	This study

The abrasion resistance of thermal sprayed coatings is significantly related to the relative fracture toughness [40]. The indentation fracture method is often employed to characterize the relative fracture toughness of coatings [40]. In this study, an indentation fracture examination is performed and the results are shown in Figure 17 (a) to (d). Under the same load, indentation marks in the nanostructured coating are smaller than those in the conventional coating because the nanostructured coating has a higher hardness. Under a load of 1000 grams, many cracks caused by an indentation along the phase interface of carbide phase with metal binder phase are observed in the conventional coating, and some cracks are also found in the nanostructured

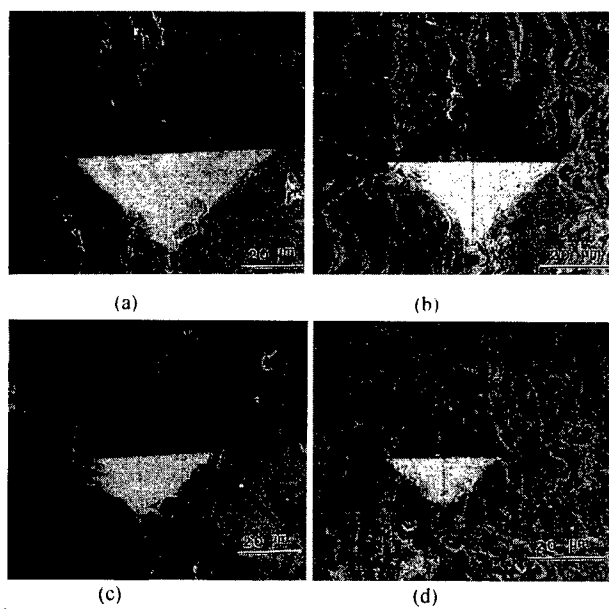


Figure 17. Indentation cracking: (a) conventional coating at 1000 grams; (b) nanostructured coating at 1000 grams; (c) conventional coating at 500 grams and (d) nanostructured coating at 500 grams.

coating. When the load is decreased to 500 grams, a few cracks around the indentation are still observed in the conventional coating, whereas none are present in the nanostructured coating. These results suggest that the nanostructured  $\text{Cr}_3\text{C}_2\text{-NiCr}$  coating possesses a higher apparent fracture toughness relative to that of the conventional material. Further work in this area is continuing in an effort to provide more insight into the fracture behavior of nanostructured coatings.

## 5. Summary

In this paper, the synthesis of nanocomposite coatings is described in detail as related to: (1) synthesis of nanocomposite feedstock powder; (2) characteristics of milled powder; (3) milling mechanism of a duplex structure powder; (4) thermal spraying process of nanocomposite coatings and (5) microstructures and properties of nanocomposite coatings.

## 6. Acknowledgments

The authors gratefully acknowledge financial support provided by the Office of Naval Research (Grants No.: N00014-94-1-0017, N00014-97-1-0844 and N00014-98-1-0569).

## 7. Reference

1. Pawlowski, L (1995) *The Science and Engineering of Thermal Spray Coatings*, John Wiley & Sons, England.
2. Roseberry, T. J. and Boulger, F. W. *A plasma flame spray handbook*, U. S. Department of Commerce Report No. MT-043, National Technical Information Service, Springfield, VA.
3. Lavernia, E. J., Lau, M. L. and Jiang, H. G. (1998) Thermal spray processing of nanocrystalline materials, in G. M. Chow and N. I. Noskova (eds.), *Nanostructured Materials*, Kluwer Academic Publishers, Dordrecht, The Netherlands, pp. 283-302.
4. Eidelman, S. and Yang, X. (1997) *NanoStructured Materials*, **79**, 9.
5. Sobolev, V.V. and Guilemany, M. (1996) *Int. Mat. Rev.*, **41** (1), 13.
6. Knotek, O. and Schnaut, U. (1992) Process modeling of HVOF thermal spraying systems, in C. C. Berndt (ed), *Thermal Spray: International Advances in Coatings Technology*, ASM International, Materials Park, Ohio, pp. 811-816.
7. Parker, D. W. and Kutner, G. L. (1991) *Adv. Mat. Process* **139**, 68.
8. Varacalle, D. J., Ortiz, M. G., Miller, C. S., Steeper, T. J., Rotolico, A. J., Nerz, J. and Riggs (II), W. L. (1992) HVOF combustion spraying of Inconel powder, in C. C. Berndt (ed), *Thermal Spray: International Advances in Coatings Technology*, ASM International, Materials Park, Ohio, pp. 181-187.
9. Srivatsan, T.S. and Lavernia, E. J. (1992) Review-Use of spray techniques to synthesize particulate-reinforced metal-matrix composites, *J. Mat. Sci.* **27**, 5965.
10. Apelian, D., Wei, D. and Farouk, B. (1989) *Metall. Trans.* **20B**, 251.
11. Hackett, C. M. and Settles, G. S. (1996) in C. C. Berndt (ed), *Thermal Spray: Practical Solutions for Engineering Problems*, Materials Park, Ohio, p665.
12. Birringer, R. (1994) in G. C. Hadjipanayis and R. W. Siegel (eds.), *Nanophase Materials: Synthesis-Properties-Applications*, Kluwer Academic Publishers, Dordrecht, The Netherlands, p.157.
13. Birringer, R. (1989) *Mat. Sci. & Engr.*, **A117**, pp. 33.
14. Lau, M. L., Jiang, H. G., Nuchter, W., and Lavernia, E. J. (1998) *Phys. Stat. Sol. (a)*, **166**, pp. 257.
15. Suryanarayana, C. (1995) Nanocrystalline materials, *Int. Mat. Rev.* **40**, 41.
16. Benjamin, J. S. (1992) Fundamentals of mechanical alloying, in P. H. Shingu (ed), *Mechanical Alloying* (Mater. Sci. Forum, Vol. 88-89), Trans Tech Publications, Switzerland, pp.1-17.
17. Koch, C. C. (1992) The synthesis of non-equilibrium structures by ball-milling, in P. H. Shingu (ed), *Mechanical Alloying* (Mater. Sci. Forum, Vol. 88-89), Trans Tech Publications, Switzerland, pp.243-262.
18. Jang, J. S. C. and Koch, C. C. (1990), *J. Mat. Res.*, **5**, 498.

19. He, J., Ice, M. and Lavernia, E. J. (1998) Synthesis and characterization of nanostructured  $\text{Cr}_3\text{C}_2\text{-NiCr}$ , *NanoStructured Mater.*, **10**, 1271.
20. He, J., Ice, M. and Lavernia, E. J. (1999) Synthesis of nanostructured WC-12%Co coating using mechanical milling and HVOF thermal spraying, submitted to *Metall. Trans.*
21. He, J., Ice, M. and Lavernia, E. J. (1999) Synthesis of nanostructured  $\text{Cr}_3\text{C}_2\text{-25(NiCr)}$  coatings, submitted to *Metall. Trans.*
22. Ahn, J. H., Chung, H.S., Watanabe, R. and Park, Y.H. (1992) Microstructural refinement & amorphization in Ti-Al, Ti-Si and Si-W system by mechanical alloying, in P. H. Shingu (ed), *Mechanical Alloying* (Mater. Sci. Forum, Vol. 88-89), Trans Tech Publications, Switzerland, pp.347-354.
23. Guilemany, J. M. and Calero, J. A. (1997) Structural characterization of chromium carbide-nickel chromium coatings obtained by HVOF spraying, in C. C. Berndt (ed.), *Thermal Spray: A United Forum for Scientific and Technological Advances*, ASM, Materials Park, Ohio, pp. 717-721.
24. Gullity, B. D. (1978) *Elements of X-ray Diffraction*, Addison-Wesley, Reading, MA(1978).
25. Luton, M.J., Jayanth, C.S., Disko, M.M., Matras, S. and Vallone, J. (1989) *Mater. Res. Soc. Proc.*, **132**, 79.
26. Lau, M.L., Huang, H., Perez, R.J., Juarez-Islas, J. and Lavernia, E.J. (1996), *NanoStruct. Mater.* **7**, 847.
27. Vuoristo, P., Niemi, K., Mantyla, T., Berger, L.M. and Nebelung, M. (1995) Comparison of different hard, metal like coatings sprayed by plasma and detonation gun processes, in C. C. Berndt and S. Sampath(eds.), *Thermal Spray Science & Technology*, ASM International, 1995, pp. 309-315.
28. Russo, L. and Dorfmann, M. (1995) A structural evaluation of HVOF sprayed  $\text{NiCr-Cr}_3\text{C}_2$  coatings, in A. Ohmori (ed.), *Thermal Spraying: Current Status and Future Trends*, High Temperature Society of Japan, 1995, pp. 681-686.
29. Reardon, J. D., Mignogna, R. and Longo, F. N.. (1981) Plasma and vacuum plasma-sprayed  $\text{Cr}_3\text{C}_2$  composite coatings, *Thin Solid Films*, **83**, 345-351.
30. Houck, D. L. and Chency, R. F. (1984) Comparison of properties of  $\text{Cr}_3\text{C}_2\text{-NiCr}$  coating thermally sprayed from pre-alloyed and mechanical mixed powders, *Thin Solid Films*, **118**, 507-513.
31. Sasaki, M., Kawakami, F., Komaki, C. and Ishida, M.(1992) Characterization of HVOF sprayed  $\text{Cr}_3\text{C}_2$  coating, in C. C. Berndt (ed.), *Thermal Spray: International Advances in Coatings Technology*, ASM International, pp. 165-170.
32. Vuoristo, P., Niemi, K., Makela, A. and Mantyla, T. (1994) abrasion and erosion wear resistance of  $\text{Cr}_3\text{C}_2\text{-NiCr}$  coatings prepared by plasma, detonation and HVOF spraying, in C. C. Berndt and S. Sampath (eds.) *Thermal Spray Industrial Applications*, ASM International, pp. 121-126.
33. Niemi, K., Vuoristo, P., Mantyla, T., Barbezat, G., and Nicoll, A. R. (1992) Abrasion wear resistance of carbide coatings deposited by plasma and high velocity combustion process, in C. C. Berndt (ed.) *Thermal Spray: International Advances in Coatings Technology*, ASM International, pp. 685-689.
34. Liu, X. D., Nagumo, M. and Umemoto, M. (1997) *Mater. Trans., JIM*, **38**, 1033-1039.
35. Suryanarayana, C., Mukhopadhyay, D., Patankar, S.N. and Froes, F. H.(1992) *J. Mater. Res.*, **7**, 2114-2117
36. D. A. Konstantinidis, D. A., and Aifantis, E. C. (1998) *NanoStructured Mater.*, **10**, 1111-1118.
37. Kear, B. H. and McCandlish, L. E. (1993) *Nanostructured Mater.*, **3**, 19-30.
38. Crawmer, D.C., Krebsbach, J. D. and Riggs, W. L.(1992) Coating development for HVOF process using design of experiments, in C. C. Berndt (ed.), *Thermal Spray: International Advances in Coatings Technology*, ASM International, pp. 127-136.
39. Fukuda, Y and Kumon, M. (1995) Application of high velocity flame sprayings for the heat exchanger tubes in coal fired boilers, in A. Ohmori (ed), *Thermal Spraying: Current Status and Future Trend*, High Temperature Society of Japan, pp. 107-111.
40. Usmani, S., Sampath, S. and Herman, H. (1998) in C. C. Berndt and E. J. Lavernia (eds.), *Thermal Spray Processing of Nanoscale Materials-A Conference Report with Extended Abstracts*, *J. of Thermal Spray Technol.*, **7**, p 429.

---

## NANO-ENGINEERED THERMOELECTRIC COATING

*M. Toprak, Yu Zhang and M. Muhammed\**

Materials Chemistry Division, Royal Institute of Technology  
SE-100 44 Stockholm, Sweden

*A.A. Zakhidov, R. H. Baughman and I. Khayrullin*  
Allied Signal Inc, Morristown, NJ 07962-1021, USA

### 1. Abstract

A nano-engineering approach has been developed for the synthesis of the thermoelectric composite materials. A possible way for enhancing ZT is to incorporate thermoelectric materials, e.g. Skutterudite, into the nano-sized pores of three-dimensional periodic arrays. The present study reports the development of a method for making a Nano-Engineered Thermoelectric (NETE) coating on silica particles. The coated particles are assembled into three-dimension array of opals to form NETE composite. The process consists of coating silica particles with gold and then with thermoelectric material. Gold coating has the advantage that post-coating assembly provides a continuous network of Skutterudite-filled gaps between gold interconnects. The second coating was carried out by chemical co-precipitation of Co and Sb precursors from a solid solution onto the surfaces of the gold-coated particles under controlled conditions. Through further heat-treatments (calcination, reduction and alloying), a Skutterudite layer has been formed in high purity. Both the gold- and gold/Skutterudite-coated particles retain the morphology of the original silica particles. In this paper, the processing conditions and materials characterizations are reported and discussed

### 2. Introduction

Thermoelectric (TE) materials are of major interest for both heat pump and electrical generator applications. The figure of merit ZT determines the achievable efficiencies of such devices. This dimensionless quantity is defined as  $ZT = TS^2\sigma/k$ , where T is the absolute temperature, S is the Seebeck coefficient,  $\sigma$  is the electrical conductivity, and  $k$  is the thermal conductivity (which is composed of electronic and lattice components). The unavailability of thermoelectrics with ZT much larger than unity presently limits to the applicability of thermoelectrics for both heat pumps and electrical generation. In order to obtain the high ZT that is required for high efficiency devices, materials with high S, high  $\sigma$ , and low  $k$  are being sought.

One approach being pursued for increasing ZT is through introducing nanoscale structures. Mahan [1-3] and Rowe [4] have predicted that  $k$  will be suppressed in nanoparticle arrays due to increased phonon scattering. Nano-engineered materials with grain sizes below 100 nm have a very high interface to volume ratio - e.g., about 50% of the atoms are at the interface for 30-40 nm diameter grains. Such a high density of interfacial material is expected to increase phonon scattering - thereby decreasing the lattice thermal conductivity. Worlock [5] reported that a large  $k$  decrease was obtained for NaCl by the incorporation of a very small concentration of colloidal silver particles. While the presence of enhanced photon scattering at interfaces will decrease thermal conductivity, electronic carrier scattering at these interfaces may also decrease electrical conductivity. Hence, the overall goal is to obtain an enhancement of  $\sigma/k$ .

The synthesis of Nano-Engineered Thermoelectrics (NETE) with properly tailored structures for increasing ZT provides the motivation for the present research.

As an alternative to the surface scattering approach, atomic-scale phonon scattering centers can be introduced to increase ZT with increasing  $\sigma/\kappa$ . For example, non-stoichiometric TE compositions can be made by doping, either by partially substituting an element on lattice sites or by filling interstitial atoms into oversized cages within the lattice. In order to reach the required composition and distribution of a dopant, nano-engineered materials are advantageous - since a large volume of disordered intergranular phase can facilitate doping. Lattice defects, vacancies or interstitial atoms, are important determinants for both electrical and thermal conductivity. A large fraction of lattice defects may greatly decrease the lattice thermal conductivity, while increasing the concentration electrical carriers for both n- and p-type TE materials [6,7].

Among a number of promising materials, the most interesting is a large family of Skutterudites having a general formula  $R_xM_4X_{12}$  ( $X = Sb, As, or P; M = Co, Fe, Ru, or Os; R$  is a rare earth, and  $x = 0-1$ ) [7]. This structure belongs to a cubic space group  $Im\bar{3}$ . Its unit cell contains 8  $MX_3$  groups and 2 oversized atomic cages, which can be filled by interstitial atoms R (which are called "rattler" atoms). There is major opportunity for optimizing the thermoelectric properties of these Skutterudites. For example, doping Skutterudites with suitable elements, by either substituting M or X or filling R into the cages, can significantly increase electrical conductivity, and/or decrease its thermal conductivity, thus enhancing ZT.

A new concept for enhancing ZT is to incorporate TE materials, e.g. a Skutterudite, into the nano-sized pores of three-dimensional periodic arrays to form a NETE composite. Either zeolites or self-assembled silica opal might be suitable for this purpose. The NETE composite is expected to have intergranular TE phase between particles, resulting in a network of nano-sized TE junctions. This could drastically decrease the thermal conductivity while perhaps limiting the negative effect on the electrical conductivity. Also, enhancement in the Seebeck coefficient is possible for a suitably designed NETE.

Since it is generally difficult to fill nano-sized pores with a complex material of defined composition, such as Skutterudite  $CoSb_3$ , an alternative approach is to coat the desired material on the individual particles before assembling them. After assembly of the coated particles, the particle surfaces form the interparticle interfaces. The present work is focused on the development of such a process. As the first step in this direction, we will describe the synthesis of Skutterudite on monodispersed gold-coated  $SiO_2$  particles. The strategy of first coating the  $SiO_2$  particles with gold (prior to formation of the Skutterudite layer and particle assembly) has the advantage that post-coating assembly provides a continuous network of Skutterudite-filled gaps between gold interconnects. For suitably thin Skutterudite gaps, ballistic electron transport across these gaps might be possible – leading to a cooling effect that is the solid-state analogue of thermoionic cooling.

We recently developed a novel chemical route for the synthesis of NETE powders of  $CoSb_3$  Skutterudite [8,9]. The present study is to establish the technical feasibility of applying this low-temperature chemical alloying route for making a NETE coatings on silica particles.

### 3. Solution Chemistry

Computer-aided thermodynamic modeling was applied for choosing the synthesis conditions used for particle coating including both dissolution and precipitation processes. For this purpose we used the computer software and database for multi-component aqueous systems similar to that we developed for chemical equilibrium calculations [10,11]. In this section, some typical calculation results are discussed in order to illustrate the utility of this approach.

The present process for coating particles with cobalt-antimony compounds is based on our previous development of a synthetic route to bulk powders of the same materials [8,9]. In this paper, we present some typical calculated chemical equilibrium results for a system of  $\text{H}^+$ - $\text{Co}^{2+}$ - $\text{Sb}^{3+}$ - $\text{Cl}^-$ - $\text{C}_2\text{O}_4^{2-}$ - $\text{NH}_3$  [9].

When dissolved in water, an antimony salt usually decomposes into a basic precipitate in the following two steps:



The reaction described in Eqn. 2 can be avoided only if the acid concentration is sufficiently high. Complete dissolution of  $\text{SbCl}_3$  in 3 M HCl can be expected for a stock solution having the atomic ratio of  $\text{CoSb}_3$  (containing 0.75 M  $\text{Sb}^{3+}$  and 0.25 M  $\text{Co}^{2+}$ ). Moreover, the solubility of  $\text{SbCl}_3$  in HCl solution is increased by the formation of soluble complexes of  $\text{SbCl}_n$  ( $n = 1$ -6). Also,  $\text{CoCl}_2$  is very soluble in water.

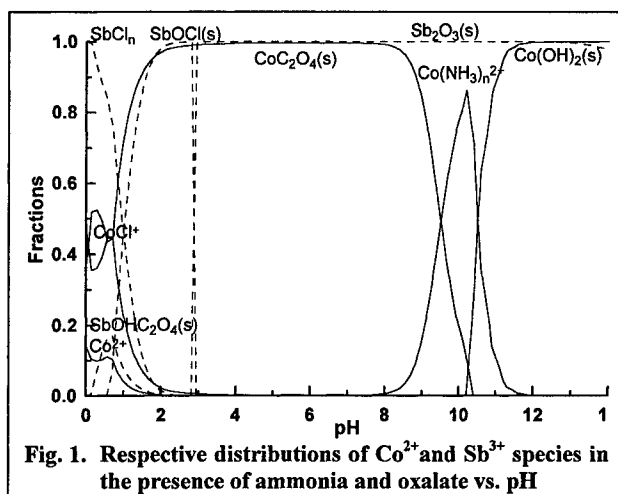


Fig. 1. Respective distributions of  $\text{Co}^{2+}$  and  $\text{Sb}^{3+}$  species in the presence of ammonia and oxalate vs. pH

According to the calculation results plotted in Fig. 1, complete co-precipitation of  $\text{Sb}_2\text{O}_3$  and  $\text{CoC}_2\text{O}_4$  with  $\text{Sb}/\text{Co} = 3$  is expected at  $\text{pH} = 3$ -8, which is mainly limited by the solubility of  $\text{CoC}_2\text{O}_4$ . The presence of ammonia results in the formation of soluble complexes of  $\text{Co}(\text{NH}_3)_n^{2+}$  ( $n = 1$ -6) at  $\text{pH} > 8$ . Neither the addition of ammonia or oxalate would affect the precipitation of  $\text{Sb}_2\text{O}_3$  in the same pH region - although the precipitation of  $\text{SbOCl}$  and  $\text{SbOHC}_2\text{O}_4$  could take place in more acidic region at  $\text{pH} < 3$  and  $< 2$ , respectively. When Ni was used for partial substitution of Co to form a final product of  $\text{Co}_{1-x}\text{Ni}_x\text{Sb}_3$ , the dissolution and precipitation of nickel species are similar to those of cobalt species. The solution chemistry of such a system including  $\text{Ni}^{2+}$  will be presented elsewhere.

#### 4. Experimental

##### 4.1 SOLUTION PREPARATION

The p.a. grade chemicals and de-ionized water were used for preparation of the stock solutions.

The solution of 0.25 M Co and 0.75 M Sb was prepared by dissolving  $\text{CoCl}_2$  and  $\text{SbCl}_3$  in 3 M HCl in order to avoid the precipitation of  $\text{SbOCl}$ . The alternative solutions including  $\text{NiCl}_2$  were also prepared in the same way, but in this case the molar ratio was  $\text{Sb}/(\text{Co}+\text{Ni}) = 3$ .

The solutions of 0.2 M  $\text{H}_2\text{C}_2\text{O}_4$  and 1 M  $\text{NH}_3$  were prepared by dissolving the respective chemicals in water. The precise concentrations of metals were analyzed by atomic absorption spectroscopy (AAS), while that of  $\text{H}_2\text{C}_2\text{O}_4$  was titrimetrically determined.

#### 4.2 MATERIALS PROCESSING

Figure 2 presents a conceptual scheme for the overall process for generating a double-layer coating on the silica particles. The experiments were carried out using the following:

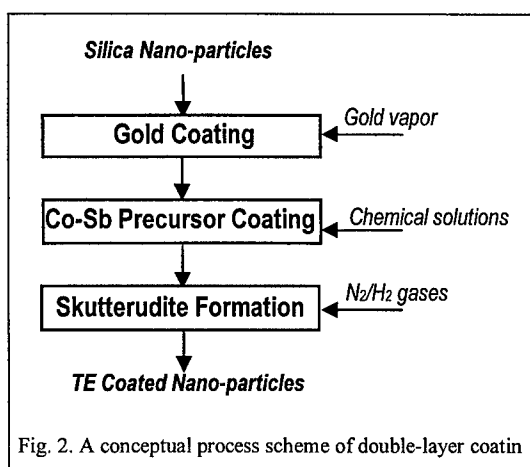


Fig. 2. A conceptual process scheme of double-layer coating

**Gold coating:** The uniform-sized silica sphere particles (300 nm) were coated by sputtering gold until the white color of silica disappeared. In order to obtain full coverage of the  $\text{SiO}_2$  sphere surface, the particles were processed through several repetitions of shaking and sputtering procedure:

**Co-Sb precursor coating:** About 8mg of the Au-coated particles were dispersed in 100 ml of  $\text{NH}_4\text{C}_2\text{O}_4$  solution under ultrasonic vibration for 5-10 minutes. Then 80 ml of Co(-Ni)-Sb solution was slowly added to the suspension, drop by drop, while maintaining pH = 5-7 (2-3 when including Ni) by regularly adding ammonia solution. After 2-5 hours of reaction equilibration, the precursor-coated particles were filtered, washed several times with water, and then dried at 100°C for more than 3 hours.

**Skutterudite formation:** The  $\text{SiO}_2$  particles coated with the Co-Sb precursor was calcined in flowing nitrogen gas at 300-400°C for 1-2 hour, then heated in a flowing hydrogen gas at 450-550°C for 2-3 hour, and then cooled to room temperature.

The samples obtained at different processing steps were characterized by several techniques: Scanning Electron Microscopy (SEM), Transmission Electron Microscopy (TEM), Energy Dispersed X-ray Analysis (EDX), Thermogravimetric Analysis (TGA), and X-ray Diffraction (XRD).

## 5. Results and Discussions

### 5.1 GOLD COATING

The initial white color of the silica particles eventually changed to golden brown during the sputtering of gold onto the  $\text{SiO}_2$  particles. As shown by the SEM photograph for Au-coated silica particles (Fig. 3), most of the gold coated particles have the spherical shape of the original  $\text{SiO}_2$ . However, a few smaller particles are also present in the sample, and are identified by EDX to be clusters of pure gold. TEM micrographs indicate that the  $\text{SiO}_2$  spheres are coated with a layer of gold, as shown in Fig. 4. However, the thickness of the gold layer on different  $\text{SiO}_2$  spheres varies over a relatively large range (10-60 nm).

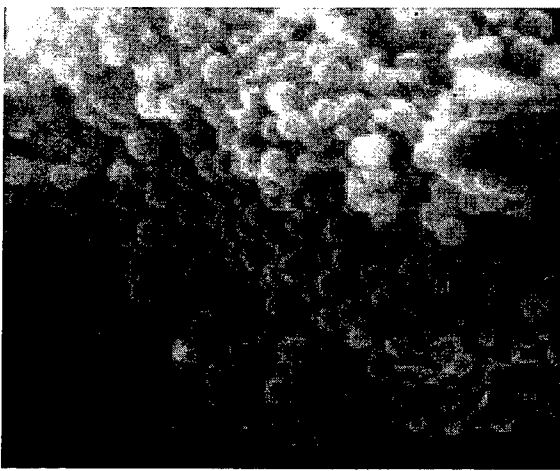


Fig. 3 SEM micrograph of Au-coated particles (bar = 1  $\mu$ )

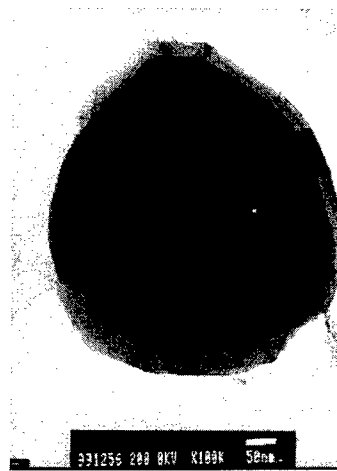


Fig. 4. TEM of gold-coated particle

### 5.2 PRECURSOR COATING

The stock solution of a mixture of  $\text{CoCl}_2$  and  $\text{SbCl}_3$  in  $\text{HCl}$  was purple in color. After precipitation and filtration, the solution obtained at  $\text{pH} = 5-7$  was colorless. Chemical analysis of those filtrate liquors indicated that more than 99% of Sb and Co was precipitated. The color of the coated particles changed to pink, lighter than that of the pure  $\text{CoC}_2\text{O}_4$  precipitate, while the pure  $\text{Sb}_2\text{O}_3$  precipitate was white. Similar to the pattern for the co-precipitated powders [8,9], the XRD pattern of the coated silica particles indicates very low crystallinity, as shown in Fig. 5. The crystalline XRD peaks of the as-coated particles correspond to  $\text{Sb}_2\text{O}_3$ , while the  $\text{CoC}_2\text{O}_4$  and any other possible deposited material appear to be amorphous. The low crystallinity of the as-coated layer is one of main characteristics for metastability, which is preferred for obtaining relatively high reactivity in the further treatments of the precursor-coated layer. Interestingly, a SEM image (Fig. 6) indicates the

formation of a novel morphology. The coating layer links the  $\text{SiO}_2$  particles into long wire-like bead arrays (Fig. 6), which are up to 10  $\mu\text{m}$  long [9].

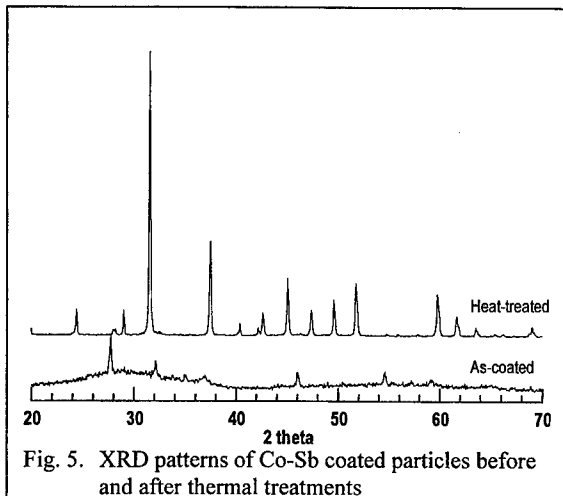


Fig. 5. XRD patterns of Co-Sb coated particles before and after thermal treatments



Fig. 6. SEM micrograph of precursor-coated silica particles (bar = 10  $\mu\text{m}$ )

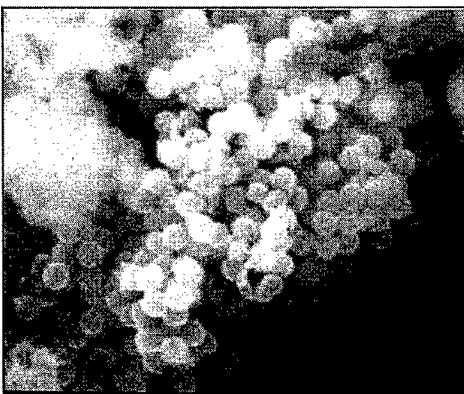


Fig. 7. SEM micrograph of  $\text{CoSb}_3/\text{Au}$  coated particles (bar = 1  $\mu\text{m}$ )

### 5.3 SKUTTERUDITE FORMATION

After the thermochemical treatments first in nitrogen and then hydrogen, the coated  $\text{SiO}_2$  particles became dark gray in color. As indicated by the XRD pattern in Fig. 5, the crystalline phase in the heat-treated sample is the desired phase of the  $\text{CoSb}_3$  Skutterudite, with very little detectable impurity (< 3%). There is no indication in the XRD of either crystalline or amorphous forms of silica. Figure 7 shows a SEM photograph of the  $\text{CoSb}_3/\text{Au}$  coated silica particles. This micrograph shows that, after the heat treatments, the doubly-coated particles have regained their spherical shape and uniform size, thus resembling the original or Au-

coated silica particles. The assembly of the NETE coated particles into particle arrays and the TE properties of the assembled sphere arrays will be presented in future work.

## 6. Conclusions

A chemical alloying route has been demonstrated for NETE coating on silica particles. The conclusions for this route are:

- 1) The chemical route for the synthesis of bulk powders of Skutterudite compounds can be directly utilized for NETE coating, without significant modification of synthesis conditions;
- 2) The primary coating of gold on the particles by sputtering is simple to accomplish, although there is significant polydispersity in the thickness of the gold layer on different particles.
- 3) Both the gold- and gold/Skutterudite-coated particles retain the morphology of the original silica particles. However, we find that the  $\text{SiO}_2$  particles assemble into chains that are internally linked by the coating that is precursor to the Skutterudite.
- 4) The NETE layer of Skutterudite structure has the same or higher purity than Skutterudite powders produced by the same technique.

## 7. Acknowledgments

We would like to thank Dr. Lingna Wang and Mr. Hans Bergqvist for their assistance in SEM and TEM characterizations. This work was supported by DARPA Contract DAAB07-97-J036 (USA).

## References

1. Bartkowiak, M. and Mahan, G.D. (1995) Nonlinear current in Voronoi networks, *Phys. Rev. B* **51**, 10825-10832.
2. Mahan, G.D. and Sofo, J.O. (1996) The best thermoelectrics, *Proc. Natl. Acad. Science* **93**, 7436-7439.
3. Mahan, G.D. (1997) Good thermoelectrics, in Ehrenreich, H. and Spaepen, F. (eds), *Solid State Physics*, p81, Academic Press, New York.
4. Rowe, D.M. and Bhandari, C.M. (1980) Effect of grain size on the conversion efficiency of semiconductor alloys at high temperatures, *Appl. Energy* **6**, 347-351.
5. Tighe, T.S., Worlock, J.M. and Roukes, M.L. (1997) Direct thermal conductance measurements on suspended monocrystalline nanostructure, *Appl. Phys. Lett.* **70**, 2687-2689.
6. Terry, M. (1995) Thermoelectrics run hot and cold, *Science* **272**, 1276-1277.
7. Sales, B.C. (1998) Electron crystals and phonon glasses: a new path to improved thermoelectric materials, *MRS Bulletin* **23**, 15-21.
8. Wang, M., Zhang, Y. and Muhammed, M. (1997) Synthesis and characterisation of thermoelectric skutterudite  $\text{CoSb}_3$  via solution chemistry route, *Nanostruct. Mater.* **12**, 237-240.
9. Wang, M., Zhang, Y. and Muhammed, M. (1999) A novel chemical alloying route for the preparation of nano-engineered thermoelectric skutterudite  $\text{CoSb}_3$ , in M. Wang's doctoral thesis: Thermodynamic modelling of aqueous solutions and applications in some functional materials synthesis, ISBN 91-7170-412-4, The Royal Institute of Technology, Stockholm.

10. Puigdomenich, I. (1983), INPUT, SED and PREDOM: computer programs drawing equilibrium diagrams. Report TRITA-OOK-3010, The Royal Institute of Technology, Stockholm.
11. Wang, M. and Muhammed, M., to be published.

## PHOTOLUMINESCENCE FROM PRESSURE - ANNEALED NANOSTRUCTURED SILICON DIOXIDE AND NITRIDE FILMS

A. MISIUK<sup>a</sup>, L. REBOHLE<sup>b</sup>, A. ILLER<sup>c</sup>, I. E. TYSCHENKO<sup>d</sup>, J. JUN<sup>e</sup>  
and A. PANAS<sup>a</sup>

(a) *Institute of Electron Technology, Al. Lotników 46, 02-668 Warsaw, Poland*; (b) *Institut für Ionenstrahlphysik und Materialforschung, Dresden, POB 510119 Dresden, Germany*; (c) *Institute of Vacuum Technology, Długa 44/50, 00-241 Warsaw, Poland*; (e) *Institute of Semiconductor Physics RAS, 630090 Novosibirsk, Russia*; (d) *High Pressure Research Centre, Sokolowska 29/37, 01-142 Warsaw, Poland*

### Abstract

Light emission in thin films ( $\text{SiO}_2$ ,  $\text{SiO}_2:\text{Si}$  and  $\text{Si}_3\text{N}_4$ ) on a single crystalline silicon surface has been investigated after treatment at enhanced argon pressure, HP. Pronounced effect of HP up to 1.5 GPa during annealing up to 1550 K on photoluminescence, PL, of the  $\text{SiO}_2$ ,  $\text{SiO}_2:\text{Si}$  and  $\text{Si}_3\text{N}_4$  films of 0.1 - 1.2  $\mu\text{m}$  thickness has been stated. The pressure - temperature treatment results in development and enhancement of ultraviolet and visible PL at about 290 - 320, 360, 460, 600 and 680 nm, related to stress induced creation of PL active silicon nanoclusters and other oxygen deficient defects.

### 1. Introduction

Nanocrystalline materials have been attracting rapidly increasing interest in the last decade in the areas of magnetics, catalysts, mechanics and optoelectronics. The last is related, among others, to the hopes of obtaining visible light emission from silicon or silicon - related materials. Light emission from  $\text{SiO}_2$ ,  $\text{SiO}_2$  implanted by Si ( $\text{SiO}_2:\text{Si}$ ) or Ge,  $\text{Si}_3\text{N}_4$  and from porous silicon, pSi, has been intensively investigated because of their usefulness in silicon based optoelectronics. Silicon based optoelectronics refers to the integration of photonic and electronic components on a Si chip or wafer. The photonics adds value to the electronics, and the electronics offers low cost mass production benefits [1].

Bulk silicon (with bandgap value  $E = 1.12$  eV) is an indirect bandgap semiconductor, and so phonons must assist in radiative electron hole recombination. It results in the low photoluminescence, PL, efficiency, of the order of  $\sim 10^{-5}$  which can be increased in the case of a dislocation - free crystal with perfectly passivated surface [2].

Efficient room temperature PL at about 1.8 eV from pSi prepared by electrochemical etching of single crystalline Si has been reported. However, PL from pSi degrades in ambient conditions; moreover, pSi is fragile and of very poor thermal conductivity so, in spite of enormous efforts, it is still far from being introduced into wide use.

There are two general explanations of visible PL from pSi. One mechanism is related to the presence of some PL active surface contaminants; the other one is related to a quantum - size effect. In nanometer sized Si crystal the effective mass approximation predicts bandgap upshift for  $\Delta E \sim d^2$  where  $d$  is the nanocrystal diameter [2]. This second effect suggests possible usefulness of other materials containing semiconductor nanocrystals, e.g. Si, (C, Ge,..), dispersed in optically transparent film (e.g. SiO<sub>2</sub>). Such materials can be produced by ion implantation with subsequent annealing.

As it has been stated [3, 4], enhanced pressure of ambient gas at annealing (HT - HP treatment) of oxygen containing Czochralski grown silicon, Cz-Si, and of Si - Ge solid solution exerts pronounced effect on oxygen and germanium diffusivity, clustering etc. It inspired our recent investigations of the HT - HP treatment effect on visible PL from silicon dioxide implanted by silicon, SiO<sub>2</sub>:Si [5, 6].

Effects of the HT - HP treatment on creation of silicon nanoclusters, and on PL from the SiO<sub>2</sub>, SiO<sub>2</sub>:Si and Si<sub>3</sub>N<sub>4</sub> thin films grown (deposited) on single crystalline silicon are reported in this paper.

## 2. Experimental

Silicon dioxide, SiO<sub>2</sub> films of 0.1 - 1.2  $\mu$ m thickness on n - and p - type (001) oriented single crystalline Czochralski grown, Cz-Si, wafers were prepared by oxidation in dry oxygen at up to 1420 K, oxidation in the O<sub>2</sub> + N<sub>2</sub> mixture at 1370 K, oxidation in the O<sub>2</sub> + H<sub>2</sub> ("wet oxygen") atmosphere at 1270 - 1370 K or by low pressure chemical vapour deposition, LPCVD, at 670 - 920 K from the gas containing silicomethane and oxygen, typically with the final densification at 1270 K.

Some 500 nm thick SiO<sub>2</sub> films were implanted with Si<sup>+</sup> ions at an energy of 100 keV and then at 200 keV using respective doses of  $1.2 \times 10^{16} \text{ cm}^{-2}$  and  $2.0 \times 10^{16} \text{ cm}^{-2}$  (low dose, LD, total dose  $3.2 \times 10^{16} \text{ cm}^{-2}$ ), of  $2.3 \times 10^{16} \text{ cm}^{-2} + 4.4 \times 10^{16} \text{ cm}^{-2}$  (high dose, HD, total dose  $6.7 \times 10^{16} \text{ cm}^{-2}$ ) and of  $3.9 \times 10^{16} \text{ cm}^{-2} + 6.3 \times 10^{16} \text{ cm}^{-2}$  (very high dose, VHD, total dose  $1.02 \times 10^{17} \text{ cm}^{-2}$ ). In what follows such silicon implanted films are referred to as the SiO<sub>2</sub>: Si films.

Silicon nitride, Si<sub>3</sub>N<sub>4</sub>, films of 0.12  $\mu$ m thickness on the Cz-Si surface were prepared by LPCVD from the silicomethane - ammonia mixture at 920 K.

The SiO<sub>2</sub>/Si, SiO<sub>2</sub>:Si/Si and Si<sub>3</sub>N<sub>4</sub>/Si samples were subjected to anneals for up to 10 h up to 1550 K under enhanced (up to 1.5 GPa) hydrostatic argon pressure, HP [4, 5].

PL peaks observed at particular excitation wavelength were often accompanied by scattered radiation. To avoid possible mistakes with interpretation of the obtained results, different excitation sources were applied.

PL of the HT - HP treated SiO<sub>2</sub>, SiO<sub>2</sub>:Si and Si<sub>3</sub>N<sub>4</sub> films was excited at room temperature, RT, by ultraviolet lamp ( $\lambda_{\text{ex}} = 240 - 250 \text{ nm}$ ), He - Cd laser ( $\lambda_{\text{ex}} = 325 \text{ nm}$ ) or Ar laser ( $\lambda_{\text{ex}} = 488 \text{ nm}$ ) and recorded employing a Spex Fluoromax spectrometer and R 928 Hammatu photomultiplier (for measurements using  $\lambda_{\text{ex}} = 240 - 250 \text{ nm}$ ) or a photomultiplier with S11 cathode (for other excitations).

### 3. Results

#### 3. 1 PHOTOLUMINESCENCE FROM PRESSURE ANNEALED SILICON DIOXIDE FILMS

As deposited thermally grown  $\text{SiO}_2$  films excited by  $\lambda_{\text{ex}} = 250$  nm indicate at RT very weak PL at about 460 nm [5].

PL spectra from the 290 nm thick  $\text{SiO}_2$  films obtained at RT using 240 nm excitation wavelength are presented in Fig. 1 for the samples treated at different HT - HP conditions and in Fig. 2 - for the samples treated at 1470 K - HP. PL spectrum for the sample treated at 1550 K - 1.5 GPa - 10' is presented for comparison.

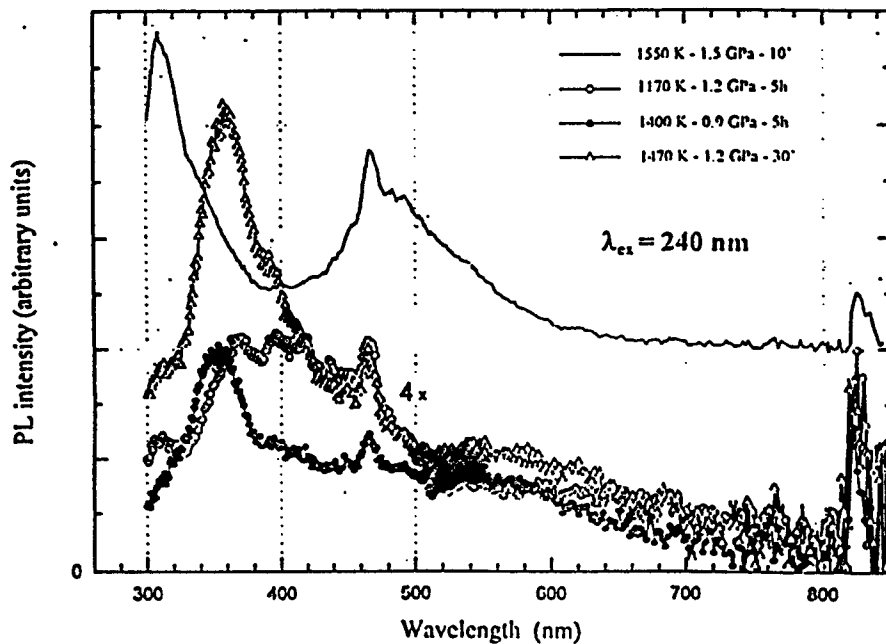


Figure 1. PL spectra from thermally grown ( $\text{O}_2 + \text{H}_2$ , 1470 K) silicon dioxide films of 290 nm thickness, subjected to HT - HP treatments at different temperatures - pressures: 1170 K - 1.2 GPa - 5 h, 1400 K - 0.9 GPa - 5 h, 1470 K - 1.2 GPa - 30' and 1550 K - 1.5 GPa - 10'. PL excitation wavelength  $\lambda = 240$  nm.

Minor PL measured for the samples treated at 1170 K - 1.2 GPa - 5 h (Fig. 1) and at 1470 K - 1.5 GPa - 10' (Fig. 2) is mostly due to scattering of exciting ( $\lambda_{\text{ex}} = 240$  nm) radiation. This seems to be also the case for the sharp PL peaks at 465 nm and 820 nm observed for almost all samples. However, as it follows from the PL results obtained using the 325 nm excitation, this scattered radiation can be superimposed on the wide "real" weak PL peak at 520 - 560 nm (at least for the sample treated at 1550 K - 1.5 GPa - 10', see also Figs 3 and 4).

Comparatively strong PL peaks at 290 - 320 nm and at 340 - 380 nm were observed for the samples treated at 1400 - 1470 K - 0.9 - 1.5 GPa for above 30' (Fig 1, 2).

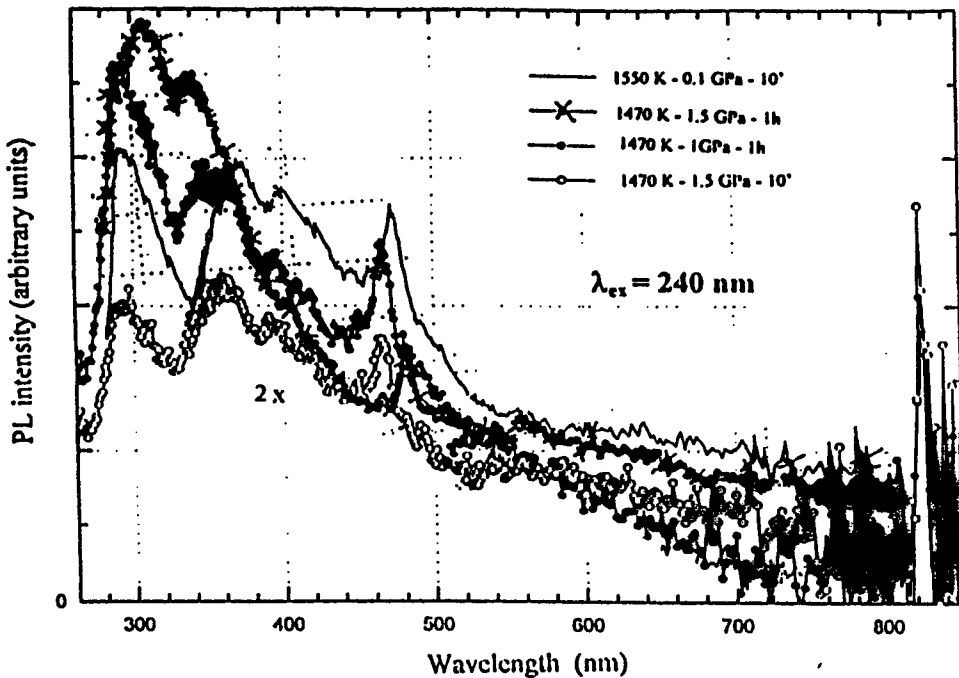


Figure 2. PL spectra from thermally grown ( $O_2 + H_2$ , 1470 K) silicon dioxide films of 290 nm thickness, subjected to HT - HP treatments at 1470 K and at 1550 K: 1470 K - 1 GPa - 1 h, 1470 K - 1.5 GPa - 10', 1470 K - 1.5 GPa - 1 h and at 1550 K - 0.1 GPa - 10'. PL excitation wavelength  $\lambda = 240$  nm.

Similar HT - HP induced PL (but peaking at 305 nm) was detected for the sample treated at 1550 K - 1.5 GPa for 10' (Fig. 1) whereas the sample treated at the same conditions but under 0.1 GPa indicated PL similar to that detected for the samples treated at 1470 K (Fig. 2).

As it follows from measurements with the 325 nm excitation, the prolonged (1 - 5 h) HT - HP treatment at  $\geq 1170$  K - 1.2 - 1.5 GPa of thermally grown  $SiO_2$  results in a wide PL band at 400 - 600 nm (Figs 3, 4). Intensity of the 400 - 600 nm PL band from the thermally grown  $SiO_2$  of 290 nm thickness (Fig. 3) was dependent on conditions of the HT - HP treatment (temperature, pressure, time) and was of the highest value for the samples HP - treated at 1400 - 1470 K for 1 - 5 h. The short time treatments (10' - 30') at 1270 - 1470 K - 0.1 - 1.5 GPa resulted in very weak PL at this wavelength range. The same concerned the samples HT - HP treated at below 1170 K.

The PL intensity from the  $SiO_2/Si$  samples treated at 1400 K - 1.2 GPa for 5 h was dependent on the preparation method. It was comparatively strong for the thin  $SiO_2$  films prepared by oxidation of Si in a dry oxygen atmosphere (Fig. 4, spectrum d) but much weaker for the case of  $SiO_2$  films prepared by oxidation of silicon in the ( $O_2 + N_2$ ) or ( $O_2 + H_2$ ) gas mixtures (Fig. 4, spectra a - c).

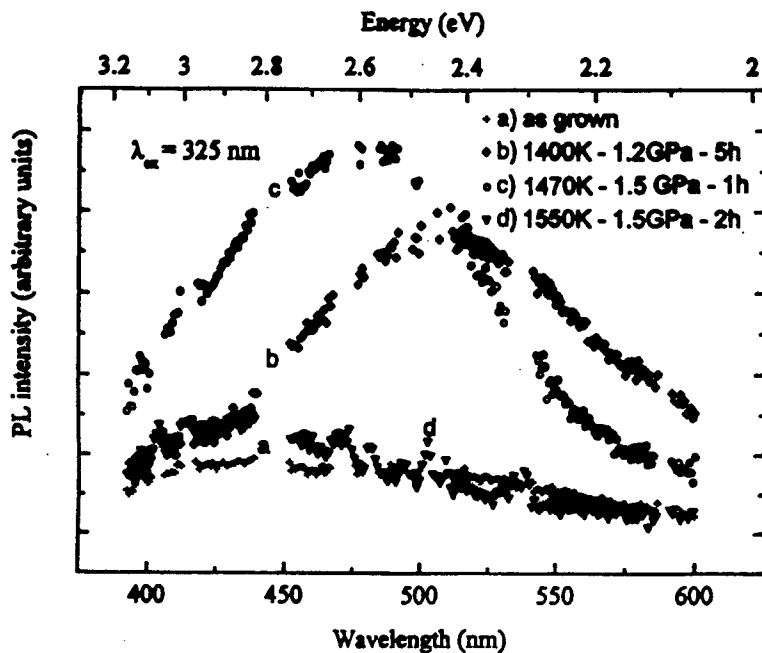


Figure 3. PL spectra from thermally grown ( $O_2 + H_2$ , 1470 K) 290 nm thick  $SiO_2$  films, as grown and subjected to HT - HP treatments at 1400 K - 1.2 GPa - 5 h, 1470 K - 1.5 GPa - 1 h and at 1550 K - 1.5 GPa - 2 h.

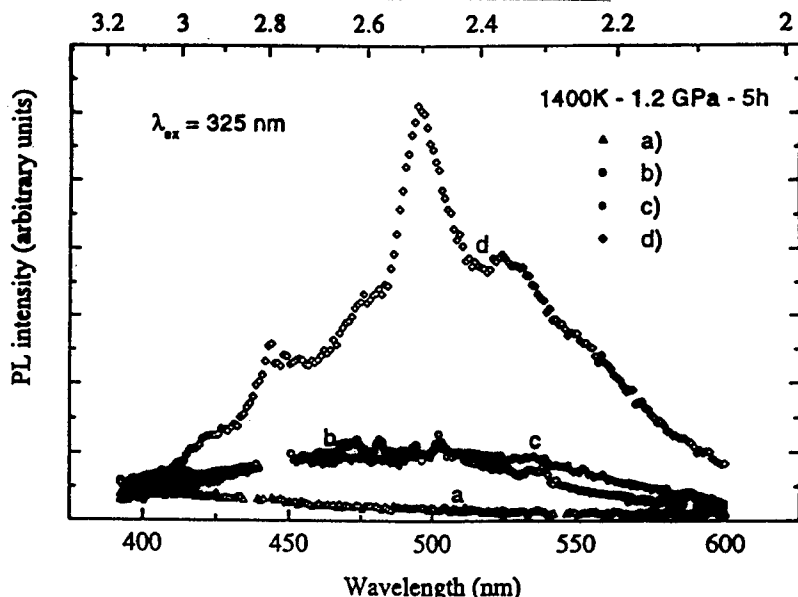


Figure 4. PL spectra from silicon dioxide films treated at 1400 K - 1.2 GPa for 5 h.  $SiO_2$  films were thermally grown at different conditions: a) ( $O_2 + N_2$ ) mixture, 1370 K, 260 nm thick; b) wet oxygen ( $O_2 + H_2$ ), 1470 K, 290 nm thick; c) wet oxygen ( $O_2 + H_2$ ), 1270 K, 470 nm thick; d) dry oxygen, 1370 K, 260 nm thick.

### 3. 2 PHOTOLUMINESCENCE FROM SILICON IMPLANTED PRESSURE ANNEALED SILICON DIOXIDE FILMS

The PL spectra from thermally grown 0.5  $\mu\text{m}$  thick  $\text{SiO}_2$  : Si / Si films (2 stage VHD implantation,  $\text{Si}^+$  energy of 100 keV,  $3.9 \times 10^{16} \text{ cm}^{-2}$  dose +  $\text{Si}^+$  energy of 200 keV,  $6.3 \times 10^{16} \text{ cm}^{-2}$  dose) as implanted and subjected to the post implantation HT - HP treatment at 720 K, are presented in Fig. 5.

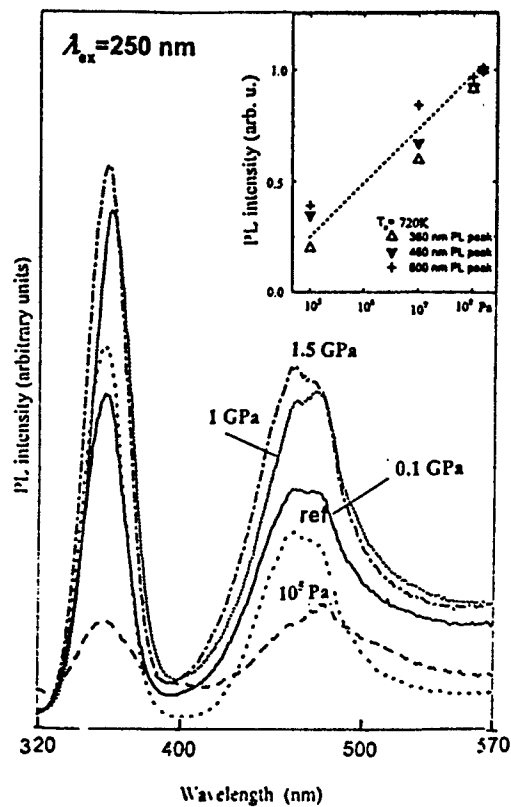


Figure 5. PL spectra (at 300 K) from thermally grown 0.5  $\mu\text{m}$  thick  $\text{SiO}_2$  films VHD implanted with silicon, as implanted (ref) and treated at 720 K - (10<sup>5</sup> Pa - 1.5 GPa) for 10 h. Insert: dependence of the PL intensity peaks at 360, 460 and 600 nm on HP during annealing at 720 K for 10 h. PL excitation wavelength  $\lambda = 250 \text{ nm}$ .

The as implanted sample exhibits two PL peaks in the short wavelength range at about 360 nm (ultraviolet) and 460 nm (blue). The PL peaks at 360, 460 and 600 nm (the last not seen in Fig. 5) were detected for the HT - HP treated samples. The peak intensity increased (see insert) with HP.

Effect of the HT - HP treatment at 1400 K on the PL spectra from thermally grown 0.5  $\mu\text{m}$  thick silicon implanted  $\text{SiO}_2$  films (2 stage implantation, low and high oxygen doses) is presented in Fig. 6 for PL excitation wavelength  $\lambda = 250 \text{ nm}$ . The intensity of the short wavelength photoluminescence at 360 nm was strong for the HD implanted samples treated at 1400 K - 1.2 GPa for 5 h, while during annealing at ambient pressure (10<sup>5</sup> Pa) this peak reached a maximum for the samples annealed at about 770 K.

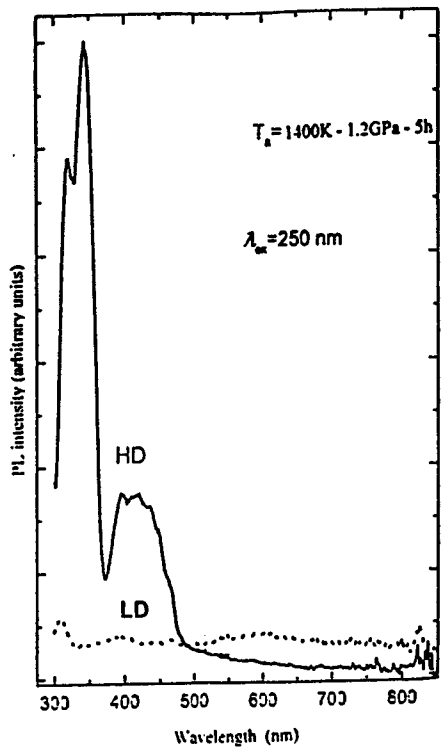


Figure 6. PL spectra (at 300 K) from thermally grown 0.5  $\mu\text{m}$  thick  $\text{SiO}_2$  films implanted with low and high silicon doses, LD and HD, treated at 1400K - 1.2 GPa for 5 h. PL excitation wavelength  $\lambda = 250\text{ nm}$ .

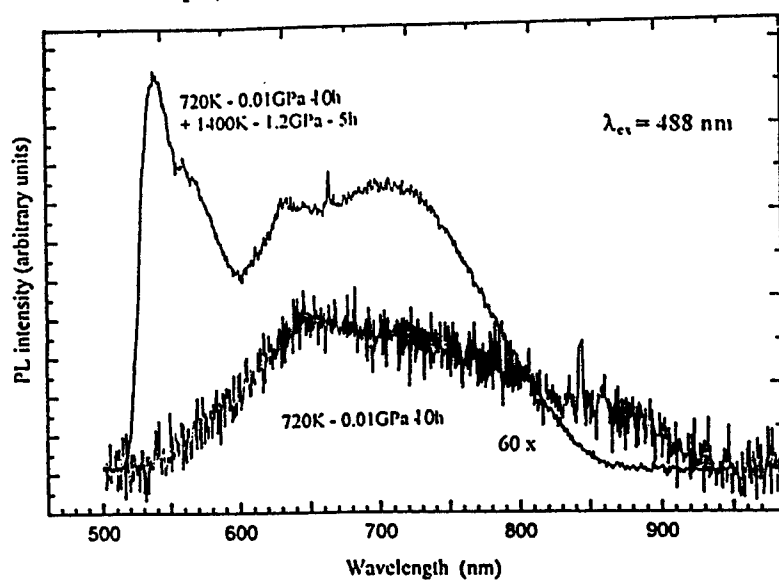


Figure 7. PL spectra from thermally grown 0.5  $\mu\text{m}$  thick VHD  $\text{SiO}_2:\text{Si}/\text{Si}$  samples subjected to treatment at 720 K - 0.01 GPa and additionally at 1400 K - 1.5 GPa. PL spectrum of the sample treated at 720 K - 0.01 GPa was magnified (60 times). PL excitation wavelength  $\lambda = 488\text{ nm}$ .

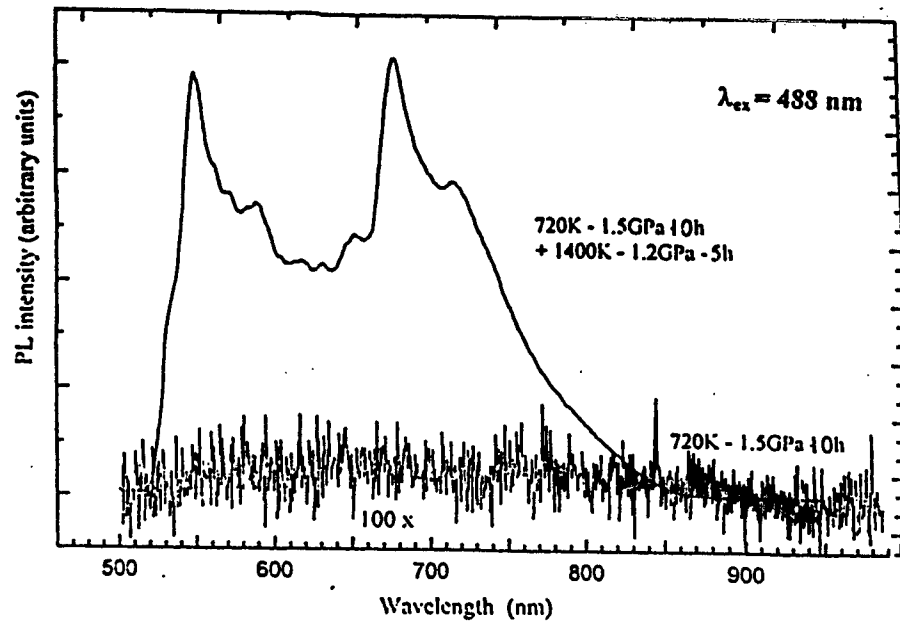


Figure 8. PL spectra from thermally grown VHD 0.5  $\mu\text{m}$  thick  $\text{SiO}_2$ : Si films treated at 720 K - 1.5 GPa and additionally at 1400 K - 1.2 GPa. PL spectrum of the sample treated at 720 K - 1.5 GPa was magnified (100 times). PL excitation wavelength  $\lambda = 488$  nm.

The effect of HT - HP treatment at 720 K and at 1400 K on PL spectra from thermally grown 0.5  $\mu\text{m}$  thick VHD  $\text{SiO}_2$ : Si films is presented in Figs 7 and 8 for PL excitation wavelength  $\lambda = 488$  nm. The higher - energy PL peak at 550 nm is related probably to scattered radiation whereas that at 660 - 750 nm corresponds to the "real" PL.

Enhanced pressure during sample annealing at 720 K leads to practically complete quenching of PL at 660 - 750 nm whereas additional treatment at 1.2 GPa resulted in PL peaking at about 680 nm, being dependent on conditions of the treatment.

### 3. 3 PHOTOLUMINESCENCE FROM PRESSURE ANNEALED SILICON NITRIDE FILMS

The effect of the HT - HP treatment on PL from silicon nitride (Figs 9 - 11) was investigated for  $\text{Si}_3\text{N}_4$  films of 0.12  $\mu\text{m}$  thickness deposited at 920 K on the Cz-Si surface by LPCVD method from the silicomethane - ammonia mixture. PL at 380 and 520 nm [7] (excited by ultraviolet lamp,  $\lambda_{\text{ex}} = 350$  nm) has been reported for the silicon nitride films deposited at 1060 K by LPCVD method from the  $\text{NH}_3$  -  $\text{SiH}_2\text{Cl}_2$  mixture. The HT - HP treatment of the  $\text{Si}_3\text{N}_4$ /Si samples resulted in PL (excitation by ultraviolet lamp,  $\lambda_{\text{ex}} = 240$  nm or He - Cd laser,  $\lambda_{\text{ex}} = 325$  nm) peaking at about 290, 360 and 450 nm.

The  $\text{Si}_3\text{N}_4$  / Si sample treated at 1550 K - 0.1 GPa - 10' indicates PL at 290 and 360 nm (the sharp peak at 460 nm can be related to scattered excitation light).

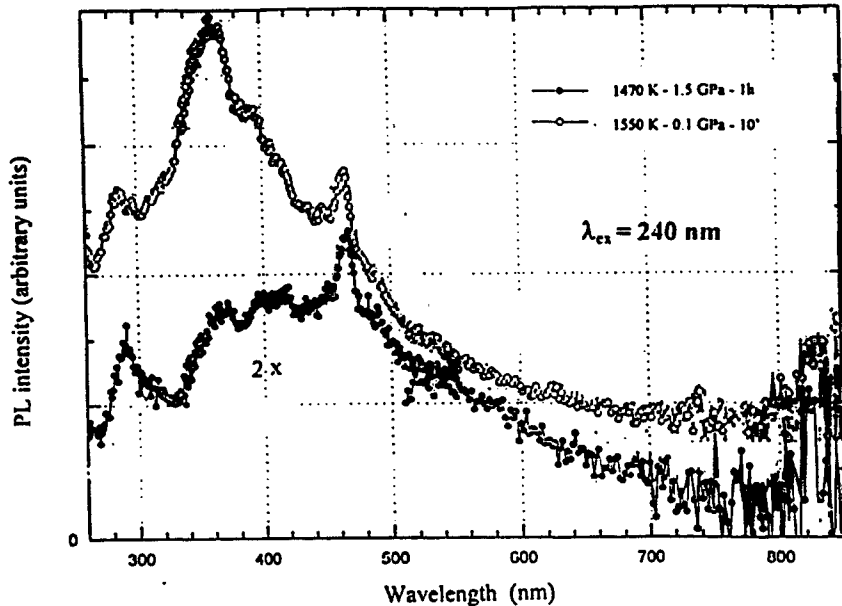


Figure 9. PL spectra from 120 nm thick  $\text{Si}_3\text{N}_4$  / Si samples ( $\text{Si}_3\text{N}_4$  deposited at 920 K by LPCVD method from silane -  $\text{NH}_3$  mixture) after subjecting to HT - HP treatments at 1470 K - 1.5 GPa for 1 h and at 1550 K - 0.1 GPa for 10'. PL excitation wavelength  $\lambda = 240$  nm.

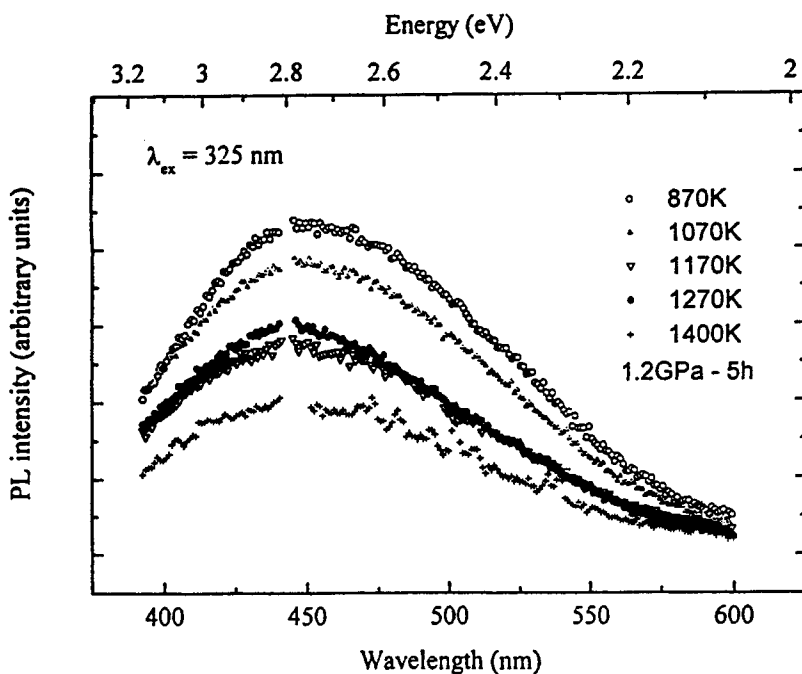


Figure 10. PL spectra from 120 nm thick  $\text{Si}_3\text{N}_4$  / Si samples treated at 870 - 1400 K - 1.2 GPa for 5 h.

The treatment of such samples at 1470 K - 1.5 GPa for 1 h resulted in much weaker PL (Fig. 9). A very broad PL band in the 400 - 550 nm region was observed for the  $\text{Si}_3\text{N}_4$  / Si samples treated at 870 - 1400 K - 1.2 GPa for 5 h ( $\lambda_{\text{ex}} = 325$  nm). The intensity of this PL band diminished with increasing treatment temperature (Fig. 10). The intensity of PL in the 400 - 550 nm region did not depend much on pressure and time of treatment at 1470 K but practically disappeared for the  $\text{Si}_3\text{N}_4$  / Si samples treated at 1550 K - 1.5 GPa for 30' (Fig. 11).

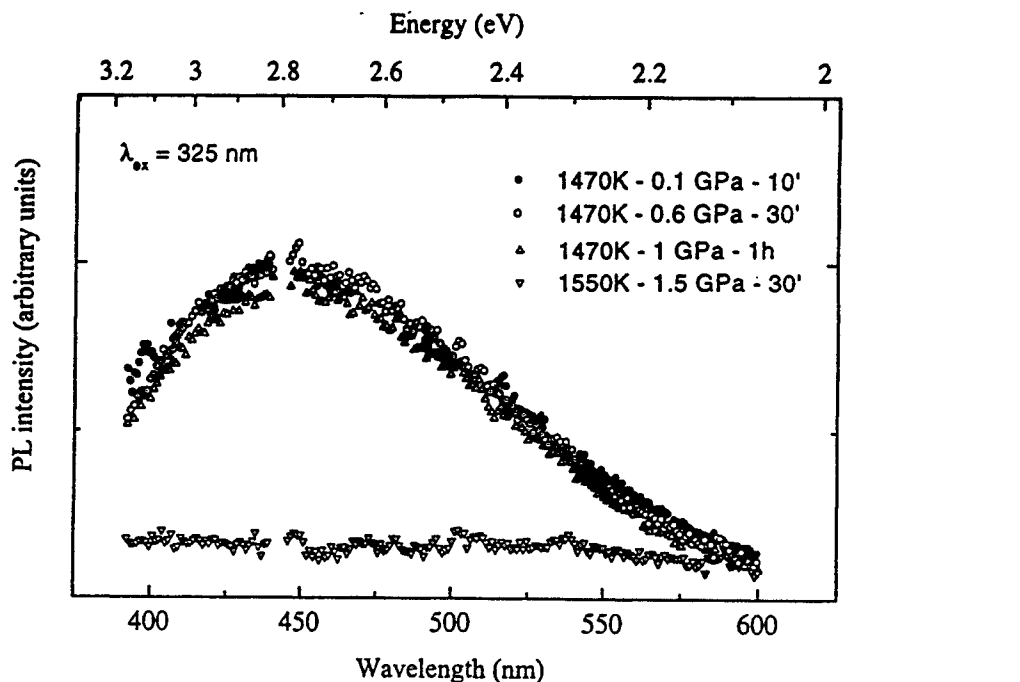


Figure 11. PL spectra from 120 nm thick  $\text{Si}_3\text{N}_4$  / Si samples after subjecting to HT - HP treatments at 1470 and 1550 K. PL excitation wavelength  $\lambda = 325$  nm.

#### 4. Discussion

The HT - HP treatment effect (at up to 1550 K, 1.5 GPa, 10 h) on the photoluminescence properties of thin films (up to 1.2  $\mu\text{m}$  thickness) of  $\text{SiO}_2$ ,  $\text{Si}_3\text{N}_4$  and of silicon implanted silicon dioxide,  $\text{SiO}_2$  : Si, on the single crystalline Cz-Si surface, is investigated in this work. All investigated films were prepared by oxidation of Cz-Si or by deposition of the respective material, so in fact the HT - HP effect on PL of the  $\text{SiO}_2$  / Si,  $\text{SiO}_2$  : Si / Si and  $\text{Si}_3\text{N}_4$  / Si systems was investigated.

Our results are "hot": they are the first obtained on the title subject. This paper contains mostly new results (only some of them were already published [5, 6, 8]). In spite of performed investigations, many problems need further investigation and many questions remain to be answered. The presented discussion and conclusions are of preliminary character and demand deepening in future.

Most results were obtained on the HT - HP treated  $\text{SiO}_2/\text{Si}$  and  $\text{SiO}_2 : \text{Si}/\text{Si}$  samples. They will be discussed jointly because, as it seems, the effects of HT - HP treatment are somewhat similar in both systems.

#### 4. 1. PHOTOLUMINESCENCE FROM HT - HP TREATED SILICON DIOXIDE AND SILICON IMPLANTED SILICON DIOXIDE FILMS

To avoid, at least partially, problems with distinguishing real PL and the peaks from scattered radiation, we performed PL measurements using different excitation wavelengths (240, 250, 325 and 488 nm). One rather striking observation concerned lack of proportionality between the  $\text{SiO}_2$  thickness and the PL signal intensity, which suggests that the "PL - related" HT - HP induced transformations in  $\text{SiO}_2 / \text{Si}$  are related to that at the  $\text{SiO}_2 / \text{Si}$  interface. Some PL results for the  $\text{SiO}_2 / \text{Si}$  samples are recapitulated (see also Figs 1 - 4) in the simplified form (only positions of PL peaks are presented, not accounting for their width and shape) in Table 1.

Table 1. PL peaks observed at RT from the  $\text{SiO}_2 / \text{Si}$  samples subjected to specified HT - HP treatment. 290 nm thick  $\text{SiO}_2$  film was grown on Cz-Si wafer by annealing at 1470K in a wet oxygen ( $\text{O}_2 + \text{H}_2$ ) for 10 minutes.

HT - HP, K - GPa - time	Excitation wavelength, nm	PL peaks, nm
1170 - 1.2 - 5 h	240	360 (?), 460(?)
" " " " "	325	480
1470 - 1.5 - 1 h	240	305, 340, 460(?)
" " " " "	325	460
1550 - 1.5 - 10'	240	305, 460

The PL peak at 460 - 480 nm was detected for the HT - HP treated  $\text{SiO}_2/\text{Si}$  samples (for excitation wavelength  $\lambda_{\text{ex}} = 325$  nm). In the case of excitation by 240 nm wavelength, this PL line seems to be superimposed on the scattered radiation peak. The 460 nm peak was shifted to higher energies for the samples treated at "severe" HT - HP conditions and disappeared after the 1550 K - 1.5 GPa - 2 h treatment (Fig. 3).

If using  $\lambda_{\text{ex}} = 240$  nm the peaks at 290 - 305 nm and 340 nm were detected for the samples treated at the highest temperatures and pressures (Figs 1, 2, Table 1), whereas the 360 nm PL peak (Fig. 10) was observed for the samples treated at lower temperature and pressures or for more short time.

The violet (at 432 nm) and yellow (at 561 nm) PL bands were reported for silicon dioxide thin films annealed by the RTA method [9]. PL at about 2.9 eV (430 nm) was detected for silicon oxide thin films prepared by dual plasma CVD [10]. This may be related to a defect associated with the OH groups. Radiation - induced PL from silica

reported for about 2.7 eV (460 nm), 3.1 eV (410 nm) and 4.3 eV (290 nm) is probably related to the presence of an "oxygen deficient center" (ODC) [11].

The PL band at 420 - 480 nm can originate from the nanocrystalline silicon formed in the  $\text{SiO}_2/\text{Si}$  interface by thermal energy and thermal strain [9]. Other PL peaks can be related to some defects created in the  $\text{SiO}_2$  film volume at HT - HP.

Photoluminescence spectra from the HT - HP treated  $\text{SiO}_2 : \text{Si}$  samples are presented in Figs 5 - 8 and data are summarised for some samples in Table 2.

Table 2. PL peaks from the  $\text{SiO}_2 : \text{Si}/\text{Si}$  samples subjected to specified HT - HP treatment. 500 nm thick  $\text{SiO}_2$  film on Cz-Si wafer was VHD - implanted with  $\text{Si}^+$  ions.

HT - HP, K - GPa - time	Excitation wavelength, nm	PL peaks, nm
720 - 0.01 - 10h	250	360, 460, 600 [5]
- „ - „ - „ -	488	650
720 - 1.5 - 10h	250	360, 460, 600 [5]
- „ - „ - „ -	488	not observed
720- 0.01-10 h + 1400K-1.2GPa-5h	488	700
720 - 1.5-10 h + 1400K-1.2GPa-5h	488	680

For the samples subjected to treatments at 720 K, the PL lines at 360, 460, 600 and 650 nm were detected (see also [5, 6]), whereas for that treated additionally at 1400K - 1.2 GPa - at 340 and 420 nm (for  $\lambda_{\text{ex}} = 250$  nm). A quite different PL band (at about 640 - 700 nm) was detected for such samples if excited by  $\lambda_{\text{ex}} = 488$  nm. This band is similar to that reported for the HT - HP treated bulk silicon samples [12].

An unique explanation of PL induced by HT - HP treatments in the  $\text{SiO}_2/\text{Si}$  and  $\text{SiO}_2:\text{Si}/\text{Si}$  samples is impossible at present. It is probable, however, that the origin of PL (especially at 460 nm) is the same for  $\text{SiO}_2/\text{Si}$  and  $\text{SiO}_2:\text{Si}/\text{Si}$  samples, and that the wide PL band at 460 nm is related to silicon nanoclusters created at the Si rich region of the  $\text{SiO}_2/\text{Si}$  interface in effect of pressure and thermally induced strains [9].

It is known that diffusivity of oxygen and probably of silicon decreases at HP [13] and that more small cluster - like defects are created at HT - HP, at least for the case of Si - O system [14]. This means that at HT - HP conditions, more silicon - related defects (possibly of the  $\equiv\text{Si}-\text{Si}\equiv$  centres [5], "responsible" mainly for PL at 360 nm) will be created in the  $\text{SiO}_2:\text{Si}$  film volume, whereas Si clusters ("responsible" for PL at 460 nm) would be created at the  $\text{SiO}_2/\text{Si}$  and  $\text{SiO}_2:\text{Si}/\text{Si}$  interfaces. Because of the mentioned diminished silicon diffusivity at HT - HP, the dimensions and concentration of the Si - related defects in the  $\text{SiO}_2:\text{Si}$  thin film volume would be comparatively less dependent on the treatment temperature and time (but not on HP, because just HP results in larger concentration of such defects).

Such qualitative explanation accounts for ultraviolet / visible PL from the HT - HP treated  $\text{SiO}_2$  / Si samples (creation of Si nanoclusters at the Si rich regions of the  $\text{SiO}_2$  / Si interface [9]) and the shift of this PL line to higher wavelength with treatment time (related to the growth of dimensions of the Si nanoclusters created at the mentioned interface). The rise of PL intensity with HP in the  $\text{SiO}_2$ :Si/Si system can be related to stress stimulated creation of the  $\equiv\text{Si-Si}\equiv$  centres in the  $\text{SiO}_2$  "bulk" [5]. Above explanation does not exclude, of course, other possible sources of HP - HT induced ultraviolet or visible PL: creation of "oxygen sufficient structures" [9] or of ODC [11].

#### 4. 2. PHOTOLUMINESCENCE FROM HT - HP TREATED SILICON NITRIDE FILMS

As it follows from our rather preliminary investigations (Figs 9 - 11), the HT - HP treatment of the  $\text{Si}_3\text{N}_4$ /Si samples results in PL at about 290 and 360 nm (for excitation at  $\lambda_{\text{ex}} = 240$  nm) or in the wide PL band peaking at about 450 nm (for excitation at  $\lambda_{\text{ex}} = 325$  nm). The last is probably also present in the PL spectra obtained using  $\lambda_{\text{ex}} = 240$  nm, but it is "hidden" because of the overlap with scattered radiation (Fig. 9). The intensity of PL at 450 nm decreases with treatment temperature at constant HP = 1.2 GPa (Fig. 10) and as a result of the treatment at 1550 K - 1.5 GPa - 30' (Fig. 11). The intensity of PL lines at 290 nm and 360 nm was the highest after the short time sample treatment at 1550 K (Fig. 9).

As prepared thin (120 nm)  $\text{Si}_3\text{N}_4$ /Si samples did not indicate measurable PL. For the thicker samples (300 nm) the wide PL band at 450 - 600 nm as well as comparatively narrow PL line at 390 nm and wide PL band at about 520 nm were reported (for excitation by  $\lambda_{\text{ex}} = 350$  nm) [7]. It seems that PL induced by the HT - HP treatment can be related (as in the case of discussed above  $\text{SiO}_2$ /Si and  $\text{SiO}_2$ :Si/Si) to the stress stimulated creation of silicon nanoclusters at the  $\text{Si}_3\text{N}_4$ /Si interface.

#### 5. Conclusions

High pressure - high temperature treatment of  $\text{SiO}_2$ ,  $\text{SiO}_2$ :Si and  $\text{Si}_3\text{N}_4$  thin films on single crystalline silicon surface results in the appearance of visible and ultraviolet photoluminescence, as well as in enhancement of photoluminescence intensity from the  $\text{SiO}_2$ :Si samples containing silicon nanoclusters, in comparison to that from the samples subjected to similar processing but at atmospheric pressure. Further work in this field can help to reveal the physics of processes responsible for ultraviolet / visible PL in such systems and in improving of the existing technology.

**Acknowledgements** The authors thank m.sc. A.Wnuk from the Institute of Electronic Materials Technology, Warsaw and Mr F. Froeb from the Technical University, Dresden for their help in PL measurements as well as Mr T. Koska and Mr M. Rozental from the Institute of Electron Technology, Warsaw for sample preparation. This work was supported in part by the Polish Committee for Scientific Research (grants 8T11B 009 13 and 7T08A 057 17).

## References

1. Soref, R. (1998) Application of silicon - based optoelectronics, *MRS Bulletin*, **23**, 20-24.
2. Tsysbekov, L. (1998) Nanocrystalline silicon for optoelectronic applications, *MRS Bulletin*, **23**, 33-38.
3. Misiuk, A., Zaumseil, P. (1995) Hydrostatic pressure treatment techniques for investigation of semiconductor defect structure, *Proceed. ESC / ESSDERC Symposium ALTECH 95, Electrochemical Soc. Proceed.*, **95-30**, 194-203.
4. Misiuk, A., Zaumseil, P., Antonova, I., Bak-Misiuk, J., Bugiel, E., Hartwig, J., Romano-Rodriguez, A. (1997) Defects in pressure - annealed Cz-Si and SiGe/Si, in J.Donecker and I.Rechenberg (eds.), *Proceed. Conference DRIP VII, Templin, Germany*, Institute of Physics Conf.Ser. No. 160, pp. 273-276.
5. Tyschenko, I.E., Rebohle, L., Yankov, R.A., Skorupa, W., Misiuk, A. (1998) Enhancement of the intensity of the short-wavelength visible photoluminescence from silicon-implanted silicon-dioxide films caused by hydrostatic pressure during annealing, *Appl.Phys.Lett.*, **73**, 1418-1420.
6. Tyschenko, I.E., Rebohle, L., Yankov, R.A., Skorupa, W., Misiuk, A. , Kachurin, G.A. (1999) The effect of annealing under hydrostatic pressure on the visible photoluminescence from Si<sup>+</sup>- ion implanted SiO<sub>2</sub> films, *J.Luminescence*, **80**, 229-233.
7. Tyschenko, I.E., Volodin, V.A., Rebohle, L., Voelskov, M., Skorupa, W. (1999) Photoluminescence from Si<sub>3</sub>N<sub>4</sub> films implanted with Ge<sup>+</sup> and Ar<sup>+</sup> ions, *to be published in Semiconductors*, **33**.
8. Misiuk, A., Surma, B., Rebohle, L., Jun, J., Antonova, I.V., Tyschenko, I., Romano-Rodriguez, A., Lopez, M. (1999) Luminescence properties of oxygen-containing silicon annealed at enhanced argon pressure, *phys.stat.sol. (b)*, **211**, 233-238.
9. Choi, W.C., Lee, M-S., Kim , E.K., Kim, C.K., Min, S-K., Park, C-Y., Lee, J.Y. (1996) Visible luminescences from thermally grown silicon dioxide thin films, *Appl.Phys.Lett.*, **69**, 3402-3404.
10. Zhu, M., Han, Y., Wehrspohn, R.B., Godet, C., Etemadi, R., Ballutaud, D. (1998) The origin of visible photoluminescence from silicon oxide thin films prepared by dual-plasma chemical vapor deposition, *J.Appl.Phys.*, **83**, 5386-5393.
11. Meinardi, F., Paleari, A. (1998) Native and radiation-induced photoluminescent defects in SiO<sub>2</sub>: Role of impurities, *Phys.Rev. B*, **58**, 3511-3514.
12. Karwasz, G.P., Misiuk, A., Ceshini, M., Pavese, L. (1996) Visible photoluminescence from pressure annealed intrinsic Czochralski grown silicon, *Appl.Phys.Lett.*, **69**, 2900-2902.
13. Antonova, I.V., Misiuk, A., Popov, V.P., Plotnikov. A.E., Surma, B. (1998) Nucleation and formation of oxygen precipitates in Czochralski grown silicon annealed under uniform stress conditions, *Physica B*, **B 253**, 131-137.
14. Misiuk, A. (1997) Uniform stress effect on initial stages of oxygen precipitation in Czochralski grown silicon, in J.Zmija, A.Majchrowski, J.Rutkowski, J.Zielinski (eds.) *Solid State Crystals: Growth and Characterisation, Proceed. SPIE*, **3278**, 230-237.

---

## CoPt AND FePt THIN FILMS FOR HIGH DENSITY RECORDING MEDIA

J. A. Christodoulides <sup>1</sup>, Y. Zhang <sup>1</sup>, G. C. Hadjipanayis <sup>1</sup>,  
I. Panagiotopoulos <sup>2</sup> and D. Niarchos <sup>2</sup>

<sup>1</sup> Department of Physics & Astronomy, University of Delaware, Newark,  
DE 19716, USA

<sup>2</sup> Institute of Material Research NCSR "Demokritos", Ag. Paraskevi  
Attiki, 153 10 Greece

### Abstract

Granular CoPt/C and FePt/C films, consisting of nanoparticles of the highly anisotropic fct CoPt (FePt) phase embedded in a carbon matrix, were made by co-sputtering from pure Co<sub>50</sub>Pt<sub>50</sub> (Fe<sub>50</sub>Pt<sub>50</sub>) and C targets using a tandem deposition mode. The as-made films showed a disordered face centered cubic (fcc) structure, which was magnetically soft and had low coercivity. Magnetic hardening occurred after heat treatment at elevated temperatures, which led to increase in coercivity with values up to 15 kOe. The hardening originated from the transformation of the fcc phase to a highly anisotropic face centered tetragonal phase (fct) with anisotropy  $K > 10^7$  erg/cm<sup>3</sup>. Transmission electron microscopy studies showed FePt particles embedded in C matrix with a particle size increasing from below 5 nm in the as-made state to 15 nm in the fully annealed state. These results are very promising and make these materials potential candidates for high-density magnetic recording.

### 1. Introduction

FePt and CoPt alloys with compositions close to equiatomic have been studied extensively in the past, as possible candidates for permanent magnets [1], because of the large value of magnetocrystalline anisotropy of the ordered fct phase. This resulted in coercivities greater than 5 kOe. These alloys undergo a phase transformation at 1300°C for FePt and 800°C for CoPt, from a disordered face centered cubic (fcc) phase at higher temperatures to an ordered face centered tetragonal (fct) phase at lower temperatures. Recently these alloys were prepared in the form of thin films receiving considerable attention for magnetic recording and magneto-optical recording applications [2].

Requirements for higher magnetic recording density with low noise impose the need of a material consisting of magnetically isolated grains with size below 10 nm<sup>3</sup>. In such small grain sizes high magnetocrystalline anisotropy is needed to avoid thermal

fluctuations and demagnetizing fields that tend to destabilize the magnetization of the recorded bits [3]. Current studies have been focused on nanocrystalline rare-earth compounds and CoPt and FePt because of their high anisotropy. Granular CoPt/C films consisting of Co-rich hexagonal Co-Pt particles in a C matrix have been reported by Delaunay et al. [4]. However, the films had a low coercivity because of the lower anisotropy of the hexagonal Co-rich phase. We have recently started a program to obtain nanocomposite CoPt/M and FePt/M (M = Ag, C) films consisting of magnetically hard CoPt (FePt) nanoparticles in a non-magnetic matrix. In this study we prepared nanocomposite CoPt/C and FePt/C films consisting of the highly anisotropic tetragonal phase with coercivities in the range of 2-9 kOe and studied the effects of particle size, temperature and interparticle interactions on the coercivity.

## 2. Experimental

The granular structure was obtained by first depositing CoPt/C or FePt/C in a multilayer form (consisting of 100 repetitions) and subsequently annealing the samples in the temperature range of 500-900°C. The films were prepared by magnetron sputtering deposition from pure 1.3 inch targets of Co<sub>50</sub>Pt<sub>50</sub> or Fe<sub>50</sub>Pt<sub>50</sub> and C. The base pressure of the chamber was  $3 \times 10^{-8}$  Torr and high purity Ar (99.9999%) was used for deposition at ambient temperature with a pressure of 5 mTorr. The substrates used were Si(100), 600  $\mu$ m thick with a naturally grown oxide on the surface. A 150 Å buffer layer of C was used to ensure similarity of growth conditions. The C layers were sputtered using a power of 60 W DC at a rate of 0.3 Å/sec. For CoPt and FePt a DC power of about 10 W gave a growth rate of 1.4 Å/sec and the resulting stoichiometry of the layers was found to be Co<sub>54</sub>Pt<sub>46</sub> and Fe<sub>49</sub>Pt<sub>51</sub>. The chemical composition of CoPt and FePt as-made films was checked by energy dispersive x-ray analysis. X-ray diffraction (XRD) spectra were collected with a PHILIPS powder diffractometer using Cu-K $\alpha$  radiation. Magnetic hysteresis loops were measured with an Oxford MagLab VSM and a Quantum Design MPMSR2 SQUID magnetometer. The microstructure was examined with a Philips CM20 and a Jeol JEM-2000 FX TEM transmission electron microscopes (TEM).

## 3. Results and Discussion

All the as-made films were magnetically soft and became hard after annealing at temperatures between 600-780°C. The development of hysteresis loops was found to be sensitive to the layer thickness. A summary of the hysteresis loop parameters of CoPt/C samples, with different bilayers thickness, after annealing at different temperatures and times

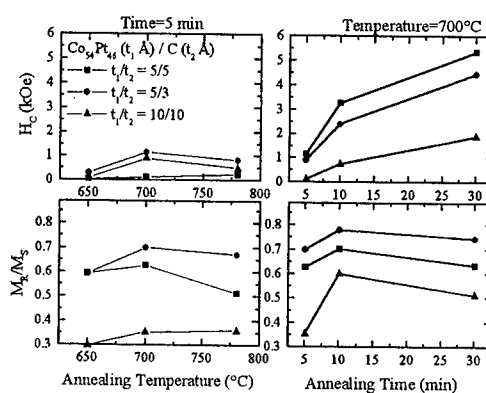


Figure 1. Coercivity and reduced remanence as a function of annealing temperature and time.

is shown in figure 1. Higher reduced remanence ( $M_r/M_s$ ) reaching a value of 0.78, is obtained for the less C-containing  $\text{Co}_{54}\text{Pt}_{46}(5\text{\AA})/\text{C}(3\text{\AA})$  sample whereas a higher coercivity (5.4 kOe) is observed for the higher C-content  $\text{Co}_{54}\text{Pt}_{46}(5\text{\AA})/\text{C}(5\text{\AA})$ . The loops were measured with the applied field in the film plane. Thus the remanence enhancement above the value expected (0.5) for randomly distributed uniaxial single-domain particles [5] must be attributed to interparticle interaction effects. In figure 2 (a-c) the demagnetization curves for  $\text{Co}_{54}\text{Pt}_{46}/\text{C}$  samples annealed at 700°C for 5-30 min with various layer thickness are shown. For longer annealing times the coercivity increases but the  $M_r/M_s$  ratio decreases and finally a shoulder in the demagnetization curves develops after long annealing times. This shoulder is more pronounced in samples with higher Pt content ( $\text{Co}_{45}\text{Pt}_{55}$ ) where it develops even for short annealing times. There are several possibilities for this behavior. One of them may be related to the formation of large multidomain particles. The other reasons may be related to the formation of fcc CoPt phases, which form during aging. An indication for the  $\text{CoPt}_3$  phase is the fact that the shoulder is more pronounced in samples with higher Pt content. Furthermore these Pt-richer samples show a greater reversibility in the demagnetization curves as would be expected in nanocomposite magnets where the soft-phase exchange coupled to the magnetically hard fct-CoPt phase [6]. Figure 3 shows magnetic data on FePt/C samples with different bilayer thickness annealed at 700°C for 10 minutes where the fct-FePt phase was observed. At smaller carbon thickness (3 Å) the  $H_c$  values were larger and the hysteresis loops showed a higher  $M_r/M_s$  ratio (0.82).

The development of magnetic hysteresis in annealed samples was closely related to the microstructure, which was obtained by transmission electron microscopy. The evolution of microstructure with aging heat treatment at 700°C is shown in figure 4 for the  $\text{Co}_{54}\text{Pt}_{46}(5\text{\AA})/\text{C}(3\text{\AA})$ . The as-deposited films were found to consist of tiny particles (5 nm) with the disordered fcc structure (Fig. 4a). Upon aging, the ordered fct phase is formed and the particle size increases. After 10 minutes at 700°C the electron

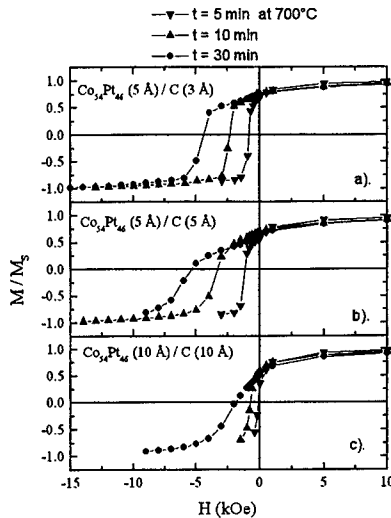


Figure 2. Demagnetization curves for  $\text{Co}_{54}\text{Pt}_{46}(t_1 \text{\AA})/\text{C}(t_2 \text{\AA})$  samples annealed for 5-30 minutes at 700°C with different  $t_1, t_2$ .

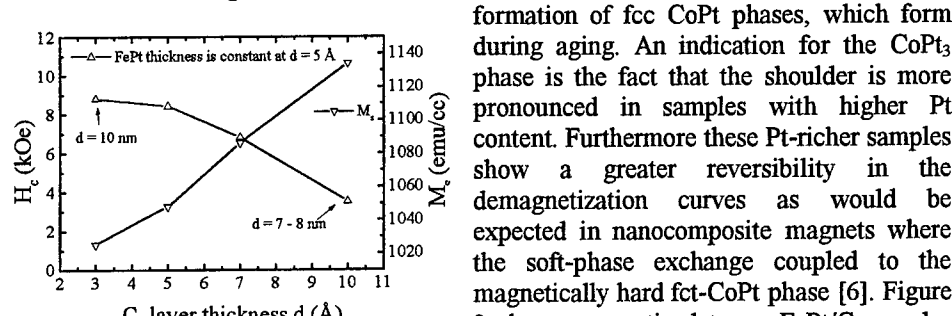


Figure 3. Coercivity and magnetization saturation as a function of carbon layer thickness.

Figure 3 shows magnetic data on FePt/C samples with different bilayer thickness annealed at 700°C for 10 minutes where the fct-FePt phase was observed. At smaller carbon thickness (3 Å) the  $H_c$  values were larger and the hysteresis loops showed a higher  $M_r/M_s$  ratio (0.82).

The development of magnetic hysteresis in annealed samples was closely related to the microstructure, which was obtained by transmission electron microscopy. The evolution of microstructure with aging heat treatment at 700°C is shown in figure 4 for the  $\text{Co}_{54}\text{Pt}_{46}(5\text{\AA})/\text{C}(3\text{\AA})$ . The as-deposited films were found to consist of tiny particles (5 nm) with the disordered fcc structure (Fig. 4a). Upon aging, the ordered fct phase is formed and the particle size increases. After 10 minutes at 700°C the electron

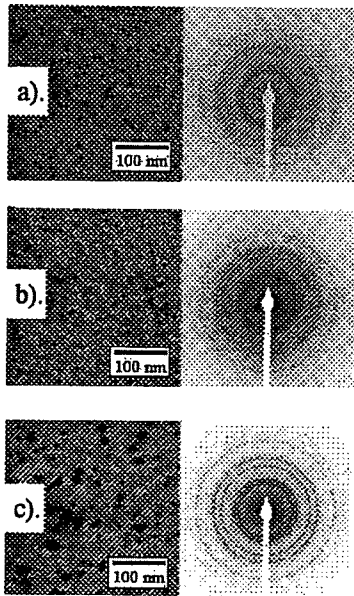


Figure 4. Evolution of microstructure of CoPt/C films: (a) as-made, (b) annealed at 700°C for 10 min and (c) annealed at 700°C for 60 min.

completely due to the long-range nature of the dipole interactions.

For most of the samples studied the size of the CoPt particles is well below the single domain size of the fct-CoPt phase which is around  $0.6 \mu\text{m}$ , so magnetization reversal should be based on a coherent rotation mechanism. For coherent rotation in a random distribution of non-interacting particles with uniaxial anisotropy  $K$  the coercivity is given by  $H_c = 0.96K/M_s$  [9]. This would lead to an  $H_c \sim 59 \text{ kOe}$  if the bulk value of  $K \sim 4.9 \cdot 10^7 \text{ erg/cm}^3$  is used. The values of the measured coercivity are smaller by one order of magnitude. This large discrepancy may be due to several factors. One could attribute this to the size dependence of coercivity, which for an assembly of randomly orientated non-interacting particles will be [10] proportional to  $1-(V_p/V)^{2/3}$  where  $V_p$  is the critical volume for superparamagnetism, estimated by  $KV_p = 25kT$ . Our TEM studies show that particle size is in the range 7-26 nm that would account only for a reduction of coercivity around 20%. Another

diffraction patterns show clearly the presence of ordered peaks corresponding to fct CoPt and the particles grow bigger (7-12 nm) (Fig. 4b). After prolonged heat treatment (60 min) the SAD patterns are more ordered and the particles become larger (8-26 nm) (Fig. 4c). In addition very large (micron size) particles of CoPt are found to coexist with the smaller particles.

An important parameter that is known to determine media noise is the magnetic isolation of the grains. This parameter can be controlled basically by the amount of carbon in the system, which determines the interparticle separation and therefore the interparticle interactions.  $\delta M$  plots [7] have been used to study interaction effects as shown in figure 5. Positive  $\delta M$  ( $\delta M_{\text{norm}} = M_d - 1 + 2M_p$ ) indicates the presence of exchange interactions while negative means dipolar interactions. The optimally annealed CoPt(5 Å)/C(5 Å) sample shows, around  $H_c$ , a small amount of positive exchange-type interactions (Fig. 5a) superimposed over a negative contribution due to magnetostatic interactions. Positive interactions are completely suppressed in higher C content samples CoPt(5 Å)/C(10 Å) (Fig. 5b) where only the negative magnetostatic part remains. This part of course is difficult to eliminate

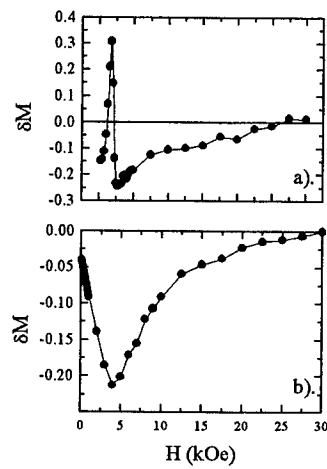


Figure 5.  $\delta M$  plots for (a) Co<sub>45</sub>Pt<sub>55</sub>(5 Å)/C(5 Å) and (b) Co<sub>45</sub>Pt<sub>55</sub>(5 Å)/C(10 Å) samples.

possibility for the explanation of this discrepancy is the consideration of the interaction effects, which are expected to lead to remanence enhancement accompanied by reduction of the coercivity [11]. However, for interactions large enough to give  $M_r/M_s = 0.78$  the expected reduction of coercivity is around 10% [12]. Therefore, interaction effects may lead to some coercivity reduction in the samples where the grains are not magnetically isolated but cannot explain the large difference that is observed even in samples with isolated grains. This difference must be attributed mainly to the fact that for the relatively short annealing times, which are used to optimize the microstructure, the ordering of the fct phase is not complete. The splitting of the (002)-(200) reflections in the XRD patterns corresponds to a ratio  $c/a = 0.99$  compared to the bulk value of  $c/a = 0.97$ . Because of this the anisotropy is expected to be lower than that of the bulk value.

#### 4. Conclusions

In summary, we were very successful in fabricating high coercivity CoPt/C and FePt/C granular films consisting of highly anisotropic ordered fct CoPt or FePt nanoparticles embedded in an amorphous C matrix. The particle size and isolation and therefore the coercivity of the films can be varied by controlling the layer thickness and the aging heat treatment conditions. The results of this study are very promising and make these materials attractive as candidates for magnetic recording.

#### 5. Acknowledgments

This work has been supported by NSF-DMR 9307676.

#### 6. References

1. Darling, S. (1963), *Platinum Met. Rev.* **7**, 96; Gebhardt, E. and Köster, W. (1940), *Z. Metallkunde* **32**, 253.
2. Yanagisawa, M. Yamaguchi, N. and Suganuma, Y. (1983), *IEEE Trans. Mag.* **19**, 1638.
3. Tsang, C. Chen, M. M. and Yogi, T. (1993), *Gigabit-Density Magnetic Recording*, Proc. IEEE **81**, 1344.
4. Delaunay, J. Hayashi, T. Tomita, M. Hirono, S. and Umemura, S. (1997), *CoPt/C Nanogranular Magnetic Thin Films*, *Appl. Phys. Lett.* **71**, 3427.
5. Stoner, E. C. and Wohlfarth, E. P. (1948), *A Mechanism of Magnetic Hysteresis in Heterogeneous Alloys*, *Philos. R. Soc. A* **240A**, 599.
6. Panagiotopoulos, I. Withanawasam, L. and Hadjipanayis, G. (1996), *Exchange Spring Behavior in Nanocomposites Hard Magnetic Materials*, *J. Magn. Magn. Mat.* **152**, 353.
7. Henkel, O. (1974), *Phys. Stat. Sol.* **7**, 919.
8. Joffe, I. (1969), *J. Phys. C* **2**, 1537.

---

1

9. Cullity, B. D. (1972) *Introduction to Magnetic Materials*, Addison-Wesley.
10. Pfeifer, H. (1990), *Phys. Stat. Sol. A***118**, 295.
11. Crabbe, M. W. Davies, H. A. and Buckley, R. A. (1994), *Remanence Enhancement in Nanostructured Melt Spun Sm(Fe<sub>0.209</sub>Cu<sub>0.061</sub>Zr<sub>0.025</sub>Co<sub>0.704</sub>)<sub>7.61</sub>*, *IEEE Trans. Mag.* **30**, 696.
12. Hadjipanayis, G. (1979), Ph.D. Thesis, University of Manitoba.

## UNIDIRECTIONAL ANISOTROPY IN MANGANITE BASED FERROMAGNETIC-ANTIFERROMAGNETIC MULTILAYERS

I. PANAGIOTOULOS<sup>1</sup>, C. CHRISTIDES<sup>2</sup>,  
M. PISSAS<sup>1</sup>, AND D. NIARCHOS<sup>1</sup>

1. *Institute of Materials Science, NCSR “Demokritos”*,

*Ag. Paraskevi Attiki, 153 10 Greece*

2. *Department of Engineering Sciences, School of Engineering*  
*University of Patras, 26110 Patras, Greece*

### 1. Introduction

In mixed valence manganites a large negative magnetoresistance (MR), termed colossal magnetoresistance [1] (CMR), can be obtained due to a metal-insulator transition at the ferromagnetic Curie point [2]. However little progress has been made towards using these materials in applications, mainly due to the strong temperature dependence of the CMR effect and the large saturation fields (of the order of Tesla) required. Tunneling and grain boundary effects [3-8] as well as interface scattering [9] seem promising towards getting useful MR in these materials. In particular the high degree of spin polarization [10] makes these materials promising for spin-electronic device applications.

In view of the above considerations, recently several publications have focused on the study of trilayers and multilayers based on mixed valence manganites [11-20]. The magnetic and magnetotransport properties of such structures are not a mere superposition of the response of the individual layers. This is a result of possible interface scattering [11-17], interlayer interactions [19,20] and stress effects due to lattice mismatch between the layers [11,12,14,16].

The sensitivity of double exchange and superexchange interactions to Mn-O bond lengths and Mn-O-Mn bond angles has been used as a structural tuning mechanism of magnetic and MR properties in bulk CMR manganites [21,22]. Such changes can be engineered through various substitutions that alter the configuration of Mn-O octahedra. In epitaxial thin films, strain due to lattice mismatch can give rise to structural deformations. Thus, depending on the substrate used, the film can be under ductile or tensile strain that results in changes of magnetic anisotropy and MR properties [23-27].

In what follows we report on the magnetic structural and MR properties of  $\text{La}_{2/3}\text{Ca}_{1/3}\text{MnO}_3/\text{La}_{1/3}\text{Ca}_{2/3}\text{MnO}_3$  multilayers showing exchange biasing effects. The  $\text{La}_{2/3}\text{Ca}_{1/3}\text{MnO}_3$  layers are ferromagnetic (FM) and  $\text{La}_{1/3}\text{Ca}_{1/3}\text{MnO}_3$  layers are antiferromagnetic (AF) [28]. The structural compatibility of the AF and FM layers permits coherent growth of the superlattices that satisfy the conditions for magnetic coupling at the interfaces.

The existence of unidirectional anisotropy due to exchange coupling between a FM and an AF phase was first reported in oxide-coated fine particles of Co [29]. The exchange anisotropy results in a displaced magnetic hysteresis loop when the sample is field cooled through the Néel temperature of the AF phase. In early studies, this loop displacement has been explained by assuming an ideal FM/AF interface with uncompensated moments in the atomic-plane of the AF layer at the FM/AF boundary [29]. Up to date exchange anisotropy effects have been studied mainly in AF/FM systems consisting of transition metal alloys and metallic oxides (e.g. FM= Co, NiFe,  $\text{Fe}_3\text{O}_4$ , and AF=CoO, FeMn) [30], but not in manganites where the magnetic interactions cannot be described by direct-exchange.

## 2. Experimental details

The films were deposited on (001)  $\text{LaAlO}_3$  substrates by pulsed laser deposition (PLD) from bulk stoichiometric  $\text{La}_{2/3}\text{Ca}_{1/3}\text{MnO}_3$  target samples. The targets were prepared by standard solid state reaction from  $\text{La}_2\text{O}_3$ ,  $\text{CaCO}_3$  and  $\text{MnO}_2$  powders sintered at  $1300^\circ\text{C}$  for 5 days with two intermediate grindings. MR measurements were performed with a four-probe method and with the current parallel to the applied magnetic field. The  $\theta$ - $2\theta$  X-ray diffraction data were obtained with a Siemens D500 diffractometer using  $\text{CuK}\alpha$  radiation and a secondary graphite monochromator. The magnetic measurements were performed in a SQUID magnetometer (Quandum Design). A series of  $\text{La}_{2/3}\text{Ca}_{1/3}\text{MnO}_3/\text{La}_{1/3}\text{Ca}_{2/3}\text{MnO}_3$  multilayers with equal AF ( $t_{\text{AF}}$ ) and ( $t_{\text{FM}}$ ) FM layer thickness and bilayer thickness ( $\Lambda$ ) ranging from 2 to 32 nm were grown along the (001) direction of the simple pseudocubic perovskite unit cell. The structural compatibility of the AF and FM layers permits coherent growth that favors magnetic coupling. In order to deposit in a multilayer form, the targets were mounted on a step-motor controlled rotatable carrier that allows the  $\text{La}_{2/3}\text{Ca}_{1/3}\text{MnO}_3$  and  $\text{La}_{1/3}\text{Ca}_{2/3}\text{MnO}_3$  targets to be sequentially exposed in the beam path. The substrate was located at a distance of 6 cm from the target, by the edge of the visible extent of the plume. The substrate temperature ( $T_s$ ) was  $700^\circ\text{C}$  and the oxygen pressure in the chamber during the deposition was 0.03 Torr. The resulting rate at fluence of  $1.5 \text{ J/cm}^2$  on the target was  $0.4 \text{ \AA/pulse}$ .

## 3. Structural Characterization

The existence of the superstructure has been confirmed from the presence of low-angle superlattice Bragg-peaks and multiple satellite peaks around the (001), (002) and (003) Bragg-reflections of the constituents. In the low angle diffraction patterns the even order satellites are not observed due to the  $t_{\text{AF}}=t_{\text{FM}}=\Lambda/2$  condition.

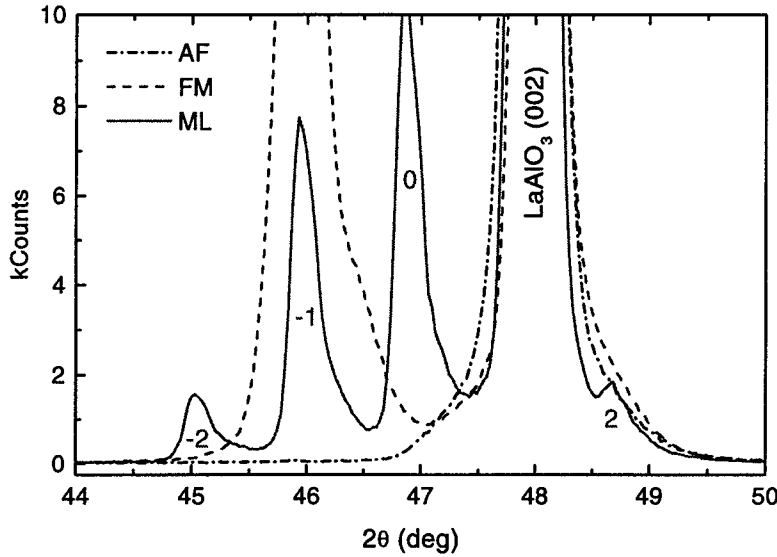


Figure 1. The XRD pattern of a multilayer sample compared to those of single AF and FM layers.

The main Bragg peak lies between the Bragg peaks observed in single AF and FM layer films and is surrounded by satellite peaks due to the layered structure (Fig.1). The existence of an average Bragg peak for  $\Lambda \leq 10\text{nm}$  indicates that for this range of bilayer thickness we have a coherent layer growth. The values of  $\Lambda$  were estimated by the formula  $\Lambda = n\lambda_{\text{Cu}}/2(\sin\theta_n - \sin\theta_0)$  where  $\theta_n$  are diffraction angles of the  $n$ -th order satellite and  $\theta_0$  is the average Bragg peak. The  $(00\ell)$  LAO Bragg-peaks ( $\ell=1, 2$ , and 3) interfere with the satellite peaks adjacent to the fundamental (zeroth order) peaks of the multilayer, introducing uncertainties in the quantitative analysis of the XRD spectra. Asymmetric intensity of the satellite peaks has been reported in multilayers in which a chemical and/or strained interfacial profile is assumed along the growth direction of the superlattice. Since for all the examined  $\Lambda$  values there are no traces of mixed  $(001)$  and  $(110)$  textures, cumulative roughness effects resulting to extra surface roughness and mosaic spread with increasing  $\Lambda$  can be excluded.

#### 4. Magnetization and Magnetoresistance Measurements

Magnetic hysteresis loops, measured at 10 K after cooling down from 300 K in zero field (ZFC) and in 10 kOe (FC), for a  $\text{LaAlO}_3/[\text{FM}(5\text{ nm})/\text{AF}(5\text{ nm})]_{15}$  sample are shown in Fig.2. It is evident that the ZFC loop is symmetric around the zero field, while the FC loop is shifted towards negative fields. This effect can be attributed to exchange biasing at the AF/FM interface, since single-layered FM films do not exhibit any loop displacement after the FC process. If  $H_1$  is the lower and  $H_2$  is the higher field value where the average film magnetization becomes zero, then the exchange biasing field is

defined as the loop shift  $H_{EB} = -(H_1 + H_2)/2$  and the coercivity as the halfwidth of the loop  $H_C = (H_1 - H_2)/2$ . Thus, we calculate for the FC loop an  $H_{EB} = 880$  Oe, and a  $H_C = 800$  Oe which is almost double compared to the  $H_C$  value obtained from the ZFC loop. Additional magnetic measurements were performed in order to investigate the origin of this effect. The temperature dependence of  $H_{EB}$  and  $H_C$  values is shown in

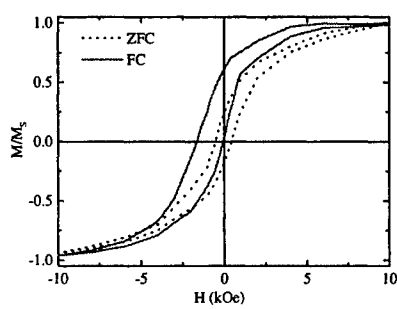


Figure 2. Hysteresis loops, measured at 10 K after cooling down from 300 K in zero field (ZFC) and in 10 kOe (FC), for the  $\Lambda=10$  nm multilayer.

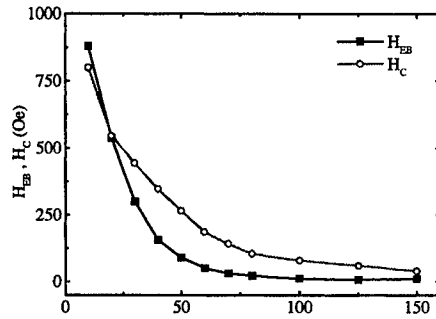


Figure 3. Temperature dependence of exchange biasing field ( $H_{EB}$ ) and coercive field ( $H_C$ ) for  $\Lambda=10$  nm multilayer.

Fig.3. These values were estimated from isothermal loops measured in constant temperature intervals, after FC the sample from 300 K down to 10 K in 10 kOe and then warming up. It is evident that  $H_{EB}$  decreases and disappears around the blocking temperature  $T_B$  of 70 K. The  $H_C$  values exhibit a similar trend, indicating a connection between the mechanisms that give rise to coercivity and loop displacement. The excess coercivity observed below  $T_B$  is induced by random exchange fields at the AF/FM interfaces. This low-temperature anisotropy can be treated as an additional energy barrier in the magnetic free energy, as in the case of superparamagnetic particles [23].

Since exchange biasing is an interface related phenomenon a strong dependence on the individual FM and AF layer thickness is expected. The maximum  $H_{EB}$  is observed for the sample with  $\Lambda=10$  nm.  $H_C$  follows the variation of  $H_{EB}$  with  $\Lambda$ , indicating that there is a significant contribution in  $H_C$  from the exchange anisotropy at the AF/FM interfaces. A decrease of  $H_{EB}$  at higher  $\Lambda$  is observed as expected due to the decreased contribution of the interfaces. However  $H_{EB}$  also decreases at lower  $\Lambda$  due to the decreased contribution of the AF layers.

Additional magnetic measurements were performed in order to investigate the origin of this effect. In Fig.4 the ZFC and FC measurements of the magnetization, normalized to the total FM volume of the sample, are shown for the above series of multilayers as a function of temperature. Both measurements were performed by warming up in 1 kOe after having cooled in zero field and 10 kOe respectively. The ZFC and FC curves coincide at temperatures higher than 100 K and become zero at about 250 K, where the Curie point  $T_C$  of the FM layers is expected. The ZFC curve exhibits a broad peak around the  $T_B$  70 K, whereas the FC curve exhibits a steep increase just below  $T_B$ . It is reasonable to assume that in the FC measurement an increase of magnetization results from the alignment of interfacial magnetic moments, giving rise to unidirectional

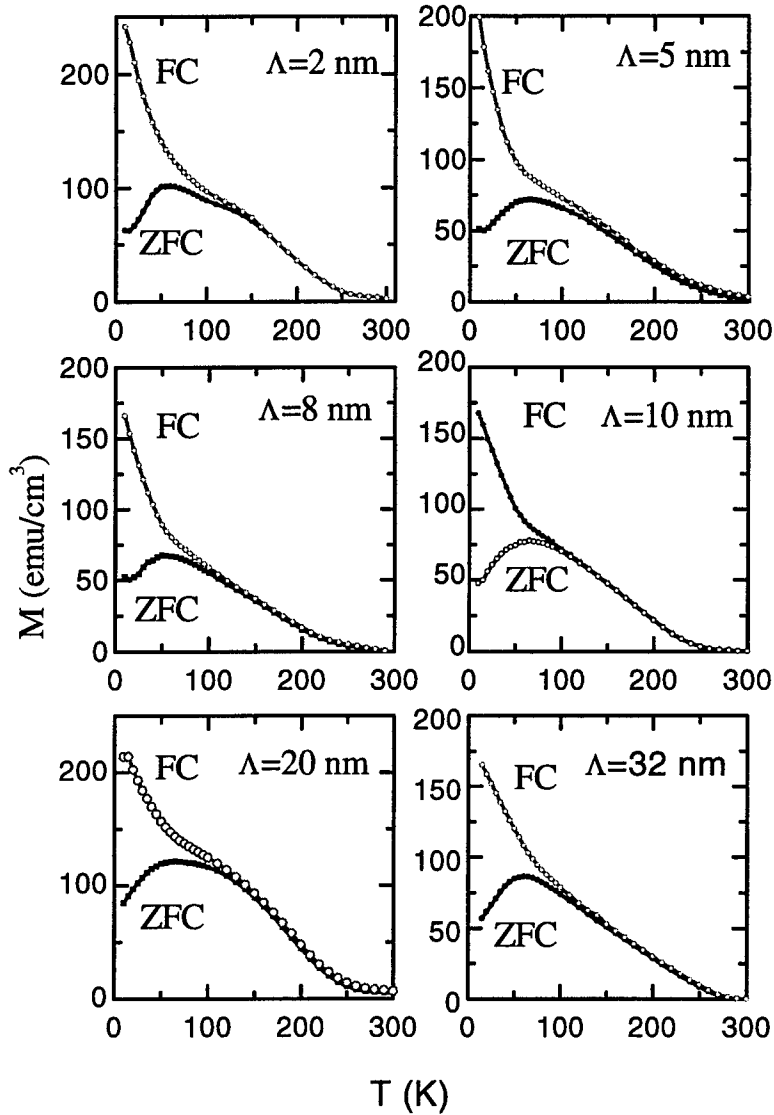


Figure 4. Magnetization as a function of temperature for the series of  $[FM(\Lambda/2nm)/AF(\Lambda/2nm)]_{15}$  multilayers. The measurements were performed by warming up in 1 kOe after having cooled down to 10 K, in zero field (ZFC) and 10 kOe (FC) respectively.

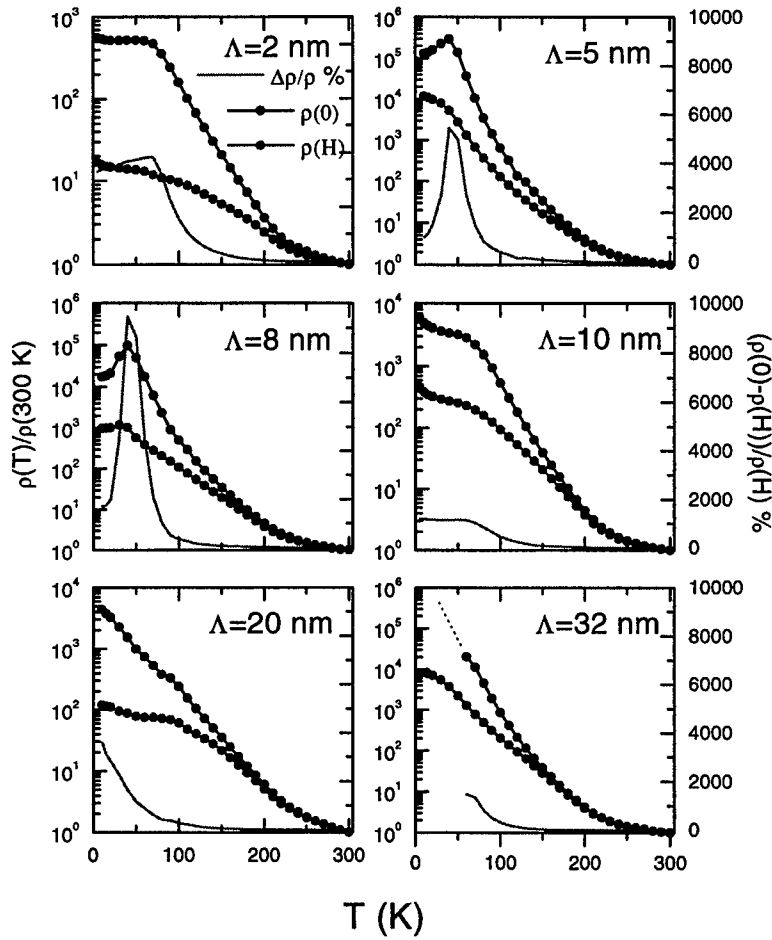


Figure 5. Resistivity, normalized to the 300 K value, as a function of temperature, measured in 50 kOe ( $\rho_H$ ) and in zero applied field ( $\rho_0$ ) for the series of  $[FM(\Lambda/2)/AF(\Lambda/2)]_{15}$  multilayers. The CMR ratio  $\Delta\rho/\rho_0 = [\rho_0 - \rho_H]/\rho_H$  is plotted as a solid line.

anisotropy [16] below  $T_B$ . Hence, the observed hump below  $T_B$  in the ZFC curve can be attributed to thermally activated magnetic rotation over energy barriers caused by random exchange coupling at the AF/FM interfaces. Our magnetothermal measurements indicate that the  $T_B$  does not change in the examined range of bilayer thickness and occurs at 70 K for all samples. To answer why  $T_B$  remains more or less the same in the examined range of  $\Lambda$  values it is reasonable to consider that interfacial spin ordering is confined within a few atomic planes near the AF/FM interfaces, defining an active film volume  $V_{int}$ . Thus, the appearance of exchange-biasing depends on the magnetic ordering of interfacial atomic planes which define a critical volume where thermal-activation energy becomes comparable to the magnetic energy at a certain blocking temperature, independent of  $\Lambda$ . Figure 5 shows the variation of the normalized resistivity as a function of temperature, measured in 50 kOe ( $\rho_H$ ) and in zero applied field ( $\rho_0$ ). The resistivity increases drastically as we cool down from 300 K, spanning almost four orders of magnitude. Also, the CMR ratio becomes maximum in the temperature range below  $T_B$ . In Fig.5 the steep increase of resistivity at low temperatures is in contrast to the decrease of  $\rho$  observed in epitaxial FM films [24,25]. This provides further experimental evidence that the insulating behavior [26] of the AF layer is dominant at low-temperatures. This extra contribution in  $\rho$  is different for every specimen and modifies the shape of the resultant CMR curves (Fig.6). Clearly, the multilayers with  $\Lambda=5$  and 8 nm exhibit a peak in the CMR response, indicating a special arrangement of spins at the AF/FM interfaces. As a consequence the characteristic CMR peak, that is usually reported nearby the ferromagnetic  $T_C$  of  $\text{La}_{2/3}\text{Ca}_{1/3}\text{MnO}_3$  films [27] is not observed in the  $\rho_0$  versus temperature curve. This behavior is in agreement with the magnetothermal measurements (Fig.5), where it is evident that the most drastic change of the average film magnetization does not occur near the  $T_C$  of the individual FM layers but at  $T_B$ .

## 5. Conclusion

In summary, we have studied the variation of exchange biasing and coercive field as a function of  $\Lambda$  and temperature in  $\text{La}_{2/3}\text{Ca}_{1/3}\text{MnO}_3/\text{La}_{1/3}\text{Ca}_{2/3}\text{MnO}_3$  multilayers grown by PLD. The maximum  $H_{EB}=880$  Oe was observed for the sample with  $\Lambda=10$  nm. The exchange biasing mechanism sets-in below a blocking temperature of 70 K and induces: (i) an enhancement of  $H_C$  in the FC hysteresis loops, (ii) an increase of the MR ratio due to interface scattering around  $T_B$ . It is interesting to note that in the series of multilayers studied here despite all variations in the AF and FM layer thicknesses  $T_B$  does not vary considerably, signifying that the mechanism of spin ordering is confined within a few atomic planes near the AF/FM interfaces. This may be attributed to weak coupling of the interfacial spins to the core of the AF layer.

## References

1. Jin, S., Tiefel, T.H., McCormack, M., Fatsnacht, R.A., Ramesh, R. Chen, L.H. (1994) Thousandfold change in resistivity in magnetoresistive La-Ca-Mn-O films, *Science* **264**, 413-415
2. Radaelli, P.G., Cox, D.E., Maresio, M., Cheong, S-W., Schiffer, P.E., and Ramirez, A.P. (1995) Simultaneous Structural, Magnetic, and Electronic Transitions in  $\text{La}_{1-x}\text{Ca}_x\text{MnO}_3$  with  $x=0.25$  and  $x=0.50$ , *Phys. Rev. Lett.* **75**, 4488-4491
3. Yu Lu, Li, X.W., Gong, G.Q., Gang Xiao, Gupta, A., Lecoeur, P., Sun, J.Z., Wang, Y.Y. and Dravid, V.P. (1996) Large magnetotunneling effect at low magnetic fields in micrometer scale epitaxial  $\text{La}_{0.67}\text{Sr}_{0.33}\text{MnO}_3$  tunnel junctions *Phys. Rev. B* **54**, R8354-8360
4. Mathur, N.D., Burnell, G., Isaac, S.P., Jackson, T.J., Teo, B.-S., MacManus-Driscoll, J.L., Cohen, L.F. Evetts, J.E. and Balmire, M.G. (1997) Large low field magnetoresistance in LaCaMnO induced by artificial grain boundaries, *Nature* **387**, 266-268.
5. Steenbeck, K., Eick, T., Krisch, K., Schmidt, H-G., and Steinbeissh, E., (1998) Tunneling-like magnetoresistance in bicrystal  $\text{LaSrMnO}$  thin films, *Appl. Phys. Lett.* **73**, 2506-2508.
6. Srinitiwarawong, C., and Ziese, M. (1998) Magnetoresistance of mechanically induced grain boundaries in LaCaMnO films, *Appl. Phys. Lett.* **73**, 1140-1142.
7. Ziese, M. (1999) Grain-boundary magnetoresistance: Spin-polarized inelastic tunneling through spin-glass-like barrier, *Phys. Rev. B* **60**, R738-R741.
8. Coey, J.M.D. (1999) Powder Magnetoresistance *J. Appl. Phys.* **85**, 5576-5581.
9. Ziese, M., Sena, S., Shearwood, C., Blythe, H.J., Gibbs, M.R.J., Gehring, G.A. (1998) Voltage-controlled colossal magnetoresistance in manganite/normal-metal heterostructures *Phys. Rev. B* **57**, 2963-2967
10. Wei, J.Y.T., Yeh, N.-C., Vasquez, R.P., Gupta, A., (1998) Tunneling evidence of half-metallicity in epitaxial films of ferromagnetic perovskite manganites and ferrimagnetic mangetite, *J. Appl. Phys.* **83**, 7366-7368
11. Gong, G.Q., Gupta, A., Gang Xiao, Lecoeur, P., and McGuire, T.R., (1996) Perovskite oxide superlattices: magnetotransport and magnetic properties *Phys. Rev. B* **54**, R3742-3745.
12. Kwon, C., Kim, K.-C., Robson, M.C., Gu, J.Y., Rajeswari, M., Venkatesan T, and Ramesh, R. (1997) Desirable magnetotransport properties in doped Mn-oxide-based superlattices *J. Appl. Phys.* **81**, 4950-4952
13. Ghosh, K., Ogale, S.B., Pai, S.P., Robson, M., Eric Li, Jin, I., Zi-Wen Dong, Greene, R.L., Ramesh, R., Venkatesan, T., and Johnson, M., (1998) Positive giant magnetoresistance in a  $\text{Fe}_3\text{O}_4/\text{SrTiO}_3/\text{La}_{0.5}\text{Sr}_{0.3}\text{MnO}_3$  heterostructure *Appl. Phys. Lett.* **73**, 689-691.
14. Rongsheng Cheng, Kebin Li, Shouguo Wang, Zhixiang Chen, Caoshui Xiong, Xiaojun Xu and Yuheng Zhang, (1998). The special magnetoresistive effect in trilayered films of manganite perovskites, *Appl. Phys. Lett.* **72**, 2475-2477.
15. Sun, J.Z., Abraham, D.W., Roche, K., and Parkin, S.S.P. (1998) Temperature and bias dependence of magnetoresistance in doped manganite thin film trilayer junctions, *Appl. Phys. Lett.* **73**, 1008-1010.
16. Wiedenhorst, B., Hoefener, C., Yafeng Lu, Klein, J., Alff, L Gross, R. Freitag, B.H. Mader, W. (1999) Strain effects and microstructure of epitaxial manganite thin films and heterostructures, *Appl. Phys. Lett.* **74**, 3636-3638
17. Sahana, M., Hedge, M.S., Prasad, V., and Subamanyam, S.V. (1999) Electrical resistivity and enhanced magnetoresistance in  $\text{LaPbMnO}/\text{LaMnO}$  superlattices *J. Appl. Phys.* **85**, 1058-1061
18. Panagiotopoulos, I., Christides, C., Pissas, M., and Niarchos, D. (1999) Exchange biasing mechanism in  $\text{La}_{2/3}\text{Ca}_{1/3}\text{MnO}_3/\text{La}_{1/3}\text{Ca}_{2/3}\text{MnO}_3$  multilayers *Phys. Rev. B* **60**, 485-491
19. Izumi, M., Murakami, Y., Konishi, Y., Manako, T., Kawasaki, M., Tokura, Y., (1999) Structure characterization and magnetic properties of oxide superlattices  $\text{LaSrMnO}/\text{LaSrFeO}$  *Phys. Rev. B* **60**, 1211-1215.
20. Nikolaev, K.R., Bhattacharya A., Kraus, P.A., Vas'ko, V.A., Cooley, W.K., and Goldman, A.M., (1999) Indications of antiferromagnetic interlayer coupling in  $\text{La}_{2/3}\text{Ba}_{1/3}\text{MnO}_3/\text{LaNiO}_3$  multilayers *Appl. Phys. Lett.* **75**, 1118-120
21. Fontcuberta J., Martinez, B., Seffar, A., Pinol S., Garcia-Munoz, J.L. and Obradors, X. (1997) Colossal magnetoresistance of ferromagnetic manganites: Structural tuning and mechanisms *Phys. Rev. Lett.* **76**, 1122-1125.
22. Kuwahara, H., Moritomo, Y., Tomioka, Y., Asamitsu, A., Kasai, M. and Tokura, Y. (1997) Low-field colossal magnetoresistance in bandwidth-controlled manganites *J. Appl. Phys.* **81**, 4954-4957
23. Koo T.Y., Park, S.H. Lee K-B., Jeong, Y.H. (1997) Anisotropic strains and magnetoresistance of  $\text{La}_{0.7}\text{Ca}_{0.3}\text{MnO}_3$  *Appl. Phys. Lett.* **71**, 977-979

24. Wang H. S. and Qi Li, (1998).Strain-induced large low-field magnetoresistance in  $\text{Pr}_{0.67}\text{Sr}_{0.33}\text{MnO}_3$  ultrathin films *Appl. Phys. Lett.* **73**, 2360-2362
25. O'Donnell, J. Rzchowski, M.S. Eckstein, J.N. and Bozovic, I. (1998).Magnetoelastic coupling and magnetic anisotropy in LaCaMnO films *Appl. Phys. Lett.* **72**, 1775-1777
26. Wang, H. S. Qi Li, Kai Liu and Chien, C.L. (1999).Low-field magnetoresistance and anisotropy in ultrathin PrSrMnO films grown on different substrates *Appl. Phys. Lett.* **74**, 2212
27. Nath, T. K. Rao, R. A. Lavric, D. Eom, C. B. Wu, L. and Tsui, F. (1998).Effect of three-dimensional strain states on magnetic anisotropy of LaCaMnO epitaxial thin films *Appl. Phys. Lett.* **73**, 1615-1617
28. Millis, J. (1998) Lattice effects in magnetoresistive manganese perovskites *Nature* **392**, 147-150
29. Meiklejohn, W. H. and Bean, C. P. (1957) New Magnetic Anisotropy *Phys. Rev.* **105**, 904 -913
30. For a recent review on Exchange Biasing phenomena see Nogues, J. and Schuller, Ivan K. (1999) Exchange Bias *J. Magn. Magn. Mat.* **192**, 203-232

---

## **SURFACE CHARACTERIZATION OF NANOSTRUCTURED COATINGS: STUDY OF NANOCRYSTALLINE $\text{SnO}_2$ GAS SENSORS**

Marie-Isabelle BARATON  
SPCTS - UMR 6638 CNRS, University of Limoges (France)  
e-mail: baraton@unilim.fr

### **1. Introduction**

In principle, all the properties of bulk materials can be determined provided that the composition and the structure of the material are sufficiently well defined. But, it is easy to realize that the properties at a solid surface are altered because of the very presence of the surface constituting a fundamental discontinuity. When the size of the solid is decreased down to the nanometer scale, the nanoparticles can be considered as *surfaces in three dimensions* and the relationships between bulk structure and material properties are no longer valid. In nanostructured coatings, the constituent phase or the grain structure may have sizes of the order of 10 nm or less, leading to a high number of atoms either at the external surface or at the grain boundaries. Besides, the material synthesis history and the preparation method of the layers govern the surface structure and the surface composition of coatings. Therefore, precise surface characterization is a strong requirement to control the surface properties and to further improve the nanostructured coating performances.

As a general requirement, the methods used to characterize clean or real surfaces must be sensitive enough to detect the small number of surface atoms. But, when applied to nanostructured materials, the surface characterization techniques must additionally be capable of analyzing a depth significantly smaller than the size of the grain to solely take the surface layer into consideration. Most of the techniques for surface analysis are essentially based on the scattering, absorption or emission of photons, electrons, atoms or ions. But no single technique can provide all necessary information about surface atoms [1].

As an example, the study by Fourier transform infrared (FTIR) surface spectrometry of semiconductor nanostructured thick films used as chemical gas sensors will be discussed. It will be shown that this cost-effective technique allows one to identify the surface chemical species, to test the reproducibility of the surface oxidation state and to determine the type of semiconductivity. In addition, emphasis will be put on the capability of FTIR surface spectrometry to provide information simultaneously on the chemical reactions taking place at the gas-sensing layer interface and on the resulting

---

variations of the electrical conductivity of the surface layer. Besides, because the gas sensing properties are essentially dependent on the surface reactivity, it will be shown how modifications of the chemical species of the sensor surface can affect the gas detection.

## 2. Surface Analysis

### 2.1. GENERAL CONSIDERATIONS

The definition of a surface is highly subjective. The phenomena to be studied generally define the depth of the surface layer to take into consideration [2]. For example, adsorption only concerns the adsorbed molecules or atoms and the very first atomic layer (monolayer) of the solid. On the contrary, changes in the electrical properties of a semiconductor usually affect over one hundred atomic layers. Therefore, the technique for the analysis of a specific surface phenomenon must be chosen by carefully comparing the thickness of the surface layer that will be perturbed and the depth that the envisaged method can sample. This is not an easy task because this depth mainly depends on the material and on the energy of the probing particles (photons, electrons, atoms or ions). In addition, some techniques can be used at grazing angle of the incident beam instead of normal incidence, thus greatly influencing the depth of sampling [3]. Since different techniques (or eventually the same technique but under different conditions) have different depths of sampling, it must be kept in mind that discrepancies can occur between the results obtained on the same sample by different methods. Moreover, because the characterization technique has to be chosen with respect to the property to be analyzed, the simultaneous study of correlated properties involving the surface layer at different thicknesses seems like trying to "square the circle".

On the other hand, a complete surface characterization should reveal the chemical nature of the surface atoms, their concentrations, their electronic states as well as their arrangements with respect to each other and with respect to the underlying atoms [4]. The thorough investigation of the surface composition and structure should lead to the control of the electronic and chemical properties of this surface. However, no single technique can provide both structural and chemical complete information.

Despite all these difficulties, the critical need for the control of materials surfaces, and particularly of nanomaterials surfaces, leads to a constant development and improvement of instrumentation for surface analysis. This paper does not intend to review the techniques used for the study of surface structure and chemical composition. Several books describe these methods with respect to their field of interest [2-5] such as X-ray photoemission spectroscopy (XPS or ESCA), extended X-ray absorption fine structure (EXAFS), electron energy loss spectroscopy (EELS), Auger electron spectroscopy (AES), atomic force microscopy (AFM) and scanning tunneling microscopy (STM), ion-scattering spectroscopy (ISS), to name only a few. Among the methods that do not involve probing particles, let us quote: thermal desorption

spectroscopy (TDS) and temperature programmed desorption (TPD). Instead, the emphasis will be put on the possibilities offered by Fourier transform infrared (FTIR) spectrometry.

Although FTIR spectrometry is not usually considered as a surface-sensitive technique, under particular configurations it can be a high-performance tool for the surface analysis of nanosized powders [6-7]. When non-transparent materials have to be studied, the transmission mode is no longer appropriate. Then, the infrared radiation diffused by the sample becomes the most relevant effect to be investigated. Diffuse reflectance infrared Fourier transform spectrometry (DRIFTS) allows the analysis of films and coatings deposited on absorbing substrates and of the surface layer of bulk samples as well.

## 2.2. DIFFUSE REFLECTANCE SPECTROMETRY

In 1978, Fuller and Griffiths [8] published an optical arrangement for the measurement of diffuse reflectance infrared spectra of powdered samples. The schematic design is represented in Figure 1. An off-axis paraboloid mirror (focusing mirror) is used to focus the infrared beam onto the sample whereas an on-axis paraboloid mirror (collecting mirror) collects the radiation diffusely reflected from the sample. The specularly reflected radiation is eliminated through a hole drilled on the axis of the collecting mirror. The recent attachments for diffuse reflectance measurements are still based on this original design.

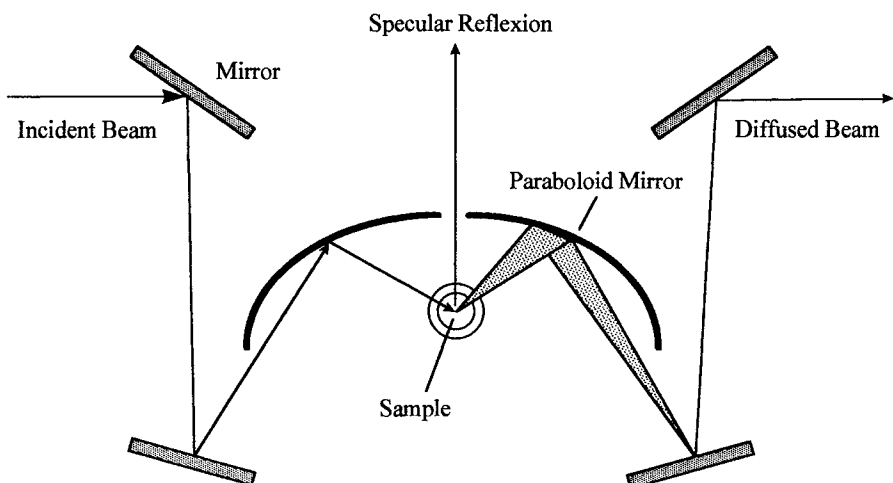


Figure 1. Optics for the diffuse reflectance infrared Fourier transform spectrometry

The theory of the diffuse reflectance is extremely complex and the determination of the penetration depth of the infrared radiation into the sample is not straightforward. Many theories have been proposed based on various models, each of them being valid under a specific set of conditions. A critical discussion of different theories can be found in [9] for example. Without going into details, it should be borne in mind that the diffuse reflectance is highly dependent upon the nature of the absorbent (refractive index, particle size, particle shape and particle size distribution etc) and upon the surface roughness. Note that a very smooth surface is not appropriate for such analysis because the specular reflectance is very intense whereas the diffuse reflectance becomes negligible. But, in any case, it must be clearly realized that, whatever the sample, a diffuse reflectance spectrum not only contains information on the surface species (very first atomic layer) but also on the bulk. To discriminate the bands due to the surface species from those originating from the bulk vibrations, a specific cell called environmental chamber must be attached to the diffuse reflectance accessory. Like in the case of transmission measurements [6-7, 10], this cell allows a thermal treatment of the sample under vacuum or controlled pressures of gases. Indeed, a thermal treatment of the sample under dynamic vacuum clears the surface from impurities, thus allowing the characterization of the surface chemical species such as hydroxyl groups, carbonates and hydrocarbon residues etc. In addition, selected probe-molecules can be purposely adsorbed on the film/coating surface to identify possible surface reactive sites. Under those conditions, the very first atomic layer of a film/coating can be fully characterized in the same way as that of a nanosized powder [6-7]. Moreover, the gas-surface interactions can be followed *in situ* as a function of the temperature and/or the gas pressure.

When a powdered sample is mixed with a nonabsorbing salt, such as potassium bromide, the infrared radiation can propagate into the salt grains and then undergoes several external and internal reflections before it emerges from the sample. In this case, the contribution of the surface species to the diffuse reflectance spectrum is relatively larger than in the case of the same powder studied in transmission mode. Obviously when the sample to be analyzed is a thick film, the diffuse reflection is limited to the external surface layer. As a consequence, the intensity of the bands originating from the surface species is weaker. This is the reason why the surface study by diffuse reflectance of thick films or bulk samples can only be successfully performed with highly sensitive infrared detectors. However, the nanocrystalline structure of films and coatings leads to an increase of the external surface area, thus facilitating their surface analysis by DRIFTS.

### 3. Semiconductor Coatings and Thick Films

When the material to be analyzed is a semiconductor, FTIR spectrometry can bring additional information on the electrical conductivity variations. According to the Drude-Zener theory [11], the infrared energy absorbed by a semiconductor is essentially due to surface states and to free carriers. Therefore, the absorbed infrared energy is related to the electrical conductivity of the semiconductor. Obviously, the more the infrared energy

is absorbed by the sample, the less it is scattered. In other words, a decrease of the infrared energy diffused by a semiconductor means an increase of its electrical conductivity provided that the surface states are not strongly modified.

Because of the optical properties of semiconductors and metals, it is not expected that DRIFTS can sample more than a few nanometers deep in such materials [8]. The surface layer corresponding to these few nanometers may actually represent the depletion layer in a semiconductor. For example, in tin oxide the depletion layer is estimated around 3 nm [12] which is probably close to the analyzed depth of a  $\text{SnO}_2$  thick film by DRIFTS. Keeping in mind that DRIFTS allows the analysis of the very first atomic layer and the study of the gas-surface interactions thanks to the use of the environmental chamber, it can be easily realized that, with this technique, the modification of the first atomic layer and its consequence on the electrical conductivity can be simultaneously followed under the same environment. This is the basis of fundamental studies of gas detection mechanisms in semiconductor-based sensors.

To clearly explain the dual possibility of DRIFTS, let us consider a semiconductor gas sensor based on tin oxide. The sensor is usually fabricated from a paste, consisting of a dispersion of the tin oxide particles in an appropriate solvent, deposited over a substrate (e.g. an alumina tile) and then fired to ensure a network of interconnected tin oxide grains [13]. It must be noted that preventing undesirable nanoparticle agglomeration during dispersion of the nanopowder and during further thermal treatment of the layers requires a state-of-the-art knowledge in surface chemistry. Depending on the temperature, oxygen adsorption onto the surface of these grains causes the removal of electrons from the conduction band and therefore a decrease of the electrical conductivity. An electron-depleted zone (space charge layer) is thus created at the surface and it generates a potential barrier between neighboring grains. When a reducing gas is adsorbed on the tin oxide surface, electrons are injected into the conduction band, decreasing the depth of the space charge layer and increasing the electrical conductivity. These changes in the electrical conductivity translate into variations of the background absorption of the sample in the infrared range. Note that, when the tin oxide particle size is considerably greater than the depth of the depletion layer, the electrical conductivity is controlled by the grain boundaries. But, when the sensing layer is constituted of nanoparticles, the depth of the depletion layer becomes comparable to the particle radius and then the electrical conductivity is controlled by the grains themselves. Therefore, the oxygen adsorption will result in fully depleted grains and to a high resistance of the material. As a consequence, the sensitivity of the sensor is increased and the effects on the background infrared absorption of the sample become more pronounced. As previously explained, a gas adsorption or ionosorption on the  $\text{SnO}_2$  first atomic layer has consequences on several hundreds of atomic layers in depth. Because the chemical reactions occurring at the very surface can be studied by DRIFTS and because the variations of the electrical conductivity generated by these chemical reactions are related to the variations of the infrared energy diffused by the sample, DRIFTS appears as a very relevant tool for the study of the gas detection mechanism in a semiconductor-based sensor.

#### 4. Study of a nanocrystalline tin oxide-based sensor

The sensors considered in the following are fabricated from nanosized tin oxide powder [13] obtained by laser evaporation of a tin oxide rod under specific conditions [14]. The size of the tin oxide primary particles is 8 nm and these particles are shown not to significantly grow during the firing step of the sensing layer preparation [13]. These sensors show an excellent sensitivity toward carbon monoxide in presence of oxygen. Details on the sensors fabrication and on their electrical characteristics can be found in [13].

##### 4.1. DETERMINATION OF THE TYPE OF THE SEMICONDUCTOR BY DRIFTS

Even though it is well known that tin oxide is a n-type semiconductor under standard conditions, the following procedure illustrates how it is possible to determine the type of the semiconductivity by DRIFTS without using any electrode.

A non-fired sensor without electrode, that is the sensing thick film deposited onto the alumina tile and dried at 373 K, is placed in the DRIFTS environmental chamber. The infrared spectrum recorded at room temperature in air is presented in Figure 2a.

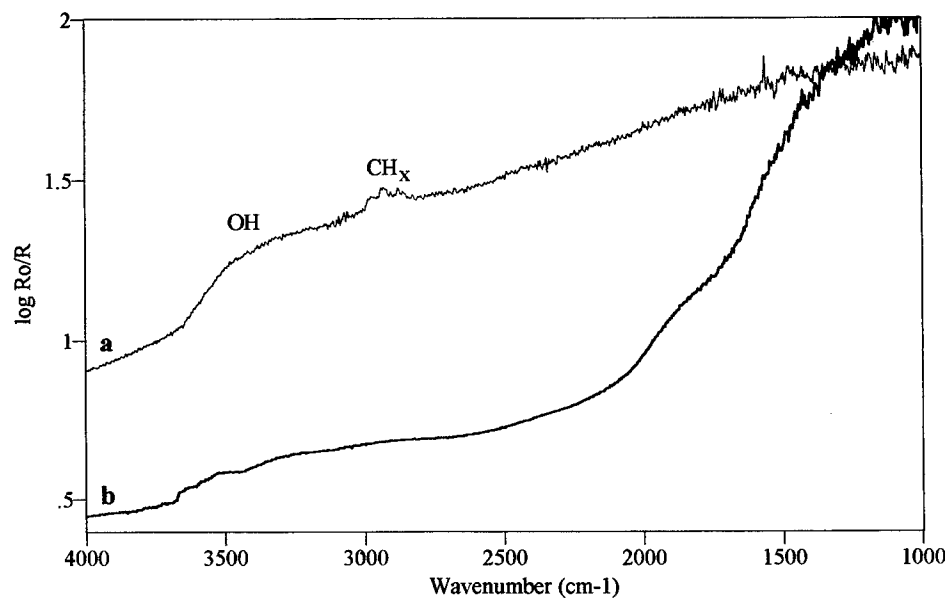


Figure 2. Diffuse infrared spectra of the n-SnO<sub>2</sub>-based sensor:  
a) at room temperature under atmosphere; b) after heating at 673 K under atmosphere.

The broad band centered around  $3300\text{ cm}^{-1}$  has been proved to correspond to atmospheric molecular water adsorbed on the Sn-OH surface hydroxyl groups [15] whereas the group of weaker bands in the  $3000\text{ cm}^{-1}$  region is due to the  $\text{CH}_x$  groups of the organic binder. When the sensor is heated under atmosphere, the  $\text{CH}_x$  groups are steadily eliminated as well as part of adsorbed molecular water (Figure 2b). But the most important modification of the infrared spectrum of the sensor during the thermal treatment is the decrease of the background absorption. This is due to the oxygen ionosorption on the sensor surface when the temperature increases. As previously explained, the oxygen ionosorption leads to an increase of the depth of the depletion layer, that is to a decrease of the free carrier density. As a consequence, a decrease of the background absorption of the infrared radiation by the free carriers is observed, which is related to the decrease of the electrical conductivity. This is the proof that the sample is a n-type semiconductor. Conversely, when the sensor is heated under dynamic vacuum (Figure 3), the absorption of the sample increases with temperature, thus proving an increase of the electrical conductivity. Indeed, this thermal treatment under vacuum is a reducing treatment and leads to oxygen loss mainly from the surface layer of the sample. Obviously, for a p-type semiconductor, the oxygen ionosorption causes the opposite effect on the background infrared absorption. This simple experiment is therefore an easy and fast method to determine the type of the semiconductor material while avoiding the perturbation which may be caused by the use of metallic electrodes.

#### 4.2. GAS DETECTION MECHANISM

Various infrared experiments have been performed on the sensing layer described above to simulate the gas detection by the semiconductor-based sensor. As a first step, the pretreatment conditions of the sensor [13] are reproduced by heating the sensing layer at 673 K under 50 mbar of oxygen and then cooling it to the chosen operating temperature while still under oxygen. As previously explained, this procedure decreases the electrical conductivity because oxygen adsorbs on the surface as different ionized species. By studying the original nanosized tin oxide powder, these species have been identified as mainly  $\text{O}^-$  and  $\text{O}_2^-$  [15] whose relative amount depends on the temperature [16]. Note that the adsorption of oxygen onto the as-received nanopowder surface allows one to identify defect sites where molecular oxygen is preferentially adsorbed at room temperature. These defect sites are destroyed by annealing under oxygen [15]. From the electrical measurements, it has been determined that this undoped sensor is sensitive toward reducing gases at an operating temperature ranging from 373 to 773 K [13] with two sensitivity local maxima at 393 K and 623 K. The experiments described below have been performed at these latter temperatures.

After the thermal pretreatment under oxygen, the sensor surface is subjected to 10 mbar of carbon monoxide (CO) at 623 K in presence of oxygen for 10 minutes. The electrical conductivity increases, which on the infrared spectrum translates into an increase of the background absorption (Figure 4a,b). Moreover, by looking closer at the

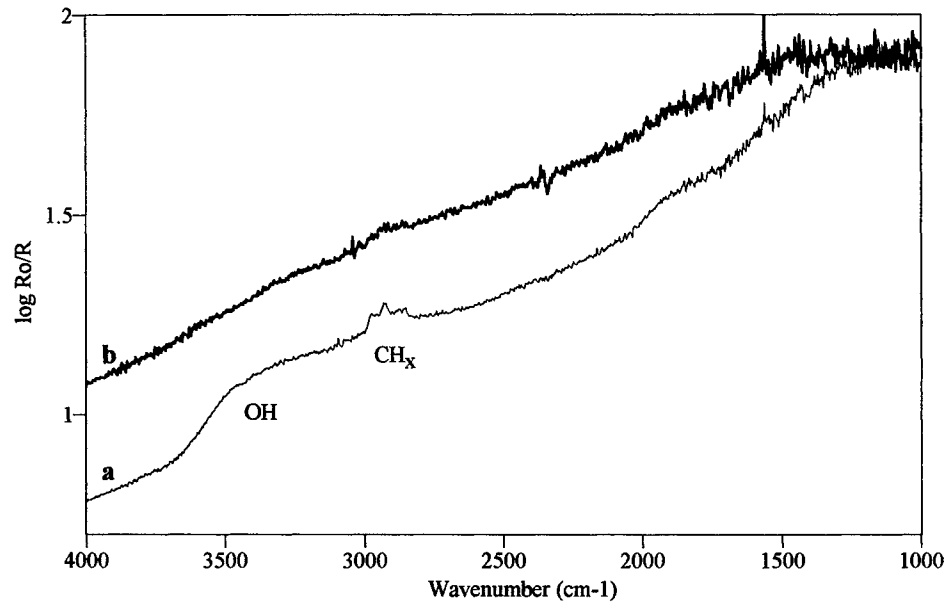


Figure 3. Diffuse infrared spectra of the n-SnO<sub>2</sub>-based sensor:  
a) at room temperature under vacuum; b) after heating at 673 K under dynamic vacuum.

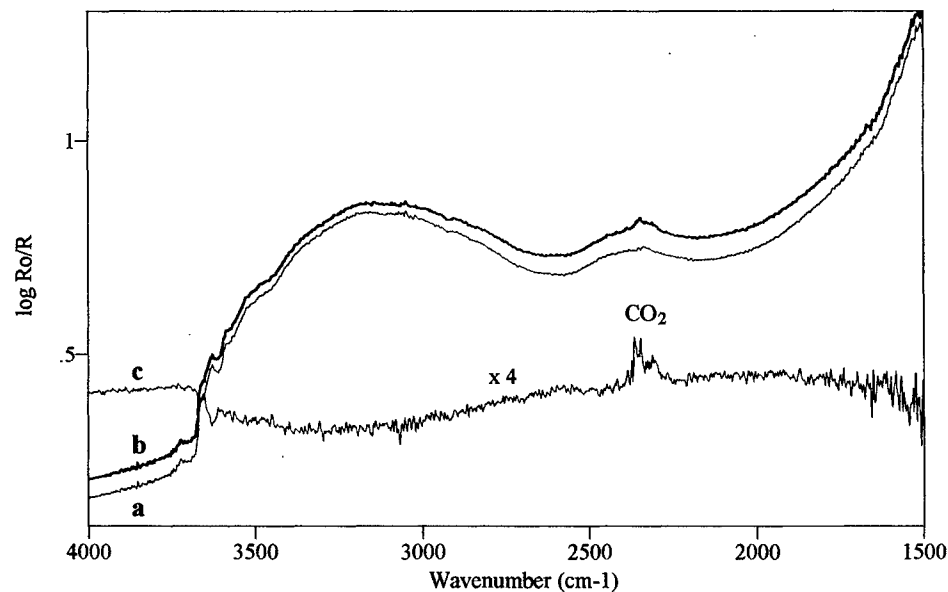


Figure 4. Diffuse infrared spectra of the n-SnO<sub>2</sub>-based sensor at 623 K:  
a) under 50 mbar O<sub>2</sub>; b) after addition of 10 mbar CO; c) difference spectrum: b-a.  
The Y axis refers to spectra a and b, spectrum c has been translated for clarity sake.

infrared spectra, it is possible to detect the formation of carbon dioxide as shown on the difference spectrum (Figure 4c). Then, the gases ( $O_2$ , CO and the newly formed  $CO_2$ ) are quickly evacuated and a new dose of oxygen (50 mbar) is added for 10 minutes followed by 10 mbar CO. This additions/evacuation sequence is repeated several times and the infrared energy diffused by the sensing layer in the entire wavenumber range scanned by the spectrometer ( $7800-450\text{ cm}^{-1}$ ) is reported versus gas exposures in Figure 5. The variations of the diffuse infrared energy can be related to the sensor response. It can be seen that under oxygen the electrical conductivity of the sensor decreases whereas it increases under CO. This increase can be related to the  $CO_2$  formation observed on the infrared spectra. During the evacuation of all of the gases present in the cell, the sample is reduced as expected from the oxygen desorption and from the removal of ionosorbed oxygen species used for the  $CO_2$  formation. When the sample is again subjected to oxygen, the oxidation state of the surface is totally regenerated.

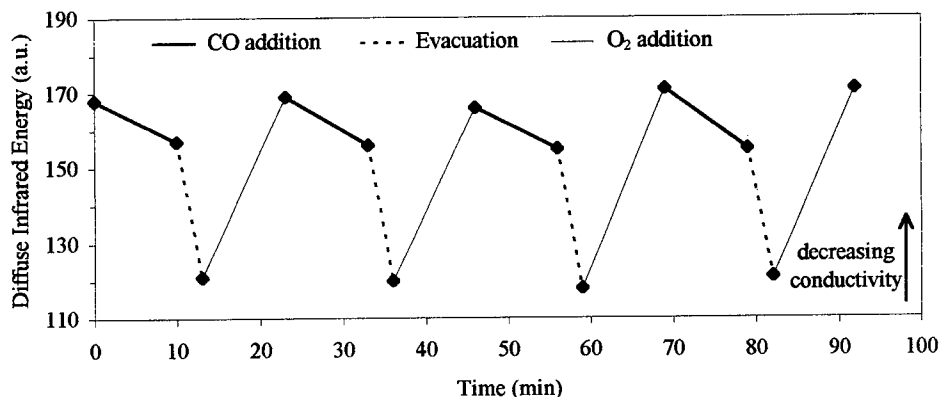


Figure 5. Infrared energy diffused by the n-SnO<sub>2</sub>-based sensor at 623 K versus gas exposures.

In another experiment at 623 K, oxygen was quickly evacuated before CO addition (10 mbar). The introduction of the reducing gas causes a strong decrease of the infrared energy diffused by the sensing layer (Figure 6). Taking into account the detection limits of our system, the formation of  $CO_2$  is either very weak or absent. A rapid evacuation does not lead to significant changes. Whereas the addition of a second CO dose may be responsible for a very slight increase of the electrical conductivity, further evacuation or CO addition is not detected by the sensor. The sensor seems unable to undergo further reduction, thus proving that the nanosized tin oxide particles are totally reduced after the first CO addition. But, when the sensing layer is subjected to oxygen, the recovery is immediate (Figure 6).

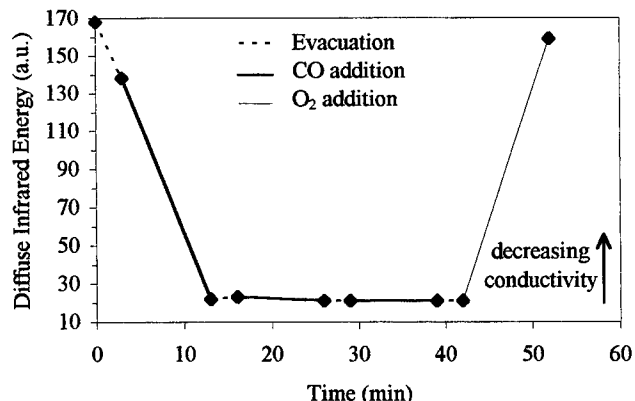


Figure 6. Infrared energy diffused by the n-SnO<sub>2</sub>-based sensor at 623 K versus gas exposures.

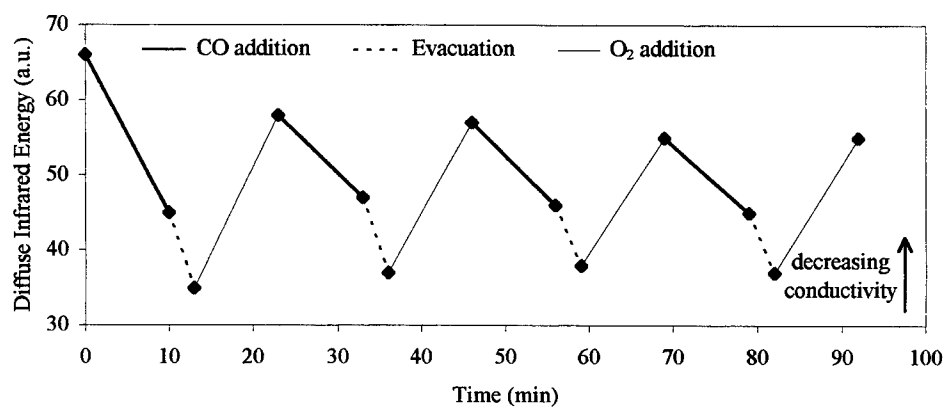


Figure 7. Infrared energy diffused by the n-SnO<sub>2</sub>-based sensor at 393 K versus gas exposures.

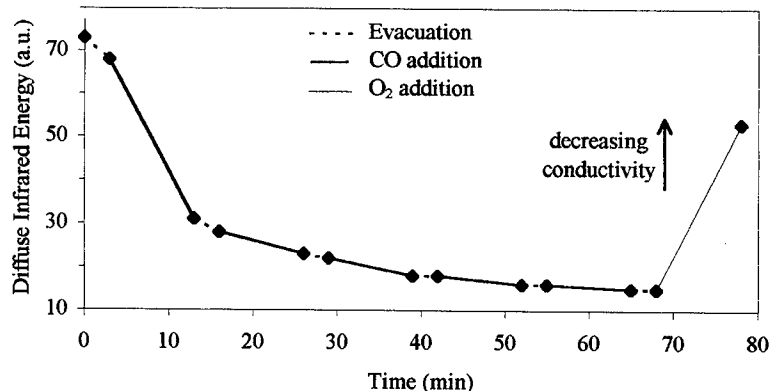


Figure 8. Infrared energy diffused by the n-SnO<sub>2</sub>-based sensor at 393 K versus gas exposures.

The two above experiments prove that the nanostructured tin oxide-based sensor strongly requires an oxygen environment for normal operation. It is amazing how fast the reduction of the nanoparticles can be, thus strengthening the need for oxygen to balance out the complete depletion of the nanoparticles in a reducing atmosphere.

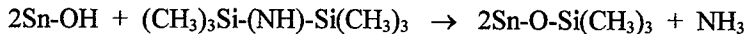
Similar experiments (CO additions in presence or in absence of oxygen) were performed on the same sensing layer at 393 K. The variations of the diffuse infrared energy versus gas exposures are given in Figures 7 and 8. The major difference with the experiments performed at 623 K is that the formation of CO<sub>2</sub> is not observed even in presence of oxygen. This is not completely surprising because this lower temperature should prevent the CO combustion. However, the response of the sensor is far from being negligible and this phenomenon is in good agreement with the electrical measurements showing a sensitivity local maximum around 393 K [13]. We tentatively explain the sensor response toward CO, without formation of CO<sub>2</sub>, by the adsorption of the CO molecules on the sensing layer surface. Indeed, this adsorption, only possible around room temperature, should modify the thickness of the depletion layer and therefore the electrical conductivity of the semiconductor material. By comparing the results obtained at 393 K and at 623 K, we note that the recovery of the oxidation state of the sensor surface is slower at 393 K, and that the total reduction of the sensor by subsequent CO additions in absence of oxygen is slower as well (Figure 8).

With these DRIFTS experiments, we have correlated the variations of the electrical conductivity of the sensing layer with the oxidation of carbon monoxide into carbon dioxide on the sensor surface. Moreover, in agreement with the electrical conductivity measurements, we have demonstrated that, at low temperature, the response of the SnO<sub>2</sub>-based sensor is not due to the CO combustion. We have also produced the proof that the presence of oxygen is essential for the reproducibility of the sensor response whatever the operating temperature.

#### 4.3. MODIFICATION OF THE SURFACE SPECIES AND CONSEQUENCES ON THE SENSOR RESPONSE

The gas detection mechanism is essentially a surface phenomenon generating modifications in the depletion layer of the semiconductor material. Besides, the surface properties of a film or coating may be changed when organic substances are adsorbed [17]. Therefore, when the surface chemistry of the sensing layer is modified, consequences should be observed on the sensor response. For example, the response toward CO is mainly dependent on the oxygen ionosorbed species but this response can be strongly affected by the presence of humidity. The hydroxyl groups present on all metal oxide surfaces are known to play an important role in the surface properties since they can act as adsorptive or reactive sites [17]. Particularly, humidity interacts with these OH groups although the precise mechanism correlating the chemical interactions and the electrical response of the semiconductor is not completely understood [18]. Therefore, chemical modifications of surface hydroxyl groups are expected to change the sensor sensitivity toward humidity.

To check this hypothesis, hexamethyldisilazane (HMDS) is grafted on the hydroxyl groups of the tin oxide surface. A thorough infrared study of the grafting mechanism has been previously performed on the tin oxide nanopowder [19] which is used to fabricate the sensing layer. HMDS reacts with the surface OH groups according to the following reaction:



When the grafted sample undergoes a subsequent oxidation, the  $\text{Si}(\text{CH}_3)_3$  groups prove to transform into new Si-OH groups linked to the tin oxide surface [19]. Obviously, these newly formed Si-OH groups do not have the same acid-base properties as that of the Sn-OH groups on the original tin oxide surface. Therefore, their reactivity toward water molecules should be different.

The surface of the sensing layer has been modified according to a procedure previously described [19-20]. The diffuse reflectance spectra of the sensing layer before HMDS grafting and after HMDS grafting followed by a thermal treatment under oxygen at 673 K are presented in Figure 9.

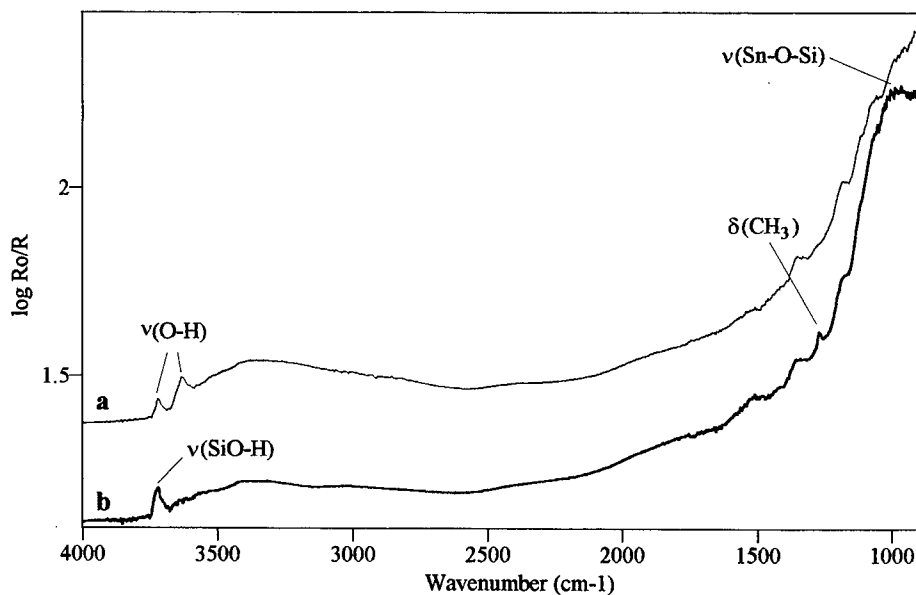


Figure 9. Diffuse infrared spectra of the n-SnO<sub>2</sub>-based sensor:  
a) after oxidation at 673 K; b) after HMDS-grafting followed by an oxidation at 673 K.  
The Y axis refers to spectrum a, spectrum b has been translated for clarity sake.

After the grafting and the oxidation (Figure 9b), the band at  $3630\text{ cm}^{-1}$  assigned to the  $\nu(\text{OH})$  stretching vibration of Sn-OH surface groups on the tin oxide grains [15] has completely disappeared because of the reaction of the corresponding OH groups with HMDS. The band at  $3717\text{ cm}^{-1}$ , also assigned to  $\nu(\text{OH})$  of surface groups, is not strongly modified by the grafting. This band that does not exist in the spectrum of the pure  $\text{SnO}_2$  nanosized powder may be due to OH groups remaining from the organic binder. After HMDS grafting, the shoulder which appears at  $3726\text{ cm}^{-1}$  on the high-wavenumber side of the  $3717\text{ cm}^{-1}$  band is assigned to the  $\nu(\text{OH})$  stretching vibration of new Si-OH surface groups. The sharp band at  $1270\text{ cm}^{-1}$  is due to the  $\delta_s(\text{CH}_3)$  bending vibration of the  $(\text{CH}_3)$  groups of the grafted HMDS [19]. At lower wavenumbers, the broad band around  $1000\text{ cm}^{-1}$  has been assigned to the  $\nu(\text{Sn-O-Si})$  stretching vibration [19]. All of these features prove that HMDS is grafted on the sensor surface and that the oxidation of the grafted species proceeds like on the tin oxide powder surface.

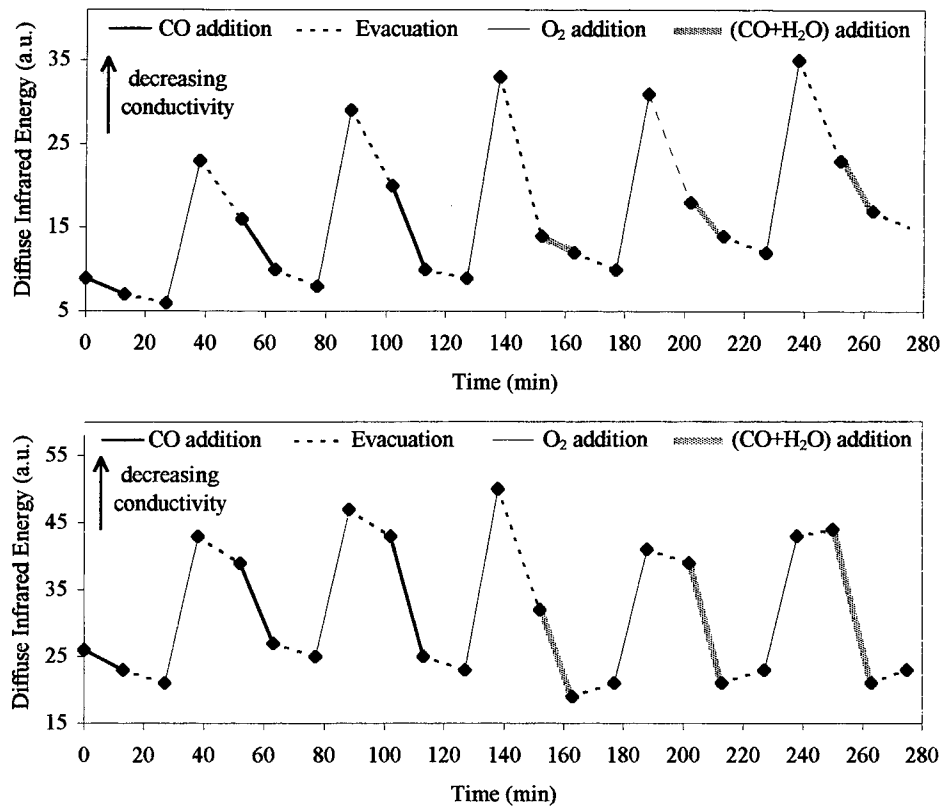


Figure 10. Infrared energy diffused by the n- $\text{SnO}_2$ -based sensor at  $523\text{ K}$  versus gas exposures: top) before grafting; bottom) after HMDS grafting.

To analyze the effects of the surface modifications on the sensor response, the sensitivity of the sensor is tested before and after grafting. The same addition/evacuation sequences are followed in both cases: oxygen addition, quick evacuation, pure carbon monoxide addition, quick evacuation. This sequence is repeated twice and from the forth sequence, carbon monoxide is replaced by a mixture of water vapor and carbon monoxide at increasing  $H_2O/CO$  pressure ratios (10, 20, 40%). The variations of the diffuse infrared energy versus gas exposures is reported in Figure 10. It can be seen that, before grafting (Figure 10a), the presence of humidity strongly affects the sensor response toward CO, whereas after grafting (Figure 10b), the amplitude of the response is stable whatever the humidity level. This experiment clearly demonstrates the importance of the chemical composition of the first atomic layer in the gas detection mechanism.

The different behavior of the non-grafted and grafted sensor toward humidity is explained by the drastic modification of the chemical nature of the surface hydroxyl groups. The Si-OH surface groups formed after HMDS grafting and subsequent oxidation should have an acid-base property close to that of the OH groups on a silica surface, that is quite different from that of the Sn-OH groups originally on the sensor surface. The constant amplitude of the response toward CO in presence of humidity indicates a stabilizing surface effect by HMDS, which has been already observed on titania [21] but its complete mechanism is still unknown. The Si-OH groups are believed to play an important part in neutralizing the effect of humidity possibly because their amphoteric character gives them equal opportunity to interact with  $OH^-$  and  $H^+$  ions originating from the dissociation of a water molecule.

## 5. Conclusion

Surface studies of materials are generally difficult to perform mainly because the adequacy between the property to be analyzed and the investigation tool is not easily satisfied. Obviously, the difficulty increases in the case of nanomaterials.

Diffuse reflectance infrared spectrometry, often used to analyze the bulk of standard materials, has been demonstrated to be relevant for surface studies of nanostructured films and coatings under particular conditions. The first atomic layer can be characterized as far as the chemical composition of the surface species is concerned. The surface reactivity can eventually be checked like in transmission infrared spectrometry for nanosized powders [7].

An important achievement of DRIFTS is to allow the analysis of the chemical reactions or interactions taking place at the very first atomic layer of a semiconductor layer simultaneously with their consequences on the electrical conductivity possibly involving a depth of few nanometers. Under those conditions, DRIFTS is an invaluable investigation tool in the field of chemical gas sensors for the comprehension of the fundamental mechanisms.

## 6. References

1. Somorjai, G.A. (1998) From Surface materials to Surface Analysis, *MRS Bulletin* **23**(5), 11-29.
2. Somorjai, G.A. (1994) *Introduction to Surface Chemistry and Catalysis*, Wiley, New York.
3. Morrison, S.R. (1990) *The Chemical Physics of Surfaces*, Plenum Press, New York.
4. Prutton, M. (1994) *Introduction to Surface Physics*, Oxford University Press, Oxford.
5. Göpel, W., Hesse, J., and Zemel, J.N. eds. (1991) *Sensors - A Comprehensive Survey, Chemical and Biochemical Sensors*, Vol. 2, VCH, Weinheim.
6. Baraton, M.-I. (1998) The Surface Characterization of Nanosized Powders. Relevance of FTIR Surface Spectrometry, in G.M. Chow and N.I. Noskova (eds.), *Nanostructured Materials: Science and Technology*, NATO-ASI Series, Kluwer Academic Press, Dordrecht, pp. 303-317.
7. Baraton, M.-I. (1999) FTIR Surface Spectrometries of Nanosized Particles, in H.S. Nalwa (ed.), *Handbook of Nanostructured Materials and Nanotechnology*, Academic Press, San Diego, in press.
8. Griffiths, P.R. and de Haseth, J.A. (1986) *Fourier Transform Infrared Spectrometry*, Wiley, New York.
9. Hecht, H.G. (1976) The Interpretation of Diffuse Reflectance Spectra, *J. Research Nat. Bureau Standards* **80A**, 567-583.
10. Baraton, M.-I. (1994) IR and Raman Characterization of Nanophase Ceramic Materials, *J. High Temp. Chem. Processes* **3**, 545-554.
11. Harrick, N.J. (1967) *Internal Reflection Spectroscopy*, Interscience, Wiley, New York.
12. Ogawa, H., Nishikawa, M., and Abe, A. (1982) Hall Measurement Studies and an Electrical Conduction Model of Tin Oxide Ultrafine Particle Films, *J. Appl. Phys.* **53**, 4448-4455.
13. Williams, G and Coles, G.S.V. (1998) Gas Sensing Properties of Nanocrystalline Metal Oxide Powders Produced by a Laser Evaporation Technique, *J. Mater. Chem.* **8**, 1657-1664.
14. Riehemann, W. (1998) Synthesis of Nanoscaled Powders by Laser-Evaporation of Materials, *Proc MRS Symp.*, MRS ed., Warrendale, **501**, 3-13.
15. Tribout, J., Chancel, F., Baraton, M.-I., Ferkel, H., and Riehemann, W. (1998) Oxygen Adsorption on Tin Oxide Nanosized Powders Characterized by FTIR Spectrometry and Relation with the Sensor Properties, *Proc MRS Symp.*, MRS ed., Warrendale, **501**, 95-100.
16. Lantto, V. and Romppainen P. (1987) Electrical Studies on the Reactions of CO with Different Oxygen Species on SnO<sub>2</sub> Surfaces, *Surf. Sci.* **192**, 243-264.
17. Takeda, S., Fukawa, M., Hayashi, Y., and Matsumoto, K. (1999) Surface OH Group Governing Adsorption Properties of Metal Oxide Films, *Thin Solid Films* **339**, 220-224.
18. Heinrich, V.E. and Cox, P.A. (1994) *The Surface Science of Metal Oxides*, Cambridge University Press, Cambridge.
19. Chancel, F., Tribout, J., and Baraton, M.-I. (1998) Effect of Surface Modification on the Electrical properties of TiO<sub>2</sub> and SnO<sub>2</sub> Nanopowders, *Proc MRS Symp.*, MRS ed., Warrendale, **501**, 89-94.
20. Chancel, F., Tribout, J., and Baraton, M.-I. (1997) Modification of the Surface Properties of a Titania Nanopowder by Grafting: A Fourier Transform Infrared Analysis, *Key Eng. Mater.* **132** **136**, 236-239.
21. Baraton, M.-I. and Merhari, L. (1998) Surface Property Control of Semiconducting Metal Oxide Nanoparticles, *Nanostruct. Mater.* **10**(5), 699-713.

## PHASE DIFFERENTIATION AND CHARACTERIZATION OF NANOSTRUCTURED COMPOSITES BY SYNCHROTRON RADIATION TECHNIQUES

Y.K. HWU

*Institute of Physics, Academia Sinica,  
Nankang, Taipei 11529, Taiwan, R.O.C.*

G.M. CHOW and W.C. GOH

*Department of Materials Science, National University of Singapore,  
Kent Ridge, Singapore 117543, Republic of Singapore*

T.S. CHO, and J.H. JE

*Department of Materials Science and Engineering  
Pohang University of Science and Technology,  
Pohang, 790-784, Korea*

D.Y. NOH

*Department of Materials Science and Engineering  
Kwangju Institute of Science and Technology,  
Kwangju, 506-712, Korea*

H.-M. LIN,

*Department of Materials Engineering, Tatung University,  
Taipei, Taiwan, R. O. C.*

C. K. LIN

*Department of Materials Science, Feng Chia University  
Taichung, Taiwan, R.O.C.*

### Abstract

The complexity of nanostructured materials presents challenging difficulties in characterization using conventional techniques. For example, conventional x-ray diffraction may not provide accurate information on the structure (solid solution or phase separation) of nanostructured materials. Complementary advanced characterization methods are often required in the detailed understanding of structures. In this paper we report our work on characterization of two nanostructured systems, namely, AgNi powder and NiCo films, using synchrotron radiation techniques of x-ray diffraction, anomalous x-ray scattering and x-ray absorption spectroscopy.

## 1. Introduction

Structural characterization of alloys by conventional x-ray diffraction (XRD) has been well established [1]. For materials with coarse grain size, the appearance of a single set of diffraction peaks and the disappearance of elemental peaks are commonly accepted as evidence of formation of an alloy. In a random, substitutional solid solution, the lattice parameter changes with composition and the variation can be qualitatively followed using Vegard's law. When the crystallite size (or x-ray coherence length) of a material is decreased to below a certain critical length scale, a nanostructured solid solution cannot be unequivocally determined from a composite using conventional x-ray diffraction [2]. In a nanocomposite where the two phases have close lattice parameters and x-ray structural coherence, the Bragg peak of one phase has some degree of overlap with that of the other phase. Because of the effects of size broadening and the contribution to diffraction amplitude by structural coherence of the two phases, a single peak will appear for a particular Bragg reflection when the size is below a certain limit. However, this single peak has an average lattice spacing that has no correspondence in real space, and can be easily mistaken as evidence of formation of an alloy. Therefore, conventional XRD, used for probing long-range ordered atomic structure, should not be used alone to study the structure of nanostructured alloys and composites made of structurally coherent and immiscible materials. Instead, other tools, or more often a vast combination of different techniques, which do not suffer from such limitations should be considered.

The structural characterization of nanostructured metastable alloys, prepared by non-equilibrium processing such as mechanical alloying and vapor quenching, has already required the use of techniques other than conventional XRD. For example, techniques such as Extended X-ray Absorption Fine Structure spectroscopy (EXAFS) and solid-state nuclear magnetic resonance spectroscopy (NMR) were used to investigate the average local atomic environment of Co-Cu, in order to confirm if the nanostructured material was a solid solution or a composite [3]. Both techniques rely on the use of suitable reference standard materials for comparison. However, in certain composites where the elements have very similar scattering potentials, such as Ni-Co, EXAFS cannot be used to separate the scattering effects from different elements and the advantage of being an element-specific structural analysis tool is greatly reduced. Further, since the primary EXAFS signal is given rise by the short-range order of the sample, one will not be able to separate different phases of different long-range order coexisting in the composite.

Diffraction anomalous fine structure (DAFS)[4,5], a technique combining diffraction and XAS (X-ray Absorption Spectroscopy, a general term covering EXAFS and XANES), can be used to selectively provide short-range order information of the long-range ordered atoms associated with a particular Bragg reflection, and the information on specific chemical valence at inequivalent atomic site. The spatial selectivity can be used to study the local atomic structure of multiple-phase materials, when the phases in the sample give rise to diffraction peaks at different locations. In the case of a random,

homogeneous, nanostructured alloy, x-ray absorption spectra should display the characteristic of the constituent elements of each phase as well as their binding and local structure associated with the Bragg peaks. However, in the case of nanostructured alloy, the diffraction peaks are rather weak and broad and therefore hamper the generation of a detailed radial distribution function by the standard Fourier transform due to the low signal intensity. Nevertheless, the elemental information can be easily obtained by the similar method, anomalous x-ray scattering (AXS), and yields information on the formation of solid solution. In this article, we report the structural investigation of nanostructured  $\text{Ag}_x\text{Ni}_{1-x}$  powders and  $\text{Ni}_x\text{Co}_{100-x}$  films, using synchrotron radiation techniques of x-ray diffraction, anomalous x-ray scattering and X-ray absorption.

## 2. Experimental

Nanocrystalline  $\text{Ag}_{1-x}\text{Ni}_x$  ( $x=0.2-0.8$ )[6] powders were prepared by the gas condensation method [7]. The deposition chamber was first evacuated to  $\leq 1 \times 10^{-5}$  Torr and then back-filled with helium of  $\sim 2$  Torr before metal evaporation. Pure Ag and Ni were co-evaporated by resistive heating from a tungsten boat. Following rapid evaporation of the metals, small particles formed by condensation from Ag and Ni atoms in helium. They were then transported via the convection of helium gas and deposited on a liquid nitrogen cooled trap. The distance between the cold trap and the evaporation source was approximately 4 cm. Such distance was optimized to ensure that the smallest nanocrystalline particles were synthesized. The evaporation and condensation typically occurred in a very short time. The compositions of powders were controlled by using different evaporation source contents.

As-synthesized powders were examined by X-ray diffraction (XRD) and transmission electron microscopy (TEM). A Rigaku D/MAX IIIA  $\theta$ - $2\theta$  diffractometer with filtered  $\text{Cu K}\alpha$  radiation (wavelength = 1.5406 Å) was used in conjunction with a graphite monochromator. The diffraction profiles were analyzed quantitatively using a profile fitting program to obtain accurate peak position and full-width at half-maximum (FWHM) values. Line broadening was used to estimate the average crystallite size whenever such analysis is possible. Under conditions optimized for the synthesis of the finest particles, an average particle size range of 5-20 nm was obtained in these samples. High-resolution TEM (HRTEM) (JOEL 2010F) with electron diffraction capability confirmed the nanocrystalline nature of these materials. Synchrotron radiation experiments were conducted at two third-generation synchrotron facilities: Synchrotron Radiation Research Center (SRRC), Taiwan and the Pohang Light Source (PLS), Korea. EXAFS measurements were performed at B11-DCM beamline, (SRRC) and 3C1 beamline (PLS) using both fluorescence and transmission modes of detection. Soft-x-ray XAS and photoemission spectroscopy experiments were carried out in the 6m-HSGM (High energy Spherical Grating Monochromator) beamline (SRRC) in an ultrahigh vacuum chamber.

The  $\text{Ni}_x\text{Co}_{100-x}$  magnetic films were deposited on Cu substrates using the non-aqueous electroless method known as the Polyol [8]. It involved the reduction and deposition of constituent atoms in refluxing ethylene glycol at 194 °C. The films with

compositions of  $\text{Ni}_{100}$ ,  $\text{Co}_{100}$ ,  $\text{Ni}_{90}\text{Co}_{10}$  and  $\text{Ni}_{50}\text{Co}_{50}$  were studied using conventional XRD and synchrotron techniques of EXAFS and anomalous x-ray scattering. The study was carried out at beamlines DB-11 of SRR and 5C2 at PLS. Anomalous x-ray scattering (AXS) provided site-selective, structural information of nanostructured films that could not be obtained by either XRD or EXAFS alone, or combined.

### 3. Results and discussion

#### 3.1 AgNi nanocomposite powders

According to the phase diagram of binary alloys, solid solutions of AgNi cannot be formed [9]. The solid solubility of Ni in Ag is as low as 0.1% even at 750 °C. Several efforts to produce such a solid solution by creating metastable states under extreme conditions, such as liquid quenching, did not lead to a reproducible fabrication procedure. The formation of the solid solution was only reported on thin films using laser ablation deposition [10,11], co-evaporation method [12], and recently mechanical alloying [13]. Taking advantage of the high surface-to-bulk energy ratio, which is characteristic of nanocrystals, we were able to prepare samples [7] containing significant amounts of AgNi alloy phase with a wide range of compositions using a co-evaporation of Ag and Ni.

As-synthesized nanocrystals had average particle size of 5-20nm as examined by TEM [7]. Three types of X-ray absorption spectra were measured: X-ray Absorption Near Edge Spectroscopy (XANES), Extended X-ray Absorption Fine Structure (EXAFS) and soft-X-ray absorption spectroscopy, to investigate the electronic properties, the local structure and the stability of the AgNi binary alloys. Photoemission spectroscopy was used to identify the chemically different species. Our results indicate that, by controlling the processing parameters and therefore varying the particle size, materials with new properties can be obtained which can be potentially important for industrial applications such as catalysis, magnetic recording and sensor technology.

Note that XAS has a rather large probing length and this property can eliminate or at least reduce contributions from the complicated surface properties of nanoparticles, which dominate several other more surface sensitive spectroscopy techniques. Specifically, the probing length of the XAS (even by total electron yield (TEY) detection) is longer than 5 nm. This matches well with the average particle size of our samples, thus enabling us to perform “bulk” measurement.

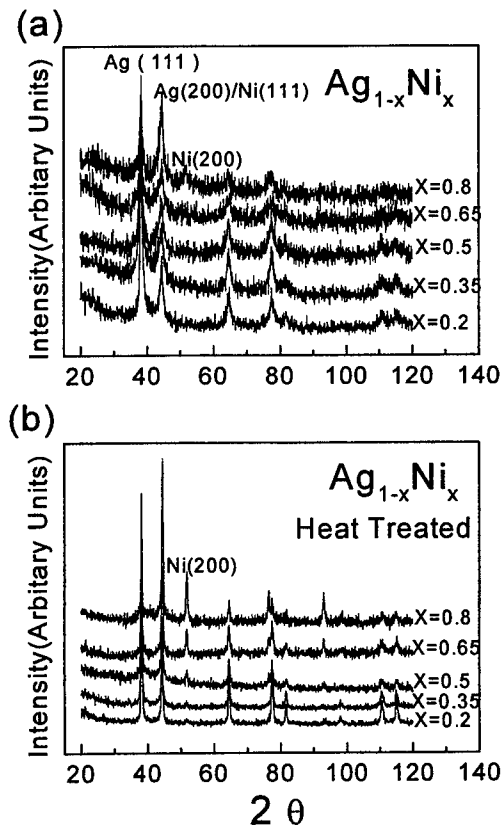


Fig. 1 - X-ray powder diffraction of the AgNi nanocrystals with different compositions. (a) as grown sample (b) after heat treatment.

The first evidence of the formation of an AgNi solid solution was suggested by the absence of the Ni (200) XRD peak in as-synthesized samples. As shown in Fig. 1(a), Ni (200) is barely visible in the sample of high Ni concentration. The measured Ni  $K$  edge absorption intensities remain nearly proportional to the Ni contents in these samples. The nearest neighbor bond lengths, 2.1-2.5 Å with a nearly linear relation with respect to the Ni composition, deduced from the Ni  $K$  EXAFS oscillations, are shown in Fig. 2(a). Similar to the Vegard's law commonly used to deduce the alloy composition from the lattice parameter [1] obtained by XRD, such a relation indicates the formation of the AgNi solid solution. The disappearance of the Ni (200) diffraction peak in the mixed Ag-Ni phase, therefore, can only be attributed to the loss of long-range order of Ni in the formation of solid solution.

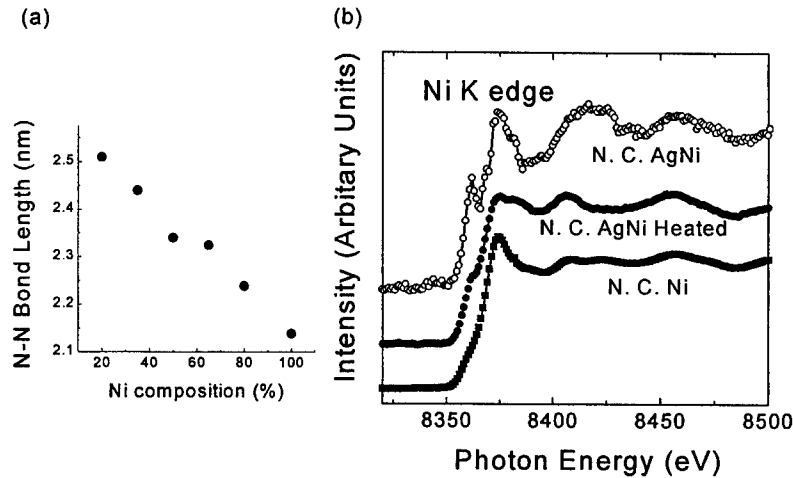


Fig. 2 - (a) The nearest-neighbor bond length deduced from the Ni *K* edge spectra of  $\text{Ag}_{1-x}\text{Ni}_x$  ( $x=0.2-0.8$ ). (b) Ni *K* absorption spectra of AgNi nanocrystals before and after high temperature annealing. The spectra are compared with commercial Ni nanocrystalline powders (bottom curve).

A similar behavior can also be expected in the case of Ag although Ag (111) and (200) diffraction peaks were observed. The widths of the Ag diffraction peaks reveal, in fact, that the corresponding domains are much larger than the average particle size of our AgNi nanocrystals. Therefore, we can conclude that the measured Ag (111) and (200) diffraction peaks are a result of Ag that did not participate in the mixing process. Such type of inhomogeneous morphology has also been imaged with HRTEM measurement of our samples. The inhomogeneous size distribution of Ag indeed created much more difficulties in the precise determination of the microstructure. For example, the EXAFS measurements of the Ag *L* absorption edge with different compositions show almost no difference, which can be again attributed to that the larger Ag particles did not participate in the formation of solid solution. They dominated the EXAFS spectra since they had higher order.

The sharp feature in the edge region — see the top spectrum in Fig 2(b) — at a photon energy of approximately 8365 eV is another strong indication that the Ni atoms of our samples are in a very different electronic structure than those of commercial Ni powders which are also in a nanocrystalline form. Samples prepared with different noble gas pressure, which usually leads to different particle sizes, do not exhibit strong differences in the X-ray absorption spectra. However, the subsequent heat treatment caused drastic changes in the near-edge region and the EXAFS region. Note the

sintering of the sample is conducted on pellets of compacts powders. It is concluded that as-prepared AgNi nanocrystals were metastable alloys and heat treatment to  $> 320$  °C caused the phase separation of the elements.

The drastic decrease of the Ni  $L_{2,3}$  absorption spectra intensity of the nanocrystalline AgNi pellets upon heating (not shown here)[14] indicates that a strong segregation of Ag and Ni occurred at the temperature above 320 °C. Since the free energies of Ag and Ni increase with temperature and become eventually larger than the free energy gained by alloying in the nanocrystals, the segregation becomes energetically favorable above a certain temperature. We also observed the dependence of phase segregation on particle size (the relative AgNi solid solution content) in samples upon heating. For samples with particle size of 50 nm and larger (under different control parameter and not included in the discussion of this work), the gain in the surface energy is not enough to form substantial amount of AgNi solid solution and, therefore, no segregation can be detected.

A simple empirical rule can be used to examine the surface segregation of transition metal alloys: the constituent with lower elemental surface tension enriches the alloy surface [15]. The same argument leads to a surface enrichment of Ag since the surface tension of the Ag in the liquid phase is lower than that of Ni [16]. The segregation temperature measured in our present experiment is consistent, within the accuracy of our temperature measurement, with that derived from the temperature dependent X-ray powder diffraction measurements. The result of the X-ray diffraction of the sample after heating to above 420 °C followed by a rapid quenching shows Ni(200) (Fig. 1b). Scanning electron microscopy (SEM) micrographs showed a sharp segregation between Ag and Ni, with Ni buried under Ag in a thin film-like arrangement. The segregation explains the decrease in the Ni  $L$  absorption signal.

In order to clarify the causes of alloying, we simulated the process by depositing Ni on Ag clusters prepared on HOPG (Highly Oriented Pyrolytic Graphite),  $\text{SiO}_2$  surfaces (natural oxide of Si (100) wafer) and on  $\text{TiO}_2$  nanocrystalline particles [17]. It is well known that small amounts of Ag on HOPG and  $\text{SiO}_2$  form clusters with small size [18]. In our case, only  $\sim 0.05$  monolayer (ML)(nominal) of Ag was deposited first and Ni was then deposited at room temperature with increasing coverage. Synchrotron photoemission spectroscopy was used to detect possible alloying or chemical reactions. Both valence and core level spectra were collected and their spectral intensities are also used as a quantitative indication of the metal deposition. Typical valence band spectra in such sequence are shown in Fig. 3(a) on which Ag and Ni were deposited on sample substrate, a Ta foil, covered with  $\text{TiO}_2$  nanocrystals.

We did not find any evidence of Ag-Ni bonding or atomic exchange on the Ni/Ag covered HOPG and  $\text{SiO}_2$  surfaces by examining both valence and core level spectra. However, in the case of deposition on the  $\text{TiO}_2$  nanocrystalline particle surfaces, the Ag  $3d$  core level spectrum, shown in Fig. 3(b), exhibits a clear shoulder on the low-binding energy side, compared to the Ag  $3d$  spectrum taken on the freshly deposited Ag. The amount of Ni deposited here was approximately 0.03 ML, a small amount not yet sufficient to metallize the surface. Based on the valence band spectra in Fig. 3(a), more than 0.1 ML of Ni is needed to produce spectral intensity at the Fermi level, indicating the metallized surface is metallized. In this case, the shoulder appearing on the low-

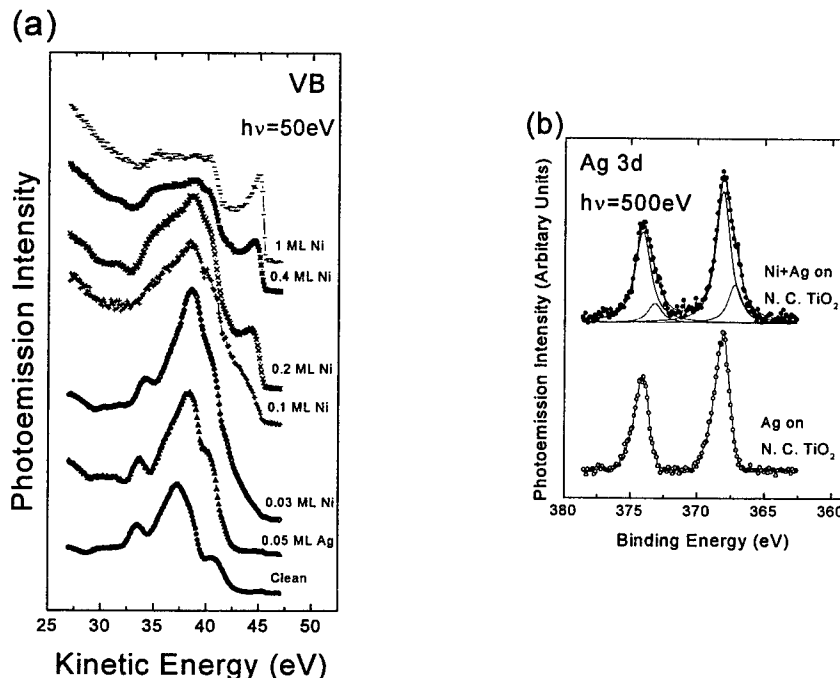


Fig. 3 – (a) Valence band photoemission spectra of the metal deposition sequence taken at a photon energy of 50 eV. The substrate is  $\text{TiO}_2$  covered Ta foil. (b) Photoemission Ag 3d core level spectra taken at a photon energy of 500 eV. New components are developed on the low binding energy side of the spectrum of Ag nanocrystals (deposited on  $\text{TiO}_2$ ) covered with Ni. Spectrum with open circles is taken with Ag nanocrystals.

binding energy side of the spectrum is not likely due to local charging related to the partial metal coverage. Instead, it indicates the existence of a new phase of AgNi similar to what was observed in the nanocrystalline samples grown by gas evaporation.

Subsequent XANES measurements on the Ni  $K$  edge on these samples also confirms this phase by giving rise to a similar near edge structure. The particle size of AgNi grown on  $\text{TiO}_2$  is as small as the AgNi nanocrystalline particles grown by the gas evaporation method. Ag and Ni grown on the HOPG and  $\text{SiO}_2$  apparently have much larger particle size, approximately 500 nm, according to SEM micrographs. This difference in the particle size again is consistent with the spectroscopy measurements. Thus, it is likely that the major driving force for the AgNi alloy formation is the high surface energy of nanocrystals. The only apparent role of the growth kinetics during the gas evaporation process is on small particle size.

In summary, X-ray diffraction and EXAFS measurements revealed the existence of the solid solution phase by the disappearance of Ni(200) diffraction peaks and by the linear relation of the Ni nearest neighbor bond length with respect to the Ni composition. The new feature in the XANES spectra further indicates that the AgNi solid solution is formed.

The alloy is stable from room temperature up to 320 °C. Heating the pellet samples above 320°C causes Ag and Ni to segregate and thin films of Ag and Ni are formed with Ag on top of Ni. The near edge spectra of heat-treated samples are much closer to bulk Ag and Ni than before heat treatment. An effort to simulate the gas evaporation process with a procedure under ultrahigh vacuum failed to yield similar alloy particles on the HOPG and SiO<sub>2</sub> surface. On the other hand, Ni and Ag deposited on TiO<sub>2</sub> give rise to a new component on the low-binding-energy side of the Ag 3d spectrum which can be explained by the formation of an AgNi alloy. This indicates that the surface energy plays the key role in allowing the production of the new alloy.

### 3.2 NiCo nanocomposite films [19]

Nickel and cobalt have mutual solubility at equilibrium. The lattice parameters for fcc Ni and fcc Co are 3.5238 Å and 3.5447 Å, respectively. The K absorption edges for Co and Ni are 7.709 keV and 8.333 keV, respectively. Although EXAFS has been widely accepted as a very useful tool to study nanostructured metastable alloys, it is not suitable for investigating materials consisted of elements (such as Ni and Co) with very close lattice parameters, backscattering amplitudes and phase shifts. Therefore, the EXAFS results of the Ni edge and Co edge of Ni<sub>50</sub>Co<sub>50</sub> and Ni<sub>90</sub>Co<sub>10</sub> (not shown here) did not show noticeable difference from the elemental films. The EXAFS data were therefore inconclusive regarding the mixing of these elements in the films.

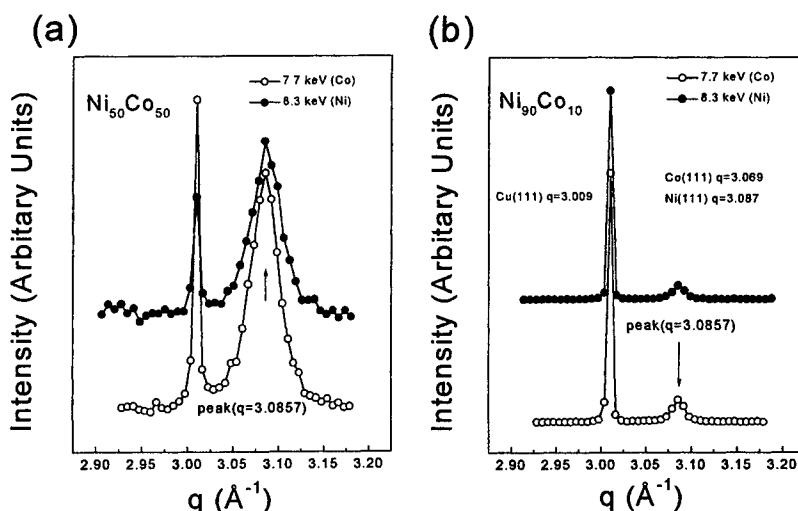


Fig. 4 - XRD powder scans of (a) Ni<sub>50</sub>Co<sub>50</sub> and (b) Ni<sub>90</sub>Co<sub>10</sub>.

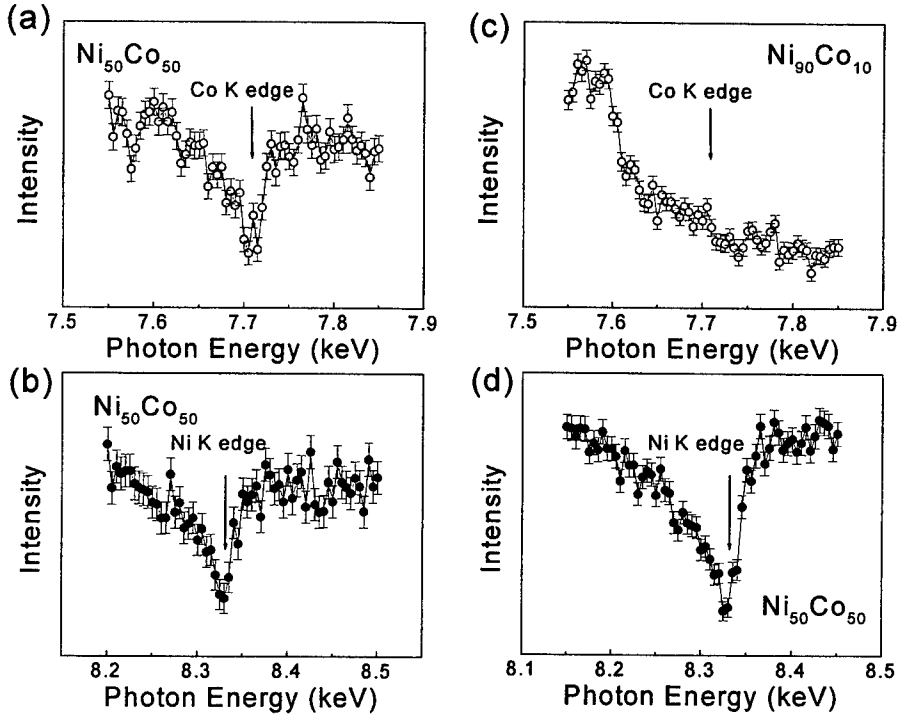


Fig. 5 - AXS results of the XRD peak at  $q=3.085 \text{ \AA}^{-1}$  of (a)  $\text{Ni}_{50}\text{Co}_{50}$  scanning across Co, (b) Ni absorption edges, and (c) of  $\text{Ni}_{90}\text{Co}_{10}$  scanning across Co and (d) Ni absorption edges.

Conventional XRD results showed these films were polycrystalline and had a single set of fcc diffraction peaks without any sign of elemental separation. Because of the close lattice parameters of fcc Ni and fcc Co, the formation of alloy or composite could not be ascertained, as also reported for  $\text{Ni}_{80}\text{Co}_{20}$  powders synthesized using similar method [20]. The average crystallite size of  $\text{Ni}_{100}$ ,  $\text{Co}_{100}$ ,  $\text{Ni}_{90}\text{Co}_{10}$  and  $\text{Ni}_{50}\text{Co}_{50}$  was in the range of 15 to 64 nm. For anomalous x-ray scattering measurements, powder diffraction experiments were first performed to determine the position of the (111) Bragg reflection of the films ( $q = 3.086 \text{ \AA}^{-1}$ ) at each photon energy. The powder scans of  $\text{Ni}_{50}\text{Co}_{50}$  and  $\text{Ni}_{90}\text{Co}_{10}$  are shown in Figs. 4(a) and 4(b). Only a single peak at the (111) reflection existed in these films. The momentum transfer was fixed to the (111) reflection of the film, i.e.  $q = 3.086 \text{ \AA}^{-1}$ , and the scattering intensity was monitored as the x-ray energy was varied through Ni and Co absorption edges, respectively.

If the element in question is related to the specified Bragg peak, then the elemental absorption causes a decrease in the Bragg intensity at its absorption edge. A cusp, caused by the interference between the Thomson scattering amplitude and the real part

of the anomalous scattering amplitude [4], is observed in the energy scan of the Bragg peak. Such behavior was observed for the Ni<sub>100</sub> and Co<sub>100</sub> films.

Figure 5 shows the AXS measurement of the (111) peaks of Ni<sub>50</sub>Co<sub>50</sub> and Ni<sub>90</sub>Co<sub>10</sub>. Both Ni and Co were related to this Bragg peak for Ni<sub>50</sub>Co<sub>50</sub>. For Ni<sub>90</sub>Co<sub>10</sub>, only Ni was found in this Bragg peak. However Co absorption was absent. It is noted that EXAFS and energy dispersive analysis confirmed the existence of Co in this sample. Thus, within our detection limit of AXS, Co was not associated with the (111) Bragg peak of this film. Only Ni solely contributed to this long-range order. The detection limit of long range order using XRD is roughly 3 nm. The absence of Co in the (111) Bragg peak of Ni<sub>90</sub>Co<sub>10</sub> suggested that Co did not alloy with Ni in this atomic arrangement. Further AXS work using other Bragg peaks of the films is in progress to investigate if Co was associated with other peaks or amorphous.

In summary, for AgNi nanocomposite powders, EXAFS, XANES, soft-x-ray and photoemission spectroscopy were used to identify the miscible phase and its most likely origin. For NiCo nanocomposite films, AXS technique was added to this approach in order to gain more specific information on the alloy formation. It is clear, regardless of the apparent success, that further work needs to be performed on exploiting the AXS technique with more sophisticated peak fitting and simulation, as well as on improving the resolution limit.

### Acknowledgment

The work is supported by National Science Council, Taiwan. G.M. Chow would like to acknowledge the support of this work by the Academic Research Fund of National University of Singapore and the grant from the US Office of Naval Research. W.C. Goh was supported by the NUS postgraduate research scholarship.

### References

1. Cullity, B. D. (1978) *Elements of x-ray diffraction*, 2nd edition, Addison-Wesley, Menlo Park, USA, , p. 375.
2. Michaelson, C. (1995) On the structure and homogeneity of solid solutions: the limits of conventional x-ray diffraction, *Phil. Mag. A*, **72**, 813.
3. Chow, G. M., Kurihara, L. K., Kemner, K. M., Schoen, P. E., Elam, W. T., Ervin, A., Keller, S., Zhang, Y. D., Budnick, J. and Ambrose, T. (1995) Structural, morphological, and magnetic study of nanocrystalline cobalt-copper powders synthesized by the polyol process, *Journal of Materials Research*, **10**, 1546.
4. Stragier, H., Cross, J.O., Rehr, J.J., Sorensen, L.B., Bouldin, C.E. and Woicik, C.E. (1992) Diffraction anomalous fine structure: A new x-ray structural technique, *Phys. Rev. Lett.*, **69**, 3064.
5. Pickering, I. J., Sansone, M., Marsch, J. and George, G. N. (1993) Diffraction Anomalous Fine Structure: A New Technique for Probing Local Atomic Environment, *Journal of American Chemical Society*, **115**, 6302.
6. Note that the actual stoichiometry was not determined due to the lack of reliable reference to index the materials. Therefore, compositions given in this work were only referred to the source contents.
7. Tung, C. -Y., Gu, J. M., Lin, H. -M., Hwu Y. and Cheng, N. -F. (1997) X-Ray Absorption Spectroscopy Study of Ag<sub>x</sub>Ni<sub>1-x</sub> Nanocrystalline Solid Solution, *Nanostructured Materials*, **9**, 351;

---

Tung, C. -Y. Ph.D. Thesis, Tatung University, Taipei, Taiwan.

8. Chow, G. M., Ding, J., Zhang, J., Lee, K. Y., Surani D. and Lawrence, S. H. (1999) Magnetic and hardness properties of nanostructured Ni-Co films deposited by a nonaqueous electroless method, *Appl. Phys. Lett.*, **74**, 1889.
9. Massalski, T. B. Okamoto, H. Sabramamian, P. R. and Lacprzak L. (eds.) (1990) *Binary Alloy Phase Diagrams*, ASM International, Materials Park, OH, 2nd Ed., Vol. 1, p. 64.
10. van Ingen, R. P., J. Fastenau, R. H. and Mittemeijer, E. J. (1994) Formation of Crystalline Ag<sub>x</sub>Ni<sub>1-x</sub> Solid Solutions of Unusually High Supersaturation by Laser Ablation, *Phys. Rev. Lett.* **72**, 3116.
11. Rodmacq, B., Mangin, P. and Vettier, C. (1991) Evidence for Antiferromagnetic Coupling in Ag/Ni Superlattices: a Neutron Scattering Study, *Europhys. Lett.*, **15**, 503; dos Santos, C. A. Rodmacq, B. Vaezzadeh, M. and George, B. (1991) Oscillatory magnetic coupling in Ag/Ni superlattices, *Appl. Phys. Lett.* **59**, 126; Tonnerre, J. M., Jergel, M., Raoux, D., Idir, M., Soullier, G., Barchewitz, R. and Rodmacq, B. (1993) Resonant magnetic soft X-ray diffraction at Ni L<sub>II</sub> edge: ferro- and antiferromagnetism in Ag-Ni multilayers, *J. of Magnetism and Magnetic Materials* **121**, 230.
12. Bitti R. R. and Dixmier, J. (1969) Production of Meatable Phase and Solid Solutions by C-evaporation of elements non-miscible in the Liquid State, *Solid State Commun.* **7** 1345.
13. Xu, J., Herr, U., Klassen, T. and Averback, R. S. (1996) Formation of supersaturated solid solutions in the immiscible Ni-Ag system by mechanical alloying, *J. Appl. Phys.* **79**, 3935.
14. Tung, C. Y., Gu J. M., and Lin, H. M., Cheng, N.-F., Hwu, Y. (1996) *SRRC 1995 Annual Activity Reports*, Synchrotron Radiation Research Center, Hsinchu, Taiwan.
15. Zangwill, A. (1988) *Physics at Surfaces*, Cambridge University Press, Cambridge, p.87.
16. Schmit, J. N. Ph. D. Thesis, University of Liege.
17. Hwu, Y., Yao, Y. D., Cheng, N. -F., Tung C. -Y., and Lin, H. -M. (1997) X-Ray Absorption of Nanocrystal TiO<sub>2</sub>, *Nanostructured Materials*, **9**, 355.
18. See, for example, Faraci, G., Costanzo, E., Pennisi, A. R., Hwu Y., and Margaritondo, G. (1992) Binding energies and cluster formation at low metal deposition: Ag on Si and SiO<sub>2</sub>, *Z. Phys. D* **23**, 263.
19. Chow, G.M., Goh, W.C., Hwu, Y.K., Chow, T.S., Je, J.H., Lee, H.H., Kang, H.C., Noh, D.Y., Lin, C.K., and Chang, W.D., (1999) Structure determination of nanostructured Ni-Co films by anomalous x-ray scattering, *Appl. Phys. Lett.*, **75**, 2503.
20. Viau, G., Ravel, F., Acher, O., Fiévet -Vincent, F. and Fiévet, F., (1994) Preparation and microwave characterization of spherical and monodisperse Co<sub>20</sub>Ni<sub>80</sub> particles, *J. Appl. Phys.* **76**, 6570.

## X-RAY STUDY OF MICROSTRUCTURE AND GRAIN BOUNDARY

### STATISTICS IN NANOCRYSTALLINE MATERIALS

A.P. ZHILYAEV, I.V. ALEXANDROV AND R.Z. VALIEV

*Institute for Physics of Advanced Materials*

*Ufa State Aviation Technical University*

*12, K. Marx St., 450000 Ufa, Russia*

#### 1. Introduction

Recently the attention of many scientists has been attracted to nanostructured materials possessing novel physical and mechanical properties [1, 2]. Nanoscale microstructures can form during processing of nanostructured materials using different methods, e.g. condensation in inert gas atmosphere, rapid quenching, electrodeposition, ball milling, severe plastic deformation and during oxidation (see [1, 3]). Among them only severe plastic deformation and ball milling give bulk nanostructured samples while others yield thin films. It is well known that internal interfaces or the grain boundaries (GB) control behavior of nanostructured materials. Such properties as strength, ductility, hardness, resistance to failure, corrosion resistance, fatigue and electromigration are all greatly affected by grain boundaries and their behavior as an whole ensemble [4-7]. Two major methods are used to characterize GB: transmission electron microscopy can analyze the atomic structure of individual grain boundaries and X-ray diffractometry may be used to examine volume-averaged characteristics. This paper presents a review of recent results obtained in ultra-fine grained (UFG), nanocrystalline (NC) metals, and oxide films using X-ray analysis. Both fine structure (crystallites' size, microdistortions) and statistical features (texture and grain boundary character distribution) have been calculated from experimental measurements. Different techniques (severe plastic deformation, electrodeposition, oxidation etc.) have been used to process metals and alloys where mean grain size is less than 1  $\mu\text{m}$  for UFG and less than 100 nm for NC materials.

#### 2. Methods of Sample Processing

Samples of Cu and Ni with UFG structure (a mean grain size less than 0.2  $\mu\text{m}$ ) were processed by torsion straining and equal channel angular pressing. Nanostructured nickel samples with grain size about 20 nm were made by electrodeposition. Zirconium oxide thin film formed during oxidation of Zr-2.5%Nb alloy. Mean grain size of  $\text{ZrO}_2$  film formed is less than 50 nm by TEM.

To process the UFG microstructure in bulk Cu and Ni the method of severe plastic deformation was applied. It was carried out using intense shear deformation by torsion straining under high imposed pressure of several GPa and equal channel angular pressing [3] (Figure 1).

Torsion straining under high imposed pressure of several GPa (Figure 1a) was used for fabrication of disk type samples 10 mm in diameter and 0.2 mm in thickness from massive ingot and ball milled powder as well. The logarithmic torsion strain of samples was 7 at the perimeter of the disks.

During equal channel angular pressing cylindrical ingots were machined and pressed through a special die to give a continuous repeating passage (Figure 1b). Following pressing, the samples were pressed again through the same die. Equal channel angular pressing was conducted up to 12 passes. Each pass corresponded to true strain equal approximately to 1. Equal channel angular pressing facility used in these experiments had an angle of intersection of two channels equal to  $90^\circ$ . The processed samples had a cross section diameter about 20 mm and the length of about 80 mm.

### 3. X-ray Analysis

The results of conducted experimental studies [3] indicate that a general view of X-ray diffraction patterns of nanostructured materials processed by severe plastic deformation differs from that of corresponding coarse-grained materials (Figure 2). The X-ray patterns of nanostructured materials are characterised by changed relative intensity, significant broadening, a shift in position of centroids, change in a X-ray peak profile shape and elevated diffusion background of X-rays scattering [5,9]. Note a growth of relative intensity of X-ray peak (111) in respect to other peaks that is typical for nanostructured Cu (Fig. 2) and Ni.

X-ray diffraction patterns of these materials requires their careful examination and interpretation. For example, long tails and considerable broadening lead to necessity of

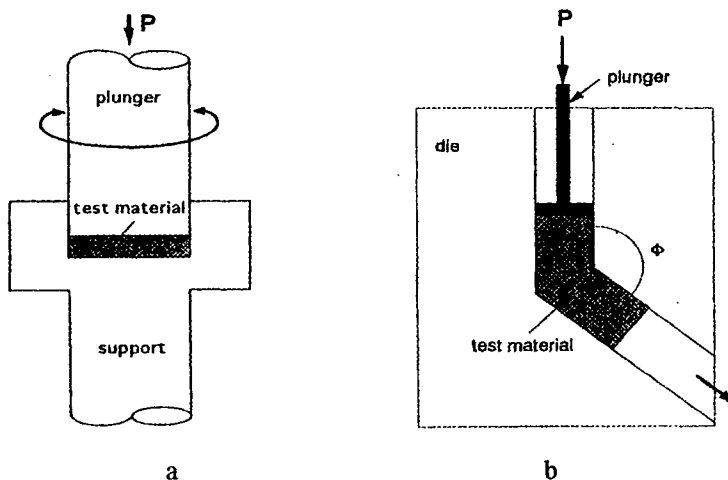


Figure 1. Principles of severe plastic deformation methods: torsion straining under high pressure (a), equal channel angular pressing (b).

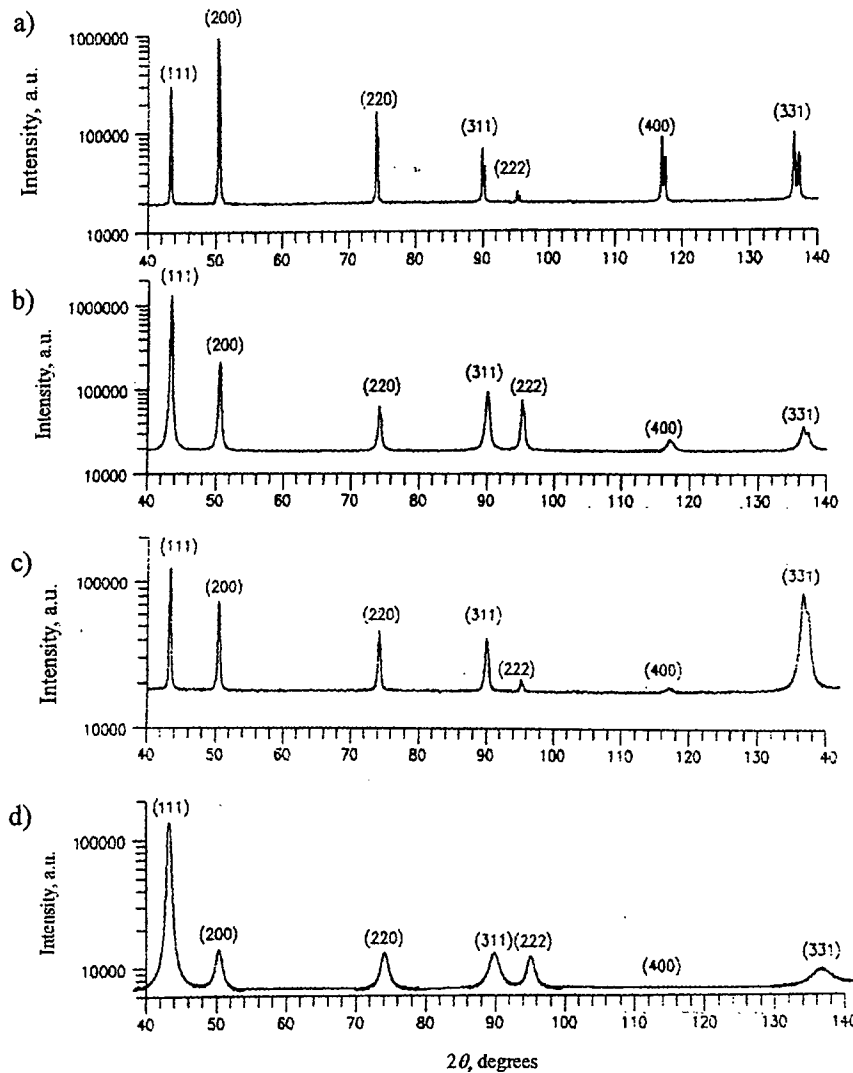


Figure 2. X-ray diffraction patterns of Cu: coarse-grained (a); nanostructured, processed by torsion straining (b), equal channel angular pressing (c), consolidation of powder by torsion straining (d).

obtaining experimental information from the very wide intervals in vicinities of X-ray peaks. The very small intensity of high angle peaks should be taken into account as well.

The changes observed in the general view of X-ray diffraction patterns testify that the evolution of structure of the studied materials resulted from severe plastic deformation. The data obtained in different experiments indicate changes in lattice parameter, structure refinement, elevated microdistortions of a crystal lattice, high static and dynamic atomic displacements, and decrease in the Debye temperature.

Moreover, severe plastic deformation results in changes in preferential orientations of grains, i.e. crystallographic texture. The low temperature experimental studies revealed that the thermal expansion coefficient  $\alpha_T$ , equalled to  $(3.75 \pm 0.10) \times 10^{-5} \text{ K}^{-1}$  in

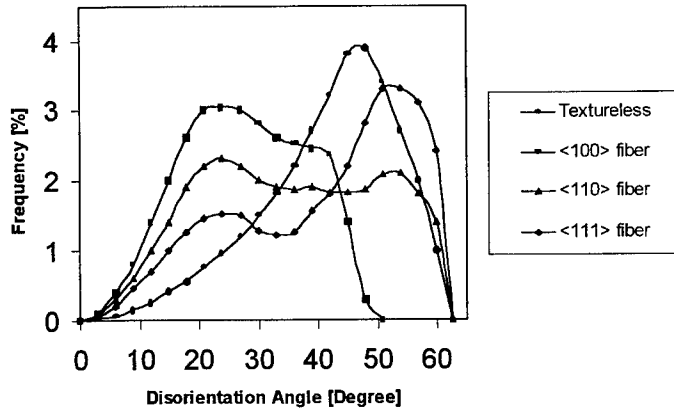


Figure 3. Disorientation angle distributions for variously textured model polycrystals

nanostructured Ni exceeds a corresponding tabular value of coarse-grained Ni by approximately a factor of 3 [9]. These observations correlate with the data of the Young's modulus measurements previously conducted by the ultrasonic method [10]. According to these data the Young's modulus in the nanostructured Cu processed by severe plastic deformation is lower than in the corresponding coarse-grained one by 12±13%. At the same time a decrease in the Debye temperature was revealed in these nanostructured materials. Thus, in the nanostructured Ni the Debye temperature calculated on the basis of the X-ray data is equal to  $293\pm7$  K [9] which is lower than a tabular value of the coarse-grained Ni by 22%. The calculated Debye temperature in the nanostructured Cu is  $233\pm6$  K which is lower than a tabular value of the coarse-grained Cu by 23%.

#### 4. Grain Boundary Statistics (General Consideration)

In recent years, the relationships between grain boundary misorientation distributions and texture have been studied both experimentally and by means of computer simulation [10]. While there have been attempts to derive misorientation distributions from texture data only, our studies have shown that in general the relationship between the two distributions is not straightforward but rather ambiguous. Complications arise due to the orientation correlation, which may exist between various crystallites of the polycrystalline aggregate. These two factors, texture and orientation correlations, determine the grain boundary character distribution in a sample. Contributions of these factors to the misorientation distribution as a whole and to the fractions of specific grain boundary types are dependent on the material. In some materials, for example b.c.c. alloys, grain boundary distribution is primarily determined by texture [11]. However, the orientation correlations play a dominant role in f.c.c. alloys. The same may be true for other materials with a high propensity to formation of special (twin) boundaries. The results obtained on nanocrystalline monoclinic zirconia film give evidence in favor of this conclusion. That the misorientation distribution depends on texture can be seen e.g. from Fig. 3, which displays the misorientation angle distributions for differently textured model polycrystal with the cubic crystal lattice. Of course, the use of texture

data for evaluating the grain boundary misorientation (and hence character) distribution is very attractive because the determination of grain boundary statistics is much more laborious and time-consuming as compared to the texture measurement. However, such an approach must be treated with caution since the spatial correlations between neighboring grain orientations may have a dominant effect in the grain boundary statistics. The procedure of evaluation of the misorientation distribution from the texture data consists of assigning orientations corresponding to some model or real orientation distribution function (ODF) to a model set of grains and computing misorientations at the boundaries between these grains. Detailed description of the technique can be found elsewhere [4-7].

#### 4.1. EXAMPLES OF DIFFERENT MATERIALS

##### 4.1.1. BCC Materials

The data accumulated to date indicate that the role (contribution) of texture and orientation correlations in the misorientation distribution depends on the type of material. Apparently, there are little orientation correlations in metals and alloys with the BCC crystal structure. Therefore, obtaining the grain boundary character distribution directly from the experimentally determined ODF, as was done e.g. for a Fe-6%Si alloy [12], seems to produce reasonable results for such materials. Some selected results from paper [13] are presented in Table 1.

TABLE 1. Percentages of some grain boundary types in an electrical steel

GB Type	$\Sigma 3$	$\Sigma 5$	$\Sigma 7$	$\Sigma 9$
Simulation	2.2	0.9	1.0	1.0
Experiment	2.8	0.8	0.8	1.0

##### 4.1.2. FCC Materials

On the other hand, experimental data show that the grain boundary distributions in FCC materials are dominated by the correlations in the orientations of contiguous grains. In aluminum the predominant type of correlation is the formation of low-angle boundaries, with the formation of twin ( $\Sigma 3$ ) boundaries being the secondary correlation. The grain boundary character distribution obtained from the experimentally (x-ray) determined ODF assuming these correlations, agrees well with the grain boundary distribution measured independently using transmission electron microscopy [9] (see Table 2). We must admit, however, that the agreement between the simulated and experimental misorientation angle and axis distributions was not as good as in the case of the  $\Sigma$ -distributions.

TABLE 2. Percentages of different grain boundary types in some fcc materials

GB Type	Aluminum		AISI 316L	
	Experiment	Simulation	Experiment	Simulation
LAB, $0 < 15^\circ$	30.0	32.4	8.9	7.3
$\Sigma 3$	4.0	2.6	33.1	27.6
Random	66.0	65.0	58.0	65.1

#### 4.1.3. Zirconium Oxide Films

TABLE 3. Percentages of different grain boundary types in  $\text{ZrO}_2$  formed on  $\text{Zr-2.5\%Nb}$  alloy during oxidation.

GB Type	Grain Growth Texture	Fiber Texture [001]	Mixture
LAB, $\theta < 15^\circ$	—	11,4	2,1
$\Sigma 3$	33,4	12,1	—
$\Sigma 71$	66,6	13,6	—
Random	—	62,9	97,9

Recently, an interesting type of twin boundaries has been observed in corrosion films formed on a zirconium alloy [14]. The oxide layer consists of predominantly monoclinic zirconia with crystallite dimensions in the nanometer range. Vast areas in the film contain zirconia grains of only eight distinct orientations. These orientations can be explained by growth of zirconia crystallites in the [001] and [100] directions of the monoclinic lattice with misorientations between adjacent grains described by the  $180^\circ$  and  $90^\circ$  rotations about the above axes. In such areas only few types of intercrystallite boundaries are possible, all of them being special, coherent and semi-coherent twins and pseudo-twins. Unlike the cubic structure, where there is only one type of twin boundary –  $\Sigma 3$ , several non-equivalent twin variants are possible in the monoclinic lattice, and grain boundary networks built entirely of twins are possible in zirconia. In this particular case, exchange of grain positions would create the grain boundaries of the same set, i.e. the grain boundary character distribution would not change. Thus, a specific strong crystallographic texture in such regions of the microstructure is determined by the correlations that provide for certain special misorientations between contiguous crystallites.

#### 4.1.4. Nickel Oxide Films Formed At Single Crystal Of Nickel

TABLE 4. Percentages of different grain boundary types in  $\text{NiO}$  formed on (100) and (111) crystal faces of Ni

GB Type	(100) Substrate	(111) Substrate
LAB, $\theta < 15^\circ$	40.4	6.4
$\Sigma 3$	3.1	27.6
Random	56.5	66

Grain boundary diffusion of reactants in oxide layers makes a dominant contribution to the transport mechanisms during the oxidation of metals at temperatures less than one half of the melting point of the oxide. Qualitative evidence for the importance of grain boundary transport was found in recent work [15, 16] where it was shown that the difference between the oxide growth rates on (100) Ni and (111) Ni crystals is more than one order of magnitude. The microstructural examination indicates that this difference cannot be attributed solely to the density of short circuits paths but the character of individual grain boundaries should also be considered. A computer model

was developed to simulate the diffusion of Ni through both the grain boundaries and lattice in NiO at elevated temperatures. The grain boundary network was defined by the shape and size of oxide grains and by the grain boundary character distribution. Two sets of GBCD describing the oxide grown on (100) and (111) crystals faces of Ni (Table 4) were employed to simulate transport through the NiO film. The model was found to be effective in predicting of the difference in diffusivity through the nickel oxide grown on (100) and (111) faces. The ratio of parabolic constants for NiO for two different oxide films obtained from simulation equals 11 while from the experiments this ratio found is 14. It proves that the GBCD greatly influence and control the Ni diffusion through NiO layer.

## 5. Concluding Remarks

The conducted experimental X-ray structural studies showed that X-ray diffraction patterns of nanocrystals processed by severe plastic deformation significantly differ from the corresponding coarse-grained ones. These differences consist in significant broadening, shift of positions of centroids, change in X-ray peak profile shape and increase in diffusion background of X-rays scattering.

The significance of grain boundary character distribution discussed in this paper is that GBCD can vary in metals with different type of crystalline lattice, texture and microstructure. These affect spatial correlation in orientation of neighbours determining grain boundary clustering.

**Acknowledgments.** One of the authors, A.P.Zhilyaev would like to thank Drs. V.Yu.Gertsman and F. Czerwinski for helpful discussion of the results.

## 6. References

1. Schiøtz J.D., Di Tolla Francesco and Jacobsen K. W. (1998) Softening of nanocrystalline metals at very small grain sizes, *Nature* **391**, 561-563.
2. McFadden S. X., Mishra R S., Valiev R. Z., Zhilyaev A. P. and Mukherjee A. K. (1999) Low-temperature superplasticity in nanostructured nickel and metal alloys, *Nature* **398**, 684-686.
3. Valiev R. Z., Islamgaliev R. K. and Alexandrov I. V. (1999) Bulk nanostructured materials processed by severe plastic deformation, *Progress in Material Science* (accepted for publication).
4. Gertsman V. Y., Zhilyaev A. P., Pshenichnyuk A. I., and Valiev R. Z. (1992) Modeling of grain boundary spectrum in polycrystals with crystallographic texture, *Acta Metall. Mater.* **40**, 1433-1441.
5. Zhilyaev A. P., Gertsman V. Y., Mishin O. V., Pshenichnyuk A. I., Aleksandrov I. V. and Valiev R. Z. (1993) Grain boundary misorientation spectra determined by real ODF in f.c.c. materials susceptible to annealing twinning, *Acta Metall. Mater.* **41**, 2657-2665.

---

6. Gertsman V. Y., Tangri K. and Valiev R. Z. (1994) Overview No.116: On the grain boundary statistics in metals and alloys susceptible to annealing twinning, *Acta Metall. Mater.* **42**, 1725-1804.
7. Zhilyaev A. P., Pshenichnyuk A. I., and Valiev R. Z. (1994) Energetical approach to modelling grain boundary misorientation spectrum determined by real ODF, *Strength of Materials (Proc. Int. Conf.)*, Eds. H.Oikawa et al, Sendai: JIM, 997-890.
8. Alexandrov I. V., Zhang, K., Kilmametov A. R., Lu, K., Valiev R. Z. (1997) The x-ray characterization of the ultrafine-grained Cu processed by different methods of severe plastic deformation, *Materials Science & Engineering A* **234-236**, 331-334.
9. Zhang K., Alexandrov I.V., Kilmametov A. R., Valiev R.Z., Lu K., (1997) The crystallite-size dependence of structural parameters in pure ultrafine-grained copper. *J. Phys. D: Appl. Phys.* **30**, 3008-3015.
10. Mulyukov R. R., Akhmadeev N. A., Valiev R. Z., Mikhailov S. B. (1993) Strain amplitude dependence of internal friction and strength of submicrometre-grained copper, *Materials Science and Engineering A* **131**, 143-149.
11. V.Y.Gertsman, A.P.Zhilyaev and J.A.Szpunar (1998) On the role of orientation correlations in the grain boundary character distribution in textured polycrystals, in *Proceedings of ICGG-III*. (accepted for publication).
12. Morawiec A., Szpunar J. A. and Hinz D. C. (1993) Texture influence on the frequency of occurrence of CSL-boundaries in polycrystalline materials, *Acta Metall. Mater.* **41**, 2825-2832.
13. Hayakawa Y., Szpunar J. A., Palumbo G. and Lin P. (1996) The role of grain boundary character distribution in Goss texture development in electrical steels. *J. of Magnetism and Magnetic Materilas* **160** 143-144.
14. Gertsman V. Y., Lin Y. P., Zhilyaev A. P. and Szpunar J. A., Special grain boundaries in zirconia corrosion films. *Phil. Mag.* (accepted for publication)

---

## XRD STRAIN AND STRESS DETERMINATION IN NANOSTRUCTURED FILMS AND COATINGS

Thomas Tsakalakos, Department of Ceramic and Materials Engineering  
Mark Croft, Department of Physics  
Rutgers University  
Piscataway, NJ 08854, USA

### 1. Abstract

The residual stress determination of nanostructured films and coatings is reviewed. A method of measuring the depth dependence of the stress profile using energy dispersive x-ray diffraction with a high-energy "white" beam synchrotron radiation source is presented. The profiling is accomplished with the aid of a highly collimated incident and scattered x-ray beams and with micro positioning of the sample-interface. The depth of the profiling is on the order of mm and the resolution of the profiling is on the order of a few microns. The technique allows the three dimensional profiling of the stress distribution in these materials.

### 2. Introduction

X-ray diffraction has of course been the central technique for nearly a century for determining interatomic distances in solids. Applications of this technique to profiling residual strains, as a function of depth from a surface, have also been developed on a more limited basis. Such conventional residual surface strains analysis has utilized the "sin 2 $\Psi$ " diffraction method [1], where the varying penetrating power of the x-rays with varying incident angle is exploited. This technique is limited both by the rather broad convolution of scattering depths via the exponential penetration function, and by the limitation of the penetration length to a few microns.

At the nanoscale level Tsakalakos has worked extensively on stress distribution around interfaces of similar or dissimilar multilayered materials using advanced x-ray methods [2,3]. Earlier work [4] on fatigue, corrosion-fatigue and stress-corrosion-cracking demonstrated the ability to measure excess dislocation densities near the surface by x-ray rocking curve analysis. This method, however, failed to quantify the residual stress as a function of distance because it relied on successive removal of surface layers, which resulted in redistribution of the stresses in the remaining material.

In this paper we review some aspects of the energy dispersive diffraction technique as a nondestructive method from which the three dimensional state of stress

can be deduced. We also report some new results on WC/Co nanostructured coatings prepared by plasma spraying coating methods.

The expansion of the availability of high-energy synchrotron "white beam" sources (20-100 keV) has led to the expansion of the use of energy dispersive x-ray diffraction. This technique (see Fig. 1. for a schematic) has several unique advantages: these x-rays penetrate deeply; the data collection geometry is extremely stable with stationary incident/diffracted-beam paths; this stability and the high intensity of the synchrotron beam allow extremely high incident/diffracted beam collimation thereby defining very small highly position-specific diffraction volumes; the data collection is very efficient/rapid allowing good signal-to-noise diffraction spectra to be taken quickly on small volumes; and finally, recent advances in precise sample micro positioning allow precision scanning of the diffraction volume laterally and as a function of depth through the sample.

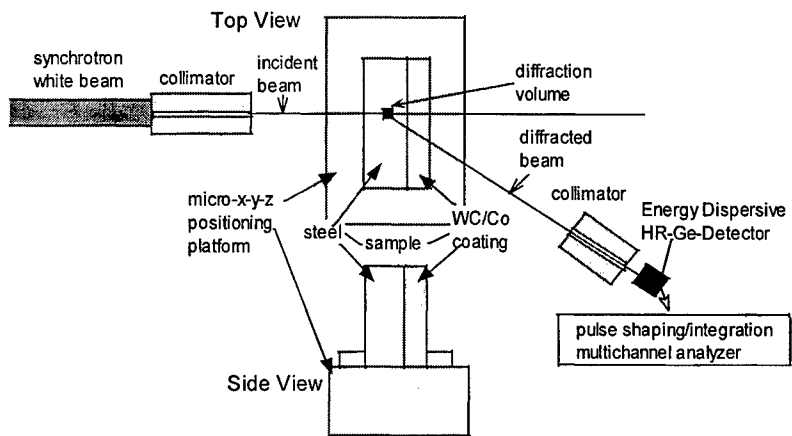


Fig. 1. A schematic of the experimental geometry for energy dispersive x-ray diffraction for WC/Co coatings on steel.

This energy dispersive x-ray diffraction (EDXRD) technique has been widely used for many years for high-pressure diffraction measurements on the small diffraction volumes inside diamond anvil high-pressure cells. The use of this technique for profiling strains in engineering materials has more recently evolved [1,5]. In this section of paper we will note some aspects of applying the energy dispersive diffraction technique to probing the three-dimensional homogeneity and state of stress in WC/Co wear resistant coatings on steel.

It is of great technological importance to be able to predict the failure of materials subjected to static stressing in aggressive environments or dynamic or repeated loading in mechanical and structural applications. This ability is often hindered when inhomogeneous distributions of residual, interfacial or other type of elastic

stresses due to the processing or manufacturing conditions, are present. Thus, for deformation processes which are known to be highly sensitive to preexisting large elastic stresses, the evaluation of these inhomogeneous stresses with respect to depth from the surface or interface is equally essential to the comprehensive characterization of deformation induced damages. Because the EDXRD method is nondestructive, it represents an ideal tool with which to elucidate structural changes, and the degradation in mechanical performance such as fatigue failure and fracture.

### 3. Energy dispersive technique

Energy dispersive x-ray diffraction involves considering the traditional Bragg equation (1) at a constant scattering angle,  $2\theta$ , (usually a few degrees) as a function of the x-ray energy.

$$E_{hkl} = \frac{hc}{\lambda} = \frac{hc}{2 \sin \theta} \frac{1}{d_{hkl}} \quad (1)$$

Here the interatomic plane spacings,  $d_{hkl}$ , are uniquely related to the energies at which the corresponding Bragg reflections occur,  $E_{hkl}$ . Since the scattered x-ray energies are typically measured by Ge-detector (see Figure 1) calibrated in units of keV, a more useful version of this equation is

$$E_{hkl} [\text{ in KeV}] = \frac{6.22}{d_{hkl} \sin \theta}. \quad (1a)$$

With this technique [1] the strain ( $\epsilon$ ), related to the shifts in the plane spacings ( $\Delta d_{hkl}$ ), is determined by the energy-Bragg-line shifts ( $\Delta E_{hkl}$ ).

$$\epsilon = -\left(\frac{\Delta d}{d}\right)_{hkl} = -\left(\frac{\Delta E}{E}\right)_{hkl} \quad (2)$$

The strain-resolution that this technique has can be estimated from the differential of equation (2).

$$\left| \left( \frac{\delta d}{d} \right)_{hkl} \right| = \left| \left( \frac{\delta E}{E} \right)_{hkl} \right| + |\operatorname{ctn} \theta| \Delta \theta \quad (3)$$

For a typical scattering geometry (2)  $\Delta\theta$  can be about 2 mrad with  $\theta$  in the  $2^\circ$  to  $8^\circ$  range, however, substantial improvements on these figures have been and are being made. The  $\delta E$  is the limit of our ability to determine the shift in the centrum of the Bragg-energy peak. Although energy resolution of the cryogenically cooled Ge-detector is only on the order of 0.2 KeV at 60 KeV (or better) the detectable shift in the peak centrum position of such peaks (fitted to Gaussian line shapes) can be far higher. Indeed with such methods Kuntz et. al. [1] has emphasized that the strain requiring sensitivities of  $10^{-4}$  can be obtained. Kuntz et. al. [1] profiled and separated stress and strain variations in the radial and "hoop strain" directions for cylindrical composite materials.

Here we report some preliminary EDXRD measurements on small diffraction volumes in a WC/Co coating on a high-strength-steel base micro-positioned to separately probe the base and coating. These measurements were carried out on Beam Line X17C at the National Synchrotron Light Source at Brookhaven Lab with the indispensable aid of Dr. J. Z. Hu. The enhanced high energy white beam on this line is supplied by a superconducting wiggler insertion device. A schematic of the typical geometry for these preliminary measurements is shown in Fig. 1.

The standard columniation slits on this beam line allow aperturing of the incident beam down to 10 microns. The diffracted beam columniation depends on the variable detector distance from the fixed scattering volume. The existing micro-positioning stage on the line was also utilized. The sample used consisted of a 100 micron WC/Co coating plasma sprayed onto a 2-mm thick steel base.

In Fig. 2, the diffraction pattern for a small volume in the steel is shown along with its bcc indexing. This pattern was collected over just a couple of minutes in the geometry shown in the schematic Fig. 1. This spectrum emphasizes the utility of this hard radiation for collection of high quality diffraction data on small volumes even when buried beneath a high-Z coating.

In Fig. 3, EDXRD pattern for the WC/Co coating is displayed along with the WC indexing. The weak W<sub>2</sub>C impurity lines labeled are typical for such materials. The W-K and W-L fluorescence lines are also noted.

Figures 4 and 5 demonstrate the applicability of the method in terms of strain resolution, which is about  $10^{-4}$  and the penetration depth, which reaches 3 mm depth with a diffracting volume size of about  $5 \mu\text{m}$  [1]. The measurements were performed on controlled samples of Al<sub>2</sub>O<sub>3</sub> cylindrical fibers embedded in CP Titanium matrix composite. The solid lines represent the theoretically obtained stress distributions from the interface showing the excellent agreement between theory and experiment.

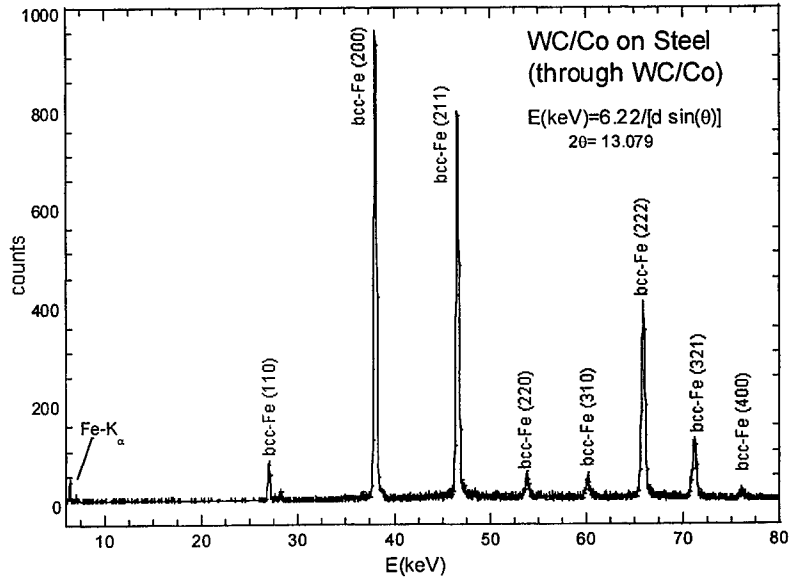


Fig. 2. The EDXRD from the steel layer of a WC/Co on steel sample. Note that this pattern was taken in the geometry where the entered the steel surface normally and the diffracted beam exited the coating surface at an angle  $2\theta$  to the normal (as in the schematic).

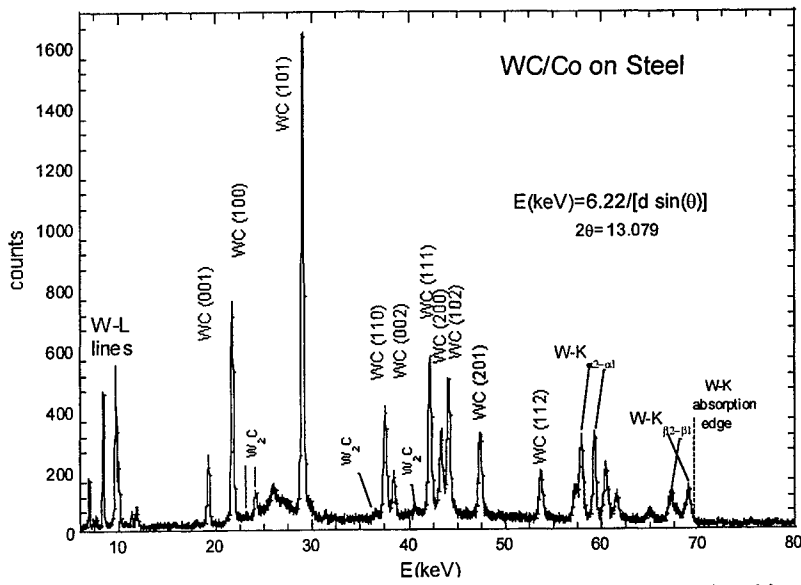


Fig. 3. The EDXRD from the WC/Co layer of a WC/Co on steel sample. Note that this pattern was taken in a reflection geometry to obtain a high quality near surface pattern for the coating.

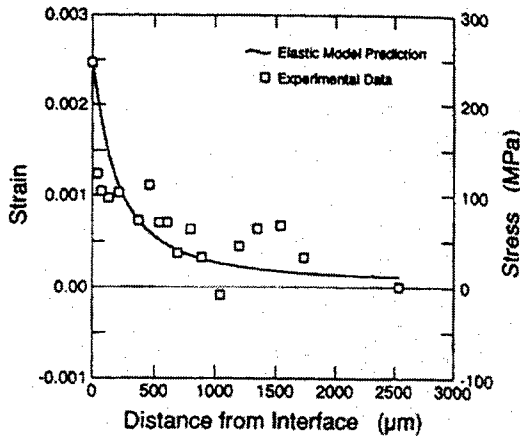


Fig. 4 - Hoop residual strain profile for the CP titanium/Al<sub>2</sub>O<sub>3</sub> (HIPO) sample

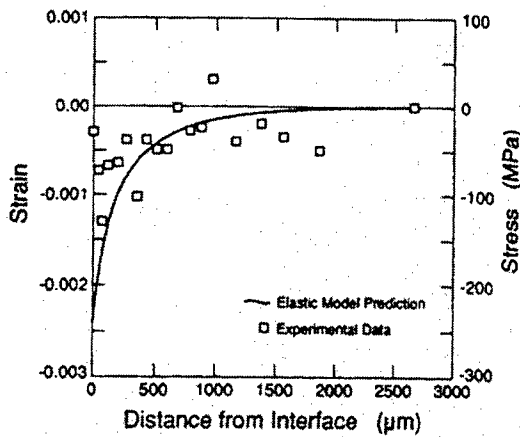


Fig. 5 - Radial residual strain profile for the CP titanium/Al<sub>2</sub>O<sub>3</sub> (HIPO) sample

#### 4. Discussion and Conclusions

In this paper we have reviewed a new technique for measuring residual stresses in nanostructured films and coatings using energy dispersive x-ray diffraction. The scattering volume was scanned through this interface of substrate/coating via micro positioning of the sample. The samples were placed into a geometry that allowed x-ray access in various orientations. Lateral profiling of the strains, approaching the edges, were also possible to be performed to probe for strain relief effects at such surfaces.

These experiments were carried out on beam lines at the National Synchrotron Light Source at Brookhaven Lab.

A key factor for the accurate measurement of the residual and interfacial stress distribution is the ability to penetrate the coating and the substrate sufficiently to allow for long range stress relaxation from the surface and interface of the nanostructured coatings.

The energy dependence of the absorption length ( $1/e$  decay length) for x-rays in WC/Co is shown in Fig. 6. Note that the density of commercial WC/Co of  $15 \text{ g/cm}^3$  was used. The effective penetration lengths in the 30 -150 keV range are sufficiently large to allow the proposed diffraction profiling. Indeed, as shown in Fig. 6, the penetration depth for WC/Co is in the range of a few mm for the working energy conditions.

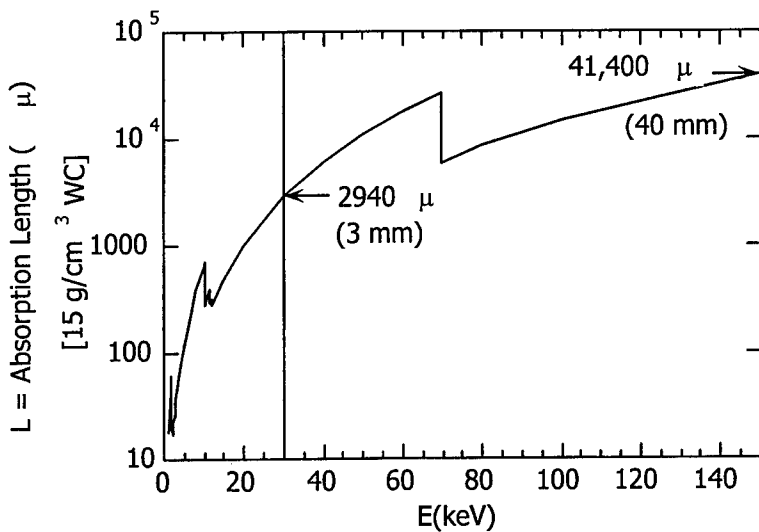


Fig. 6. The energy dependence of the absorption length ( $1/e$  decay length) for x-rays in WC/Co.

The detected volume is determined by the intersection of the collimated beam and the diffracted beam. Incident beam columniations of down to  $5 \mu\text{m}$  have been reported as possible both at NSLS [6] and CHESS [7]. Additional incident and diffracted beam aperturing will be used.

The diffraction experiments proposed utilize a constant incident and diffracted beam positions. Thus positioning of the diffraction volume is determined by the translational positioning of the sample. Sample micro positioning is typically available on beamlines (e.g.  $2.5 \mu\text{m}$  step size reported for X23A3 Beamline at NSLS). For additional required accuracy Newport Corporation produces a wide range precision positioners (e.g.  $0.1 \mu\text{m}$  repeatable positioning with 400 mm travel).

In summary, for nanostructured films and coatings with thickness in the range of 100  $\mu\text{m}$  we can measure the stress distributions with spatial resolution down to 1  $\mu\text{m}$  due to new developments in beam aperturing and micro-position devices. We can measure strains down to  $10^{-4}$  with accuracy of about 2 to 5 % (as determined by the peak position described above). Our original control experiments of WC/Co coatings demonstrated the feasibility of the method and revealed some of the expected working conditions for the stress determination. For films of larger thickness, a better resolution can be obtained by increasing the diffracted volume.

In the future, it is hoped that this approach to the problem of the residual stress distribution can eventually transcend the laboratory research stage and be used directly as a diagnostic tool for technological applications. For example, an in-situ fatigue stage development in conjunction with the EDXRD technique could provide invaluable information on the determination of prefracture damage, crack initiation and the remaining lifetime of the materials.

### Acknowledgments

The Authors gratefully acknowledge the support of the Office of Naval Research under contract ONR N000149910424- 99PRO4801-00. These measurements were carried out on Beam Line X17C at the National Synchrotron Light Source at Brookhaven Lab with the indispensable aid of Dr. J. Z. Hu.

### References

1. Kuntz, T., Wadley, H. and Black D. (1993) Residual strain gradient determination in metal matrix composites by Synchrotron X-ray Energy Dispersive Diffraction Metallurgical Transactions A, 24A, 1117.
2. Lee, J-W., Mayo, W.E. and Tsakalakos, T. (1992) Elastic and plastic contributions to x-ray line broadening of InGaAsP/InP heterostructures, Journal of Electronic Materials, 21, 867-875.
3. Chassapis, C.S. and Tsakalakos, T. (1997) Multidimensional optimization of a stochastic model for X-ray diffraction from superlattices, Computer Physics Communications 99, 163-179.
4. Panborn R.N., Yazici, R., Tsakalakos, T., Weissmann, S. and Kramer, I.R. (1980) Determination of prefracture damage in fatigued and stress-corroded materials by x-ray double crystal diffractometry, National Bureau of Standards Special Publication 567, Proceedings of Symposium on Accuracy in Powder Diffraction held at NBS, Gaithersburg, MD, 433-49.
5. see numerous references in Advances in X-ray analysis: Volume 39. Proceedings of the Forty-Fourth Annual Conference on Applications of X-Ray Analysis (Col. Springs Col., 1995), Gilfrich, J., Goldsmith, C. Huang, T., Jenkins, R., Predecki, P. K. and Smith, D. (eds.) (Plenum Press, NY, 1997).
6. see Microbeam Diffraction at NSLS (July 97 NSLS Newsletter).
7. see CHESS B1 Beamline Facilities Description.

---

## INTERFACES IN NANOSTRUCTURED FILMS AND COATINGS

I.A.OVID'KO

*Laboratory for Theory of Defects in Materials*

*Institute for Problems of Mechanical Engineering*

*Russian Academy of Sciences*

*Bolshoj 61, Vas.Ostrov, St.Petersburg 199178, Russia*

### 1. Introduction

This paper reviews theoretical models of interfaces in nanostructured films and coatings with the special attention being paid to their nano-scale structural features and the properties associated with such features. The paper deals with many models which, however, are discussed briefly, in a non-detailed way.

In general, nanostructured films and coatings exhibit outstanding physical and mechanical properties, in which case they are thought of as advanced materials with wide applications in different areas of technology, e.g. [1-6]. The outstanding properties of nanostructured films and coatings crucially depend on both the structure and the properties of interfaces, that is, intergrain and interphase boundaries whose total volume fraction ranges from 10 to 50 % in such materials. The interfacial structures have been revealed as those ranging rather widely in nanostructured solids. They include the specific interfacial structures that are inherent to only nanostructured solids and conventional interfacial structures that exist also in conventional films and coatings. (Hereinafter, by conventional films and coatings are meant coarse-grained polycrystalline films and multilayer coatings that consist of meso-scale single crystalline or coarse-grained polycrystalline layers.) In this context, the present paper is concerned with not only interfaces in nanostructured films and coatings, but, in part, also with interfaces in conventional films and coatings.

The specific features of interfacial structures in nanostructured films and coatings are caused, in particular, by the following: (1) The volume fraction of the interfacial phase is extremely high in nanostructured films and coatings. (2) Interfaces as structural elements mostly have extremely short dimensions in nanostructured films and coatings, in contrast to the situation with conventional solids. (3) There is a strong elastic interaction between neighbouring interfaces, because (extremely short) distances between them are close to the characteristic scales of their stress fields. (4) In nanocrystalline films and coatings there is a strong effect of triple junctions and nanograins on interfaces and vice versa, in contrast with conventional

films and coatings, because the volume fraction of triple junctions is extremely high in nanocrystalline solids and because nanograins commonly are more distorted than conventional grains in polycrystalline films and coatings. (5) Formation of nanostructured films and coatings frequently occurs at highly non-equilibrium conditions that essentially influence the interfacial structures.

The aforesaid aspects should be taken into account in theoretical models of the interfacial structures in nanostructured films and coatings, which, in most cases, can not be unambiguously identified with the help of contemporary experimental methods. Below we will briefly review “fresh” models of interfaces in nanostructured films and coatings while focusing on highly defected and non-periodic interfaces whose structural features are related to nano-scale effects.

## 2. Misfit Disclinations at Interfaces in Nanostructured Films

Let us consider the specific features of misfit defect structures that can exist in systems consisting of a single crystalline substrate and a nanocrystalline film. In general, misfit stresses (that occur in films due to a geometric mismatch between crystalline lattices of films and substrates) essentially contribute to the properties of films. Misfit stresses are commonly viewed to effectively relax via generation of “standard” misfit dislocations with crystal lattice Burgers vectors. Such dislocations commonly form dislocation rows at interphase (film/substrate) boundaries, partly compensate misfit stresses and, therefore, often improve functional physical characteristics of films, e.g. [7-10]. At the same time, misfit dislocation cores are located at interphase boundaries, and, therefore, negatively affect functional physical characteristics of interphase boundaries. This causes high interest in searching for alternative effective micromechanisms for relaxation of misfit stresses.

In nanocrystalline films with their high-density ensembles of grain boundaries, there is an effective alternative to the standard physical micromechanism for relaxation of misfit stresses, namely formation of special interfacial disclinations (Fig. 1) [11]. Such disclinations induce stresses that compensate, in part, misfit stresses in the film and are located at junctions of the interphase boundary and grain boundaries (Fig. 1a). In general, as with disclinations in polycrystalline and nanocrystalline bulk solids synthesized at highly non-equilibrium conditions [12, 13], the discussed disclinations can exist also at triple junctions of grain boundaries in a nanocrystalline film (Fig. 1b). Hereafter we shall call such disclinations (Fig. 1a and 1b) as misfit disclinations.

Following the estimations [11] of energetic characteristics of a nanocrystalline film with misfit disclinations periodically arranged at an interphase boundary between a substrate and the film (Fig. 1a), the existence of misfit disclinations is more energetically favourable than the existence of “standard” planar rows of misfit dislocations with lattice Burgers vectors. More than that, following estimations [11],

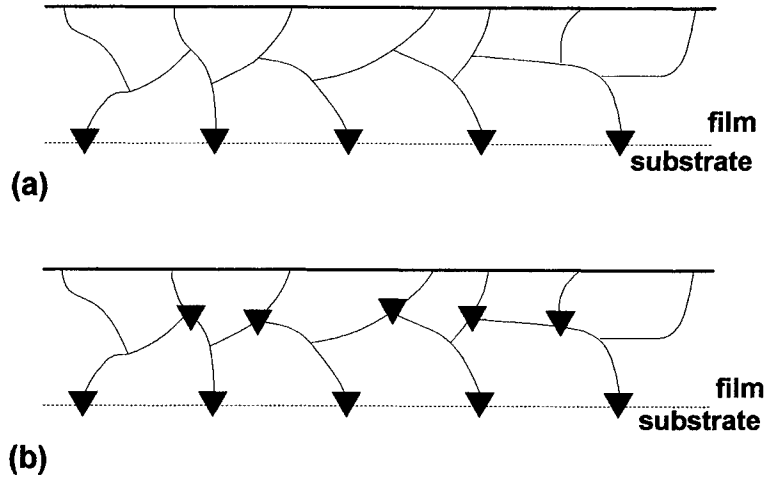


Figure 1. Misfit disclinations at interfaces in nanostructured films. (a) Periodically arranged ensemble of misfit disclinations at nanocrystalline film/substrate interface. (b) Misfit disclinations at interfaces — intergrain and interphase boundaries — in nanocrystalline film.

the critical thickness,  $h_c$ , for the generation of misfit disclinations in nanocrystalline films is  $h_c = 0$ , at least, for characteristic values of misfit parameter ranging from  $10^{-4}$  to  $10^{-2}$ . It means, in particular, that the generation of misfit disclinations is more energetically favourable than the existence of a coherent interphase boundary between a substrate and a nanocrystalline film at any value of its thickness.

Misfit disclinations and their configurations can be formed also in polycrystalline films. The partial case of misfit disclination configurations, namely dipoles of misfit disclinations located at junctions of an interphase boundary and twin boundaries, has been observed experimentally in epitaxial rhombohedral ferroelectric films (see paper [14] and references therein).

Generally speaking, misfit disclinations can also be generated as defects that bound walls of misfit dislocations in single crystalline films and multilayer coatings (Fig. 2) [15]. Such dislocation walls have been observed experimentally in films resulted from convergence of island films [16].

### 3. Grain Boundary Dislocations and Their Configurations as Misfit Defects in Nano-Film/Substrate Systems

In general, due to the presence of high-density ensembles of grain boundaries, their triple junctions, and junctions of grain boundaries and interphase boundaries in nanocrystalline films and coatings, the generation of grain boundary dislocations

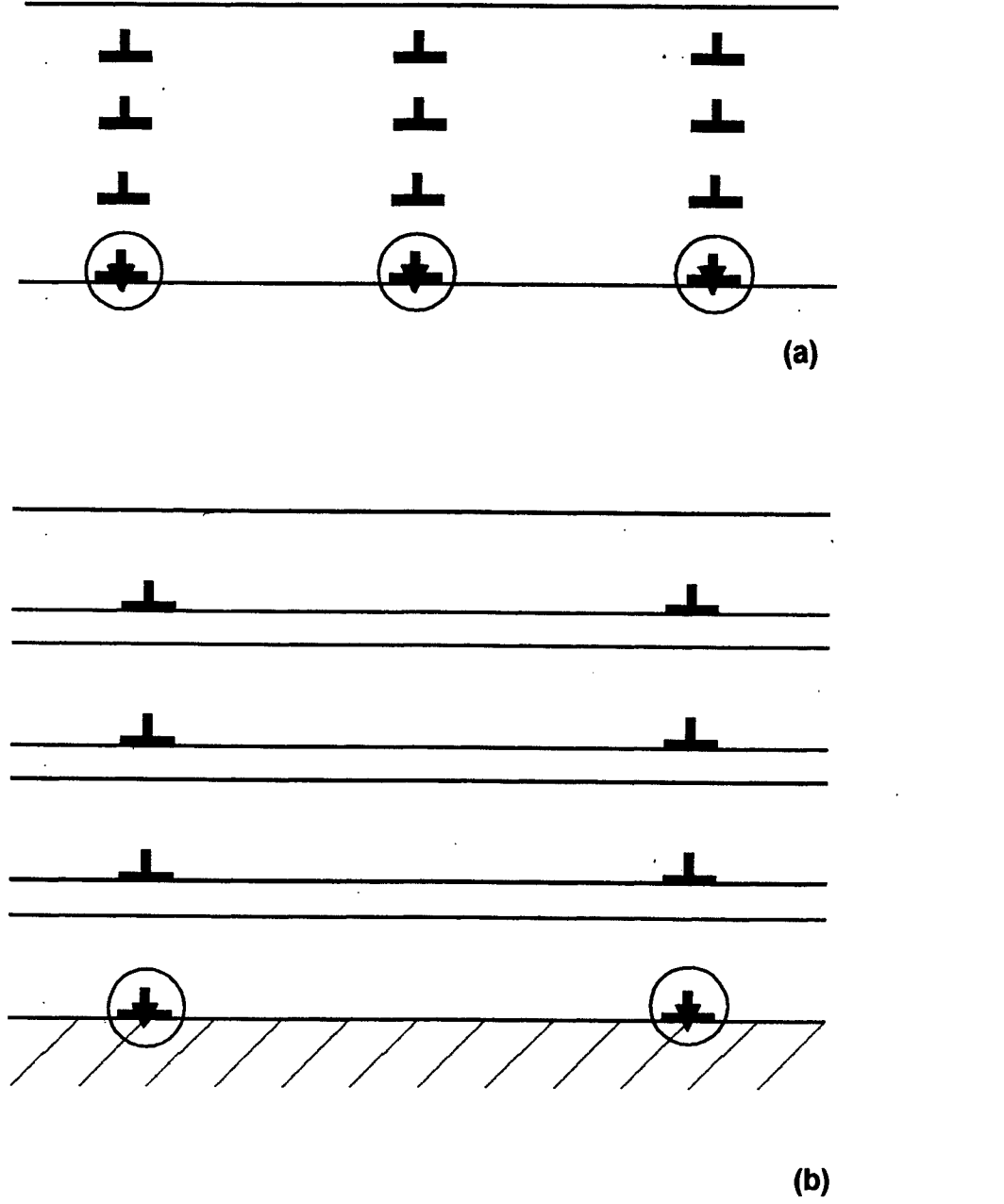


Figure 2. Disclinations (located at open circles) at ragged walls of misfit dislocations in (a) single crystalline film and (b) multilayer coating.

and their configurations as misfit defects, is capable of effectively contributing to relaxation of misfit stresses. For instance, let us consider a periodically arranged ensemble of grain boundary dislocations located at junctions of grain boundaries and the interphase boundary between a single crystalline substrate and a nanocrystalline film (Fig. 3). In context of the general theory of misfit dislocations (e.g., [7-10]), such dislocations create stress fields that compensate misfit stresses generated due to the geometric mismatch between the crystalline phases matched at an interphase boundary. In doing so, the most spatially homogeneous distribution of misfit dislocations is characterized by minimal elastic energy density and, therefore, is most stable.

Grain boundary dislocations are commonly characterized by Burgers vectors being essentially lower than those of "standard" misfit dislocations being crystal lattice dislocations. This specific feature allows grain boundary dislocations to be more homogeneously distributed along an interphase boundary as compared with "standard" misfit dislocations with the proviso that the sum Burgers vectors of the misfit dislocation ensembles are the same per unit of the boundary length. As a corollary, the existence of grain boundary dislocations as misfit dislocations is more energetically favourable than that of "standard" misfit dislocations.

In general, due to the presence of high-density ensembles of grain boundaries in nanocrystalline films, complicatedly arranged configurations of grain boundary dislocations can be formed as defect configurations causing the effective relaxation of misfit stresses in nanocrystalline film/substrate systems. Examples of such configurations are compensated and non-compensated dipoles of grain boundary dislocations (Fig. 4a), networks of grain boundary dislocations distributed within a nanocrystalline film (Fig. 4b), grain boundary dislocation-dislocation ensembles (Fig. 4c), etc.

#### 4. Partly Incoherent Interfaces

An interphase boundary between a single crystalline substrate and a nanocrystalline film is featured by the existence of many boundary fragments bordered by junctions of the interface boundary and grain boundaries of the nanocrystalline film. In these circumstances, one of the effective micromechanisms for misfit stress relaxation that are specific for nanocrystalline film/substrate systems is the formation of a partly incoherent interface, a partly incoherent interphase boundary. Each such a partly incoherent interface consists of both coherent and incoherent fragments and is characterized, in the first approximation, by a modified misfit parameter,  $\tilde{f} = f(1 - \delta)$ , depending on the ratio,  $\delta = l_i/l_c$ , of the sum length,  $l_i$ , of the incoherent fragments to the sum length,  $l_c$ , of the coherent fragments. In general, when the thickness,  $h$ , of a film increases resulting in an increase in the elastic energy, this energy effectively relaxes via generation of new incoherent fragments. In these circumstances, a nanocrystalline film is characterized by two critical values,  $h_{c1}$  and  $h_{c2}$ , of its thick-

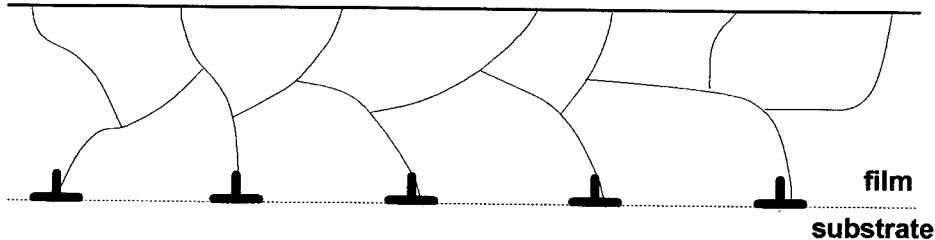
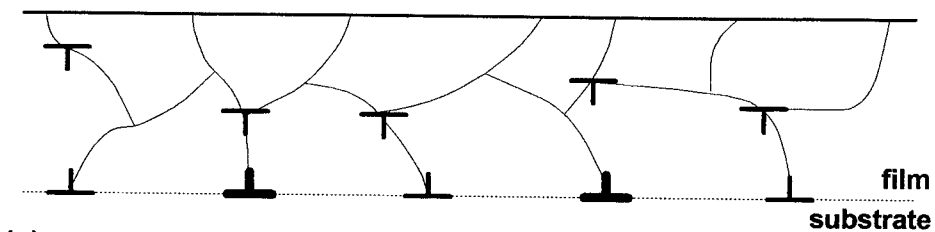
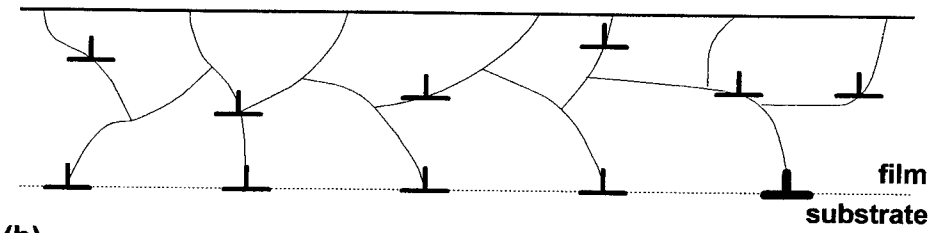


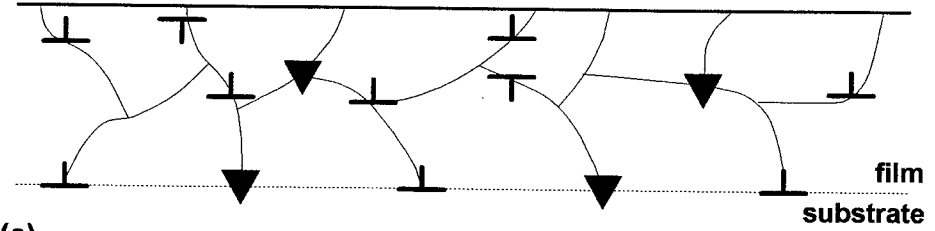
Figure 3. Periodically arranged ensemble of misfit, grain boundary dislocations.



(a)



(b)



(c)

Figure 4. Configurations of interfacial dislocations and disclinations in nanocrystalline films.

ness. Generation of incoherent fragments is energetically favourable in films with thickness above  $h_{c1}$  (Fig. 5 a and b). The existence of a totally incoherent interface is energetically favourable in films with thickness above  $h_{c2}$  (Fig. 5 c).

## 5. Crystal/Glass Interfaces

The properties of advanced crystal-glass nanocomposites essentially depend on crystal/glass interfaces, e.g. [17-19], in which case the characteristics of crystal/glass interfaces are of great interest. Recently, a model [11, 20] has been developed describing crystal/glass interfaces as semi-coherent interfaces containing misfit disclinations and dislocations. In the framework of this model, misfit disclinations are generated at crystal/glass interfaces as extensions of disclinations inherent to the adjacent glassy phase. Misfit dislocations at crystal/glass interfaces provide a partial compensation of the so-called dilatation misfit stresses occurring due to the difference between the characteristic interatomic distances in the adjacent crystalline and glassy phases.

Crystal/glass interfaces modeled [11, 20] as semi-coherent interfaces contain coherent fragments, in which case such interfaces have to be sensitive to crystallographic peculiarities of the adjacent crystalline phase. In this context, experimental observations of faceted crystal/glass interfaces [17, 21] and pronounced textures in polycrystalline films on glassy substrates [19] support the theoretical model [11, 20].

In the framework of the model [11, 20], the total elastic energy density of a crystal/glass interface (calculated as the elastic energy density of misfit disclinations and dislocations) is as follows:

$$W \approx k G a, \quad (1)$$

where  $k$  ranges from 0.06 to 0.18,  $G$  denotes the shear modulus, and  $a$  the mean interatomic distance in the glassy phase. In general,  $W$  is either larger or smaller than values of the energy density (per unit area) of high-angle grain boundaries in crystals (for example, [22]), depending on parameters of grain boundaries and crystal/glass interfaces.

## 6. Amorphization at Interphase Boundaries in Multilayer Coatings

Solid state amorphizing transformations occur in multilayer coatings consisting of alternate layers, say,  $\alpha$  and  $\beta$  [23, 24]. In these circumstances, layers of the new amorphous alloyed phase  $\alpha - \beta$  nucleate at  $\alpha/\beta$  interfaces due to diffusional mixing of atoms  $\alpha$  and  $\beta$  (Fig. 6). Recently, it has been experimentally revealed that the solid state amorphization does not occur in Ni/Ti multilayer composites having the crystalline layer thickness in a composite below some critical thickness  $h_c^{am}$  (being several nanometers) [23].

Solid state amorphizing transformations in layered composites have been theo-

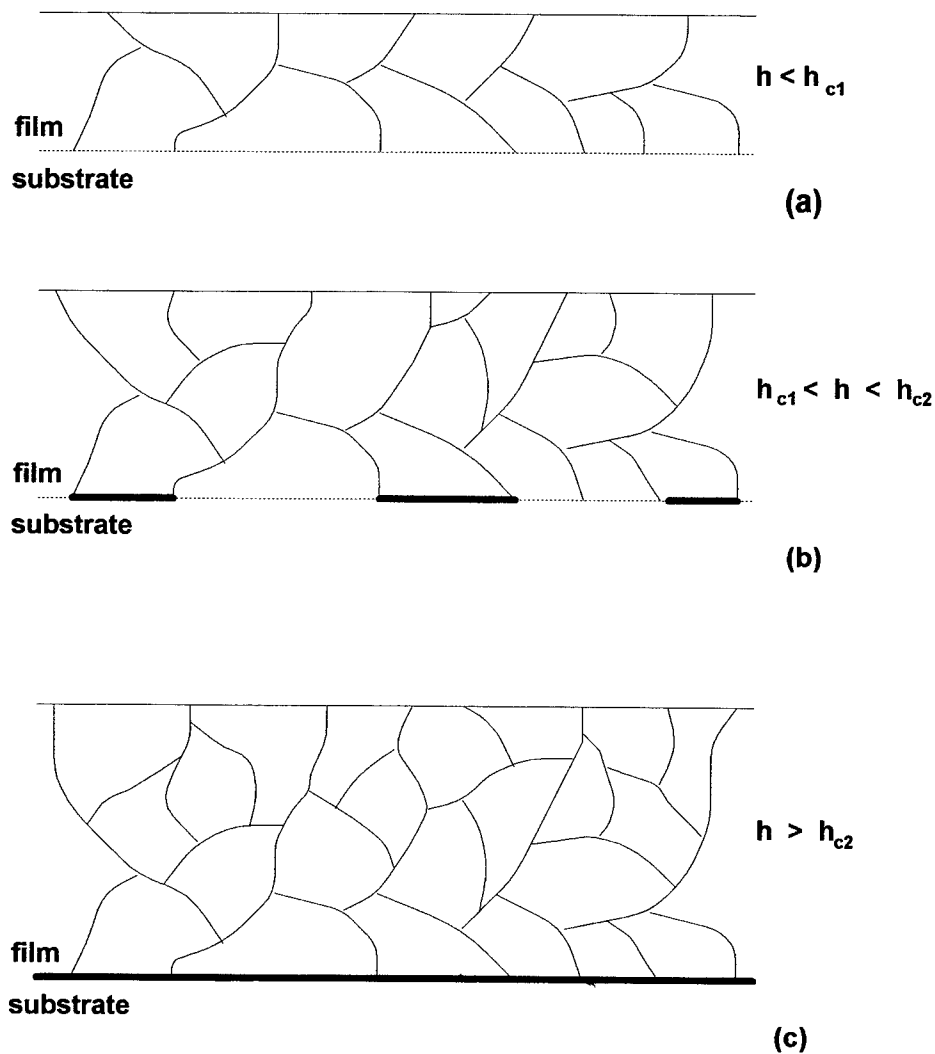


Figure 5. Coherent-to-incoherent transformation of interphase boundary as a micromechanism for misfit stress relaxation.

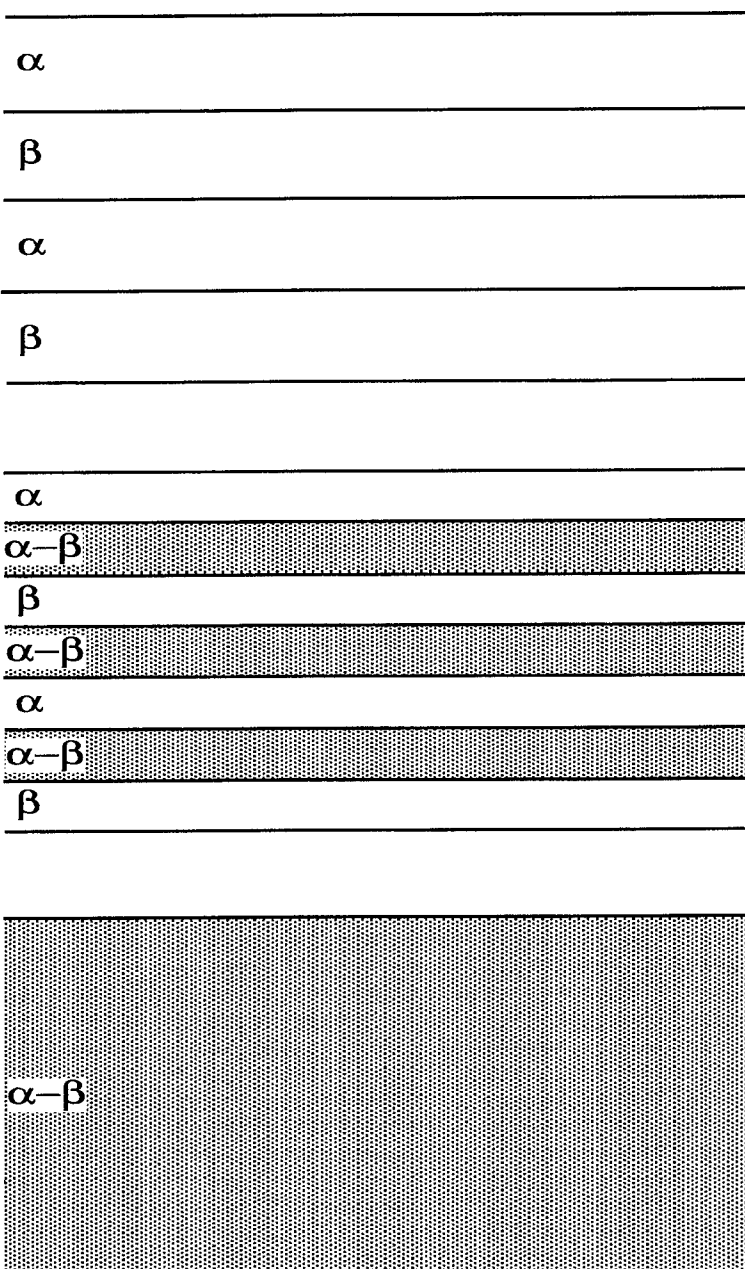


Figure 6. Solid state amorphization in multilayer coatings.

retically described in [25] as phase transformations affected by misfit strains. It has been found that there is a misfit-stress-induced minimal critical thickness  $h_c^{am}$  which characterizes the solid state amorphization in layered composites: composites consisting of layers with thickness whose values are above  $h_c^{am}$ , are amorphized, whereas below are not amorphized.

## 7. Amorphous and Quasioperative Grain Boundaries

Let us briefly outline models that describe amorphous and quasiperiodic interfaces in nanostructured films and coatings. These models are beyond the applicability of the standard concept [22] of periodic interfaces in solids.

Grain boundaries in nanostructured materials are characterized by extremely short lengths, in which case tilt boundaries of finite extent are theoretically recognized to be more often quasiperiodic than periodic [10, 26, 27]. The presence of such quasiperiodic tilt boundaries in nanostructured materials, in particular, is capable of effectively contributing to the experimentally observed deviations of the yield stress dependence on grain size from the standard Hall-Petch relationship [10, 26].

Amorphous grain boundaries are often experimentally observed in nanocrystalline and polycrystalline ceramics [28, 29]. Following computer experiments (see [30, 31] and references therein), such boundaries can exist also in nanostructured metals and silicon. The elastic energy and stress fields of amorphous grain boundaries are effectively calculated as those of special ensembles of grain boundary dislocations.

## 8. Technological Aspects

The above representations on new interfacial defect structures potentially can be used in both optimization of conventional technologies and design of new technologies for synthesis of nanostructured films and coatings with desired properties. So, in the light of the representations of new interfacial defect structures, interphase boundaries in nanostructured films and coatings strongly affect grain boundaries within nanocrystalline films and vice versa. As a corollary, one can use technologies that control interphase boundary parameters in order to form grain boundary structures with desired properties in nanocrystalline layers. And, on the contrary, one can use technologies that control grain boundaries in order to form interphase boundaries with desired properties in nanostructured coatings.

In particular, the effect of relaxation of misfit stresses via formation of grain boundary defects on nanocrystalline films potentially allows one to design films and coatings with spatially variable stable structure which consists of single crystalline

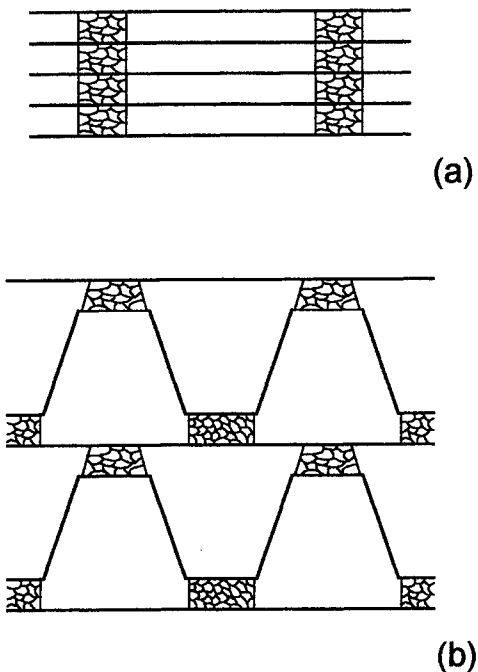


Figure 7. Coatings with spatially variable structures containing single crystalline and nanocrystalline regions.

regions divided by ideal coherent boundaries and nanocrystalline regions causing effective relaxation of misfit stresses. In these circumstances, single crystalline regions with ideal coherent matching exhibit desired functional properties, while nanocrystalline regions play the role of structural elements that provide misfit stress relaxation. Some illustrations of the coatings with spatially variable structures and various geometries are shown in Fig. 7.

The coatings with spatially variable structures potentially can be synthesized, for instance, in a two-step manner. At the first step, a coating with the completely nanocrystalline structure is synthesized by conventional methods. At the second step, local heating can be used to induce local recrystallization processes that result in a desired spatially variable structure. This method can serve as a kind of nanolithography.

Also, local regions with the nanocrystalline structure in either film or substrate of a heteroepitaxial system are capable of effectively contributing to misfit stress relaxation in the system, even if such nanocrystalline regions are located far from

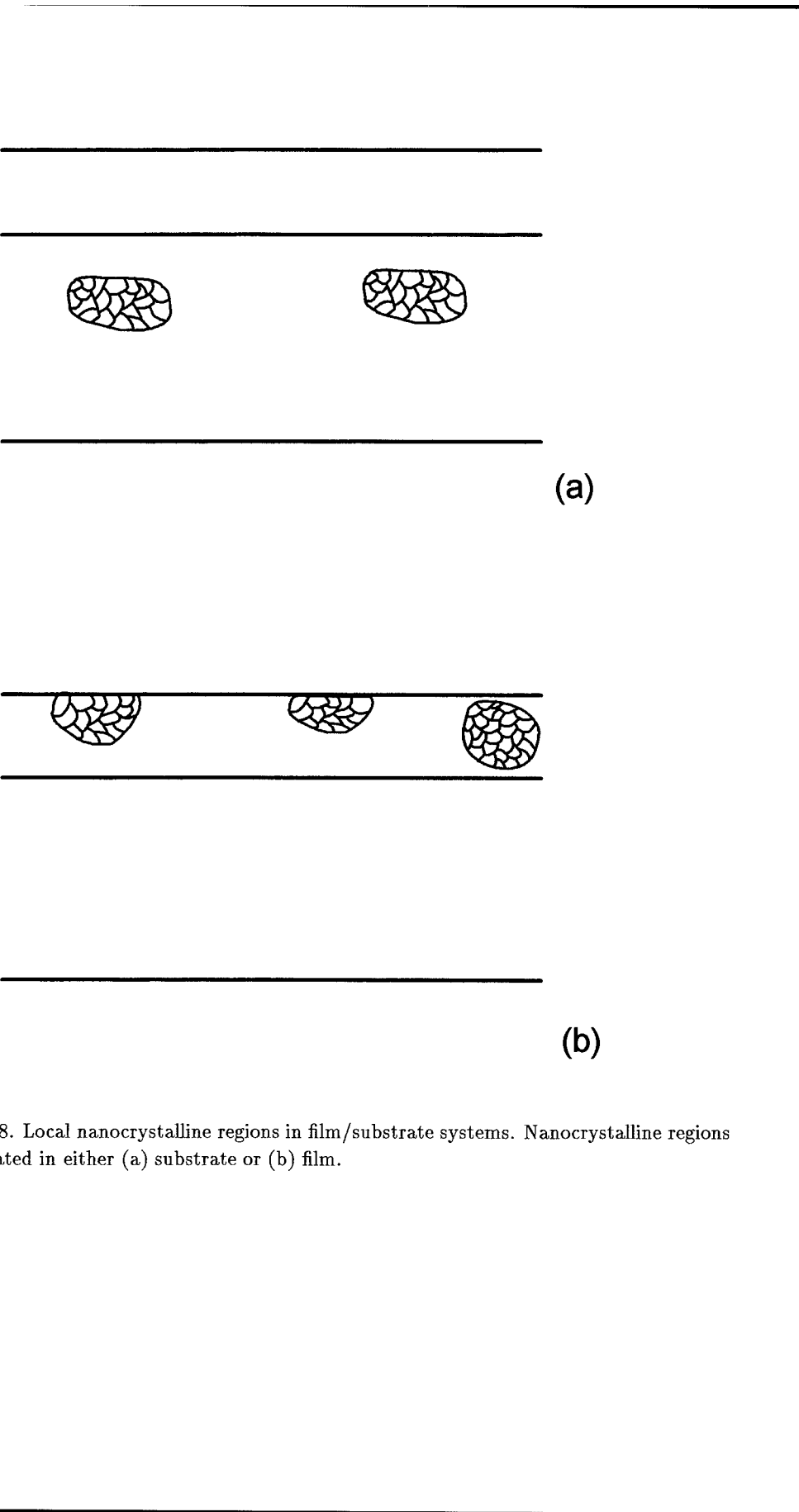
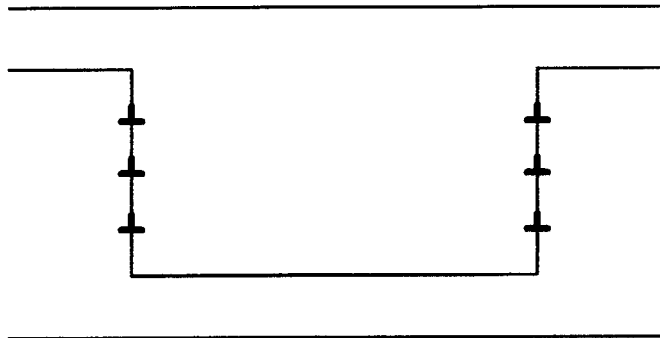
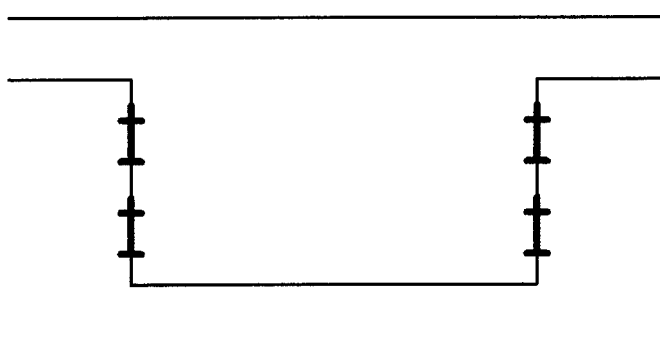


Figure 8. Local nanocrystalline regions in film/substrate systems. Nanocrystalline regions are located in either (a) substrate or (b) film.



(a)



(b)

Figure 9. Film/substrate systems with interface containing walls of (a) perfect and (b) partial misfit dislocations.

the interphase boundary (Fig. 8). This effect can be potentially used in technologies, too.

Also, multilayer coatings with single crystalline layers divided by interfaces having a complicated geometry and containing walls of either perfect or partial misfit dislocations (Fig. 9) potentially can be synthesized as coatings with unusually wide areas of the ideal coherent matching. This is important for applications of coatings with the functional properties dependent on the coherent matching of thick single crystalline layers.

## 9. Concluding Remarks

Thus, such defected and non-periodic interfaces as quasiperiodic tilt boundaries, partly incoherent interfaces, interphase boundaries with misfit disclinations, misfit grain boundary dislocations, and misfit partial dislocations, crystal/glass interfaces, quasiperiodic and amorphous interfaces between crystalline phases are inherent structural elements of nanostructured films and coatings. Both the specific structure and the specific properties of defected and non-periodic interfaces in nanostructured films and coatings cause the specific effects of such interfaces on the macroscopic properties of nanostructured films and coatings. These effects should definitely be taken into account in experimental research and theoretical description of the structure and behavior of advanced nanostructured materials.

**Acknowledgements.** This work was supported, in part, by the Russian Foundation of Basic Researches (grant 98-02-16075), Office of US Naval Research (grant N00014-99-1-0569), and Volkswagen Foundation (Research Project Nr. 05019225).

## References

1. *Nanomaterials: Synthesis, Properties and Applications* (eds. A.S. Edelstain and R.C. Cammarata), Institute of Physics Publ., Bristol and Philadelphia, 1996.
2. Gleiter H. (1991) Nanocrystalline solids. *J. Appl. Cryst.*, **24**, 79-90.
3. *R&D Status and Trends in Nanoparticles, Nanostructured Materials, and Nanodevices in the United States.*, (eds. R.W. Siegel, E. Hu and M.C. Roco), International Technology Research Institute, Baltimore.
4. Shull R.D. (1996) Viewpoint update: nanocrystalline and nanophase materials. *Nanostruct. Mater.*, **7**, Nos. 1/2, 265-268.
5. Holtz R.L., Provenzano V. and Imam M.A. (1996) Overview of nanophase metals and alloys for gas sensors, getters, and hydrogen storage. *Nanostruct. Mater.*, **7**, Nos. 1/2, 259-264.

6. *Nanostructured Materials: Science and Technology, NATO ASI Series* (eds. G.-M. Chow and N.I.Noskova), Kluwer, Dordrecht, 1998.
7. Tkhorik, Yu.A., and Khazan, L.S. (1983) *Plastic Deformation and Misfit Dislocations in Heteroepitaxial Systems*, Naukova Dumka, Kiev (in Russian).
8. Merwe, J.H. van der (1991) Misfit dislocation generation in epitaxial layers, *Critical Reviews in Solid State and Materials Science* **17**, 187- 209.
9. Jain, S.C., Harker, A.H., and Cowley, R.A. (1997) Misfit strain and misfit dislocations in lattice mismatched epitaxial layers and other systems, *Phil.Mag. A* **75**, 1461-1515.
10. Ovid'ko, I.A. (1998) Quasiperiodic and disordered interfaces in nanostructured materials, in G.-M. Chow and N.I.Noskova (eds.), *Nanostructured Materials: Science and Technology, NATO ASI Series*, Kluwer, Dordrecht, pp.183-206.
11. Ovid'ko I.A. (1999) Misfit disclinations at "crystal/crystal" and "crystal/glass" interfaces. *Phys. Sol. State*, **41**, No. 9.
12. Romanov A.E., and Vladimirov V.I. (1992) Disclinations in crystals, in F.R.N.Nabarro, (ed.), *Dislocations in Solids* **9**, North-Holl. Publ., Amsterdam, 191-314.
13. Gryaznov, V.G., and Trusov, L.I. (1993) Size effect in micromechanics of nanocrystals, *Progr.Mater.Sci.* **37**, 290-400.
14. Romanov A.E., Lefevre M.J., Speck J.S., Pompe W., Streiffer S.K. and Foster C.M. (1998) Domain pattern formation in epitaxial rhombohedral ferroelectric films. II. Interfacial defects and energetics, *J.Appl. Phys.*, **83**, 2754.
15. Ovid'ko I.A. (1999) Misfit dislocation walls in solid films. *J.Phys: Cond. Matter*, **11**, 6521-6527.
16. Ievlev V.M., Trusov L.I. and Kholmyanskii V.A. *Structural Transformations in Thin Films*, Metallurgiya, Moscow, 1988 (in Russian).
17. Mallamaci M.P. and Carter C.B. (1998) Faceting of the interface between  $\text{Al}_2\text{O}_3$  and anorthite glass, *Acta Mater.*, **46**, 2895-2907.
17. Donzel, L., Lakki, A., and Schaller, R. (1997) Glass transition and  $\alpha$  relaxation in Y-Si-Al-O-N glasses and in  $\text{Si}_3\text{N}_4$  ceramics studied by mechanical spectroscopy, *Phil.Mag. A* **76**, 933-944.
18. Veprek, S., Haussmann, M., and Reiprich, S. (1996) Structure and properties of novel superhard nanocrystalline/amorphous composite materials, in R.Bormann, G.Mozzone, R.D.Shull, R.S.Averbach and R.F.Ziolo (eds.), *Metastable Phases and Microstructures, MRS Symposium Proc.* **400**, MRS, Pittsburgh, pp.261-266.
19. Lee T.-S., Gu G.L. and Tseng B.-H. (1996) Microstructure and stress in Mo films sputter-deposited on glass substrates, in H.J.Frost et al (eds.), *Polycrystalline Thin Films: Structure, Texture, Properties and Applications II, MRS Symposium Proc.*, **403**, MRS, Pittsburgh, 119-124.
20. Ovid'ko I.A. (1999) Misfit disclinations and dislocations at crystal/glass interfaces, *Phil.Mag.Lett.*, **79**, 709-713.
21. Dusher G., Mullejans H., Werner J. and Ruhle M. (1996) Amorphous  $\text{SiO}_2$  precipitates at silicon grain boundaries, *Mater. Sci. Forum*, **207-209**, 713-716.
22. Sutton, A.P., and Balluffi, R.W. *Interfaces in Crystalline Materials*, Clarendon Press, Oxford, 1995.
23. Jankovski, A.F., Sandoval, P., and Hayes, J.P. (1995) Superlattice effects on solid-state amorphization, *Nanostruct. Mater.* **5**, 497-503.

---

- 24. Samwer, K. (1988) Amorphization in solid metallic systems, *Phys. Rep.* **161**, 1-41.
- 25. Gutkin, M.Yu., and Ovid'ko, I.A. (1999) Misfit strains and phase transformations in layered composite solids, *J.Phys: Cond. Matter*, in press.
- 26. Ovid'ko, I.A. (1997) Quasi-nanocrystalline materials, *Nanostruct. Mater.* **8**, 149-153.
- 27. Ovid'ko, I.A. (1999) Quasiperiodic interfaces and tilt boundaries of finite extent, *Mater.Sci.Eng. A*, in press.
- 28. Pan., X. (1997) Atomistic structure of silicon nitride/silicate glass interfaces, *J.Am. Ceram. Soc.* **79**, 2975-2979.
- 29. Gu, H., Pan, X., Tanaka, I., Cannon, R.M., Hoffmann, Mullejans, H., and Ruhle, M. (1996) Structure and chemistry of intergranular films in Ca-doped  $\text{Si}_3\text{N}_4$ , *Mater.Sci.Forum*, 207-209, 729-732.
- 30. Kebinski, P., Phillipot, S.R., Wolf, D., and Gleiter, H. (1997) Relationship between nanocrystalline and amorphous microstructures by molecular dynamics simulation, *Nanostr.Mater.* **9**, 651-660.
- 31. Kebinski, P., Phillipot, S.R., Wolf, D., and Gleiter, H. (1997) Amorphous structure of grain boundaries and grain junctions in nanocrystalline silicon by molecular dynamics simulation, *Acta Mater.* **45**, 987-998.
- 32. Kolesnikova, A.L., Ovid'ko, I.A., and Reizis, A.B. (1998) Elastic energy and equilibrium thickness of intergranular amorphous boundaries in ceramics, *J. Mater. Proc. Manuf. Sci.*, **7**, 5-14.

## NANOSCALE ELASTIC PROPERTIES OF DISLOCATIONS AND DISCLINATIONS

M.YU. GUTKIN\* and E.C. AIFANTIS†

*Aristotle University of Thessaloniki, Thessaloniki 54006, GREECE*

*\*Institute of Mechanical Engineering Problems, Russian Academy of Sciences, Bolshoj 61, Vas. Ostrov, St. Petersburg 199178, RUSSIA*

*†Michigan Technological University, Houghton, MI 49931, USA*

### 1. Introduction

A correct description of the behavior of defects in thin-film and nanostructured systems needs to take into account both the strong influence of outer and inner interphase boundaries and the fact that the size of a defect core, where classical solutions are singular and incorrect, occurs in the same order as the characteristic length of the system (film thickness, grain size, etc.). To take into account the influence of interphase boundaries, many solutions of boundary value problems for defects have been obtained in the framework of the classical theory of elasticity (see [1–5] for a review). To solve the second problem, some approaches have been proposed which have been aimed at dispensing with classical singularity of elastic fields within defect cores (see [6, 7] for a review). The present paper represents a brief description of our recent results [6–10] dealing with nanoscale elastic fields within and near cores of disclinations [6, 7] and dislocations [6–10] in the framework of gradient elasticity. The main result shown there was an elimination of displacement, strain, stress and energy singularities at the defect line. It is worth noting, that previous continuum models for such kind of defects which have taken into account couple stresses or non-locality (see [6, 7] for a review), do not dispense with the singularity in the displacement or strain field, even though some of them [11–13] claim elimination of stress singularity.

We have started with a simple gradient modification of the linear theory of elasticity in the form [14]

$$\sigma = \lambda(\text{tr } \varepsilon)I + 2\mu\varepsilon - c\nabla^2 [\lambda(\text{tr } \varepsilon)I + 2\mu\varepsilon], \quad (1)$$

where  $\lambda$  and  $\mu$  are the Lamé constants,  $\sigma$  and  $\varepsilon$  are the stress and strain tensors,  $I$  is the unit tensor,  $\nabla^2$  denotes Laplacian and  $c > 0$  is the gradient coefficient. Using (1) or similar theory, the authors of [14–20] have demonstrated the elimination of classical singularity from the solution for the strain field at the crack tip.

Encouraged by these results, we first employed [8, 9] the same gradient theory described by (1) to consider dislocations. In particular, four dislocation configurations (i.e. a screw dislocation, an edge dislocation, and the dipoles of such dislocations) have been considered. It has been shown that in the case of screw dislocation [8], the elastic strain is zero at the dislocation line and achieves a maximum value ( $\approx \pm b_z / 10\pi\sqrt{c}$ ), at a distance  $\simeq \sqrt{c}$  from it. It is worth noting that for an atomic lattice, the gradient coefficient,  $c$ , can be estimated [14] as  $\sqrt{c} \approx a/4$ , where  $a$  is the lattice constant. With the Burgers vector,  $b_z$ , taken to be equal to  $a$ , it follows that the aforementioned maximum value is estimated as  $\approx 12\%$ . In the case of edge dislocations [9, 10], we have also shown that all strain components are equal to zero at the dislocation line achieving maximum values (3-14)% within the dislocation core ( $r \leq 4\sqrt{c}$ ).

It has also turned out for both types of dislocations that beyond the dislocation core ( $r_0 \simeq 4\sqrt{c}$ ) the classical and gradient solutions coincide. Furthermore, it has been shown that the total displacement varies smoothly across the dislocation line in contrast to the classical solution which suffers a jump there. In addition, some of the displacement components which are singular in the classical theory now become finite (edge dislocation). We have also considered the displacement and strain distributions for dislocation dipoles and shown that the values of relative displacements of the cut surfaces depend on the dipole arm, in contrast to the classical theory where these displacements are always the same. As a result, two characteristic distances appear naturally in this approach:  $r_0 \approx 4\sqrt{c}$  which may be viewed as the radius of dislocation core and  $d_0 \approx 10\sqrt{c}$  which may be viewed as the radius of strong short-range nanoscale interaction between dislocations.

In [6], we have considered the elastic fields of disclinations within the gradient theory described by (1). We have found the elastic strains for all kinds of straight disclinations, and examined the interactions between disclinations in dipoles. It has been shown that the main features of the gradient solutions are very similar to the case of dislocations: the singularities at the disclination lines are eliminated from the strain fields which are equal to zero or attain finite values there. The non-vanishing values depend strongly on the dipole arm,  $d$ , and exhibit a regular and monotonous (in the case of wedge disclinations) or non-monotonous (in the case of twist disclinations) behavior for short-range nanoscale ( $d < 10\sqrt{c}$ ) interactions between disclinations. When the disclinations annihilate ( $d \rightarrow 0$ ), the elastic strains tend to zero value. Far from the disclination line ( $r \gg 10\sqrt{c}$ ) gradient and classical solutions coincide. When  $d \ll \sqrt{c}$ , the elastic fields of a dipole of wedge disclinations transform into the elastic fields of an edge dislocation [9] as is the case in the classical theory of elasticity.

It is important to emphasize, however, that in the framework of the gradient elasticity theory described by (1), the stress fields of dislocations [8, 9] and disclinations [6] remain as in the classical theory of elasticity (same as in the case of crack problems [14-17, 20]). In order to eliminate the singularities also from the elastic stresses of defects, we used in [7, 10] a more general version of gradient elasticity theory which has been also utilized by Ru and Aifantis [21] (see also

[22]). The constitutive equation of this theory reads

$$(1 - c_1 \nabla^2) \boldsymbol{\sigma} = (1 - c_2 \nabla^2) [\lambda(\text{tr } \boldsymbol{\varepsilon}) \mathbf{I} + 2\mu \boldsymbol{\varepsilon}], \quad (2)$$

with two different gradient coefficients  $c_1$  and  $c_2$ . In [21] a rather simple mathematical procedure analogous to the one contained in [15] has been outlined for the solution of (2) in terms of solutions of classical elasticity for the same boundary value problem. In fact, it is easily established (see [15], also [6–10]) that the right hand side of (2) for the case of  $c_1 \equiv 0$ , gives the classical solution for the stress field which we denote here by  $\boldsymbol{\sigma}^0$ , while the solution for the displacement is determined through the inhomogeneous Helmholtz equation given by

$$(1 - c_2 \nabla^2) \mathbf{u} = \mathbf{u}^0, \quad (3)$$

where  $\mathbf{u}^0$  denotes the solution of classical elasticity for the same traction boundary value problem. Eq. (3) implies a similar equation for strain,  $\boldsymbol{\varepsilon}$ , of the gradient theory

$$(1 - c_2 \nabla^2) \boldsymbol{\varepsilon} = \boldsymbol{\varepsilon}^0, \quad (4)$$

in terms of the strain  $\boldsymbol{\varepsilon}^0$  of the classical elasticity theory for the same traction boundary value problem. With the displacement or strain field thus determined (which is obviously independent of whether  $c_1 \equiv 0$  or  $c_1 \neq 0$ ), it follows that the stress field  $\boldsymbol{\sigma}$  of (2) can be determined (for the case  $c_1 \neq 0$ ) from the equation

$$(1 - c_1 \nabla^2) \boldsymbol{\sigma} = \boldsymbol{\sigma}^0, \quad (5)$$

where  $\boldsymbol{\sigma}^0$  denotes the solution obtained for the same boundary value problem within the classical theory of elasticity.

Thus, in order to solve equation (2), one can solve separately equations (4) and (5) by utilizing the classical solutions  $\boldsymbol{\varepsilon}^0$  and  $\boldsymbol{\sigma}^0$  provided that appropriate care is taken for the extra (due to the higher order terms) boundary conditions or conditions at infinity. For dislocations and disclinations, this problem's solutions are accounted for by assuming that the strain and stress fields at infinity have the same characteristic features for both the gradient and classical theory. The approach has already been applied [21] to the cases of screw dislocations and mode-III cracks where the asymptotic solutions at the dislocation line and crack tip have been found demonstrating the elimination of both strain and stress singularities there.

Below we report the exact analytical solutions of (2) obtained for straight dislocations and disclinations.

## 2. Dislocations

### 2.1. CLASSICAL SOLUTION

Consider a mixed dislocation whose line coincides with the  $z$ -axis of a Cartesian coordinate system. Let its Burgers vector be  $\mathbf{b} = b_x \mathbf{e}_x + b_z \mathbf{e}_z$  thus determining

the edge ( $b_x$ ) and screw ( $b_z$ ) components. In the framework of classical elasticity theory, the total displacement field is described by

$$\begin{aligned} \mathbf{u}^0 &= \frac{b_x \mathbf{e}_x + b_z \mathbf{e}_z}{2\pi} \left\{ \arctan \frac{y}{x} + \frac{\pi}{2} \text{sign}(y)[1 - \text{sign}(x)] \right\} \\ &+ \frac{b_x}{4\pi(1-\nu)} \left\{ \mathbf{e}_x \frac{xy}{r^2} - \mathbf{e}_y \left[ (1-2\nu) \ln r + \frac{x^2}{r^2} \right] \right\}, \end{aligned} \quad (6)$$

where  $\nu$  is the Poisson ratio,  $r^2 = x^2 + y^2$ . Here we use a single-valued discontinuous form suggested by de Wit [23]. The elastic strain field  $\varepsilon_{ij}^0$  reads [23, 24] (in units of  $1/[4\pi(1-\nu)]$ ) by

$$\begin{aligned} \varepsilon_{xx}^0 &= -b_xy [(1-2\nu)r^2 + 2x^2]/r^4, & \varepsilon_{yy}^0 &= -b_xy [(1-2\nu)r^2 - 2x^2]/r^4, \\ \varepsilon_{xy}^0 &= b_x x (x^2 - y^2)/r^4, & \varepsilon_{xz}^0 &= -b_z(1-\nu)y/r^2, & \varepsilon_{yz}^0 &= b_z(1-\nu)x/r^2, \end{aligned} \quad (7)$$

and elastic stress field  $\sigma_{ij}^0$  is [23, 24] (in units of  $\mu/[2\pi(1-\nu)]$ )

$$\begin{aligned} \sigma_{xx}^0 &= \varepsilon_{xx}^0 (\nu = 0), & \sigma_{yy}^0 &= \varepsilon_{yy}^0 (\nu = 0), & \sigma_{zz}^0 &= \nu(\sigma_{xx}^0 + \sigma_{yy}^0), \\ \sigma_{xy}^0 &= \varepsilon_{xy}^0, & \sigma_{xz}^0 &= \varepsilon_{xz}^0, & \sigma_{yz}^0 &= \varepsilon_{yz}^0, \end{aligned} \quad (8)$$

Fields (6) ( $y$ -component), (7) and (8) are singular at the dislocation line.

The elastic energy  $W^0$  of the dislocation per unit dislocation length is [24]

$$W^0 = \frac{\mu}{4\pi} \left( b_z^2 + \frac{b_x^2}{1-\nu} \right) \ln \frac{R}{r_0}, \quad (9)$$

where  $R$  denotes the size of the solid and  $r_0$  is a cut-off radius for the dislocation elastic field near the dislocation line. When  $r_0 \rightarrow 0$ ,  $W^0$  becomes singular.

## 2.2. GRADIENT SOLUTION

Let us now consider the corresponding dislocation fields within the theory of gradient elasticity given by (2). As described in *Section 1*, one can obtain the solution of (2) by solving separately equations (3)–(5). They can be solved [9] by using the Fourier transform method. Omitting intermediate calculations, we give here only the final results. For the total displacements, solution of (3) gives [8, 9]

$$\begin{aligned} \mathbf{u} &= \mathbf{u}^0 - \frac{b_x}{4\pi(1-\nu)} \left\{ [\mathbf{e}_x 2xy + \mathbf{e}_y (y^2 - x^2)] r^2 \Phi_2 + \mathbf{e}_y \Phi_0 \right\} \\ &+ \frac{b_x \mathbf{e}_x + b_z \mathbf{e}_z}{2\pi} \text{sign}(y) \int_0^{+\infty} \frac{s \sin(sx)}{\frac{1}{c_2} + s^2} e^{-|y|\sqrt{\frac{1}{c_2} + s^2}} ds, \end{aligned} \quad (10)$$

where  $\mathbf{u}^0$  is given by (6),  $\Phi_0 = (1-2\nu) K_0(r/\sqrt{c_2})$ ,  $\Phi_2 = [2c_2/r^2 - K_2(r/\sqrt{c_2})]/r^4$ ,  $K_n(r/\sqrt{c_2})$  is the modified Bessel function of the second kind and  $n = 0, 1, \dots$  denotes the order of this function.

For the elastic strain, solution of (4) gives [8, 9]  $\varepsilon_{ij} = \varepsilon_{ij}^0 + \varepsilon_{ij}^{gr}$ , where  $\varepsilon_{ij}^0$  are given by (7) and  $\varepsilon_{ij}^{gr}$  (in units of  $1/[2\pi(1-\nu)]$ ) by

$$\begin{aligned}\varepsilon_{xx}^{gr} &= b_{xy}[(y^2 - \nu r^2)\Phi_1 + (3x^2 - y^2)\Phi_2], & \varepsilon_{xz}^{gr} &= b_z(1-\nu)yr^2\Phi_1/2, \\ \varepsilon_{yy}^{gr} &= b_{xy}[(x^2 - \nu r^2)\Phi_1 - (3x^2 - y^2)\Phi_2], & \varepsilon_{yz}^{gr} &= -b_z(1-\nu)xr^2\Phi_1/2, \\ \varepsilon_{xy}^{gr} &= -b_{xx}[y^2\Phi_1 + (x^2 - 3y^2)\Phi_2],\end{aligned}\quad (11)$$

where  $\Phi_1 = K_1(r/\sqrt{c_2})/(\sqrt{c_2}r^3)$ . For the stresses, the solution of (5) gives [10]  $\sigma_{ij} = \sigma_{ij}^0 + \sigma_{ij}^{gr}$ , where  $\sigma_{ij}^0$  are given by (8) and  $\sigma_{ij}^{gr}$  (in units of  $\mu/[\pi(1-\nu)]$ ) by

$$\begin{aligned}\sigma_{xx}^{gr} &= \varepsilon_{xx}^{gr}(\nu = 0, c_2 \leftrightarrow c_1), & \sigma_{yy}^{gr} &= \varepsilon_{yy}^{gr}(\nu = 0, c_2 \leftrightarrow c_1), & \sigma_{zz}^{gr} &= \nu(\sigma_{xx}^{gr} + \sigma_{yy}^{gr}), \\ \sigma_{xy}^{gr} &= \varepsilon_{xy}^{gr}(c_2 \leftrightarrow c_1), & \sigma_{xz}^{gr} &= \varepsilon_{xz}^{gr}(c_2 \leftrightarrow c_1), & \sigma_{yz}^{gr} &= \varepsilon_{yz}^{gr}(c_2 \leftrightarrow c_1).\end{aligned}\quad (12)$$

The main feature of the solution given by (10)–(12) is the absence of any singularities in the displacement, strain and stress fields. In fact, when  $r \rightarrow 0$ , we have  $K_0(r/\sqrt{c_k})|_{r \rightarrow 0} \rightarrow -\gamma + \ln(2\sqrt{c_k}/r)$ ,  $K_1(r/\sqrt{c_k}) \rightarrow \sqrt{c_k}/r$ ,  $K_2(r/\sqrt{c_k}) \rightarrow 2c_k/r^2 - 1/2$ , ( $k = 1, 2$ ) and, thus,  $u_y$  is finite,  $\varepsilon_{ij} \rightarrow 0$ ,  $\sigma_{ij} \rightarrow 0$ . The fields of displacements (10) and strains (11) have been discussed in detail in [8, 9] within a special version of gradient elasticity theory ( $c_1 \equiv 0$ ). The stress fields (12) have been examined in [10]. It has been shown there that they attain their extreme values ( $|\sigma_{xx}| \approx 0.45 \mu$ ,  $|\sigma_{yy}| \approx |\sigma_{xy}| \approx 0.27 \mu$  and  $|\sigma_{xz}| \approx 0.25 \mu$  for  $b_i = a = 4\sqrt{c_1}$  and  $\nu = 0.3$ ) at a distance  $\approx a/4$  from the dislocation line. Far away from the dislocation core ( $r \geq r_0 \approx 4\sqrt{c_k}$ ), the gradient solutions coincide with the classical ones [8–10].

Using (12), one can find the elastic energy of the dislocation within the gradient elasticity given by (2) as follows [10]

$$W = \frac{\mu}{4\pi(1-\nu)} \left\{ \frac{b_x^2}{2} + [b_x^2 + (1-\nu)b_z^2] \left( \gamma + \ln \frac{R}{2\sqrt{c_1}} \right) \right\}, \quad (13)$$

where  $\gamma = 0.57721566\dots$  is Euler's constant. Thus, we obtain a strain energy expression which is not singular at the dislocation line.

### 3. Disclinations

#### 3.1. CLASSICAL SOLUTION

Consider a disclination of general type with Frank vector  $\omega = \omega_x e_x + \omega_y e_y + \omega_z e_z$  in an infinite elastic medium. The scalars  $\omega_x$  and  $\omega_y$  determine the twist components of the disclination while  $\omega_z$  determines its wedge component. Let its line coincides with the  $z$ -axis of the above coordinate system. For such an isolated disclination, both classical and gradient solutions themselves have no physical meaning because they are not screened but they may be used in modeling screened disclination

configurations as basic elements. The classical solution for elastic strain fields  $\varepsilon_{ij}^0$  reads [23] (in units of  $1/[4\pi(1-\nu)]$ )

$$\begin{aligned}\varepsilon_{xx}^0 &= \omega_x z x \frac{2\nu r^2 - x^2 + y^2}{r^4} + \omega_y z y \frac{2\nu r^2 - 3x^2 - y^2}{r^4} + \omega_z \left\{ (1-2\nu) \ln r + \frac{y^2}{r^2} \right\}, \\ \varepsilon_{yy}^0 &= \omega_x z x \frac{2\nu r^2 - x^2 - 3y^2}{r^4} + \omega_y z y \frac{2\nu r^2 + x^2 - y^2}{r^4} + \omega_z \left\{ (1-2\nu) \ln r + \frac{x^2}{r^2} \right\}, \\ \varepsilon_{xy}^0 &= (\omega_y x - \omega_x y) z \frac{x^2 - y^2}{r^4} - \omega_z \frac{xy}{r^2}, \quad \varepsilon_{xz}^0 = \omega_y \frac{xy}{r^2} - \omega_x \left\{ (1-2\nu) \ln r + \frac{y^2}{r^2} \right\}, \\ \varepsilon_{yz}^0 &= \omega_x \frac{xy}{r^2} - \omega_y \left\{ (1-2\nu) \ln r + \frac{x^2}{r^2} \right\},\end{aligned}\quad (14)$$

and for the stress fields it may be written (in units of  $\mu/[2\pi(1-\nu)]$ ) as

$$\begin{aligned}\sigma_{xx}^0 &= \varepsilon_{xx}^0(\nu=0), \quad \sigma_{yy}^0 = \varepsilon_{yy}^0(\nu=0), \quad \sigma_{xy}^0 = \varepsilon_{xy}^0, \quad \sigma_{xz}^0 = \varepsilon_{xz}^0, \quad \sigma_{yz}^0 = \varepsilon_{yz}^0, \\ \sigma_{zz}^0 &= -\omega_x z 2\nu \frac{x}{r^2} - \omega_y z 2\nu \frac{y}{r^2} + \omega_z 2\nu \ln r.\end{aligned}\quad (15)$$

Most of the components in (14) and (15) contain singular terms  $\sim \ln r$ .

### 3.2. GRADIENT SOLUTION

The gradient solutions have been originally obtained for a disclination dipole within both the gradient theories considered in *Section 1*. Solving (4), we solve finally for an individual disclination under consideration the strain field [6]  $\varepsilon_{ij} = \varepsilon_{ij}^0 + \varepsilon_{ij}^{gr}$ , where  $\varepsilon_{ij}^0$  are given by (14) and  $\varepsilon_{ij}^{gr}$  (in units of  $1/[4\pi(1-\nu)]$ ) by

$$\begin{aligned}\varepsilon_{xx}^{gr} &= \omega_x 2xz \{ (y^2 - \nu r^2) \Phi_1 + (x^2 - 3y^2) \Phi_2 \} \\ &+ \omega_y 2yz \{ (y^2 - \nu r^2) \Phi_1 + (3x^2 - y^2) \Phi_2 \} + \omega_z \{ \Phi_0 + r^2(x^2 - y^2) \Phi_2 \}, \\ \varepsilon_{yy}^{gr} &= \omega_x 2xz \{ (x^2 - \nu r^2) \Phi_1 - (x^2 - 3y^2) \Phi_2 \} \\ &+ \omega_y 2yz \{ (x^2 - \nu r^2) \Phi_1 - (3x^2 - y^2) \Phi_2 \} + \omega_z \{ \Phi_0 - r^2(x^2 - y^2) \Phi_2 \}, \\ \varepsilon_{xy}^{gr} &= \omega_x 2yz \{ -x^2 \Phi_1 + (3x^2 - y^2) \Phi_2 \} \\ &- \omega_y 2xz \{ y^2 \Phi_1 + (x^2 - 3y^2) \Phi_2 \} + \omega_z 2xyr^2 \Phi_2, \\ \varepsilon_{xz}^{gr} &= \omega_x \{ -\Phi_0 - r^2(x^2 - y^2) \Phi_2 \} - \omega_y 2xyr^2 \Phi_2, \\ \varepsilon_{yz}^{gr} &= \omega_y \{ -\Phi_0 + r^2(x^2 - y^2) \Phi_2 \} - \omega_x 2xyr^2 \Phi_2,\end{aligned}\quad (16)$$

where  $\Phi_i$  are the same as in *Section 2.2*. For the stress field, the solution of (5) gives [7]  $\sigma_{ij} = \sigma_{ij}^0 + \sigma_{ij}^{gr}$ , where  $\sigma_{ij}^0$  are given by (15) and  $\sigma_{ij}^{gr}$  (in units of  $\mu/[2\pi(1-\nu)]$ ) by

$$\begin{aligned}\sigma_{xx}^{gr} &= \varepsilon_{xx}^{gr}(\nu=0, c_2 \leftrightarrow c_1), \quad \sigma_{yy}^{gr} = \varepsilon_{yy}^{gr}(\nu=0, c_2 \leftrightarrow c_1), \\ \sigma_{zz}^{gr} &= 2\nu \{ (\omega_x x + \omega_y y) z r^2 \Phi_1 (c_2 \leftrightarrow c_1) + \omega_z \Phi_0 (\nu=0, c_2 \leftrightarrow c_1) \}, \\ \sigma_{xy}^{gr} &= \varepsilon_{xy}^{gr}(c_2 \leftrightarrow c_1), \quad \sigma_{xz}^{gr} = \varepsilon_{xz}^{gr}(c_2 \leftrightarrow c_1), \quad \sigma_{yz}^{gr} = \varepsilon_{yz}^{gr}(c_2 \leftrightarrow c_1).\end{aligned}\quad (17)$$

Using the limiting transitions noted in *Section 2.2*, it is easy to show the total elimination of classical logarithmic singularity from elastic fields (16) and (17). In [6, 7], we have considered similar elastic fields of disclination dipoles in detail and found that they are equal to zero or attain finite values at the disclination lines. The non-vanishing values depend strongly on the dipole arm,  $d$ , and exhibit a regular and monotonous (wedge disclinations) or non-monotonous (twist disclinations) behavior for short-range nanoscale ( $d < 10\sqrt{c}$ ) interactions between disclinations. When the disclinations annihilate ( $d \rightarrow 0$ ), the elastic strains and stresses tend to zero. Far from the disclination line ( $r \gg 10\sqrt{c}$ ) gradient and classical solutions coincide. When  $d \ll \sqrt{c}$ , the elastic fields of a dipole of wedge disclinations transform into the elastic fields of an edge dislocation [9, 10] as is the case in the classical theory of elasticity.

#### 4. Conclusions

The gradient elasticity described by (2) has been employed in the consideration of nanoscale short-range elastic fields and interactions of dislocations and disclinations. Exact analytical solutions for the displacements, strain and stress fields and elastic energies of dislocations have been reported which demonstrate the elimination of any singularity from the elastic fields and energies at the dislocation line. For disclinations, the gradient solutions have been given for the strain and stress fields where the classical singularities at the disclination lines also disappear. These new non-singular elastic fields are considered as especially useful for modeling nanoscale behavior and interactions of dislocations and disclinations in thin-film or nanostructured solids.

**Acknowledgements:** This work was supported by INTAS-93-3213-Ext.

#### References

1. Eshelby, J.D. (1979) Boundary problems, in F.R.N. Nabarro (ed.), *Dislocations in Solids 1*, North-Holland, Amsterdam, pp. 167–221.
2. Gutkin, M.Yu., and Romanov, A.E. (1991) Straight edge dislocation in a thin two-phase plate. I. Elastic stress fields, *Phys. stat. sol. (a)* **125**, 107–125.
3. Gutkin, M.Yu., Kolesnikova, A.L., and Romanov, A.E. (1993) Misfit dislocations and other defects in thin films, *Mater. Sci. Engng. A* **164**, 433–437.
4. Romanov, A.E. (1995) Continuum theory of defects in nanoscaled materials, *NanoStruct. Mater. 6*, 125–134.
5. Bonnet, R. (1996) Elasticity theory of straight dislocations in a multilayer, *Phys. Rev. B* **53**, 10978–10982.
6. Gutkin, M.Yu., and Aifantis, E.C. (1999) Dislocations and disclinations in gradient elasticity, *Phys. Stat. Sol. (b)* **214**, 245–284.

---

7. Gutkin, M.Yu., and Aifantis, E.C. (1999) Dislocations and disclinations in the theory of gradient elasticity, *Phys. Solid State.* **41**, 000–000.
8. Gutkin, M.Yu., and Aifantis, E.C. (1996) Screw dislocation in gradient elasticity, *Scripta Mater.* **35**, 1353–1358.
9. Gutkin, M.Yu., and Aifantis, E.C. (1997) Edge dislocation in gradient elasticity, *Scripta Mater.* **36**, 129–135.
10. Gutkin, M.Yu., and Aifantis, E.C. (1999) Dislocations in the theory of gradient elasticity, *Scripta Mater.* **40**, 559–566.
11. Eringen, A.C. (1977) Screw dislocation in non-local elasticity, *J. Phys. D: Appl. Phys.* **10**, 671–678.
12. Eringen, A.C. (1983) On differential equations of nonlocal elasticity and solutions of screw dislocation and surface waves, *J. Appl. Phys.* **54**, 4703–4710.
13. Eringen, A.C. (1985) Nonlocal continuum theory for dislocations and fracture, in E.C. Aifantis and J.P. Hirth (eds.), *The Mechanics of Dislocations*, American Society for Metals, Metals Park, Ohio, pp. 101–110.
14. Altan, S.B., and Aifantis, E.C. (1992) On the structure of the mode III crack-tip in gradient elasticity, *Scripta Metal. Mater.* **26**, 319–324.
15. Ru, C.Q., and Aifantis, E.C. (1993) A simple approach to solve boundary-value problems in gradient elasticity, *Acta Mechanica* **101**, 59–68.
16. Aifantis, E.C. (1994) Gradient effects at the micro, macro and nano scales, *J. Mech. Behaviour of Materials* **5**, 355–375.
17. Unger, D.J., and Aifantis, E.C. (1995) The asymptotic solution of gradient elasticity for mode III, *Int. J. Fracture* **71**, R27–R32.
18. Exadaktylos, G.E., and Aifantis, E.C. (1996) Two and three dimensional crack problems in gradient elasticity, *J. Mech. Behaviour of Materials* **7**, 93–117.
19. Vardoulakis, I., Exadaktylos, G., and Aifantis, E.C. (1996) Gradient elasticity with surface energy: mode-III crack problem, *Int. J. Solids Structures* **33**, 4531–4559.
20. Altan, B.S., and Aifantis, E.C. (1997) On some aspects in the special theory of gradient elasticity, *J. Mech. Behavior of Materials* **8**, 231–282.
21. Ru, C.Q., and Aifantis, E.C. (1993) Some studies on boundary value problems in gradient elasticity, Preprint.
22. Milligan, W.W., Hackney, S.A., and Aifantis, E.C. (1995) Constitutive modeling for nanostructured materials, in H. Mühlhaus (ed.), *Continuum Models for Materials with Microstructure*, Wiley, pp. 379–393.
23. de Wit, R. (1973) Theory of disclinations: IV. Straight disclinations, *J. Res. Nat. Bur. Stand. (U.S.)* **77A**, 608–658.
24. Hirth, J.P., and Lothe, J. (1982) *Theory of Dislocations*, John Wiley, New York.

---

## STUDY OF POROUS SILICON FORMATION AND SILICON-ON-POROUS SILICON EPITAXY (COMPUTATIONAL MODELLING)

P.L. Novikov, L.N. Aleksandrov, A.V. Dvurechenskii, V.A. Zinoviev

*Institute of Semiconductor Physics, Academy of Science,*

*Novosibirsk 630090, Russia*

*E-mail: novikov@isp.nsc.ru*

**KEYWORDS/ ABSTRACT:** porous silicon/ computer simulation/ fractal dimension/ epitaxy

By computer simulation the processes of porous silicon formation and of silicon-on-porous silicon epitaxy are studied. The model of electrochemical etching is applied for p<sup>+</sup>Si and p<sup>-</sup>Si substrates and takes into account the non-homogeneous surface charge distribution, the thermal generation of holes and quantum confinement effects. The epitaxy is studied on the basis of Gilmer model extended to the case of relief surface. The porous structures obtained by computer simulation are presented for various anodization conditions. The analysis of 3D images shows the profile of porosity over depth and multifractal properties. It is shown that the mechanism of epitaxy on PS (111) surface is provided by the thin pendant layer formation. The dependence of kinetics of epitaxy upon the porosity, molecular flow density and initial surface roughness are established.

### 1. Introduction

Porous silicon (PS), prepared by anodization, has become a very promising material for device application due to its visible luminescence [1], extremely large specific surface and wide technological opportunities [2, 3]. It is also an interesting subject for fundamental investigation, since fractal structure of PS exhibits a number of optical, transport and thermodynamic properties [4], which are not fully understood.

Along with experimental methods, the computer simulation has been used for the study of PS properties. The first step in this direction was the modelling of PS formation. The diffusion limited aggregation (DLA) model and its variations [5, 6]

appeared to be easily adapted for computer simulation. However, structures obtained in these computational experiments could hardly be used in further investigation mainly for the following reasons. First, these structures were modelled on the 2D meshes. Second, they had only visual resemblance to the real ones, while the detailed topological analysis showed that much of structural characteristics (such as shape and size distribution of pores, interface profiles etc.) were not quite adequate. The simulated porous structures obtained by Aleksandrov and Novikov [7] exhibited the variety of morphologies and the structural [8] and thermodynamic [9] properties of PS were studied. The qualitative analysis of the simulated PS layer surface was used for modelling of silicon-on-porous silicon epitaxy. The present paper includes the series of works which deal with the modelling of PS formation, structural analysis of various simulated morphologies and homoepitaxy on PS.

## 2. The model and method of calculation

## 2.1. THE MODEL OF POROUS SILICON FORMATION

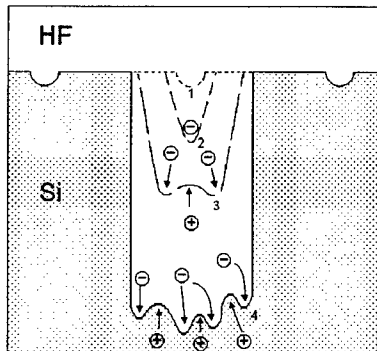


Fig.1. Schematic illustration of the pore formation relief mechanism. The contours 1-4 show the consecutive stages of Si/HF interface evolution.

Since a hole is necessary in electrochemical reaction of Si dissolution under anodization, the actual question is at what points a hole preferably crosses the Si/HF interface. We suppose that the morphology of the porous structure is determined by self-consisting correlation between potential and geometrical relief at Si/HF interface. At the first stage of pore formation the initial flat and smooth silicon anode becomes a relief as the result of random dissolution (contour 1 in Fig. 1). This stage proceeds until tips or cavities at the Si/HF interface become marked enough to trap the charge carriers (contour 2 in Fig. 1).  $F^-$  ions are trapped in the cavities, filled with HF solution, while holes drift to the hillocks (contour 3 in Fig. 1). If the electrolyte near the silicon anode is depleted (high current density approximation) then the hillocks are the effective centers for dissolution and electro-

polishing occurs. In the opposite case (low current density and/or light doping level and/or high HF concentration) electric field lines are focused on the pore tips, where the dissolution preferably takes place. In an intermediate case, when electrolyte is weakly depleted, only some randomly formed pores induce at their tips an electric field large enough to attract the holes effectively. The current density,  $j$ , at the tips of these pores is higher than the average over the surface and in the region of electrolyte near the pore tips the strong ion depletion is formed. This leads to the effect of "electro-polishing" in micro regions near pore tips rather than over the whole surface. The size

of the micro regions determines an average diameter of pores, which is constrained by the condition of the depletion in the electrolyte at the pore tip. As the diameter of the pore exceeds some critical value  $D$ , the local current density (under the fixed average one) becomes too low to provide the strong depletion in the electrolyte. Then the region of "electropolishing" gets narrow. The pore diameter value is provided by the self-consistent processes.

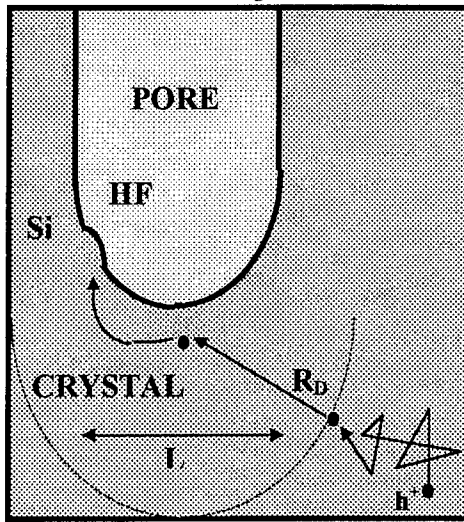


Fig.2. The illustration of the computational algorithm for  $p^+$ -PS formation.

Computer simulation of  $p^+$ -Si anodization is performed on two-dimensional ( $160 \times 160$ ) mesh. Each position on the mesh is defined as a cell. One mesh step corresponds to the real size of surface charge fluctuations. The computational algorithm is illustrated in Fig.2.  $N$  holes undergo random transport by the mesh, hopping over a distance equal to the mean free path. As soon as a hole is located within radius  $R_D$  from the nearest pore tip, drift in the direction of this tip starts.  $R_D$  is equal to the Debye radius and

expressed in mesh cells. After the hole reaches a point on the interface, the analysis of interface curvature is carried out within interval  $L$  from this point. The dissolution occurs in the most marked protuberance over the interval. The average diameter of pores,  $d$ , was estimated roughly as follows [7]:

$$d = \sqrt{\frac{4j}{Cc^{3/2} N_s}} \exp\left(\frac{E_A}{kT}\right) \quad (1)$$

where  $c$  (wt.%) is HF concentration,  $N_s$  ( $\text{cm}^{-2}$ ) is the surface density of pores,  $j$  ( $\text{mA}/\text{cm}^2$ ) is anodic current density,  $T$  (K) is the temperature,  $E_A = 343$  meV,  $C = 3300$   $\text{mA} \cdot \text{cm}^{-2} \cdot \text{wt. \%}^{-3/2}$ . The parameter  $L$  (in mesh steps) is equal to  $d$  followed by Eq. (2).

In lightly doped crystal ( $p < 10^{16} \text{ cm}^{-3}$ ) the space charge density and the local electrical field are low. Therefore, the effect of potential relief on the morphology of porous structure is expected to be negligible in this crystal. For this reason the dominant mechanisms of the pore formation are diffusion, thermal generation and recombination of holes and - in nanocrystallites - quantum confinement effect. The quantum confinement is known to increase the band gap. Consequently a barrier appears between the bulk region and nanoparticles, which prevents hole penetration inside nanoparticles. The size, at which the quantum confinement becomes significant, is denoted  $R_Q$  and equal to 10 nm and less [10].

Computer simulation of the pore formation in  $p^+$ -Si is performed on two-dimensional ( $160 \times 160$ ) and three-dimensional ( $160 \times 160 \times 80$ ) meshes. One mesh step

corresponds to the average interatomic distance. The computational algorithm differs from the one described above. Hole may disappear from the current point and appear in another position of crystal volume with probability  $G$ . The generation rate  $g$  ( $s^{-1}$ ) is linked to  $G$  by the relationship:

$$g = Gv_0/l, \quad (2)$$

where  $l \sim 10^{-6}\text{-}10^{-7}$  m is mean free path,  $v_0 \sim 10^5$  m/s - mean velocity of hole. After a hole reaches the interface, the analysis of surrounding space is carried out. If the crystal volume contains the sphere of radius  $R_Q$ , then the dissolution occurs.

## 2.2. THE MODEL OF SILICON-ON-POROUS SILICON EPITAXY

The extended diffusion model was constructed on the basis of the initial premises of the Gilmer model and includes two new assumptions. First, vacancies and overhangs are permitted. Second, the summation of the second-nearest neighbors, which determine the activation energy of diffusion, extends over all 12 positions in the second coordination sphere. Evaporation of atoms is neglected. All numerical parameters of the extended model are corrected so that the growth process on the smooth Si (111) surface will occur identically to the process in the Gilmer diffusion model [11].

The computational algorithm is performed on a  $N_x \times N_y \times N_z = 160 \times 160 \times 20$  three-dimensional grid whose nodes correspond to regular positions of atoms in the crystal structure of silicon. The state of the cells that are filled with atoms is characterized by the numbers  $N_1$  and  $N_2$  of neighbors in the first and second coordination spheres ( $1 \leq N_1 \leq 4$ ,  $1 \leq N_2 \leq 12$ ) respectively. Each atom executes a diffusion hop with probability  $p$  ( $N_1, N_2, T$ ). The final position of a diffusion hop is chosen randomly among the unoccupied cells in the first and second coordination spheres. Transitions which result in an atom not having any neighbors in the first coordination sphere are forbidden (that is why  $N_1 \neq 0$ ,  $N_2 \neq 0$ ). The probability of a diffusion hop (with the condition that the endpoint position is free) equals

$$p(N_1, N_2, T) = p_0 \exp(-E/kT), \quad E = N_1 \cdot E_1 + N_2 \cdot E_2, \quad (3)$$

where  $k$  is Boltzmann's constant,  $T$  is temperature, and  $p_0 = \exp((E_1 + 3E_2)/kT)$  is a factor chosen so that the probability of a diffusion hop on the free (111) surface equals 1. To decrease the amount of computation, a threshold probability  $p_s$ , which limits the number of "candidates" for a diffusion hop (active array) to atoms for which  $p(N_1, N_2, T) > p_s$ , is introduced. Scanning over the elements in an active array is performed during iteration. The time interval corresponding to one iteration is estimated as  $\tau = \chi \cdot p_0 / v$ , where  $v = 2.5 \cdot 10^{13}$  s<sup>-1</sup> is the frequency of atomic oscillations and  $\chi = 6/16$  is the coefficient that takes into account the ratio between the numbers of possible final positions for  $Is(111)$  in the Gilmer and the extended diffusion models.

The parameter  $E_2$  characterizes the kinetics of attachment/detachment of atoms on the faces of the elementary layers. These processes were investigated by simulation method, and the value  $E_2 = 0.2$  eV provided good agreement with experimental data [12]. Since in our model an adatom on a smooth surface has one neighbor in the first

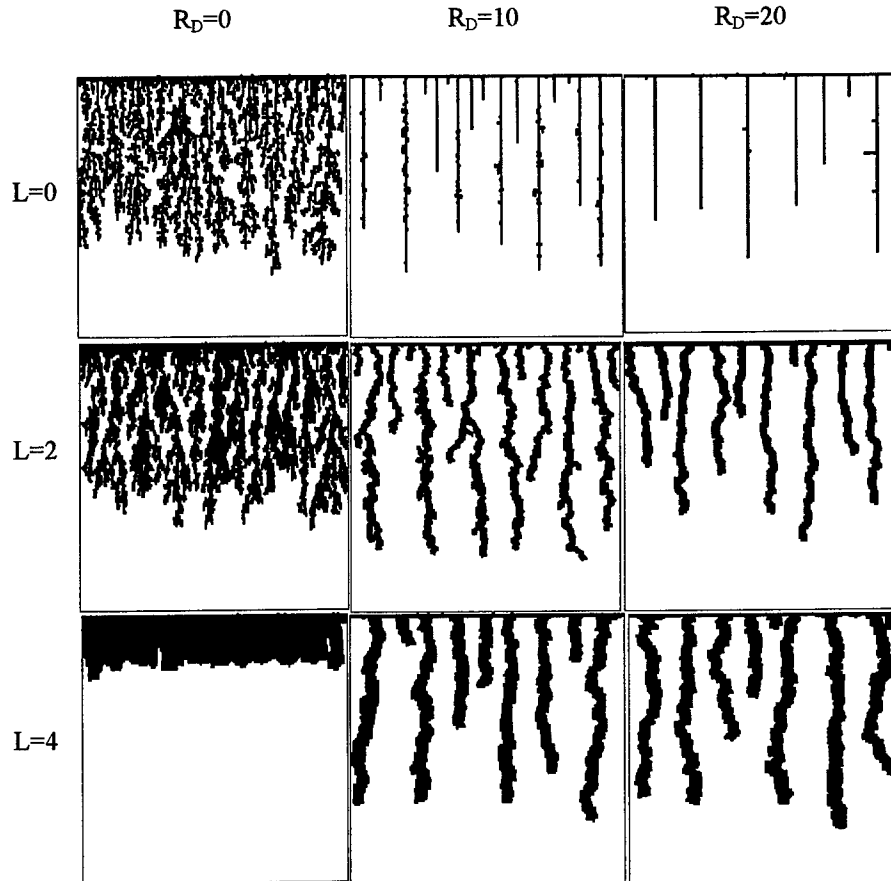


Fig. 3. A matrix of computer simulation plots with varying effective parameters  $L$  and  $R_D$  ( $N=80$ ).

and three in the second coordination spheres, the activation energy of surface diffusion can be expressed as  $E_A=E_1+3E_2$ . At the same time, the value  $E_A=1.3\pm 0.2$  eV was obtained experimentally in a number of work. We employed the value  $E_A=1.34$  eV, which corresponds to  $E_1=0.74$  eV.

The probability that an atom from a molecular beam reaches the surface over time  $\tau$  is

$$p_F=2F\tau N_X N_Y, \quad (4)$$

where  $F$  (bilayer/s) is the molecular flux density.

The  $160\times 160\times 14$  meshes speckled with bottomless cylindrical pores were used as the initial layer for simulation. The cylinders were randomly distributed over the surface and oriented normally to it. The number and radius of cylinders were the parameters of simulation.

### 3. Results and discussion.

#### 3.1. RESULTS OF SIMULATION OF POROUS SILICON FORMATION.

A matrix of plots, obtained by computer simulation on two-dimensional mesh ( $160 \times 160$ ), with  $N=80$  is shown at Fig.3. Black colour corresponds to pores. The pores grow downwards from the top of each plot. The effective parameters  $R_D$  and  $L$  (in mesh steps) are shown for each line and column of the matrix. The pore diameter is seen to

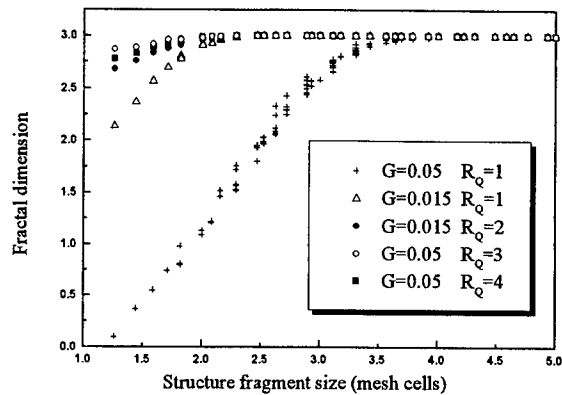


Fig. 4. Fractal dimension of structures formed by computer simulation on three-dimensional mesh *vs* size of detail.

Fig. 4. Fractal dimension of structures formed by computer simulation on three-dimensional mesh *vs* size of detail.

Fig. 4. Fractal dimension of structures formed by computer simulation on three-dimensional mesh *vs* size of detail.

Fig. 4. Fractal dimension of structures formed by computer simulation on three-dimensional mesh *vs* size of detail.

The three-dimensional images of simulated structures ( $160 \times 160 \times 80$ ) were obtained. The calculations show that the porosity  $P$  changes over the depth,  $h$ , of the porous layer in accordance with SIMS data [17].  $dP/dh$  decreases with increasing  $G$ . In order to interpret this result, it is necessary to first explain why the gradient in DLA model rises without hole generation ( $G=0$ ). In the growth process limited by diffusion, holes can not penetrate from the bottom to the top of the growth layer since they are effectively captured by the branches of the ramified structure. For this reason the growth preferably proceeds in thin front layer. Let us characterize it at any time by the current active surface defined as the number of possible centres of growth in the front layer. The initial flat Si/HF interface has the highest active surface. As the cluster develops, the active surface decreases (even though the whole specific surface may increase). The evolution of the active surface determines the porosity profile, so the change in active surface leads to the porosity gradient. The hole generation permits

increase with the increase of  $L$ , which corresponds to current density increase and/or HF concentration decrease. This result agrees with experimental data [13, 14]. Within radius,  $L$ , pores are continuous in plane-parallel directions, which agrees with high-resolution and cross-sectional TEM photographs of the mesoporous Si layers [15]. For  $L=4$  and  $R_D=0$  current density is great enough to achieve polishing.  $R_D$  increase leads to straightening of the pores and increasing distance between them. By the conditions  $L=0$  and  $R_D=10$  and 20, the direction of growth is practically predetermined, since the active zone for each pore is limited by its lowest point. Similar conditions were provided by Lehmann et. al. [16] in n-Si, using inducing pits and backside illumination.

The three-dimensional images of simulated structures ( $160 \times 160 \times 80$ ) were obtained. The calculations show that the porosity  $P$  changes over the depth,  $h$ , of the porous layer in accordance with SIMS data [17].  $dP/dh$  decreases with increasing  $G$ . In order to interpret this result, it is necessary to first explain why the gradient in DLA model rises without hole generation ( $G=0$ ). In the growth process limited by diffusion, holes can not penetrate from the bottom to the top of the growth layer since they are effectively captured by the branches of the ramified structure. For this reason the growth preferably proceeds in thin front layer. Let us characterize it at any time by the current active surface defined as the number of possible centres of growth in the front layer. The initial flat Si/HF interface has the highest active surface. As the cluster develops, the active surface decreases (even though the whole specific surface may increase). The evolution of the active surface determines the porosity profile, so the change in active surface leads to the porosity gradient. The hole generation permits

holes to appear at any depth of PS layer, and the active surface is no longer limited by the front layer. Then the pore diameter increases until the quantum confinement in crystal nanoparticles becomes essential. So the simultaneous action of hole generation and quantum confinement leads to smoothing of the porosity profile. It was shown that

a porosity averaged over the porous layer depth increases while  $R_Q$  decreases. This result is reasonable since the quantum confinement effect tends to prevent dissolution on the local scale.

The fractal dimension was calculated for the crystal part of the porous structures, formed by computer simulation on three-dimensional mesh. The dependence of fractal dimension upon size is shown in Fig.4. It changes from 0.1 to 3 as the size of the structure varies from 1.3 to 4 mesh steps, which corresponds to real sizes from 0.3 to 1 nm. The X-ray scattering experiment [18] showed that mesoporous structures are characterized by fractal dimension at sizes up to 100 nm. Nanoporous structures should display the fractal properties at smaller sizes.

### 3.2. THE RESULTS OF SIMULATION OF SILICON-ON-POROUS SILICON EPITAXY.

Three-dimensional images of grown layers were obtained for various porosity, pore size and molecular beam density,  $F$ . The typical fragments of layer surface before, during and after Si deposition on PS are shown in Fig. 5 ( $F=1$  bilayer/s) and Fig. 6 ( $F=10$  bilayer/s). The cross sections at the edges with the insets illustrate the pore morphology evolution. The difference in the kinetics of epitaxy for the cases of various  $F$  is clearly seen. Under low flow density, pores are the effective traps for adatoms and the Si island formation is suppressed until pores are covered. At high flow density, the adatoms form the islands between the pores. The islands are formed as far from the pores as a diffusion length. This is marked in case of large distance between the pores. Thus, the porosity chosen for Fig. 1 and Fig. 2 is rather low. It is an interesting result to find that a change in pore structure occurs only in the upper (of 1-2 bilayer thick) layer.

In order to specify the detailed mechanism of the Si growth over pores, the statistical analysis of random atomic bond configurations for adatoms inside pores was carried out. Figs. 6 a,b,c illustrate the idealized scheme for formation of Si pendant layer. Circles show the regular atom positions in (111) plane. Fig. 6 d shows the fragment of diamond-type structure elucidating the location of the positions over depth: the

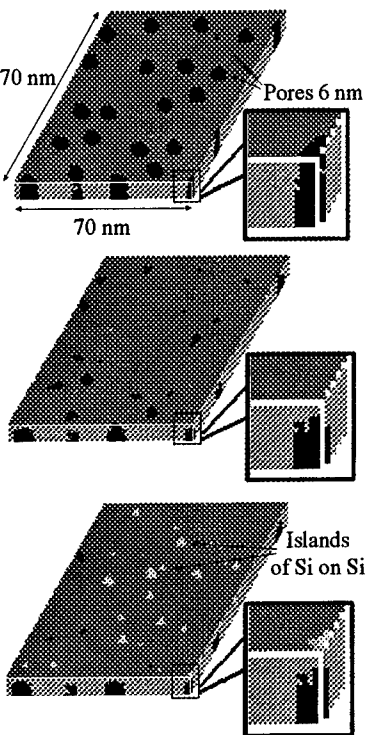


Fig.5. Fragment of PS (111) at different stages of Si epitaxy ( $P=0.18$ ,  $T=1000$  K,  $F=1$  bilayer/s).

large circles correspond to the upper surface layer. The positions occupied by atoms are marked in black, those most probable to be occupied - in grey in Figs. 6a,b,c. A white circle inside a black one denotes an atom in the inner bilayer. At first, the metastable nucleus (a chain of atoms or a single atom linked with the structure by two bonds) is formed at the edge of a pore (Fig. 6a). Under certain conditions, depending on temperature and molecular beam density, the metastable nucleus exists long enough to form a bond with a new atom arriving with the surface diffusion flow. The most probable positions to be occupied (grey circles in the Figs. 6a,b,c) are linked with the structure by two bonds at least. At all stages of pendant layer formation these positions appear to be located inside two upper bilayers. Obviously this factor determines the thickness of the pendant layer growing by the perimeter over pore. The analogous series of enlarged fragments near a pore obtained during the computational experiment showed close resemblance with those presented at Figs. 6. The

b

c

d

e

f

g

h

i

j

k

l

m

n

o

p

q

r

s

t

u

v

w

x

y

z

aa

bb

cc

dd

ee

ff

gg

hh

ii

jj

kk

ll

mm

nn

oo

pp

qq

rr

ss

tt

uu

vv

ww

xx

yy

zz

aa

bb

cc

dd

ee

ff

gg

hh

ii

jj

kk

ll

mm

nn

oo

pp

qq

rr

ss

tt

uu

vv

ww

xx

yy

zz

aa

bb

cc

dd

ee

ff

gg

hh

ii

jj

kk

ll

mm

nn

oo

pp

qq

rr

ss

tt

uu

vv

ww

xx

yy

zz

aa

bb

cc

dd

ee

ff

gg

hh

ii

jj

kk

ll

mm

nn

oo

pp

qq

rr

ss

tt

uu

vv

ww

xx

yy

zz

aa

bb

cc

dd

ee

ff

gg

hh

ii

jj

kk

ll

mm

nn

oo

pp

qq

rr

ss

tt

uu

vv

ww

xx

yy

zz

aa

bb

cc

dd

ee

ff

gg

hh

ii

jj

kk

ll

mm

nn

oo

pp

qq

rr

ss

tt

uu

vv

ww

xx

yy

zz

aa

bb

cc

dd

ee

ff

gg

hh

ii

jj

kk

ll

mm

nn

oo

pp

qq

rr

ss

tt

uu

vv

ww

xx

yy

zz

aa

bb

cc

dd

ee

ff

gg

hh

ii

jj

kk

ll

mm

nn

oo

pp

qq

rr

ss

tt

uu

vv

ww

xx

yy

zz

aa

bb

cc

dd

ee

ff

gg

hh

ii

jj

kk

ll

mm

nn

oo

pp

qq

rr

ss

tt

uu

vv

ww

xx

yy

zz

aa

bb

cc

dd

ee

ff

gg

hh

ii

jj

kk

ll

mm

nn

oo

pp

qq

rr

ss

tt

uu

vv

ww

xx

yy

zz

aa

bb

cc

dd

ee

ff

gg

hh

ii

jj

kk

ll

mm

nn

oo

pp

qq

rr

ss

tt

uu

vv

ww

xx

yy

zz

aa

bb

cc

dd

ee

ff

gg

hh

ii

jj

kk

ll

mm

nn

oo

pp

qq

rr

ss

tt

uu

vv

ww

xx

yy

zz

aa

bb

cc

dd

ee

ff

gg

hh

ii

jj

kk

ll

mm

nn

oo

pp

qq

rr

ss

tt

uu

vv

ww

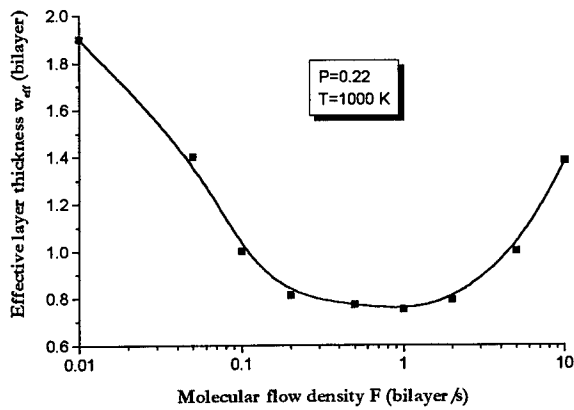


Fig. 7. The effective thickness of layer deposited vs flow density ( $P=0.22$ ,  $T=1000$  K).

porous layer. This decreases the effectiveness of overgrowth.

The atomic force microscopy data [19] give an evidence that the surface between pores is rough (with an average relief height  $\sim 0.1$ - $0.2$  nm). The initial smooth 3D grid ( $160 \times 160 \times 16$ ,  $P=0.14$ ) was exposed to an artificial roughening procedure,

during which the surface atoms one by one were randomly removed from the grid. The meshes obtained at various intervals were used as the initial substrates in simulation of epitaxy. For numerical characterization of porous layer surface morphology the roughness function,  $S$  [12], was calculated and defined as the relative number of atoms situated in the vertical sections of surface.

The dependence of roughness upon the amount of Si deposited is shown in Fig. 8 for various initial surface morpholo-

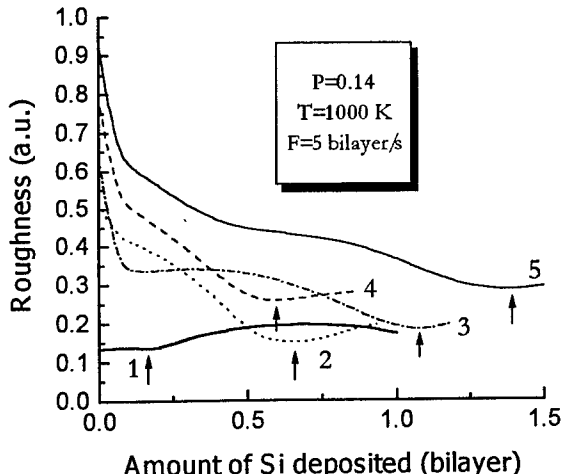


Fig. 8. The dependence of surface roughness upon the amount of Si deposited for various initial surface morphologies ( $P=0.14$ ,  $T=1000$  K,  $F=5$  bilayer/s).

gies (curves 2-5). For comparison, curve 1 is plotted corresponding to the initial surface which is smooth between pores. At the initial stage, curves 2-5 have a sharply descending section, illustrating the effect of polishing. This effect arises due to the intensive capture of adatoms in micropores. The next stage of growth is defined by the competition between the formation of a pendant layer and the growth of islands between pores. Arrows show the points in the curves which correspond to the overgrowth of pores. The interesting result is that  $w$  increases non-monotonously with the initial roughness  $S$ . The brief explanation of this is as follows. Roughening changes the ratio between the surface areas occupied by the upper and the lower monolayers compiling the (111) bilayer. This leads to a critical change in the effectiveness of the nucleation of islands and accounts for the non-monotonous dependence of  $w$  upon initial  $S$ . The dependence is not periodical because the removal of monolayers is coupled with the increase in surface roughness.

#### 4. Conclusion

The present model provides a more accurate description of PS formation by electrochemical etching in HF. The simulated structures exhibit close resemblance to those obtained in experiment. The 3D meshes, corresponding qualitatively to nanoporous Si structures, are taken for simulation of Silicon-on-Porous Silicon Epitaxy. The simulation is carried out on the basis of the Gilmer model extended for the case of a relief surface. The possible mechanism of overgrowth of the porous layer is proposed via the pendant layer formation. In terms of this mechanism the dependence of growth kinetics upon the porosity, molecular flow density and initial surface roughness are interpreted.

This work was supported in part by the Russian National Programs "Surface atomic structures" under grant 97-3.21 and "Solid nanostructure physics" under grant 99-1131.

#### References

1. Canham L.T. (1990) Silicon quantum wire array fabrication by electrochemical and chemical dissolution of wafers, *Appl. Phys. Lett.* **57**, 1046-1048.
2. Foll H. (1991) Properties of silicon-electrolyte junctions and their application to silicon characterization, *Appl. Phys. A53*, 8-19.
3. Shengurov V.G., Shabanov V.N., Gudkov N.V., Tkatch B.Ya. (1993) Epitaxial silicon films formed on the porous silicon surface, *Microelectronics* **222**, 19-23.
4. Yakimov A.I., Stepina N.P., and A.V.Dvurechenskii (1998) Stretched-exponential conductivity relaxation and 1/f noise on fractal networks of porous amorphous silicon, *Phys. Low-Dim. Struct.* **5/6**, 111-130.
5. Smith R.L., Chung S.-H., and Collins S.D. (1988) A theoretical model of the formation morphologies of porous silicon, *J. Electron. Mater.* **17**, 533-547.

6. He J., Huang Y.P., Kwor R. (1995) A modified computer-model for the formation of porous silicon, *Thin Solid Films* **265**, 96-100.
7. Aleksandrov L.N. and Novikov P.L. (1997) Simulation of the formation of porous silicon structures, *JETP Letters* **65**, 714-719.
8. Aleksandrov L.N. and Novikov P.L. (1998) Morphology of porous silicon structures formed by anodization of heavily and lightly doped silicon, *Thin solid films* **330**, 102-107.
9. Aleksandrov L.N. and Novikov P.L. (1996), Kinetics of phase transitions in porous silicon, *phys. stat. sol. (a)* **158**, 419-426.
10. Collins R.T., Fauchet P.M., Tischler M.A. (1997) Porous silicon - from luminescence to LEDs, *Physics Today* **50**, 24-31.
11. Novikov P.L., Aleksandrov L.N., Dvurechenskii A.V., and Zinovyev V.A. (1999) Modelling of initial stage silicon epitaxy on porous silicon (111) Surface, *Phys. Low-Dim. Struct.* **1/2**, 179-188.
12. Vvedensky D.D. and Clarke Sh. (1990) Recovery kinetics during interrupted epitaxial growth, *Surf. Sci.* **225**, 373-389.
13. Smith R.L. and Collins S.D. (1992) Porous silicon formation mechanisms, *J. Appl. Phys.* **71**, R1-R22.
14. Sasaki Y. and Kitahara M. (1994), Micro-Raman spectroscopy of nanoporous silicon, *J. Appl. Phys.* **76**, 4344-4346.
15. Lehmann V., Hofmann F., Muller F., Cruming U. (1995) Resistivity of porous silicon - a surface effect, *Thin Solid Films* **255**, 20-22.
16. Lehmann V., Hönlein W., Reisinger H., Spitzer A., Wendt H., and Willer J. (1996) A novel capacitor technology based on porous silicon, *Thin Solid Films* **276**, 138-142.
17. Karanovich A.A., Romanov S.I., Kirienko V.V., Myasnikov A.M., and Obodnikov V.I. (1995) A secondary ion mass spectrometry study of p<sup>+</sup> porous silicon, *J. Phys. D- Appl. Phys.* **28**, 2345-2348.
18. Goudeneau P., Naudon A., Bomchil G., and Herino R. (1989) X-ray small-angle scattering analysis of porous silicon layers, *J. Appl. Phys.* **63**, 86-88.
19. Hoppo N., Fujiwara M., and Horii K. (1998) Atomic-force microscopy study of self-affine fractal roughness of porous silicon surfaces, *Jap. J. Appl. Phys. P1* **37** (1998) 3951-3953.

---

## EVOLUTION OF PHASE COMPOSITION AND ASSOCIATED PROPERTIES IN THE PROCESS OF GROWTH OF NANOSTRUCTURED FILMS

S.A.Kukushkin and A.V.Osipov

*Laboratory of Structural and Phase Transitions in Condensed Media  
Institute of Problems of Mechanical Engineering, Russian Academy of  
Science, 199178, St.-Petersburg, Russia,  
e-mail: ksa@math.ipme.ru; fax: (812) 321-47-71*

### 1. Introduction

Nanostructured films are widely used in optics, microelectronics, laser engineering and many other fields of science and technology [1]. The materials must possess certain properties, for instance, mechanical or electrophysical depending on the application. The properties, as a rule, are determined by the composition of the growing films and also by the size of the crystalline grains forming the films [2]. Both systems can be studied in a similar way. Film systems are examined here only as an example since now they are widely used.

Irrespective of the preparation techniques, the films in the process of their growth pass a series of stages typical for a first-order phase transition [1, 3–9]. These stages are the nucleation of nano-clusters of a new phase [1, 10–17], their growth [10], Ostwald ripening [1, 3–8, 17], coagulation [11] and formation of a continuous film. When the nucleation process occurs under considerable supersaturation, the density of islands of new phase and the degree of substrate filling are high and the stages following nucleation may not take place [1]. In this case, both composition and structure are determined by the nucleation processes which have a complicated non-linear nature [12–16]. To control the process at this stage is not possible. Special methods such as nucleation process control are to be used. As shown in Refs [3–9], the growth parameters can be controlled only at the Ostwald ripening stage, where nucleation of new islands does not take place and a continuous film has still not formed. The possibility of composition and structure control is based on the fact that at this stage an ensemble of islands of new phase begins to interact with

generalized diffusion and thermal fields formed on the substrate's surface, and fluxes of atoms incident on it.

The aim of this work is to find out the dependence of the distribution function of nano-islands on their composition and, accordingly, the distribution functions with respect to one or another property (such as, conductivity, mobility and so on) dependent on the initial composition. It was shown previously that there is a great difference between evolution of nano-islands grown from substances forming a continuous series of solid solutions and stoichiometric substances formed as a result of chemical reactions. This leads to a significant difference in the growth processes of films both at the nucleation stage and the Ostwald ripening stage [3-9]. For this reason, these cases are analyzed separately.

## 2. Evolution of the phase composition of nano-islands at the Ostwald ripening stage.

### 2.1. EVOLUTION OF PHASE COMPOSITION IN SOLID SOLUTION

Let the equilibrium state diagram of a system for a growing film be the state diagram of a binary system with continuous solubility of components in a solid phase (see Fig 1). This means that both nucleation and Ostwald ripening processes are possible only when the system is supercooled to a temperature between the liquids line and the  $T_a$  line (see Fig 1). When the system is cooled in such a way that the temperature rapidly arrives at values lying between the  $T_a$  — line and the solidus curve, then the system readily solidifies without separation into phases and the composition of the solid phase corresponds to that of the liquid phase [18]. These processes are not discussed in this paper.

If a nano-island ensemble on the substrate surface is at the Ostwald ripening stage and is supercooled to a temperature in the interval between  $T_a$  and the liquidus line, then the composition of each island is related with its size,  $R$ , by the following equation [6, 7]:

$$C_{SR} = \frac{2\sigma w C_{L0}}{k_B T R} + C_{L0} + \psi \left( \frac{2\sigma w C_{L0}}{k_B T R} + C_{L0} \right), \quad (1)$$

where  $\sigma$  is the surface tension on the island-vapor (solution) interface;  $k_B$  is the Boltzmann constant ;  $T$  is the absolute temperature;  $C_{L0}$  is the equilibrium concentration of a component, for instance,  $A$  on the liquidus line (Fig.1), i.e. in a liquid phase;  $w$  is the volume per atom in an island;  $\psi$  is the functional relationship for the solidus-liquidus line, i.e.  $C_{S0} - C_{L0} = \psi(C_{L0})$ , describing the diagram of state (Fig.1);  $C_S$  — is the equilibrium concentration of a component of a solid solution, for instance,  $A$  in the solid phase.

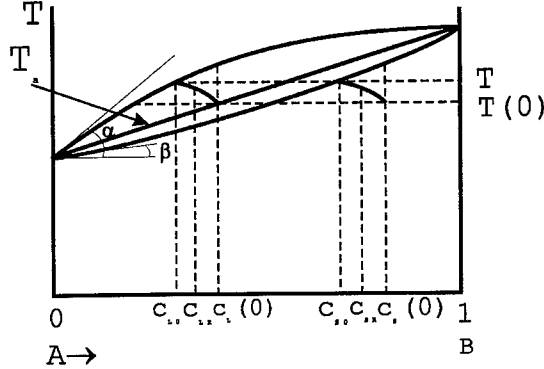


Figure 1: Diagram of states for a binary system with continuous solubility of components in a solid phase. Here  $C_{S0}$  and  $C_{L0}$  are equilibrium concentrations of a component in solid and liquid phases, respectively.  $C_{SR}$  is the composition of islands of radius  $R$ ;  $T_a$  is the temperature below which an alloy solidifies without changes in composition;  $\bar{T}(0)$  and  $\bar{C}_L(0)$  are the initial temperature and concentration in melt and solid phase, respectively;  $\alpha$  is the slope angle of the liquidus line for  $C \rightarrow 0$ ;  $\beta$  is the slope angle of the solidus line for  $C \rightarrow 0$ .

Let us consider the ranges of values of the  $\psi$  function near small values of  $C_{L0}$  concentration of the component  $A$ , i.e. near the origin of coordinates. In this case the  $\psi$  function can be approximated by two straight lines. In this case

$$C_{SR} = \frac{2\sigma w C_{L0}}{k_B T R} + C_{L0} + \gamma \left( \frac{2\sigma w C_{L0}}{k_B T R} + C_{L0} \right). \quad (2)$$

Here  $\gamma = \operatorname{tg} \alpha / \operatorname{tg} \beta - 1$ ;  $\operatorname{tg} \alpha$  is the angle coefficient of the straight line binding liquidus line and  $\operatorname{tg} \beta$  is the angle coefficient of the solidus line;  $(1 + \gamma)$  is the distribution coefficient of liquid and solid phases within the equilibrium one, i.e.  $1 + \gamma = C_{S0}/C_{L0}$ . Note, that if  $\gamma < 0$ , concentration of the component in the liquid is higher than in the solid (i.e. an easily fusible component is analyzed). In the case when  $(1 + \gamma) > 1$ , i.e.  $\gamma > 0$ , concentration of this component is higher in the solid phase than in the liquid. The expression for the island radius  $R$  could be obtained from (2):

$$R = \frac{2\sigma w C_{L0}(1 + \gamma)}{k_B T [C_{SR} - C_{L0}(1 + \gamma)]}. \quad (3)$$

Let us define  $C_{SR} - C_{L0}(1 + \gamma)$  as  $\xi_R$ . It is seen from equation (3) that there is an unambiguous relation between the island radius,  $R$ , and composition. Thus, if  $C_{SR} \rightarrow C_{L0}(1 + \gamma)$ , i.e.  $\xi_R \rightarrow 0$ , then  $R \rightarrow \infty$ . If  $\xi_R \rightarrow \infty$ , then  $R \rightarrow 0$ . It was shown previously in Refs [6-8], that in order to find out the size distribution function of islands,  $f(R, t)$  at the Ostwald ripening stage, it is necessary to solve the set of equations that involves the

continuity equation for the distribution function, the matter-and-heat balance equation, the equation describing relation between the flux of matter arriving at an island and the flux of heat released during the growth of the island; the coupling equation of the melting point for an island with radius,  $R$ , with the concentration of matter which is in equilibrium with it and the equation expressing the dependence of the growth rate of an island on its radius.

Since there is an unambiguous correlation between  $R$  and  $\xi_R$ , let us consider the distribution function  $f(R, t)$  - the distribution function of island versus inverse composition values, i.e.  $\varphi\left(\frac{1}{\xi_R}, t\right)$ . In accordance with (3), for  $t \rightarrow \infty$ , and  $R \rightarrow \infty$ ,  $\xi_R \rightarrow 0$ , it is more convenient to use the reciprocals of the compositions, i.e.  $1/\xi_R \rightarrow \infty$  at  $t \rightarrow \infty$ . So, we pass from  $f(R, t)$  to  $\varphi(1/\xi_R, t)$ , i.e.  $f(R, t)dR = \varphi(1/\xi_R, t)d(1/\xi_R)$ . In this case the set of equations describing the size distribution function  $f(R, t)$ , derived in Refs [6, 7] for the function  $\varphi(1/\xi_R, t)$ , could be written as:

$$\frac{\partial \varphi(1/\xi_R, t)}{\partial t} + \frac{\partial}{\partial(1/\xi_R)} \left[ \varphi\left(\frac{1}{\xi_R}, t\right) \frac{d(1/\xi_R)}{dt} \right] = 0 \quad (4)$$

$$Q_D(t) = N_0 \Delta C(t) + \kappa \int_0^\infty \varphi(1/\xi_R, t) (1/\xi_R^3) d(1/\xi_R) \quad (5)$$

$$Q_T(t) = \lambda C_P \rho \Delta T(t) + \kappa^* \int_0^\infty \varphi(1/\xi_R, t) (1/\xi_R^3) d(1/\xi_R) \quad (6)$$

$$L J_{D,R} = J_{T,R} \quad (7)$$

$$T_R = \varphi(C_L, R) \quad (8)$$

$$\frac{d(1/\xi_R)}{dt} = \frac{A_P}{\alpha^P (1/\xi_R)^{p-1}} \left[ \frac{\alpha(1/\xi_R)}{R_c} - 1 \right]. \quad (9)$$

Here Eqn. (4) is the continuity equation of the distribution function of islands versus island composition; Eqn. (5) is the equation of the matter conservation law expressed via the distribution function in terms of composition; Eqn. (6) is the equation of heat conservation law expressed through the distribution function in terms of composition; Eqn. (7) is the equation coupling heat and matter fluxes on the surface of an island of composition  $C_{SR}$ ; Eqn. (8) is the equation coupling the melting point of an island of radius,  $R$ , and its composition; Eqn. (9) is the equation describing the change of an island composition in time;  $Q_D(t)$  and  $Q_T(t)$  are the power carried by the matter flux arriving at the substrate and the power in the heat flow, respectively;  $\Delta C(t)$  and  $\Delta T(t)$  are the supersaturation and supercooling on a substrate or in the melt, respectively [6, 7];  $C_P$  and  $\rho$  are the heat capacity and density of a melt or substrate, respectively depending on where the ripening process takes place;  $\lambda$  is the thickness of the melt or substrate layer,

where the Ostwald ripening process takes place,  $\lambda$  is of the order of average island size, i.e.  $\lambda \sim \bar{R}$  (more information about  $\lambda$  value and its calculation can be found in [1]);  $A_P$  and  $p$  are the coefficients dependent on the mechanism of island growth [1, 6, 7]; the coefficient  $p$  can take the values of  $p = 2, 3, 4$  (in the case of evolution of faceted islands  $p = 5$ );  $R_c$  is the critical radius of islands;  $\chi_{cr} = \frac{2\sigma w C_{L0}(1+\gamma)}{k_B T} \frac{2}{3} \frac{\pi}{w N_0} [\chi(\theta)]^{-1}$ ;  $\kappa^* = \kappa/L$ ;  $L$  is the latent heat of crystallization per atom of the precipitated phase;  $N_0$  is the number of adsorption sites on the substrate,  $N_0 \sim 1/a^2$  (or the total number of atoms in solution,  $N_a$  depends on the kind of heat/mass transfer mechanism realized in a system [6, 7];  $a$  is the lattice constant of the substrate;  $\chi(\theta) = 2(2 - 3 \cos \theta + \cos^3 \theta)^{-1}$ ;  $\theta$  is the wetting angle;  $\alpha = 2\sigma w C_{L0}(1 + \gamma)$ ). Note, that in the general case, as shown in Refs [6, 7], the values of  $Q_D(t)$  and  $Q_T(t)$  can be represented in the form  $Q_D(t) = Q_{0D} + g_{0D} t^n$ ,  $Q_T(t) = Q_{0T} + g_{0T} t^n$ , where  $Q_{0D}$  and  $Q_{0T}$  are the total amount of matter and heat on a substrate at the beginning of the Ostwald ripening, respectively;  $g_{0D}$  and  $g_{0T}$  are the strengths of sources (sinks) of matter and heat;  $n$  is an arbitrary number,  $n \geq 0$  at the Ostwald ripening stage, i.e. when  $t \rightarrow \infty$ ,  $Q_D(t) \rightarrow g_{0D} t^n$  and  $Q_T(t) \rightarrow g_{0T} t^n$ .

Equations (4)–(9) were derived by substitution of variables from Eqn. (3) into the equations describing evolution of the size distribution function [6, 7]. Since  $R_c(t) = \frac{\alpha}{\Delta(t)}$ , where  $\alpha' = \frac{\alpha \cdot C_{L0}}{C_{L0}(1+\gamma)}$ , then

$$\frac{\alpha/\xi_R}{R_c(t)} = \frac{(\bar{C}(t) - C_{L0})(1 + \gamma)}{C_R - C_{L0}(1 + \gamma)} \quad (10)$$

As  $C_{L0}(1 + \gamma) = C_{S0}$ , then

$$\frac{\alpha}{\xi_R R_c(t)} = \frac{(\bar{C}(t) - C_{L0})C_{S0}}{(C_R - C_{S0})C_{L0}} \quad (11)$$

In accordance with (11) we can rewrite (9), as

$$\frac{d(1/\xi_R)}{dt} = \frac{A'_p}{(1/\xi_R)^{p-1}} \left[ \frac{(\bar{C}(t) - C_{L0})(1 + \gamma)}{C_R - C_{S0}} - 1 \right], \quad (12)$$

where  $A'_p = A_p/\alpha$ .

Finally the set of Eqns (4)–(8) and (12) completely describes the evolution of phase composition at the stage of the Ostwald ripening of a substance with the state diagram of a binary system with continuous solubility of components in a solid phase. Let us introduce the following variables:  $U = \frac{(\bar{C}(t) - C_{L0})(1 + \gamma)}{C_R - C_{S0}}$ ;  $x = \frac{\Delta_0}{\Delta(t)}$ ;  $\tau = \ln x^p$ , where  $\Delta_0$  and  $\Delta(t)$  are the supersaturation at the initial stage of ripening process  $n$  at time  $t$ . Equations (4)–(9) written with these variables are completely identical to the equations describing the process of non-isothermal Ostwald ripening [6–8]. Their solutions in variables  $u$  and  $\tau$  will be the same. The solution of the equations are given in [6–8]. By passing from variables  $u$  and  $\tau$  to variables  $1/\xi_R$  and  $t$  and also to the function  $\varphi(1/\xi_R, t)$ , we shall

obtain the relationship of island distribution with respect to composition in time. This solution is essentially dependent on a technique of deposition of material on a substrate as well as on the intensity of cooling (or heating) of the substrate. It is well known, that the Ostwald ripening stage starts only in the presence of weak sources of matter at  $0 \leq n < 3/p$ . In this case, as analysis shows [6, 7].

$$\varphi(1/\xi_R, t) = \frac{2\sigma\omega C_{L0}(1+\gamma)N(t)}{k_B T R_C(t)} P_p(U). \quad (13)$$

Here,  $P_p(U)$  is the probability density for  $U$  to range between  $U$  and  $(U + dU)$ ; the index  $p$  indicates the particular mechanism of heat/mass transfer realized in the system;  $N(t)$  is the density of islands on a substrate at the time  $t$ , the analytical expressions of this value are given in [1, 3–8];  $R_C(t)$  is the critical size of islands at the time  $t$ . In Eqn. (13) instead of the critical radius  $R_C(t)$  one can use the average radius, since they are related to each other by equation  $\bar{R}(t) = R_C(t)C_{pn}$ , (see Refs [1, 3–5]). Coefficient,  $C_{pn}$ , depend on the mechanism of heat/mass transfer and the power carried by sources of matter and heat. Numerical values of  $C_{pn}$  can be found in Refs [1, 3–5]. The value  $\frac{2\sigma C_{L0}(1+\gamma)\omega}{k_B T R_C(t)} = \frac{2\sigma C_{S0}\omega}{k_B T R_C(t)} = \Delta(t)$  is supersaturation.

The value of supersaturation in accordance with [7] changes in time as:

$$\Delta(t) = \frac{2\sigma\omega C_{L0}}{k_B T C_{pn}} (\bar{R}_0^p + A_p^0 t)^{-1/p} \quad (14)$$

Here,  $\bar{R}_0$  is the average size of islands at the initial stage of the Ostwald ripening. Coefficient  $A_p^0$  is the kinetic coefficient associated with the coefficient,  $A_p$ , derived above and it depends on the heat/mass transfer mechanism realized in the system. Values of these coefficients for all possible mechanism of heat/mass transfer are given in [6, 7]. In particular, when the islands are in the form of spherical segments and their growth occurs, as a rule, due to heat/mass transfer on the substrate surface with  $\lambda_s \gg R_1$   $p = 4$

$$A_p^0 = \frac{27}{32} \frac{D_a \sigma w^2 N_0 C_{sb0} K_s \ell_{sb} \phi_1(\theta)}{(D_a N_0 C_{Lsb0} L^2 \ln(H/R_1) + K_s \ell_{sb} k_B T_0^2 \ln(\lambda_s/R_1))},$$

where  $\lambda_s$  is the free path length of adatoms;  $D_a$  is the Brownian diffusion coefficient of adatoms;  $\sigma$  is the surface tension at the old phase-island interface (solution, melt, vapor);  $\phi_1(\theta)$  is the geometrical factor;  $K_s$  is the thermal conductivity of the substrate,  $K_s [J m^{-1} K]$ ;  $\ell_{sb}$  is the thickness of a substrate layer where the ripening process takes place [1, 7];  $L$  is the latent heat of crystallization per atom of a precipitated phase;  $C_{Lsb0}$  is the equilibrium concentration of adatoms on a substrate;  $T_0$  is the equilibrium temperature of crystallization (of solution, vapor or melt);  $H$  is the average distance between islands on a substrate [7];  $R_1 = R \cdot \sin \theta$ ;  $\theta$  is the wetting angle.

Analytical expressions of  $P_p(U)$  functions for all values of  $p$  are given in [1, 3–8], that is why in Fig 2 only the plots of  $P_p(U)$  values for  $p = 2, 3$  and  $4$  for  $n = 0$  are presented.

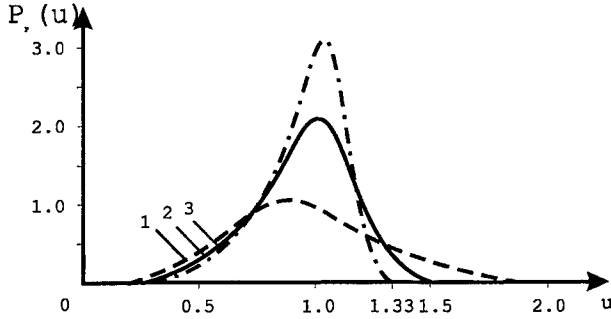


Figure 2:  $P_2(U)$ ,  $P_3(U)$  and  $P_4(U)$  functions for nano-islands with the spherical shape.

$P_p(U)$  functions can be experimentally found using the technique described in [1], i.e. by expressing  $U$  via the average radius of islands  $U = R \cdot C_{pn}/\bar{R}$ . This way is more convenient than to express  $U$  via concentrations  $U = (\bar{C}(t) - C_{s0})/(C_R - C_{s0})$ , which are hardly measurable values in the experiment. The distribution function in terms of composition (13) can be actually expressed through values independent of composition (except the  $C_{s0}$  value)—this is an advantage of our approach. Equilibrium concentrations  $C_{L0}$  and  $C_{s0}$  as well as equilibrium temperature  $T_0$  are determined from the solution of Eqns (5)–(8) for  $t \rightarrow \infty$ . For  $t \rightarrow \infty$  the equations transform into algebraic equations. The equations can be easily solved and, as a result, the values of  $C_{L0}$ ,  $C_{s0}$  and  $T_0$  can be obtained (for more details see [6, 7]).

The average composition of nano-islands is calculated from the equation

$$\bar{\xi}(t) = \left[ \int_0^\infty \frac{1}{\xi_R(t)} \cdot \varphi(1/\xi_R, t) d\left(\frac{1}{\xi_R}\right) \right]^{-1}. \quad (15)$$

Taking into account Eqn. (3) and expressing  $\varphi(1/\xi_R, t) d(1/\xi_R)$  via  $f(R, t) dR$ , as it is done before, we shall get

$$\bar{\xi}(t) = \frac{2\sigma\omega C_{L0}(1+\gamma)}{k_B T} [\bar{R}(t)]^{-1}. \quad (16)$$

Finally we shall obtain:

$$\bar{\xi}(t) = \frac{2\sigma\omega C_{L0}(1+\gamma)}{k_B T} [\bar{R}_0^p + A_p^0 t]^{-1/p}. \quad (17)$$

Comparing Eqn. (17) with (14),  $\Delta(t) = \bar{\xi}(t)/(1+\gamma)$  is readily obtained. This result is associated with the fact that compositions of solid and liquid phases are related to each

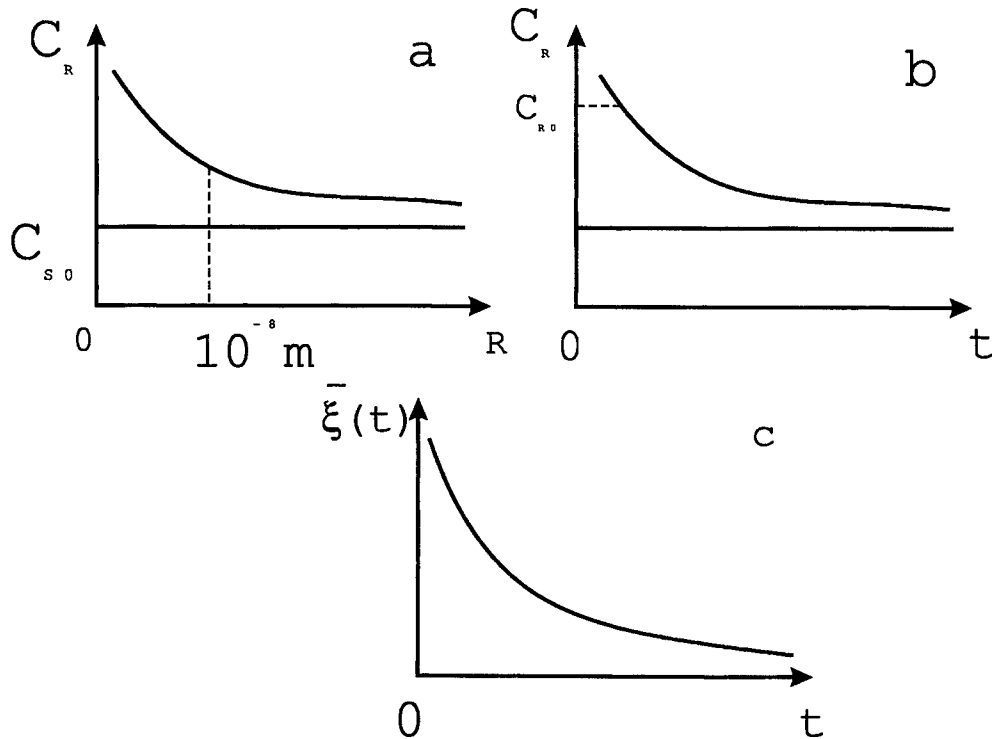


Figure 3: Dependence of composition of nano-islands on size (a) and composition of nano-island on time (b); time dependence of the mean composition of nano-islands (c).

other by the state diagram presented in Fig.1.

The changes in composition in an island can be obtained from the following relationship

$$C_R = C_{S0} + \frac{\Delta(t)}{U}, \quad (18)$$

where  $\Delta(t)$  is determined from Eqn. (14), whereas  $U = R/R_c$ .

The dependence of island compositions on their sizes are shown in Figures 3a,b,c (for composition of the particular island dependent on its growth time and dependence of the average composition of islands on time).

Let us do some estimates. As follows from Eqn. (18).  $C_R = C_{S0} + \frac{2\sigma\omega C_{S0}}{k_B T R}$ . Let us assume,  $\sigma$  to be  $\sim 10^{-1} \div 10 J/m^2$ , and  $kT \sim 10^{-19} J$ , we shall get for:  $C_R \sim C_{S0} \left(1 + \frac{10^{-10}}{R}\right)$ . For this reason, the main change in composition of islands takes place for  $R \leq 10^{-8} m$ . In this case, the change of composition will be within a few tens of atomic percents and this fact

is of particular importance for the measurement electrophysical properties.

## 2.2. EVOLUTION OF THE COMPOSITION OF A NANO-ISLANDS OF STOICHIOMETRIC COMPOSITION.

When islands are of strictly stoichiometric composition, as it is shown in Refs [1, 3–5, 8], the regions of phase coexistence and accordingly, the composition of island films are determined from the solution of the system of equations derived in [1, 5]. Detailed analysis of the set of equations is performed in Ref. [1, 3–5, 8] and some particular solutions for specific systems are given. Now we shall pass to the description of phase composition evolution at the nucleation stage.

## 3. Evolution of phase composition in new phase islands at the nucleation stage

### 3.1. EVOLUTION OF PHASE COMPOSITION IN SOLID SOLUTION ISLANDS.

At the nucleation stage there is no unambiguous relation between size and composition as compared to the Ostwald ripening stage. Note, that new phase nucleation processes in such systems were investigated by many authors [12, 14, 15, 20, 21]. It turned out that fluctuations of components involved in a nucleus happen independently of each other. The control of the composition is impossible at this stage.

### 3.2. EVOLUTION OF PHASE COMPOSITION IN ISLANDS OF STOICHIOMETRIC COMPOSITION.

When islands of new phase are stoichiometric compounds, the nucleation process can occur in several stages (see Ref. [20]). It is shown that the nucleation process is essentially dependent on whether or not chemical reactions in multicomponent adsorbed gas occur simultaneously with the formation of the end reaction product. We have shown in [20] that for specific conditions it is possible to observe self-oscillations of the number of nuclei and self-organization phenomena are possible.

#### 4. Evolution of the composition-dependent properties of growing nanostructured films

It is well known that many properties of solids are essentially dependent on their chemical and phase composition. The properties can be the concentration of charge carriers in semiconductors, their mobility, conductivity of metals and alloys, absorption and electromagnetic wave scattering, strength properties [2, 18], etc. Without claiming any consistent investigation of the properties, we show here merely the main principle for calculation of their evolution in the process of nanostructured film growth.

##### 4.1. EVOLUTION OF PROPERTIES IN SOLID SOLUTION NANO-ISLANDS.

Let  $F(C, t)$  be the function describing the relation between certain properties of the solid (in this case, an island) on composition. Let us find the distribution function of properties of different composition. To do this we shall pass from the function  $\phi(1/\xi_R)$ , expressing distribution function of island in terms of composition to the distribution function with respect to properties,  $\Theta(F, t)$ :

$$\Theta(F, t) d(F) = \varphi\left(\frac{1}{\xi_R}, t\right) d\left(\frac{1}{\xi_R}\right), \quad (19)$$

In the general case, the average value of properties in nano-islands changes in time as

$$\bar{F}(t) = \int_0^\infty F(t)\Theta(F(t), t) d(F). \quad (20)$$

Note, that Eqns (4)–(9) describe not only the evolution of composition and, accordingly, properties in nano-island films but the meaning of these values in continuous films as well. For this purpose it is necessary to estimate the time of coalescence of islands into a solid layer using the equations given in Ref. [3] and the distribution functions of islands in terms of composition in time. In this case, it is necessary to take into account that Eqn. (4)–(9) and, accordingly, (13)–(18) are valid, strictly speaking, only for total coverage close to zero. In the case when the total coverage essentially exceeds zero, the collision integral is to be introduced into Eqns (4)–(9), [22]. However, as it follows from calculations [22], the function values are only slightly changed. Therefore, Eqns (13)–(18) provide an adequate approximation.

When some property of islands depends both on their size and composition, i.e.  $\Theta = \Theta(C, R, t)$ , it is necessary to pass from variable  $R$  in the terms for  $\Theta(C, R, t)$  to variable  $C_{SR}$  by means of Eqn. (3). In a consequence, we again get the function  $\Theta(C, t)$ . In the case, when the property, in question, is only the distribution function, i.e.  $\Theta(R)$ ,

conditions for its evolution can be expressed through the size distribution function  $f(R, t)$  [1].

#### 4.2. EVOLUTION OF PROPERTIES IN NANO-ISLANDS OF STOICHIOMETRIC COMPOSITION.

The nano-islands of stoichiometric composition are homogeneous. Therefore, the property function depends on the islands' size only. The properties of a nano-film are determined by the number of islands of one or another phase and by the size distribution of islands colliding with each other. The technique for the phase coexistence regions determination is described in detail in Ref. [1, 3–5]. The diagram of phase coexistence regions for a three-component two-phase system (where one of the components is simultaneously included in both phases) is constructed therein. If there is an unambiguous relation between the distribution function of property values  $F$  for  $s$ -phases,  $\Theta^s(F, t)$ , and size of particles, then the distribution function for  $n < 3/p$  can be derived in a similar way as in (13):

$$\Theta^s(F, t) = \frac{N^s(t)}{R_c^s(t)} \frac{dR}{dF^s} P_p^s(U), \quad (21)$$

where  $N^s(t)$ ,  $P_p^s(U)$ ,  $R_c^s(t)$  are the functions of the number of islands  $N^s(t)$ , probability density  $P_p^s(U)$  and critical radius of islands of  $s$ -phase [1, 3–5];  $dF^s/dR$  is the derivative of relation between the properties and radius of an island of  $s$ -phase;  $p = 2, 3, 4$  in accordance with the island growth mechanism. Evolution of the average value of a property can be described by an equation similar to Eqns (15).

Consequently, all conclusions on influence of heating or cooling of a substrate and the power of component sources presented in Refs [1, 3–5] for the size distribution function  $f^s(R, t)$  of islands of phase  $s$  over a substrate can be extended for the function  $\Theta^s(F, t)$ . When islands of different phases (chemical compounds) have regions of mutual solubility, i.e. they can be solid solutions, evolution of their properties can be described in a similar way as in section 2.

On the contrary, when properties depend on sizes of islands and the function  $\Theta(F, t)$  is known, the relative number of  $s$ -phase can be expressed as  $J^s = \frac{1}{V_m^s N_0} \frac{\kappa(\theta) 4}{3} \pi \int_0^\infty f^s(R, t) R^3 dR$ ; (here  $V_m^s$  is the volume of molecules of phase  $s$ ;  $N_0$  is the number of adsorption sites on the substrate surface  $N_0 \sim 1/a^2$ ;  $a$  is the lattice constant of a substrate) can be expressed as follows:

$$J^s = \frac{1}{V_m^s N_0} \kappa(\theta) \int_0^\infty \Theta^s(F, t) Z^3(F) d(F), \quad (22)$$

taking into account the condition  $f^s(R, t) dR = \Theta^s(F, t) dF^s$ .  $R = Z(F)$  is the inverse function from the function  $F = Z(R)$ . Thus, the coexistence region of different compo-

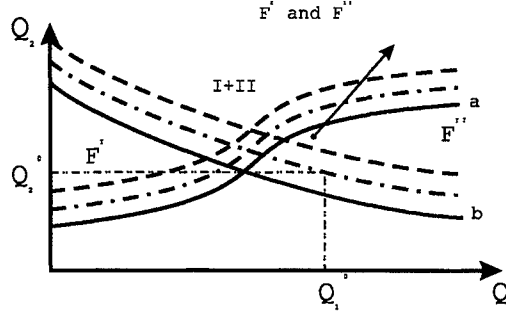


Figure 4: Values diagram of properties in the space of components  $Q_1$  and temperature (in projection on the  $Q_1, Q_2$  plane). Boundaries of the values of properties in a system are indicated with the continuous line; displacement of the boundaries due to temperature change is indicated with dashed and chain-dotted line.  $Q_1^0$  and  $Q_2^0$  are certain initial quantities of components;  $I$  and  $II$  are the regions of different phases;  $F^I$  and  $F^{II}$  are the values of a property in islands of different chemical composition. The trajectory of a system in the presence of sources of components is indicated with arrow.

sitions can be determined by known values of  $F$ . The diagram of values of the property function for a two-phase tree-component system where one of the components is simultaneously included into both phases, is given in Fig.4. The diagram is calculated in accordance with the technique described in [1, 3-5]. Fig. 4 shows that in the case when islands form a continuous film, the structure with a number of properties determined only by its dependence on the size of islands exists in regions  $I$  and  $II$ . Within the region  $I + II$ , islands of mixed composition, i.e. with a different value of properties  $F^I$  and  $F^{II}$  will grow. In the process of growth, the islands give rise to non-homogeneous properties of thin films. The regions of  $F$  values can be varied in the presence of sources of components (or through cooling heating of the substrate). For this purpose, it is necessary to choose a certain value of the decay degree of sources,  $n$ , in accordance with the island growth mechanism [1, 3-5].

Now, we pass to the nucleation of new phase islands in multicomponent systems during chemical reactions. It is shown in Ref. [21] that for some specific relation between chemical components and islands of different phases complex non-linear interactions occur. This causes periodic change of the number of islands in space and time. As a result periodic changes in thin films properties are observed. The value will change periodically in space and time as well (see Fig. 5a and 5b).

In the case of the formation of islands of several phases (chemical compounds), the behavior of properties is more complicated. However, when self-organization or self-induced oscillations occur in a system, appropriate properties will also periodically change either in space, or in time.

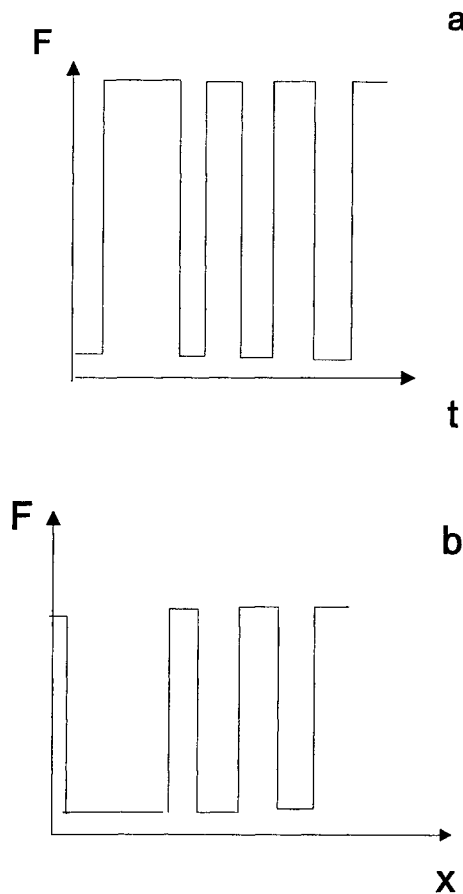


Figure 5: The scheme of the change in the values of properties for the case of new phase nucleation in multi-component systems in the presence of self-induced oscillations of composition — (a) or self-organization — (b).

## 5. Discussion

The relationship between size and composition of new phase nano-islands formed in the course of condensation of solid solution films is elucidated in the work. Analysis shows that the most favorable ways to control the composition of the nanostructured films are at the Ostwald ripening stage. At this stage there is an unambiguous relation between the size distribution function of islands and distribution function in their properties. This allows to pass from equations describing evolution of the size distribution function to equations of evolution of distribution function of properties in solid solution nano-islands. The analysis shows that considerable changes in composition occur for sizes less than  $10^{-8}m$ . In this case, their composition can be changed by tens of atomic percent that corresponds to  $10^{12} \div 10^{13}m^{-3}$ . For values of island radius  $R > 10^{-8}m$  the composition of islands is independent of size actually regardless of substance.

It is shown that the coexistence diagrams can be constructed for stoichiometric compounds, and by means of change of atomic fluxes and controlling the degree of cooling or heating of a substrate one can pass from one property to another.

It is found that the control of properties at the nucleation stage is restricted. Only in the case with nucleation of stoichiometric compounds the structures with given properties may be obtained, provided that self-induced oscillations and self-organization take place. However, in this case it is necessary either to calculate beforehand the oscillation period of the composition [21], or to determine it experimentally and to stop the growth when the desired composition is achieved.

This work was partially supported by the Russian Foundation for Basic Research (code 99-03-32768 and 98-03-32971), grant "Integration" No. A0121, NATO Grant SfP #973252.

## References

- [1] Kukushkin, S.A. and Osipov, A.V. (1996) New phase formation on solid surfaces and thin film condensation Prog. in Surf. Sci **56**, 1.
- [2] Mott, N.F. and Davis, E.A. (1979) Electron processes in non-crystalline materials (Second Edition) Clarendon press. Oxford.
- [3] Kukushkin, S.A. (1992) Evolution processes in multicomponent and multiphase films Thin Solid Films **207**, 302.
- [4] Kukushkin, S.A. (1994) Evolution processes in multicomponent and multiphase film growth from solutions Thin Solid Films **239**, 16.
- [5] Kukushkin, S.A. (1993) Evolutionary processes in ensembles of disperse particles on the surfaces of solids. Mechanisms of initial stages of formation of thin multicomponent films. I. Conservative systems Phys. Solid. State **35**, 797.

[6] Kukushkin, S.A. and Slyozov, V.V. (1995) Crystallization of binary melts and decay of supersaturated solid solutions at the Ostwald ripening stage under nonisothermal conditions *J. Phys. Chem. Solids* **56**, 1259.

[7] Kukushkin, S.A. and Slyozov, V.V. (1996) Growth of island films from binary melts or a vapor phase at the Ostwald ripening stage under non-isothermal conditions *J. Phys. Chem. Solids* **57**, 601.

[8] Kukushkin, S.A. and Slyozov, V.V. (1996) Theory of the Oswald ripening in multicomponent systems under non-isothermal *J. Phys. Chem. Solids* **57**, 195.

[9] Kukushkin, S.A. and A.V. Osipov, A.V. (1993) Microscopic theory of epitaxial film growth on vicinal surfaces *Thin Solid Films* **227**, 119.

[10] Osipov, A.V. (1993) Kinetic model of vapour-deposited thin film condensation : nucleation stage *Thin Solid Films* **227**, 111.

[11] Osipov, A.V. (1995) Kinetic model of vapour-deposited thin film condensation : stage of liquid-like coalescence *Thin Solid Films* **231**, 173.

[12] Kukushkin, S.A. and Osipov, A.V. (1997) Perturbation theory in the kinetics of first-order phase transitions *J. Chem. Phys.* **107**, 3247.

[13] Katz, J.L., Donohue, M.D. (1979) A kinetic approach to homogeneous nucleation theory *Adv.Chem.Phys.* **40**, 137.

[14] Mirabel, P. and Katz, J.L. (1974) Binary homogeneous nucleation as a mechanism for the formation of aerosols *J. Chem. Phys.* **60**, 1138.

[15] Kozisek, Z. and Demo, P. J. (1995) Transient nucleation in binary ideal solution *Chem. Phys.* **102**, 7595.

[16] Shi, F.G. (1995) Direct measurement of free-energy barrier to nucleation of crystallites in amorphous-silicon thin-films *Chem.Phys.* **212**, 421.

[17] Voorhees, P.W. (1990) Coarsening in binary solid-liquid mixtures *Met. Trans.* **21**, 27.

[18] Cahn, R.W. and Haasen, P. (1983) *Physical Metallurgy*, North-Holland, Amsterdam; Elsevier Science, New York.

[19] H. Reiss (1950) The kinetics of phase transition in binary systems *J. of Chem. Phys.* **18**, 840.

[20] Kukushkin, S.A. and Osipov A.V. (1995) Crystallization of binary melts and decay of supersaturated solid solutions at the Ostwald ripening stage under non-isothermal conditions *J. Phys. Chem. Solids* **56**, 1259.

[21] Kukushkin, S.A. and Osipov, A.V. (1997) Self-organization in the process of multicomponent film nucleation *J. Phys. Chem. Solids*, **58**, 1115.

[22] I.M. Lifshits, and Slyozov, (1962) The kinetics of precipitation from supersaturated solid solution *J. Phys. Chem. Solids*. **1**, 1258.

---

## REVIEW OF FATIGUE OF COATINGS/SUBSTRATES

K. SADANANDA\* AND R. L. HOLTZ  
Materials Science and Technology Division  
Code 6323, Physical Metallurgy Branch  
Naval Research Laboratory, Washington D.C.  
\*Currently on Sabbatical as Visiting Professor  
At Indian Institute of Technology, Madras, India.

### ABSTRACT

A review of fatigue of coatings/substrates is presented. Fatigue damage is either local or general, depending on the range of cyclic loads. Local fatigue damage includes rolling contact fatigue (RCF), fretting fatigue, fatigue-wear and general wear. Applied loads are localized consisting of rolling contacts or sliding contacts, and the resulting damage is mostly surface related. Crack initiation, surface pitting, delamination, spalling, buckling and enhanced wear can result from local fatigue damage of coatings. General fatigue damage results when the loads are of longer range such as cyclic bending, torsion or uniaxial or biaxial tension/compression etc. The mechanics of fatigue, role of microstructure, micromechanics in terms of crack nucleation, growth and fracture are reviewed. Defects produced during processing form precursors for crack nucleation. It is shown that optimization of the processing conditions to minimize defect density is essential to enhance fatigue resistance of coatings/substrates.

### 1. INTRODUCTION

The integrity of coatings/substrate composite depends on the nature of applied loads, environment, temperature and internal stresses introduced from the processing route as well as on the accommodating micromechanisms present. Understanding of the interplay of these factors, and the mechanics of the failures is important for the development of efficient and cost effective coatings. In this review, we examine the fatigue behavior of coating/substrates composites to evaluate the mechanical and microstructural factors that are involved in their fatigue damage. Since the microstructure and intrinsic defects that are formed depend on the processing conditions, we limit our discussion mainly to

thermal-spray coatings that are of current interest to US Navy, although the general principles discussed are applicable to all coatings. Through microstructural refinement, new nano-structured coatings are being developed to improve wear and corrosion resistance for many Navy structural components. The fatigue properties of these new nanostructured coatings are of interest, particularly in comparison to the conventional coatings. Some of these developments are also of interest to commercial sector under dual use technology.

## 2. MECHANICAL AND MICROSTRUCTURAL CONSIDERATIONS

Mechanical incompatibilities at bimaterial interfaces involving coatings/substrates result in internal stresses that affect the integrity of the coatings. The sources of internal stresses include:

- (a) Elastic modulus mismatch
- (b) Thermal coefficient of expansion mismatch
- (c) Lattice parameter mismatch
- (d) Plastic flow mismatch

Several analyses and reviews [1-7] exist in the literature quantifying the nature of the internal stresses that are generated at interfaces in coatings/substrates and resulting from these mismatches in the material properties at the bimaterial interfaces.

On the macroscale, response of coating/substrate composite to internal or external stresses depends on its flow behavior. Figure 1, for example, illustrates two contrasting coatings compared to stress strain curve of a substrate. Coating I has higher strength but lower ductility than the substrate, in comparison to coating II which is weaker but more ductile [8]. If such coating/substrate composite is stressed under equi-strain condition, the stronger but less ductile coating breaks giving rise to cracks in the coating. If interface is weaker, cracks can propagate along interface resulting in delamination and spalling of the coating. If the coating has lower strength but is more ductile than the substrate, then the coating deforms plastically, accommodating the stresses. In that case the composite will survive until the substrate fails or until the coating cracks when its fracture strain is reached. Most of the wear resistant coatings [9-12] such as WC/Co on steels or Al-alloys, are of the first type which are generally stronger and less ductile than the substrate. Their strength provides the needed wear protection.

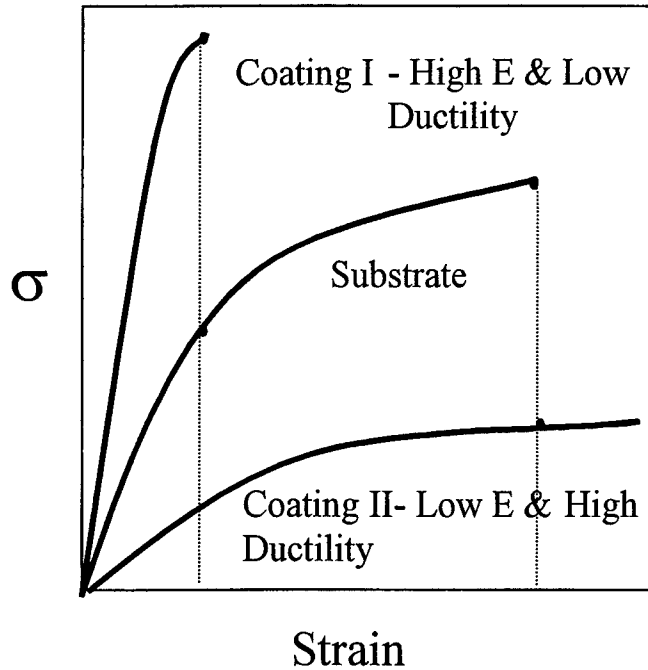


Fig. 1 Contrasting stress-strain behavior of ductile versus brittle coatings.

## 2.1 RESIDUAL STRESSES

Residual stresses arise from all of the above sources, but the thermal coefficient of expansion mismatch across the coating/substrate interface provides their major source. Residual stresses play a dominant role in the integrity of the coatings/substrates [13-17].  $\Delta\alpha$  is defined as  $(\alpha_c - \alpha_s)$ , where  $\alpha_c$  and  $\alpha_s$  are the coefficients of thermal expansion of coating and substrate, respectively. If the stresses are compressive in the coating, which is the case when cooled from high processing temperature to the application temperature and when  $\Delta\alpha$  is negative. The residual stresses inhibit the nucleation and growth of cracks. On the other hand, they can augment the compressive forces that will be introduced during contact fatigue and accentuate failures associated with contact fatigue. In addition the compressive forces can cause buckling of the coating if the cracks are formed parallel to the stress axis. This leads to delamination and spalling of the coatings. Another source of residual stresses which is not discussed above, occurs due to mechanical impact when the coating particles impinge on the substrate at high velocities,

such as during plasma spray or thermal spray processes [18]. Figure 2, for example, shows the nature of the residual stresses introduced in thermally sprayed WC/Co coatings, where spraying is done using high velocity guns.

### 3. CLASSIFICATION OF FATIGUE DAMAGE

One can classify the fatigue damage of coating/substrate assembly broadly into two types. They are (a) local fatigue damage and (b) bulk fatigue damage. The local fatigue damage is such that the scale factor is less than the coating thickness or volume. Local fatigue damage includes (a) rolling contact fatigue (RCF), (b) fretting fatigue, and (c) fretting wear, wherein the damage scale is smaller than the thickness of the coatings.

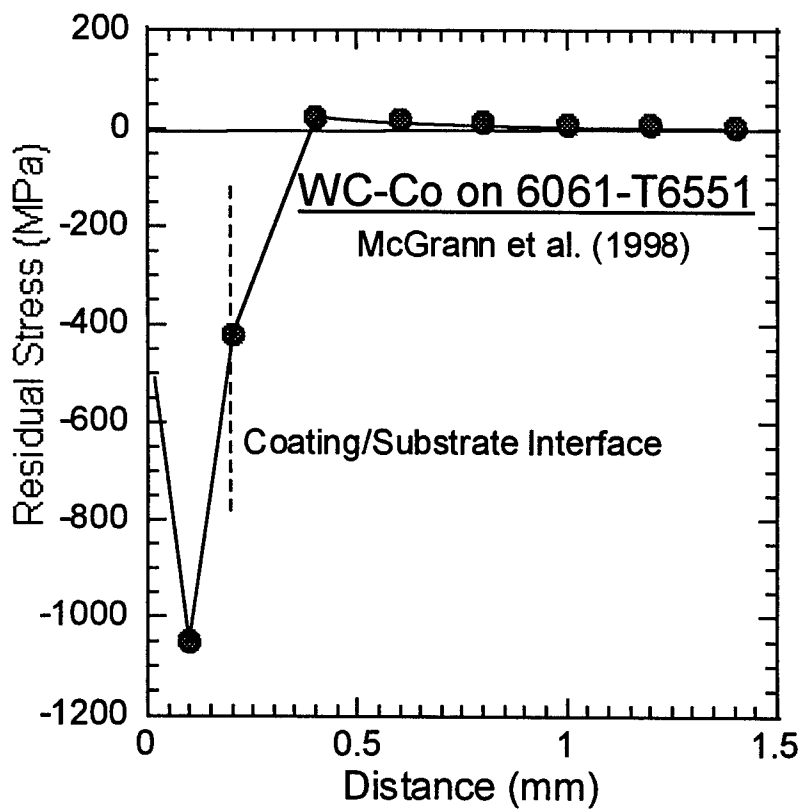


Fig. 2. Compressive residual stresses in WC-Co coating on an Al-alloy.

The bulk fatigue damage, on the other hand, involves intrinsic fatigue properties of the coating and substrate, bulk stresses, which extend to larger volume and the presence of defects or formation of cracks that are larger than the coatings thickness. Fatigue evaluation tests of the coatings/substrates such as push-pull or four-point bend tests etc., fall under this category.

### 3.1. LOCAL FATIGUE DAMAGE

Local fatigue damage consists of fluctuating loads on a local scale, which could occur due to high frequency vibrations with associated small tangential displacements between two contacting components. The two components may be in close mechanical locking or in rolling contact with one or both components rolling, such as wheels on rails, rolling ball bearings or gear contacts etc. Hard wear resistant coatings are deposited on the substrates to provide surface protection. Failure of these coatings generally involve fretting fatigue, fretting wear or rolling contact fatigue with crack formation, formation of pits, delamination and spalling of coatings at a local scale. If the two contacting surfaces are relatively stationary, then small tangential cyclic displacements can lead to fretting fatigue especially when there are normal forces to reinforce their mutual contact.

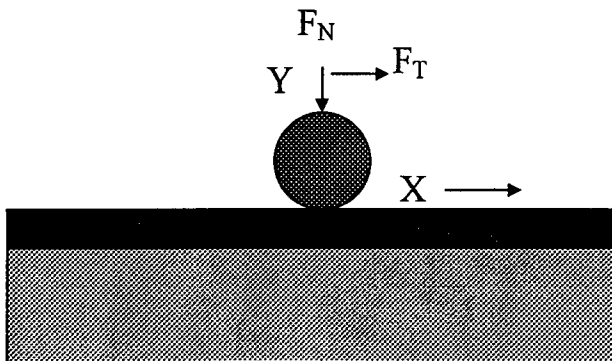


Fig 3. Rolling contact of a sphere on a half-space

The mechanics of the problem is somewhat similar for all local fatigue problems involving rolling contact, fretting fatigue, or fatigue wear etc. Complexities arise because of the three dimensional nature of the problem with local irreversible plasticity causing fatigue damage. Several analytical and numerical analysis techniques [19-24] have been presented in the literature considering the three dimensional nature of the contact problem. The problem has been simplified by considering an elastic analysis of a ball pressed against a flat surface characterized by half-space as shown in Fig. 3.

Fretting occurs in the regime depending on the frequency, displacement amplitude,  $\delta$ , or amplitude of the tangential force. Examining the nature of the damage during cyclic contact displacement, Madlin [22-23] has shown that under contact pressure, the shear stress required to overcome the static frictional resistance will have a maximum at the center of the circular contact area. While Madlin's analysis assumes elastic conditions, the three-dimensional nature of the problem and local plasticity effects have been considered recently using numerical techniques[24-28]. There are three conditions - stick, partial slip and general slip [29-32]. The load-displacement curves for the three are schematically represented in Fig.4 based on which fretting maps have been developed. Case A is considered elastic with tangential displacements being small.  $F_T$  -  $d$  curve shows transition from predominately elastic to plastic shear, which represents the plastic yield of not only the asperities but also of the underlying bulk material.

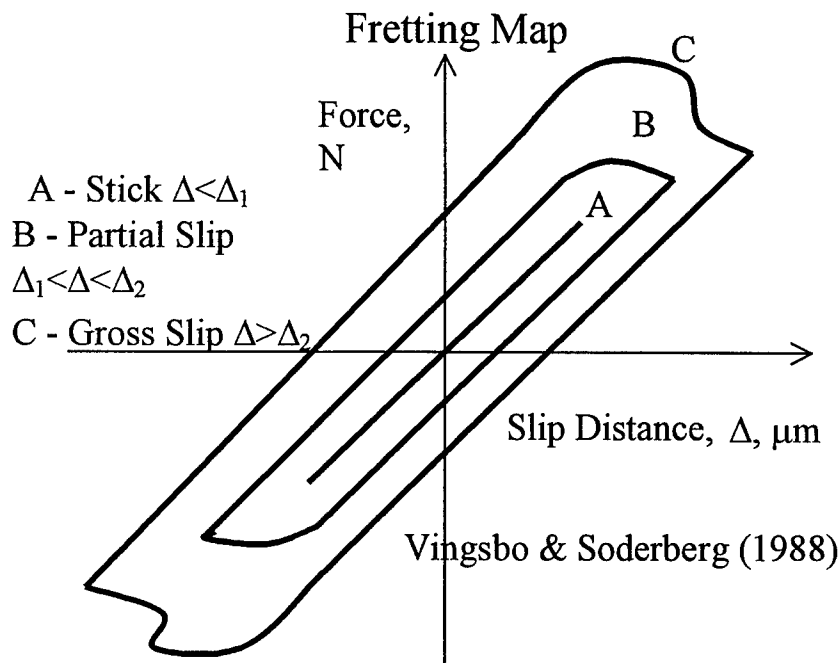


Fig. 4. Force-distance curve of contact bodies, stick, partial slip and gross slip regimes.

A second contribution to the leveling-off of the tangential force above a certain displacement stems from the fact that part of the applied shear stress is relaxed by the introduction of slip in the annular slip region. Figure 4 indicates that there are two

critical displacements,  $\Delta_1$  and  $\Delta_2$ , defining the three regimes, stick, partial slip and gross slip. Nonlinear displacements in contact fatigue, Figure 4, result in fatigue damage. If the frequency and the number of cycles become sufficiently large, the damage becomes significant and is termed fretting fatigue. Cyclic straining during continued fretting might lead to the nucleation and propagation of surface fatigue cracks, particularly along the rim of the contact area. Generally the displacement amplitudes are within the range of 1-2 $\mu\text{m}$  for fretting fatigue. But the damage can be significant when the number of cycles are in the range of  $10^7$  cycles.

Since fretting and wear both result from local fatigue damage, the fretting map can be superimposed on wear map using displacement amplitude as the independent variable. Although wear damage is not discussed here, the same region subjected to repeated rubbing by two contact surfaces exhibits both fatigue and wear. In fact wear itself could be due to fatigue, although characteristically referred to as wear fatigue to separate it from other forms of fatigue. Thus fretting damage manifests in two forms, fretting wear and fretting fatigue, which are somewhat related. Fretting wear starts when particles are formed within or at the edge of the contacts.

#### 4. BULK FATIGUE

In addition to local fatigue problems, which are surface contact induced fatigue damage, the coatings/substrates are subjected to fluctuating gross scale loads that cause general or bulk fatigue. The mechanics of the problems and the nature and the extent of the damage are sufficiently general requiring separate evaluation. There have been several analyses of the coating/substrate mechanics to evaluate the fracture and fatigue properties of the coated material [1-7,33,34]. The analyses have been done considering combined Mode I and Mode II stresses for a body bonded by a thin adhesive layer. The difference in strength and elastic properties of the bimaterial and the strength of the interface along with the nature of the applied or induced stresses dictate the behavior of the coating/substrates.

##### 4.1 FAILURE MODES

Under general loading conditions, there are three types of fatigue failures observed depending on the nature of residual stresses[5]. These correspond to delamination of the interface, splitting of the film and substrate cracking. There is also a fourth mechanism of failure that involves buckling of the coating and subsequent delamination of the interface. The later mode of failure relies on the existence of compressive stresses within the coating. The presence of a superimposed tensile stress can cause delamination along the interface, or cracking in the film or substrate. Failure

induced by a compressive stress involves a complex interaction between buckling of the film and delamination along the interface.

Microstructure also plays a major role in crack nucleation and growth process. Process induced defects such as voids and inclusions etc. form nucleation centers for cracks. Grain size is expected to have dual roles. It is well known that decreasing grain size increases the endurance limit under fatigue. From the dislocation pile up analysis it is clear that decrease in grain size decreases the slip band length and hence increase the number of cycles (or endurance stress) for crack nucleation life. On the other hand, reducing grain size has been found to increase the resistance to crack growth particularly in planar slip materials. For coatings, in general, a reduction in grain size is expected to be beneficial in terms of fatigue life, since crack nucleation life has more sensitive dependence on grain size than the crack propagation life. In addition, fine grain size in the nano-range is expected to be beneficial in terms of increasing the strength of the coatings and in relaxing the residual stresses by grain boundary sliding.

## 5. APPLICATION TO THERMAL SPRAY COATINGS

In the following we discuss the application of the above understanding of the fatigue damage process to thermal spray coatings which are increasingly being used for many applications. The available experimental results on fatigue will be examined in terms of the resulting microstructure and the associated local and bulk fatigue damage.

Thermal spray coatings have a unique microstructure that affect their properties. It was noted earlier, Fig. 2, that compressive residual stresses are present in the coating due to high velocity impact of the particles during thermal spray [18]. As the molten or semi-molten feed particles impact on the cold substrate surface, they flatten and freeze. In addition to the impact stresses there will also be some residual stresses due to mismatch in thermal coefficient of expansion. The next incoming particle falls on the previous one thus forming a layer structure. In the inter-layers, the inter-particle boundaries called splat boundaries are formed, which are significantly weak[7-12]. Major concern is that these weak boundaries are parallel to the surface hence parallel to shearing forces that arise during Rolling Contact Fatigue. In addition to splat boundaries, there is grain nucleation and growth perpendicular to the splat boundaries. Thus each projectile particle during thermal spray forms a multigrain particles each separated from the others by splat boundaries. The size of each splat depends on the size of the feed particles. For micron size particles, high velocity oxy-fuel (HVOF) process resulted in splat boundaries that are about 30-40  $\mu\text{m}$  wide, while the size of grain boundaries within the splat is about 2  $\mu\text{m}$ . The aspect ratio of splat boundaries is very high [12].

### 5.1. FATIGUE OF THERMAL SPRAY COATINGS

The extent of the study of fatigue damage of thermal spray coatings is limited. McGrann *et al.* [18] have investigated the performance of WC-17%Co thermal spray coatings on SAE 4130 steel and 6061-T6511 Al-alloy substrates. The WC-Co coatings were applied by HVOF. Residual stresses in Fig. 2 were also determined. Fatigue tests were done using bending tests with zero mean stress. Three sets of thermal spray-coated Al-specimens were tested: Al-L, Al-M and Al-H, where L, M and H corresponds to light, medium and heavy coatings in terms of compressive residual stresses present. The stresses are of the order of 80, 500, and 760 MPa, respectively. For steel specimens,

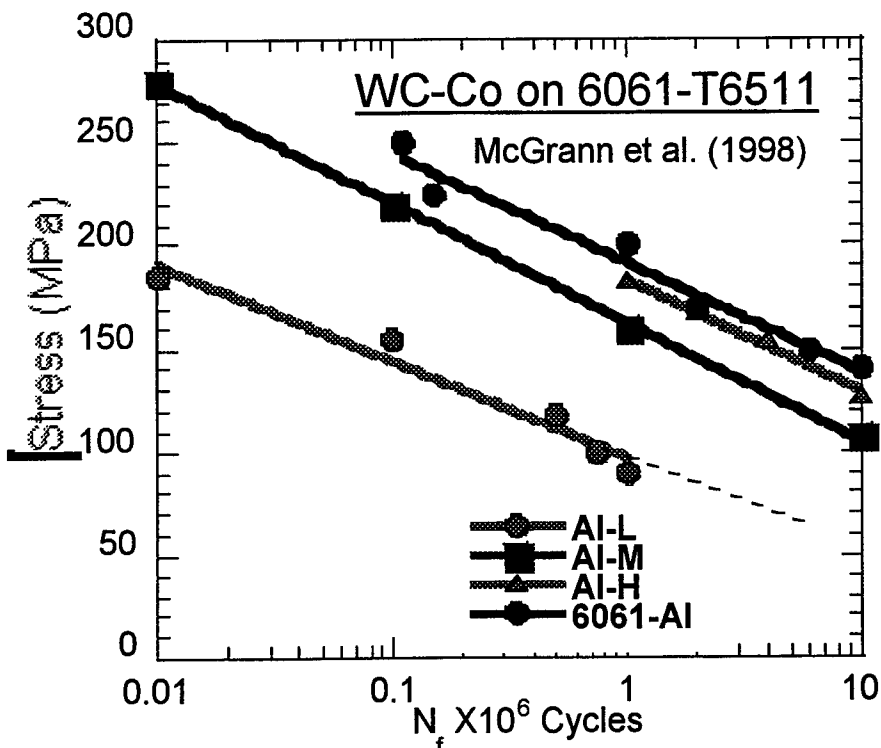


Fig. 5 Effect of WC-Co coatings on an Al-alloy substrate.

the coatings are of L and H types in addition to conventional chrome plated and shot-peened specimens. The average residual compressive stresses in the steel specimens were 125 and 365 MPa for L and H types, respectively. Figures 5 and 6 show the fatigue

results in terms of maximum applied stress versus the number of cycles to failure for each of the coated and uncoated specimens. For Al-alloys, in comparison to uncoated specimens, there is significant improvement (30 times) in life with coating. Examination of the results indicates that improvement is associated solely with the compressive residual stresses than coatings properties per sec, since with increasing residual stresses (for the same thickness) the fatigue life is increased significantly. Similar results are obtained for the steel specimens. The WC-Co with H type of coatings fared well in par with the shot peened specimens, where compressive residual stresses are deliberately introduced. The WC-Co coatings are much better than the conventional chrome plated specimens. Clearly the improvement arises from the compressive residual stresses since WC-Co coatings of L type did not show noticeable improvement due to low residual stresses. Figures 5 and 6 clearly demonstrate the importance of the residual stresses. The materials are coated to improve the wear resistance and bulk fatigue tests are only part of the acceptance tests for these coatings. There is no degradation of the properties as a result of the coatings. If fatigue is the life or performance-limiting factor then processing needs to be optimized to arrive at improved fatigue resistant coatings. The results thus indicate that WC-Co coatings can improve fatigue resistance compared to the conventional coatings currently used.

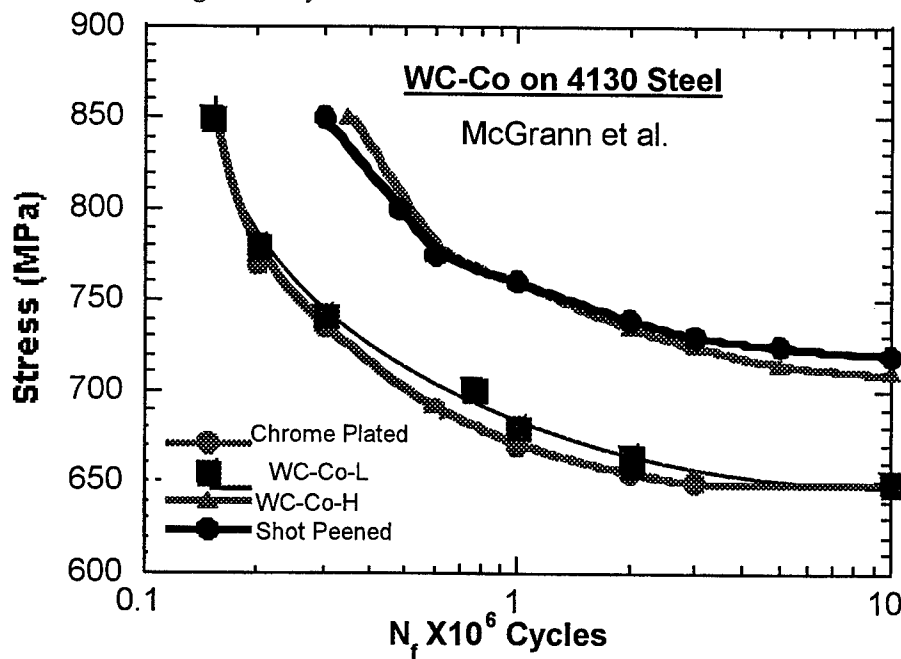


Fig. 6. Effect of WC-Co coating on fatigue life of 4130 Steel.

## 6. SUMMARY AND CONCLUSIONS

Coatings are provided to improve wear, corrosion, and oxidation of the substrates including as thermal barriers for high temperature components. Since the components are subjected to variable loads, the fatigue resistance of the coatings is of concern. Fatigue damage can result from local variations in loads such as in rolling contact fatigue, fretting fatigue or wear-fatigue or from global application of loads. Fatigue damage in general manifests in terms of irreversible plasticity, crack initiation, crack propagation and failure. Failure processes include cracking, pitting, particle decohesion, delamination, spalling, buckling etc. Mechanics of these are examined along with the review of available results. It is shown that fatigue performance of the coatings depends on the microstructure and residual stresses, and defect density and distribution. Processing optimization is essential in order to improve performance of the coatings.

## 7. ACKNOWLEDGEMENTS

The authors express their gratitude to Professor S. Sampath for providing data of thermal spray coatings. The review was completed when one of the authors (K.S) was on sabbatical at the Indian Institute of Technology, Madras. K.S expresses his appreciation to the Director of the Institute for hosting him during his sabbatical. The work is supported by the Office of Naval Research. Helpful discussions with Drs. L. Kabacoff and A.K. Vasudevan and their support are gratefully acknowledged.

## 8. REFERENCES

1. Evans, A.G. and Hutchinson J. W. (1984) *Int. J Solids and Struct.* **20**, 455.
2. Rice, J.R.(1988), "Elastic Fracture mechanics for interfacial cracks" , *J. Appl. Mech. Trans ASME*, **55**, pp. 98-103.
3. Hu, M.S., Thouless, M.D. and Evans, A.G., (1988), "The de-cohesion of thin films from brittle substrates", *Acta Met.* **36**, pp. 1301-1307.
4. Sue, Z and Hutchinson, J.W., (1990) "Interface crack between two elastic layers", *Int. J. Fracture*", **43**, 1-18.
5. Thouless, M.D. (1991), "Cracking and Delamination of coatings", *J. Vac. Sci and Tech.* **9a**, 2510-2515.
6. Evans, A.G. and Hutchinson, J.W. (1989) "Effect of non-planarity on the mixed mode fracture resistance of bimaterial interfaces", *Acta Met.*, **37**, 909-916.
7. Thouless, M.D. Evans, A.G., Ashby, M.F. and J.W. Hutchinson, J.W., (1988), *Acta Metall.* **35**, 1333-1341.

---

8. Grunling, H.W., Schneider, K., and Singheiser, L., (1987), "Mechanical Properties of Coated Systems", *Mat. Sci. Engrg.*, **88**, 177-189.
9. Ramaswamy, S and Herman, H., (1986), "Metallurgical characterization of Plasma Sprayed WC-Co Coatings, in Advances in Thermal Spraying", Pergamon Press, pp. 101-110.
10. M.E. Vinayo, F. Kassabji, J. Guyonnet and P. Fauchais, Plasma Sprayed WC-Co Coatings: Influence of Spray Conditions, on the Crystal Structure, porosity, and Hardness, (1985), *J. Vac. Sci. Technol. A*, **3**, pp. 2483-2489
11. Ramnath, V, and Jayaraman, N., (1989), "Characterization and Wear Performance of Plasma Sprayed WC-Co Coatings", *Mater. Sci. Tech.*, **5**, 382-388
12. Sampath, S, and Wayne, S.F, (1994) "Microstructure and Properties of Plasma-Sprayed Mo-Mo<sub>2</sub>C composites", *J. Thermal Spray Technology*, **3**, 282-288.
13. Johnson, K.L. and Jefferis, M.A., (1963), "Plastic flow and Residual Stresses in Rolling and Sliding Contact", *Proc. Symp. on Fatigue in Rolling Contact*, pp. 54-65.
14. Cao, H.C., Thouless, M.D. and Evans, A.G., "Residual stresses and cracking in brittle solids bonded with a thin ductile layer", *Acta Met.*, **36**, 2036-2046.
15. Charalambides, P.G., and Evans, A.G. (1989), "Debonding properties of residually stressed brittle matrix composites", *J Amer. Ceram. Soc.* **72**, 746-753.
16. Drory, M.D, Thouless, M.D. and Evans, A.G. (1988), "On the decohesion of residually stressed thin films", *Acta Met.* **36**, 2019-2028.
17. Landgraf, R.W., Chermenoff, R.A. (1988), "Residual stress effects on fatigue surface processed steels, analytical and experimental methods", *ASTM-STP 1004*, 1-12.
18. McGrann, R.T.R., Greving, D.J., Shadley, J.R., Rybicki, E.F., Kruecke T.L. and Bodger, B.E., (1984), "The Effect of Coating Residual Stress on the Fatigue Life of Thermal Spray-Coated Steel and Aluminum", *Surface and Coating Technology*, **108-109**, 59-64.
19. Hertz., H.,(1882) "Uber die Beruhrang fester elastischer Korper" ( On the contact of Elastic Solids", *J. reine und angewandre Mathematik*, **92**, 156-171. (English translation in Miscellaneous Papers by Hertz, H., Eds., Jones and Schott, (1986) MacMilan, London).
20. Timoshenko, S.P. and Goodier, J. N. (1970), "Theory of Elasticity", Third edition, MacGraw-Hill New York, pp. 409-420.
21. Bentall, R. H., and Johnson, K.L. (1968), "An elastic strip in plane rolling contact", *Int. J. Mech. Sci.*, **10**, pp. 637-663.
22. Madlin, R.D., (1949), *J. Appl. Mech.* **16**, 259.
23. Madlin, R.D. and Deresiewicz, H., (1953), "Elastic Spheres in Contact Under Varying Oblique Forces", *J. Appl. Mech.*, **20**, 327-344.
24. Hamilton, G.M. and Goodman, L.E., (1966), *J. Appl. Mech.* **33**, p.371.

25. Lin, W. Kuo, C.H., and Keer, L.M., (1991), "Analysis of transversely isotropic half space under normal and tangential loading", ASME J. Tribol. **113**, 335-338.
26. Hanson, M.T., (1992), "The elastic field for conical indentation including sliding friction for transverse isotropy", ASME, J. Appl. Mech., **59**, 123-130.
27. Hamilton, G.M., (1983), Proc. Inst. Mech. Engng, **197C**, p53.
28. Merwin, M., and Johnson, K.L., (1963), "An Analysis of Plastic Deformation in Rolling Contact", "Proceedings of the Institute of Mechanical Engineers", London, Vol. 177, 676-685, 1963.
29. Vingsbo, O., and S. Soderberg, S., (1988), "On Fretting Maps", Wear, **126**, 131-147.
30. Vingsbo, O., Odfolk, M., and Shew, N.E., (1989), "Fretting maps – Fretting wear of some fcc metals and alloys", Wear Mater, 275-282.
31. Vincent, L, Berthier, Y., Dubourg, M.C.,and Godet, M.D., (1992) "Mechanics and Materials in Fretting", Wear, **153**, 135-148.
32. Sheppard, S.D., Barber, J.R., and Comninou, M., (1987), "Subsurface Cracks under conditions of Slip, Stick, and Separation Caused by a Moving Compressive Load", J. of Appl. Mech., **54**, 393-398.
33. Hutchinson, J.W., Mear, M.E., and Rice, J.R., (1987), "Crack Paralleling an interface between dissimilar materials J Appl. Mech. (Trans ASME)", **54**, 828-832.
34. He, M.Y., and Hutchinson, J.W., (1989), "Crack Deflection at an interface between dissimilar elastic materials", Int J solid struct. **25**, 1053-1067.

---

## NANOINDENTATION / NANOSCRATCHING AND STRESS STUDIES IN MONOLITHIC AND NANOLAYERED AMORPHOUS CARBON FILMS

S. LOGOTHETIDIS, C. CHARITIDIS AND M. GIOTI

*Department of Physics, Aristotle University of Thessaloniki,  
540 06 Thessaloniki, Greece.*

### Abstract

We have recently reported that monolithic amorphous carbon (a-C) films deposited by RF magnetron sputtering exhibit a high level of  $sp^3$  sites when a negative bias voltage ( $V_b$ ) is applied onto the substrate. This type of a-C films are dense ( $\sim 2.65 \text{ g/cm}^3$ ), hard ( $>20 \text{ GPa}$ ) and highly stressed (6-7 GPa). The latter, however, limits their thickness below to  $\sim 40 \text{ nm}$ . Thus, we have developed nanolayer structured a-C thick films with alternating  $V_b$  (positive / negative) which are stable, hard and rich in  $sp^3$  content. Nanoindentation and low load scratch test results demonstrate that the layers rich in  $sp^2$  content promote the stress relaxation of the films during a compositional rearrangement when a layer rich in  $sp^3$  content is deposited. Possible explanations on the origin of the stress relaxation and the enhancement of the elastic properties in nanolayered a-C films are proposed and discussed based on the formation of compositional smooth interfaces between the two different types of layers.

### 1. Introduction

The use of sputter deposited amorphous carbon (a-C) thin films has enlarged in a wide range of technological and industrial applications, such as micro-electronic, optical, biomedical applications, wear-, corrosion-resistant materials and protective overcoats for hard disks in the magnetic storage industry. Sputtering offers a number of benefits such as low cost, process simplicity and control, and film homogeneity. It is also not time-consuming. All the above characteristics make sputtering an attractive and powerful technique for a-C production, especially for industrial scale production. The present trend in a-C thin film technology is largely dictated by the urgent need for the development of new processes, materials and their fabrication for applications in surface engineering and submicron microelectronics.

The high internal stresses as measured in sputtered a-C films are closely related to adhesion problems and crack creation in the films, and thus limit their maximum thickness for good adherence on the substrate at  $\sim 40 \text{ nm}$ . Consequently, the search for processes reducing film stress, improving thermal stability and low toughness of a-C films, are some major technological challenges in a-C research. Recently, it has been

shown that reduction of the internal stress in thick a-C films with high hardness can be obtained by developing layer structured (consisting of sequential soft and hard nanolayers) films [1].

Amorphous carbon films 30 nm thick, deposited with negative  $V_b$  were found to be rich in  $sp^3$  sites (45%), dense ( $\sim 2.65 \text{ g/cm}^3$ ) and with compressive stress above 6 GPa. On the other hand, films deposited with positive  $V_b$  are rich in  $sp^2$  sites, exhibit low density ( $1.9 \text{ g/cm}^3$ ) and compressive stress ( $\sim 1 \text{ GPa}$ ). It was also found that the development of a-C films in the form of nanolayered structure, consisting of sequential layers of the above mentioned two different types of a-C films, provides stable, thick and rich in  $sp^3$  sites a-C films [1] potentially for many practical applications.

In this work, emphasis is placed upon the study of the elastic properties of these two types of a-C films and their dependence on the substrate bias voltage ( $Ar^+$  ion energy). The enhancement of elastic properties and their comparison with those so far reported for sputtered a-C films, and the scratching behavior of nanolayered structures (consisting of sequential layers deposited with alternating  $V_b$ ) are also presented. In view of the obtained results, possible explanations on the origin of the stress relaxation and enhancement of the elastic properties in nanolayered a-C films are proposed and discussed, based on the formation of compositional smooth interfaces between the different type of layers.

## 2. Experimental Details

The sputtered a-C films studied here were deposited in an Alcatel SCM 600 magnetron sputtering apparatus which has been described elsewhere [2,3]. Briefly, the a-C thin films were deposited on c-Si (001) substrates using a graphite (99.999% purity) target. During deposition, the sputtering Ar gas was at a partial pressure of  $1.5 \times 10^{-2}$  Torr, the target to substrate distance was fixed at 65 mm, and the discharge power equal to 100 W. The only parameter that was varied was the substrate bias voltage  $V_b$ . A phase modulated ellipsometer, mounted on the deposition system, allows in-situ and real-time spectroscopic ellipsometry (SE) measurements in the energy region 1.5-5.5 eV, and was used to estimate the thickness and the composition ( $sp^2$  and  $sp^3$  content) of the deposited film [3].

To investigate the mechanical behavior of a-C thin films three series of a-C films with thickness 30, 280 and 200 nm, respectively, were prepared. The a-C films with thickness 30 nm were deposited either with negative or positive  $V_b$  and those of 200 nm thick with positive  $V_b$ . The films with thickness 280 nm were deposited in sequential thin layers with alternating (positive/negative)  $V_b$ . In detail, first a layer of  $\sim 15$  nm was deposited with  $V_b=+10$  V and consequently a layer of  $\sim 23$  nm with  $V_b=-20$  V. In the next bilayers the thickness of each one was  $\sim 5$  nm and  $\sim 23$  nm, respectively, for the development of films with total thickness  $\sim 280$  nm. We have found by analyzing SE (nanoindentation) measurements that films deposited with negative  $V_b$  were rich in  $sp^3$  content (hard), while films deposited with positive  $V_b$  were rich in  $sp^2$  content (soft) [4].

The elastic (hardness, H and elastic modulus, E) and tribological properties of the films were conducted using a Nano Indenter XP system with the continuous stiffness measurements (CSM) and lateral-force measurements (LFM) options. The H and E of

each of the films were measured with a Berkovich, three-sided pyramid diamond indenter with nominal angle of 65.3° between the tip axis and the faces of the triangular pyramid, which was forced into the specimen surface by using a coil and magnet assembly. Nanoindentation measurements were obtained with both conventional indentation (CI) and CSM. The system has load (displacement) resolution of 50 nN (<0.01 nm). A detailed description of the system has been presented elsewhere [5]. Prior to each indentation test, two indents in 100 nm depth were conducted in fused silica to evaluate the tip condition. When CSM technique [5,6,7] is employed, the stiffness is measured continuously allowing the H and E to be calculated at every displacement point acquired during the indentation experiment. In all CI and CSM depth-sensing tests a total of ten indents were averaged to determine the mean H and E values for statistical purposes, with a spacing of 50  $\mu$ m.

A different diamond Berkovich indenter was used for scratch testing. Scratches were made with an edge of the indenter (point-on orientation). Prior to each scratch test, three indents were made in aluminum to clean the tip, and then two 100 nm indents were made in fused silica to evaluate the condition of the tip. A precision X-Y table with a resolution of 1  $\mu$ m was used to slide the film under the tip with a minimum of vibration and electrical noise. Lateral deflection was measured using two separate capacitive displacement gauges to sense the lateral displacement of the indenter column in the X and Y directions. Lateral (friction) forces were then calculated from stiffness of the column determined in calibration experiments. Coefficient of friction ( $\mu$ ) can be calculated afterwards [8]. Since scratch-induced damage of a film, specifically fracture or delamination, was monitored by in-situ friction force measurements there was no need to obtain an image of the scratch event but only to confirm the experimental results. Depths of scratches with increasing scratch length or normal load were measured in-situ by profiling the surface of the film before, during and after the scratch event, resulting in a total length of the test of 700  $\mu$ m, while the scratch length was 500  $\mu$ m long. The load for initial and post-scratch scan was 0.02 mN. Data from these regions were used to account for both the slope and curvature of the sample surface so that the entire scratch can be viewed with the surface of the sample as the baseline for deformation [9].

Stress measurements were immediately performed after each layer or thin film was deposited and exposed to air. The stresses were measured using a commercial instrument by Tencor, and calculated by measuring the radius of the curvature of the substrate before and after film deposition by the modified Stoney expression [3]. The films were also studied by Transmission Electron Microscopy in cross-section geometry (XTEM) [10].

### 3. Results and Discussion

#### 3.1. MECHANICAL PROPERTIES OF a-C FILMS, AND THEIR DEPENDENCE ON $V_b$ AND THICKNESS

Figure 1 shows the plots of hardness and elastic modulus as a function of contact depth obtained from two a-C films, deposited with  $V_b$ =+10 and -10 V, with the same

thickness 30 nm. For the film deposited with  $V_b=-10$  V the maximum  $H$  ( $E$ ) value was  $\sim 18$  (185) GPa, whereas that deposited with  $V_b=+10$  V was  $\sim 8$  (130) GPa. Since the a-C films were deposited on Si, their hardness (elastic modulus) approaches at large contact depths, the value of Si, 12.5 (168) GPa. The above values of  $H$  and  $E$  for each  $V_b$  were estimated from the regime of the shallow data points (Fig.1) as more representative of the film properties. Hardness of hydrogenated carbon films with almost the same thickness was found to be 9.4 GPa [11].

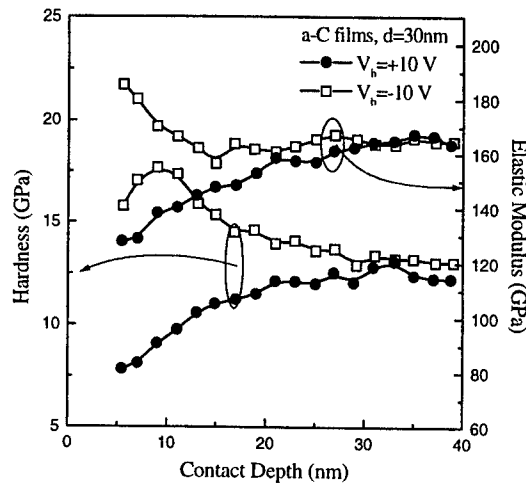


Figure 1. Nanoindentation data of  $H$  and  $E$  vs. indentation contact depth obtained from single a-C films 30 nm thick, deposited with  $V_b=+10$  V (circles) and  $V_b=-10$  V (squares). The CSM data obtained in contact depth 40 nm.

The development of a-C films rich in  $sp^3$  C-C sites is based on incident energetic species ( neutrals or ions) that penetrate the growing surface and induce subsurface growth [12]. A negative  $V_b$  achieves the energetic ion bombardment during sputter deposition [3,13,14]. Films produced with positive  $V_b$  exhibit low hardness because the mean energy of the deposited neutral species is lower than a critical one to penetrate the film's surface. Thus, in these films the  $sp^2$  bonding is dominant, both hardness and density [15] are low and the films exhibit a large amount of voids [16]. We measured in these films a  $sp^2$  ( $sp^3$ ) volume fraction  $\sim 60$  (20)% and density  $1.9$  g/cm $^3$ . When a negative  $V_b$  is applied the  $Ar^+$  ions are oriented towards the substrate with kinetic energy  $E$ , which in first approximation is given by the following expression:  $E=e|V_b|+E_0$ , where  $E_0$  is the mean energy of the discharge. The transfer of energy from  $Ar^+$  ions to deposited C species results in the formation of rich in  $sp^3$  C-C bond films [15,16]. The results from SE data analysis [5] have shown that when  $V_b=-10$  V promotes the formation of  $sp^3$  sites ( $\sim 50\%$ ) all over the film (except the initial stages of growth) resulting in a hard material with density, measured with X-ray reflectivity,  $2.6$  g/cm $^3$  [15]. The above experimental data and the qualitative interpretation suggest that an interrelation exist between the hardness and elastic modulus and the  $sp^3$  bonding of a-C films.

The dependence of hardness on the  $V_b$  for a-C films, 30 nm thick, is shown in Fig. 2. The elastic modulus exhibits the same dependence on  $V_b$  with the hardness. Both of these quantities do not exhibit the same dependence with the  $sp^3$  content [17] on  $V_b$ . There is a sharp increase in going from positive (the film is rich in  $sp^2$  content) to negative  $V_b$  (rich in  $sp^3$  content). In the regime  $-100 V < V_b < 0 V$  (30-130 eV, low energy ion bombardment) there is a near plateau in  $H$  and  $E$  values that indicates the existence of a subplantation mechanism (probably indirect) during deposition. That is,  $Ar^+$  transfer their energy to the surface C atoms which subplant below the surface. In the energy window 30-130 eV the produced a-C films were rich in  $sp^3$  sites and hard. For  $V_b < -100 V$  (ion energy above 130 eV) it was found a reduction in stress (Fig. 3a), which in concurrent with the decrease of the  $sp^3$  content but not with density [17].

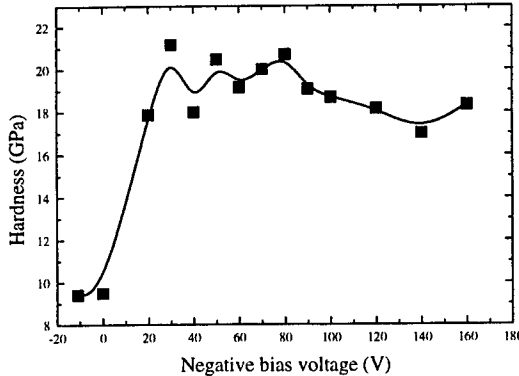


Figure 2. Hardness of sputtered 30 nm thick a-C films versus  $V_b$ . The data was obtained from indentations at a contact depth of 20 nm using the CSM technique.

The dependence of compressive stress on the  $V_b$  for a-C single films, 30 nm thick, is shown in Fig. 3a. Stress exhibits the same dependence with the  $sp^3$  content on  $V_b$ , as proposed by the densification model [18,19]. There is a sharp increase in going from ground to negative  $V_b$  and a broad non-symmetric peak at  $V_b = -40V$ . The stress behavior can be described successfully by Davis' formula [19]. Stress values measured at films deposited with negative (positive) bias voltage support that stresses in a-C films are an intrinsic property and arise from the deposition mechanism that creates the  $sp^3$  ( $sp^2$ ) bonding. The film deposited in sequential layers with alternating  $V_b$  leads to the development of stable and highly  $sp^3$  bonded material. Figure 3b shows the evolution of stress with the thickness for the nanolayered structure film 280 nm thick. The first deposited soft layer exhibits low stress (1.35 GPa). Consequently, it provides good adhesion of the film to the substrate. The next deposited hard layer increases rapidly the average stress of the film to 4.5 GPa. Further depositions of layers either with positive or negative  $V_b$  do not affect much the situation that was established during the deposition of the first two layers. Above the 180 nm film thickness the stress values saturate to ~5.2 GPa.

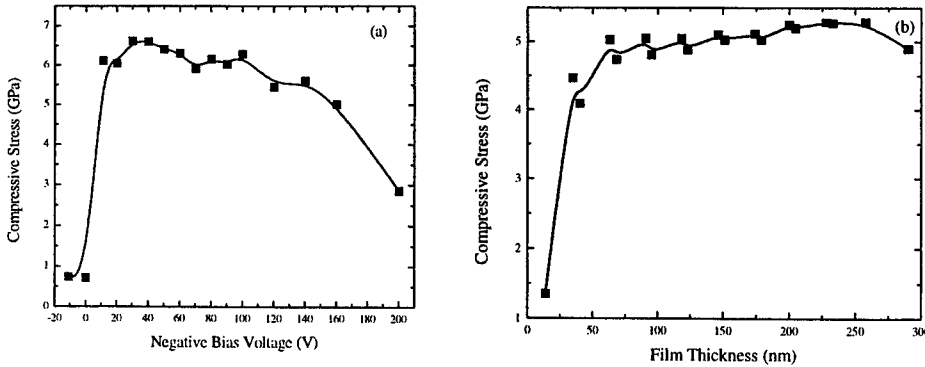


Figure 3. The variation of compressive stress of single a-C films vs  $V_b$  (a), the evolution of stress with thickness in an a-C film in sequential layers with alternating  $V_b$  (b).

What is important about the nanolayer a-C film is that there are large stress gradients in the film between the individual layers. Even the average stress is relatively small (~5.2 GPa, Fig. 3b) within the  $sp^3$  layers, stresses are larger. The resulting large stress gradients in the film can act as an additional driving force for atomic diffusion at the  $sp^3$ -rich to  $sp^2$ -rich interfaces.

### 3.2. ENHANCEMENT OF ELASTIC PROPERTIES AND STRESS RELAXATION IN NANOLAYERED a-C FILMS

Figure 4 shows the nanoindentation results for an a-C film 280 nm thick, where  $H$  and  $E$  are plotted as a function of contact depth.

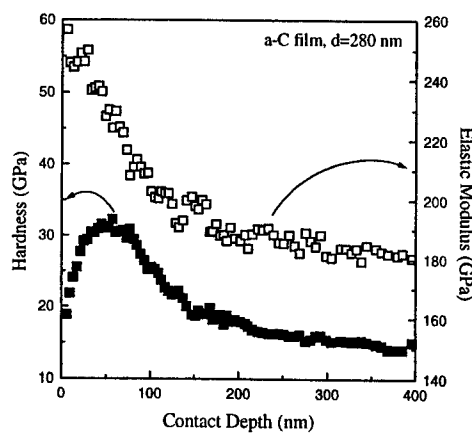


Figure 4. Hardness and elastic modulus vs. indentation contact depth obtained from a-C films 280 nm thick, deposited in sequential layers with alternating  $V_b$ , using the CSM technique.

Indentation was conducted by applying both the CI, in different contact depths, and the CSM technique for penetration depth 400 nm. At shallow depths, about 20-50 nm,

elastic properties more representative of the films were obtained but still influenced by the substrate. Comparing these values of  $H$  and  $E$  with those obtained from an a-C:H film ( $H=17$  and  $E=175$  GPa), 300 nm thick prepared by sputter deposition on Si [20], we conclude that hydrogen-free a-C film deposited in sequential layers with alternate positive/negative  $V_b$  of layers are harder by a factor of  $\sim 2$ .

Figure 5 compares the load-displacement curves for 30 nm thick a-C films deposited either with positive or with negative  $V_b$ , both tested with identical indentation cycles to a maximum load of 0.11 mN. Low-load indentation experiments have revealed that a-C films deposited with positive  $V_b$  exhibit more plastic deformation than those developed with negative  $V_b$ . Figure 6 shows representative CI load-displacement curves for 200 and 280 nm thick a-C films at specific loads to achieve contact depths at the same percentage ( $\sim 12\%$ ) of each one thickness.

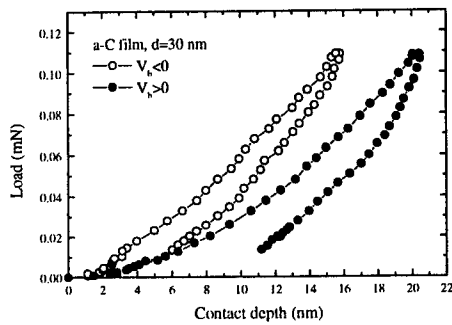


Figure 5. Load-displacement curves for 30 nm thick a-C films deposited with positive and negative  $V_b$  at the same maximum load.

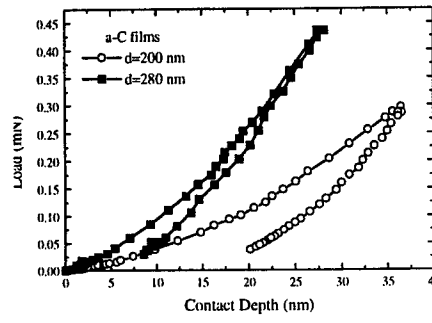


Figure 6. Load-displacement curves for 200 and 280 nm thick a-C films obtained at a penetration depth of about 12% of film thickness.

Figures 5 and 6 display the qualitative differences between the three series of a-C films concerning not only their hardness but their elastic deformation behavior, too. From the maximum penetration depth and the residual depth for each case, we have found that a-C films deposited in sequential layers by altering  $V_b$  exhibit much higher hardness and elastic deformation  $\sim 80\%$  than the films deposited with  $V_b > 0$ ,  $\sim 50\%$  and higher to those deposited with  $V_b < 0$ ,  $\sim 70\%$ .

The film deposited in sequential layers with alternating  $V_b$  led to the development of stable and rich in  $sp^3$  bonded material, resulting in harder a-C films than the ones developed solely with negative  $V_b$  (Fig. 1). The deposited layers with  $V_b > 0$  seem to be essential for the stress relaxation of the whole film and was made practicable to grow thicker and stable a-C films [1].

In order to study the geometrical characteristics of the nanolayered structure of the a-C films we performed an XTEM study of the a-C specimens [10]. As it is shown in Fig. 7, the film consisted of 10 bilayers with almost the same modulation period  $\sim 26$  nm, except the first one on the top of the substrate ( $\sim 35$  nm) and an ultra-thin layer ( $\sim 1.5$  nm), which was deposited with  $V_b = +10$  V, on top of the film. Since the layers had the same chemical nature (amorphous carbon), the existing contrast difference indicates the different bonding and density in the layers. Thus, the light colored layers are attributed to the  $sp^2$ -rich layers whereas, the dark colored to the  $sp^3$ -rich ones. From the

XTEM [10] and SE and XRR [21] results, modifications in thickness and composition of soft layers were found to occur during the deposition of hard (rich in  $sp^3$  bonds) layers. Namely, a reduction in the thickness of soft layers was observed when a hard layer was deposited on it.

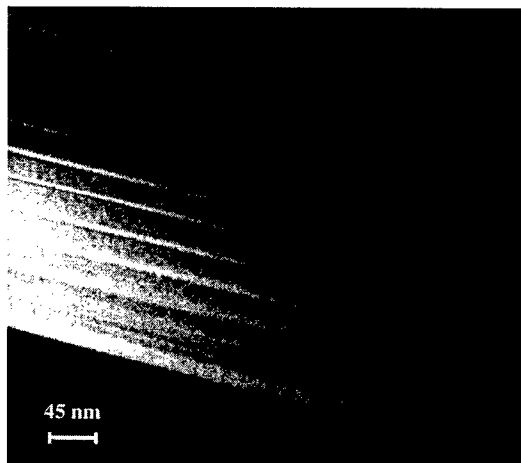


Figure 7. A TEM cross-section image of nanolayer a-C film made of alternating rich in  $sp^2$  / rich in  $sp^3$  layers.

### 3.3. NANOSCRATCH TESTS ON NANOLAYERED a-C FILMS

The objective of the nanoscratch tests was to investigate the elastic and tribological properties of the films developed in layered structure (rich in  $sp^3$  content) and their comparison with those of films rich in  $sp^2$  content. We focused on the adhesion and deformation response of the films using the scratch test as main experimental characterization tool. Film deformation response was studied in order to gain a better understanding on the mechanisms governing the failure of thin films.

In Fig. 8 nanoscratch test results for a-C films, 280 nm thick, at various normal loads are presented. Figure 8 includes plot of the vertical displacements of the diamond during the initial scan (prescan), the load-ramped scratch (scratch scan), and the post scratch scan (post scan) for each film. The scratch proceeds from left to right in the figure. The initial scan profiles the unscratched surface of the film and the post-scratch scan was used to determine the surface damage due to the scratch event. Negative displacements correspond to the scratch tip being pushed into the specimen, and positive displacements that appear in the post-scratch scan, indicate the outward blistering of the surface or the accumulation of debris in the scratch trace. Four scratches were made at each load at different areas of specimen.

In Fig. 8a the scratch can be divided into two regimes based on differences in the appearance of the scratch profile. The first regime was defined by the first 300  $\mu$ m of the scratch. In this regime, the scratch is extremely smooth and shallow as can be seen both by comparing the post scan to the prescan and by optical microscopy. A closer examination revealed that there are no remnants of the scratch, corresponding to fully recovered elastic contact. The second regime extended from 400 to 600  $\mu$ m. In this

regime, film recovery was highly elastic (~90%). It is marked by a change in the scratch displacement. In this regime, the film blisters by partial delamination between layers [9]. Examination of the film by optical microscopy revealed an amount of small particle debris surrounding the scratch trace in this regime, suggesting that damage was limited to cracking and small areas of pull-off contained entirely within the scratch track.

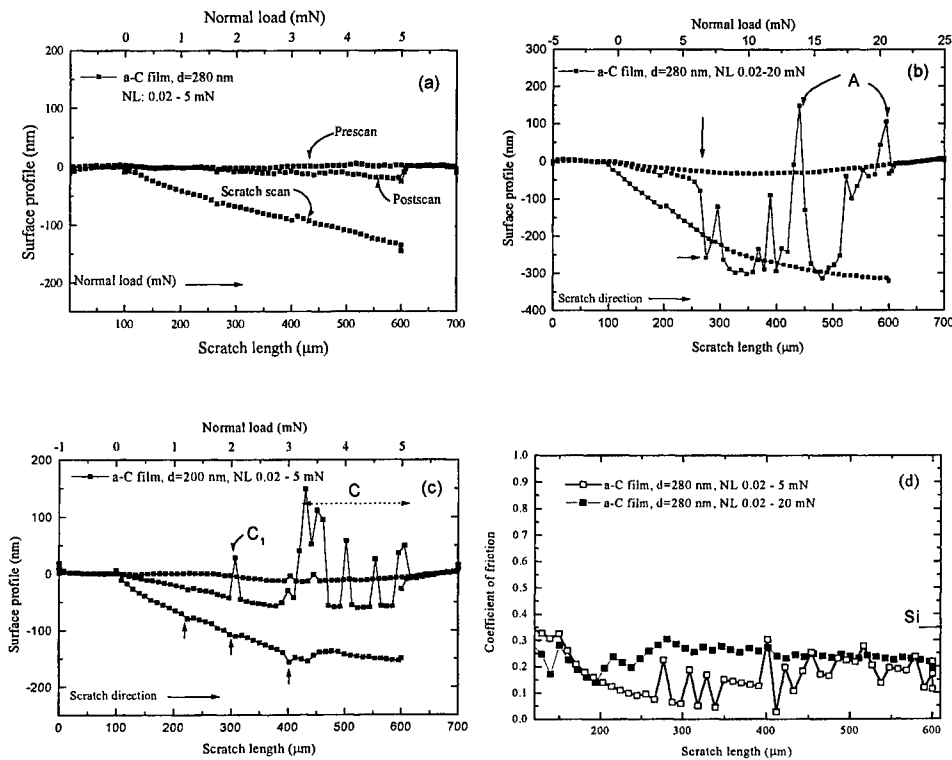


Figure 8. Surface profiles of the a-C films rich in  $sp^3$  content developed in nanolayered structure, 280 nm thick, scratched with ramping normal loads of 0.02 – 5 mN (a) and 0.02 – 20 mN (b), and a-C films rich in  $sp^2$  content (200 nm thick) scratched with ramping normal loads of 0.02 – 5 mN (c). Coefficient of friction profiles of a-C films rich in  $sp^3$  content, 280 nm thick, as a function of scratching length (ramping normal load) (d).

The behavior of the a-C film, 280 nm thick at load up to 20 mN, was examined to monitor the adhesion and strength of the film. As shown in Fig. 8b, the regime from 100 to 250 μm was characterized by almost fully elastic recovery. In the regime above 250 μm (i.e. load above 5 mN) there was a large change in post scan, failure begun abruptly by brittle fragmentation in the film and substrate. The post scan trace showed that the fragmentation has occurred at a depth near the film thickness, indicating complete failure and removal of the film [22,23] (position A in Fig. 8b). In details, the height measured at position A is ~150 nm, and it was the half of the film thickness, which also implies the absence of a significant portion of the a-C film, at a load ~14 mN.

Deformation response of the a-C film rich in  $sp^2$  content (Fig. 8c) was mainly plastic all over the scratch length, and at  $\sim 400$   $\mu m$  of the scratch length (i.e. load 3 mN) failure begun abruptly by brittle fragmentation in the film. The ripple structures (observed in area C in Fig. 8c) pronounced along the track seems to be influenced by the tensile-type cracks. The depth measured in area C is  $\sim 150$  nm, and it was more than the half of the film thickness, which implies the absence of a-C film at a load  $> 3$  mN and possibly is correlated to the delamination of the film. The poor adhesion of the a-C film to the substrate produced cracks and small regions of film pull-off at loads above 1 mN, which resulted in the displacement roughness at scratch track positions between 200 and 300  $\mu m$  (indicated by arrows in Fig. 8c). The large positive displacements between 300 and 600  $\mu m$  represent the positions at which the stylus was forced over the delaminated film that was piled up in its path. Friction coefficient values for these films were found to be  $\sim 0.35$ .

Figure 8d is a plot of the friction coefficient ( $\mu$ ) versus scratch length (normal load) for a-C film 280 nm thick. The  $\mu$  was calculated by taking the ratio of the lateral force and normal load on the indenter [8]. Until the tip begins to slide with respect to the sample, the  $\mu$  is indeterminate. At the start of the scratch, the lateral force data is noisy indicating a stick-slip phenomenon [24]. Once the normal load reaches about 0.5 mN, the  $\mu$  settle to nearly constant values. Friction coefficient values for these films were found to be  $\sim 0.2$ , below those for a-C films rich in  $sp^2$  content. Figures 8a,b and 8d show that both scratch depth and  $\mu$ , respectively, increase with increasing scratch load. Friction coefficient clearly increased at, or close to, the point at which the film blisters (at  $\sim 300$   $\mu m$  of the scratch length, Fig. 8a) or detaches begun (at  $\sim 250$   $\mu m$ , Fig 8b). The measured increase in  $\mu$  could be due to the indenter climbing over small (large) particle debris, for a scratch load 5 (20) mN, as it passes over the surface. The fluctuation in friction coefficient values is promoted by point-on orientation of the tip or the layered structure of the films or it could be due to nanoscale fracture events.

Based on the above findings we will discuss the possible explanations of the stability and the enhancement of the elastic properties of the nanolayered structured, rich in  $sp^2/sp^3$  content a-C films. The soft (plastic) layers, deposited with  $V_b > 0$ , seem to act as a reservoir of energy transferred to the film. As a result the soft layer sandwiched by the two elastic hard layers may not easily deform even under loading. An explanation for this behavior can be the following. The layered structure of the film with a smooth compositional transition at an interface (the layers have the same chemical nature but different bonding and density), is thought to result in preventing penetration of cracks into the film across an interface due to the difference in mechanical properties of two alternating layers. A compositional smooth interface can prevent the delamination of layered structured films at an interface providing the noticeable stability and adhesion of the layered structured films. The lamination of plastic and elastic layers prevents the energy from dispersing into the deeper layers or the substrate by causing an elastic displacement in the hard layer.

The material removal, with the formation of surface materials on the side of the scratch which were plastically torn away, indicates that scratching on films rich in  $sp^2$  content took place mainly by plastic deformation typical of soft materials. This type of deformation of soft layers is possibly responsible for delamination and buckling effects observed in nanolayered structure films when the former are subjected to high normal

loads during the scratch test. A detailed examination of the scratch profiles in nanolayered structure films supports the above speculation. For the design of tough nanolayered structure a-C films we have to take into account the following mechanisms: i) the stress relaxation in the hard layer by plastic deformation in the soft layer [1], and ii) the termination of cross-sectional cracks by their deflection at interfaces and braking in a soft layer with energy dissipation by plastic deformation. For a-C nanolayered structure films the important question is whether the termination of plastic deformation in a soft layer is required. From the strengthening mechanisms, (i) and (ii), interlayer plasticity is necessary to blunt cracks and relax stresses in hard a-C bilayers. Thus, a minimum thickness of the soft layer is required to activate strengthening mechanisms (i) and (ii) for a-C layered structure. However, for larger soft layer thicknesses, there is a probability of failure of the total film stack by buckling or crack propagation along the soft layer. In conclusion, an optimal thickness of the individual layers is thought to be critical in the design of layered structure films with good properties. On the other hand, a layered structure film with a high number of interfaces exhibits an increase in toughness and crack propagation resistance [25]. Interfaces in films with layered structure are sites of energy dissipation and crack deflection leading to a toughening of the layer material. Further studies are in progress to determine the minimum thickness of soft layers and the number of interfaces in order to produce films with improved adhesion and toughness under high local loading and to reduce the amount of residual compressive stresses associated with the kinetically forced formation of  $sp^3$  bonds in hard layers.

#### 4. Conclusions

Hardness and elastic deformation enhancement for nanolayered structured films has been thought to occur possibly because of the formation of a compositional smooth interface when a rich in  $sp^3$  sites layer deposited on a rich in  $sp^2$  sites layer. Further work, however, is required to completely unravel the complex phenomena related to structure, processing and properties in this interesting and promising class of a-C films. This will allow us to understand the mechanisms of the elastic properties enhancement.

The results of the systematic investigation of scratch performance of sputtered a-C films in this work confirm the enhanced elastic behavior of the nanolayered films. Nanolayered films exhibit better adhesion strength comparing with those that are rich in  $sp^2$  content, so that they can sustain film cracking without debonding. The direct and in-situ depth measurement can provide the elastic/plastic depth profile along the scratch track. Application of this useful information in scratch process, modeling and understanding of fundamental mechanisms may lead to increased toughness and adhesion of hard a-C films.

#### 5. Acknowledgements

This work was supported in part by the Greek General Secretariat of Research and Technology.

## 6. References

1. Gioti, M., Logothetidis, S. and Charitidis, C. (1998) *Appl. Phys. Lett.* **73**, 184.
2. Logothetidis, S. (1996) *Appl. Phys. Lett.* **69**, 158.
3. Logothetidis, S. and Gioti, M. (1997) *Mater. Sci. Eng. B* **46**, 119.
4. Charitidis, C., Logothetidis, S. and Douka, P. (1999) *Diam. Relat. Mater.* **8**, 558.
5. Logothetidis, S. and Charitidis, C. (1999) *Thin Solid Films* (in press).
6. Oliver, W.C. and Pharr, G.M. (1992) *J. Mater. Res.* **7**, 1564.
7. Nano Instruments, Inc. (1997) *Nano Indenter<sup>®</sup> XP, Operating Instructions V1.1*.
8. Scharf, T.W. and Barnard, J.A. (1997) *Thin Solid Films* **308-309**, 340.
9. McAdams, S.D., Tsui, T.Y., Oliver W.C. and Pharr, G.M. (1995) *MRS Symp. Proc.* **356**, 809.
10. Logothetidis, S., Gioti, M., Charitidis, C., Patsalas, P., Arvanitidis, J., Stoimenos, J. (1999) *Appl. Surf. Sci.* **138-139**, 244.
11. Wei, B. and Komvopoulos, K. (1996) *ASME Journal of Tribology* **118**, 431.
12. Lifshitz, Y., Lempert, G.D. and Grossman, E. (1994) *Phys. Rev. Lett.* **72**, 2753.
13. Ullmann, J., Schulze, S., Erben, J., Grunewald, W., Heger, D., Muhling, I. (1992) *Thin Solid Films* **219**, 109.
14. Schwan, J., Ulrich, S., Theel, T., Roth, H., Ehrherdt, H., Becker, P. and Silva, S.R.P. (1997) *J. Appl. Phys.* **82**, 6024.
15. Logothetidis, S. and Stergioudis, G. (1997) *Appl. Phys. Lett.* **71**, 2463.
16. Gioti, M. and Logothetidis, S. (1998) *Diam. Relat. Mater.* **7**, 444.
17. Logothetidis, S., Gioti, M., Patsalas, P. and Charitidis, C. (1999) *Carbon* **37**, 765.
18. Robertson, J. (1994) *Diam. Relat. Mater.* **3**, 361.
19. Davis, C.A. (1993) *Thin Solid Films* **30**, 226.
20. Tsui, T.Y., Pharr, G.M., Oliver, W.C., Bhatia, C.S., White, R.L., Andres, S., Anders, A. and Brown, I.G. (1995) *Mat. Res. Soc. Symp. Proc.* **383**, 447.
21. Logothetidis, S., Gioti, M., Charitidis, C., Patsalas, P. (1999) *Vacuum* **53**, 61.
22. Deng, H., Scharf, T.W. and Barnard, J.A. (1997) *J. Appl. Phys.* **81**, 5396.
23. Li, X., Bhushan, B. (1999) *Thin Solid Films* **340**, 210.
24. Li, K., Ni, B.Y., Li, J.C.M. (1996) *J. Mater. Res.* **11**, 6.
25. Holleck, H., Schier, V. (1995) *Surf. Coat. Technol.* **76-77**, 328.

## FORMATION OF NANOSTRUCTURED SURFACE REGIONS UNDER A CONCENTRATED LOAD

M.SH.AKCHURIN and V.R.REGEL  
*Institute of Crystallography, Russian Academy of Sciences  
Leninsky pr., 59, Moscow, Russia*

### 1. Introduction

The methods of concentrated loading (indenting, scratching) have been widely used for a long time to assess the mechanical properties of solids, and to study the mechanisms of deformation. For this reason, the deformation structure around indentations and scratches on different crystals have been studied [1-3]. However, the question of what happens in the material in the direct proximity of the contact with the tip of the indenter, where the maximum stresses (of the order of shear modulus) are generated, has not been well studied. A number of authors have made different suggestions concerning the state of the material under the indenter: from creation of an enormous density of dislocations, forming a strong stationary network [1,2], to the complete absence of dislocations [4] and phase transformations [5].

The investigations of the structure, created directly under the indenter tip have shown [6,7] that less than 10 % of the energy dissipation are used on dislocation and cracks formation, and more than 90 % evidently are consumed on the structural changes under indenter during deformation. Apparently, it is the inadequate understanding of the processes occurring directly at the point of contact of the indenter with the crystal that prevents the provision of an unequivocal physical meaning to the concept of microhardness [8]. The aim of this work is to investigate experimentally the character of structural changes taking place under the indenter tip, and also to describe the structural changes in terms of an orbifold model of deformation.

### 2. Results and Discussion

Single crystals of different structure and hardness have been investigated. Among these are refractory oxides, alkali halides, and semiconductors. The samples were deformed at room temperature using a Vickers diamond pyramid, sapphire spheres of different radii, and silicon whiskers. The materials were studied by scanning electron microscopy-cathodoluminescence (SEM-CL), X-ray microanalysis (XMA), X-ray-structural analyses, and X-ray photoelectron spectroscopy (XPS).

In our preceding works [9,10] we have shown that the relaxation of the high stresses under an indenter proceeds via the formation and displacement of point defects, and that this process results in a reconstruction of the structure with the formation of the nanocrystalline (NC) state. This reconstruction is accompanied by strong changes in physical properties of the material in regions with NaCl structure. SEM-CL investigation showed that:

Firstly, the NC regions located in direct contact with the indenter of all of the crystals exhibit enhanced luminescence capability. Figure 1 displays a schematic diagram and a cathodoluminescence image of contact regions (light-colored in CL) on the surface and in the volume under a scratch in NaCl (the surface with a scratch and a perpendicular cleavage surface are visible). The size of this region depends on the load, and the radiation disperses diffusely at depths close in magnitude to the half-diameter of the scratch. The enhancement of the CL in this case is associated with the increase in the intensity of excitonic emission bands [10]. This indicates a relative improvement of the nanocrystalline structure, i.e. a decrease in the number of other defects, which form competing channels for dissipation of the energy of the electron beam.

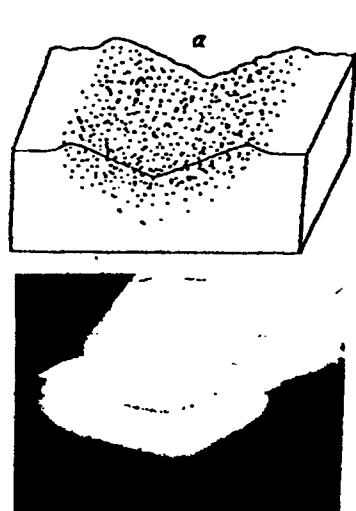


Fig.1. Schematic (a) and CL image of the scratch on a vertical cleavage plane of a NaCl single crystal. The scratch is  $30\mu\text{m}$  wide.

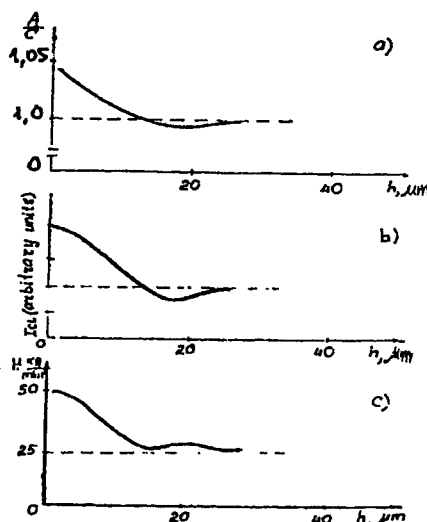


Fig.2. Changes in stoichiometry (a), CL intensity (b), and microhardness (c) with the depth under the imprint (NC regions).

It should be noted that the CL intensity at the imprint bottom may be higher or lower than that in the undeformed matrix. The increased luminescence in the contact zone between indenter and specimen is observed only at loads below the value  $P_{\text{lim}}$  typical for each crystal studied. Loads above this value cause luminescence quenching [11]. Studies of the degree of perfection of crystal structure using electron channeling microscope [12] have confirmed the above suggestion that the CL quenching at  $P > P_{\text{lim}}$  is connected with the distortion in crystal structure of imprint bottoms, and scratches up to the amorphous structure.

Secondly, the microhardness of the NC regions (light areas in CL image of Fig.1) is tens of percent higher than that of the undeformed matrix and it diminishes with depth (Fig.2c). This fact was established by means of indentation of the bottom of the imprint produced by sapphire of comparatively large diameters (about 3 mm) and of a perpendicular cleavage faces.

Thirdly, it was found by backscattering electron modes in SEM [13] that the density variations in the deformed materials are less compared to that in the undeformed matrix. It is known [14] that the density of NC materials is much lower than that of poly- and single crystals due to the specific structure of the boundaries.

Fourthly, this region has a peculiar chemical composition. The studies carried out by XPS and XMA methods have shown the change of stoichiometry in the NC regions (Table 1), with the remarkable cation-deficiency.

Crystals	MgO	LiF	NaCl	KCl
C/A	0,91	0,95	0,96	0,98

TABLE 1. Ratio between numbers of cations (C) and anions (A) in the imprint bottom (NC regions) (the ratio for undeformed regions is 1).

Figure 2a demonstrates the stoichiometric changes with depth in NaCl. It is seen that near the surface the sodium-deficiency is the highest (up to 4%), whereas in the bulk there is a smaller deficiency. Near the boundary of the bright region (in Fig. 1) the deficiency is not observed, and farther away an excess of sodium is detected. At great depths (beyond the regions with NC structure), the relation of sodium and chlorine quantity is similar to that in the undeformed single crystalline matrix.

It should be noted that in practically all crystals under investigation (especially the covalent crystals) XPS spectra show a displacement of the maximal energies of the photoelectrons in nanocrystalline regions relative to that in the single crystal matrix (Fig. 3). This indicates a change in the interatomic bonds that occur most likely at grain boundaries.

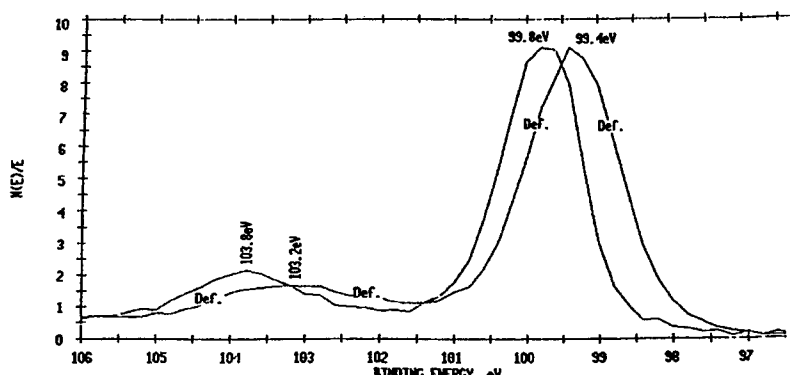


Fig.3. XPS (2P<sub>1</sub> and 2P<sub>3</sub>) spectra from the surface of single and nano (def) crystal of silicon.

We emphasize that nanocrystalline regions under the indenter are metastable. The storage of the deformed specimens (alkali halides) in air or the annealing causes the oriented grain growth. This is accompanied with recovery of the CL intensity, density and hardness of the material in these regions to the original ones, i.e. these regions lose the properties characteristic of the NC state. In the case of unsuccessful attempts to reveal the grains on the imprint bottom by SEM observation with a 10-nm resolution immediately after the indentation, one can resolve the recrystallized grains having size of several tens of nanometers. The analysis of the kinetics of the grain growth [15] and the extrapolation of the observed dependence of the grain size on annealing duration to zero time lead to the conclusion that the mean grain size (D) in alkali halides due to indentation is comprised of several nanometers (for NaCl, D≈10nm). In addition to the experimental data concerning the recrystallization process the energetic estimations of microimprinting will be made to evaluate the mean size of the grains formed. The work, W, done by indenter penetration can be measured quite exactly:  $W=Ph$ , where P is the load on indenter and h is the depth of recovered imprint. This energy (mainly above 90% of total) is expended largely on the formation of a region with NC structure. Let us assume that the total energy, W, is spent on the formation of the surfaces of grain boundaries in the volume with NC structure, i.e.  $W=\delta S$ , where  $\delta$  is a specific surface energy and S is the total area of boundaries. Also,  $S=V/D$ , where D is the mean grain size and V is the volume of a region with NC structure. Thus,  $D=V\delta/W$ , where V is determined from the CL picture of the imprint profile (Fig.1),  $V\approx d^3/4$ , where d is an imprint diameter, W is measured, and  $\delta$  is from 100 to 1000 erg/cm<sup>2</sup>. Under the assumption that on formation of the NC structure 0.9W is consumed, the mean size of nanocrystallites, D, in alkali halides crystals should be several nanometers.

Besides the empirical estimations, a theoretical evaluation of the mean size of the nanocrystals formed by indentation is given based on energy assessments of micropressing:  $D=K(\delta/H)$ , where  $H$  is the microhardness and  $K$  is the coefficient depending on binding energy and shape of the indenter. Similar dependence can be obtained from the influence of nanocrystal size on CL intensity, density and stoichiometry of NC materials.

In view of the complexity of the concept of hardness, its physical meaning depends on the testing methods employed [8]. In accordance with our investigations it seems natural to return to the definition given by P.A. Rehbinder in 1936 [16]. According to which, the hardness is equal to the work required to form a unit area of a new surface of the solid. Thus, the experiment shows, that the deformation of a material under the indenter tip causes the formation of nanocrystalline structure. It seems that theoretically this process can be connected with so-called orbifold model of deformation of crystals.

### 3. Orbifold Model of the Deformation of Crystals

The peculiarities of NC materials are in accordance with their defect structures. However, they can be explained also from the point of view of an ideal crystal. The ideal crystal is a community of atoms of the definite Fedorov symmetry group. In the Euclidean space an ideal crystal is infinite. As distinct from an ideal crystal the real one has the finite dimension and contains the volume defects. Any ideal crystal consists of cells that can be considered as independent ranges of the corresponding Fedorov group. The independent range of such Fedorov group is a part of the space without equivalent atoms according to this group. The equivalent atoms can be in the boundaries of independent range. The authentic view of the independent ranges of Fedorov group lies in the fact that the equivalent points in the boundaries are identified. In such a manner the compact local Euclidean ranges (orbifolds) appear in topology [17]. In the case of two-dimensional space the orbifolds have a shape of the tore (Fedorov group Pb), Klein's bottle (Fedorov group Pg), Meubius ribbon (Fedorov group Cm) etc. Consequently, for every Fedorov group of any dimensionality there is its own orbifold [18].

At present the orbifold concept of crystal growth starts its advancement [19,20]. According to this concept the growth entities can be not only separate atoms but also atomic groups consisting of definite number of atoms present in the independent range of the correspondent Fedorov group. As a result of small dimensions these groups may shrink on themselves the free chemical bounds and become the quasineutral particle. The topology of this particle corresponds to the volume of an ideal crystal. When considering the deformation process of the crystals as opposite to the growth, the relaxation of enormous stresses causing the stability loss can be due to the break up of crystal structure into orbifolds. This permits the consideration of the orbifolds as a mathematical model of nanocrystal - a finite ideal crystal having the compensated bonds. However, in reality it is very difficult to obtain the total bond compensation on account of identifying orbifold. So, one can assume the compensation of only the strongest bonds.

According to the orbifold model the nanocrystals should have the following properties: 1. The nanocrystal is quasineutral, the closed bonds being relatively easy to break. 2. The volume of nanocrystal is a multiple of the integral number of the volumes of elementary cells. 3. The shape of nanocrystals is not rigid and it can be changed. 4. The nanocrystal can break up and unite into any combination of the whole elementary cells. 5. The smaller the nanocrystal size the stronger it compensates its unsaturated bonds, and hence weaker interactions with neighbors. 6. The nanocrystal has a perfect internal structure, the structural defects can only be in the boundaries, which have a fractal character making its contribution to the crystal properties.

These properties of the nanocrystals suggest the following model of crystal deformation. Initially at small stresses the usual dislocation mechanisms are operating. At high stresses and deformations (the action of a concentrated load, explosion deformation, rolling, etc.) the decomposition of blocks (orbifolds) to the smaller ones originates. The result of this should be the increase of the hardness of a material, which depends on particle dimension, i.e. on dispersion work according to A.P. Rehbinder [16]. The rise in hardness will be analogous with the Petch-Hall effect until the strongest bonds in each orbifold is compensated. Under these conditions each structure has an orbifold of definite size, its shape is determined mainly by the deformation conditions. After further reducing orbifold size the hardness will tend to decrease (anomaly of Petch-Hall effect) as a consequence of a continued compensation of the weakening of bonds between orbifolds. This facilitates the intergrain sliding. In the limiting case after the total compensation of the bonds inside the orbifolds the superplasticity should be revealed. Thus, the specific

properties of the materials are determined mainly by the orbifold dimensions (nanocrystals), which influence the boundary properties.

#### 4. Conclusion

The high stresses arising under an indenter relax via the formation and migration of interstitial atoms, which result in the structural rearrangement with the formation of the NC state. The orbifold model of the crystal deformation based on new aspects of the peculiarity of the structure and properties of nanocrystalline materials is presented.

#### 5. Reference

1. Predvoditelev A.A., Rozhanskii, and Stepanova V.M. (1962) *Kristallografiya* [in Russian], v.7, p.418-424.
2. Boyarskaya Yu.S. (1972) *Deformation of Crystals During Microhardness Tests* [in Russian], Shtiintsa, Kishinev.
3. Velednitskaya M.A., Rozhanskii V.M. et al . (1975) *Deformation Mechanism of MgO Crystals Affected by Concentrate Load*, *Phys Stat. Sol.*, A, v.3, p. 123-132.
4. Akchurin M.Sh. and Galstyan V.G. (1980) *Dokl. Akad. Nauk SSSR* [in Russian], v.252, p.870-872.
5. Pharr G.M., Oliver W.C., and Clarce D.R (1990) *The Mechanical Behavior of Silicon During Small-Scale Indentation*, *J. of Electronic Materials*, v.19, №9, p. 881-887.
6. Golovin Yu.I. and Tyurin A.I. (1996) *Dynamics and Micromechanisms of the Deformation of Ionic Crystals in Pulsed Microindentation*, *Phys. Solid State*, v.38, №6, p.1000-1003.
7. Farber B.Ya., Orlov V.I., Heuer A.H. (1998) *Energy Dissipation During High Temperature Displacement Sensitive Indenation in Cubic Zirconia Single Crystals*, *Phys. Stat. Sol. (a)*, v.116, p. 115-126.
8. Tsinzerling L.G. (1974) *In Progress in Testing for Microhardness* [in Russian], Nauka, Moscow, p.86-92.
9. Akchurin M.Sh., Galstyan V.G., Mikhina E.Yu. and Regel V.R. (1991) *Plastic Deformation Localisation by Concentrated Load on Crystals*, *Latvian J. of Phys. and Techn. Sci.*, v. 4, p.72-82.
10. Akchurin M.Sh., Galstyan V.G., Regel V.R. (1992) *SEM-CL Studies of Plastic Deformation Processes in Crystals*, *Scanning*, v.14, p.194-202.
11. Akchurin M.Sh., Regel V.R. (1998) *Specific Features of Crystal Deformation Under a Concentrated Load*, *Chemistry Reviews*, v.23, p.59-88.
12. Enomoto Y.,Yamanaka K.(1982) *Cathodoluminescence at Frictional Damage in MgO Single crystals*, *J. of Mat. Sci.*, v.17, p.3288-3292.
13. Galstyan V.G. and Akchurin M.Sh. (1993) *Izv. Akad. Nauk SSSR ser. fiz* [in Russian], v.57, p.59-61.
14. Froes F.H. and Suryanarayana (1989) *Nanocrystalline Metals for Structural Applications*, *JOM* v.6, p.12-17.
15. Akchurin M.Sh., Galstyan V.G. and Regel V.R. (1995) *Fiz. Tverd. Tela* [in Russian], v.37, №3, p.845-851.
16. Rebinder P.A. (1936) *Izv. Akad. Nauk SSSR, Ser. Khim.* [in Russian],v.5, p.639-644.
17. Nikulin B.B., Shapharevich I. R. (1983) *Geometry and Groups* [in Russian], Moscow, Nauka.
18. Phomenko A.T. (1998) *Visual Geometry and Topology* [in Russian], Moscow, MGU.
19. Galiulin R.V. (1998) *Kristallografiya* [in Russian], v.43, №2,p. 366-374.
20. Aschabov A.M., Galiulin R.V. (1998) *Dokl. Akad. Nauk SSSR* [in Russia], v.363, №4, p.513-514.

---

## NON-DESTRUCTIVE MECHANICAL CHARACTERISATION OF MECHANICAL PROPERTIES OF NON-HOMOGENEOUS NANOSTRUCTURED COATINGS

S.M. AIZIKOVICH, J.-P. CELIS\*, L.I. KRENEV, N.A. SEROVA

*Rostov State University Institute for Mechanics and Applied  
Mathematics, Rostov-on-Don, Russia, E-mail: aizsm@gis.rnd.runnet.ru;*

*\* - Katholieke Universiteit Leuven Department Metaalkunde en  
Toegepaste Materiaalkunde de Croylaan, 2 B.3001 Heverlee, Belgium.*

### Abstract

The experimental model permitting the detection of coating non-homogeneity is suggested for standard depth sensing indentation tests.

It is assumed that the shear modulus varies arbitrarily with depth in a nanostructured coating. It is defined a notion of the stiffness as a function of radius of a contact zone for nanostructured coating coupled with homogeneous half-space, which makes it possible to classify the non-homogeneity of a coating.

Using numerical examples, the influence of different laws of shear modulus variation in a coating on the stiffness is studied.

### 1. Introduction

The protection of materials by means of non-homogeneous coatings is now a well-established technology, and is an extremely versatile means of improving component performance [1]. Coating elasticity is a crucial parameter for the performance and reliability of a coated part. The determination of mechanical properties arises when one wants to control the coating quality.

At present nano-indenters are high-precision instruments which allow the performance of non-destructive tests on thin non-homogeneous coatings. But the interpretation of such test results is still under development. In this paper a mathematical simulation of standard nano-indentation tests is presented. The predictions from this simulation for different non-homogeneous coatings are reported.

The elastic contact problem, which plays a key role in the analysis procedure, was originally considered in the late 19th century by Boussinesq [2] and Hertz [3]. Hertz analysed the problem of the elastic contact between two spherical surfaces with different radii and elastic constants. His now classic solutions form the basis of much experimental and theoretical work in the field of contact mechanics.

In the early 1980's, it was realised that load and depth sensing indentation methods could be very useful in the measurement of the mechanical properties of very

thin films and surface layers, and instruments for producing submicron indentations were developed.

Oliver, Hutchings, and Pethica [4,5] suggested a simple method based on measured indentation load-displacement curves and knowledge of the indenter area function (or shape function); that is, the cross-sectional area of the indenter is related as a function of the distance from its tip.

The shortcoming of these methods is that precise evaluation of the elastic modulus is performed only for samples with constant elastic modulus at depth. In the case of a non-homogeneous coating coupled with a homogeneous half-space, the obtained modulus is some mean of both the elastic modulus of a coating and the elastic modulus of a substrate.

Suresh et al. [6] proposed the method based on the finite element simulation for estimation of Young's modulus variations through a compositionally graded layer by recourse to spherical indentation.

The problem of properties investigation of non-homogeneous materials attracts the attention of many researchers by its actuality and complexity, mathematically as well as experimentally [6,7]. Published solutions of a contact problem for non-homogeneous materials were constructed in most cases numerically (using finite element method).

In this work the authors suggest the value of the numerical-analytical method. This method makes it possible to more deeply analyze the cause of problems which arise in investigation of mechanical properties of non-homogeneous nanostructured materials. Derived analytical expressions, which define the solution of the contact problem for a non-homogeneous coating coupled with homogeneous half-space degenerate into the classic Hertzian solution in the case of homogeneous half-space. In numerical examples, the stiffness of a material has been considered and analysed. The relation between the law of shear modulus variation with depth and the stiffness of a material as a function of radius of a contact zone is presented.

For the determination of properties of a non-homogeneous coating the size of contact zone of an indenter with a coating is an essential value in contrast to that of a homogeneous material. In this paper it is shown that the experiment which is performed with a view to investigate the elastic properties of a non-homogeneous coating should at least be carried out for contact zones commensurate with the thickness of a coating (from  $1/4 T$  to  $4T$ , here  $T$  is the thickness of a coating).

To analyse the non-homogeneous character of a nanostructured coating it is necessary to determine the dependence of the stiffness value from the size of a contact zone for the wide range of its variation. However an experiment should be carried out within the limits of the linearly elastic deformation of a material. Depth sensing indentation tests using the set of spherical indenters with different diameters settle this problem.

## 2. Formulation of the contact problem simulating an indentation test

A non-deformable spherical indenter of radius  $R$  is impressed into a surface  $\Gamma$ , of a non-homogeneous elastic half-space  $\Omega$ , by a normal force  $P$  (Fig. 1). Cylindrical  $(r, \varphi, z)$

coordinates are bound to the half-space. It is assumed that all deformations are elastic and that the size of the contact zone,  $a$ , is small with respect to the radius  $R$  of the sphere, and that friction force does not exist between the indenter and the surface of half-space.

The spherical indenter surface is approximated by a quadratic shape  $z = \psi(r) = \beta r^2$  in the vicinity of the original point of contact. This approximation is valid for small contact radii,  $a < 0.1R$  for homogeneous solids [6], which covers essentially all practical cases of elastic spherical indentations.

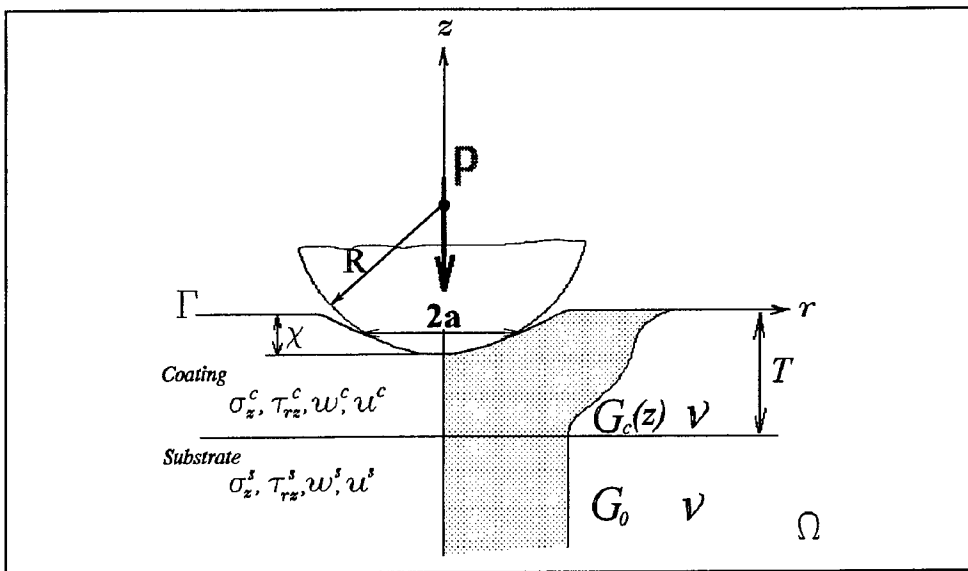


Figure 1. Scheme of indentation test.

The half-space is not loaded outside the indenter. Under the action of the normal force,  $P$ , the indenter moves a distance  $\chi$  along the  $z$  axis.

We assume a Poisson ratio,  $\nu$  is a constant, and consider the shear modulus,  $G(z)$ , in the half-space to exhibit a well defined variation. The shear modulus can thus be arbitrarily continuous or a piece-wise continuous function of the depth  $z$ , as thus expressed as follows:

$$\begin{aligned}
 1. \quad G(z) &= G_c(z), & -T \leq z \leq 0 \\
 2. \quad G(z) &= G_c(-T) = G_0, & -\infty < z \leq -T
 \end{aligned} \tag{1}$$

Let us denote  $G_c(0) = G_1$ . Under the above assumption, the boundary conditions have the form:

$$\begin{aligned}
 z=0 : \quad \tau_{zr} &= \tau_{z\varphi} = 0, \quad \sigma_z = 0, \quad r > a, \\
 w &= \chi(r) = \chi - \psi(r), \quad r \leq a
 \end{aligned} \tag{2}$$

Here  $w$  is the displacement along the  $z$  axis, while  $\tau_{zr}$ ,  $\tau_{z\varphi}$ , and  $\sigma_z$  are the radial, tangential and normal stresses respectively.

Using the method of works [8,9,10], the solution to the contact problem was constructed and the relation between an impressing force and the size of a contact zone was determined [11].

$$P = 4 \frac{a^3}{R} \frac{G_1}{1-\nu} \left( \frac{2 G_0}{3 G_1} + \sum_{i=1}^N C_i (-\cosh a_i + a_i^{-1} \sinh a_i) \right).$$

Here  $C_i$  and  $a_i$  are certain constants defined by non-homogeneity laws.

### 3. The Stiffness Concept of the Depthwise Non-homogeneous Material

As a result of the penetration of the indenter into the non-homogeneous material we can obtain the relation between the impressing force and the displacement of the indenter. These values by themselves are not very informative, as it is difficult to use these values to determine the existence of the non-homogeneous layer on the surface of the foundation.

We define an expression which is referred to as the stiffness of the material

$$S = \frac{3}{4} \frac{P}{a \chi (1 - \nu^2)},$$

where  $a$  is the contact zone radius,  $\chi$  is the displacement of the indenter,  $\nu$  is the Poisson's ratio. For the homogeneous material the stiffness is a constant, equivalent to the shear modulus of the foundation [12].

For the non-homogeneous material,  $S(a)$  is a function dependent upon the size contact zone.

### 4. Testing method for determination of the non-homogeneity of a material

Our aim is to detect the character of the non-homogeneity of a material by using standard indentation measurements.

The method described here is based on a spherical indenter and aims at investigating the elastic properties of materials. Thus, the test must be carried out under elastic deformation only. This is the basis of the method, and it allows the depth distribution of material properties to be investigated.

Practically all existing materials deform elastically in a narrow range of loading. One of the starting problems is the determination of that range.

The goal of the test is to determine the force-displacement relation for the penetration of a non-deformable spherical indenter into the continuously non-homogeneous coating coupled with a homogeneous half-space. To guarantee the non-

destructive character of the test, it is necessary to fulfil the following condition : the stresses must not exceed the elasticity limits.

### 5. Numerical Results

The numerical analysis has been carried out for non-homogeneous nanostructured coatings which have applications in magnetic recording systems, printing industries and motor engines. In this case, the value of the ratio of the shear modulus on the coating surface to the shear modulus in any interior point of substrate (denoted  $n$ ) was bounded such as

$$1 / 3.5 < n < 3.5$$

Shear modulus is assumed to vary with depth, according to the relation

$$G(z) = \begin{cases} G_0 f_i(z) & -T \leq z \leq 0, \\ G_0 & z \leq -T, \quad i = 1, 2, 3, 4 \end{cases} \quad (3)$$

$$f_1(z) = 3.5, \quad f_2(z) = \frac{1}{3.5},$$

$$f_3(z) = 3.5 + 2.5 \frac{z}{T}, \quad f_4(z) = \frac{1}{3.5} - \frac{2.5}{3.5} \frac{z}{T}$$

Fig. 2 shows the values  $f_i(z')$ ,  $z' = z/T$  ( $i = 0, 1, 2, 3, 4$ ) which characterise non-homogeneity laws described above.

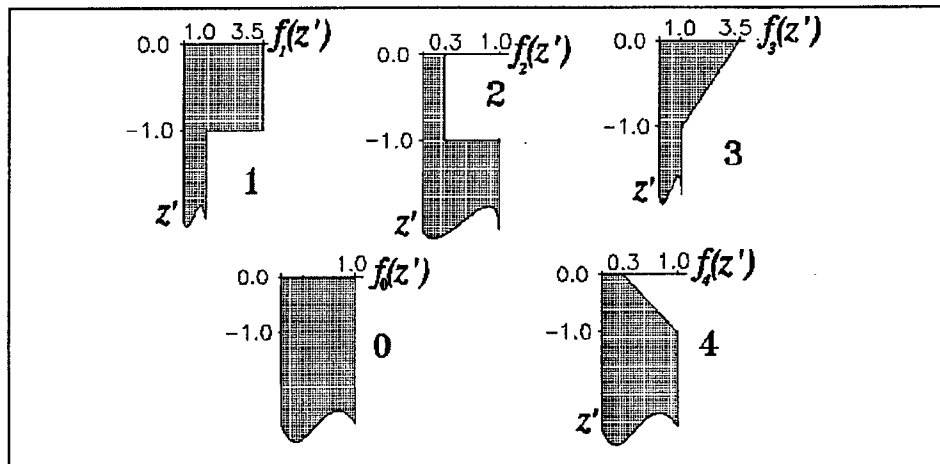


Figure 2. Nonhomogeneity laws describing the variation of shear modulus with depth.

Fig. 3 shows graphs  $S(\lambda^{-1})/S_0$  ( $\lambda=T/a$ ) — the ratio of the stiffness of non-homogeneous coatings,  $S$ , to the stiffness of substrate — a homogeneous half-space,  $S_0$  for the 5 cases given in Fig. 2. To make the graph more descriptive we present them using a logarithmic scale. The curve numbers correspond to the variation laws of elasticity modulus.

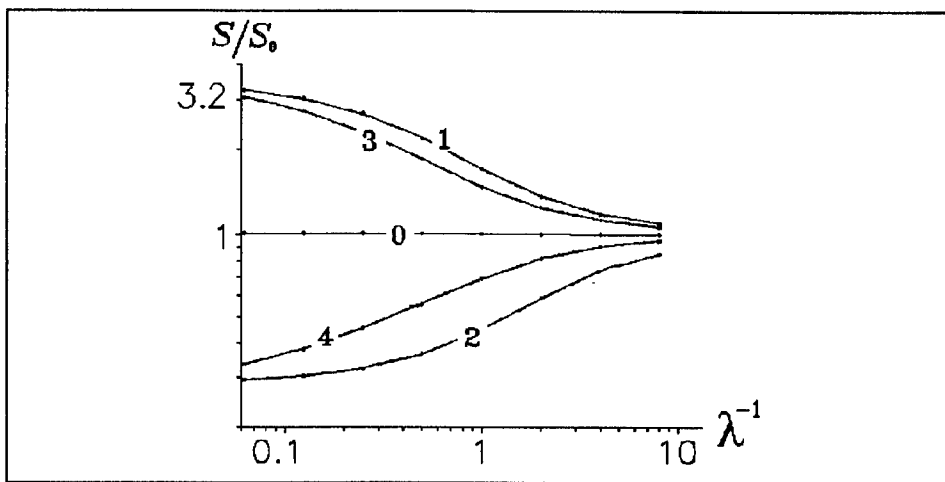


Figure 3. Graphs of the ratio  $S(\lambda^{-1})/S_0$  for the cases shown in Fig 2.

Fig. 3 shows that by using the results of non-destructive indentation experiments we can evaluate the variation of elasticity modulus with depth. Moreover, it shows that this kind of test gives the possibility of distinguishing changes in surface layer properties not only in terms of being softer or harder, but also in terms of the variation of elastic properties of coatings with depth (blended or layered). A potential application of interest is the characterisation of compositionally modulated multilayers in microelectronics [13].

The values on the graphs are obtained from calculations in which the contact zone,  $a$ , is varied from  $1/16 T$  to  $16 T$ . This is practically impossible to reproduce in one experiment within elastic deformations limits. Hence, the solution of the problem of extrapolation of values obtained for the narrow interval of indenter penetration values and, respectively, of contact zones on the whole domain of definition is of great interest.

It is obvious from Fig. 3, that the middle region of the stiffness change graph is the most informative ( $1/4 T \leq a \leq 4 T$ ).

## 6. Conclusion

In this work the estimation of relevant parameters for the non-destructive testing of the mechanical properties of non-homogeneous coatings has been carried out. The method

is based on a depth sensing indentation test performed within the elastic limits of the tested coated materials.

The method presupposes the mathematical simulation of the testing process that involves the penetration of spherical indenter into a functional non-homogeneous coating with an arbitrary variation of the elasticity modulus along its depth.

This method permits the interpretation of indentation test results performed in the elastic deformation region on non-homogeneous coatings by existing standard equipment.

From the point of view suggested in this paper regarding the testing method for determination of non-homogeneity of a coating, we analysed similar experimental data presented in the paper of Suresh et al. [6]. In this work the authors considered two kinds of coatings which correspond with above mentioned laws 3 and 4 — linear increasing and linear decreasing laws. The authors simulated a non-homogeneous coating by the model of a material with elastic properties varying exponentially with depth. Presented data correspond to small values of a contact zone in our terms, e.g.  $\lambda_1 > 29.2$ ,  $\lambda_2 > 13.3$  (here  $\lambda = T/a$ ,  $T_1 = 2.92$  mm,  $T_2 = 1.33$  mm,  $a < 0.1$  mm). Such values of  $\lambda$  conform to the very beginning of the stiffness curve and correspond with properties of practically homogeneous material and reflect properties only of layers attached to the surface layer. In other words, the experimental data do not give the opportunity to observe the non-homogeneity variation with depth because of small variation of a contact zone.

The main conclusion of our work is that in the investigation of non-homogeneous coatings, the size of a contact zone should vary at least up to the value comparable with the thickness of coating.

## 7. References

1. Rickerby, D. and Matthews, A. (1991) *Advanced Surface Coatings*, A Handbook for Surface Engineering, Blackie, London.
2. Boussinesq, J. (1885) *Applications des Potentiels a l'etude de l'équilibre et du mouvement des solides élastiques*, Gauthier-Villars, Paris.
3. Hertz, H. (1882) Über die Berührungen fester elastischer Körper (On the contact of elastic solids), *J. reine und angewandte Mathematik* **92**, 156-171.
4. Oliver, W.C., Hutchings, R. and Pethica, J.B. (1986) In ASTM STP 889, edited by Blau and B.R. Lawn (American Society for Testing and Materials), Philadelphia. PA., 90-108.
5. Pharr G.M. and Oliver W.C. (1992) Measurement of thin film mechanical properties using nanoindentation, *MRS Bulletin* **7**, 28-33.
6. Suresh, S., Giannakopoulos, A.E. and Alcalá, J. (1997) Spherical indentation of compositionally graded materials: theory and experiments. *Acta mater.* **45**, No 4, 1307-1321.
7. Anderson, I.A. and Collins, I.F. (1995) Plane strain stress distributions in discrete and blended coated solids under normal and sliding contact. *Wear* **185**, 23-33.

---

8. Aizikovich S.M., Aleksandrov V.M. (1984) Axisymmetrical Problem about Indentation of Round Punch into Elastic Inhomogeneous with Depth Half-Space. *Izv. Akad. Nauk SSSR. Mech. Tverd. Tela* **2**, 73-82
9. Aizikovich, S.M. (1990) An asymptotic solution of one class of dual equations for small values of the parameter, *Doklady Akademii Nauk SSSR* **313**, No. 1, 48-52.
10. Aizikovich, S.M. (1992) An asymptotic solution of one class of dual equations for large values of the parameter, *Doklady Akademii Nauk SSSR* **319**, No. 5, 1037-1041.
11. Aizikovich S.M., Krenev, L.I. and Serova, N.A. (1998) Non-Destructive Determination of Mechanical Properties of Non-Homogeneous Coatings. *7-th European Conference on Non-destructive Testing*, Copengagen, Denmark, May 26-29, Proceedings **1**, 1063-1069.
12. Johnson, K.L. (1985) *Contact Mechanics*, Cambridge University Press, Cambridge.
13. Haseeb, A., Celis, J.-P. and Roos, J.P. (1995) An Electrochemical Deposition Process for the Synthesis of Laminated Nanocomposites, *Materials Manufacturing Processes*, **10**, (4), 707-716.

## HIGH REFRACTIVE INDEX Si/SiO<sub>x</sub> BASED NANOCOMPOSITES

T. PHELY-BOBIN, D.E. BHAGWAGAR, F. PAPADIMITRAKOPoulos\*

*Dept. of Chemistry, Polymer Science Program, Nanomaterials Optoelectronics  
Lab., Institute of Materials Science, University of Connecticut, Storrs, CT 06269*

### 1. Introduction

Nanosized materials and their composites have generated enormous interest in recent years.[1-3] The need for high refractive index materials that readily conform to the elaborate structures proposed for photonic band-gap structures,[4,5] have attracted considerable attention in high loading nanocomposites.[6-8] The potential benefits in generating materials that gradually bridge the large refractive index gap between organics and inorganics along with maintaining reduced absorption and scattering, could benefit an array of photonic devices by improving the optical-coupling efficiencies between semiconductors and plastics or glass.[9] For example, the refractive indices of polymers vary between 1.3 and 1.7, while those of inorganic semiconductors vary between 2 and 5.[10] Some specialty polymers can exhibit refractive index greater than 2, such as poly(thiophene) with  $n = 2.12$ ,[11] although this is strongly coupled to optical absorbance in the visible region. Inorganic high band-gap materials, such as TiO<sub>2</sub>, could reach up to refractive indices of 2.9 in their crystalline state, but above this limit it is necessary to consider composites of inorganic semiconductors such as those presented in Table 1.[10]

TABLE 1. Refractive indices and absorption coefficients in the visible range for some of the ultra-high refractive index semiconductor inorganics

Material	Refractive Index ( $n$ )			Absorption Coefficient ( $k$ )		
	400 nm	500 nm	620 nm	400 nm	500 nm	620 nm
Crystalline Si	5.57	4.30	3.91	0.387	0.073	0.022
Amorphous Si	4.38	4.47	4.23	2.02	0.992	0.461
Ge	4.14	4.34	5.59	2.215	2.384	0.933
GaP	4.20 <sup>f</sup>	3.59	3.32	0.275	$2.5 \times 10^{-3}$	$2.8 \times 10^{-7}$
InP	4.42	3.82	3.55	1.735	0.511	0.317
PbS	3.62	4.35	4.19	2.015	2.238	1.773

High refractive index nanocomposites of PbS nanoparticles in gelatin or polyethylene oxide have been thoroughly investigated by Suter *et al.*[6-8] Their studies indicate that both PbS particle size and loading influence the overall refractive index of the nanocomposite. Very small particles show reduced refractive index as compared to that of particles with diameter equal or greater than 25 nm which approach the refractive index of bulk PbS.[8] The absorption coefficient of PbS nanoparticles showed similar

nanoparticle-size behavior to that of refractive index. Based on their experimental data Suter *et. al.*[8] have shown that the overall refractive index of the nanocomposite  $n$  is to the first approximation proportional to the volume fractions  $v_i$  and refractive indices  $n_i$  of its components respectively ( $n = n_1v_1 + n_2v_2$  for a two component system).

The technological challenges to achieve high refractive index inorganic-organic nanocomposites ( $n > 2.5$ ) of increased transparency requires the use of high refractive index nanoparticles with low absorption coefficient in the visible range and diameter between 20 to 40 nm (well below one tenth of the wavelength of light (400-800 nm) in order to suppress Rayleigh scattering). For the same reasons, agglomerates and large sized scatterers, such as voids, should be scrupulously excluded. Based on the absorption coefficient of ultra-high refractive index inorganics listed at Table 1, GaP appears to be the material of choice with second to best crystalline Si[10]. When one incorporates the inherently low density and cost of Si along with various safety reasons of nanofabrication, Si and its nanocomposites overweighed the advantages of GaP.

Several preparation techniques for silicon nanoparticles have been reported such as chemical-vapor pyrolysis or deposition,[12-17] sputtering,[18-20] gas evaporation,[21] anodic etching,[22-26] and high-energy milling.[27] Electrochemical etching followed by electropolishing have been used to prepare porous silicon films of increased transparency with the index of refraction  $n$  calculated to be 2 in the IR.[28] Ultimately, high energy milling was chosen based on its environmental friendliness, low cost, and relative ease of nanoparticle separation. However this techniques introduces some limitation with respect to chemical purity and partial amorphization (which results in increased absorption, see Table 1) as a result of milling. This paper describes our current results on the characterization of these nanoparticles along with our recent attempts to fabricate high refractive index nanocomposites.

## 2. Results and Discussion

### 2.1. PREPARATION AND CHARACTERIZATION OF COLLOIDAL SILICON:

The profound technological importance of the silicon-based industry has stimulated considerable investigation into attaining well-controlled nanosized Si.[12-15,17-27,29] Recently, Shen *et. al.*[27] reported the use of high energy milling for nanosizing silicon in order to attain crystal grain sizes ranging from 3 to 20 nm. This has prompted us to employ this technique in order to produce nanosized Si, in large quantities, for the fabrication of high refractive index nanocomposites. Dispersing the freshly milled Si powder into solvents such as ethanol, water and tetrahydrofuran (THF) has resulted in black suspensions that quickly flocculate to leave a clear supernatant. Mild sonication has resulted in similar suspensions that require considerably longer time to settle down. Figure 1(a) indicates that high-energy nanomilling yields particles with very broad size distributions (3 to 500 nm), clearly unsuitable for use in photonic applications.

Significant effort was put into the extraction of Si nanoparticles with well defined average size (20 - 30 nm) and narrow size distributions. Several different methods were

employed to achieve separation including filtration and centrifugation. A series of trials were performed and parameters such as exposure to oxygen and sonication time and temperature were proven crucial. The formation of an ultra-thin silicon oxide that will be discussed later on in this paper appeared to be instrumental into stabilizing nanosilicon colloids.[12,13,17,26] Filtration of sonicated suspensions proved to be a less effective technique for separation of colloidal nanosilicon, highly likely due to the fact that small particles are attracted and halted during percolation through larger agglomerates. On the other hand, centrifugation quickly separates the large agglomerates from nanosilicon leaving a bright orange, lightly opalescent supernatant of colloidal Si. Optimization of

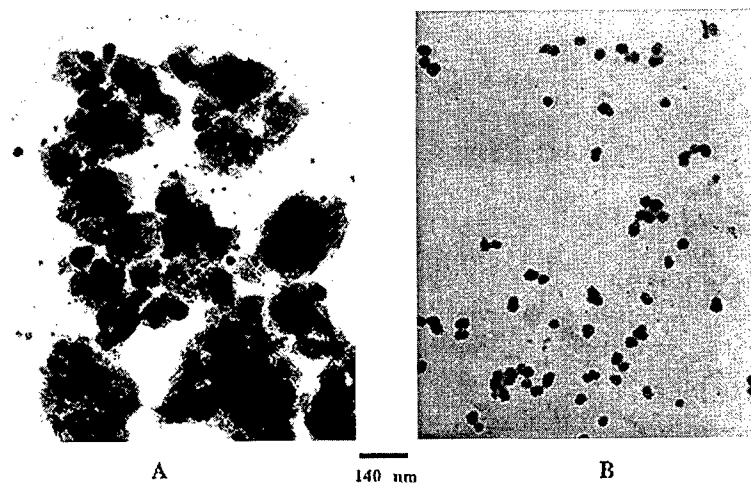


Figure 1. Transmission electron micrograph of Si, (A) as-milled, and (B) after separation by centrifugation

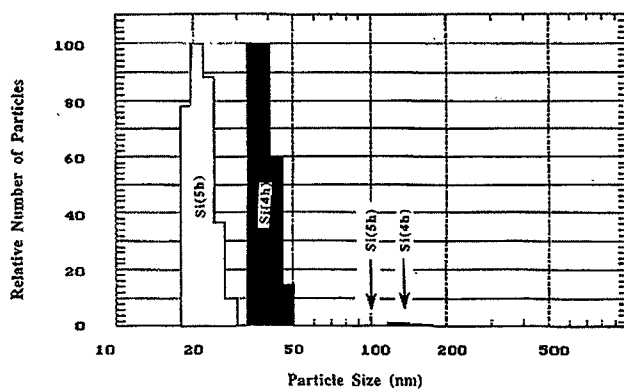


Figure 2. Number average particle size distribution obtained by dynamic light scattering from centrifuged colloidal Si suspensions as a function of milling time.

sonication temperature (c.a. 10 °C) and centrifugation time and speed (90 min. at 3000 rpm) has yielded colloidal Si with the desired average size and size distribution shown in Figure 1(b).

The average size of these nanoparticles, as determined by TEM was corroborated by size distribution analysis obtained by Dynamic Light Scattering (DLS) shown in Figure 2. For five hours milling time, the majority of nanoparticles lies between 20 and 30 nm (see Figure 1(b)). The correlation function obtained by DLS clearly does not obey Gaussian statistics. An alternative fitting procedure (Nicomp) developed especially for lightly agglomerated colloids (less than 1% agglomeration) has shown a near perfect fit based on a bimodal distribution shown in Figure 2. The small fraction of particles in the range between 100 to 150 nm sizes is present in all colloidal nanosilicon suspensions, even at very dilute concentrations. Based on the fact that microfiltration through 100 nm Nylon as well as Teflon filters has failed to remove these agglomerates, it is believed that they originate from a dynamic agglomeration - deagglomeration process slow enough to be measured by DLS. These agglomerates might look like those present in Figure 1(b), although considerable caution has to be exercised based on the markedly different nature of sample preparation (liquid vs. solid).

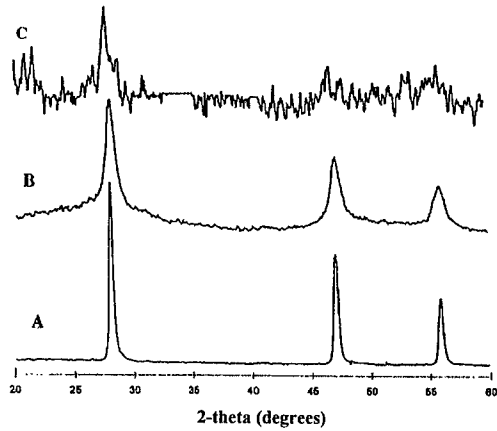


Figure 3. Radial X-ray diffraction profiles of (A) bulk Si, (B) as-milled sample Si, and (C) Si after separation by centrifugation.

The X-ray diffraction (XRD) profiles for bulk silicon, as-milled powder (before separation) and separated nanoparticles are presented in Figure 3. Line broadening is clearly the biggest difference between bulk silicon and as milled sample (Figure 3A and 3B respectively). This is in agreement with the thorough investigation of Shen *et al.*[27], on the high energy ball-milling of Si, where nanocrystalline grains of Si ranging from 3 to 20 nm were obtained, based on high resolution TEM and XRD line broadening analysis.[27] A combination of pressure induced amorphization and crystallite-refinement-induced amorphization was proposed to be responsible for this thermodynamically unfavorable process. The authors also verified that the partial

amorphous (c.a. 15%) character of the milled Si powder was distributed heterogeneously among the nanocrystalline portions while isolated nanocrystals were surrounded by a layer of amorphous silicon, surprisingly enough not oxidized by the adsorbed oxygen.[27] The XRD profile of the isolated nanosilicon in Figure 3C, although attained with significantly lower signal to noise ratio due to instrumentation shortcomings, resembles that of as milled powder with marginally increased line-broadening. Based on the work of Shen *et al.*[27], and the work presented below, it is currently believed that these nanoparticles consist of nanocrystalline Si interior with an amorphous Si exterior, partially coated with surface oxide which assists formation of colloidal suspensions in polar solvents.[12,13,26]

## 2.2. HIGH REFRACTIVE INDEX GELATIN NANOCOMPOSITES:

These Si nanoparticles were used to fabricate high refractive index nanocomposites, with refractive indices up to 3.2, when dispersed in gelatin.[30] Gelatin and poly(ethyleneoxide) have been extensively used for the fabrication of high refractive index nanocomposites with PbS.[6-8] The multiple functional sites in gelatin, a denatured protein, and its solubility in polar protic solvents such as water and ethanol makes it a matrix of choice for the fabrication of silicon based nanocomposites. Mixing an aqueous solution of gelatin with the ethanolic suspension of Si nanoparticles and concentrating by bubbling N<sub>2</sub>, a viscous brown liquid was obtained. The color of this liquid offers a first indication that gelatin strongly interacts with the silicon nanoparticles and prevents them from agglomerating which would otherwise have resulted in a black, non transparent liquid. Low speed, slow acceleration spin coating results in high quality films (c.a. 30 - 50 nm) that are further densified by vacuum annealing at 150 °C.

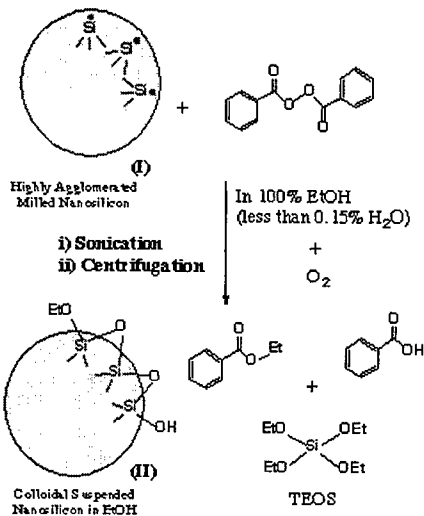
## 2.3. SELF-ASSEMBLED Si/SiO<sub>x</sub> NANOCOMPOSITES:

In an attempt to minimize concentration fluctuation, our research was recently shifted towards spontaneous nanoparticle adsorption on surfaces from dilute solutions. As it will quickly become apparent, this method offers significant advantages over highly filled systems for films below 1,000Å on various substrates such as glass, quartz, silver or gold.

The formation of stable Si colloids in polar solvents has been attributed to the growth of a thin surface oxide layer.[13,26,30,31] The thickness of such layer has been postulated to be particularly important to enable these relatively large particles to remain suspended,[30] although its minimum value is presently undetermined. With this in mind, a number of oxidizing agents were investigated to promote facile oxidation during sonication in EtOH. It was quickly recognized that when the moisture levels in 100% ethanol were kept low (H<sub>2</sub>O concentration < 0.15 %), and sonication took place in sealed containers, metastable Si colloids were produced that uniformly coat the inside wall of their glass container upon storage. The high energies achieved during sonication, apart from keeping the nanoparticles suspended in EtOH, also provide the means for performing chemistry, in the presence of oxidizing agents such as benzoyl peroxide or 3-

chloroperbenzoic acid.[32,33] A small amount of benzoyl peroxide ( $1.79 \times 10^{-4}$  M) was found to produce the optimum results in terms of concentration of Si nanoparticles.

Scheme 1 illustrates the chemistry performed during sonication as analyzed by GC/MS of the silicon colloid and FTIR spectroscopy. The presence of benzoic acid, benzoylethyl ester and tetraethoxysilane (TEOS), along with unreacted benzoyl peroxide indicate that sonication can provide considerable amount of energy not only to perform chemical reactions, such as the cleavage of benzoyl peroxide, the formation of benzoic acid and benzoylethyl ester but also convert some of the milled Si to TEOS.



*Scheme 1.* Schematic representation of the sonication-assisted oxidation of silicon nanoparticles

Figure 4A illustrates the FTIR spectrum of silicon nanoparticles (II), subjected to three consecutive centrifugation/decantation/resuspension cycles to remove all reactants and products of Scheme I that are non-bonded to nanoparticles. The underlying reactions of Scheme I facilitate the controlled release of H<sub>2</sub>O which in turns slowly oxidizes the surface of the Si nanoparticles forming Si-OH and Si-O-Si groups.[34] The silanol (SiOH) groups are witnessed with two doublets centered around 3712 and 3612 cm<sup>-1</sup> (associated with non-hydrogen bonded Si-O-H stretching) along with a much broader peak, centered around 3300 cm<sup>-1</sup>, from the hydrogen bonded Si-O-H stretching. At present, the origin of the two clearly resolved Si-O-H doublets is not entirely understood. Parameters such as the degree of association (between the neighbor SiOH and SiOH/SiOEt groups), the number of OH substitutions (single vs. geminal OH groups), variety in fractured crystal planes during nanomilling, and the degree of surface oxidation could affect the spectral signature of the Si-O-H stretching mode.[35-37] The strong absorption envelop between 1170-1050 cm<sup>-1</sup>, originates from Si-O-Si and Si-O-C stretching modes.[34,38] The shoulders at 1170 and 1055 cm<sup>-1</sup> correspond to ethoxysiloxane (SiOEt) groups (1170 cm<sup>-1</sup> for the CH<sub>3</sub> rocking absorption and 1055 cm<sup>-1</sup>

for the Si–O–Si stretching of  $\text{Si(OEt)}_n$  ( $n = 1,2,3$ ) groups).[38] The strong absorptions associated with C–H stretching (between  $2975 - 2850 \text{ cm}^{-1}$ ) and C–H deformation (five peaks between  $1700 - 1300 \text{ cm}^{-1}$ ) are additional evidence for the presence of ethoxysiloxane groups on the surface of these nanoparticles.[37]

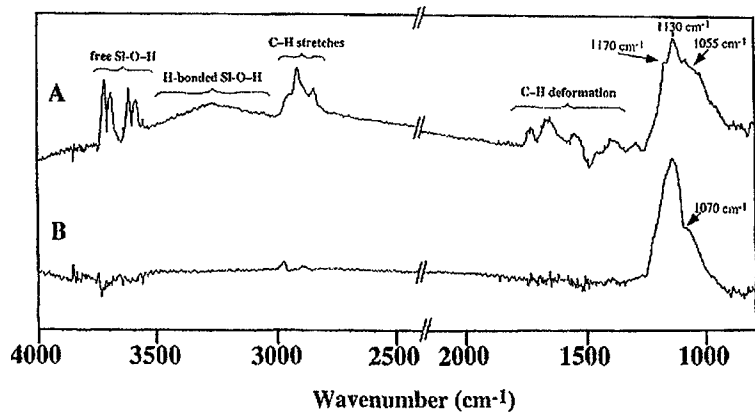


Figure 4. FTIR spectra of silicon nanoparticles II before (A) and after (B) their assembly on a  $\text{SiO}_2$  coated (ca. 400 Å) double-polished silicon substrate. (See text for details)

The thermally grown oxide on the double polished silicon substrate allows these nanoparticles to self-assemble on both sides, resulting in highly uniform films. Figure 4B depicts the FTIR spectrum of a 12 hrs. grown film. The relatively strong adhesion of these nanoparticle assemblies to the substrate prevent them from been lifted-off during subsequent washing in fresh ethanol to remove all reactants and products of Scheme I that are non-bonded to these assemblies. The significant reduction of the shoulders at  $1170$  and  $1055 \text{ cm}^{-1}$  indicates the formation of  $\text{SiO}_x$  network ( $1030$  and  $1070 \text{ cm}^{-1}$ ) at the expense of the ethoxysiloxane groups.[39] This is also confirmed by the disappearance of both free and hydrogen bonded SiOH groups along with a dramatic reduction in absorbance of the C–H stretching ( $\sim 2900 \text{ cm}^{-1}$ ) and C–H deformation ( $1700 - 1300 \text{ cm}^{-1}$ ) peaks.[40]

The formation of  $\text{SiO}_x$  network is strongly dependent on the pH of the ethanolic suspension.[41-43] The generation of benzoic acid (see Scheme 1) lowers the pH of the nanosilicon suspensions to  $5.0 \pm 0.5$ . At this range, the hydrolysis of TEOS and the ethoxysiloxane groups on the nanoparticles tends to be faster than the condensation of silanol groups to silica.[41,42] On the other hand, the surface oxidation of Si nanoparticles keeps the  $\text{H}_2\text{O}$  concentration in these suspensions sufficiently low which corroborates with the presence SiOEt groups at this pH (see Figure 4A). In addition, at pH of 5, the partial protonation of the ethoxysiloxane groups decorates these nanoparticles with a positive surface charge, which contributes to the stability of their suspensions.[42,43] Upon immersion of a fresh silica surface (glass or quartz substrates) in these suspensions, the following mechanisms are set in gear.

(i) The weaker nucleophilicity of SiOH and SiOSi groups (present at the surface of glass or quartz substrates) versus the SiOEt groups (on the nanoparticles) makes these substrates less prone to protonation at pH of 5.[42,43] This offers a plausible mechanism that accounts why nanoparticles of (II) are not repelled away from the surface of these substrates.

(ii) Upon substrate-nanoparticle contact, the slow condensation of silanol groups results in the formation of SiOSi bridges and generation of additional H<sub>2</sub>O. At pH of 5, this H<sub>2</sub>O will further promote the fast hydrolysis of SiOEt groups (from nanoparticles as well as TEOS) to SiOH groups, eventually to yield a SiO<sub>x</sub> matrix around the nanoparticles.[41-43] This is further corroborated by the complete elimination of the Si-O-H stretching in Figure 4B, which creates the slightly negative free Si-O-H absorption ( $\sim 3735\text{ cm}^{-1}$ ) as a result of substrate SiOH groups, which participate to this condensation (note that the FTIR spectra of double polished SiO<sub>2</sub>/Si/SiO<sub>2</sub> wafers were included into the spectrometer's background).[38]

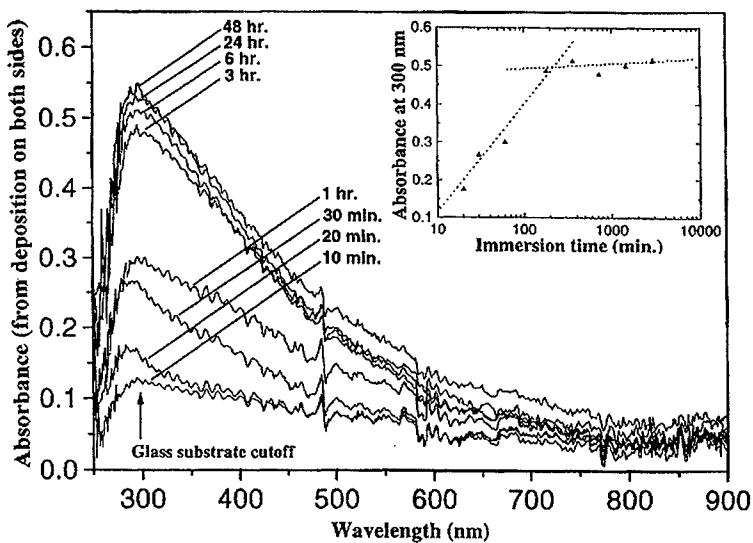


Figure 5. UV-vis absorption spectra of self-assembled Si/SiO<sub>x</sub> nanocomposites on both sides of glass substrates as a function of immersion time in a colloidal suspension of (II).

Figure 5 illustrates the UV-VIS absorption spectra of the adsorbed Si/SiO<sub>x</sub> nanocomposite on glass substrates as a function of immersion time in a colloidal suspension of (II). The rapid initial adsorption of this nanocomposite slows beyond 3 hours immersion time, revealing what appears to be a self-limiting deposition process. The optical quality and uniformity of such deposits are impressive, providing a nearly scatter-free coating on glass and quartz substrates. However, after 12 hours of immersion time, this coating begins to exhibit some scattering, which can be witnessed at the red spectral portion of Figure 5.

#### 2.4. RAMAN CHARACTERIZATION OF Si/SiO<sub>x</sub> NANOCOMPOSITES:

Raman spectroscopy has been shown to be suitable technique to study Si morphology.[44-46] Room temperature micro-Raman spectra were recorded on a Renishaw ramanoscope system equipped with a microscope attachment, in which the laser spot size could be focused to 1 mm in diameter (x100 objective), and with a power output of 35 mW. The excitation source was a 514.5-nm line of an argon ion laser. Figure 6 A illustrates the Raman spectrum of the starting polycrystalline Si powder (325-mesh size) as obtained from Alfa Aesar, with its equivalent XRD-spectrum illustrated in Figure 3A. Table 2 indicates that this is microcrystalline Si sample ( $c\text{-Si} = 511 \text{ cm}^{-1}$ )

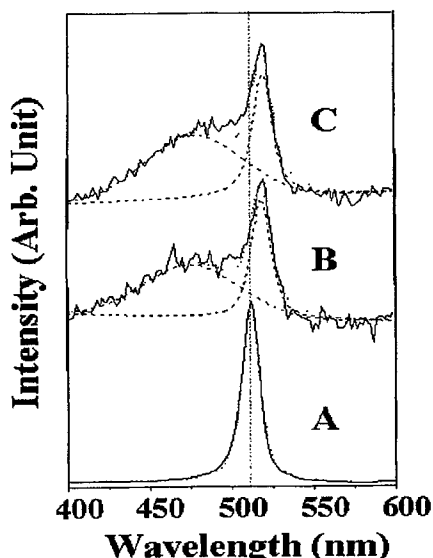


Figure 6. Room temperature Raman spectra of (A) mesh silicon, (B) as-milled Si, and (C) self-assembled Si/SiO<sub>x</sub> nanocomposites on a gold substrate.

TABLE 2. Raman peak values as determined by a Gaussian-Lorenzian fit of the Figure 6 spectra.

Material/Process	c-Si component			a-Si component		
	peak center cm <sup>-1</sup>	FWHM* cm <sup>-1</sup>	Relative Area	peak center cm <sup>-1</sup>	FWHM* cm <sup>-1</sup>	Relative Area
325-mesh polycrystalline Si powder <sup>†</sup>	511 ± 2	12 ± 1	c.a. 100%			
as-milled Si sample (5 hrs in inert atmosphere)	518 ± 2	14 ± 1	c.a. 36%	475 ± 2	67 ± 2	c.a. 64%
self-assembled Si/SiO <sub>x</sub> nanocomposites on gold	519 ± 2	12 ± 1	c.a. 30%	480 ± 2	69 ± 2	c.a. 70%

\* FWHM stands as full-width at half maximum.

<sup>†</sup> Obtained from Alfa-Aesar, (99.5% nominal purity).

with a nearly undetectable amorphous components. Raman shifts between 505 and 513  $\text{cm}^{-1}$  for crystalline Si have been reported by Kamiya *et al.*[44] A 512  $\text{cm}^{-1}$  centered Raman peak for microcrystalline Si phase is due to TO phonons confined in microcrystals with diameter of several hundred angstroms. Iqbal and Veprek have shown that the peak frequency decreases from the single crystal value of 520  $\text{cm}^{-1}$  to 512  $\text{cm}^{-1}$  for a crystallite size of 35  $\text{\AA}$ .[45]

Figure 6B depicts the Raman spectrum of the as-milled Si (5 hours in inert atmosphere). Please note that the sample were exposed to air during the collection of its Raman spectrum as well as its equivalent XRD spectrum illustrated in Figure 3B. The broad *a*-Si Raman line, peaking at 475  $\text{cm}^{-1}$  indicates considerable amorphization as a result of high-energy milling as reported by Shen *et al.*[27] and concurred by the significant line broadening shown in Figure 3. Contrary to the expected, the 518  $\text{cm}^{-1}$  *c*-Si Raman peak indicates a pressure induced crystallite-refinement, also witnessed by Shen *et al.*[27] This was explained on the basis of elevated temperatures reached during high energy milling causing a small fraction of the crystals to grow to more perfect crystallites which are responsible for the up-shift of *c*-Si Raman peak to higher frequencies.

Olego *et al.*[46] proposed a model of the microcrystalline structure of annealed  $\text{SiO}_x$  semi-insulating polycrystalline silicon (SIPOS) films grown by low-pressure chemical vapor deposition. Based on Olego's model and corroborating unreported X-ray Photoelectron Spectroscopy data, these  $\text{Si}/\text{SiO}_x$  nanoparticles appear to have a nanocrystalline Si interior, coated with an amorphous Si shell, quite amenable for sonication assisted oxidation.

### 3. References

1. Klabunde, K.J. (1994) *Free atoms, clusters, and nanoscale particles*, Academic Press, San Diego.
2. Moser, W.R. (1996) *Advanced catalysts and nanostructured materials: modern synthetic methods*, Academic Press, San Diego.
3. Hoch, H.C., Jelinski, L.W. and Craighead, H.G. (1996) *Nanofabrication and biosystems: integrating materials science, engineering and biology*, Cambridge University Press, Cambridge.
4. Busch, K. and John, S. (1998) Photonic Band Gap Formation in Certain Self-Organizing Systems, *Physical Review E* **58**, 3896.
5. Joannopoulos, J.D., Meade, R.D. and Winn, J.N. (1995) *Photonic Crystals: Molding the Flow of Light*, Princeton University Press, Princeton, NJ.
6. Weibel, M., Caseri, W., Suter, U.W., Kiess, H. and Wehrli, E. (1991) Preparation of Polymer Nanocomposites with "Ultrahigh" Refractive Index, *Polymers for Advanced Technologies* **2**, 75-80.
7. Zimmermann, L., Weibel, M., Caseri, W. and Suter, U.W. (1993) High refractive index films of polymer nanocomposites, *J. Mater. Res.* **8**, 1742.

8. Kyprianidou-Leodidou, T., Caseri, W. and Suter, U.W. (1994) Size Variation of PbS Particles in High-Refractive-Index Nanocomposites, *J. Phys. Chem.* **98**, 8992.
9. Kitai, A.H. (1993) *Solid State Luminescence*, Chapman & Hall, London.
10. Palik, E.D. (1985) *Handbook of Optical Constants of Solids*, Academic Press, Orlando.
11. Sugiyama, T., Wada, T. and Sasabe, H. (1989) Optical nonlinearity of conjugated polymers, *Synth. Metals* **28**, C323.
12. Fojtik, A., Weller, H., Fiechter, S. and Henglein, A. (1987) Preparation of Colloidal Silicon and Preliminary Photochemical Experiments, *Chemical Physics Letters* **134**, 477.
13. Littau, K.A., Szajowski, P.J., Muller, A.J., Kortan, A.R. and Brus, L.E. (1993) A luminescent silicon nanocrystal colloid via a high-temperature aerosol reaction, *J. Phys. Chem.* **97**, 1224.
14. Takagi, H., Ogawa, H., Yamazaki, Y., Ishizaki, A. and Nakagiri, T. (1990) Quantum size effects on photoluminescence in ultrathin Si particles, *Appl. Phys. Lett.* **56**, 2379.
15. Rueckschloss, M., Ambacher, O. and Veprek, S. (1993) Structural aspects of light emitting nc-Si prepared by plasma CVD, *J. Lumin.* **57**, 1.
16. Zhang, D. *et al.* (1994) Light emission from thermally oxidized silicon nanoparticles, *Appl. Phys. Lett.* **65**, 2684.
17. Nakajima, A., Sugita, Y., Kawamura, K., Tomita, H. and Yokoyama, N. (1996) Microstructure and Optical Absorption Properties of Silicon Nanocrystals Fabricated with Low Pressure Chemical Vapor Deposition, *J. Appl. Phys.* **80**, 4006.
18. Furukawa, S. and Niyasato, T. (1988) Quantum size effects on optical band gap of microcrystalline Si:H, *Phys. Rev. B* **38**, 5726.
19. Osaka, Y., Tsunetomo, K., Toyomura, F., Myoren, H. and Kohno, K. (1992) Visible photoluminescence from Si microcrystals embedded in silica glass films, *Jpn. J. Appl. Phys.* **31**, L365.
20. Sun, Y., Nishitani, R. and Miyasato, T. (1994) Study of hydrogen ion bombardement effect on the growth of Si:H films prepared by hydrogen plasma sputtering of silicon, *Jpn. J. Appl. Phys.* **33**, L1645.
21. Morisaki, H., Ping, F.W., Ono, H. and Yazawa, K. (1991) Above-band-gap photoluminescence from silicon fine particles with oxide shell, *J. Appl. Phys.* **70**, 1869.
22. Canham, L.T. (1990) Silicon quantum wire array fabrication by electrochemical and chemical dissolution, *Appl. Phys. Lett.* **57**, 1046.
23. Lehmann, V. and Gösele, U. (1991) Porous silicon formation: a quantum wire effect, *Appl. Phys. Lett.* **58**, 856.
24. Nakajima, A., Itakura, T., Watanabe, S. and Nakayama, N. (1992) Photoluminescence of porous silicon, oxidized then deoxidized chemically, *Appl. Phys. Lett.* **61**, 46.
25. Heinrich, J.L., Curtis, C.L., Credo, G.M., Kavanagh, K.L. and Sailor, M.J. (1992) Luminescent Colloidal Silicon Suspensions from Porous Silicon, *Science* **255**, 66.
26. Bley, R.A., Kauzlarich, S.M., Davis, J.E. and Lee, H.W.H. (1996) Characterization of Silicon Nanoparticles prepared from porous Silicon, *Chem. Mater.* **8**, 1881.

---

27. Shen, T.D. *et al.* (1995) The structure and property characteristics of amorphous/nanocrystalline silicon produced by ball milling, *J. Mater. Res.* **10**, 139.

28. Behren, J.v., Tsybeskov, L. and Fauchet, P.M. (1995) Preparation and Characterization of Ultrathin porous Silicon Films, *Appl. Phys. Lett.* **66**, 1662.

29. Zhang, C. *et al.* (1994) Blue electroluminescent diodes utilizing blends of poly(p-phenylene vinylene) in poly(9-vinylcarbazole), *Synthetic Metals* **62**, 35.

30. Papadimitrakopoulos, F., Wisniecki, P. and Bhagwagar, D.E. (1997) Mechanically Attrited Silicon For High Refractive Index Nanocomposites., *Chem. Mat.* **9**, 2928.

31. Bhagwagar, D.E., Wisniecki, P. and Papadimitrakopoulos, F. (1997) Characterization of Nanosized Silicon Prepared by Mechanical Attrition for High Refractive Index Nanocomposites, *Mat. Res. Soc. Symp. Ser.* **457**, 439.

32. Suslick, K.S., Fang, M. and Hyeon, T. (1996) Sonochemical Synthesis of Iron Colloid, *J. Am. Chem. Soc.* **118**, 11960.

33. Suslick, K.S., Hyeon, T. and Fang, M. (1996) Nanostructured Materials Generated by High-Intensity Ultrasound: Sonochemical Synthesis and Catalytic Studies, *Chem. Mater.* **8**, 2172.

34. Liao, W.S. and Lee, S.C. (1996) Water-Induced room-temperature Oxidation of Si-H and -Si-Si- bonds in Silicon Oxide, *J. Appl. Phys.* **80**, 1171.

35. Mawhinney, D.B., Glass, J.A. and Yates, J.T. (1997) FTIR Study of the Oxidation of Porous Silicon, *J. Phys. Chem. B* **101**, 1202.

36. Hoffmann, P. and Knozinger, E. (1987) Novel Aspects of Mid and Far IR Fourier Spectroscopy Applied to Surface and Adsorption Studies on SiO<sub>2</sub>, *Surface Science* **188**, 181-198.

37. Tedder, L.L., Lu, G. and Crowell, J.E. (1991) Mechanistic Studies of Dielectric Thin Film Growth by Low Pressure Chemical Vapor Deposition: The Reaction of Tetraethoxysilane with SiO<sub>2</sub> Surfaces, *J. Appl. Phys.* **69**, 7037.

38. Deshmukh, S.C. and Aydil, E.S. (1995) Investigation of SiO<sub>2</sub> Plasma Enhanced Chemical Vapor Deposition Through Tetraethoxysilane Using Attenuated Total Reflection Fourier Transform Infrared Spectroscopy, *J. Vac. Sci. Technol. A* **13**, 2355.

39. Ishii, K., Ohki, Y. and Nishikawa, H. (1994) Optical Characteristics of SiO<sub>2</sub> Formed by Plasma-enhanced Chemical-Vapor Deposition of Tetraethoxysilane, *J. Appl. Phys.* **76**, 5418.

40. Bao, T.I., Wu, M.S. and I., L. (1995) Infrared Studies of Room Temperature Deposition of Hydrogenated Silicon Oxide Films in RF Magnetron Discharges, *J. Appl. Phys.* **78**, 3342.

41. Keefer, K.D. (1990) Structure and Growth of Silica Condensation Polymers, in Zeigler, J. M. & Gordon-Fearon, F. W. (eds.), *Silicon-Based Polymer Science; A Comprehensive Resource*, ACS, Washington, **224**, 227-240.

42. McNeil, K.J., DiCaprio, J.A., Walsh, D.A. and Pratt, R.F. (1980) Kinetics and Mechanism of Hydrolysis of a Silicate Triester, Tri(2-methoxyethoxy)phenylsilane, *J. Am. Chem. Soc.* **102**, 1859.

43. Pohl, E.R. and Osterholtz, F.D. (1983) Kinetics and Mechanism of Aqueous Hydrolysis and Condensation of Alkyltrialkoxysilanes, in Ishida, H. & Kumar, G.

(eds.), *Molecular Characterization of Composite Interfaces*, Plenum Press, New York, 27.

44. Kamiya, T., Kishi, M., Ushirokawa, A. and Katoda, T. (1981) Observation of the amorphous-to-crystalline transition in silicon by Raman scattering, *Appl. Phys. Lett.* **38**, 377.

45. Iqbal, Z. and Veprek, S. (1982) Raman scattering from hydrogenated microcrystalline and amorphous silicon, *J. Phys. C: Solid State Phys.* **15**, 377.

46. Olego, D.J. and Baumgart, H. (1987) Semi-insulating polycrystalline Si thinn films, *J. Appl. Phys.* **63**, 2669.

---

## **PREPARATION AND CHARACTERISATION OF METALLIC THIN FILMS FOR ELECTROLUMINESCENT DEVICES BASED ON POROUS SILICON**

Irina Kleps, Anca Angelescu and Mihaela Miu  
National Institute for Research and Development in Microtechnologies  
(IMT), P.O.Box 38-160, Bucharest, Romania, fax: 40.1.2307519,  
tel.: 40.1.2313040/33, e-mail: <irinak@imt.ro>

### **Abstract**

For porous silicon (PS) electroluminescent (EL) devices, metallisation is a key process. The state of the art of the main preparation methods of thin metallic films used in PS EL devices is described. Experimental results concerning the structural and electrical characterisation of the metal/PS/p-Si structures are also presented. Different materials, like Au, In, Au-In, In-Sn, Al, etc., in a variety of preparation conditions were used as a solid-state contact on the PS layers. The luminescent properties of these structures were checked after metallic layer deposition by exciting the samples with an UV lamp. It is known that the transparency of a thin layer of 15 nm thickness is 60% or lower, finally only the luminescent structures were evaluated. Scanning Force Microscopy was used to investigate the film morphology; from the I-V characteristics of the metal/PS/p-Si structures it was determined:  $n < 3$ , series resistance  $< 500 \Omega$ , low values for contact resistance. The structures with low series resistance values, present the EL properties at lower value of the applied voltage, and are indicated for LED on PS type.

### **1. Introduction**

The porous silicon (PS), composed by Si nanocrystallites, prepared by the electrochemical etching opened the way to Si optoelectronic devices fabrication because it shows strong visible photoluminescence (PL) at room temperature [1]. Since 1991 many EL devices have been realised [2-5]. Most of them are made in a two step process: anodisation and deposition of a contact layer. Very thin metallic layers are often used as a solid contact on PS electroluminescent devices.

Metallisation is a key process with several requirements as follows: (i) it must ensure a good electrical contact between the metal layer and PS; (ii) the metal layer must be thin, to transmit as much light as possible from the PS beneath; (iii) there must be good control over the penetration depth of the metal into the pores.

The aim of this paper is to investigate the properties of different metallic contacts on porous silicon layers related to the preparation methods.

### **2. State of the art regarding the metallic thin films contacts for PS electroluminescent devices**

EL devices with different structures and characteristics have been reported. A very comprehensive study regarding different PS EL device structures was made by T. I. Cox [6]. So, there are described the following types of PS EL devices: (i) with top

contact on PS single layer (ii) p-n porosified junction, (iii) PS layer impregnated with another material, (iv) PS oxidised layer, (v) PS layer contacted by a non-porous semiconductor, (vi) PS layer in a microcavity, (vii) PS formed by stain etching. These varieties in EL device technologies make the comparison between the device characteristics more difficult. One of the major problems in the implementation of PS layers as solid-state light-emitting elements is the formation of a top electrode on the PS surface. Until now, different preparation methods for solid contact on PS EL device have been reported. An important drawback of the existing methods is related to the high electrical resistance of the contacts that require working voltages as high as 10-30 V, and result in a low quantum efficiency of the light emitting structures. The high value of the contact resistance is due to poor penetration of the deposited material into the PS pores. Additional problems of this poor contact are related to the insufficient adhesion of the deposited material.

The first EL devices were made by porosification of n- [2] or p- [3, 7] type Si with a top contact of either gold or indium tin oxide. The reported device [2] emitted red light at 200 V with a low efficiency. Later variants have threshold voltages as low as 1.35 V [8] and efficiency up to 0.05 % [9]. In any case, there are many factors which depend on the EL device properties. The efficiency of the PS EL devices is usually low ( $10^{-3}$  %), although some groups have reported lower values. The effect of using different metals [10] to contact PS layer produced by anodising under UV light has been studied. The peak wavelengths depend on the metal contact, and can be varied in the range 455 nm (indium) to 700 nm (antimony). One group has obtained a structure in which optically transmitting windows are produced in an opaque aluminium contact layer by anodically oxidising the aluminium to form transparent aluminium oxide [11-15]. The synthesis of the main PS solid contact preparation methods is presented below.

## 2.1. Physical vapour deposition (PVD) methods: thermal heating/electron beam evaporation and sputtering

The most usual methods for PS EL devices contact fabrication are evaporation and electron beam sputtering. In order to obtain a better penetration of the metallic layer in PS pores, the dynamic deposition regime at an angle of  $30^\circ$  is usually used for PS solid contacts.

It is generally known that PS fabricated by low-current density ( $1-100 \text{ mA/cm}^2$ ) anodisation has a spongelike structure with low carrier mobility [16]. For electroluminescent device applications, a sufficient electrode contact over the inside of PS, such as aqueous electrolyte contact [17], is necessary. However, these contacts are difficult to achieve by normal evaporation techniques, so that, the electrode-contact area is limited to the top of the surface, and the rest of the PS layer acts only as a resistor in such kind of diodes. Moreover, the large inner surface of the PS layer interacts with the air, and the oxidised PS causes the increase of the series resistance and the instability of the devices. The PS solid contact can be a single metal such as Au, Cr, Al, or can be formed by successive layers In/Au, In/Sn, Sn/Au or by the respective alloys. In the case of In-Au contact on PS, the device EL increase 150 times, and the emission light peak shifts towards lower wave numbers. In addition, the efficiency increases twice [10,18-19].

## 2.2. Electroplating method

In order to avoid the PS deterioration of luminescence properties, it is indicated to use a method to fill the pores with some material, such as the electrochemical processing. Metals such as gold, indium, or polymers such as polyaniline, polypyrrole, polyfuran and polythiophene have been deposited on PS as solid contacts.

This process is conducted in a liquid solution which penetrates over the entire depth of the pores and is stimulated by an electric field, thus making it possible to form a contact layer at the pore bottoms where the maximum electric field is localized. The conducting material is not required to completely fill the inner pore because this could short circuit the active layer. The best solution to increase the light device efficiency is to cover the Si skeleton walls with a very thin conductive layer in order to ensure the contact transparency. There are only a few published papers [20] on this subject because it is very difficult to approximate the PS area and the cathode/anode current density, in order to cover the Si skeleton walls and not to fill the pores.

## 2.3. Chemical vapour infiltration and deposition (CVID)

In this process a PS substrate is placed in a vacuum and is warmed. The process is monitored in such a way that the vapour precursor molecules have enough time to penetrate and decompose inside the PS pores. The vapour which has not penetrated into the pores will decompose above the warmed PS, resulting in a metal cap over the PS substrate surface. By this method, Co was deposited on and in a porous silicon layer using deuterated cobalt carbonyl hydride  $DCo(CO)_4$ . [21].

This precursor is unstable, and below  $22^\circ C$  decomposes and reacts with Si-H bonds on the pore walls to give Si-Co bonds.

## 3. Experimental data

Different materials such as Au, In, Au-In, Sn-Au, In-Sn, Al Cr, Ni, Mo, Ti, doped and undoped polypyrrole, obtained in a variety of preparation conditions have been used as solid-state contact on the PS layers for EL device applications (Table 1).

The luminescence from the metal/PS structures was observed by exciting the samples with an UV lamp. Only the properties of the luminescent structures were determined. Metal/PS morphology was investigated by scanning force microscopy (SFM) [22]. UV-visible spectra of the metals used as solid contact on PS were determined. The electrical characterisation of the metal/PS/p-Si structures was performed by current-voltage (I-V) measuring using a computer-interfaced Keithley apparatus. The structures were measured under forward (positive bias applied to p-Si) and reverse bias conditions, at room temperature.

### 3.1. Solid contacts preparation

The starting material was crystalline p-Si wafers (100) oriented and with  $6-10 \Omega cm$  resistivity. The PS layers formation was performed in an electrochemical process. The concentrations of the ethanoic HF solutions were 12% and the current densities  $10 \text{ mA/cm}^2$ , in order to obtain 80% porous silicon porosity [23].

Table 1. Experimental data

No	Solid contact layer			Luminescent properties of the contact/PS/Si structures		Electrical properties of the contact/PS/Si structures	
	Preparation	Thickness (nm)	Transmission (%) $\lambda = 660$ nm	Rs (k $\Omega$ )	$\phi B$ (eV)		
1.	Al, electron beam sputtering 10 <sup>-5</sup> torr, 1-2 A/sec	10 20	18 12	weak very weak	0.25	0.83-0.89	
2.	Au, electron beam sputtering, 10 <sup>-6</sup> torr	10	47	very good	0.45	0.79-0.84	
3.	Cr, electron beam sputtering 10 <sup>-6</sup> torr	6 10 20	43.5 30.5 14.8	very good good weak	-	-	
4.	Ti vacuum evaporation 5x10 <sup>-6</sup> Torr, 10 A/sec	10	38	good	-	-	
5.	Ni vacuum evaporation 5x10 <sup>-6</sup> Torr, 10 A/sec	10	32	good	-	-	
6.	Au vacuum evaporation 5x10 <sup>-6</sup> Torr, 10 A/sec	10	46	very good	-	-	
7.	Cr vacuum evaporation 5x10 <sup>-6</sup> Torr, 10 A/sec	10	31	good	-	-	
8.	Mo vacuum evaporation 5x10 <sup>-6</sup> Torr, 10 A/sec	10	30	good	-	-	
9.	In-Sn (9:1) vacuum evaporation, 10 <sup>-4</sup> Torr, air annealing at 120°C	100	35	good	0.38	0.9	
10.	In-Au (1:1) vacuum evaporation, 10 <sup>-5</sup> Torr, air annealing at 120°C	20	18	weak	25	0.98	
11.	In electrochemical deposition, 0.025M InCl <sub>3</sub> ,	undetermined	undetermined	very good	-	-	
12.	0.25 mA/cm <sup>2</sup> , 2 min, air annealing at 120°C t=2 min, air annealing at 120°C	undetermined	undetermined	very good	-	-	
13.	Au chemical deposition T=2 min, air annealing at 120°C	undetermined	undetermined	very good	-	-	

For the solid-state contact, after anodisation, conducting materials were formed on PS by (i) vacuum evaporation: Au, In, Au-In, In-Sn, Sn-Au, ITO, Al, Ti, Mo, Cr, Ni (2-3 A/sec and 25-30 A/sec), (ii) electrochemical deposition: Au, In, doped/undoped polypyrrole. The technological conditions were chosen in order to obtain thin, 10-20 nm metallic layers. The current densities for the electrochemical deposition processes were calculated for geometric surfaces of the samples: if the deposition takes place at the pore bottom only, current densities are the same, if the reaction takes place at the entire surface, real current densities are much lower.

### 3.2. Thin metallic films optical characterisation

The extinction coefficient changes with wavelength for each compound due to the changes in absorption (raising of energy states of the electrons) of the compound at different wavelengths (energy levels). A plot of the molar extinction coefficient versus wavelength will thus give a continuous curve of the wavelengths of absorption of a given compound. The extinction index values for different metals, after Johnson and Christy [24], indicate a better transmission in high energy zone,  $E=2-2.75$  eV, (450-550 nm). It can be observed that gold is the best metal to be used as contact for the electroluminescent devices emitting in the blue zone, while chromium, and after that gold, cooper, and titanium are more suitable for the red light zone.

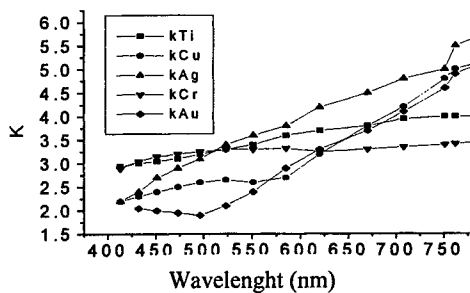


Fig. 1. The extinction index of some usual metals used as contacts on PS (after Johnson and Christy [24]).

The UV-visible transmission light of the metallic thin layer used as PS contact was determined (Fig.2). The transmission light through the investigated materials was in good agreement with the literature data [24]. It can be seen that the light transmission decreases dramatically with the film thickness; practically only very thin film,  $d \leq 10-12$  nm can be used as solid contacts on PS. The In, In-Au, and In-Sn light transmission was not determined, but all these layers have good light transmission properties, even though they are thicker than 20 nm, due to their partial oxidation in air atmosphere.

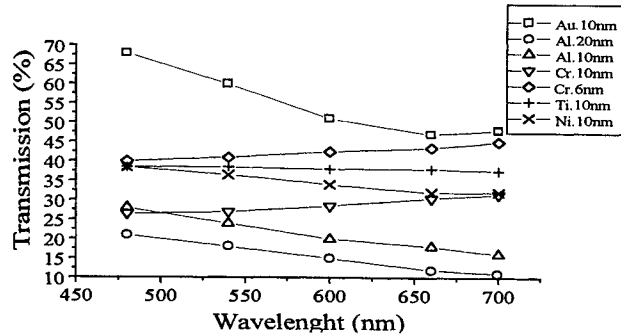


Fig. 2. The transmission spectra of vacuum evaporated metallic films, in the wavelength interval characteristic for PS light emission.

### 3.3. Metal/PS structures morphology

Metal layers cover the PS layers. 80% PS layers without metallic contact (Fig. 3a) and with Au contacts on its surface (Fig. 3b) was investigated by SFM.

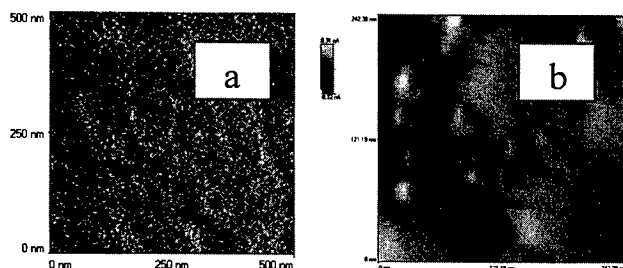


Fig 3. AFM image for 80% PS (a) and for Au/80% PS/p-Si (b)

Due to the small dimensions of PS fibrils (3-5 nm), the thin metallic film does not follow the shape of the PS surface, it is only applied on the top of the Si fibrils. However, from the SIMS spectra indicated a penetration of the metallic layer into the PS pores of about 20 nm (Fig. 4) [23].

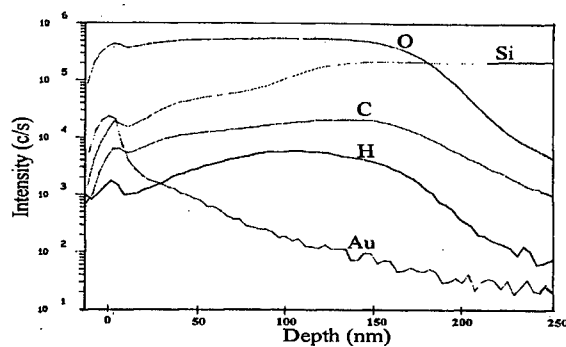


Fig. 4. SIMS depth profile of the Au/PS structure.

### 3.4. Electrical characterisation

To explore the mechanism of room-temperature visible EL from LED/PS, it is very important to characterize the electrical properties of the conducting material/PS interface. From the current-voltage measurements, the characteristics of the different metallic contacts / 80%PS / Si-p structures show a rectifying behavior (Fig. 5). These curves were analyzed using the thermionic emission equation.

At low injection levels (< 0.2V) the I-V characteristics are different for Al contacts and InSn, Au, and In contacts. An explanation is that the better contact metal / PS was electrochemically obtained for InSn, Au, and In compared to vacuum deposited Al. This is due to the better penetration of the pores by the electrolyte solution. The lower  $n$  values at low injection levels are due to the reduction of the interface states, as a result of the good stabilization of the PS surface.  $\phi_b$  is in the same range of values: 0.83 eV (Al), 0.72 eV (InSn), 0.75 eV (Au). The best contact with lower series resistance and lower ideality factor is realized by electrochemically deposited In. These type of structures are indicated for LED on PS.

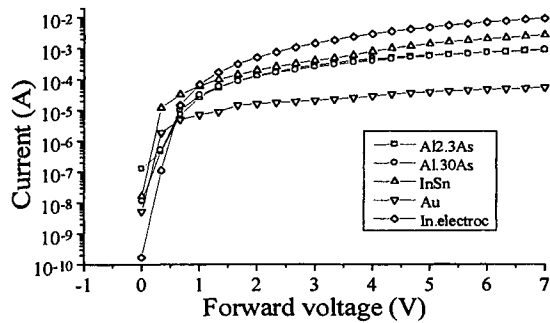


Fig. 5. I-V forward characteristics for some metallic layers used as LED solid contacts

### 4. Conclusions

Different thin films were investigated as the solid contact for PS electroluminescent devices. The electrical measurements demonstrated that the electrochemical processes are suitable for preparing metallic contacts on PS electroluminescent devices. The gold represents the best choice due to its high light emission transmission, on the whole wavelength light emission domain of the PS. Also, good results were obtained using electrochemical In and vacuum deposited In-Sn contacts, annealed in air at 120°C.

### Acknowledgements

The authors acknowledge the support of the European Community through the INCO-COPERNICUS program, contract SBLED No. 7037 / 1998 and the support of the National Agency for Science, Technology and Innovation.

## References

1. Canham, L. T. (1990) Silicon quantum wire array fabrication by electrochemical and chemical dissolution of wafers, *Appl. Phys. Lett.* 57, 1046-1049.
2. Richer, A., Steiner, P., Kozlowski, F. and Lang, W. (1991) Current induced light emission from porous silicon device, *IEEE Electron Dev. Lett.* 12, 691.
3. Koshida, N. and Koyama, H. (1992), Visible electroluminescence from porous silicon, *Appl. Phys. Lett.* 60, 347-350.
4. Steiner, P., Kozlowski F. and Lang, W. (1993) Blue and green electroluminescence from a porous silicon device, *IEEE Electron Device Letters*, vol. 14, no. 7, 317-319.
5. Lang, W. (1998), Porous silicon Electroluminescent Devices in G. Amato, C. Delerue, H. J. Bardeleben, (eds.), *Structural and Optical Properties of Silicon Nanostructures*, Gordon and Breach Science Publishers, pp. 539-555.
6. Cox T. I. (1997), Electroluminescence from porous silicon using solid state contacts, in L. Canham (ed.), *Properties of porous Silicon*, EMIS Dataviews Series No. 18, Published by INSPEC, IEEE London, UK, pp. 290-310.
7. Muraska, H. P., Namavar, F., Kalkhoran, N. M., (1992) Visible electroluminescence from porous silicon np heterojunction diodes, *Appl. Phys. Lett. (USA)*, vol. 61, 2514.
8. Kozlowski, F., Steiner, P., Lang, W. (1993) Electroluminescence from porous silicon in D. C. Bensahel, L. T. Canham, S. Ossicini (eds), *Optical properties of low dimensional silicon structures*, Proc. NATO-ARW, Series E, Applied Sciences, vol. 244, 123-132.
9. T. Oguro, H. Koyama, T. Ozaka, N. Koshida (1997) Mechanism of the visible electroluminescence from metal/porous silicon /n-Si devices, *J. Appl. Phys. (USA)* vol. 81 1407-1412.
10. Steiner, P., Wiedenhofer, A., Kozlowski, F., Lang, W., (1996), Influence of different metallic contacts on PS electroluminescence, *Thin Solid Films*, vol. 276, 159-163.
11. Lazarouk S., Bondarenko V., Jaguairo P., Lacquaniti N., Maiello G., La Monica S., Masini G., Ferrari A. (1996) Electrical characterization of visible emitting electroluminescent Schottky diodes based on n-type porous silicon and on highly doped n-type porous polysilicon , *Journal of Non-Crystalline Solids*, v.198-200, 973-976.
12. Lazarouk, S., Jaguairo, P., Katsouba, S., Prohorenko, A., Masini, G., La Monica, S., Maiello, G., Ferrari, A. (1996) Silicon-based optical interconnections, MRS Symposium Q, *Advances in Microcrystalline and Nanocrystalline Semiconductors*, 2 - 6.
13. Jaguairo, P., La Monica, S., Balucani, M., Lazarouk, S., Maiello, G., Masini, G., Ferrari, A. (1997) Characterization of Porous Silicon Light Emitting Diodes in High Current Density Conditions, *Solid State Phenomena*, Vol. 54, 21-26.
14. Lazarouk, S., Jaguairo, P., Katsouba, S., Masini, G., La Monica, S., Maiello, G., Ferrari, A., (1996) Stable electroluminescence from reverse biased n-type porous silicon-aluminum Schottky junction device, *Appl. Phys. Lett.*, vol. 68, 2108-2110..
15. Lazarouk, S., Jaguairo, P., Katsouba, S., La Monica, S., Maiello, G., Masini, G., Ferrari, A. (1996) Visible light from aluminium-porous silicon Schottky junctions, *Thin Solid Films*, vol. 276, 168-170.
16. Gosele, U. and Lehmann, V. (1994), Porous silicon, Porous Silicon Quantum Sponge Structures: Formation Mechanism, Preparation Methods and Some Properties, in Z. C. Feng and R. Tsu (eds.), *Porous silicon*, World Scientific, Singapore, p. 17.
17. Bsiesy, A., Muller, F., Ligeon, M., Gaspard, F., Herino, R., Romenstain, R. and Vial J. C. (1994) , Voltage-tuned electroluminescence of porous silicon, *Appl. Phys. Lett.*, 65, 3371-3374.
18. Steiner, P. Kozlowski, F. Wiedenhofer, A. Knoll, B. Lang, W.(1996) Fabrication and performance of electroluminescent porous silicon devices, *Proceedings of the International Symposium on Advanced Luminescent Materials*, 48-57.
19. Lang, W., Kozlowski, F., Steiner, P., Knoll, B., Wiedenhofer, A., Kollewe, D., Bachmann, T., (1997) Technology and RBS analysis of porous silicon light-emitting diodes, *Thin Solid Films*, vol. 297, no. 1-2, 268-271.
20. Lang, W., Steiner, P., Kozlowski, F. (1994) Optoelectronic properties of porous silicon-The electroluminescence devices, in J. C. Vial, J. Derrien (eds), *Porous silicon science and technology*, Springer-Verlag, Les Editions de Physique, pp. 293-305.
21. Aylett, B. J., Harding, I. S., Earwarker, L. G., Forcey, K., Giaddui, T. (1996) Metallisation of PS by chemical vapour infiltration and deposition, *Thin Solid Films*, 276, 253-256.
22. Matsumoto, T., Minura, H., Kanemitsu, Y. (1995) Photo- and electroluminescence from electrochemically polished silicon, *Jpn. J. Appl. Phys*, vol 34, , nr. 10B, L.1318-L1321.

23. Kleps, I., Angelescu, A. (1998) Porous silicon: material processing, properties and applications in light and field emission devices, *Romanian Journal of Information Science and Technology*, vol 1, nr. 2, 167-182.
24. Johnson, P. B. and Christy, R. W. (1972) Optical constants of noble metals, *Phys. Rev. B*, 6, 4370.

## PHOTOELECTROCHEMICAL BEHAVIOR OF CHLOROPHYLL a IN THIN FILMS

LAURA TUGULEA  
*Faculty of Physics-University of Bucharest  
P.O.Box Mg-11, Bucharest-Magurele  
76900 Romania*

### Abstract

The photoelectrochemical behavior of chlorophyll a species P740 (polymerized water adduct of chlorophyll a, absorbing at 740nm) was investigated using chlorophyll a thin films, electrodeposited on both  $\text{SnO}_2$  and  $\text{SnO}_2/\text{TiO}_2$  electrodes. The photocurrent action spectra of chlorophyll a in electrochemical devices are used to explain the chlorophyll a behavior in the process of charge generation under illumination and in the transfer of electrons. The use of nanoparticle-coated electrodes is promising for the building of efficient devices for light conversion, based on chlorophyll a.

### Keywords

Chlorophyll a, electron transfer, electronic structure, light activation, modeling, nanostructure, photoconversion, photoelectrochemistry

### 1. Introduction

Chlorophyll a is the major pigment in plant photosynthesis, being responsible for both light absorption and light induced charge separation. There has been much interest in photovoltaic and photoelectrochemical investigation of chlorophyll a and related pigments. Different types of photovoltaic devices have been studied; most of them using chlorophyll a in the form of solid layers coated on metal or semiconductor electrodes [1, 2]. In some photovoltaic experiments the chlorophyll a film sandwiched between two electrodes is sensitizing large bandgap semiconductors and extending their photoresponse in the visible domain [3, 4]. In photoelectrochemical measurements chlorophyll a was deposited on metal electrodes [5], but higher efficiencies for light photoconversion have been reported when chlorophyll was adsorbed on nanostructured semiconductor electrodes [6, 7]. As an extension of our previous work, done on photovoltaic devices with chlorophyll a [4, 8], we developed photoelectrochemical devices using chlorophyll a species absorbing at 740 nm. The experiments performed

on electrochemical devices using P740 chlorophyll a in thin films, electrodeposited on both  $\text{SnO}_2$  and  $\text{SnO}_2/\text{TiO}_2$  electrodes lead to a comparative study, and to the explanation of chlorophyll a behavior in the process of charge separation under illumination and of transfer of electrons.

## 2. Experimental section

### 2.1. MATERIALS

Chlorophyll a (Chla) was prepared from fresh spinach leaves by the Strain & Svec method and checked for purity (absorption and fluorescence in VIS). The chlorophyll a species P740 (polymerized water adduct of chlorophyll a, absorbing at 740nm) was obtained by dissolving the freshly prepared chlorophyll a in n-pentane (Merck), and maintaining the solution/suspension at temperatures below -10°C. Analytical grade solvents were used without further purification. The  $\text{SnO}_2$  coated electrode was cut from a commercial transparent conducting glass plate, having the dimension  $3 \times 3 \text{ cm}^2$  and sheet resistance  $20 \Omega/\text{sq}$ . The optical transparency of the electrode was 85% in the visible wavelengths. The transparent conducting glass was chemically cleaned before use to remove any residual grease. The  $\text{SnO}_2/\text{TiO}_2$  electrode was cut from a coated glass plate prepared at University of Uppsala. The Lindquist's procedure [9] for nanocrystalline  $\text{TiO}_2$  film electrodes preparation yields films of  $4 \mu\text{m}$  thickness, porous from the outer layer to the transparent conducting glass ( $\text{SnO}_2$ ), with relatively uniform particle size of 15 nm in diameter [9]. The  $\text{SnO}_2/\text{TiO}_2$  glass electrode ( $3 \times 3 \text{ cm}^2$ ) was heated for 10 min at 500°C, and then immersed in n-pentane. The chlorophyll a film was subsequently formed on the glass electrode.

### 2.2. FILM PREPARATION

Thin films of chlorophyll a were prepared by electrodeposition. On both types of electrodes,  $\text{SnO}_2$  and  $\text{SnO}_2/\text{TiO}_2$ , a thin layer of chlorophyll a (of various thickness) was electrodeposited from the suspension/solution of chlorophyll a in n-pentane. The suspension/solution of chlorophyll a was sonicated before use, in order to get uniform size for suspended chlorophyll a molecular aggregates. The  $\text{SnO}_2$  or  $\text{SnO}_2/\text{TiO}_2$  coated glass electrode was the cathode, and the applied electric field had an intensity of 1000V/cm. The film thickness was controlled by varying the molar concentration of Chla solution and/or by varying the electrodeposition time. The film thickness was estimated from the absorption spectra, using the O.D. at 740 nm. The optical absorption spectra of the films were obtained on a double beam UV - VIS spectrophotometer Lambda 2S Perkin Elmer & PECSS software.

### 2.3. PHOTOELECTROCHEMICAL MEASUREMENTS

The  $\text{SnO}_2$  and  $\text{SnO}_2/\text{TiO}_2$  electrodes coated with a thin film of P740 chlorophyll a represented the working electrode in a three-electrode electrochemical cell. A Pt foil was used as the counter electrode and a standard  $\text{Ag}/\text{AgCl}$  (saturated  $\text{KCl}$  in water) electrode as the reference. Solutions of  $\text{Na}_2\text{SO}_4$  of different ionic strengths in phosphate

buffers (pH range: 6.9 - 8) were used as electrolytes.  $\mu$ AUTOLAB (Eco-Chemie) electrochemical analyzer and GPES software were used to perform the experiments on the electrochemical cell. The working electrode (on area of about  $0.4\text{ cm}^2$ ) was illuminated by monochromatic light (in the spectral range 350 - 800 nm) using a halogen lamp of 650 W. The amperometric mode was used and the photocurrents represented the difference between the currents under illumination (different wavelengths) and dark currents. All measurements were performed in air and at room temperature. Photocurrent action spectra were obtained by plotting the photocurrents, measured for a given electrode voltage at different wavelengths. The action spectra were corrected to equal photon density at each wavelengths and normalized (the peak at 800 nm is unity).

### 3. Results and discussions

#### 3.1. PHOTOELECTROCHEMICAL STUDIES

The spectral behavior of the photoelectrochemical cells was investigated and compared with the absorption spectrum of chlorophyll a films. Anodic photocurrents have been observed at both  $\text{SnO}_2$  and  $\text{SnO}_2/\text{TiO}_2$  electrodes with electrodeposited chlorophyll a film under potential-controlled conditions, in the range more anodic than  $-0.17\text{ V}$  vs.  $\text{Ag}/\text{AgCl}$ . Typical photocurrent spectra are illustrated in Figures 1 and 2 together with the corresponding absorption spectra of chlorophyll a films.

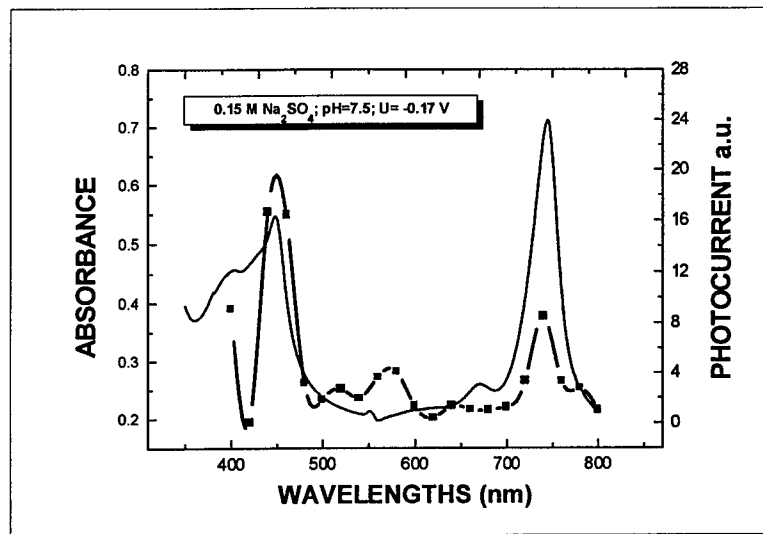


Figure 1. Photocurrent spectrum of Chl a on  $\text{SnO}_2/\text{TiO}_2$  electrode (dotted line) and absorption spectrum of the chlorophyll a film

As is evident from Figure 1, the action and absorption spectra coincide fairly well when chlorophyll a was electrodeposited on the  $\text{SnO}_2/\text{TiO}_2$  electrode. This means that chlorophyll a is sensitizing the  $\text{SnO}_2/\text{TiO}_2$  composite system. The absorption spectrum of the chlorophyll a film shows the Soret band and the red ( $Q_y$ ) band shifts to 740 nm. This indicates that the polymerized water adduct of chlorophyll a, absorbing at 740 nm, determines the photoresponse of the composite system. This special molecular aggregate of chlorophyll a is known as "microcrystalline chlorophyll a" [10] or as "micelle chlorophyll a" [11]. The size of these molecular aggregates (P740), either crystalline or micelle, having a specific absorption at 740 nm, is in the range of tens to hundred of nm. The chlorophyll a film thickness was in the range of 100 nm, as estimated from optical density at 740 nm.

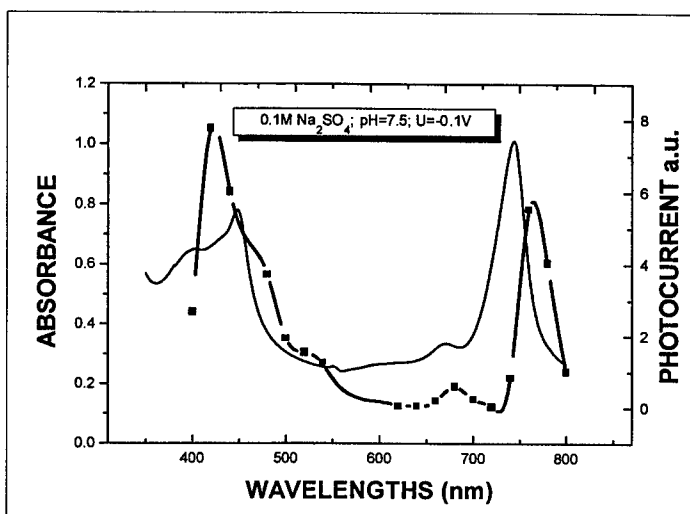
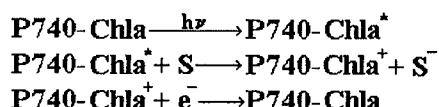


Figure 2. Photocurrent spectrum of Chl a on  $\text{SnO}_2$  electrode (dotted line) and absorption spectrum of the chlorophyll a film

The same chlorophyll a species, as resulting from the absorption spectrum presented in Figure 2, but electrodeposited on  $\text{SnO}_2$  electrode, is responsible for the photoeffects represented by the action spectrum in the same figure. The red band in the action spectrum presents a small shift of about 20 nm, as compared with the  $Q_y$  band of chlorophyll a film absorption. All investigated photoelectrochemical cells, prepared by electrodeposition of chlorophyll a on  $\text{SnO}_2$  electrodes, presented the same type of behavior, regardless of chlorophyll a film thickness or electrolyte characteristics.

Generation of anodic photocurrents was interpreted schematically in terms of the electron donation from excited P740-chlorophyll a to  $\text{SnO}_2$  or  $\text{SnO}_2/\text{TiO}_2$  electrode, followed by the reduction of Chl a cation by the free electrons from the electrolyte solution:



S being the semiconductor electrode ( $\text{SnO}_2$  or  $\text{SnO}_2/\text{TiO}_2$ ) of the electrochemical cell.

The energy diagram (Figure 3) depicts the band energies of electrodes and oxidation potential of chlorophyll a. In both cases, the more negative value of the excited state of chlorophyll a facilitates the photoinduced electron transfer from chlorophyll a to the semiconductor electrode. In case A, there is a close interaction between the large molecular aggregates of P740 chlorophyll a and the polar surface of  $\text{SnO}_2$ . As a consequence, the electric field at the interface chlorophyll a/ $\text{SnO}_2$  electrode affects the energy levels of the photoactive P740-chlorophyll a. This explains the difference between photocurrent action spectrum and film absorption in the case of photoelectrochemical cells with P740-chlorophyll a electrodeposited on  $\text{SnO}_2$  electrodes.

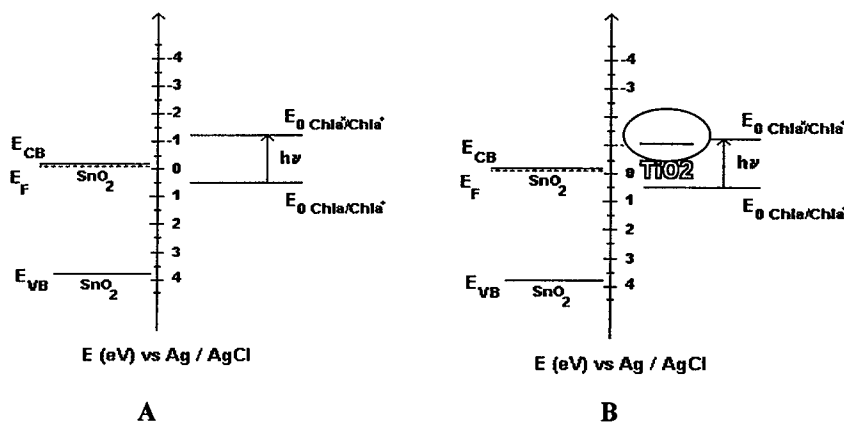


Figure 3. Schematic energy diagrams at the interface:  
chlorophyll a/ $\text{SnO}_2$  electrode (A), chlorophyll a/ $\text{SnO}_2/\text{TiO}_2$  electrode (B)

In case B, the electrolyte ions permeate the nanocrystalline  $\text{TiO}_2$  film and, as in normal solution electrochemistry, the mobile ions neutralize any electric field. At normal concentrations (0.1- 0.5 M), the electrolyte prevents the extension of an electric field of over more than 20-50 nm [12]. As a consequence, a coincidence between the action spectrum and the absorption spectrum of P740 chlorophyll a is expected. This coincidence is illustrated in Figure 1. This also means that in the case of nanostructured electrode  $\text{SnO}_2/\text{TiO}_2$ , the photoinduced electron transfer from chlorophyll a to electrode is not field-assisted. Under illumination chlorophyll a, excited to a higher electronic state, injects electrons into  $\text{TiO}_2$  particles. These electrons are then collected at the interface  $\text{SnO}_2/\text{TiO}_2$  to produce anodic photocurrents.

A further conclusion is that the large chlorophyll a molecular aggregates, electrodeposited on porous film of  $\text{TiO}_2$  nanoparticles, are closer outside the ionic double layer at the solid/solution interface. This is also supported by the observed dependence of the electrochemical cell photoresponse on the pH value of the electrolyte solution.

Figure 4 presents the pH dependence of the photoresponse when using electrochemical cells with the same thickness of chlorophyll a film, and electrolyte solutions with the same ionic strength. The value of 7.5 was found to be the optimum pH. Chlorophyll a loses the central Mg through chemical reaction with protons; at acidic pH, chlorophyll undergoes a decomposition resulting in the formation of pheophytin a. This known instability of chlorophyll a species could be the explanation for the observed behavior of photoresponse in electrochemical cells using more acidic electrolytes.

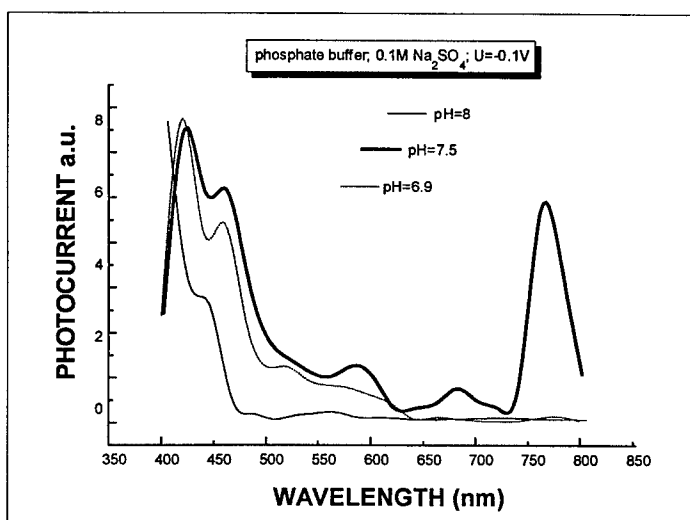


Figure 4. Photocurrent spectra of Chl a on  $\text{SnO}_2/\text{TiO}_2$  electrode at different pH values of the electrolyte

A change in the pH of the electrolyte solution causes, in many situations, a shift of the semiconductor electrode potential, induced by the dissociation equilibrium of protons at the electrode surface [13]. In the studied electrochemical cells, the electrode potential can exhibit cathodic shift by increasing pH. A shift of the electrode potential to more negative values affects the driving force for the photoinduced electron transfer from chlorophyll a to the electrode. The energy difference between the excited dye and the semiconductor is critical in controlling the electron transfer. This explains the situation illustrated in Figure 4: a photoresponse is only present when illuminating with the wavelengths corresponding to the Soret band of chlorophyll a absorption spectrum, i.e. exciting chlorophyll species to the second (higher) singlet state.

### 3.2. EFFICIENCY OF PHOTOCURRENT GENERATION

As already shown, P740 chlorophyll a manifests the ability to sensitize large bandgap semiconductors like  $\text{SnO}_2$  and  $\text{TiO}_2$ . The electron transfer is taking place from the excited state of chlorophyll a to the semiconductor. Photoelectrochemical solar cells based on chlorophyll a could be easily obtained. The incident photon to current

conversion efficiency (IPCE), is obtained from the measurements of short circuit photocurrents at various wavelengths and using the following equation [14]:

$$IPCE(\%) = \frac{I_{sc}}{I_{inc}} \frac{1240}{\lambda} 100$$

where  $I_{sc}$  is the short circuit photocurrent,  $\lambda$  is the wavelength and  $I_{inc}$  is the light intensity incident on chlorophyll a. A maximum IPCE of 1.2%, at 740 nm incident light, was obtained for the photoelectrochemical cell, with photocurrent action spectrum presented in Figure 5. The chlorophyll a film thickness is less than 100nm. Making the corrections for absorption, a value of about 2% can be considered.

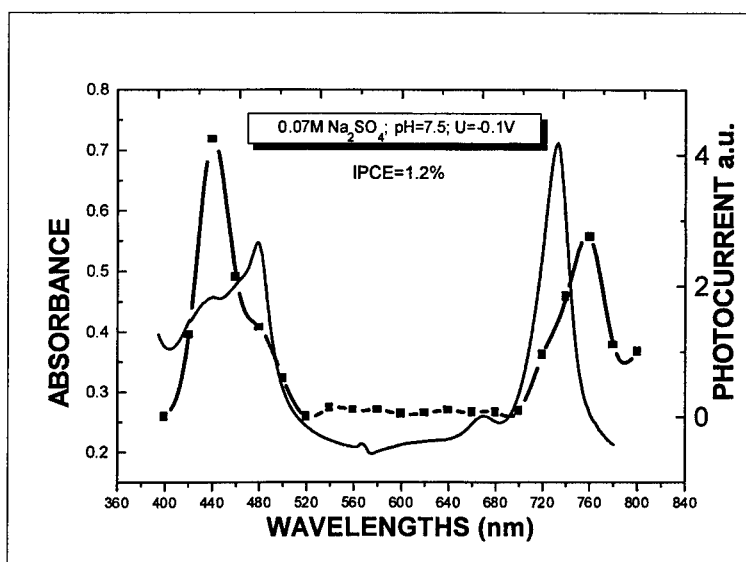


Figure 5. Photocurrent spectrum of Chl a on  $\text{SnO}_2$  electrode (dotted line) and absorption spectrum of the chlorophyll a film

Optimization of the photoelectrochemical cell, with respect to the efficient charge photogeneration and reduction of recombination losses, can be achieved by controlling the parameters of both chlorophyll a sensitized electrode and electrolyte solution.

#### 4. Conclusion

The present study of photoelectrochemical devices based on P740 chlorophyll a, electrodeposited as thin films on large band gap semiconductors, leads to the conclusion that chlorophyll a is the photoactive component. The nature of the semiconductor electrode (i.e. nanoparticulate, porous or uniform film) at the interface with P740 chlorophyll a thin film proved to be the dominant factor in controlling the photoinduced electron transfer.

### Acknowledgments

The author would like to thank Professor Sten-Eric Lindquist, University of Uppsala, Sweden for providing the  $\text{SnO}_2/\text{TiO}_2$  glass plates and for helpful discussions.

### References

1. Tang, C.W., Albrecht, A.C. (1975) Photovoltaic effects of metal-chlorophyll a-metal sandwich cells, *J. Chemical Physics* **62**, 2139-2149
2. Dodelet, J.P., Le Brech, J., Chapados C., Leblanc R.M. (1979) Photovoltaic action spectra and efficiencies of chlorophyll species absorbing near 700 nm, *Photochem. Photobiol.* **31**, 143-155
3. Segui J., Hotchandani S., Baddou D., Leblanc R.M. (1991) Photoelectric properties of ITO/CdS/Chlorophyll a/Ag heterojunction solar cells, *J.Phys.Chemistry* **95**, 8807-8812
4. Tugulea L., Antohe S. (1992) Photovoltaic characteristics of Si/Chlorophyll a structure, in N.Murata (ed.), *Research in Photosynthesis, II*, Kluwer Academic Publishers, pp. 845 - 848
5. Miyasaka T., Fujishima A., Honda K. (1981) Photoelectrochemical behavior of chlorophyll a-lipid films on a platinum electrode in an aqueous electrolyte, *Bull.Chem.Soc.Jpn.* **54**, 957-951
6. Kay A., Gratzel M. (1993) Artificial Photosynthesis. 1. Photosensitization of  $\text{TiO}_2$  solar cells with chlorophyll derivatives and related natural porphyrins, *J.Phys.Chemistry* **97**, 6272-6277
7. Bedja I., Kamat P.V., Hotchandani S. (1996) Fluorescence and photoelectrochemical behavior of chlorophyll a adsorbed on a nanocrystalline  $\text{SnO}_2$  film, *J.Appl.Physics* **80**, 4637-4643
8. Antohe S., Tugulea L., Gheorghe V., Ruxandra V., Caplanus I., Ion L.(1996) Electrical and photovoltaic properties of ITO/chlorophyll a /TPyP/Al junction cell, *Phys. Stat. Solidi (a)*, **153**, 581-588
9. Solbrand A., Lindstrom H., Rensmo H., Hagfeldt A., Lindquist S-E., Sodergren S. (1997) Electron transport in the nanostructured  $\text{TiO}_2$ -electrolyte system studied with time-resolved photocurrents, *J.Phys. Chemistry*, **101**, 2514-2518
10. Gheorghe V., Tugulea L., Teodorescu V. (1979) Transmission electron microscopy observation of chlorophyll a microcrystals, in V.Gheorghe, N.Gherbanovschi (eds.), *Experimental Trends in Physics*, IAP Press, Bucharest, pp.239 – 251
11. Worcester D.L., Michalski T.J., Katz J.J. (1986) Small-angle neutron scattering studies of chlorophyll micelles: Models for bacterial antenna chlorophyll, *Proc.Natl.Acad.Sci.USA*, **83**, 3791-3795
12. Gregg B.A., Zaban A., Ferrere S., Pichot F.(1998) Dye sensitized cells and organic semiconductors, *Twelfths International Conference on Photochemical conversion and storage of solar energy*, August 9-14, Berlin, pp.V4 (Book of abstracts)
13. Miyasaka T., Watanabe T., Fujishima A., Honda K. (1978) Light energy conversion with chlorophyll monolayer electrodes. In vitro electrochemical simulation of photosynthetic primary processes, *J. Am. Chem. Soc.* **100**, 6657-6665
14. Hotchandani S., Kamat P.V.(1992) Modification of electrode surface with semiconductor colloids and its sensitization with chlorophyll a, *Chem. Phys. Letters* **191**, 320- 326

## LEAN-BURN NATURAL GAS ENGINE EXHAUST REMEDIATION USING NANOSTRUCTURED CATALYSTS AND COATINGS

MARK D. FOKEMA, ANDREY J. ZARUR AND JACKIE Y. YING\*

*Department of Chemical Engineering, Massachusetts Institute of Technology  
77 Massachusetts Avenue, Cambridge, MA 02139, USA*

### Abstract

We have developed nanocrystalline catalytic systems with excellent thermal stability that reduce NO, CH<sub>4</sub> and CO emissions from exhaust streams containing excess oxygen. Magnesium oxide, yttrium oxide and samarium oxide catalysts were synthesized using a controlled wet-chemical precipitation technique. This process produces nanocrystalline, high surface area metal oxide powders that can be easily coated onto monoliths and substrates. Greater than 50% conversion of NO to N<sub>2</sub> was achieved in excess O<sub>2</sub> at high space velocities with the nanocrystalline oxide catalysts. Nanostructured barium hexaaluminate coated with manganese oxide was used to aid in the complete oxidation of CO and CH<sub>4</sub>. The nanocrystalline oxide systems have superior hydrothermal stability compared to noble metal and zeolitic catalysts. Presence of water vapor in the feed stream resulted in only a slight loss of activity for the nanocrystalline Y<sub>2</sub>O<sub>3</sub> system, the full activity of which was restored upon removal of water from the feed stream.

### Introduction

The development of catalytic materials that can simultaneously reduce NO<sub>x</sub>, and oxidize CO and hydrocarbons has been pursued for decades. So-called three-way catalysts are successfully used in automotive exhaust treatment, but are only effective at reducing NO<sub>x</sub> to N<sub>2</sub> at stoichiometric ( $\lambda=1$ ) or fuel-rich ( $\lambda<1$ ) conditions. New challenges for automotive catalytic systems have arisen in the past few years in response to new technologies that aim to increase automobile fuel efficiency and decrease exhaust emissions.

The use of natural gas (>90% methane) as a fuel source has actively been investigated because of the lower global warming impact of methane combustion compared to gasoline combustion. The combustion of natural gas produces 54 g of CO<sub>2</sub> per MJ, whereas the combustion of gasoline releases 74 g CO<sub>2</sub>/MJ [1]. The use of natural gas also allows engine operation at a higher compression ratio (due to the higher

\* Author of correspondence

octane number of methane) and this increases the thermal efficiency of the engine [2]. Unfortunately, current noble metal-based catalytic converters are not as efficient at oxidizing unburnt methane in the exhaust stream as they are at converting longer chain hydrocarbons that are typically found in the exhaust of conventional gasoline engines. Natural gas vehicles equipped with such conventional catalysts are thus only able to meet non-methane hydrocarbon (NMHC) emission standards, but not the total hydrocarbon (THC) emission standards [3].

The application of lean-burn technology has been touted as the most efficient approach to minimizing exhaust emissions from small and medium engines [1]. This technology involves engine operation under fuel-lean conditions. The presence of excess air results in more complete combustion at a lower combustion temperature, which also reduces  $\text{NO}_x$  formation during combustion. Although this technique significantly lowers engine-out  $\text{NO}_x$  emissions, further removal of  $\text{NO}_x$  from the exhaust gas is required in order to reach regulated ultra-low emissions levels. However, conventional three-way catalysts are unable to effectively reduce exhaust levels of  $\text{NO}_x$  in the presence of even small amounts of excess oxygen ( $\lambda > 1.01$ ) [4,5].

Thus, there is a need for developing catalytic systems that are able to oxidize  $\text{CH}_4$  and  $\text{CO}$  and reduce  $\text{NO}_x$  to  $\text{N}_2$  under oxidizing conditions. While several zeolitic materials have been found to catalyze these reactions, high-temperature hydrothermal stability is a problem for these catalysts [6-8]. Thermal stability for automotive catalysts is required well beyond their usual operating temperatures of 400 to 500°C, due to temperature excursions that may occur during heavy acceleration or engine misfiring. One of the major issues with three-way catalyst durability is the thermal deactivation that takes place at temperatures of 900°C and higher [4,9].

Group IIIB metal oxides [10] and lanthanide oxides [11] have been reported to be very active for the catalytic reduction of nitrogen oxides under oxidizing conditions. They also have excellent activity for the oxidation of carbon monoxide and hydrocarbons, and possess good hydrothermal stability when prepared in a nanocrystalline form [10]. We have focussed our work on nanocrystalline magnesium oxide, yttrium oxide and samarium oxide as catalysts for the reduction of  $\text{NO}_x$  to  $\text{N}_2$  in excess  $\text{O}_2$ . A second component has been examined as a catalyst to promote the complete oxidation of  $\text{CO}$  and  $\text{CH}_4$ . Noble metal oxidation catalysts lack the high-temperature stability required for this application, so we have chosen to employ nanostructured barium hexaaluminate (BHA) coated with transition metal oxide as the oxidation catalyst.

## Experimental

Magnesium oxide, yttrium oxide and samarium oxide catalysts were synthesized using a wet-chemical precipitation technique. This consisted of mixing aqueous solutions (0.25 M) of metal nitrate ( $\text{Mg}(\text{NO}_3)_2$  – 99%, Aldrich;  $\text{Y}(\text{NO}_3)_3$  – 99.99%, Alfa Aesar;  $\text{Sm}(\text{NO}_3)_3$  – 99.9%, Alfa Aesar) and tetraethylammonium hydroxide (35 wt%, Aldrich) at a pH between 12 and 13. The precipitate was then aged for 24 hours. After thoroughly washing the precipitate with ethanol, the material was air-dried, ground in a mortar and pestle, and then oven-dried at 120°C to remove any residual alcohol. The powder was calcined in flowing oxygen for 4 hours at 900°C to

convert the hydroxide or hydroxynitrate precipitate to a pure oxide phase that is stable at the high reaction temperatures.

The barium hexaaluminate support was prepared using a reverse emulsion-assisted sol-gel technique [12,13]. Barium isopropoxide was prepared by reacting metallic barium (99.8%, Aldrich) with isopropanol (99.99%, Mallinckrodt) by refluxing under air-free conditions at 70°C for 24 hours. Aluminum isopropoxide (99%, Aldrich) was dissolved in hot isopropanol by refluxing at 70°C for 24 hours. Stoichiometric amounts of the solutions containing barium and aluminum isopropoxides were mixed, prior to hydrolysis, in degassed 2,2,4-trimethylpentane (99.9%, Aldrich). A reverse microemulsion with a water:oil weight ratio of 15:85 was prepared by mixing doubly-deionized H<sub>2</sub>O, 2,2,4-trimethylpentane and a surfactant mixture. The surfactant mixture contained 67 wt% polyethoxylated linear alcohols (Neodol 91-6, Shell) and 33 wt% 1-pentanol (99.9%, Aldrich). The amount of surfactant added was calculated taking into account the amount of isopropanol and water liberated by the hydrolysis and polycondensation reactions of the alkoxide precursors. The final composition of the emulsion was 12.8 wt% H<sub>2</sub>O, 72.5 wt% 2,2,4-trimethylpentane, and 14.7 wt% surfactants.

The solution containing the alkoxide precursors was added drop-wise to the reverse emulsion with slow stirring. The hydrolyzed mixture was allowed to age for 24 hours before recovery by freeze drying. The BHA nanoparticles recovered were washed with isopropanol, supercritically dried, and then calcined at 800°C for 4 hours.

The active MnO<sub>2</sub> coatings were applied onto the surface of the BHA nanoparticles by impregnation. The BHA powders were suspended in H<sub>2</sub>O, and then manganese nitrate (99%, Aldrich) was added to the suspension and stirred for 30 minutes. Air was then bubbled through the suspension to promote oxidation of the manganese nitrate on the surface of the BHA nanoparticles. The MnO<sub>2</sub>/BHA sample was then air-dried and calcined to 900°C.

Dip-coating was employed to coat the nanocrystalline yttrium oxide catalyst onto a commercially available magnesia-stabilized zirconia monolith. By dip-coating from an aqueous suspension containing 25 wt% nanocrystalline yttrium oxide and 1 wt% polyethylene oxide, a loading of 11 wt% yttrium oxide on the magnesia-stabilized zirconia monolith was achieved. The composite was calcined to 800°C.

Catalyst surface area was determined by N<sub>2</sub> adsorption using a 5-point BET (Brunauer-Emmett-Teller) method on a Micromeritics ASAP 2000 instrument. Phase identification was performed by powder X-ray diffraction (XRD) using a Siemens D5000 diffractometer (45 kV, 40 mA, Cu-K $\alpha$ ). Scherrer's analysis of the X-ray peak broadening was employed to determine crystallite size. Transmission electron microscopy (TEM) was performed on a JEOL 2010 microscope. Scanning electron microscopy (SEM) was performed on a JEOL 6320 microscope.

Catalytic activity measurements were obtained at atmospheric pressure under steady-state reaction conditions in a 1/4"-O.D. quartz tube reactor with the catalyst supported on a porous quartz frit. Type K thermocouples were located above and below the catalyst bed, and were used in conjunction with an Omega temperature controller and a Lindberg tube furnace to maintain the catalyst within 2°C of the desired operating temperature. High-purity gases (He, 10.0% O<sub>2</sub>-He, 1.48% NO-He, 2.01% CH<sub>4</sub>-He and 2.06% CO-He) were metered into the top of the quartz reactor with five

independent MKS mass flow controllers. The reactor effluent was analyzed with a Perkin Elmer Autosystem gas chromatograph equipped with a 10' x 1/8"-O.D. molecular sieve 5A column and a 12' x 1/8"-O.D. Porapak Q chromatographic column. This allowed oxygen, nitrogen, nitrous oxide, methane, carbon dioxide, carbon monoxide and hydrogen in the reactor effluent to be separated and quantified. Carbon balances to within 2.5% were achieved in all runs.

## Results and Discussion

The BET surface areas and XRD crystallite sizes of the catalysts, following calcination to 900°C and catalytic testing, are presented in Table 1. The BHA material had a surface area of 248 m<sup>2</sup>/g and a TEM particle size of approximately 5 nm prior to MnO<sub>2</sub> loading. The crystallite size of the manganese oxide in the 14.7 wt% MnO<sub>2</sub>/BHA composite was too small to be determined through XRD. The Y<sub>2</sub>O<sub>3</sub>-coated magnesia-stabilized zirconia monolith had a specific surface area of approximately 3 m<sup>2</sup>/g, and a yttrium oxide crystallite size of 29 nm. The low surface area is not unexpected, given the 11 wt% loading of nanocrystalline Y<sub>2</sub>O<sub>3</sub>, the original 38 m<sup>2</sup>/g surface area of the unsupported Y<sub>2</sub>O<sub>3</sub>, and the negligible surface area of the uncoated ceramic monolith.

TABLE I. Surface area and crystallite size of catalysts

Catalyst	Surface Area, m <sup>2</sup> /g	Crystallite Size, nm
MgO	71	20
Y <sub>2</sub> O <sub>3</sub>	38	22
Sm <sub>2</sub> O <sub>3</sub>	16	31
MnO <sub>2</sub> /BHA	167	N/A

Transmission electron micrographs of the Y<sub>2</sub>O<sub>3</sub> and MnO<sub>2</sub>/BHA catalysts are presented in Figures 1 and 2, respectively. The Y<sub>2</sub>O<sub>3</sub> catalyst is composed of submicron-sized aggregates containing primary particles with dimensions on the order of 25 nm. This is in good agreement with the XRD crystallite size of 22 nm. The MnO<sub>2</sub>/BHA nanocomposite has a similar aggregate size, but the primary BHA particles are on the order of 5 nm. High-resolution TEM reveals the presence of a crystalline manganese oxide phase on the surface of the amorphous BHA particles (Figure 2b).

Figure 3 shows the microstructure of the Y<sub>2</sub>O<sub>3</sub>-coated magnesia-stabilized zirconia monolith. The morphology of a heavily coated area of the monolith is shown in Figure 3a. Submicron-sized particles of Y<sub>2</sub>O<sub>3</sub> completely cover the magnesia-stabilized zirconia surface. Figure 3b shows a region of slightly lower Y<sub>2</sub>O<sub>3</sub> loading, where the highly dense ceramic monolith support of micron-sized grains can be observed through a patchy coating of Y<sub>2</sub>O<sub>3</sub> particles.

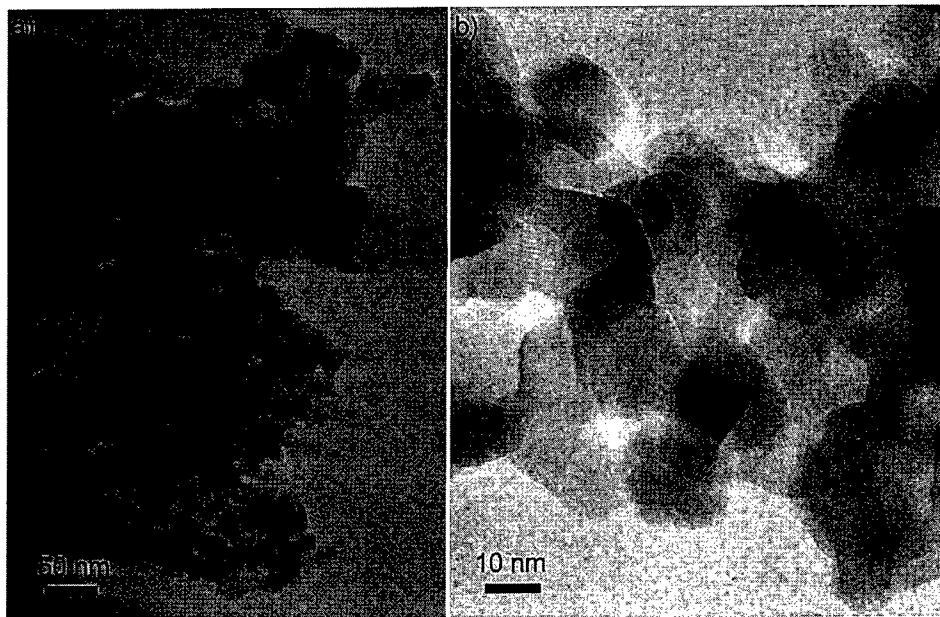


Figure 1. TEM images of nanocrystalline  $\text{Y}_2\text{O}_3$ .

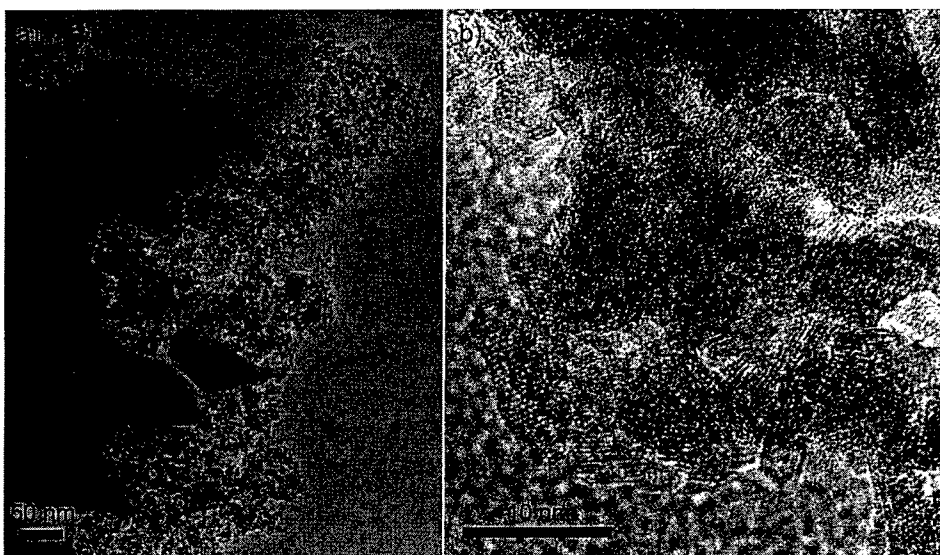


Figure 2. TEM images of  $\text{MnO}_2/\text{BHA}$  nanocomposite.

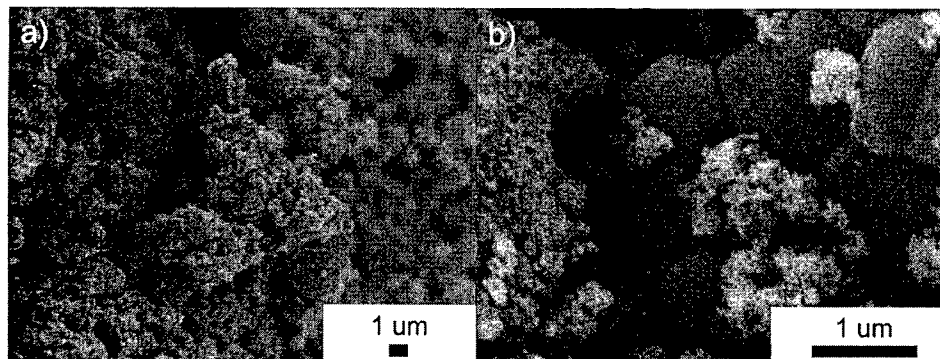


Figure 3. SEM images of  $\text{Y}_2\text{O}_3$ -coated magnesia-stabilized zirconia monolith.

The activities of the magnesium oxide, yttrium oxide and samarium oxide catalysts in a gas stream containing 5000 ppm NO, 5000 ppm CO, 5000 ppm  $\text{CH}_4$  and 1.67%  $\text{O}_2$  at a space velocity of  $30\ 000\ \text{h}^{-1}$  are shown in Figures 4 and 5. High removal rates of all undesirable gases can be achieved at temperatures as low as  $450^\circ\text{C}$  and are maintained to temperatures above  $800^\circ\text{C}$ . For NO removal, samarium oxide is the most active catalyst below  $550^\circ\text{C}$ , yttrium oxide is the most active system between 550 and  $750^\circ\text{C}$ , and magnesium oxide exhibits the highest activity above  $750^\circ\text{C}$ . Hydrocarbon and CO oxidation is best achieved by samarium and yttrium oxides, with magnesium oxide exhibiting significantly lower activity. Yttrium oxide appears to be the most effective overall catalyst, with a large temperature window for NO reduction and relatively low light-off temperatures for oxidation of CO and  $\text{CH}_4$ .

The temperature range for which these catalysts are most active exceeds the temperatures typically encountered in conventional catalytic converter systems ( $400$ - $500^\circ\text{C}$ ). The high thermal stability of these materials would, however, allow them to be employed in a close-coupled engine exhaust configuration, where the exhaust catalyst is placed near the engine. The higher exhaust temperature in this configuration would allow the operation of the catalyst within its optimal temperature range. An additional benefit of the close-coupled system is decreased cold-start emissions in comparison to the conventional downstream catalytic converter.

The stoichiometric air-to-fuel ratio for methane combustion is 17.1 [3]. Lean-burn natural gas engines typically operate at air-to-fuel ratios of 20 to 27 ( $\lambda=1.2$ -1.6), with corresponding exhaust redox ratios (molar ratio of oxidizing species to reducing species =  $\text{CO}_2/(2\text{C}_{\text{CH}_4} + 0.5\text{C}_{\text{CO}})$ ) of 5 to 50 [3]. We have examined the catalytic activity of nanocrystalline yttrium oxide at higher partial pressures of oxygen, and lower partial pressures of NO, CO and  $\text{CH}_4$  to determine how the catalyst behaves at redox ratios more representative of actual lean-burn engine exhaust. Figure 6 shows the activity of nanocrystalline  $\text{Y}_2\text{O}_3$  for  $\text{NO}_x$  reduction,  $\text{CH}_4$  oxidation and CO oxidation in a gas mixture containing 1000 ppm NO, 1000 ppm  $\text{CH}_4$ , 1000 ppm CO and 0.5-7.5%  $\text{O}_2$  (redox ratios of 2-30) at  $600^\circ\text{C}$  and a space velocity of  $30\ 000\ \text{h}^{-1}$ .

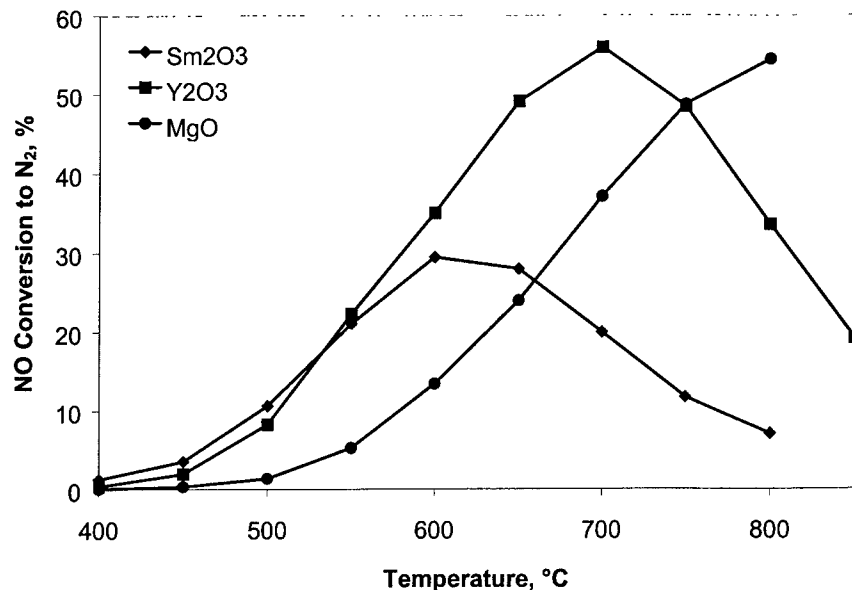


Figure 4. NO reduction activity of nanocrystalline oxide catalysts.

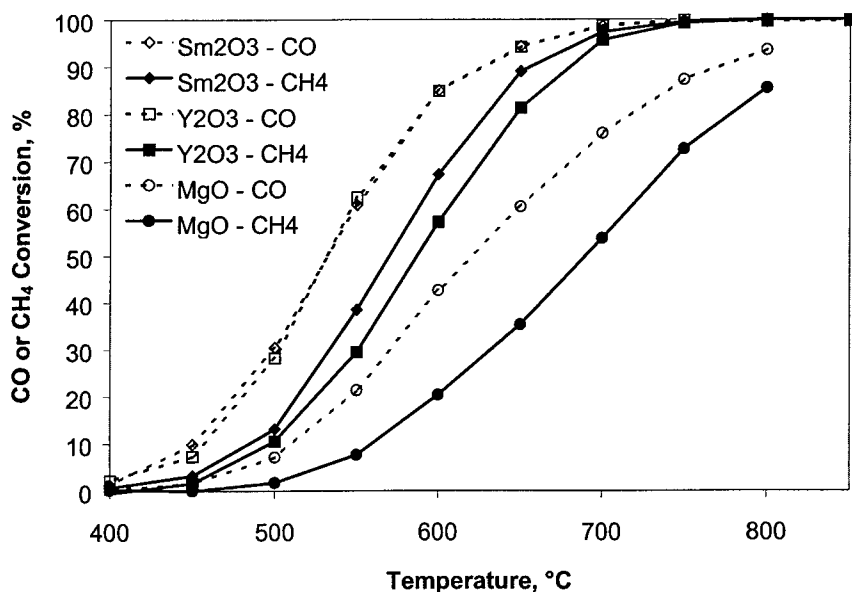


Figure 5. Activity of nanocrystalline oxide catalysts for oxidation of CO or CH<sub>4</sub>.

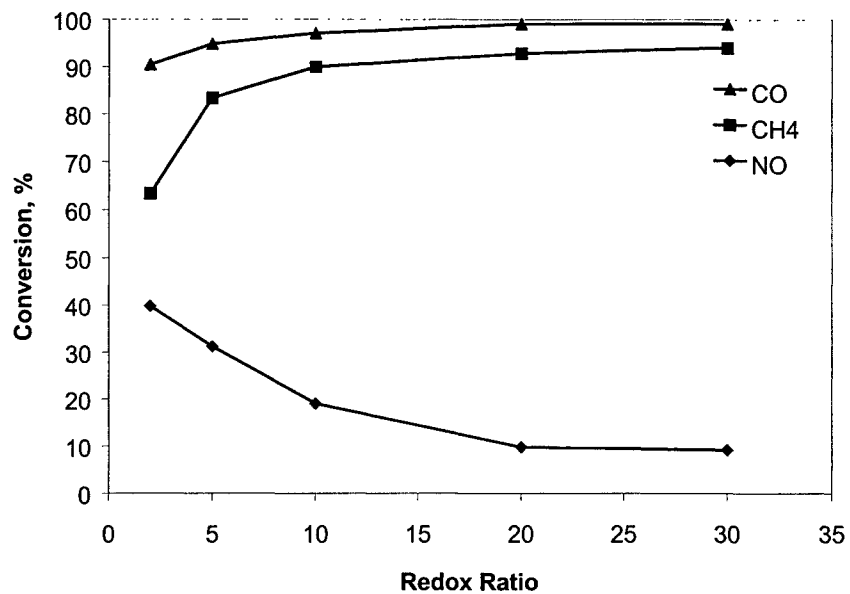


Figure 6. Effect of redox ratio on the catalytic activity of nanocrystalline  $\text{Y}_2\text{O}_3$ .

Clearly, oxygen has an inhibitory effect on the NO reduction activity, while it enhances the oxidation activity of the yttrium oxide catalyst. The lowered NO reduction activity is due to the increased competition between NO and  $\text{O}_2$  for reaction with the reducing agent,  $\text{CH}_4$ . As the partial pressure of oxygen in the exhaust increases, a larger proportion of the  $\text{CH}_4$  reacts nonselectively with  $\text{O}_2$  to produce  $\text{CO}_2$  and  $\text{H}_2\text{O}$ , and a smaller fraction of the  $\text{CH}_4$  reacts with NO through a pathway that ultimately produces  $\text{N}_2$ . However, even at a redox ratio of 30, substantial  $\text{NO}_x$  reduction is achieved with the nanocrystalline  $\text{Y}_2\text{O}_3$  catalyst.

At temperatures below 700°C or redox ratios below 10, significant amounts of  $\text{CH}_4$  and CO remain unconverted after passing through the  $\text{Y}_2\text{O}_3$  catalyst bed. Barium hexaaluminate coated with manganese oxide was added to the catalyst system in order to fully oxidize these unwanted exhaust components. The key to improving oxidation capacity without significantly affecting the reduction activity was to place the additional oxidation catalyst downstream of the nanocrystalline  $\text{Y}_2\text{O}_3$  catalyst. Through this configuration, the concentration of reducing agents was maximized throughout the  $\text{Y}_2\text{O}_3$  catalyst bed to promote the reduction of  $\text{NO}_x$  to  $\text{N}_2$ . Any unreacted  $\text{CH}_4$  or CO exiting the  $\text{Y}_2\text{O}_3$  catalyst bed was then oxidized downstream over the  $\text{MnO}_2/\text{BHA}$  catalyst bed.

By employing a catalyst system containing 75%  $\text{Y}_2\text{O}_3$  and 25%  $\text{MnO}_2/\text{BHA}$  by volume, CO conversion was increased from 95% to 100%, while  $\text{CH}_4$  conversion

was increased from 83% to 92% at 600°C and a redox ratio of 5. The  $\text{NO}_x$  reduction activity of the system under these conditions was only lowered slightly from 31% to 26%. The same system was used to remediate a gas stream containing 5000 ppm NO, 5000 ppm CO, 5000 ppm  $\text{CH}_4$  and 1.67%  $\text{O}_2$  (redox ratio = 1.34) at a space velocity of 30 000  $\text{h}^{-1}$  (Figure 7). At these conditions, the  $\text{NO}_x$  reduction activity was essentially unchanged, while the  $\text{CH}_4$  and CO conversions were significantly enhanced. The  $\text{MnO}_2/\text{BHA}$  component of the catalyst system was particularly helpful towards improving CO oxidation at low temperatures.

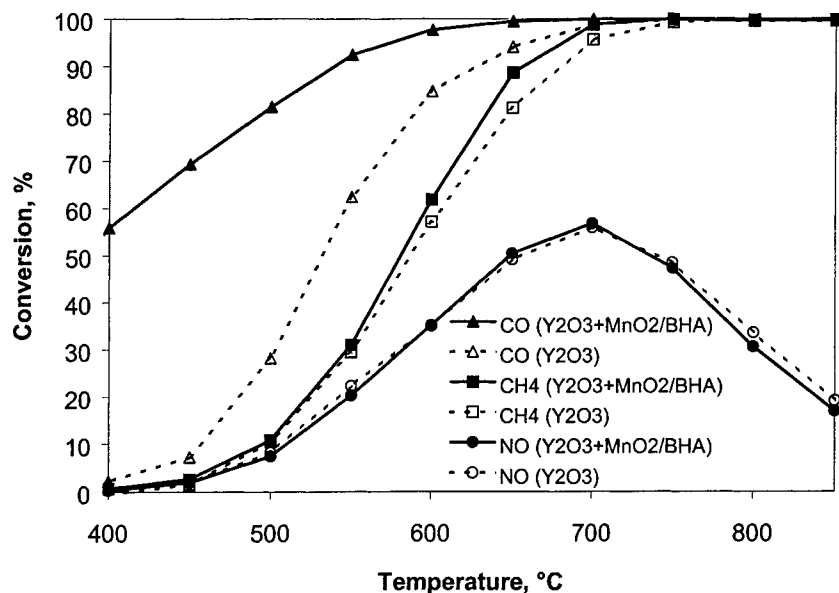


Figure 7. Catalytic activity of (i) the nanocrystalline  $\text{Y}_2\text{O}_3$  system and (ii) the nanocrystalline  $\text{Y}_2\text{O}_3 + \text{MnO}_2/\text{BHA}$  system for CO oxidation,  $\text{CH}_4$  oxidation and NO reduction.

The successful implementation of a new catalyst for automotive applications requires that the catalytic converter remains active for an exceptionally long time period. The presence of water vapor in the exhaust gas is a major source of problems for many materials that are possible alternatives to the existing three-way catalyst. Steam may induce lattice dealumination and irreversible deactivation in many zeolitic systems at temperatures ranging from 500 to 800°C [8,14]. The catalytic activity of nanocrystalline yttrium oxide was examined in the presence of 1000 ppm NO, 1000 ppm  $\text{CH}_4$ , 1000 ppm CO, 1.25%  $\text{O}_2$  and 3.5% water vapor to characterize the hydrothermal stability of this catalyst. At 650°C, a decrease in NO conversion to  $\text{N}_2$  from 25 to 20% was observed upon addition of water vapor to the reactant stream for 12 hours. However, upon removal of the water vapor from the feed stream, the initial

NO reduction activity (25% conversion) was fully restored. Furthermore, no loss of surface area from steaming of the catalyst was observed under these conditions.

The practical application of this multifunctional catalyst system requires that the active catalyst be dispersed on a mechanically and thermally stable support. A ceramic monolith was selected for this purpose because of the high-temperature stability needed for this system. Specifically, a magnesia-stabilized zirconia monolith was employed because it has similar thermal expansion coefficient and crystal structure as yttrium oxide, and will not react with yttrium oxide to form inactive phases. The catalytic activity of the  $\text{Y}_2\text{O}_3$ -coated reticulated monolith in the presence of 5000 ppm NO, 5000 ppm  $\text{CH}_4$ , 5000 ppm CO and 1.67%  $\text{O}_2$  at a space velocity of  $6000 \text{ h}^{-1}$  is presented in Figure 8. The activity of 11 wt%  $\text{Y}_2\text{O}_3$ -coated monolith is lower than that of the unsupported  $\text{Y}_2\text{O}_3$  powder catalyst, with complete oxidation of CO and  $\text{CH}_4$  requiring temperatures of  $\sim 800^\circ\text{C}$  in the former. Improvements in catalytic activity can be realized by an increased loading of the active  $\text{Y}_2\text{O}_3$  nanocrystals onto the ceramic monolith.

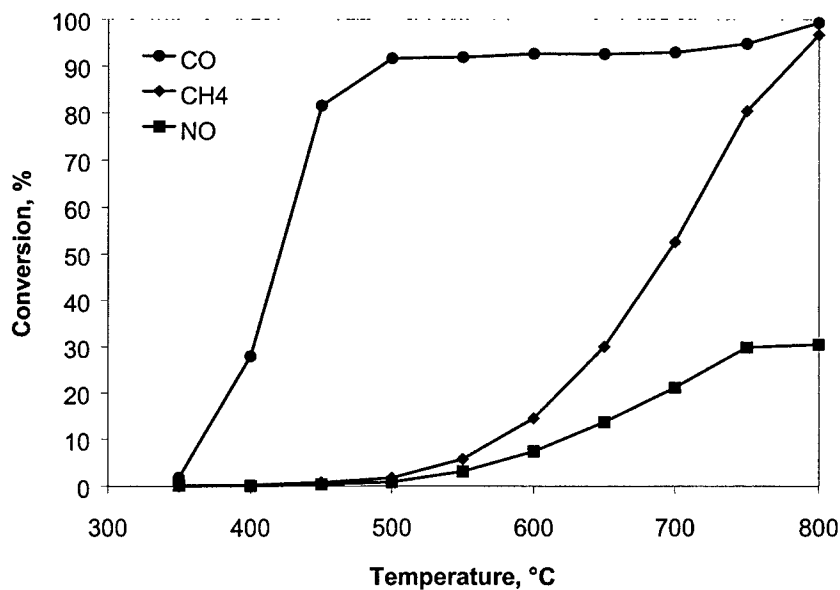


Figure 8. Catalytic activity of 11 wt%  $\text{Y}_2\text{O}_3$ -coated magnesia-stabilized zirconia monolith.

## Conclusions

We have found that nanocrystalline yttrium oxide, samarium oxide and magnesium oxide are promising catalysts for the remediation of exhaust streams from lean-burn natural gas engines. 95% conversion of CO, 83% conversion of CH<sub>4</sub> and 31% conversion of NO to N<sub>2</sub> can be achieved by nanocrystalline Y<sub>2</sub>O<sub>3</sub> at a redox ratio of 5 at 600°C. Introduction of an additional oxidation catalyst (MnO<sub>2</sub>/BHA) downstream of the nanocrystalline Y<sub>2</sub>O<sub>3</sub> catalyst significantly improves the oxidation capability of the catalytic system with only a slight decrease in NO<sub>x</sub> reduction capability. These nanocrystalline oxide catalysts are thermally stable to at least 900°C, allowing for application in close-coupled exhaust systems. They can be easily applied onto dense ceramic monoliths as nanostructured coatings for practical applications.

## Acknowledgments

The authors acknowledge the financial support of the National Science Foundation (CTS-9731396).

## References

- [1] Poulton, M. L. (1997) *Fuel Efficient Car Technology*, Computational Mechanics Publications, Southampton, UK.
- [2] Erjavec, J. (1997) *Natural Gas Vehicles – System Integration and Service*, Delmar Publishers, Albany, NY.
- [3] Lampert, J. K., Kazi, M. S., and Farrauto, R. J. (1997) Palladium catalyst performance for methane emissions abatement from lean burn natural gas vehicles, *Appl. Catal. B: Env.*, **14**, 211.
- [4] Taylor, K. C. (1987) Automobile catalytic converters, in A. Crucq and A. Frennet (eds.), *Catalysis and Automotive Pollution Control*, Elsevier Science Publishers B. V., Amsterdam, 97.
- [5] Corbo, P., Gambino, M., and Iannaccone, S. (1998) Lean burn natural gas engines as a possible power unit in urban fleets of heavy duty vehicles with low environmental impact, *Int. J. Vehicle Design*, **20**, 231.
- [6] Li, Y. and Armor, J. N. (1992) Catalytic reduction of nitrogen oxides with methane in the presence of excess oxygen, *Appl. Catal. B: Env.*, **1**, L31.
- [7] Li, Y. and Armor, J. N. (1993) Selective catalytic reduction of NO<sub>x</sub> with methane over metal exchanged zeolites, *Appl. Catal. B: Env.*, **2**, 239.
- [8] Budi, P. and Howe, R. F. (1997) Steam deactivation of CoZSM-5 NO<sub>x</sub> reduction catalysts, *Catal. Today*, **38**, 175.
- [9] Hammerle, R. H. and Wu, C. H. (1984) Effect of high temperatures on three-way automotive catalysts, Society of Automotive Engineers Paper No. 840549.
- [10] Fokema, M. D. and Ying, J. Y. (1998) The selective catalytic reduction of nitric oxide with methane over scandium oxide, yttrium oxide and lanthanum oxide, *Appl. Catal. B: Env.*, **18**, 71.
- [11] Zhang, X., Walters, A. B., and Vannice, M. A. (1995) NO adsorption, decomposition, and reduction by methane over rare earth oxides, *J. Catal.*, **155**, 290.
- [12] Zarur, A. J. and Ying, J. Y. (1999) Nanostructured complex oxides for catalytic combustion, submitted.
- [13] Zarur, A. J., Hwu, H. H., and Ying, J. Y. (1999) Reverse emulsion-mediated synthesis and structural evolution of barium hexaluminate nanoparticles, submitted.
- [14] Zhang, Y., Sun, T., Sarofim, A. F., and Flytzani-Stephanopoulos, M. (1995) Decomposition of NO over metal-modified Cu-ZSM-5 catalysts, in U. S. Ozkan, S. K. Agarwal, and G. Marcellin (eds.), *Reduction of Nitrogen Oxide Emissions*, American Chemical Society, Washington, DC, 133.

---

## **POLYMER-LAYERED SILICATE NANOCOMPOSITES: EMERGING SCIENTIFIC AND COMMERCIAL OPPORTUNITIES**

**Emmanuel P. Giannelis**

*Department of Materials Science and Engineering  
Cornell University, Ithaca, NY 14853, USA*

**ABSTRACT:** Polymer nanocomposites represent a radical alternative to conventionally (macroscopically) filled polymers. Because of their nanometer-size dispersion the nanocomposites exhibit markedly improved properties when compared to the pure polymers or conventional composites. These include increased modulus and strength, outstanding barrier properties, increased solvent and heat resistance and decreased flammability. In this paper the physical and mechanical properties of nanocomposites are reviewed and discussed in terms of their static and dynamic properties.

### **1. Introduction**

Polymer nanocomposites represent a radical alternative to conventionally filled polymers. Because of their nanometer-size dispersion the nanocomposites exhibit markedly improved properties when compared to the pure polymers or conventional composites [1]. These include increased modulus and strength, decreased gas permeability, increased solvent and heat resistance and decreased flammability [2-11]. For example, a doubling of the tensile modulus and strength without sacrificing impact resistance is achieved for nylon-layered silicate nanocomposites containing as little as 2 vol.% inorganics. In addition, the heat distortion temperature of the nanocomposites increases by up to 100 °C extending the use of the composite to higher temperature environments, such as automotive under-the-hood parts. Furthermore, the heat release rate in the nanocomposites is reduced by up to 63 % at heat fluxes of 50 kW/m<sup>2</sup> without an increase in the CO and soot produced during combustion. Applications include low-cost alternatives of high performance composites, food packaging, microelectronics and biotechnology.

### **2. Synthesis of Nanocomposites**

Melt intercalation of high polymers is a powerful new approach to synthesize polymer-layered silicate nanocomposites [12]. This method is quite general and is broadly applicable to a range of commodity polymers from essentially non-polar polystyrene, to weakly polar poly(ethylene terephthalate) to strongly polar nylon. The nanocomposites are, thus, processable using current technologies and easily scaled to manufacturing quantities.

In general, two types of hybrids are possible: **intercalated**, in which a single, extended polymer chain is intercalated between the silicate layers resulting in well ordered polymer/inorganic multilayers, and **dispersed or disordered**, in which the silicate layers (1 nm thick) are exfoliated and dispersed in a continuous polymer matrix (Fig 1).

The silicates used belong to the general family of so-called 2:1 layered silicates. Their crystal structure consists of layers made up of two silica tetrahedra fused to an edge-shared octahedral sheet of either alumina or magnesia. Stacking of the layers leads to a regular van der Waals gap between the layers called the interlayer or gallery. Isomorphic substitution within the layers generates negative charges that are normally counterbalanced by cations residing in the interlayer.

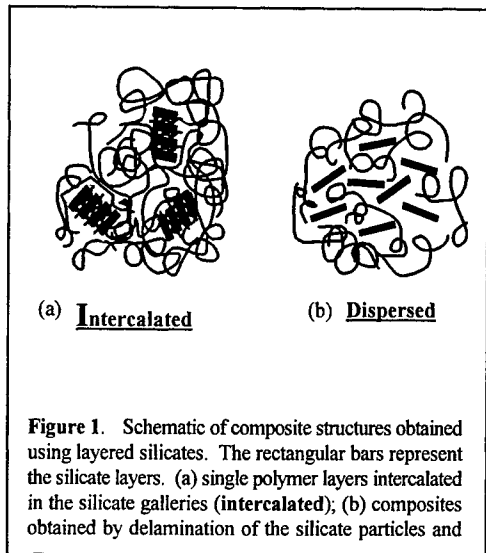


**Figure 1.** Schematic of composite structures obtained using layered silicates. The rectangular bars represent the silicate layers. (a) single polymer layers intercalated in the silicate galleries (intercalated); (b) composites obtained by delamination of the silicate particles and

Pristine layered silicates usually contain hydrated  $\text{Na}^+$  or  $\text{K}^+$  ions. Ion exchange reactions with cationic surfactants including primary, tertiary and quaternary ammonium ions render the normally hydrophilic silicate surface organophilic, which makes intercalation of many engineering polymers possible. The role of the alkyl ammonium cations in the organosilicates is to lower the surface energy of the inorganic and improve the wetting characteristics with the polymer. Additionally, the alkyl ammonium cations can provide functional groups that can react with the polymer or initiate a polymerization of monomers to improve the strength of the interface between the inorganic and the polymer.

Similarly to polymer blends any mixture of polymer and layered silicate does not necessarily lead to a nanocomposite [13]. In most cases the incompatibility of the hydrophobic polymer and the hydrophilic silicate leads to phase separation resulting in macroscopically filled systems. In contrast, by using surface modified silicates as noted earlier one can fine tune their surface energy and render them miscible (or compatible) with different polymers. The approach is based on a chemical (rather than a mechanical) driving force, which leads to nanoscopic dispersion.

### 3. Structure and Dynamics of Polymer Nanocomposites

The combination of enhanced modulus, strength and toughness is a unique feature of the nanocomposites. In conventionally-filled polymer systems increases in modulus typically compromise toughness. Additionally, the decrease in barrier properties of the

nanocomposites cannot be explained only on the high aspect ratio afforded by the exfoliation of the inorganic nanolayers. Alternatively we suggest that the polymer chains at the interface adopt a different structure and exhibit very different dynamics compared to the chains in the bulk. Due to the nanodispersion a very large fraction of the polymer is at the interface (close to 60%) even for a few percent inorganic. As a result these nanoscopically "confined" polymer chains contribute significantly and to a large extend control the properties of the hybrid.

Even simple notions regarding the conformations of polymers confined in two dimensions are not yet fully understood. In three dimensions, it is well known that the individual molecules in long chain polymers overlap significantly. In two dimensions, it has been suggested that the different chains overlap only slightly. Therefore, the local and global conformations of polymers in the nanocomposites are expected to be dramatically different from those observed in the bulk, not only due to the confinement of the polymer chains but also due to specific polymer-inorganic surface interactions not normally present in the bulk.

From our current theoretical and experimental studies on nanocomposites a new and quite unexpected picture is emerging [14]. Despite the presence of the "confining" inorganic layers, intercalated polymer chains exhibit substantial segmental motion even at temperatures where the polymer is normally in the glassy state. Thus, in contrast to the bulk polymers where chain mobility slows precipitously around  $T_g$ , in the nanocomposites chain mobility persists well below the bulk  $T_g$ . This behavior is counterintuitive as "confinement" of the polymer chains within  $\sim 2$  nm is expected to increase their solid-like character and decrease their mobility.

We start with non-equilibrium dynamics present during polymer intercalation from the melt. The observation that polymer chains can undergo center of mass transport in essentially two dimensions is rather surprising because the unperturbed radius of gyration of the polymer is roughly an order of magnitude greater than the interlayer distance between the silicate layers. The ability of the polymer chains to undergo center of mass transport during intercalation is further evidence that the silicate layers do not completely restrict segmental motions, otherwise large-scale chain motion would not be possible.

Using X-ray diffraction (which monitors the angular shift and integrated intensity of the silicate reflections) we have studied the intercalation kinetics of polystyrene into organically modified silicates (Fig. 2) [15]. The effective diffusion coefficient,  $D_{\text{eff}}$ , is much faster than the tracer diffusion coefficient of the bulk polymer or the diffusion coefficient of the polymer in a thin film. This is because during intercalation polymer chains are moving down a concentration gradient, whereas in the other two cases polymer motion is entropic in origin. Furthermore, the diffusion coefficient exhibits an inverse dependence on molecular weight. Although the diffusion coefficient of polymers near surfaces has been predicted to have an inverse molecular weight dependence (and not scaled as  $1/N^2$ ,  $N$  is the chain length, characteristic of repetition) this represents the first experimental measurement of the diffusion of high molecular weight polymer melts in two dimensions.

As the length of the surfactant molecules increases from twelve to eighteen carbon atoms, C12 to C18, respectively, the effective diffusion coefficient increases. This is because increasing the length of the surfactant chains effectively reduces the interaction with the silicate surfaces and thus decreases the stickiness to the surface.

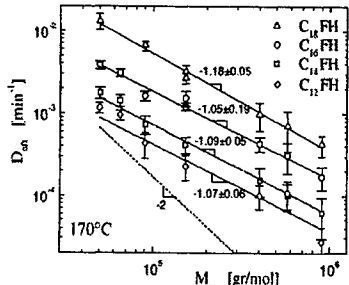


Figure 2. Diffusion coefficient as a function of molecular weight of the polymer [15].

We now turn our attention to equilibrium dynamics for the polymer chains after they have been intercalated. Local dynamics of chains “confined” between the silicate layers were probed by spin-echo NMR. In a spin-echo experiment complete refocusing of the signal is expected as long as there is no change in resonance frequency before and after the second pulse. Large intensity losses therefore take place when large amplitude dynamics commence as for example those associated with the liquid state (i.e. above the glass transition temperature,  $T_g$ ).

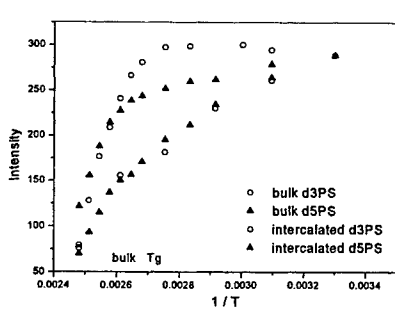


Figure 3. Spin-echo NMR of PS in bulk and nanocomposite [16].

Figure 3 shows the results of the spin-echo experiment for polystyrene and polystyrene nanocomposites [16]. To follow the respective dynamics, polystyrene deuterated at the backbone,  $d_3$ , and the ring,  $d_5$ , was used. When  $d_3$  polystyrene is used, the intensity of the NMR signal (multiplied by temperature) remains constant in the glassy regime followed by a large decrease above  $T_g$ . This is expected as backbone dynamics are absent below  $T_g$  and commence at  $T_g$ . There is some mobility for the  $d_5$  polystyrene below  $T_g$ , since the rings can independently flip  $180^\circ$  but a substantial drop in intensity is found only above the  $T_g$ . In contrast, the nanocomposites show significant amount of mobility at least for part of the polymer even at temperatures well below the  $T_g$ . Additionally, there is no distinct change from solid-like to liquid-like behavior as in the bulk polymer.

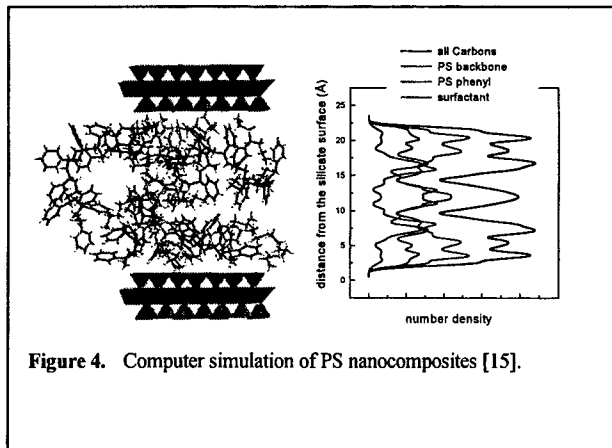


Figure 4. Computer simulation of PS nanocomposites [15].

Computer simulations offer an explanation for this behavior [15,16]. When confined between the inorganic surfaces the polymer chains order into discrete subnanometer layers (Fig. 4). This layering, clearly seen in the density profiles, imparts strong density inhomogeneity in the direction normal to the surface. The fast dynamics arise from areas of low-density or high free volume, which compensates for the confinement between the inorganic layers. Neutron scattering measurements support the above structure. The polymer chains adopt a 2D random-walk structure. Additionally, in contrast to the bulk polymer the intercalated chains do not show a single characteristic length.

#### 4. Conclusions

Mass transport of polymer chains into the silicate layers is faster than the corresponding self-diffusion. Thus hybrid formation requires no additional processing time than currently required for conventional polymer processing techniques such as extrusion.

Despite the presence of the “confining” inorganic layers, intercalated polymer chains exhibit substantial segmental motion even at temperatures where the polymer is normally in the glassy state. Thus, in contrast to the bulk polymers where chain mobility slows precipitously around  $T_g$ , in the nanocomposites chain mobility persists well below the bulk  $T_g$ . This behavior is rationalized in terms of the new structure the polymer chains adopt at the interface. When confined between the inorganic surfaces the polymer chains order into discrete subnanometer layers. The fast dynamics arise from areas of low-density or high free volume, which compensates for the confinement between the inorganic layers. Neutron scattering measurements support the above structure.

#### Acknowledgements

This work was supported in part by the Cornell Center for Materials Research, AFOSR and ONR. I would like to thank my coworkers and collaborators S.D. Burnside, H. Chen, J.D.

Gilman, J. Genzer, T. Kashiwagi, E. Manias, P.B. Messersmith, E.J. Kramer, R. Krishnamoorti, R.A. Vaia and D.B. Zax.

## References

1. Giannelis, E. P. (1996) Polymer layered silicate nanocomposites, *Adv. Mater.* **8**, 29 .
2. Usuki, A., Kawasumi, M., Kojima, Y., Okada, A., Kurauchi, T., Kamigaito, O. (1993) Synthesis of nylon 6-clay hybrid, *J. Mater. Res.* **8**, 1174
3. Kojima, Y., Usuki, A., Kawasumi, M., Okada, A., Kurauchi, T., Kamigaito, O. (1993) Synthesis of nylon 6-clay hybrid by montmorillonite intercalated with  $\epsilon$ -caprolactam, *J. Polym. Sci. Part A: Polym. Chem.* **31**, 983.
4. Yano, K. et al. (1993) Synthesis and properties of polyimide-clay hybrid, *J. Polym. Sci.: Part A: Polym. Chem.* **31**, 2493.
5. Lan, T., Kaviratna, P. D., and Pinnavaia, T. J. (1995) Mechanism of clay tactoid exfoliation in epoxy-clay nanocomposites, *Chem. Mater.*, **7**, 2144.
6. Lan, T. and Pinnavaia, T. J. (1994) Clay-reinforced epoxy nanocomposites, *Chem. Mater.*, **6**, 2216
7. Messersmith, P. B. and Giannelis, E. P. (1994) Synthesis and characterization of layered silicate-epoxy nanocomposites, *Chem. Mater.*, **6**, 1719.
8. Messersmith, P. B. and Giannelis, E. P. (1995) Synthesis and barrier properties of poly( $\epsilon$ -caprolactone)-layered silicate nanocomposites, *J. Pol. Sci. A. Pol. Chem.*, **33**, 1047.
9. S.D. Burnside and E.P. Giannelis, (1995) Synthesis and properties of new poly(dimethylsiloxane) nanocomposite, *Chem. Mater.*, **7**, 1597.
10. Gilman, J.W., Kashiwagi, K., Nyden, M., Brown, J. E. T., Lomakin, S., Giannelis, E. P. and Manias, E. (1998) Flammability studies of polymer layered silicate nanocomposites, *Proceedings Additives '98*.
11. Lee, D., Takehoshi, T. and Giannelis, E. P. (1997) Fire Resistant Nanocomposites, In *Nanophase and Nanocomposite Materials II*, Komarneni, S., Parker, J.C. and Wollenberger, H.J. (eds.) MRS Symposium Proceedings, **457**, 513.
12. Vaia, R. A., Ishii, H. and Giannelis, E. P. (1993) Synthesis and properties of 2-dimensional nanostructures by direct intercalation of polymer melts in layered silicates, *Chem. Mater.* **5**, 1694.
13. (a) Vaia, R. A. and Giannelis, E. P. (1997) Lattice model of polymer melt intercalation in organically-modified layered silicates, *Macromolecules*, **30**, 7990; (b) Vaia, R. A. and Giannelis, E. P. (1997) Polymer melt intercalation in organically-modified layered silicates: model predictions and experiment, *Macromolecules*, **30**, 8000.
14. Krishnamoorti, R., Vaia, R. A. and Giannelis, E. P. (1996) Structure and Dynamics of Polymer-Layered Silicate Nanocomposites, *Chem. Mater.* **8**, 1728.
15. (a) Vaia, R. A., Jandt, K. D., Kramer, E. J. and Giannelis, E. P. (1995) Kinetics of polymer melt intercalation *Macromolecules* **28**, 8080. (b) Manias, E., Chen, H., Krishnamoorti, R., Genzer, J., Kramer, E. J. and Giannelis, E. P. submitted.
16. Zax, D. B., Yang, D.-K., Santos, R. A., Hegemann, H., Giannelis, E. P. and Manias, E. submitted for publication.

---

## OFFICE OF NAVAL RESEARCH INITIATIVE ON WEAR RESISTANT NANOSTRUCTURED MATERIALS

L. T. Kabacoff  
Office of Naval Research  
800 N Quincy Street  
Arlington, VA 22217-5660, USA

### 1. Introduction

Every year, the U. S. Navy spends many billions of dollars in the repair and maintenance of ships, aircraft and land-based vehicles. A significant portion of this money goes to the repair or replacement of worn or eroded components such as shafts, seals, hydraulic cylinders and bearings. Because of continuing budget cuts over the last several years, it has become imperative for the Navy to find ways to reduce this maintenance burden. This need is complicated by the fact that many of the wear surfaces in question are chrome plated, which, due to increasingly stringent environmental regulations, must now be replaced by some other coating technology. As a result, the Office of Naval Research has instituted an initiative to develop and implement new coating technology that takes advantage of the outstanding properties of newly emerging nanostructured materials. Moreover, the coatings are fabricated by thermal spray processing, a mature and widely available technique, and one that is already used for refurbishing worn or otherwise damaged ship and aircraft components. The objective of the program is to establish a coatings capability which can reduce life cycle cost of navy assets either by extending the service life of components or making possible the repair, rather than replacement, of the component. The extraordinary properties of these materials make both strategies possible.

### 2. Thermal Spray Processing

Generally speaking, thermal spray consists of the heating and accelerating of solid particles by injecting them into a hot gas stream, then impacting them onto a substrate to form a coating. There are a wide variety of techniques for carrying this out. The heated gas stream can be produced by a DC arc (plasma arc spraying), by combustion of a fuel such as kerosene (high velocity oxygen fuel, or HVOF), or even simple heating of compressed air (cold dynamic gas spray, or CDGS). Each method has a characteristic range of gas velocities and temperatures. For example, plasma arc spray can produce extremely high temperature (in excess of 10,000 °C) but velocities below 1,000 ft/sec. On the other hand, HVOF produces much higher velocities, but temperatures in the 2,000 –

3,000 °C range. CDGS can produce up to Mach 4 gas velocities, but at a temperature of only about 300 °C. The choice of method depends on the material to be sprayed, the substrate, and the required quality of the coating (adhesion, porosity, etc.).

Thermal spray of nanostructured materials presents challenges not usually present when spraying conventional materials. For example, the ideal size and morphology of a particle for thermal spray is a 15–30 µm dense spherical particle. Nanostructured ceramic powder is most frequently produced in the form of individual nanoscale particles. Such particles cannot easily be fed into an thermal spray system. Moreover, it is very difficult to entrain such particles or to bring about impact on a substrate. Such particles must be agglomerated into larger, “snowball” like structures, which can be injected into and carried by the gas stream. Another important class of nanostructured materials, cemented carbides (or cermets), is produced in the form of fragile, hollow shells. Beside the low density, such shells break apart in storage and handling, resulting in fine particles that clog the powder feeders. For these materials, it is necessary to either modify the production process to create dense spheres, or to re-agglomerate the material into a more favorable structure. Another issue when spraying nanostructured materials is the degree to which the particles melt. There are two ways to form a nanoscale microstructure in a thermal sprayed coating. Either the individual particles (or one or more phases within the particle) remain solid during the spray process (since melting destroys the nanoscale nature of the material), or a nanoscale structure is recovered during solidification at the substrate. In thermal spray of conventional materials, particles are almost always allowed to melt. Finally, the extremely high surface area of nanostructured materials can lead to excessive surface reactivity which, in turn, can degrade coating quality.

### 3. Program Summary

Studies have been carried out in three general areas: cermets, ceramics, and metals.

#### 3.1 CERMETS

Two classes of cermets were investigated, WC-Co and Cr<sub>4</sub>C<sub>3</sub>-NiCr. WC-Co was manufactured in the form of hollow shells by Nanodyne with nominal compositions of 8, 12, and 15% Co. Initially, the shells were too fragile for use as thermal spray feed stock due to the presence of very fine particles (which clogged powder feeders). Three approaches were taken to solve this problem. The first involved the milling of the Nanodyne material to form micron sized particles followed by dispersal in a binder and spray drying. Further processing by a heat treatment can also be applied. Several companies are capable of this kind of processing. Under the ONR program, this work was carried out by Inframet. A second approach was to modify the parameters of the spray conversion process used by Nanodyne to manufacture the original hollow shells in order to produce shells with much thicker walls. This has been done successfully by Nanodyne, which can now produce nearly solid spheres. The third approach was to fabricate a cored wire consisting of a WC-Co core wrapped in a thin metal sheath. Thermal spray was

carried out by twin wire arc spray. Sprayable nanostructured Cr<sub>4</sub>C<sub>3</sub>-NiCr powder was fabricated by attritor milling of conventional powder followed by dispersal in a binder. In this case, rather than spray drying, the binder was allowed to harden. The resulting material was then ground to form a sprayable powder.

A very large number of cermet coatings were fabricated by several thermal spray techniques. Most were done by HVOF, with some coatings produced by plasma spray and twin wire arc. In all cases, the adhesion was outstanding, typically a factor of two better than conventional coatings of similar composition. It was also found that residual stress was very low, resulting in a capability for producing very thick coatings. In a conventional coating, stress buildup limits coating thickness to typically 500 – 800 $\mu$ m. Nanostructured coatings were made up to 0.65 cm thick and could probably be made with arbitrary thickness. It was also found that the WC-15%Co coatings were remarkably tough and could be struck hard with a hammer without cracking or spalling. The hardness and wear resistance of the coatings varied widely depending on spray techniques and parameters used. Moreover, wear resistance did not correlate to hardness. Studies show that, while bulk sintered nanostructured WC-Co is much more wear resistant than the conventional analogue, the wear resistance of the nanostructured coatings is limited by the quality of the splat boundaries and that coating quality is not yet high enough to allow the nanostructured nature of the material come into play. Development efforts are continuing. Wear data on Cr<sub>4</sub>C<sub>3</sub>-NiCr is not yet available. However, the hardness of the nanostructured coatings is somewhat higher than that of the conventional coating.

### 3.2 CERAMICS

Two types of ceramic coatings were considered: hard coatings and thermal barrier coatings. The composition for the hard coatings was Al<sub>2</sub>O<sub>3</sub> – 18%TiO<sub>2</sub> while that of the thermal barrier coating was 7YSZ (7% yttria stabilized zirconia). Sprayable powder was produced by reagglomerating individual nanoscale particles which were dispersed in a binder and spray dried, followed either by calcining or plasma densification. The resulting powders consisted of round dense particles of a size and flowability ideal for thermal spray powder feeders. Coatings were fabricated by plasma spray. Examination of the microstructure showed that partial melting had occurred and that the coatings consisted of a mixed nano/micro-scale structure. The nanoscale component varied from zero to over 60%. In the case of the hard coatings, adding proprietary dopants could increase the percentage of retained nanostructured material. The wear resistance of the hard coatings was found to be superior to that of the conventional material, being four times better in the best samples. The wear resistance correlated strongly with retained nanostructure. Adhesion was found to be much higher for the nanostructured coatings (more than twice the conventional value). It was observed that toughness was much higher, but quantitative measure of this has not yet been accomplished. It was also observed that post deposition grinding and polishing of the nanostructured coatings could be accomplished in about half the usual time and a much better final surface smoothness could be achieved.

---

In a recent effort, Inframmat has succeeded in fabricating oxide ceramic coatings by injecting an aqueous solution of salts directly into a plasma flame, thus carrying out particle synthesis and deposition in the same operation. The resulting coatings were remarkably smooth, and porosity could be controlled by controlling process parameters. The mechanical and thermal properties of the coatings are now being characterized at Inframmat and at UCONN. NEI and A&A company have also succeeded in producing coatings using a liquid, in this case using metal-organic precursors.

### 3.3 METALS

Sprayable powders of reasonably ductile alloys and metal matrix composites can most easily be obtained by attritor milling of conventional metal powders, which produces relatively large metal particles which exhibit a grain size typically 20 – 40 nm. However, these powders will almost certainly melt during deposition using most thermal spray techniques (an exception is CDGS). The nanoscale structure can be recovered upon solidification provided the material is rich in nucleation sites and solidification is rapid. These nucleation sites can be obtained by performing the milling under liquid nitrogen. This results in the creation of a fine dispersion of oxide/nitride particles which tend to collect at grain boundaries. Studies have been carried out on thermal spray of aluminum (with and without addition of micron scale SiC particles) and on a Ni-based alloy, 718. In each case, nanostructured coatings were successfully fabricated either by plasma spray in an inert atmosphere (Al, Al/SiC) or HVOF (718). These coatings have not yet been characterized. However, preliminary data indicate that the hardness of such coatings is significantly higher than that found in conventional coatings with the same composition.

### 4. Recent Publications

Much of the work described above has not been published, partly because of insufficient time, and partly because some of it is being carried out in industrial laboratories where the details are considered to be proprietary. Some of the work is presented elsewhere in these proceedings. A list of recent publications is presented below. It is suggested that interested persons contact the performers directly to obtain information.

1. Cheng, J., Jordan, E.H., Barber, B., and Gell, M. (1998) Thermal/residual stress in a thermal barrier coating system, *Acta Meterialia* **46**, 5839-5842.
2. Xiao, T.D., Jiang, S., Wang, D.M., Wang, Y., Zatorski, R., Strock, C.W. and Strutt, P.R. (1998) Thermal spray of nanostructured ceramic coatings for improved mechanical properties, in T.S. Sudarshan, K.A. Khor and M. Jeandin (eds.), *Surface Modification Technologies XII*, ASM International, Metals Park, pp. 489-493.
3. Cetegen, B.M. and Yu, W. (1999) Simultaneous particle temperature, velocity and size measurement in HVOF thermal sprays, *J. Thermal Spray Technology* **8**, 57-62.
4. Ahmed, I. And Bergman, T.L. (in press) Thermal modeling of plasma spray deposition of nanostructured ceramics, *J. Thermal Spray Technology*.
5. Wang, Y., Whang, S.H., Wang, T.D. and Strutt, P.R. (in press) Abrasive wear

characteristics of plasma sprayed nanostructured  $\text{Al}_2\text{O}_3/\text{TiO}_2$  Coatings, *Wear*.

6. Skandan, G., Glumac, N., Chen, Y.-J., Cosandey, F., Heims, E. and Kear, B.H. (1998) Low-pressure flame deposition of nanostructured oxide films, *J. Am. Ceram. Soc.* **81**, 2753-2756.
7. Usmani, S., Sampath, S., and Herman, H. (1998) HVOF processing of nanostructured WC-Co coatings and their properties, *J. Thermal Spray Technol.* **7**, 429-431.
8. He, J., Ice, M. and Lavernia, E.J. (1998) Synthesis and characterization of nanostructured  $\text{Cr}_3\text{C}_2\text{-NiCr}$ , *Nanostructured Materials* **10**, 1271-1283.
9. Lau, M.L., Gupta, V.V. and Lavernia, E.J. (1998) Mathematical modeling of particle behavior of nanocrystalline Ni during high velocity oxy-fuel thermal spray, *Nanostructured Materials* **10**, 715-722.

## 5. Performers

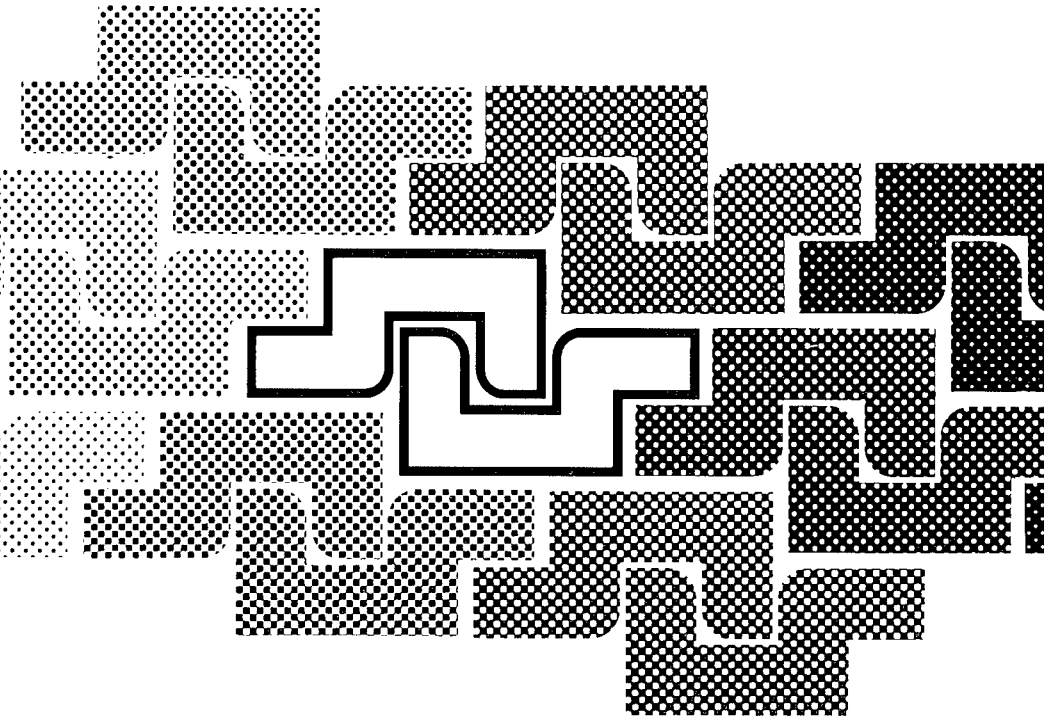
The initiative is being carried out by a large group of performers representing industry, universities, and Navy R&D centers and repair facilities. A list is given in Table 1, along with point of contact (sometimes arbitrarily chosen) and e-mail address.

TABLE 1. Performers, points of contact and e-mail addresses of participants.

Performer	Point of Contact	e-mail Address
Rutgers University	Bernard Kear	<a href="mailto:Bkear@rci.rutgers.edu">Bkear@rci.rutgers.edu</a>
University of Connecticut	Maurice Gell	<a href="mailto:Mgell@mail.ims.uconn.edu">Mgell@mail.ims.uconn.edu</a>
JC-Irvine	Enrique Lavernia	<a href="mailto:Lavernia@uci.edu">Lavernia@uci.edu</a>
SUNY Stony Brook	Sanjay Sampath	<a href="mailto:Ssampath@ms.cc.sunysb.edu">Ssampath@ms.cc.sunysb.edu</a>
Stevens Inst. Of Technology	Traugott Fischer	<a href="mailto:Tfischer@stevens-tech.edu">Tfischer@stevens-tech.edu</a>
Oregon Graduate Institute	David Atteridge	<a href="mailto:Aridge@mse.ogi.edu">Aridge@mse.ogi.edu</a>
Nanodyne, Inc	Purnesh Seegopal	<a href="mailto:Pseegopal@aol.com">Pseegopal@aol.com</a>
Inframet Materials Inc.	Peter Strutt	<a href="mailto:Inframet@aol.com">Inframet@aol.com</a>
A&A Company	Stewart Brunhouse	<a href="mailto:Info@aacoinc.com">Info@aacoinc.com</a>
PyroGenesis	George Kim	<a href="mailto:Perma@citenet.net">Perma@citenet.net</a>
Praxair	Robert Hilgenberg	<a href="mailto:Rhilgenb@sti.praxair.com">Rhilgenb@sti.praxair.com</a>
Sermatech	David Bucci	<a href="mailto:Bucci@sermatech.com">Bucci@sermatech.com</a>
Nanopowder Enterprises, Inc.	Ganesh Skandan	<a href="mailto:Skandan@aol.com">Skandan@aol.com</a>
Puget Sound Naval Shipyard	Nick Eutizzi	<a href="mailto:Eutizzin@psns.navy.mil">Eutizzin@psns.navy.mil</a>
Naval Surface Weapons Center	Ken Scandell	<a href="mailto:Scandell@nswc975.com">Scandell@nswc975.com</a>
Naval Research Laboratory	K. Sadananda	<a href="mailto:Sadananda@amvil.nrl.navy.mil">Sadananda@amvil.nrl.navy.mil</a>

## SUBJECT INDEX

alloying, 77, 203  
anomalous x-ray scattering, 203  
band gap engineering, 41  
carbon films and coatings, 25, 297  
catalysts, 355  
chemical alloying, 149  
chemical vapor synthesis, 1  
coating non-homogeneity, 315  
columnar structure, 85  
confined system, 63  
dislocation and disclination, 231, 247  
electrodeposition, 11, 85, 103  
electroforming, 11  
electroless deposition, 77  
electroluminescence, 337  
electrosleeve, 11  
EXAFS, 203  
exhaust remediation, 355  
fatigue, 283  
FTIR, 187  
gas sensor, 187  
gradient elasticity, 247  
gradient film, 1  
grain boundary, 11, 215, 231  
granular alloy, 85  
hard coating, 113  
high density recording media, 171  
high refractive index materials, 323  
HVOF spray, 113, 131  
hydrothermal synthesis, 25  
indentation, 309  
intercalation, 367  
interface, 231  
interphase boundary, 231  
magnetic films, 11, 77, 85, 171, 177  
magnetotransport properties, 177  
microporous matrix, 63  
molecular beam epitaxy, 41  
nanodispersion, 103  
nanoindentation, 297  
nanoporous material, 25  
nanoscratching, 297  
non-destructive mechanical characterization, 315  
orbifold, 309  
phase composition and growth, 267  
photoconversion, 347  
photoelectrochemistry, 347  
photoluminescence, 157  
photonics, 323  
plasma spray, 113  
polymer-layered silicate, 367  
polyol synthesis, 55, 77  
porous silicon, 255, 337  
quantum dot heterostructure, 41  
quantum wire, 63  
severe plastic deformation, 215  
sol-gel processing, 55  
strained layer heteroepitaxy, 41  
stress and strain determination, 223, 297  
surface characterization, 187  
synchrotron characterization, 203, 223  
thermoelectric coating, 149  
wear fatigue, 283  
wear resistant materials, 25, 113, 373



NATO Science Series

3. High Technology

ISBN 0-7923-6266-7



9 780792 362661

Kluwer Academic Publishers

Dordrecht/Boston/London